ENSO RESPONSE TO ALTERED CLIMATES

Andrew Thorne Wittenberg

A DISSERTATION
PRESENTED TO THE FACULTY
OF PRINCETON UNIVERSITY
IN CANDIDACY FOR THE DEGREE
OF DOCTOR OF PHILOSOPHY

RECOMMENDED FOR ACCEPTANCE
BY THE PROGRAM IN
ATMOSPHERIC AND OCEANIC SCIENCES

June 2002

Abstract

Observed secular changes in the El Niño / Southern Oscillation (ENSO) phenomenon are not well understood; nor are the major differences in ENSO simulations found among state-of-the-art general circulation models of the tropical Pacific. To address these issues, this study advances an efficient numerical model of the ocean-atmosphere system and then uses it to explore the sensitivity of ENSO to changes in the climatological background. The model includes dynamical, statistical, and stochastic components and provides a reasonably good simulation of the observed climatology and interannual variability of the tropical Pacific.

A series of idealized experiments reveals how changes in equatorial and off-equatorial zonal wind stresses, meridional stresses, and radiative forcings affect the tropical climatology. Because coupled feedbacks dominate the time-mean response, perturbed climatologies tend to resemble either an El Niño (with warm sea surface temperatures in the eastern equatorial Pacific, weakened trade winds and flattened thermocline) or a La Niña (with cool sea surface temperatures, enhanced trades and steeper-sloping thermocline).

The study then shows how these altered climates impact the behavior of ENSO, including its amplitude, frequency, spatial structure, mechanism, sensitivity to transient disturbances, and predictability. An analysis of the oceanic mixed layer thermodynamics provides a physical basis for understanding these changes. Results from a more sophisticated ocean-atmosphere model are also presented, and the problem of detecting climate-induced ENSO changes in short stochastic timeseries is discussed.

Acknowledgments

My thanks to George Philander, who shared his copious flow of ideas, encouraged my independence, and fostered beauty and clarity in my work. I enjoyed his genial personality, and the many delightful evening soireés at his home in Princeton – with their lively discussions, musical puzzles, and impromptu tangos. Thanks also to Jeff Anderson, who guided my pre-generals research and showed me how to be deliberate and thorough. His passion for applied problems, and his expertise in statistics and nonlinear dynamical systems, provided essential training for me as a scientist.

Kudos to Tony Rosati and Matt Harrison for much encouragement and support over the past few years. Tony carefully read this thesis and offered many great suggestions. Matt kindly configured the hybrid GCM for my use, and contributed numerical codes that inspired Chapter 3.

Many others contributed to this work. Geoff Vallis, Kirk Bryan, and Ants Leetmaa graciously volunteered to read this thesis and provided useful comments. Alexey Fedorov was a sounding board for theoretical ideas. Gabriel Lau, Isaac Held, Steve Griffies, Kevin Hamilton, Bin Wang, Eli Tziperman, and Lisa Goddard gave advice and encouragement at critical times. Interactions with Scott Harper, Giulio Boccaletti, Eli Galanti and Jong-Seong Kug were also helpful. Thanks to Gail Haller and Bea Amend for maintaining an excellent library; to Hans Vahlenkamp and Larry Lewis for computing solutions; to Jim Byrne for his assistance with many interoffice moves; and to the ready-room staff for their cheerful company during lonely weekends and late nights. I gratefully acknowledge NASA and the NSF for their generous fellowship awards, which were expertly administered by Laura Rossi, Anna Valerio, and Johann Callan of the AOS program. Thanks also to the TAO Project and the crew of the good ship Ka'imimoana for showing me the ropes during six unforgettable weeks at sea.

Memories I take with me from graduate school: science/policy adventures in Hokkaido with Tracey Holloway; beers and strategy games with Olivier Pauluis; New-GC parties with Tapio Schneider and the crew of "Entry 34"; biking the mountains of Oregon with Dave Baker; political discussions with Curtis Deutsch and office-mates Yunqing Zhang, Frederic Vitart, and Irina Marinov; three semesters with George Philander, Scott Harper, Barbara Winter, and Meredith Galanter teaching the science of weather and climate to undergraduates.

Thanks to Olly, Eric, Colleen, Alana, Wade, Jon, and Corrinne for pulling me away from work to celebrate life. Thanks to my family for always believing in me.

Above all, thanks to my wife Gayle for her infinite patience. Only with her bright smile, warm heart, sharp mind, and giving nature could I complete such a project. From early-morning Linux hints to afternoon pep talks and late-night suppers, she has been the most versatile and helpful companion on this journey.

Contents

Introduction

My soul is full of longing
For the secret of the sea,
And the heart of the great ocean
Sends a thrilling pulse through me.

Longfellow, *The Secret of the Sea*

1.1 Motivation

1.1.1 The big picture

Oceanography and meteorology would be rather dull were it not for two simple facts: the earth spins and is illuminated by the sun. These transform what could have been a quiet rock into one whose oceans and atmosphere are rich in structure, and alive with currents, waves and eddies spanning from the microscopic to the global and from seconds to millennia.

Knowing only this, a distant observer of earth would likely point out the equator as a region of special interest, since it receives the most sunlight per orbit, and is the only place on the globe where the vertical component of rotation changes sign. If the observer could see the configuration of earth's continents, he might also infer that the Pacific Ocean, which covers a third of the global surface, would be a major player in earth's climate. The tropical Pacific would seem a prime target for further study.

We residents of earth came to this conclusion less directly. Confined to the continents, we farmed the land and fished the coastal seas, growing accustomed to the march of the seasons and to local differences in winds, temperature and rainfall. When the usual climate patterns were disrupted, the impact on society was often devastating. We then yearned to understand and predict these strange fluctuations using the tools of science. As observations accrued and theory and simulations advanced, our perspective finally became

that of the distant observer. We now realize that something very big indeed is happening in the tropical Pacific.

1.1.2   The importance of ENSO for climate and society

A key to global climate

The El Niño/Southern Oscillation (ENSO) is now recognized as earth's dominant climate fluctuation on interannual time scales (Anderson et al., 1998). The warm phase of ENSO, which appears irregularly every two to ten years, is associated with warming of the eastern and central tropical Pacific and a weakening of the easterly trade winds. The shift of strong convection from the western Pacific into the central Pacific also reorganizes atmospheric flows on a global scale, bringing floods to Peru, droughts and fires to Australia and Indonesia, changes in weather over the United States, and worldwide changes in agricultural productivity. The weakening of the trade winds also shuts down upwelling in the eastern equatorial Pacific, reducing the inflow of nutrients from the deep. This inhibits the growth of marine microorganisms, which propagates up the food chain to affect ecosystems, fisheries, and economies along the western coast of South America. ENSO is not a new phenomenon; coral records indicate that it is over a hundred thousand years old (Tudhope et al., 2001). It thus appears that understanding ENSO is key to understanding global climate.

Hope for long-term forecasts

Since Lorenz (1963) showed that the evolution of deterministic, turbulent systems can be sensitive to initial conditions, there has been a fair amount of pessimism regarding long-term forecasts of day-to-day weather at specific locations. Such "predictions of the first kind" (Lorenz, 1975) attempt to foretell the precise chronological order in which atmospheric states will occur. Unfortunately, stretching and stirring by weather systems rapidly amplifies initial uncertainties in the state of the atmosphere, so that useful information is rapidly lost, i.e., the set of possible atmospheric states consistent with the initial conditions soon becomes indistinguishable from the climatological set of weather states. Weather-stirring is so vigorous in the atmosphere that it appears useful forecasts of day-to-day weather may be limited to two weeks or less (AMS Council, 2001).

Climate forecasts, on the other hand, are "predictions of the second kind," which aim to foretell the large-scale and long-term *statistics* of events but not their precise chronological order. Such forecasts depend less on the uncertainty of the initial state and more on the evolution of boundary conditions like sea surface temperature (SST), which are controlled by slowly-evolving components of the climate system. Fortunately, a substantial part of the global atmospheric circulation appears to be in equilibrium with tropical heating. Since this heating is modulated by slowly-evolving processes like ENSO, there is great hope for seasonal-to-interannual prediction of climate anomalies if phenomena like ENSO can be properly simulated (Barnston et al., 1994; Goddard et al., 2001).

The ability to forecast climate several seasons in advance would be of enormous benefit to society. Farmers could plant the crops best suited to the predicted rainfall. Fishermen

could target regions where ocean temperatures and plankton blooms promised an abundant catch. Governments and insurers could prepare ahead of time for droughts and floods.

Such predictions have been realized with some success since 1987, when Cane et al. (1986) issued the first experimental forecasts of ENSO using a fairly simple ocean-atmosphere model. Since then, ever more complex models, including comprehensive general circulation models (GCMs) and sophisticated statistical models, have been employed for operational seasonal prediction (Latif et al., 1998). The growth of this seasonal forecasting capability has gone hand-in-hand with the deployment of more comprehensive and accurate observing systems (McPhaden et al., 1998), and the continued development of more realistic coupled GCMs (Delecluse et al., 1998).

1.1.3   The modeling challenge

Why ENSO is difficult to simulate

Despite recent progress, El Niño has proved devilishly hard to simulate and forecast. There are many reasons this is so. First, ENSO is a fundamentally *coupled* ocean-atmosphere phenomenon. Coupled air-sea interactions are partly a blessing, since they lend seasonal predictability to the atmosphere. But they are also a curse, since coupled feedbacks make the climate system highly sensitive to errors in the formulation of a forecast model. Current coupled GCMs have trouble maintaining realistic climatologies beyond a year or so; this "climate drift" arises from inadequate resolution, incomplete model physics, or mis-tuned parameterizations and can be very difficult to diagnose and fix given the complexity and computational cost of most GCMs. As will be shown in this thesis, misrepresentation of the time-mean state can then affect the simulation of ENSO.

A second reason that ENSO is difficult to model is that it involves a very wide range of spatial and temporal scales. Processes important to ENSO occur throughout the tropical Pacific, so a model must encompass at least this region. To the extent that extratropical weather or the globe-circling Madden-Julian Oscillation (MJO) trigger ENSO events, a fully global model may even be required. The model must then run for years (to forecast a single event) or even many decades (to characterize long-term statistics). With present computational resources, such large-scale models cannot adequately resolve many important processes that occur at small scales, including mixing, surface heat fluxes, and cloud formation. Such processes must be parameterized in terms of the large-scale fields, and uncertainties in these parameterizations can lead to problems in simulating the tropical climatology and ENSO variability.

A third reason El Niño is so difficult to describe, understand and model is its irregularity in time. Although many robust features of ENSO have been identified (Rasmusson and Carpenter, 1982; Harrison and Larkin, 1998), no two events look alike, and the time between events can vary from 2 to 10 years. The behavior of the phenomenon also seems to change from decade to decade (Gu and Philander, 1995; Wang and Wang, 1996; Torrence and Compo, 1999; Torrence and Webster, 1998, 1999). It is therefore unclear just what ENSO is: a linear mode modulated by climate change, a chaotic system, a series of stochastic events, or some combination of these? This uncertainty has in turn led to disagreements over just what constitutes a good model of the system and how to approach the forecast

problem.

Forecast surprises

The difficulty of simulating ENSO has been revealed by several forecast surprises over the past few decades. In 1982, forecasters were caught completely off guard by a severe El Niño that wreaked havoc with ecosystems and economies worldwide. This spurred a decade of intense research into ENSO and led to the development of sophisticated monitoring and forecasting systems. While many of the new models were successful at "hindcasting" the 1982–1983 warm event and showed good skill for the rest of the 1980s, they began having trouble in the early 1990s when an unusual sustained series of warm events occurred. These secular changes in forecast skill have now been documented in several models (Kerr, 1993; Latif et al., 1998; Kirtman and Schopf, 1998) and have confounded researchers for more than a decade.

With further development, many models did anticipate the strong 1997 warm event (Barnston et al., 1999a,b), but none successfully forecast its unusually rapid onset, severity, and sudden demise (Landsea and Knaff, 2000). For this event and its aftermath, most state-of-the-art models failed to achieve even a modest standard of forecast skill (Kerr, 2000b; Landsea and Knaff, 2000). Fig. 1.1 shows the skill of operational forecasts of the 1997–98 event, relative to that of a simple statistical model called ENSO-CLIPER (Knaff and Landsea, 1997) which is based on historical data. No model, statistical or dynamical, was able to exceed this benchmark of skill at forecast lead times of two seasons or less. At longer leads, some of the predictions outperformed ENSO-CLIPER, but by that time their absolute errors were so large that they would have been of little use to forecasters (Landsea and Knaff, 2000).

ENSO differences among coupled GCMs

Given these recent forecast surprises, it is clear there is still room for improvement in the models used to forecast ENSO. A useful initial exercise is to compare different simulations and look for relative strengths and weaknesses. From the efforts now underway (Latif et al., 2001; AchutaRao and Sperber, 2002; Davey et al., 2002) it has become apparent that there is a wide variety of ENSO simulations in different models, and that no single coupled model affords a completely realistic simulation compared to observations (Figs. 1.2–1.3).

Although every model is different, most models tend to simulate ENSO SST variability that is too weak, too variable in the western Pacific and not variable enough along the eastern boundary, has too short a period, is too regular in time, and is too weakly phase-locked to the annual cycle compared to the observations. Interannual fluctuations of GCM wind stresses are generally weaker than observed (Davey et al., 2002) and simulated SSTAs and SOIs are less correlated than observed (AchutaRao and Sperber, 2002), suggesting that the simulated atmospheres are either too weakly coupled to SST or have too little internal variability. The zonal propagation of SST anomalies can also differ from observed; this is especially the case in models with coarse oceanic resolution, where SSTAs tend to propagate westward instead of developing in place like most observed events (Latif et al., 2001).
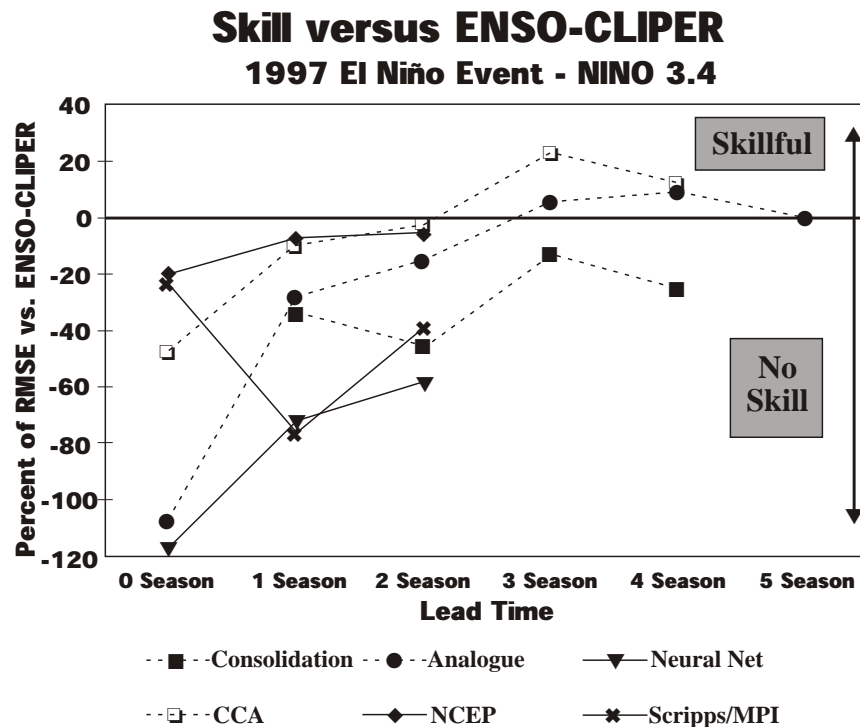
Figure 1.1: Skill assessment of operational SST anomaly forecasts of the 1997–98 warm event and its aftermath. ENSO-CLIPER, a simple statistical model, provides the benchmark of skill. Denoting the root-mean-square error relative to observations as RMSE, the relative forecast skill of a given model at a given forecast lead time is plotted as [1-RMSE(model)/RMSE(ENSO-CLIPER)] × 100%. Panel shows the relative skill of SST anomaly forecasts for the NINO3.4 region (170°W–120°W, 5°S–5°N) from four statistical models (Consolidation, CCA, Analogue, Neural Net) and three dynamical models (NCEP, Scripps/MPI). From Enfield (2001) based on Landsea and Knaff (2000).
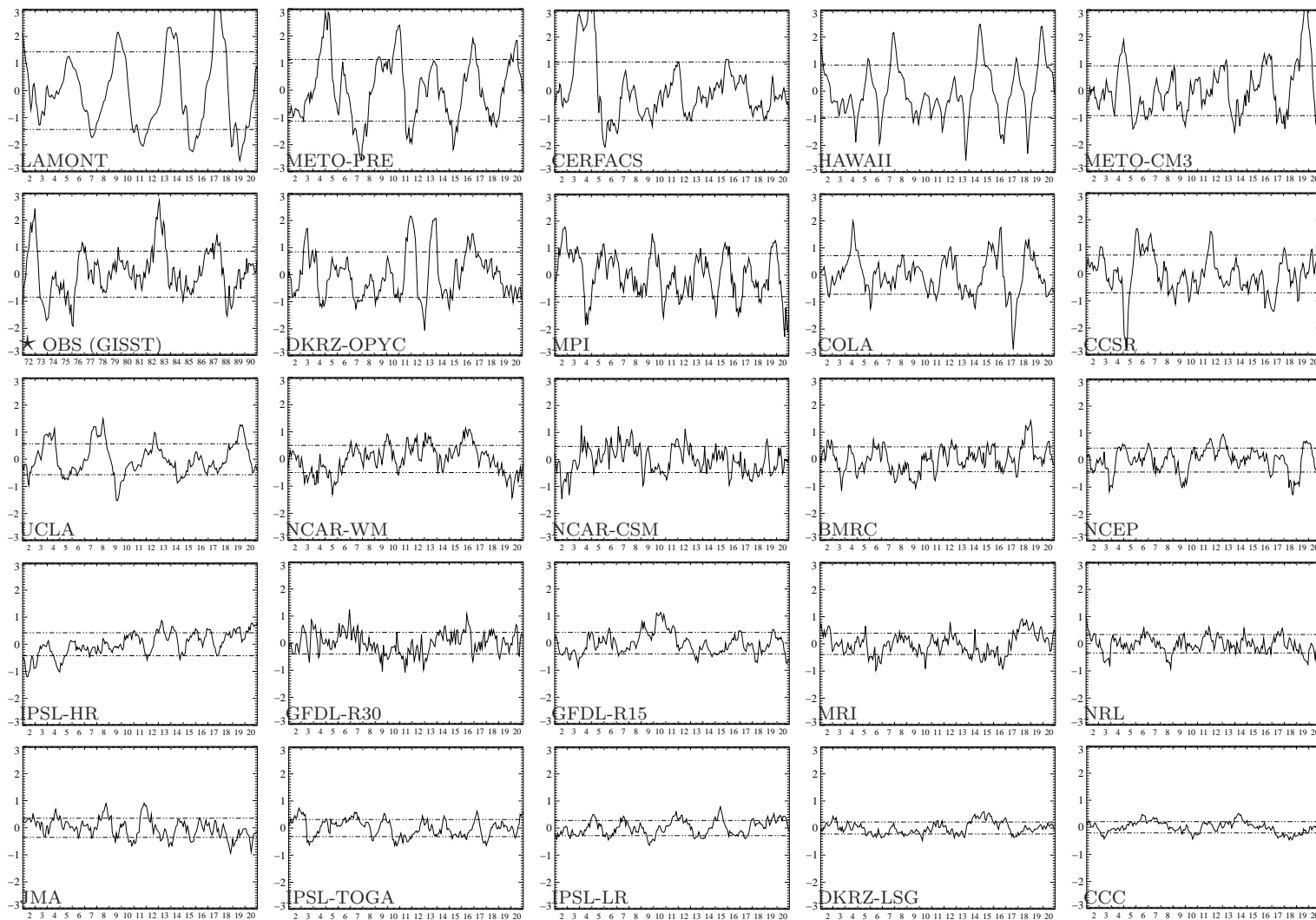
Figure 1.2: 19-year timeseries of NINO3 SST anomalies, sorted by standard deviation (dashed lines), from GISST observations (starred) and 24 coupled models. Adapted from Davey et al. (2000, 2002).

Standard Deviation of Surface air temperature (tas) (2N – 2S)
CMIP II Control Runs and Observations
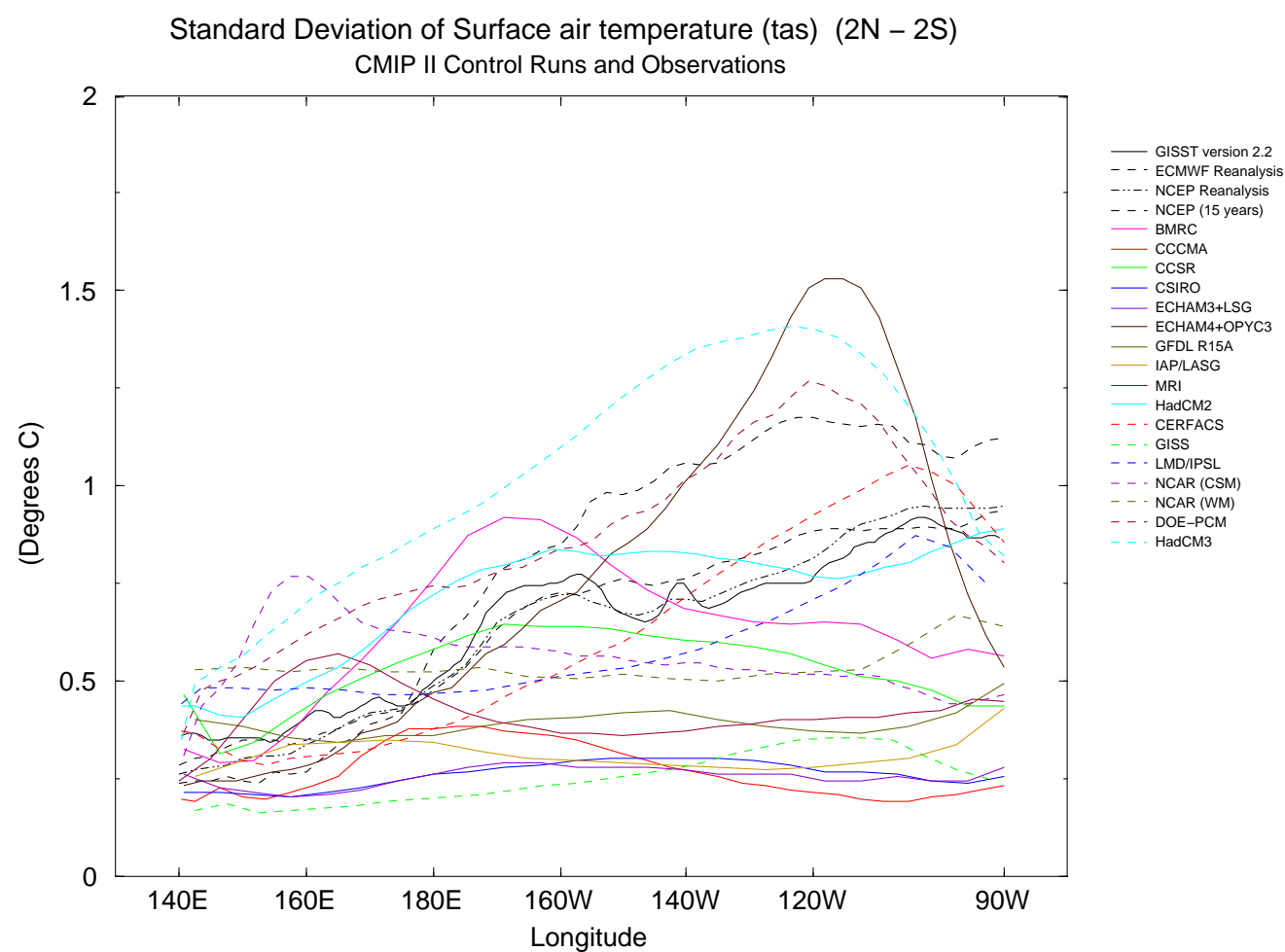
Figure 1.3: Standard deviation of tropical Pacific surface air temperature anomalies, averaged over 2°S–2°N, from the CMIP simulations. SSTs from the NCEP, ECMWF, and GISST reanalyses are shown for reference. From AchutaRao and Sperber (2002).

A role for the climatology?

That simulated ENSOs differ from each other and from reality may have partly to do with the climatological background, since there are clear differences among the climatologies of coupled models (Fig. 1.4; Mechoso et al., 1995; Latif et al., 2001; AchutaRao and Sperber, 2002; Davey et al., 2002). The majority of models tend to have a climatological cold bias in the equatorial central Pacific, a cold tongue that is too meridionally narrow, a warm bias along the western coast of South America, and an unrealistic "double ITCZ" straddling the equator. Although the climatological zonal gradient of SST is often as strong as observed, most models exhibit a mean tradewind stress that is too weak and shifted westward relative to the observations.

In addition to wind stress errors, many atmospheric GCMs also misrepresent the surface heat fluxes. This is largely due to errors in cloudiness (Kleeman et al., 2001), most notably off the coast of South America. Such errors tend to be amplified and redistributed in the coupled context, making them difficult to attribute specifically to the ocean model or the atmosphere model. Faced with two coupled models that give different simulations, sometimes the only recourse is to systematically eliminate differences between models until the sources of disparity are understood (Schneider, 2002).

Intercomparisons of coupled GCMs indicate suggestive, though not conclusive, evidence for climatological controls on ENSO. In an early study, Neelin et al. (1992) found that models with weak climatological cold tongues tended not to have strong interannual oscillations, although the evidence for climatological controls of ENSO was not very strong due to major differences in grid resolutions and physical parameterizations among the models. Meehl et al. (2001a) examined the behavior of 10 closely-related CGCMs of varying resolutions and vertical diffusivities. They found that the models with the weakest diffusivities had not only the sharpest mean thermoclines but also the strongest ENSO variability, especially in the east Pacific. Models with strong trades, furthermore, tended to have stronger zonal thermocline slopes, stronger zonal temperature contrasts, and stronger ENSO variability. Pontaud et al. (2000) compared the climatologies and ENSO simulations of four coupled GCMs in detail, and found large differences in the position and strength of equatorial mean upwelling in the models, as well as substantial differences in the spatial structure of interannual SSTAs. Models with the strongest cold tongues again appeared to support the strongest ENSO variability. The authors attempted to explain the ENSO amplitude differences with regard to the dominant terms in the mixed layer energy budget and their relation to the mean state; although their analysis was limited, it showed promise as a new way of understanding the ENSO differences among models.

Thus there appear to be some systematic links between the climatology and ENSO behavior among different GCMs. This suggests two competing hypotheses: (1) the climatology and ENSO do not interact, but instead are both controlled by a third factor such as the air-sea coupling strength; or (2) the coupling and other parameters affect the climatology, which then directly affects ENSO. It has proved difficult to falsify either hypothesis simply by intercomparing models, since the influence of climate is obscured by other major differences such as vertical and horizontal resolution, atmospheric convection, oceanic mixing, and the presence or absence of flux adjustments. To truly understand the influence of climate on ENSO, it seems that a targeted suite of sensitivity experiments in
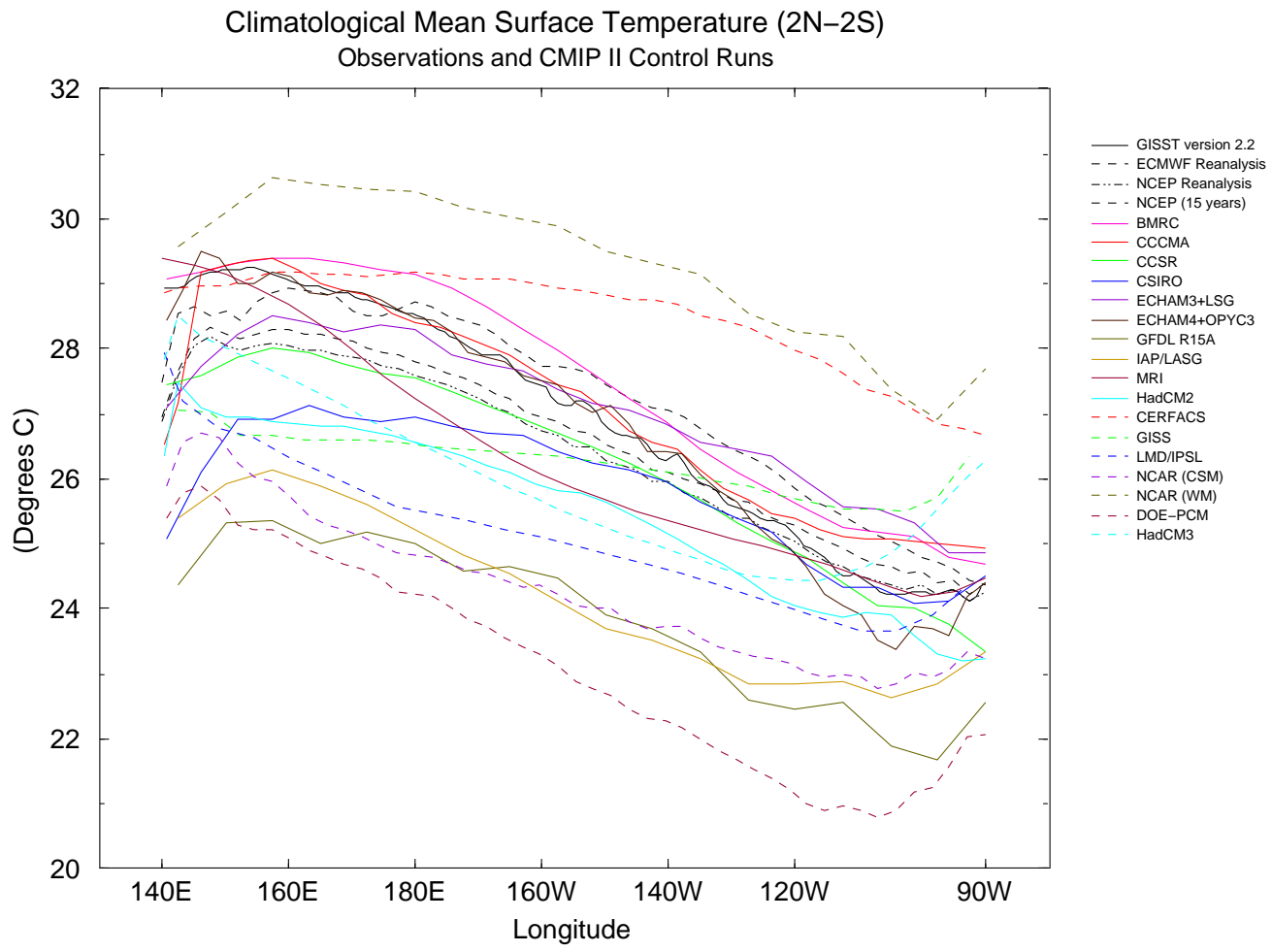
Figure 1.4: Annual-mean tropical Pacific surface air temperature, averaged over 2°S–2°N, from the CMIP simulations. SSTs from the NCEP, ECMWF, and GISST reanalyses are shown for reference. From AchutaRao and Sperber (2002); see also Fig. 1 of Latif et al. (2001).

a single model is required. This is the first key motivation for the present study.

1.1.4 Nature of the historical record

A natural place to look for climatological controls of ENSO is in historical data. Fig. 1.5a shows a timeseries of SST anomalies in the eastern equatorial Pacific from 1860–2001. Clearly the behavior of ENSO has varied substantially over the past 140 years. Interannual oscillations are strong from 1875–1930, weaker from 1930–60, and then grow stronger after 1960. The return period between events appears to be relatively long from 1875–95, shorter from 1895–1907, sporadic between 1907-60, short from 1960–77, and longer after 1980. Although most of the strongest warm and cold events peak around the end of the calendar year, the 1941 and 1987 warm events are notable exceptions. It also appears that SST in the equatorial eastern Pacific varies on decadal and longer time scales: it was relatively warm from the 1890s to the 1940s, then cooler through the 1950s and 1960s, warmed abruptly around 1976, and has since remained fairly warm.

The interdecadal changes and ENSO changes noted above have been documented in numerous datasets (see Wallace et al. (1998) for a review). The lack of data prior to 1960 and especially before 1920 (Fig. 1.5b) is problematic for detecting these changes, since it is often hard to tell whether an apparent change is real or simply an artifact of sampling error. Independent evidence from corals, however, appears to corroborate the strong decadal variability prior to 1920, and the weak and irregular ENSO behavior of the 1930s and 1940s (Urban et al., 2000). Taking Fig. 1.5a at face value, it seems that decadal connections between the slowly-evolving background state and ENSO irregularity may be subtle, and that chaos or random forcing probably play a role as well.

1.1.5 Recent changes in the background state

The interdecadal climate variability evident in Fig. 1.5a has received much attention in recent years, including two books (National Research Council, 1995; Navarra, 1999) and a workshop (Mehta et al., 2000). These studies are strongly motivated by the need to understand natural variations as a backdrop for possible human-caused climate changes. This section reviews what is known about tropical Pacific decadal variability, since (1) it provides a context for understanding and interpreting the observed changes in ENSO, and (2) it suggests how the climate-perturbation experiments in later chapters should proceed.

Over the past 50 years, the trade winds, meridional overturning circulation, and east-west thermocline slope in the equatorial Pacific appear to have weakened, in tandem with a warming of the eastern equatorial Pacific despite decreased surface heat flux entering the ocean (Curtis and Hastenrath, 1999; Chao et al., 2000; Kerr, 2000a; Levitus et al., 2000; Liu and Huang, 2000; Casey and Cornillon, 2001; Huang and Liu, 2001; McPhaden and Zhang, 2002). There is also evidence for an eastward shift of the Pacific trade winds (Curtis and Hastenrath, 1999), although as will be shown in Chapter 2 this conclusion depends on the wind dataset used. One must always keep in mind that nonstationarities of the observing system and measurement techniques have been linked to spurious trends and shifts in the data (Wright, 1988; Posmentier et al., 1989; Clarke and Lebedev, 1996, 1997; Harrison and Larkin, 1997; Huang and Liu, 2001).
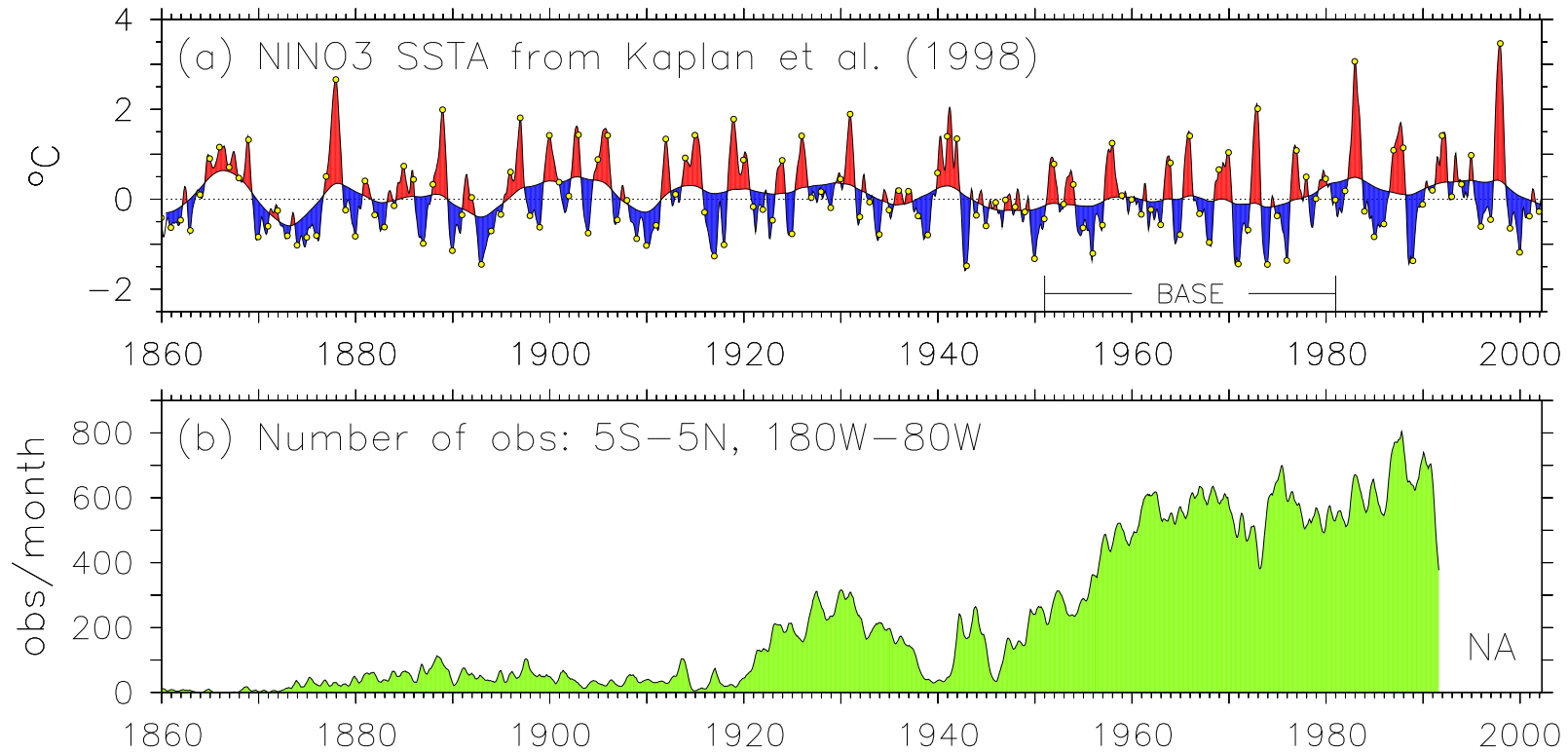
Figure 1.5: (a) SST anomalies with respect to 1951-1980. Data from 1856-1981 are reconstructed by reduced space optimal smoothing (Kaplan et al., 1998); data after 1981 are obtained by projection of the optimal interpolation analysis of Reynolds and Smith (1994) onto the reduced space of the earlier period. The data have then been low-pass filtered with half-power points at 0.5 and 10 yr. White dots are December values. (b) Number of observations per month used in the Kaplan et al. (1998) reconstruction, east of the dateline between 5°S–5°N (low-pass filtered with a cutoff at 1 yr).

Many patterns of recent decadal variability have been described which include signatures in the tropical Pacific (Kleeman et al., 1996; Kachi and Nitta, 1997; White and Cayan, 1998; Kerr, 1999a; Zhang et al., 1999; Giese and Carton, 1999; Goswami and Thomas, 2000; Tourre et al., 2001; Tomita et al., 2001; Mestas-Nuñez and Enfield, 2001). Spectral analyses indicate that interdecadal variations in Pacific climate are prevalent throughout the historical record (Mann and Park, 1994; Zhang et al., 1998; Moron et al., 1998; Lau and Weng, 1999; Tourre et al., 2001), and proxy data provide evidence of decadal variability as far back as the seventeenth century (Dunbar et al., 1994; Linsley et al., 2000; D'Arrigo et al., 2001). These decadal and interdecadal variations are stronger than the longer-term (centennial) trends over the observed record (Enfield and Mestas-Nuñez, 1999). The decadal changes often resemble abrupt shifts (Chao et al., 2000). One such shift evident in multiple atmospheric and oceanic fields, which some have argued is part of an ongoing "Pacific Decadal Oscillation" or PDO, occurred around 1976–77 and included a warming of the east Pacific that occurred nearly simultaneously with changes in the North Pacific (Graham, 1994; Trenberth and Hurrell, 1994; Talley, 1995; Zhang, 1998; Zhang and Liu, 1999; Liu and Zhang, 1999; Barnett et al., 1999; D'Arrigo et al., 2001; Stephens et al., 2001; Giese et al., 2002). The tropical radiative budget also appears to vary on decadal timescales: the 1990s saw a sharp increase in outgoing longwave radiation (OLR) and a smaller decrease in shortwave reflection, ostensibly due to altered cloudiness associated with a possible recent strengthening of the Hadley and Walker circulations (Hartmann, 2002; Chen et al., 2002; Wielicki et al., 2002). Interestingly, these very large changes in the tropical radiative balance appear to have occurred without correspondingly large changes in average tropical SST.

Whether these decadal changes interact with or can be attributed to ENSO is unknown. Some studies argue that the tropical signatures of the decadal patterns arise from mechanisms distinct from ENSO (Graham, 1994), while others suggest they may derive from random fluctuations in ENSO itself or mechanisms similar to ENSO (Zhang et al., 1997). Tropical decadal modes with differing mechanisms have been simulated in coupled climate models (Latif, 1998). In some models (Knutson and Manabe, 1998; Jin, 2000; Yukimoto et al., 2000) the decadal variability resembles ENSO, both in its spatial pattern and in its evolution by delayed-oscillator/recharge mechanisms that depend on slow oceanic adjustment via off-equatorial Rossby waves. In others (Vimont et al., 2002), the spatial patterns of variability resemble ENSO but events decay by surface heat fluxes rather than equatorial recharge.

Others have argued that interactions between the tropics and extratropics may give rise to interdecadal variability. One hypothesis (Gu and Philander, 1997) is that temperature anomalies subducted into the midlatitude pycnocline propagate slowly toward the equator, affecting the structure of the equatorial thermocline roughly a decade later. Although many observational and modeling studies support this "oceanic bridge" (Zhang et al., 1998, 1999, 2001b; Johnson and McPhaden, 1999; Weaver, 1999; Huang and Pedlosky, 2000), other studies have suggested that the effects of these subducted anomalies on Pacific surface temperatures may be relatively weak on decadal time scales, at least compared to more rapid and direct forcing by off-equatorial wave propagation/reflection and changes in shallow overturning near the equator (Zhang et al., 1997; Kleeman et al., 1999; Schneider

et al., 1999a,b; Wu et al., 2000; Hazeleger et al., 2001; McPhaden and Zhang, 2002). An "atmospheric bridge," in which decadal changes in extratropical SSTs affect the tropical trade winds, thus seems viable for explaining observed concurrent climate shifts throughout the Pacific (Barnett et al., 1999; Pierce et al., 2000a,b; Wang and An, 2001, 2002). The extratropical signals conveyed along either bridge could in turn be influenced by changes in the tropics, since it is known that ENSO affects the intensity of the Aleutian Low and associated winds and evaporation over the North Pacific (Weaver, 1999). There is little evidence in observations or models, however, to support a closed tropical/extratropical loop, and the current thinking is that extratropical decadal variability arises from oceanic integration of random atmospheric forcing (Mehta et al., 2000).

That Pacific climate is continually changing is a strong motivation for understanding the ENSO sensitivity to the background state. The apparent importance of wave dynamics and the tropical trade winds in the decadal variations of the tropical Pacific further suggests that a tropical Pacific-only model, perturbed by slowly-changing tradewind and heat fluxes, may be quite relevant to the way ENSO is modulated in the real world. This motivates the model development in Chapter 4 and the perturbation experiments of Chapters 5 and 7.

1.1.6 Recent changes in ENSO

Observed and inferred changes in ENSO behavior over the past few centuries have been extensively documented (Quinn et al., 1987; Enfield and Cid, 1991; Mann and Park, 1994; Rasmusson et al., 1995; Wang, 1995; Gu and Philander, 1995; Wang and Wang, 1996; Kestin et al., 1998; Torrence and Compo, 1999; Torrence and Webster, 1998; Setoh et al., 1999). These studies have concluded that although ENSO is reasonably stationary on centennial timescales, it shows large decadal variations in its amplitude, period, spatial structure, and propagation characteristics.

Much attention has focused on ENSO changes associated with the 1976 climate shift (An and Wang, 2000; An and Jin, 2000; Trenberth and Stepaniak, 2001; Wang and An, 2001, 2002). In the decades leading up to the shift, the climatology was apparently more La Niña-like and ENSO exhibited a short period of only 2–3 years with westward-propagating SST anomalies. After the shift to warmer temperatures, the ENSO period lengthened to 4–6 years and SST anomalies propagated eastward or remained stationary. An and Jin (2000) explain these changes in terms of increases in the mean equatorial upwelling, the entrainment temperature sensitivity to thermocline motions, and the decrease in the zonal SST contrast, all of which acted to enhance thermocline feedbacks over zonal advection feedbacks to favor eastward propagation of SST anomalies after 1976. Wang and An (2001, 2002) further suggest that an eastward shift of the mean wind convergence, equatorial upwelling, and shallow thermocline led to an eastward shift in the anomaly patterns as well. They argue that this reduced the speed of equatorial recharge of heat content, thus allowing more growth by local feedbacks in the eastern basin and permitting a longer ENSO period and larger amplitude.

Attention has also focused on the long and unpredictable series of warm events of the early 1990s, and the very strong warm events of 1982–83 and 1997–98 (Kerr, 1993; Trenberth and Hurrell, 1994; Kleeman et al., 1996; Latif et al., 1997). Whether these unusual events represent a fundamental change in ENSO behavior due to global warming,

or are the result of natural stochastic fluctuations, internal chaos, or interactions with internal or external decadal modes is a source of much debate (Cane et al., 1995; Trenberth and Hoar, 1996, 1997; Latif et al., 1997; Harrison and Larkin, 1997; Rajagopalan et al., 1997; Kirtman and Schopf, 1998; Kestin et al., 1998; Kleeman et al., 1999; Timmermann, 1999; Wunsch, 1999; Trenberth and Hurrell, 1999; Timmermann and Jin, 2002). This debate is more than academic: it bears directly on our ability to detect and forecast what will happen to ENSO in the future. Unfortunately, there are so few realizations of ENSO in the observational record that the issue appears unlikely to be resolved anytime soon without further clues.

1.1.7 Clues from the distant past

Paleoclimatology attempts to reconstruct climates of the distant past using proxy data (corals, tree rings, ice cores, ocean and lake sediments) and appropriate numerical models. Paleodata offer a potentially better signal-to-noise ratio for testing ENSO theories than the historical record, since the climate changes are larger and the records are longer. It is important to remember, however, that these data are only indirect measures of ENSO and can be affected by changes in local climate or ENSO teleconnections.

Several reconstructions of the past few centuries have been prepared. A reasonably direct thermometer is afforded by corals from the Galápagos Islands (Dunbar et al., 1994), which indicate the following long-term interdecadal and centennial-scale climate fluctuations in the eastern equatorial Pacific SSTs: cold (1640), warm (1670), moderate (1700), warm (1710-50), cold (1810), moderate (1830-1900), and cold (1950). The warm epochs appear to show a relatively weaker and shorter-period ENSO than do the moderate and cold epochs. Less direct reconstructions based on data from the periphery of the Pacific basin (Diaz and Pulwarty, 1994; Stahle et al., 1998; Mann et al., 2000; Jones et al., 2001), suggest that ENSO teleconnections were attenuated in the early 1800s, then grew more active into the 1900s in tandem with a possible strengthening of the climatological Walker circulation.

Moving farther back into the past, several authors have worked to reconstruct the tropical Pacific climate and variability of the Holocene period (10 ka–present). Cole (2001) and Enfield and Mestas-Nuñez (1999) provide reviews. Based on proxy data, ENSO appears to have been weaker prior to 5-6 ka, with a longer period between strong events (Sandweiss et al., 1996; Kerr, 1999b; Rodbell et al., 1999; Tudhope et al., 2001). Some model simulations of the early-to-mid Holocene concur with this picture of a weakened ENSO (Liu et al., 2000a), while others suggest that ENSO may have been similar to today but may have had different seasonal locking (DeWitt and Schneider, 1998), skewness (Codron, 2001), and teleconnection properties (Otto-Bliesner, 1999), the latter having important implications for distant proxy data.

There is some evidence that the climate of the early-to-mid Holocene (10–5 ka) may have been more La Niña-like than today; paleodata indicate a warmer west Pacific but are in conflict regarding temperature in the eastern Pacific (Colinvaux, 1972; Farrell et al., 1995; Ravelo and Shackleton, 1995; Sandweiss et al., 1996, 1997; DeVries et al., 1997; Wells and Noller, 1997; Gagan et al., 1998). With a few exceptions (Codron, 2001), coupled GCM simulations concur with a La Niña-like picture of the early-to-mid Holocene (Bush, 1999;

Otto-Bliesner, 1999), and at least one (Liu et al., 2000a) also produces a narrow warming along the South American coast despite cooler temperatures in the central Pacific. Liu et al. (2000a) argue that the enhanced Pacific tradewinds and lack of ENSO during the early-to-mid Holocene are due to the strengthening of the Asian summer monsoon and the deepening of the equatorial thermocline due to subduction of warm water in the South Pacific. Another hypothesis is related to the date of perihelion, which is affected by the precession of earth's orbit around the sun and has a period of roughly 22,000 years. Perihelion currently occurs in January, but in the mid-Holocene it occurred in September. Because the equatorial Pacific climatology is most zonally-asymmetric in September when the ITCZ is farthest north of the equator, Clement et al. (1999) argue that September perihelia should be most effective at enhancing convection in the western basin, strengthening the Walker Cell, and seeding coupled feedbacks that enhance the zonal contrast of SST. Model simulations by Clement et al. (1999) indicate that Holocene-like orbital parameters should have contributed to a more La Niña-like climatology and a less regular ENSO.

Still farther back in time, there is evidence for climate/ENSO connections spanning the ice ages. Ancient corals from Indonesia (Hughen et al., 1999) and New Guinea (Tudhope et al., 2001) indicate that ENSO has existed for at least 130,000 years. Tudhope et al. (2001) suggest that over this vast epoch, ENSO has never to been stronger than over the past 120 years or so. Although these records offer little evidence for prehistoric changes in the period or regularity of ENSO, they do suggest that ENSO tends to be weaker during September perihelia, and also during glacial periods, which appear to be associated with a more La Niña-like climatology in the tropical Pacific (based on studies of the very strong Last Glacial Maximum; Bush and Philander, 1998; Liu et al., 2000b; Lea et al., 2000; Nurnberg, 2000; Andreasen et al., 2001). The weaker ENSOs during glacials could result from weaker coupling due to colder SSTs, from outcropping of the climatological thermocline in the eastern equatorial Pacific that limits the ability of the system to oscillate, or perhaps to lower sea level which could expose more land area in the western Pacific and anchor convection over Indonesia (Cole, 2001). Orbitally-induced changes in ENSO/annual cycle interactions have also been shown to produce abrupt shutdowns of ENSO on glacial timescales in an intermediate model (Clement et al., 2001).

Clement et al. (1999) and Cane and Molnar (2001) have suggested that the closing of the Indonesian and/or Panama seaways around 3–4 million years ago may have heralded the establishment of the first strong zonal thermocline slope in the Pacific, and the onset of strong ocean-atmosphere interactions. This fundamental change could have had a major impact on global climate and ENSO, which Clement et al. (1999) argue might be connected to the onset of Milankovitch forcing oscillations in eastern equatorial Pacific plankton deposits around that time.

These intriguing links between ENSO and paleoclimates further motivate our study of climate/ENSO interactions. That paleodata suggest ENSO may be stronger at present than ever before brings up some fundamental questions: Is the modern climatology optimal for ENSO, such that any departure from this climatology will cause ENSO to weaken? Or are we headed toward a world with even stronger ENSO variability?

1.1.8 Where are we headed?

Perhaps the most obvious and important motivation for this study is the need to understand how ENSO may change in the future, due to possibly human-induced changes in the tropical Pacific climatology.

Model projections of future climate

What will the future climate of the tropical Pacific look like? A number of studies have addressed this question, with contradictory results (Tett, 1995; Knutson and Manabe, 1995; Meehl and Washington, 1996; Knutson and Manabe, 1998; Noda et al., 1999; Timmermann et al., 1999; Barnett et al., 2000; Boer et al., 2000; Meehl et al., 2000a,b; Washington et al., 2000; Dai et al., 2001; Jin et al., 2001; Yu and Boer, 2002). Although most coupled GCMs give a uniform or slightly El Niño-like warming of the equatorial Pacific in response to increased concentrations of greenhouse gases, others give more of a La Niña-like response with an enhanced zonal SST gradient at the equator.

Because the structure of the tropical Pacific climate response is crucial to teleconnections around the globe, many theories have been put forward to explain the different SST responses in these various simulations. The first (Knutson and Manabe, 1995) is based on the Clausius-Clapeyron relation. For a uniform downward radiative heat flux, the cold eastern equatorial Pacific must warm more than the warm west Pacific to evaporate enough water from the surface to balance the radiative heating; this would act to *reduce* the east-west SST gradient. Such an idea does not account for changes in clouds that would render the radiative heat flux zonally-asymmetric, nor does it consider the ocean circulation.

A second mechanism (Ramanathan and Collins, 1991; Meehl and Washington, 1996) invokes changes in clouds. An SST increase in the warm and convergent west could produce more cirrus cloud shielding than in the cold and divergent east. This would limit the warming in the west and thus *reduce* the zonal SST gradient. Whether cirrus clouds would actually respond in this way to SST increases has been questioned (Fu et al., 1992; Hartmann and Michelson, 1993; Lau et al., 1994; Pierrehumbert, 1995).

A third mechanism (Clement et al., 1996; Sun and Liu, 1996; Cane et al., 1997) invokes an "ocean dynamical thermostat." Given a uniform radiative heating, warming in the east is limited by continual entrainment of cold water from below the mixed layer, which thus *enhances* the zonal SST gradient. Note that the dynamical thermostat can be defeated if the radiative heating is weighted toward the eastern Pacific, and this idea does not account for long-term changes in the structure and zonal-mean depth of the equatorial thermocline.

A fourth mechanism (Gu and Philander, 1997; Liu and Huang, 1997; Seager and Murtugudde, 1997; Liu, 1998) operates on a slower timescale. Enhanced warming in the extra-tropics can subduct, reach the equatorial thermocline, and then upwell to counteract the dynamical thermostat. Because the off-equator is relatively warm, fairly small SST anomalies can balance the radiative heating there and so the subducted temperature anomalies may be too weak to fully cancel the dynamical thermostat (Seager and Murtugudde, 1997). Even if the subducted anomalies are strong, they might take a decade or more to reach the equator through the ventilated thermocline; thus if the change in radiative forcing is rapid enough, the dynamical thermostat response may be evident for some time before the

subduction has an effect.

As shown by Clement et al. (1996) any net zonal asymmetry generated by the combination of these mechanisms can be strongly enhanced by air-sea feedbacks like those involved in ENSO. The equatorial wind stress response is particularly important, since the equatorial temperature climatology appears to be mainly advection-driven, with surface heat fluxes acting primarily as a damping on ENSO and longer time scales (Huang and Liu, 2001; Jin et al., 2001; Yu and Boer, 2002).

The extent to which the mechanisms above are simulated in a given model may depend fundamentally on oceanic resolution (for the dynamical thermostat) or uncertain cloud parameterizations (for the cloud thermostat and other cloud feedbacks). The radiative forcing associated with cloud changes under enhanced CO_2 is highly model-dependent, and depends as much on changes in the atmospheric circulation (associated largely with SST gradients) as on local SST (Rind, 1987; Cess et al., 1989, 1990; Bony et al., 1997; Dutton et al., 2000). Cloud radiative forcing thus remains one of the largest uncertainties in future projections of tropical Pacific climate.

Given the large number of competing feedbacks, imperfect models, and conflicting model projections, the future of tropical Pacific climate is not at all clear. This provides another strong motivation for exploring the sensitivity of ENSO to a range of possible future climates.

Model projections of future ENSO behavior

Given that GCM projections vary so widely regarding the future of the tropical Pacific climatology, it is perhaps no surprise that they also disagree on what will happen to ENSO (Easterling et al., 2000; Hu et al., 2001; Collins, 2000a). Coupled models with low oceanic resolution near the equator (Meehl et al., 1993; Tett, 1995; Knutson et al., 1997) tend to show little change in ENSO for higher CO_2, while some higher resolution models are more sensitive. Knutson et al. (1997) and Boer et al. (2000) found slightly weaker interannual variability of the SST anomalies and surface stress, despite stronger precipitation anomalies in a greenhouse world. Greenhouse simulations by Timmermann (1999) and Timmermann et al. (1999) showed *increased* ENSO variability that was skewed more toward cold events, with little change in the ENSO period; these changes, which occurred in the context of an El Niño-like warming of the mean state and a sharpening of the equatorial thermocline, were linked by Timmermann (2001) to an increased effect of ENSO SST anomalies on the equatorial recharge of heat content. A $4xCO_2$ simulation by Collins (2000a) also showed a stronger and shorter-period ENSO, which was explained in terms of the increased climatological vertical temperature gradients at the equator and an increased efficiency of equatorial recharge due to stronger meridional temperature gradients off-equator. In contrast, a higher-resolution simulation by Collins (2000b) with an updated model showed less warming at the surface, a smaller increase in the vertical and meridional temperature gradients, and little change in the statistics of ENSO.

Thus the ENSO response appears to be very sensitive to the nature of the warming, and most GCMs have enough trouble simulating the present tropical Pacific climatology and ENSO, let alone future changes. The disparate GCM projections of future ENSO variability thus further motivate an investigation into the climate sensitivity of ENSO.

1.1.9   The role of this study

A number of previous studies have revealed links between the climatology and ENSO behavior (Hirst, 1986; Battisti and Hirst, 1989; Neelin, 1991; Wakata and Sarachik, 1991, 1992; Yang and O'Brien, 1993; Moore, 1995; Jin, 1996; Kirtman and Schopf, 1998; Dijkstra and Neelin, 1999; Codron et al., 2001; Wang and An, 2002). Some of these have explored the stability properties of ENSO over a wide range of parameter space, typically using simple models and an analytically efficient and convenient set of parameters (Neelin, 1991; Hao et al., 1993; Jin and Neelin, 1993a,b; Neelin and Jin, 1993; Neelin et al., 1998). Among the most important of these parameters are the *coupling strength*, namely the strength of the wind response to SST anomalies; the *wave adjustment time*, which is the time required for the equatorial ocean to come into balance with the wind stress by internal wave processes; and the *surface layer feedback*, i.e. the strength of the surface currents and upwelling induced by the winds. Application of these results to CGCMs, however, has been hampered by confusion over just what these parameters represent in nature.

Fedorov and Philander (2000, 2001) helped to bridge the gap between ENSO theories and observations by establishing a set of important climate parameters based on measurable quantities, like the strength of the equatorial trade winds, the zonal-mean depth of the equatorial thermocline, and the sharpness of the thermocline in the vertical. Using a simple model, the authors then constructed maps of the linear growth rate and period of ENSO as a function of tropical Pacific ocean climates forced by idealized winds. Fedorov (2002) extended these results to the time-dependent regime, by considering the impact of discrete westerly wind bursts that occur at different phases along a pre-existing ENSO cycle. Together, these studies provide a tentative road map for understanding ENSO behavior in different models and different climate regimes.

Many questions remain, however. How does coupling of the climatological ocean-atmosphere constrain the path through climate-parameter space? How relevant are the linear results to the more realistic nonlinear, stochastic, and meridionally-asymmetric regimes found in observations and models? How detectable are climate-induced ENSO changes in the stochastic context? What is the effect on the tropical climatology and ENSO of other climate parameters, like the longitude and meridional width of the trade winds, the strength of the cross-equatorial southerlies in the eastern Pacific, and the surface heat flux? To what extent do the sensitivity results from simple models apply to more comprehensive GCMs?

The purpose of this dissertation is to answer these questions and carry the simple linear road map into more realistic (but also more complex and challenging) regimes. Such a study is well-timed, because (1) a wealth of new paleodata are now coming online which should provide excellent tests for the results; (2) recent coupled-model intercomparisons are improving awareness of climate differences among models and how they affect seasonal-to-interannual forecasts; (3) the climate community may be on the verge of adequately detecting and simulating how human-induced changes in the climate system may affect ENSO; and (4) there is a growing appreciation of the strong influence of ENSO on global climate at multiple timescales, from intraseasonal to interglacial. A further investigation of the climate sensitivity of ENSO is thus strongly motivated.

1.2   Formulation of the problem

1.2.1   Central question

The central question of this study is: How do changes in the background state affect ENSO behavior? The *background state* refers to the climate of the tropical Pacific averaged over a decade or more. *ENSO* will refer to anomalous tropical Pacific variability with time scales ranging from a few months to one decade. The *behavior* of ENSO refers to its amplitude, period, structure, propagation characteristics, physical mechanism, and predictability.

Our central question is related to the question of why ENSO varies so much among coupled GCMs, since these GCMs show large differences in their climatologies. It may also be related to the question of why the behavior of the *observed* ENSO changes through time, since observed climate has low-frequency components spanning from decades to millennia.

1.2.2   Thesis

Our thesis is that *the climatology of the tropical Pacific exerts strong controls on ENSO behavior.* To test this thesis, we devise a model to represent climate/ENSO interactions, and then assess the extent to which the simulated ENSO responds to changes in the background state.

Two important points must be considered. First, there is much debate about just what constitutes an appropriate model for ENSO (Chang et al., 1996; Thompson and Battisti, 2001; Wang, 2001a,b). Is ENSO a damped linear oscillation sustained by atmospheric noise, an unstable oscillator whose irregularity arises from chaos, or some combination of the two? A complete understanding of ENSO sensitivity will necessarily involve different types of models at different levels of sophistication. The models in this study will range from a simple conceptual oscillator to a comprehensive coupled GCM, but for the most part we shall focus on a reasonable, intermediate-complexity model of ENSO. It is anticipated that a careful analysis of the intermediate model will yield insight into more sophisticated models, an approach which has proved successful in the past (McCreary and Anderson, 1991; Neelin et al., 1998).

Second, to the extent that stochastic events affect ENSO, we must pay careful attention to the statistical *significance* of changes in ENSO behavior to ensure that they are not simply chance events arising from a small number of cases. Robust determination of the stochastic climate sensitivity will therefore require long simulations containing many events. The computational burden is even higher to assess the *sensitivity* of predictability, as this requires ensembles of stochastic runs launched from a large number of initial conditions. Fortunately, the intermediate model we describe is very efficient and up to the task of generating so many runs in a reasonable time.

1.2.3   Overview of the dissertation

The structure of remaining chapters is as follows. Chapter 2 characterizes the observed climatology and interannual variability of the tropical Pacific, and Chapter 3 draws upon these results to develop a stochastic model of wind stress anomalies. Chapter 4 introduces

an intermediate coupled model for climate/ENSO interactions, describes its essential characteristics, and investigates its sensitivity to dynamical parameters. Chapter 5 describes the sensitivity of the tropical Pacific climatology to key background variables, using the intermediate model and a hybrid coupled GCM. Chapter 6 constructs a theoretical framework for thinking about the influence of climate on ENSO, which is then applied to the intermediate and GCM simulations of Chapter 7. Chapter 8 concludes with a discussion of real-world applications of the results and suggests promising avenues for further research.

Analysis of Observations

It is a capital mistake to theorize before one has data. Insensibly one begins to twist facts to suit theories, instead of theories to suit facts.

Sherlock Holmes, *A Scandal in Bohemia*

This chapter provides a comprehensive look at available observations of tropical Pacific climate over the past four decades. This analysis is undertaken for several reasons. First, it provides a ground truth for the development and evaluation of the coupled model in the next chapter. Second, it reveals the range of climate, ENSO, and noise variability that are actually observed, which is useful for orienting and interpreting the sensitivity maps of later chapters. Finally, it reveals the level of uncertainty in the observations. The climate differences between observational analyses, between decades, and between different coupled GCMs, underscore the necessity of exploring wide regions of climate parameter space.

Special attention is paid to the wind stress on the ocean surface, for the following reasons. First, the stress is a key variable for both the climatology and ENSO. It largely reflects the gradient of SST, the slope of the thermocline, and the strength of equatorial upwelling; and as one of the noisiest of climate variables, it also provides stochastic forcing to the ENSO system. Second, the wind stress is one of the few variables for which multidecadal records are available. Third, the stress is quite uncertain, so it is useful to compare analyses from different sources. Finally, the detailed analysis of the stress supports the development of the statistical atmosphere model in Chapter 3.

2.1 Preliminaries

2.1.1 Motivation

The wind stress on the ocean surface is of intense interest to the climate community. Modelers depend on realistic wind stresses to test their ocean simulations, and forecasters need them to produce accurate initial conditions for climate predictions. Since the recognition of the El Niño/Southern Oscillation (ENSO) as a major driver of Earth's climate,

greater attention has focused on the tropical Pacific Ocean and several retrospective analyses of wind stresses in that basin have been made available to researchers (McPhaden et al., 1998). Due to the sparsity of historical data, changes in observing systems, and different analysis procedures, these products do not always agree on what reality is like. The purpose of this paper is to compare two of these analyses and paint a clearer picture of the wind stress and its uncertainty.

Oceanographers have long recognized that improvements in ocean models must be supported by improvements in the wind stress forcing (Latif, 1987; McPhaden et al., 1988; Harrison et al., 1989; Landsteiner et al., 1990). Wind stresses drive not only the variations in currents and temperatures associated with the annual cycle and El Niño, but also the noisy fluctuations that confound seasonal forecasts, and the slow changes that alter ENSO behavior on decadal and longer time scales. Coupled climate models indicate that ENSO behavior is sensitive to both equatorial and off-equatorial wind stress responses to sea surface temperature (SST) changes (Neelin, 1990; Kirtman, 1997; An and Wang, 2000; Cassou and Perigaud, 2000). The behavior and predictability of ENSO are also affected by random wind stress noise (Penland and Sardeshmukh, 1995; Kleeman and Moore, 1997; Kirtman and Schopf, 1998; Roulston and Neelin, 2000). Better understanding of the wind stress is therefore essential to improving ENSO modeling and prediction.

2.1.2   Uncertainties in the wind stress

The wind stress on the surface of the ocean is difficult to estimate accurately. Until the recent advent of satellite scatterometry, stress estimates were based on wind velocities estimated from wave heights or measured by anemometers many meters above the surface. Such measurements are prone to both random errors, like incorrect assumptions of anemometer heights, and systematic errors, like incorrect conversions from the Beaufort scale to wind speed (Cardone et al., 1990; Morrissey, 1990). The sparseness of observations in time and space also presents a sampling problem. Binning to reduce random errors and aliasing from small scales must be done carefully, since the stress depends nonlinearly on the wind (Wright and Thompson, 1983), and since filling data gaps can spuriously affect the patterns of spatial variability (Sterl, 2001).

Ultimately the wind velocities or pseudostresses must be converted to surface stresses. This typically involves "bulk" formulae, whose form can depend not only on the wind speed, but also the roughness of the surface, the vertical wind shear, the vertical stability of the atmosphere, the surface currents, and even the drift of the observing platform (Smith, 1988; Cardone et al., 1990; da Silva et al., 1994; Kelly et al., 2001). Such variables can be complicated functions of the observations actually collected at sea.

Researchers interested in decadal climate variability must further contend with the gradual evolution of the observing system, including changes in data density and measurement procedures (Clarke and Lebedev, 1997). One notable change occurred in the late 1970s, as anemometers gradually replaced Beaufort estimates as the preferred method for determining wind velocities. This change is probably responsible for much of the apparent trend in observed wind speeds since 1960 (Ramage, 1987; Peterson and Hasse, 1987; Wright, 1988; Posmentier et al., 1989; Cardone et al., 1990; Michaud and Lin, 1992; Ward,

1992; Ward and Hoskins, 1996; Clarke and Lebedev, 1996), and recently the Comprehensive Ocean-Atmosphere Data Set (COADS) has been modified to account for some of these changes (da Silva et al., 1994). Two other major changes include the deployment of anemometers on the Tropical Atmosphere-Ocean (TAO) buoy array beginning in the 1980s, and the launch of scatterometers on satellites beginning in 1991. While such changes were necessary to improve wind stress estimates, they also force investigators to always consider *nonstationarity of the observing system* as one possible source of decadal changes in the observations.

2.1.3 Additional constraints

Wind stress analyses attempt to reconstruct reality from these sparse observations, biased instruments, and changing observing systems. In the face of such uncertainties, it helps to consider additional constraints besides the wind data.

One approach is to examine the self-consistency of the winds: Zebiak (1990), for example, used a set of linear momentum equations to derive a synthetic pressure field, which was then used to adjust the winds to be consistent with a simple vorticity balance. A second approach is to examine the consistency of the winds with the observed forcing. Ward (1992), Ward and Hoskins (1996), and Clarke and Lebedev (1996, 1997), for example, used observed sea level pressures to assess apparent trends in the trade winds. SST is also a useful constraint, since it largely controls the distribution of atmospheric heating and pressure gradients (Gill, 1980; Lindzen and Nigam, 1987). A third approach is to examine the response of the ocean and use it to infer the wind stress forcing. Kirtman and Schneider (1996), for example, adjusted the FSU wind stress to optimize the SST simulation produced by an ocean GCM. Another indicator of the stress is the thermocline slope, which is nearly in balance with the zonal wind stress at the equator (Neelin et al., 1998). Although decadal changes in the thermocline are hard to discern due to the paucity of subsurface data prior to the 1980s, recent work has taken advantage of ocean GCMs and full four-dimensional assimilation of the observations to infer the wind forcing (Bonekamp et al., 2001).

Present analyses combine several of these approaches to estimate the wind stress. While the analyses use largely the same data sources, they rely on different methods for quality control, filling gaps in the observations, and adjusting the data for consistency with physical expectations. *Objective analyses* attempt to represent the data faithfully, imposing few if any physical constraints between variables. *Subjective analyses* rely on experienced meteorologists to check for consistency among important dynamical variables. *Model analyses* rely on numerical models to enforce physical consistency of the data. Given this range of analysis techniques, it is important to examine results from each to help determine what the "real" wind stress actually is and quantify its uncertainty.

2.1.4 Previous studies

Although the evaluation and intercomparison of tropical wind stresses has a long history, previous studies have generally focused on a single analysis, a short time period, or a single aspect of the stress. The annual cycle of wind stress over the tropical Pacific

was described by McPhaden et al. (1988) and Landsteiner et al. (1990), who examined the 1979–1981 period in analyses from Florida State University (FSU), the University of Hawaii (UH), and the Fleet Numerical Oceanography Center (FNOC). Trenberth et al. (1990) and Yang et al. (1997) studied the annual cycle during the 1980–1986 and 1985–1992 periods, respectively, using data from the European Centre for Medium Range Weather Forecasts (ECMWF). Saji and Goswami (1997) analyzed the annual cycle of wind stress over the 1979–1988 period, using results from 17 atmospheric general circulation models (AGCMs) and data from COADS, ECMWF, and Hellerman and Rosenstein (1983).

Other researchers have investigated the total wind stress or departures from the annual cycle. Reynolds et al. (1989) compared surface winds from ECMWF, the National Meteorological Center (NMC, now NCEP), and the U.K. Meteorological Office (UKMO) between February 1987 and July 1987, and Graham (1994) described decadal changes in the FSU pseudostress between 1971–1976 and 1977–1982. Kleeman et al. (2001) examined the response of wind stress anomalies to SST, comparing results from 27 SST-forced AGCMs against the NCEP and corrected COADS products for 1979–1988. Yang et al. (2001) discussed the seasonal dependence of the wind stress anomalies using the FSU and NCEP products. Latif (1987), Harrison et al. (1989), and Auad et al. (2001) have all found substantial differences between ocean simulations forced by different wind stress products.

Auad et al. (2001) recently examined cross-statistics of the NCEP and merged COADS/FSU stress products over the 1958–1997 period, and found the NCEP product to be weaker along the equator by up to a factor of 2.5 (for the zonal stress) or 3.5 (for the meridional stress). While the two datasets were found to be well-correlated in midlatitudes, they were not well correlated in the poorly-sampled equatorial and east Pacific. Interannual stress variations were found to be coherent between the products but intraseasonal variations were not. Shinoda et al. (1999) likewise found that the NCEP stresses tended to underestimate buoy stresses in low-wind conditions in the west Pacific, and Smith et al. (2001) found that the NCEP product underestimates stresses derived from ship observations under a wide range of conditions.

Recently, studies of the wind stress have been motivated by the need to evaluate new satellite products. Busalacchi et al. (1993) compared the Special Sensor Microwave Imager (SSM/I) satellite stresses with data from ECMWF, NMC, FNOC, FSU, and UH between July 1987 and June 1988, while Meissner et al. (2001) compared the SSM/I wind speeds with those from NCEP and ECMWF between July 1987 and December 1997. The NASA scatterometer (NSCAT) stresses have also been evaluated against the ECMWF analysis over brief periods (Kelly et al., 1999; Yu and Moore, 2000).

Coupled model studies have underscored the importance of the wind stress forcing for ENSO simulation and prediction. Chen et al. (1999) showed that hindcasts of the 1997–1998 El Niño in a simple coupled model were improved when NSCAT stresses were used in place of FSU to generate the ocean initial conditions. Kug et al. (2001) showed similar improvements when the NCEP winds were used instead of FSU during the 1990s. Harrison et al. (2002) constructed several statistical models of the wind stress response to SST anomalies, using 1979–1993 stresses from ECMWF, NCEP, and an AGCM run, and 1988–1996 stresses from a satellite product. They found that coupling these different statistical atmospheres to an ocean GCM produced widely different ENSO simulations,

ranging from damped oscillations to sustained oscillations to a slow drift to a new steady state.

It has thus become clear that available wind stress analyses exhibit large differences over the tropical Pacific, and that these differences are large enough to affect simulation of the tropical climatology and ENSO. The analyses also cover different regions and time periods, complicating their use in ocean hindcasts. Current efforts aim to quantify the uncertainties in the analyses (Smith et al., 2001; Taylor, 2001), and integrate the best aspects of different analyses into a single merged solution (Putman et al., 2000). Until such products come into widespread use, researchers who study climate change or need to force ocean models with realistic winds must choose from among several different analyses. The present study should assist in that choice.

2.1.5   Goals of this study

Since the tropical Pacific wind stress plays such a pivotal role in global climate, and since the differences between wind stress products are clearly important for ENSO modeling and forecasting, we here present a more comprehensive look at this field in two widely-used analyses. We also examine the relationship between the wind stress and SST, since this relationship matters a great deal to ENSO, and since simulating it accurately remains a challenge in current atmospheric models (Saji and Goswami, 1997; Kleeman et al., 2001). The primary objectives of this study are to (1) document the similarities and differences between the analyses, (2) show how the analyzed wind stresses have changed over the past four decades, and (3) determine whether these wind stress changes are consistent with SST changes. The results should be of great interest to ENSO researchers, modelers and forecasters.

2.2   Data

The present study focuses on two different analyses of the monthly-mean wind stress. The first, referred to as FSU, is the subjectively-analyzed Florida State University pseudostress (Legler and O'Brien, 1988; Stricherz et al., 1997), available from the Center for Ocean-Atmospheric Prediction Studies. The FSU data are routinely used for climate studies, forcing ocean models, and generating initial conditions for ENSO forecasts (Chen et al., 1995; Dewitte and Perigaud, 1996, ; see also Introduction). The present study uses only the FSU research-quality product, which as of this writing is available from 1961–1999. The FSU pseudostress $\|\mathbf{u}_a\|\mathbf{u}_a$ is converted to wind stress $\boldsymbol{\tau}$ using the bulk formula

$$\boldsymbol{\tau} = \rho_a c_d \|\mathbf{u}_a\| \mathbf{u}_a \tag{2.1}$$

where $\rho_a = 1.2$ kg m^{-3} is the surface air density and $c_d = 1.3 \times 10^{-3}$ is a nondimensional drag coefficient.

The second stress product, referred to as NCEP, is the model-based NCEP/NCAR reanalysis (Kalnay et al., 1996), available from the LDEO/IRI Climate Data Library. The reanalysis is available from 1949 to the present, and has been used for climate studies (see Introduction), atmospheric model comparisons (Kleeman et al., 2001), ocean hindcasts

(Behringer et al., 1998), and operational ENSO forecasts (Ji et al., 1998). It should be noted that the reanalysis classifies the zonal stress as a type "B" variable (observed but also strongly influenced by the model), and the meridional stress a type "C" variable (derived solely from the model and forced to remain close to the atmosphere simulation).

An objective analysis of the Comprehensive Ocean-Atmosphere Data Set (COADS, da Silva et al., 1994) has also been examined but for brevity will not be presented here. These data have been used in studies of decadal climate change (Kleeman et al., 1999) due to their availability over a long period (1945-1993) and their relative freedom from analysis biases. Results for this product were very similar to those for FSU, in large part because FSU is based heavily on COADS after 1966. An overview of ENSO-related aspects of COADS can be found in Harrison and Larkin (1998).

The monthly-mean SSTs used in this study are from the reconstruction of Smith et al. (1996), available from the NOAA-CIRES Climate Diagnostics Center. These SSTs have been used for climate studies (An and Wang, 2000), because they span the entire 1950-1999 period using a uniform statistical scheme. This helps to reduce spurious discontinuities resulting from changes in analysis procedures and data density.

The monthly-mean data are averaged onto identical grids with $5.625°$ longitude by $2°$ latitude spacing over the tropical Pacific region ($129.375°E$–$84.375°W$, $20°S$–$20°N$). Land points are excluded from the analysis, but the data are not detrended. A 12-month climatology is computed for each dataset over the 1961–1999 period (468 months), and subtracted from the total fields to give monthly-mean anomalies. A similar decomposition is performed separately for the 1961–1979 period (228 months) and the 1980–1999 period (240 months). We refer to the wind stress anomalies as τ', the zonal and meridional components as τ'_x and τ'_y, and the SST anomalies as SSTA.

The split into pre-1980/post-1980 timeseries serves two purposes. First, it provides an estimate of slow trends in the wind stress. Second, it separates the earlier period of relatively sparse observations from the latter period of intensive observations and more modern methods. Changes in the analyzed stresses between these two periods will therefore be a product of two confounding effects: changes in the physical system and changes in the observing/analysis system. By comparing two different analyses, it is possible to separate these two effects somewhat. Differences between the analyses afford an estimate of the level of uncertainty in the wind stress, which can then be used to assess similar changes in the analyses.

2.3 Climatology

2.3.1 Annual mean

The annual-mean climatologies of the wind stress and SST are shown in Fig. 2.1. The zonal component of the mean stress, $\overline{\tau}_x$ (Fig. 2.1a), is easterly everywhere except in the far eastern and western equatorial Pacific. These easterlies are important for producing mean equatorial upwelling and a shoaling of the thermocline in the eastern Pacific, both of which are key to understanding the annual cycle and ENSO. The trade winds have a slanted saddle shape: they peak in the central basin $12°$–$15°$ poleward of the equator, weaken towards the equator, and then weaken further towards the equatorial coasts. Compared to FSU,

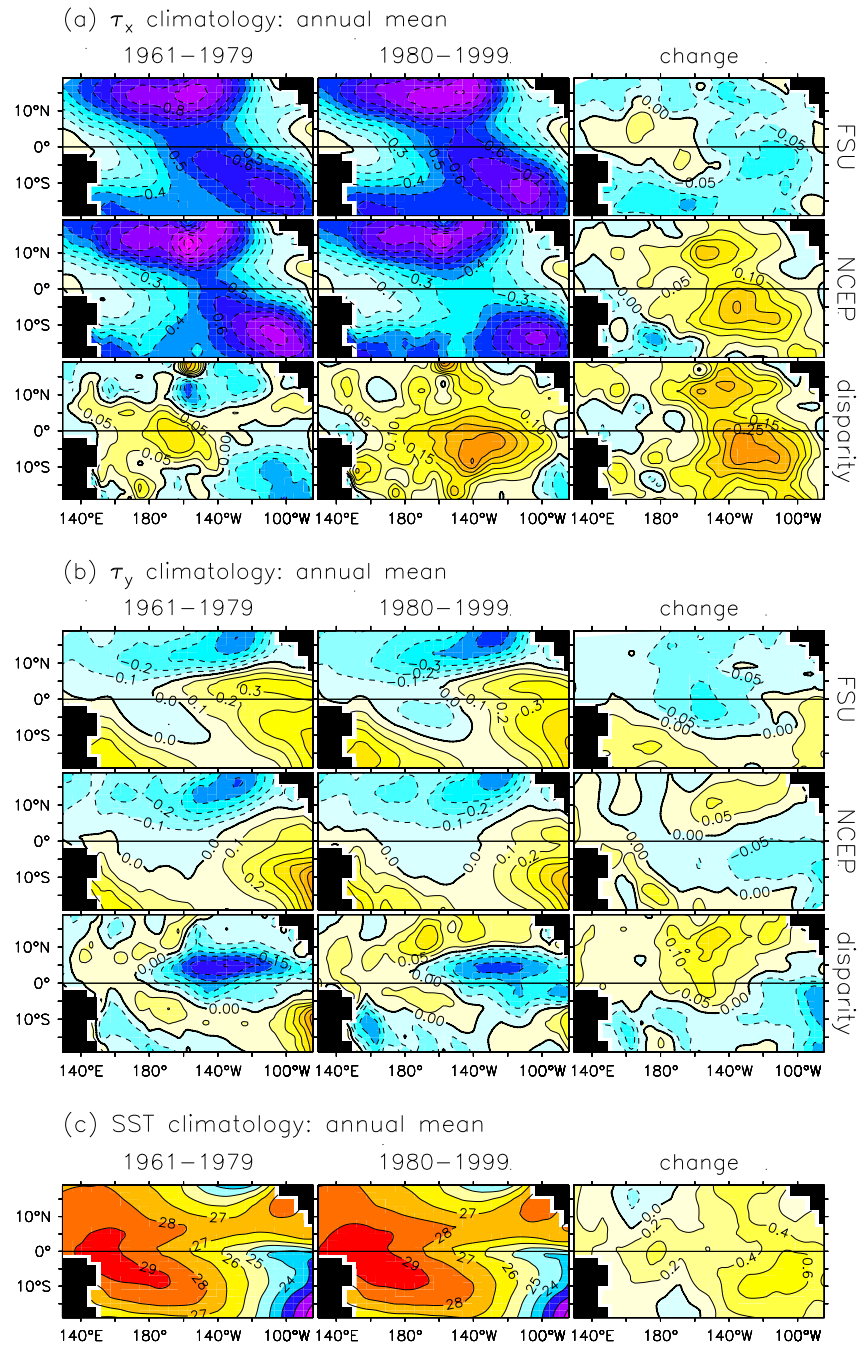Figure 2.1: Annual-mean climatology of (a) zonal wind stress (dPa), (b) meridional wind stress (dPa), and (c) SST (°C). Fields are shown for 1961–1979 (first column) and 1980–1999 (second column). The change from the former period to the latter is also shown (third column). Rows correspond to the FSU analysis (first row), the NCEP analysis (second row) and their difference (NCEP minus FSU, third row).

NCEP has a more pronounced saddle shape, with weaker easterlies at the equator. Between 1961–1979 and 1980–1999, both products show a weakening of the easterlies around the equatorial dateline and a strengthening in the southwest. However, while FSU shows a strengthening of the trade winds east of 160°W, NCEP shows a weakening in this region. In other words, while FSU suggests the climatological trade winds strengthened and shifted eastward, NCEP suggests they weakened and shifted westward.

Fig. 2.1b shows $\overline{\tau}_y$, the meridional component of the mean stress. Southerly winds cross the equator in the east Pacific and meet opposing northerlies in the Intertropical Convergence Zone (ITCZ) along 5°N–12°N. These southerlies are important for generating mean upwelling south of the equator, which increases the coupling of the surface and subsurface in the eastern Pacific. In the central basin, weak northerlies cross the equator and meet opposing southerlies in the South Pacific Convergence Zone (SPCZ) along 5°S–17°S. Compared to FSU, NCEP shows stronger southerlies in the southeast, but weaker southerlies crossing the equator in the central and eastern Pacific. Between 1961–1979 and 1980–1999, both FSU and NCEP suggest an increase of the southerlies in the southwest. Along the southeast coast, however, FSU indicates that the southerlies along the southeast coast strengthened while NCEP suggests they weakened. The decadal changes in $\overline{\tau}_y$ also contrast strongly between the analyses in the northern tropical Pacific.

The mean curl of the wind stress (not shown) is associated primarily with meridional gradients of $\overline{\tau}_x$. The curl is positive north of the equator and in the western equatorial and southeastern tropical Pacific; the curl is negative in the eastern equatorial and southwestern tropical Pacific. The mean cyclonic curl on both sides of the equator is important because it produces divergence of ocean surface currents away from the equatorial zone, raising the mean thermocline. The NCEP curl is more strongly cyclonic than in FSU. Between 1961–1979 and 1980–1999, both products show a strengthening of the cyclonic curl in the southwest, but other decadal changes are not well correlated between the products.

The mean wind divergence (not shown) is thought to be important for controlling the sensitivity of atmospheric heating to SST perturbations (Zebiak and Cane, 1987; Tziperman et al., 1997; Galanti and Tziperman, 2000; Wang, 2000a). The ITCZ and SPCZ slant equatorward toward the west and meet in the equatorial western Pacific. FSU shows much stronger convergence zones than NCEP, and stronger divergence in the equatorial eastern Pacific. Between 1961–1979 and 1980–1999, both FSU and NCEP show increased convergence in the western equatorial Pacific, but other changes are not consistent. For example, FSU shows a weakening of the mean divergence in the equatorial eastern Pacific, while NCEP shows a strengthening of this divergence.

The tropical climatology is a result of strong air-sea feedbacks (Dijkstra and Neelin, 1995; Philander et al., 1996) so that any discussion of the winds must include consideration of the SST. The SST climatology (Fig. 2.1c) consists of a vast warm pool of $> 28°$C water in the west, a smaller warm pool south of Mexico, a warm band of $> 27°$C water north of the equator that connects the warm pools, and a cold tongue of water that extends up the coast of South America and westward along the equator. The edges of these features delineate regions of strong horizontal SST gradients which give rise to the wind stress climatology: the northward SST gradient along the equator in the east induces the cross-equatorial southerlies, and the westward SST gradient in the central Pacific enhances the equatorial

easterly trade winds. The SST data suggest that between 1961–1979 and 1980–1999, there was a warming and eastward expansion of the western warm pool, a widening of the warm band, and an eastward shrinking of the cold tongue. The maximum warming occurs in the cold tongue region, indicating a weakening of the zonal SST contrast across the basin.

To the extent that the trade winds are driven by hydrostatically-induced pressure gradients associated with SST gradients (Lindzen and Nigam, 1987), the warming in the east Pacific would seem to suggest a general weakening of the easterlies, consistent with NCEP. However, in the west Pacific the latent heating of the middle troposphere is an important driver of the winds (Wang and Li, 1993). Because the supply of moisture available for latent heating depends nonlinearly on SST (through the Clausius-Clapeyron relation and horizontal moisture convergence), the winds are arguably more sensitive to SST changes in the west Pacific (where the SST is warm) than in the east (where the SST is cold). If this is the case, then the warming and eastward expansion of the warm pool would seem consistent with the strengthening and eastward shift of the trade winds seen in FSU.

Thus it is not immediately clear which of the products has the more realistic annual-mean stress, and clearly simple qualitative arguments are not sufficient to resolve this question. It is hoped that Fig. 2.1 will motivate further evaluation of the stress climatologies using comprehensive atmosphere and ocean models.

2.3.2 Annual cycle

Standard deviations associated with the climatological annual cycle are shown in Fig. 2.2. As described by McPhaden et al. (1988), there are strong variations of $\overline{\tau}_x$ and $\overline{\tau}_y$ associated with the western Pacific monsoons and the seasonal movements of the ITCZ. Most of the variability occurs in broad bands along 10°N and 10°S, west of the dateline and in the ITCZ. The annual cycle of the wind stress is substantially weaker along the equator and in the southeast Pacific. Variability of the climatological wind stress curl and divergence are concentrated at the northern and southern edges of the ITCZ. FSU generally shows much stronger seasonal variability of $\overline{\tau}_y$ and divergence due to the stronger ITCZ in that product, although NCEP does show stronger variability north of 10°N and in the far southeastern basin.

Between 1961–1979 and 1980–1999, both FSU and NCEP show increased monsoonal $\overline{\tau}_x$ variability in the southwest and decreased variability in the southeast. However, while FSU shows strengthening annual variations of the central Pacific easterlies and east Pacific cross-equatorial southerlies, NCEP indicates the opposite. For the stress curl there is little agreement between the analyses, with FSU showing increased variability near the equator and NCEP showing a broad decrease in variability across the east Pacific. For the stress divergence, both analyses show the increased seasonal variability in the central equatorial Pacific, and decreased variability of the ITCZ, but elsewhere the changes are not consistent between FSU and NCEP. Interestingly, the SST annual cycle hardly changes between 1961–1979 and 1980–1999.

Time/longitude plots of the annual cycles of $\overline{\tau}_x$ and SST at the equator are shown in Fig. 2.3. The annual cycle of SST is strongest in the eastern Pacific (near 100°W) where temperatures are warmest in March and coolest in September. The annual signal propagates westward, with SST changes in the east leading those at the dateline by 3–4
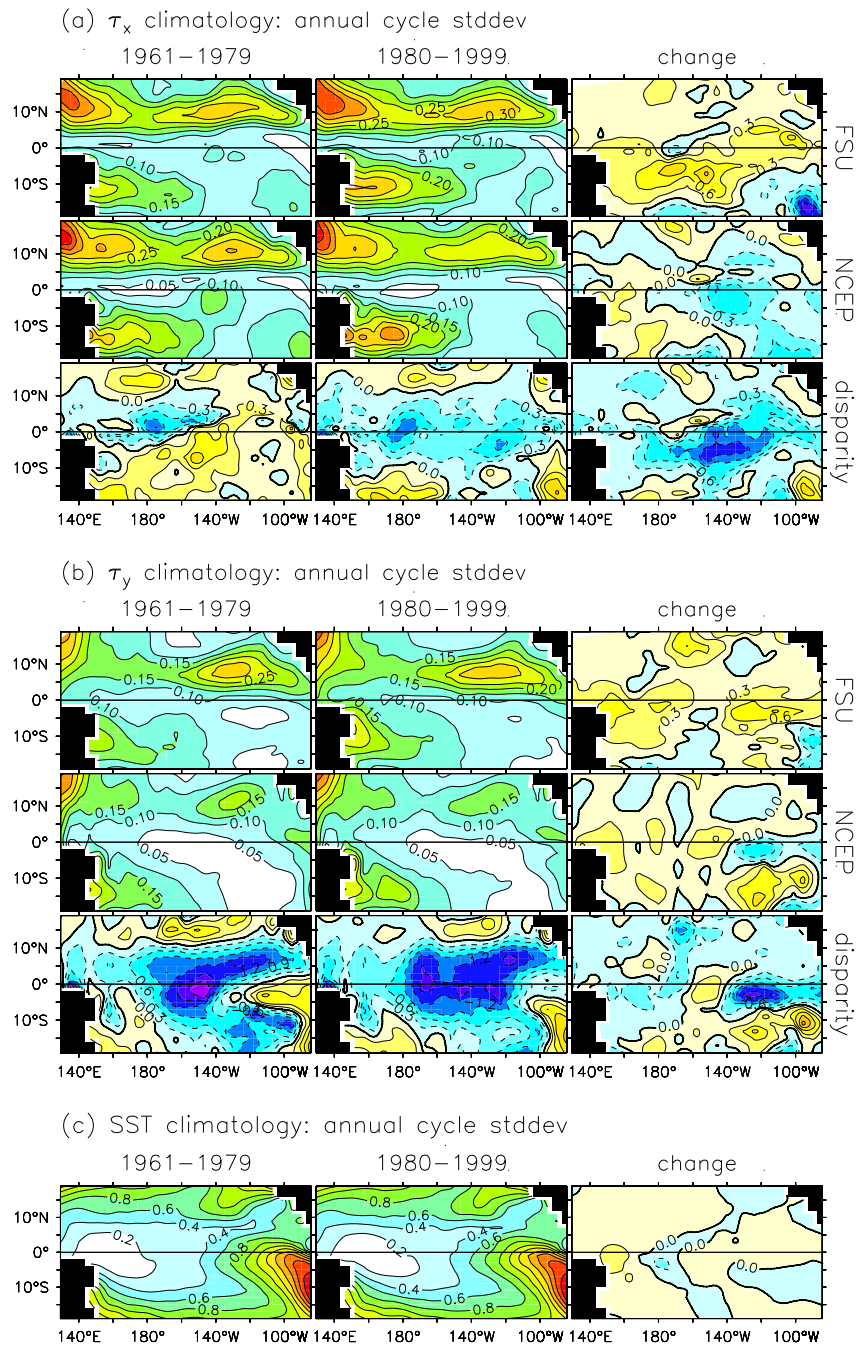
Figure 2.2: Standard deviations associated with the climatological annual cycle of (a) zonal wind stress (dPa), (b) meridional wind stress (dPa), and (c) SST (°C). Standard deviations are shown for 1961–1979 (first column) and 1980–1999 (second column). The base 2 logarithm of the ratio of the latter period over the former is also shown (third column). Rows correspond to the FSU analysis (first row), the NCEP analysis (second row), and the base 2 logarithm of their ratio (NCEP over FSU, third row).
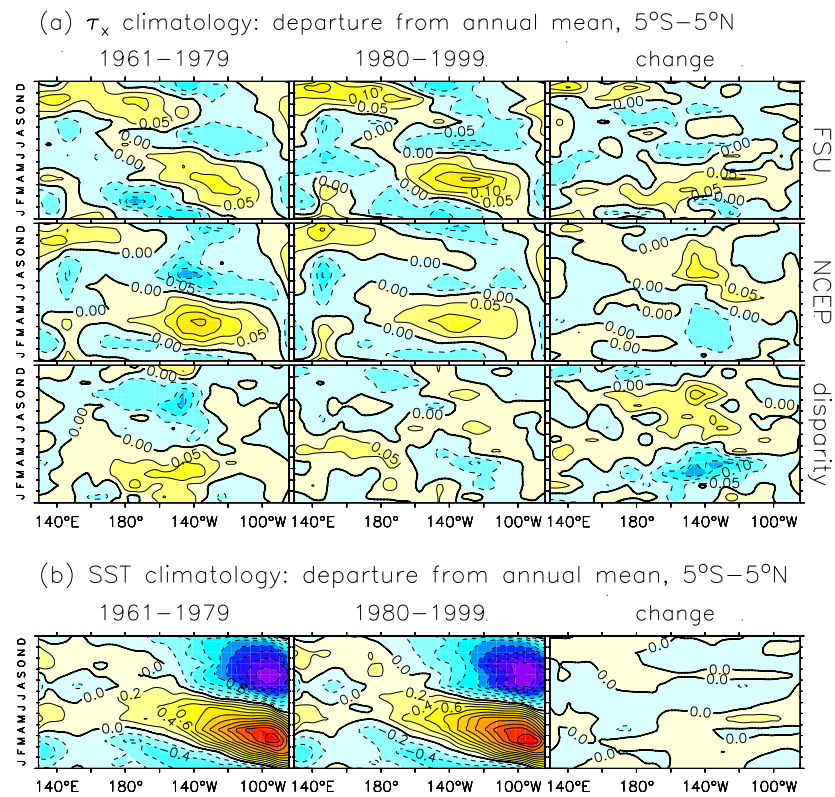
Figure 2.3: Climatological annual cycle of deviations from the annual mean, averaged over the equatorial band from 5°S to 5°N, for (a) zonal wind stress and (b) SST.
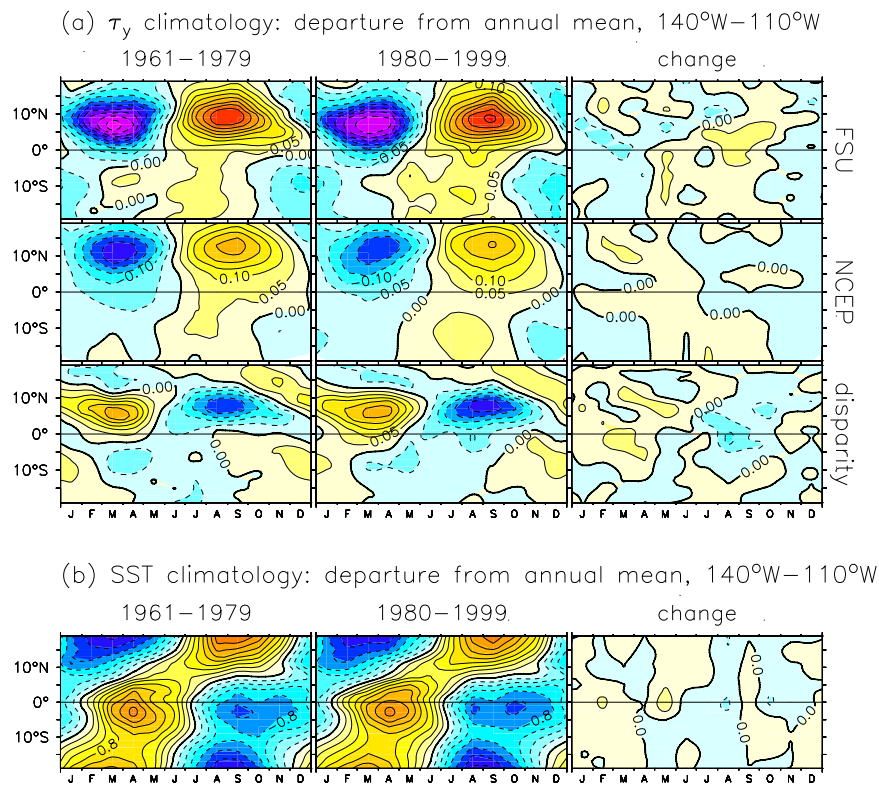
Figure 2.4: Climatological annual cycle of deviations from the annual mean, averaged over the eastern Pacific from 140°W to 110°W, for (a) meridional wind stress and (b) SST.

months. The zonal gradient of SST at the equator is weakest in boreal spring and strongest in boreal autumn, consistent with the strong annual cycle of $\overline{\tau}_x$ near 140°W that shows weakened easterlies in boreal spring. In the west Pacific there is a prominent semiannual cycle, with westerlies and warm SST in May and November, and easterlies and cool SST in February and August.

In both wind stress products between 1961–1979 and 1980–1999, the semiannual signal in the west is largely replaced by an annual signal, with westerlies in boreal winter and easterlies in boreal summer. In the eastern equatorial Pacific the annual signal strengthens in FSU but weakens in NCEP. The SST data indicate a slight decadal warming in May in the east, and a slightly *stronger* semiannual cycle in the west, but otherwise there is very little change in the annual cycle of SST at the equator.

Latitude/time plots of the annual cycles of $\overline{\tau}_y$ and SST in the eastern Pacific are shown in Fig. 2.4. Away from the equator, the SST cycle is in quadrature with the solar cycle: maximum temperatures appear in autumn following the summer season of strong solar heating, and minimum temperatures appear in spring following the winter season of weak heating. SST changes at the equator closely track those of the south Pacific, with the strongest variability occurring just south of the equator in the heart of the equatorial cold tongue. The seasonal changes of $\overline{\tau}_y$ are strongest north of the equator at the southern edge of the ITCZ. The annual cycle of $\overline{\tau}_y$ in both hemispheres is nearly in phase with the SST in the north; In contrast with the large north/south phase difference in SST, the $\overline{\tau}_y$ changes in the north lag those in the south by only 1–2 months. The northward SST gradient, cross-equatorial southerly winds, and equatorial wind divergence are all strongest in boreal summer/autumn and weakest in boreal winter/spring.

The annual cycle of $\overline{\tau}_y$ is much stronger in FSU than in NCEP, especially north of the equator associated with the stronger ITCZ in FSU. Neither the SST nor the $\overline{\tau}_y$ data indicates much change in the eastern annual cycle between 1961–1979 and 1980–1999.

2.3.3 Summary

Clearly the FSU and NCEP wind stress climatologies differ substantially. Perhaps most important for ENSO modeling are the differences in (1) equatorial $\overline{\tau}_x$ (weaker in NCEP), which controls the strength of equatorial upwelling, the zonal slope of the thermocline, and is linked with evaporative cooling of the sea surface; (2) mean off-equatorial cyclonic stress curl (stronger in NCEP), which affects the zonal-mean depth of the equatorial thermocline; (3) cross-equatorial southerlies in the eastern Pacific (weaker in NCEP), which produce upwelling just south of the equator; and (4) mean equatorial convergence (weaker and less seasonally-variable in NCEP), which in simple models controls the sensitivity of the atmosphere to heating anomalies.

The analyses also disagree regarding the nature of the mean wind stress changes between 1961–1979 and 1980–1999, with the equatorial $\overline{\tau}_x$ weakening in NCEP but strengthening and shifting eastward in FSU. Because of the subtlety of the decadal SST changes, it is difficult to say which product is the more correct regarding decadal changes in the annual mean stress. The large (and conflicting) changes in the annual cycle of $\overline{\tau}_x$ are also puzzling, given the lack of substantial changes in the annual cycle of SST between 1961–1979 and 1980–1999. Either the stress changes are not real, or they are caused by something other

than variations in SST; perhaps nonlinearity (associated with the mean warming observed in Fig. 2.1c), or changes in extratropical heating or land heating. Assuming the SST reconstruction is accurate, these puzzles could presumably be solved using an atmospheric GCM to evaluate the wind stress response to observed SST changes, or an ocean GCM to check the ocean response to the wind stress changes (e.g. Graham, 1994).

2.4   Anomaly patterns

2.4.1   Interannual variability

Fig. 2.5 shows standard deviations of the wind stress anomalies and SSTAs at periods greater than one year. The interannual variability of τ_x' (Fig. 2.5a) is concentrated in the central equatorial Pacific. These τ_x' variations are important for several reasons: they induce changes in the zonal slope of the thermocline, they generate zonal currents which advect water at the edge of the warm pool, and they alter the strength of equatorial upwelling, all of affect equatorial SST. Except for NCEP 1961–1979, the center of action for τ_x' appears just east of the dateline, near the $28°$C isotherm at the edge of the warm pool. In this region the standard deviation of interannual τ_x' is roughly twice that of the annual cycle, and is half the strength of the annual mean. There is little τ_x' variability near the coasts.

FSU and NCEP differ substantially in their representation of interannual τ_x'. For 1961–1979, the interannual variations of τ_x' in NCEP are shifted almost $40°$ east of FSU. For 1980–1999, the interannual variability in NCEP shifts westward to within $10°$ of FSU, but then its standard deviation is only $\sim60\%$ of FSU. Between these two periods, FSU shows an increase in interannual τ_x' variance almost everywhere except north of $5°$N in the central basin. NCEP, on the other hand, shows a strong *decrease* of variance across the entire eastern half of the basin.

Interannual variability of τ_y' (Fig. 2.5b) is focused near the climatological edges of the ITCZ and SPCZ. In FSU the standard deviation of τ_y' is double that in NCEP, presumably due to the stronger convergence zones in FSU. Between 1961–1979 and 1980–1999, the interannual variability of τ_y' increases along the equator in both datasets, especially FSU. The weakening of interannual τ_y' in NCEP between $5°$S–$10°$S is not as evident in FSU.

Interannual anomalies of wind stress curl (not shown) are focused in the central Pacific around $5°$N and $10°$S, at the northern and southern edges of the τ_x' variability. Variations in wind stress curl are thought to be important because they generate off-equatorial Rossby waves, which discharge warm surface waters away from the equator and terminate El Niño. The interannual curl variability is stronger in FSU than NCEP. FSU also shows a broad decadal increase in interannual curl variability across the basin, while NCEP shows *decreased* curl variability in the east. These changes are consistent with the changes in interannual τ_x' variability noted above.

Interannual anomalies of wind stress divergence (not shown) are most active in the central Pacific, especially in FSU associated with the strong ITCZ in that product. Changes in wind divergence are important because they are associated with convective changes over the eastern Pacific, which alter the surface heat balance and may affect the sensitivity of the atmosphere to SST. The analyses show relatively weak interannual variability of the
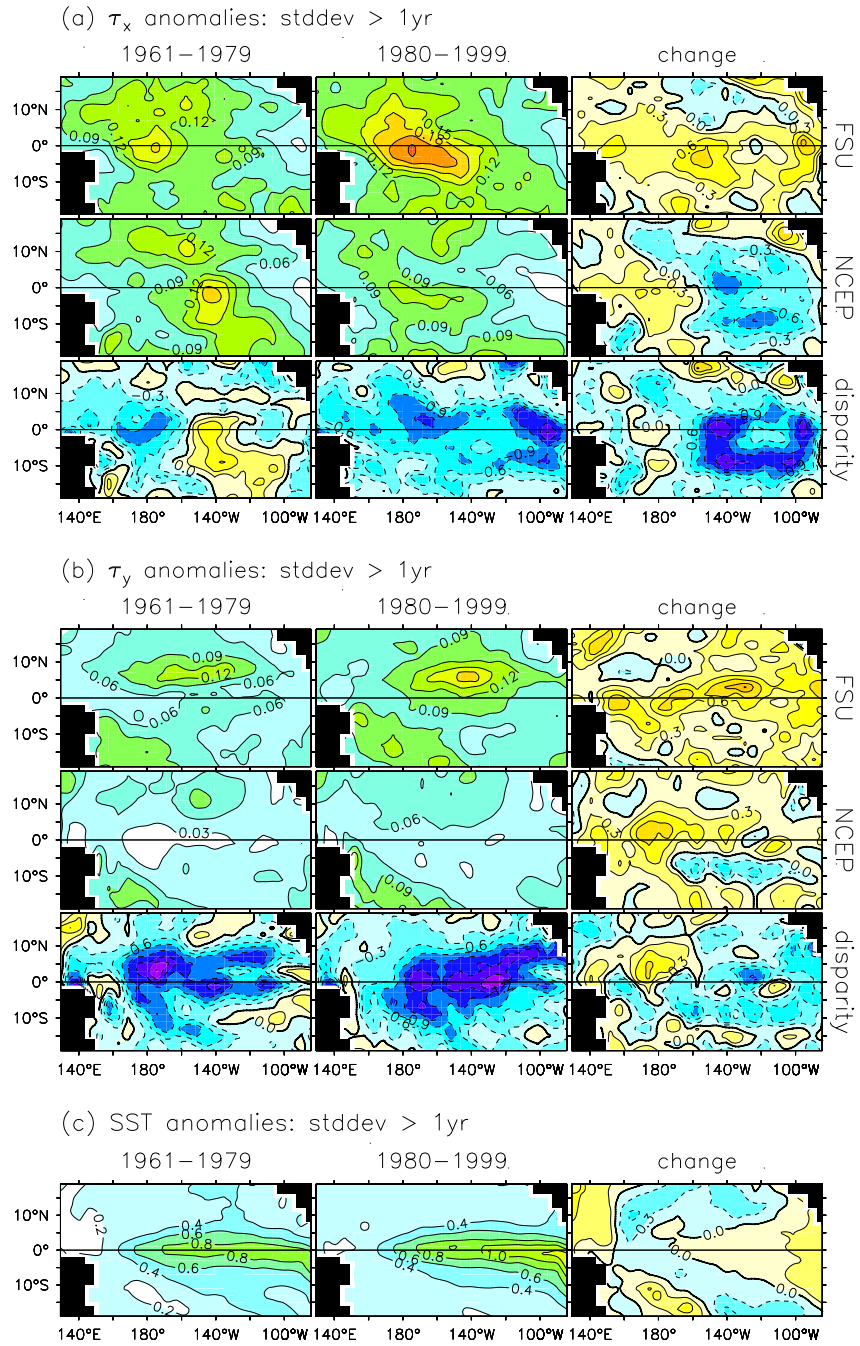
Figure 2.5: As in Fig. 2.2, but for the standard deviation of anomalies at periods greater than one year. The monthly-mean anomalies are filtered by two applications of a 6-month running mean, which gives a spectral half-power point at 12.4 months.
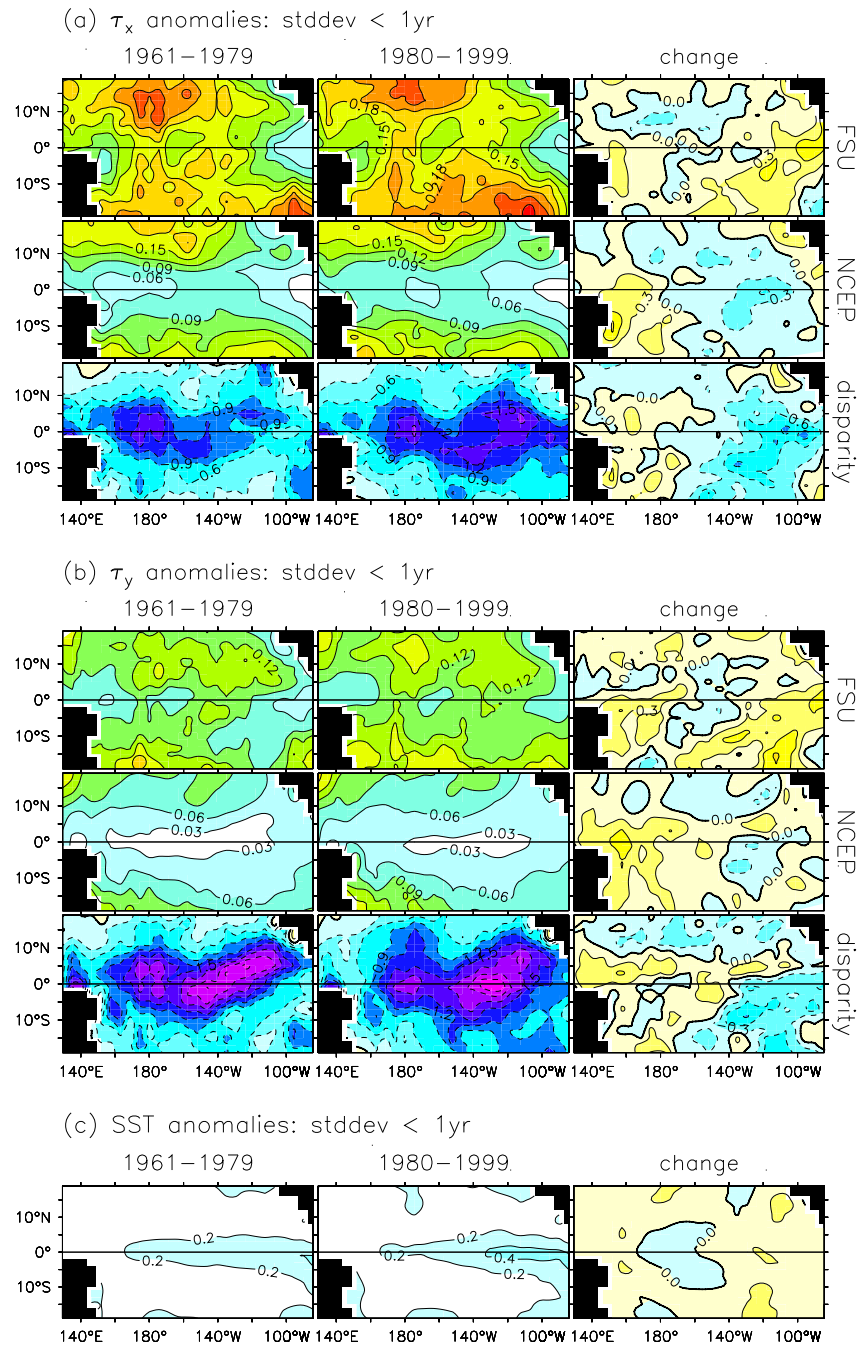
Figure 2.6: As in Fig. 2.5, but for variability at periods less than one year. This is the variability remaining when the interannual component of Fig. 2.5 is subtracted from the monthly-mean anomalies.

divergence in the far western equatorial Pacific. The interannual divergence variability is stronger in FSU than NCEP. Between 1961–1979 and 1980–1999, FSU shows an increase in interannual divergence variability in the east and a decrease in the west, while NCEP shows an *increase* in the west and a decrease off-equator in the central and eastern tropical Pacific.

For SSTA (Fig. 2.5c), interannual variability is concentrated near the equator in the eastern Pacific along the cold tongue. There is very little interannual SSTA variability in the western equatorial Pacific and away from the equator. Between 1961–1979 and 1980–1999, the SSTA variability increases in the far eastern and western Pacific, and decreases at 160°E and in the off-equatorial central basin.

2.4.2 Subannual variability

Fig. 2.6 shows standard deviations of the monthly anomalies at periods less than one year. This short-period variability is thought to play a role in triggering and amplifying ENSO events. The subannual τ_x' is weak near the coasts (especially in the east), but away from the equator the subannual component is even stronger than the interannual component. At the equator, FSU indicates the subannual τ_x' is as strong as the interannual τ_x', while NCEP shows a much weaker subannual component. Between 1961–1979 and 1980–1999, both FSU and NCEP show a strengthening of subannual τ_x' variance in the west Pacific and a weakening in the central Pacific around 5°N–10°N. In FSU, however, the subannual variance in the east Pacific increases, while in NCEP it decreases.

For τ_y', the subannual variability is generally comparable to the interannual variability. Apart from a broad minimum near the equator, there is little agreement between FSU and NCEP regarding the structure of the subannual τ_y' variance. In particular, FSU has much stronger equatorial variance than NCEP. Between 1961-1979 and 1980-1999, both products show increased variance in the west. FSU, however, shows a much stronger increase in the east than NCEP.

The subannual curl and divergence anomalies (not shown) are also much stronger in FSU than NCEP, especially near the equator. For both the subannual curl and the subannual divergence, FSU shows increased variability in the far eastern and western equatorial Pacific. The decrease in variability over the central Pacific is focused farther west in FSU than in NCEP.

For SSTA, subannual variability is focused in the cold tongue region much like the interannual variability. The subannual component, however, is much weaker than the interannual component in this region. The lack of subannual variance is partly due to the SST reconstruction procedure (Smith et al., 1996) and the regridding done in this study; in particular, tropical instability waves, which are active in the cold tongue region with a period of 20–40 days and wavelengths of 10°–20° longitude, are practically eliminated by the temporal and spatial averaging. Yet examination of high-resolution SSTs from the weekly optimal interpolation of Reynolds and Smith (1994) indicates that the subannual variance is generally less than 30% as strong as the interannual variance in the cold tongue region during 1981–2001. Thus much of the strong subannual variability in the wind stress is probably not caused by subannual SSTA. Between 1961–1979 and 1980–1999, the subannual variance of SSTA increases slightly in the east Pacific and decreases slightly

near 160°W, but such small changes could easily be due to the increase in the density of observations between the two periods.

2.4.3 Response to SST anomalies

Model studies have shown that ENSO behavior is quite sensitive to subtle changes in the wind stress response to SST anomalies (Neelin, 1990; Kirtman, 1997; An and Wang, 2000; Cassou and Perigaud, 2000), so it is important to understand the observed response. The stress response is a function of season (Yang et al., 2001) and also differs between warm events and cold events (Kang and Kug, 2002). For purposes of comparison, however, it is useful and illuminating to simply show the annually-averaged, linear response to SSTA.

Regressions of the wind stress anomalies and SST anomalies onto SSTA averaged over the NINO3 region (150°W–90°W, 5°S–5°N) are presented in Fig. 2.7. These regressions are performed without regard to the seasons or total SST, and in this sense represent the "average" response to a warm anomaly in the eastern Pacific.

Both stress products indicate equatorial westerlies and off-equatorial easterlies in the west/central basin, weak easterlies near the eastern boundary, northerlies spanning the northern tropical Pacific, and southerlies across the southwest and equatorial southeast Pacific. There is cyclonic stress curl on both sides of the equator in the central Pacific, convergence along the equator, and divergence in the off-equatorial eastern Pacific. The stress response is not entirely symmetric about the equator. The meridional center of the τ_x' response lies a degree or two south of the equator, and the center of the northern cyclone ($\sim 5°$N) is closer to the equator than the center of the southern cyclone ($\sim 10°$S). Between 1961–1979 and 1980–1999, the FSU and NCEP τ_x' responses to NINO3 SSTA (Fig. 2.7a) undergo a few similar changes; at the equator, these include stronger westerly anomalies near the dateline, stronger easterly anomalies near the western boundary, and weaker easterly anomalies near the eastern boundary.

Yet there are also many striking differences between the analyses. For 1961–1979, the equatorial westerlies (and associated off-equatorial cyclonic curl) in the two products have similar amplitudes, but in FSU the response is centered near 175°W while in NCEP it is focused near 145°W with only a weak tail extending past the dateline. For 1980–1999, the two products are in better agreement regarding the position of the westerly peak near 165°W, but the NCEP response is less than 60% as strong as that in FSU during this period. Thus while FSU indicates that the westerly response to NINO3 SSTA strengthened and spread eastward between 1961–1979 and 1980–1999, NCEP suggests just the opposite.

The meridional stress response (Fig. 2.7b) also differs substantially between FSU and NCEP. Although the NCEP response looks somewhat more similar to FSU during 1980–1999 than during 1961–1979, for both periods NCEP shows weaker southerly stress anomalies in the SPCZ region and equatorial eastern Pacific, and much weaker meridional convergence anomalies than FSU in the vicinity of the ITCZ. Between 1961–1979 and 1980–1999, FSU suggests a change toward a more northerly wind stress response at the equator near 140°W, while NCEP shows a smaller change occurring 20°–30° farther west.

Fig. 2.7c shows how SST anomalies are related to the NINO3 index. Between 1961–1979 and 1980–1999, the SSTA pattern shifted eastward by 5°–10°, and the strength of anomalies in the equatorial eastern Pacific increased. To the extent that the wind stress is
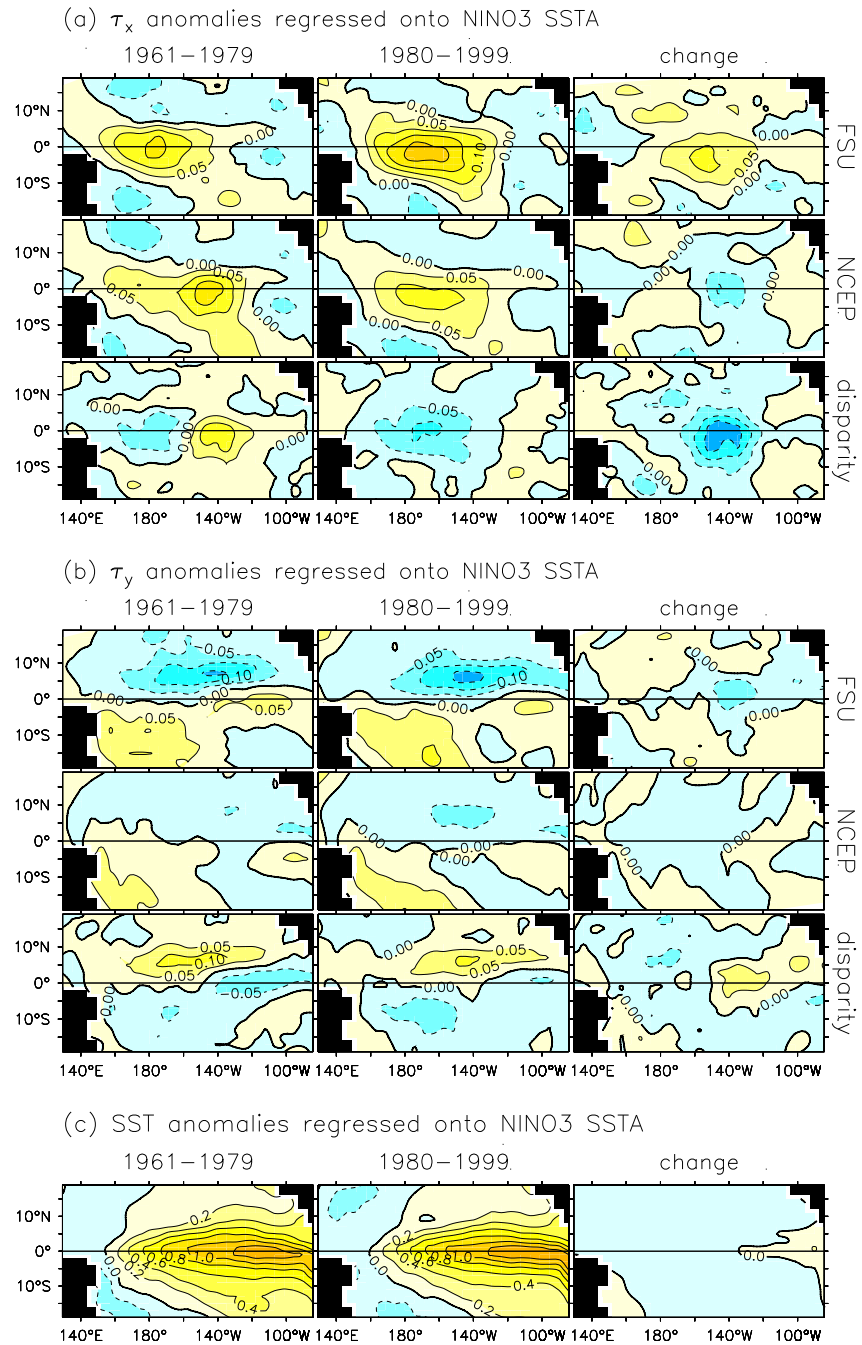
Figure 2.7: As in Fig. 2.1, but for regressions of anomalies onto NINO3-average SST anomalies. Units as in Fig. 2.1 but divided by °C.

linearly determined by SST gradients, these changes appear consistent with the eastward shift and strengthening of the stress response found in FSU. More complicated dynamics would be required to explain the westward shift and weakening of the stress response found in NCEP.

One must ask whether the very small decadal changes in the SSTA pattern can account for the rather large changes in *either* of the wind stress analyses, if indeed the stress changes are real. It is known that the atmospheric heating which drives the winds is a nonlinear function of the total SST and wind convergence (Kleeman, 1991; Wang and Li, 1993; Battisti et al., 1999; Cassou and Perigaud, 2000). Therefore it is possible that changes in mean SST and wind convergence between 1961–1979 and 1980–1999 (Fig. 2.1c) could play as large a role in modifying the stress response as the small changes in the structure of the SST anomalies. Again, qualitative arguments are not adequate to resolve this question; quantitative investigations with comprehensive atmospheric models will be required.

2.4.4 Point correlations

Point correlations of the FSU and NCEP wind stress anomalies are shown in Fig. 2.8. In general, the correlation between the two products is higher for τ_x' than τ_y', higher in the west than the east, higher for interannual periods than subannual periods, and higher for 1980–1999 than 1961–1979. Exceptions include the very low, even negative, interannual correlation in the eastern Pacific during 1961–1979, and the slight decrease in off-equatorial subannual correlation between 1961–1979 and 1980–1999.

It is no surprise that the correlations are lowest in the eastern Pacific, where the ENSO signal is weakest (Figs. 2.5–2.6), and during the earlier period, where the observations are sparse (McPhaden et al., 1998). Sampling problems are also probably to blame for the low correlations (below 0.5) of subannual anomalies near the equator. In contrast, the interannual τ_x' correlations in the western-central equatorial Pacific during 1980–1999 are quite high, approaching 0.95. Clearly recent improvements in the observing system, such as the deployment of the TAO array, have led to better agreement between the wind stress analyses.

2.5 Anomaly timeseries

Interdecadal averages and their differences tell only part of the story of the wind stress. In this section we focus on key regions for interannual τ_x' and SSTA and take a closer look at the temporal character of the data. As shown in Fig. 2.5, the center of action for τ_x' is the NINO4 region in the western equatorial Pacific (160°E–150°W, 5°S–5°N), while that for SSTA is the NINO3 region in the eastern equatorial Pacific (150°W–90°W, 5°S–5°N)

2.5.1 The timeseries

Standardized timeseries of NINO4 τ_x' and NINO3 SSTA are shown in panels (a) of Figs. 2.9–2.11. The standard deviation scale σ and lag-1-month autocorrelation ϕ_1 of the timeseries are indicated above each plot. Note that the standard deviation of FSU is nearly twice that of NCEP. The NINO3 SST anomalies ($\phi_1 = 0.91$) are more persistent in time
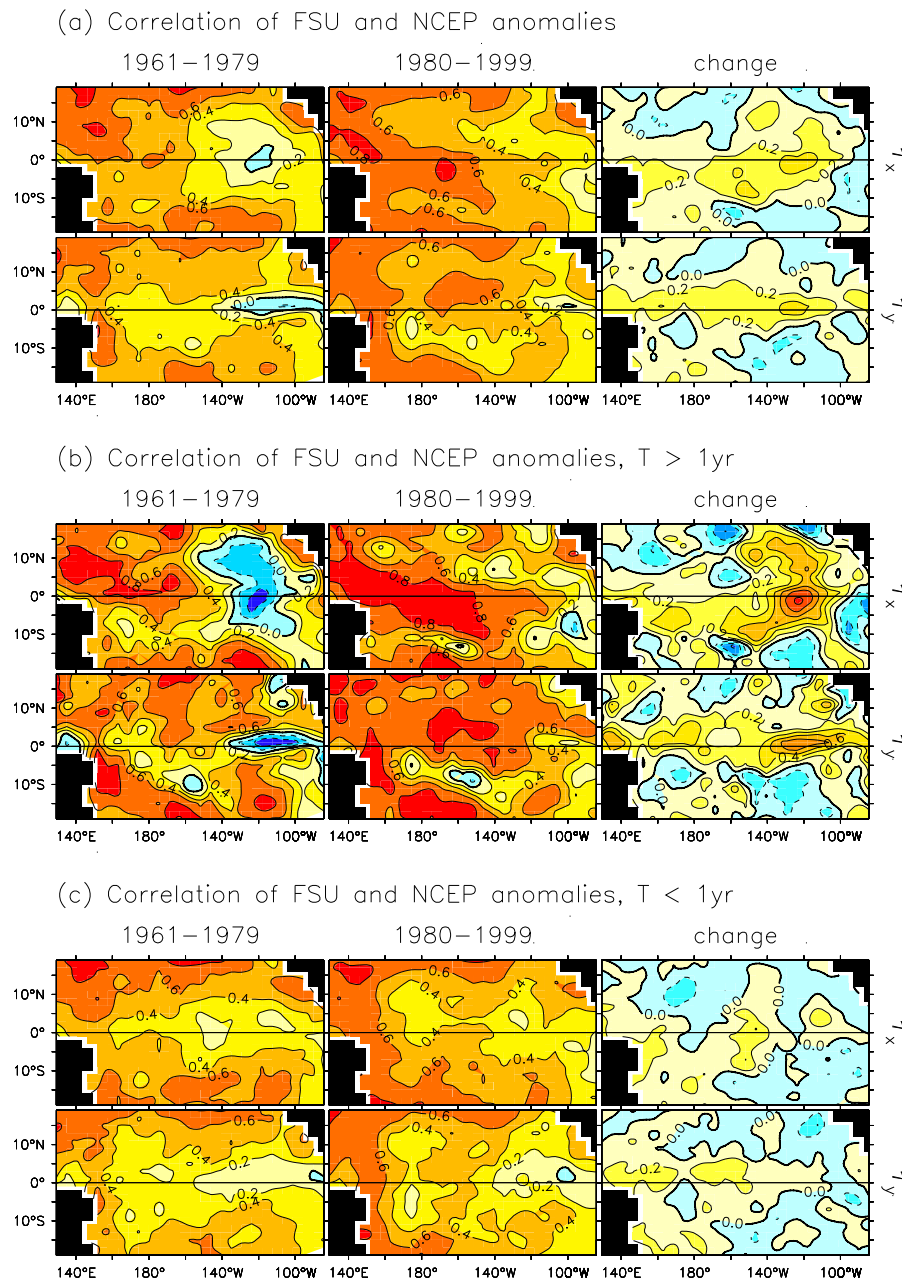
Figure 2.8: Point correlation of FSU and NCEP wind stress anomalies, for (a) the full anomalies, (b) anomalies filtered to retain only periods greater than 1 yr, and (c) anomalies filtered to retain only periods less than 1 yr. Fields are shown for 1961–1979 (first column) and 1980–1999 (second column). The change from the former period to the latter is also shown (third column). Rows correspond to the zonal stress anomalies (first row) and the meridional stress anomalies (second row).
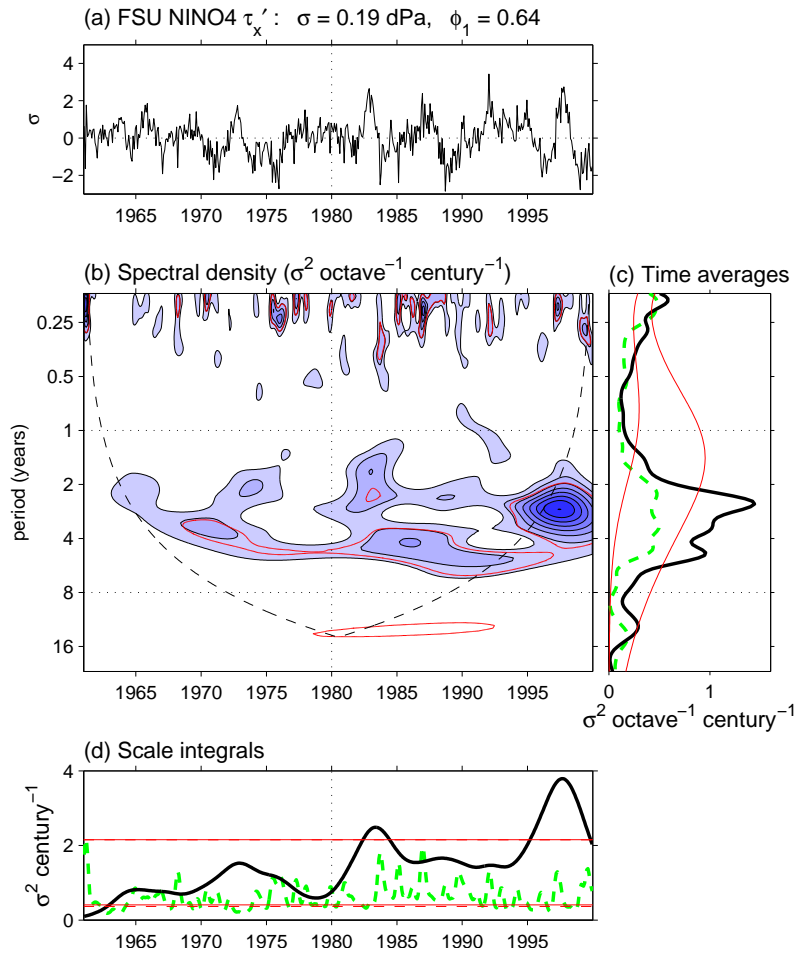
Figure 2.9: (a) Timeseries of standardized monthly anomalies for the FSU zonal wind stress averaged over the NINO4 region (160°E–150°W, 5°S–5°N). Anomalies are with respect to the 1961–1999 climatology. The standard deviation σ and lag-1 autocorrelation ϕ_1 are indicated at the top of the plot. (b) Spectral density of the timeseries, obtained by convolution with a wavenumber-6 Morlet wavelet. The base contour and contour interval are 0.5 σ^2 octave^{-1} century^{-1}. The dashed line ("cone of influence") represents twice the e-folding time for the wavelet response to a spike in the timeseries; below this line the spectral density is underestimated due to edge effects. Thick contour encloses the 95th percentile for red noise realizations with the same σ and ϕ_1 as the timeseries. (c) Time-averaged spectra for 1961–1979 (thick dashed) and 1980–1999 (thick solid). Thin lines bracket the central 90% of wavelet spectra calculated from 20-year realizations of the red noise. (d) Running variance in the 0–1 year spectral band (thick dashed) and the 1–8 year band (thick solid). Thin lines bracket the central 90% of running variances calculated from red noise.
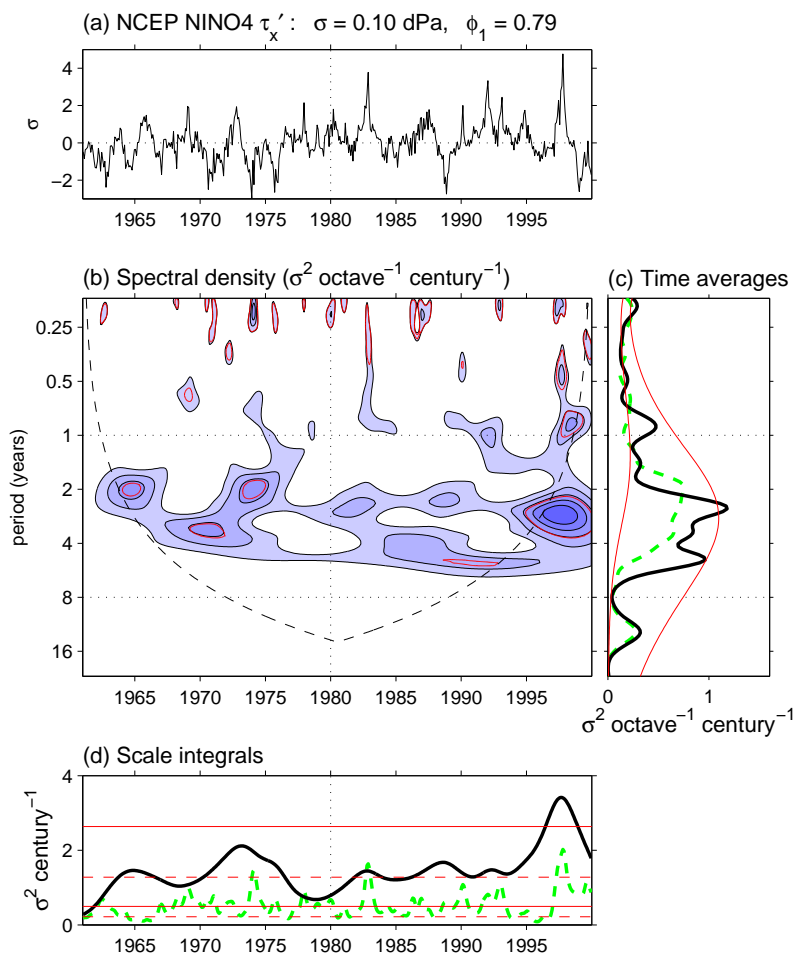
Figure 2.10: As in Fig. 2.9 but for the NCEP zonal wind stress anomalies.
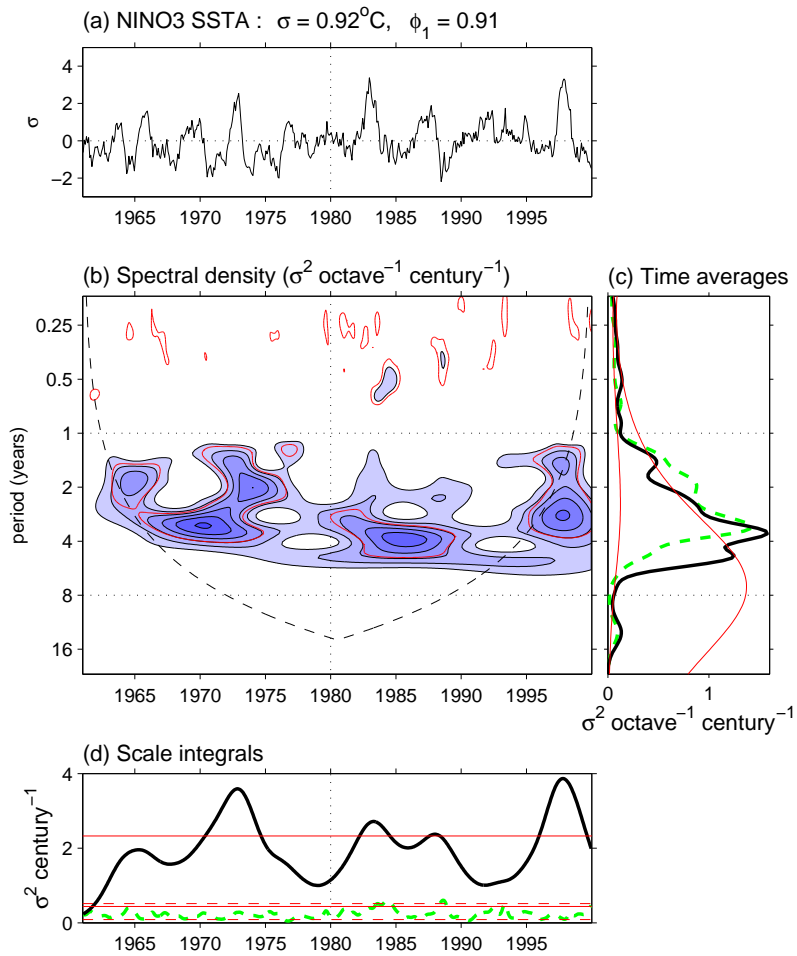
Figure 2.11: As in Fig. 2.9 but for SST anomalies averaged over the NINO3 region (150°W–90°W, 5°S–5°N).

than the NINO4 zonal stress anomalies in either NCEP ($\phi_1 = 0.82$) or FSU ($\phi_1 = 0.72$). For both stress products, τ'_x is well correlated with SSTA (0.65 for FSU, 0.74 for NCEP), with westerlies during El Niño and easterlies during La Niña.

Strikingly, the differences between the FSU and NCEP anomalies are of the same order as the stress anomalies themselves. The correlation of FSU and NCEP with each other (0.80) is only slightly larger than their correlation with SSTA. The FSU stress anomalies are generally stronger, noisier, and have broader westerly peaks than NCEP. Compared to NCEP or SSTA, FSU exhibits weaker interannual variability during the 1960s and 1970s, and weaker El Niño anomalies in 1982–83 and 1997–98. The 1991–92 El Niño event, on the other hand, is stronger in FSU than in NCEP or SSTA, stronger even than the 1982–83 and 1997–98 events in FSU. The 1996 cold event also shows up more strongly in FSU than in either NCEP or SSTA.

Around 1976–77, an upward "climate shift" is apparent in all three timeseries. This shift has been noted in a variety of datasets (Nitta and Yamada, 1989; Graham, 1994; Trenberth and Hurrell, 1994; An and Wang, 2000). Note that in NCEP, part of this shift may be an artifact related to introduction of satellite data around this time (Santer et al., 1999). However, the presence of this shift in a variety of fields, and its concurrence with changes in North Pacific climate, suggest that it may well be real and possibly independent of ENSO (Latif et al., 1997; Wang and An, 2002).

2.5.2 Spectra

Panels (b) of Figs. 2.9–2.11 give an alternate view of the timeseries. Wavelet analysis has been used by several authors to reveal interdecadal changes in ENSO (Gu and Philander, 1995; Wang and Wang, 1996; Torrence and Compo, 1999; Torrence and Webster, 1998, 1999). As pointed out by Lau and Weng (1995), a wavelet diagram amounts to a musical score for a timeseries, with low notes (long periods) at the bottom and high notes (short periods) at the top.

ENSO is evident in these diagrams as a concentration of variance between 1 and 8 yr, which is nonuniform in frequency and time. The blobs of variance are not much wider than the cone of influence, suggesting that ENSO events occur in isolated groups of one or two, separated by periods of reduced activity. The spectral power near 2 yr waxes and wanes in roughly an 8 yr cycle, while the power at 4 yr strengthens every 15 yr or so. There is also a gradual increase in variance at periods longer than 4 yr.

Panels (c) of Figs. 2.9–2.11 show the time-averaged spectra for 1961–1979 and 1980–1999. There is generally more power at subannual time scales for τ'_x than for SSTA, especially at periods of 3 months or less where τ'_x shows significantly more power than red noise. Both τ'_x and SSTA show broad peaks in the interannual band (1–8 yr) which become stronger after 1980. The spectral peaks at 12–15 yr are stronger in τ'_x than in SSTA, but the significance of these peaks is dubious since they cannot clearly be distinguished from red noise.

The spectra reveal many differences among the timeseries. The NCEP spectrum is more stationary in time than FSU, and looks more similar to SSTA than does FSU. This is perhaps to be expected since the NCEP model incorporates SST forcing into the analysis. In the 0–6 month band, FSU has relatively more power than NCEP and shows more of

an increase in variance after 1980 than either NCEP or SSTA. In the 6–12 month band, FSU shows significantly *less* power than the red noise spectrum, while NCEP and SSTA cannot be clearly distinguished from red noise. In the interannual band, FSU shows a much stronger increase in variance between 1961–1979 and 1980–1999 than either NCEP or SSTA. In FSU this increase is largest at a period of around 2.5 yr, at the short-period end of the active band. In NCEP and SSTA, the spectral change is best described as a shift of the entire active band toward *longer* periods.

Panels (d) of Figs. 2.9–2.11 show the running variances in the 0–1 yr band and the 1–8 yr band. The interannual SSTA variance has gradually changed over the past four decades, with quiet periods during the early 1960s, late 1970s, and early 1990s, and active periods during the early 1970s, mid-1980s, and late 1990s. Most of these changes are mirrored in the τ'_x data, though neither stress product shows reduced interannual variance during the early 1990s, when the decrease in variance at 4 yr was compensated for by an increase at 1–2 yr. The very strong El Niño of 1997–1998 and its aftermath correspond to highly significant interannual variance peaks in all three datasets.

The NCEP τ'_x variance is more uniform in time than either FSU or SSTA; the FSU interannual variance in particular increases strongly toward the latter half of the record. FSU and NCEP also show different changes in the 0–1 yr band: FSU shows heightened activity from 1983–1993, while NCEP shows fairly uniform noise activity apart from three prominent and isolated spikes in 1974–1975, 1982–1983, and 1997–1998.

The spectral variations of SSTA appear to be more consistent NCEP than with FSU. Again, this is not surprising since the NCEP reanalysis explicitly includes SST as a model forcing. NCEP also has a more stationary spectrum than FSU, probably because the NCEP analysis scheme is more rigorously uniform in time.

2.5.3 Seasonality of the anomaly variance

The annual cycles of NINO4 τ'_x and NINO3 SSTA variance are shown in Fig. 2.12. The standard deviation scales, labeled at the top of each plot, once again confirm that the wind stress anomalies (especially FSU) have a larger subannual component than do the SST anomalies. Column (a) indicates that the full anomaly variance depends on the calendar month. The SSTA variance, for example, is four times stronger in December than in March. The τ'_x variance also tends to peak near the end of the calendar year, though FSU is not as strongly locked to the annual cycle as NCEP. Between 1961–1979 and 1980–1999, there is not much change in the cycle of SSTA variance apart from an overall strengthening of the variance. The wind stress products, however, show more substantial changes. Both indicate an increased annual cycle of anomaly variance which peaks slightly later in the year: in NCEP, the December peak narrows and shifts to November, while in FSU the broad August–February peak shifts to September–March.

Column (b) of Fig. 2.12 shows that the interannual variances of τ'_x and SSTA are clearly phase-locked to the annual cycle, with anomalies most variable in boreal autumn and least variable in boreal spring. Between 1961–1979 and 1980–1999, all three datasets show a strengthening of the mean variance and a shift of the cycle of variance so that it peaks one month later in the year. However, while SSTA shows a weakening of the cycle of interannual variance, NCEP shows little change, and FSU actually shows a strengthening.
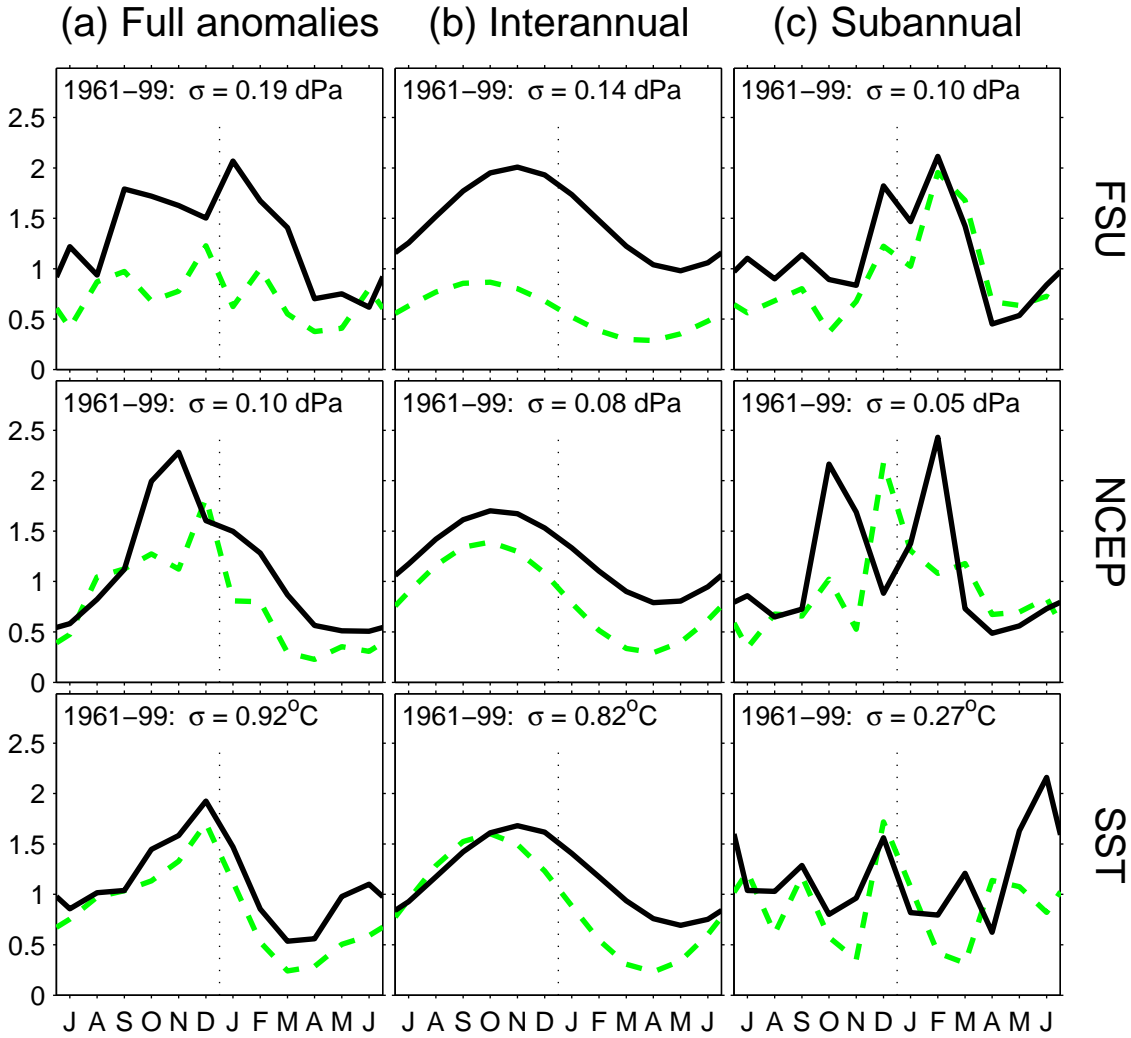
Figure 2.12: Monthly variance of the anomalies for FSU and NCEP τ'_x averaged over NINO4, and SSTA averaged over NINO3. The anomalies have been filtered to retain (a) all periods, (b) periods greater than one year, and (c) periods less than one year. The monthly variance, shown for 1961–1979 (dashed) and 1980–1999 (solid), is in units of σ^2 where σ is the standard deviation over the entire 1961–1999 period (labeled). The horizontal axis runs from July to June.

The cycles in the three datasets are all in phase during 1961–1979, but during 1980–1999 NCEP is shifted a few weeks earlier than FSU and SSTA.

Column (c) of Fig. 2.12 indicates that the seasonal cycle of subannual variance is more complex. Apart from a weak peak in December and a June peak during 1980–1999, the subannual NINO3 SSTA variance does not show much of a cycle. The subannual NINO4 τ'_x variance, however, shows a strong cycle with decreased variance in late boreal spring and summer and increased variance in boreal winter. Between 1961–1979 and 1980–1999, the subannual variance in FSU increased in every season except boreal spring, and the February peak in FSU broadened to include December and January. The December peak in NCEP, on the other hand, split into two separate peaks: one in October–November and the other in February.

Several conclusions can be drawn from Fig. 2.12. First, the calendar phasing of inter-annual anomalies is fairly robust, with little dependence on dataset and not much change between decades. Second, the phasing of the subannual "noise" is not as robust. It is usually assumed that the stress responds rapidly to SST (order of a few weeks or less), while SST responds slowly to the stress ($\sim$2 months for subsurface Kelvin waves to cross the basin, plus time for upwelling to affect SST). If this is true, then the February peaks in subannual NINO4 τ'_x variance do not appear to be caused by subannual NINO3 SSTA. It is conceivable, though, that the February peaks in τ'_x produce the June peaks in SSTA activity. In addition, the December maxima in subannual τ'_x, though curiously absent in the 1980–1999 NCEP data, could be related to the weak December peaks in subannual SSTA.

Considering the sharp features in Figs. 2.9a–2.10a, it is possible that nonlinearities contribute to the subannual maxima of NINO4 τ'_x variance. In particular, the subannual variance peaks in October–December occur at about the same time as the interannual variance peaks. Similarly, the subannual variance peaks during February–March occur at the time of year when the eastern Pacific is warmest, the ITCZ is closest to the equator, and equatorial convection is most active (Fig. 2.3). The idea that the climatology and ENSO may modulate the subannual variability is consistent with the conceptual framework of Meehl et al. (2001b).

2.5.4 Cross-correlations

Cross-correlations among the NINO4 τ'_x and NINO3 SSTA are shown schematically in Fig. 2.13. In this figure, hexagons symbolize the timeseries of Figs. 2.9a–2.11a, and connecting links indicate the correlations between the timeseries for 1961–1979 (inner links) and 1980–1999 (outer links). Clearly the interannual links are the strongest, with the correlations between the stress and SST nearly as strong as those between the stress products. The subannual correlations are much weaker: the subannual stress is completely independent of SST, and the subannual link between the stress analyses is rather tenuous. SSTAs are slightly better correlated with NCEP than with FSU, especially prior to 1980.

The changes in correlations between 1961–1979 and 1980–1999 are fairly small relative to the correlations themselves. There is almost no change in the links with SST, apart from a strengthening of the correlation between the full FSU and SST anomalies due to less negative subannual correlation. FSU and NCEP are generally in better agreement for
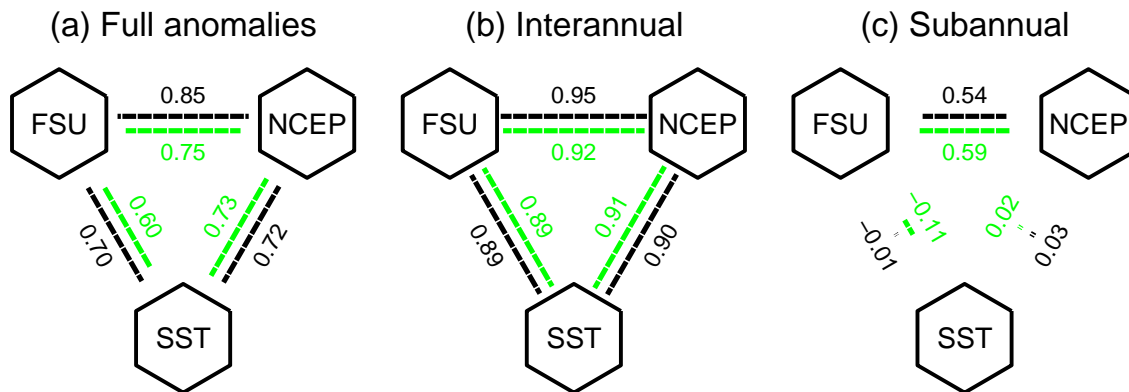
Figure 2.13: Correlations among FSU and NCEP NINO4 τ'_x, and NINO3 SSTA, represented graphically by the length of the links between variables. Inner links are for 1961–1979, outer links are for 1980–1999. Correlations are shown for (a) the full anomalies, (b) anomalies filtered to retain only periods greater than 1 yr, and (c) anomalies filtered to retain only periods less than 1 yr.

the latter period, as evidenced by the increase in their correlation with each other (except at subannual time scales), and by their more similar correlations with SST.

2.5.5 Distributions

Probability densities

Probability densities of the interannual and subannual anomalies, estimated using a Gaussian kernel (Silverman, 1986), are shown in Fig. 2.14. On the basis of such plots one can make several qualitative statements. For the full anomalies, FSU appears more normally distributed than NCEP or SSTA, and for all three datasets, the subannual component looks more normally distributed than the interannual component. The interannual anomalies appear skewed to the right, more so for SSTA than for τ'_x. The subannual SST anomalies seem almost normally distributed. Between 1961–1979 and 1980–1999, some of the distributions appear to change, especially SSTA, which becomes more skewed to the right.

Red noise comparisons

One can use probability plots to quantify these statements. To assess the normality of a sample, for example, it is common to plot the sample quantiles against theoretical quantiles from a normal distribution. The correlation coefficient for this plot can then be tested for significant departures from unity, and if the departures are large enough then the hypothesis of normality can be rejected. This is the essence of the Shapiro-Wilks W-test for normality (D'Agostino and Stephens, 1986). In the present case, the monthly data are autocorrelated, so it is more appropriate to compare the sample quantiles with the quantiles of *autocorrelated* Gaussian red noise. Furthermore, it is easier to see the nature
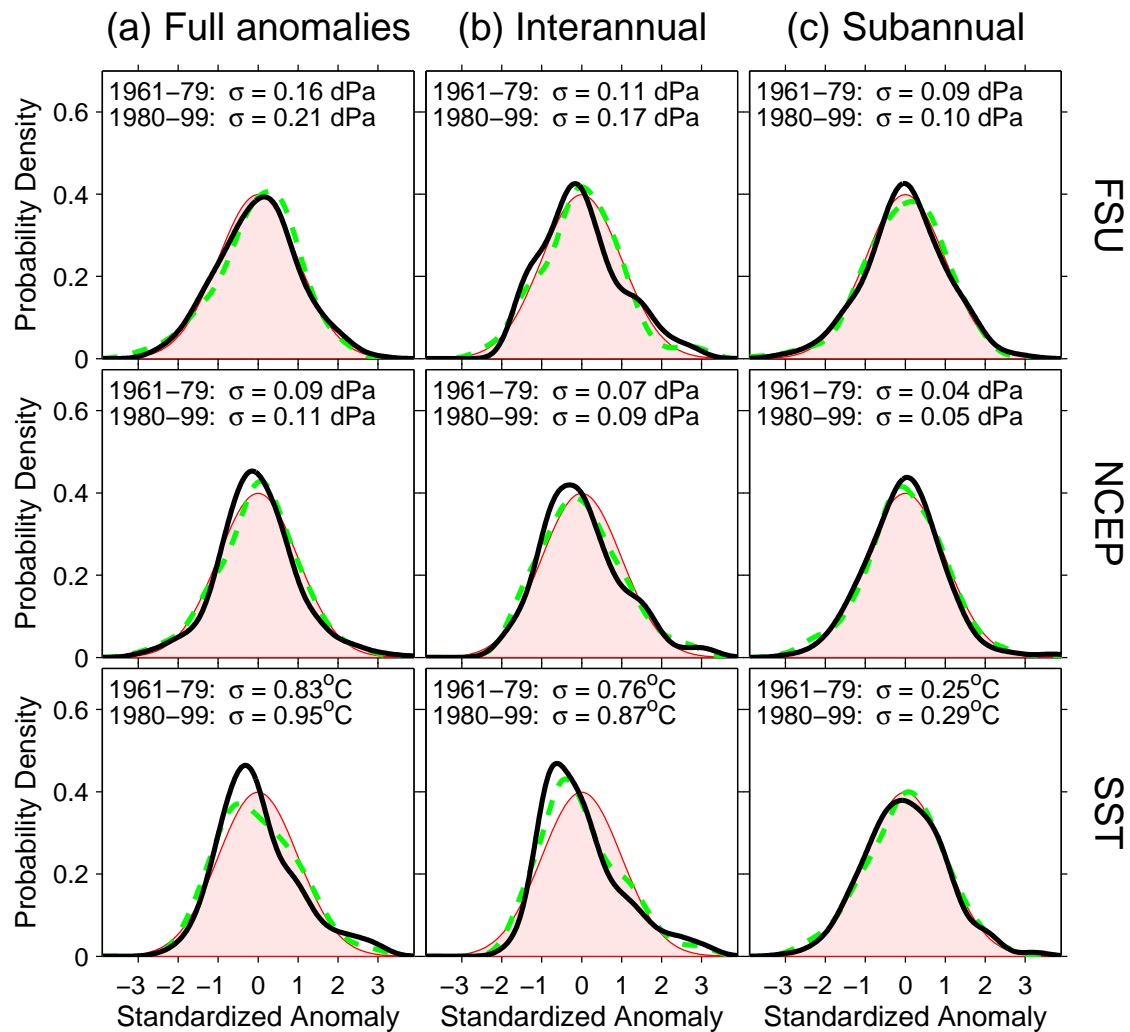
Figure 2.14: Distributions of standardized anomalies for FSU and NCEP τ'_x averaged over NINO4, and SSTA averaged over NINO3. The anomalies have been filtered to retain (a) all periods, (b) periods greater than one year, and (c) periods less than one year. The distributions, estimated using a Gaussian kernel, are shown for 1961–1979 (dashed) and 1980–1999 (solid). The normal distribution is shaded for reference.
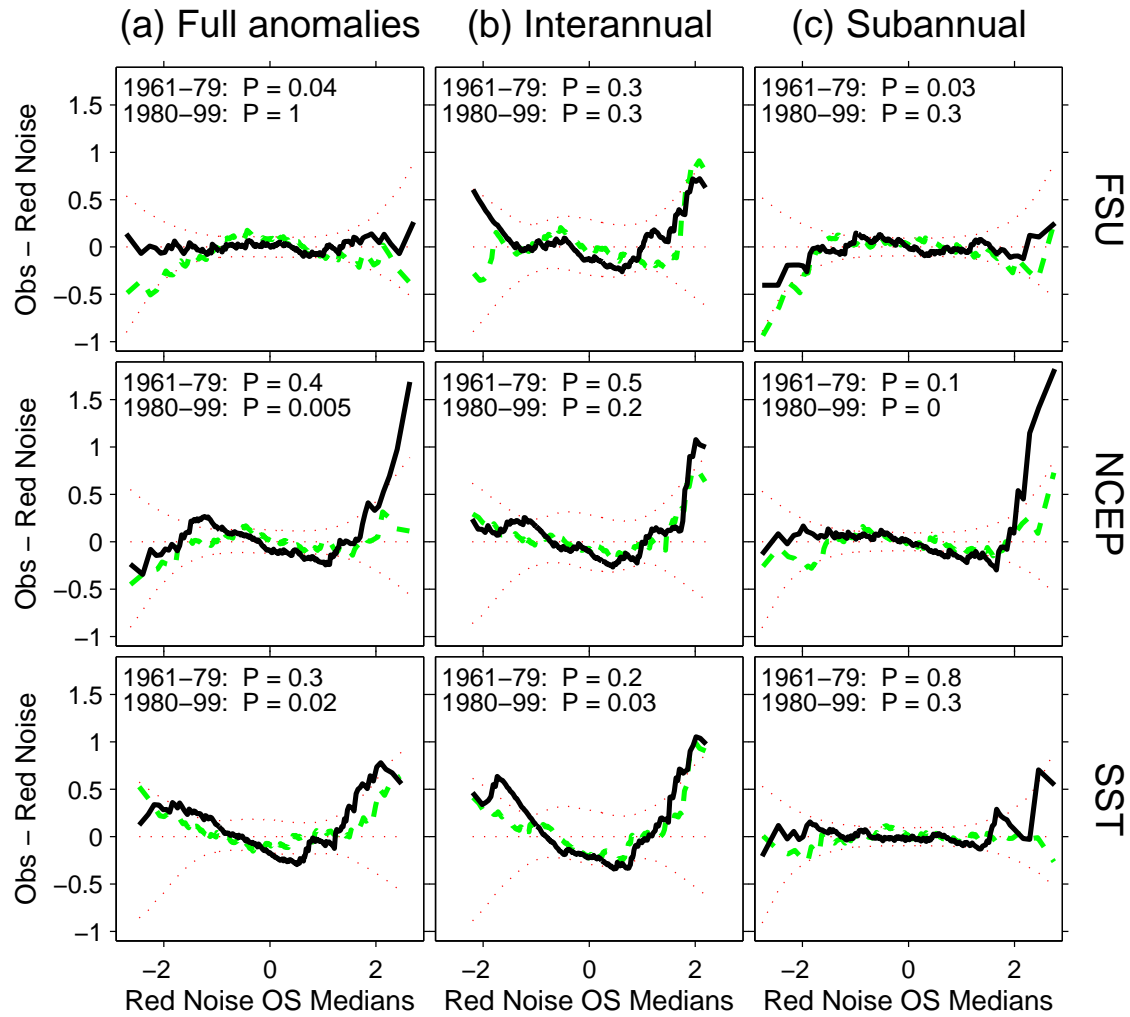
Figure 2.15: Normal probability plots of the data in Fig. 2.14, for 1961–1979 (dashed) and 1980–1999 (solid). The difference between the standardized ordered observations and the red noise order statistic medians is plotted against the latter. Under the hypothesis H_0 that the observations are red noise, one would expect this difference to be zero, apart from random fluctuations (curved dotted lines indicate the 95% confidence band from 10,000 red noise realizations). A test for normality is conducted using the correlation r between the ordered observations and the red noise order statistic medians. The probability that r could be as small as observed, under H_0, is estimated from the red noise realizations and given as P at the top of each plot.

of the non-normality if *differences* between the sample quantiles and red noise quantiles are plotted against the latter.

A set of such plots are shown in Fig. 2.15. If the data were simply Gaussian red noise, one would expect horizontal lines at zero. Concave-up curvature, on the other hand, indicates that both the smallest and the largest of the observations are larger than expected from red noise, i.e. the sample is skewed to the right. The curves may be considered consistent with red noise where they stay within the 95% confidence band (dotted lines). A test for the entire sample, similar to the W-test, is based on the correlation of the ordered data and the red noise quantiles. The probability that the correlation could be as small as observed, under the hypothesis that the observations are red noise, is given as P at the top of each plot.

With such a short data record, it is quite difficult to distinguish the observed distributions from red noise. There are simply not enough data: at interannual time scales, the 20-year timeseries essentially contain only 8 or so independent events. Thus the correlation test for red noise rejects only 6 of the 18 samples at the 0.05 level: full/subannual FSU for 1961–1979, full/subannual NCEP for 1980–1999, and full/interannual SSTA for 1980–1999.

Column (a) of Fig. 2.15 indicates the distribution of FSU anomalies is skewed to the left before 1980, but becomes indistinguishable from red noise after 1980. The NCEP distribution, on the other hand, is reasonably consistent with red noise before 1980 but becomes heavy-tailed (especially on the right) after 1980. The SSTA distribution is skewed to the right during both periods, more so after 1980.

Column (b) of Fig. 2.15 confirms that the interannual distributions are generally skewed to the right relative to red noise. However, the only sample that fails the correlation test is the post-1980 interannual SSTA. Thus the decadal changes in interannual τ'_x distributions, apparent in Fig. 2.14, are for the most part no larger than what one would expect from red noise. It would therefore be risky to interpret the apparent decadal changes in interannual distributions as anything more than random chance.

Column (c) of Fig. 2.15 shows that the subannual curves are reasonably flat over the bulk of each sample, suggesting consistency with red noise. Significant departures at extreme values, however, suggest a possible role for nonlinearity in FSU during 1961–1979 and in NCEP during 1980–1999.

Data cross-comparisons

Differenced quantile-quantile (DQQ) plots of NCEP versus FSU, and of each of these products versus SST, are shown in Fig. 2.16. Such plots offer a more direct comparison of the samples against each other. For identical samples the DQQ plot would be a flat line at zero. If the *leftmost* point in a DQQ plot of y versus x lies above the zero line, this indicates that the *smallest* value of y is larger than the *smallest* value of x. Similarly, if the *rightmost* point lies above zero, then the *largest* y is larger than the *largest* x. Finally, if the *center* point lies above zero, then the *median* of y is larger than the *median* of x.

The DQQ plots reveal some interesting relationships between the stress analyses. For the full anomalies, it is apparent that NCEP takes more extreme westerly values than FSU, especially after 1980. This is due to an increase in the subannual skewness of NCEP relative to FSU after 1980. Interannually, however, NCEP comes into better agreement
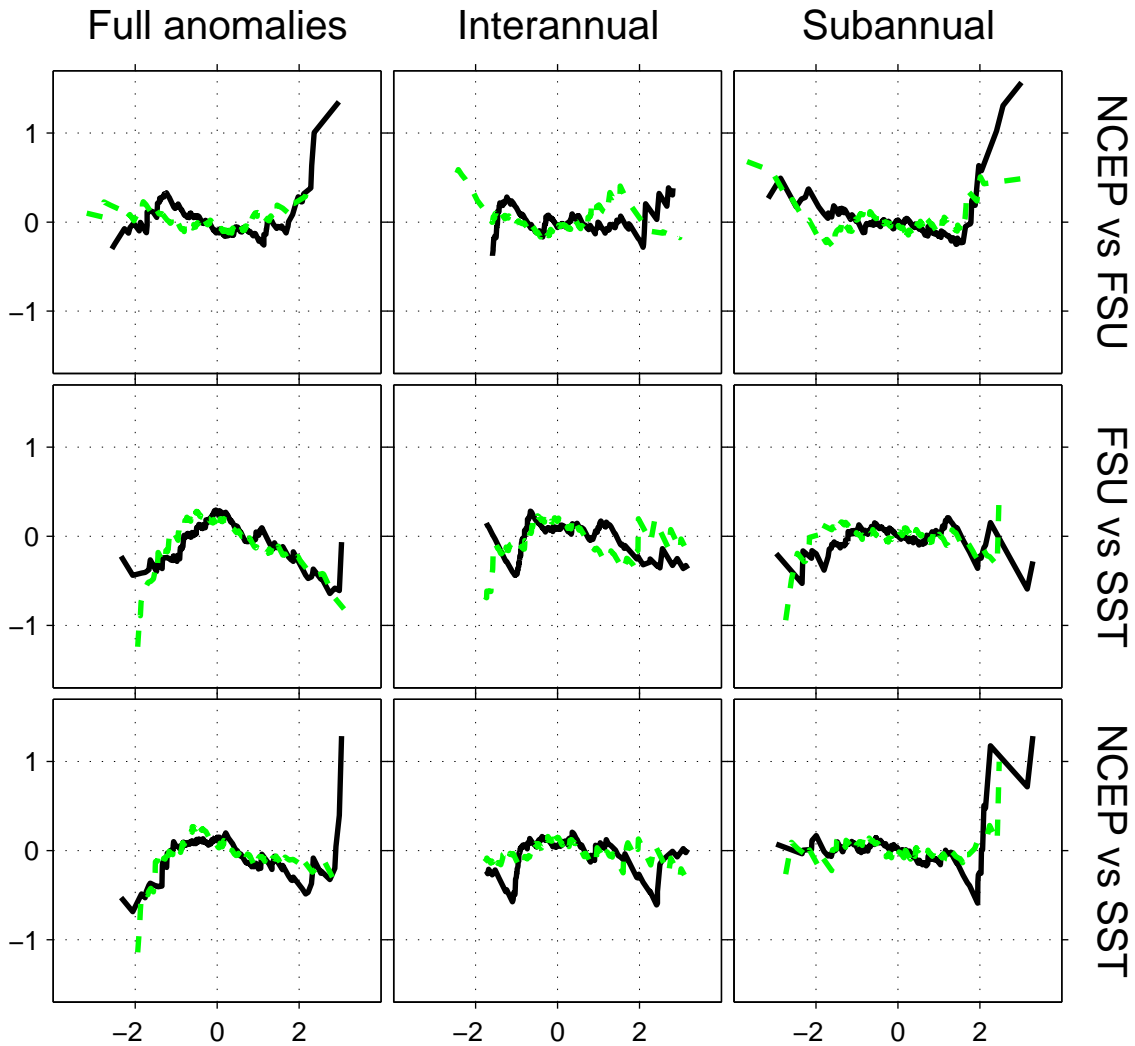
Figure 2.16: Differenced quantile-quantile plots of the data in Fig. 2.14, for 1961–1979 (dashed) and 1980–1999 (solid). Variables are indicated at the right edge of the figure; the difference between the standardized ordered observations of the first variable and those of the second are plotted against those of the second, for the full anomalies (left column), periods greater than one year (middle column), and periods less than one year (right column).

with FSU during the latter period.

The DQQ plots also reveal differences between the distributions of the wind stress anomalies and those of the SST anomalies. For the full anomalies, FSU is less skewed towards positive values than SST, although this difference decreases slightly after 1980. NCEP, however, shows an increasing tendency to take on more extreme positive values than SST, and a decreasing tendency to take on more extreme negative values than SST. The interannual distributions of τ_x' and SSTA are fairly similar. The subannual anomalies, however, indicate that FSU takes slightly more extreme *negative* values than SST, while NCEP takes much more extreme *positive* values than SST.

2.6 Conclusions

The tropical Pacific wind stress is a vital component of global climate but one which is difficult to estimate accurately. This study is the first to describe the full range of spatial and temporal variability of the observed wind stress and its consistency with observed SST in multiple datasets over a long time period. As such the results should be of great interest to researchers interested in tropical Pacific climate variability.

The NCEP stress climatology is distinguished from FSU by weaker equatorial easterlies, stronger off-equatorial cyclonic curl, weaker cross-equatorial southerlies in the east Pacific, stronger southerlies along the Peruvian coast, and weaker convergence zones with weaker annual variations. Changes in the mean state between 1961–1979 and 1980–1999 differ between the analyses, with FSU indicating an eastward shift and strengthening of the equatorial trade winds, but NCEP suggesting a westward shift and weakening of the trade winds. Modeling and data assimilation studies will be required to indicate which change is more consistent with the observed mean warming of tropical SST. Changes in the annual cycle of wind stress also differ between the analyses, but appear unrelated to changes in the annual cycle of SST.

In response to NINO3 SSTA, NCEP gives easterlies which peak farther east than in FSU. NCEP also exhibits a much weaker meridional stress response (owing to the weak convergence zones in that product) and lacks the cross-equatorial southerly anomalies evident in FSU. Between 1961–1979 and 1980–1999, FSU shows a strengthening and eastward spread of the zone of interannual τ_x' variability, while NCEP shows a weakening and westward spread of this variability. In this case the FSU change appears to be the more consistent with the observed increase in SST variability in the east Pacific. The changes in the wind stress response to NINO3 SSTA, if they are real, could be due to a slight change in the "meaning of NINO3 SSTA" over the past four decades (namely an eastward shift of the SST anomalies). Alternatively, the changes in wind stress response may be due to the observed change in climatological SST, which through nonlinearity would alter the strength and region of atmospheric heating induced by SST anomalies.

There is good temporal correlation of area-averaged western Pacific (NINO4) τ_x' between FSU and NCEP on interannual time scales. Small-scale stress anomalies, however, are not well correlated except for interannual anomalies in the western Pacific after 1980. Both interannual and subannual variability are stronger in FSU than NCEP, notably for τ_x' near the dateline and τ_y' near convergence zones. Although the anomalies are stronger and

noisier in FSU, NCEP shows more extreme westerly peaks in the NINO4 region during El Niño. Decadal changes in the distributions of subannual NINO4 τ'_x anomalies differ between FSU and NCEP, and large event-to-event differences between the analyses are evident.

The spectrum of NINO4 τ'_x in NCEP is more stationary in time than in FSU, and appears to be more consistent with NINO3 SSTA especially before 1980. Compared to FSU, NCEP shows a smaller fraction of the NINO4 τ'_x variability occurring at time scales of 3 months or less. Between 1961–1979 and 1980–1999, the interannual variability in FSU shifts toward shorter periods, while that in NCEP and SSTA shifts toward longer periods. The seasonal cycle of interannual variance becomes stronger in FSU, but does not much change in NCEP. The seasonal cycle of subannual variance and the decadal changes in this cycle are also quite different between the analyses.

Encouragingly, the wind stress analyses have come into better agreement since 1980, and many similarities are clear. At the equator between 1961–1979 and 1980–1999, both products show increased mean convergence in the far western Pacific, a weakening of the mean easterlies near the dateline, increased subannual and interannual variability in NINO4, and a stronger τ'_x response to SST anomalies. The following wind stress response to an eastern Pacific warming appears robust to dataset and time period: westerly anomalies peak in the west/central Pacific just south of the equator, while easterly anomalies appear off-equator and in the east; cyclonic stress curl anomalies in the north lie closer to the equatorial waveguide than in the south; and the anomalous stress is generally equatorward, except in the southeastern part of the basin. The interannual variance of NINO4 τ'_x peaks between October and November, the subannual variance between November and February. SST and stress anomalies are strongly correlated on interannual time scales, but uncorrelated on subannual time scales. Changes in the distribution of interannual NINO4 τ'_x between 1961–1979 and 1980–1999 are not significant.

Despite the better agreement since 1980, the FSU and NCEP stress analyses are very different. Changes in the analyses between 1961–1979 and 1980–1999 are generally smaller than the differences between the analyses, so the *true* changes in wind stress are very uncertain. Researchers should keep this uncertainty in mind when using the observed stresses to study climate variability, construct statistical atmosphere models, or drive ocean simulations.

Statistical Wind Stress Model

A field of water betrays the spirit that is in the air.

Thoreau, *Walden*

3.1 Motivation

The simulation and prediction of the El Niño–Southern Oscillation (ENSO) remains a formidable challenge (Landsea and Knaff, 2000; Latif et al., 2001). Part of the challenge stems from uncertainties about the tropical Pacific wind stress response to sea surface temperature anomalies (SSTA). Several studies have shown that this response is critical to the behavior of ENSO (Neelin, 1990; Kirtman, 1997; An and Wang, 2000; Cassou and Perigaud, 2000). Unfortunately, general circulation models of the atmosphere have had difficulty reproducing the observed response (Saji and Goswami, 1997; Kleeman et al., 2001), and even the observational analyses themselves do not fully agree on what reality is like (Chapter 2; McPhaden et al., 1998).

To solve this problem, several researchers have constructed statistical models of the wind stress based on the observational analyses. These statistical atmospheres may then be coupled to dynamical ocean models to produce "hybrid coupled models" (Barnett et al., 1993; Balmaseda et al., 1994; Syu and Neelin, 1995; Blanke et al., 1997; Eckert and Latif, 1997; Cassou and Perigaud, 2000; Kang and Kug, 2000). Recently, Harrison et al. (2002) built several such hybrid models, coupling statistical atmospheres derived from various flux products to the same ocean GCM. They found that different atmospheric responses produced very different ENSO behaviors, ranging from damped oscillations to sustained oscillations to a slow drift to a new steady state. The predictive skill of these coupled models varied as well. Such sensitivity motivated the careful investigation of the differences between available tropical Pacific wind stress products in Chapter 2, and also warrants a closer look at the statistical models derived from them.

A statistical model is much more than a "black box"— it is a powerful diagnostic tool, as it gathers a researcher's qualitative notions about a system into a consistent, quantitative framework. This tool can then be used to test ideas, e.g. to reveal the influence of SST
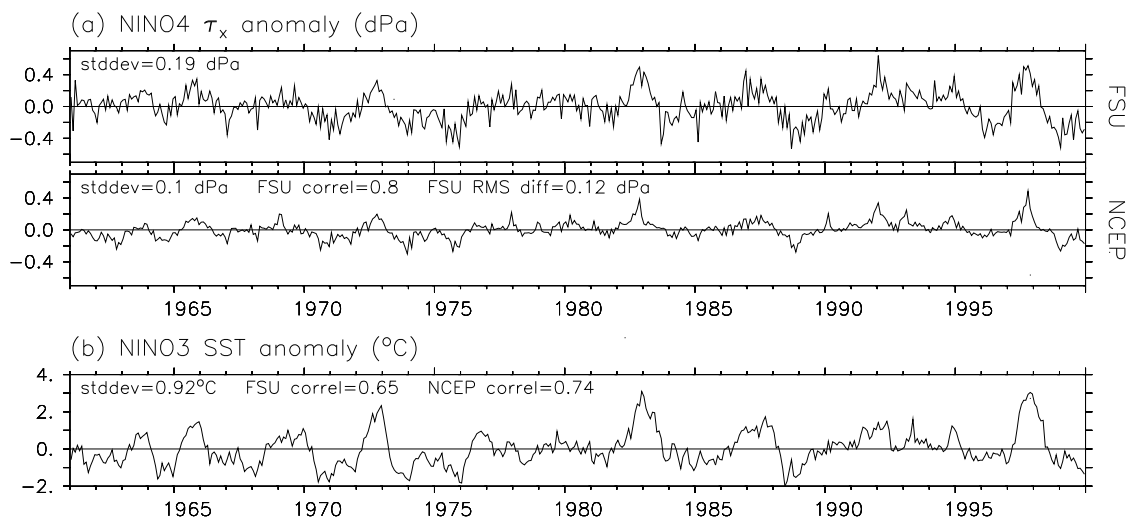
Figure 3.1: Timeseries of monthly-mean (a) zonal wind stress anomalies averaged over the NINO4 region (160°E–150°W, 5°S–5°N) and (b) SST anomalies averaged over the NINO3 region (150°W–90°W, 5°S–5°N). Anomalies are with respect to the 1961–1999 climatology. The standard deviation of each timeseries is indicated, followed by correlations and/or root-mean-square differences with the timeseries in the other panels.

forcing, nonlinearity, and noise on the observed wind stress, even (or perhaps especially) when the model is found to be incomplete. Model-building and evaluation thus represent the essence of the scientific method.

This study therefore derives statistical models from two different widely-used analyses. We assume the monthly-mean wind stress consists of three independent components: a seasonally-varying climatology, a linear response to SSTA, and random noise. After fitting this statistical model to the analyses for two different time periods, we investigate to what extent such a model actually reproduces the data. Particular attention is paid to the sizable residual that remains after SSTA dependence is subtracted from the stress anomalies, and prior hypotheses about this residual are tested.

3.2   Data

The data used in this study are the same as in the previous chapter. Fig. 3.1 shows timeseries of area-averaged monthly τ_x' and SSTA with respect to the 1961–1999 base period. The area averages comprise the regions of maximum variability for τ_x' (NINO4: 160°E–150°W, 5°S–5°N) and SSTA (NINO3: 150°W–90°W, 5°S–5°N). For both the FSU and NCEP wind stress products, τ_x' is well-correlated with SSTA, and ENSO events are stronger and have a longer period toward the latter half of the record. What is striking is that the RMS difference between the FSU and NCEP anomalies is of the same order as the stress anomalies themselves, and the correlation of FSU and NCEP with each other is not much larger than their correlation with SSTA. The FSU stress anomalies are stronger,

noisier, less correlated with SSTA, and have more persistent westerly peaks than NCEP. Prominent differences between the products are evident at the beginning of the record (1961–1965), when FSU indicates westerlies while NCEP shows easterlies. Differences are also apparent at the end of the record, particularly during the winter of 1991–1992 when FSU shows stronger westerly anomalies than NCEP, and in 1996 when FSU shows stronger easterly anomalies than NCEP. A more complete account of the differences between the FSU and NCEP products may be found in Chapter 2.

Several things are evident from Fig. 3.1. First, it is clear that subannual variance is an important component of τ'. Second, this subannual variability is probably not related to the large-scale monthly-mean SSTAs, which vary mostly on interannual time scales. Lastly, differences in τ' between the analyses are as apparent as changes between decades. This suggests any "real" changes in the stress anomalies will be difficult to extract from the "observed" changes, since the former are confounded by changes in the observing system and analysis methods. In this study, we focus not on the stress anomalies themselves, but instead on their relationship with SSTA. We hope to determine whether this relationship differs between the observational analyses, and whether there has been any change in this relationship in recent years.

As discussed in Chapter 2, most of the interannual variability of the wind stress is at key climatological "edges" where strong SST gradients exist; the warm pool/cold tongue boundary and the southern edge of the ITCZ are two such regions. Local nonlinearity may be important when these edges shift positions during ENSO events. It is therefore necessary to assess the adequacy of commonly-used linear models of the wind stress. To this end, we construct such a model and assess its validity.

3.3   Empirical bases for climate variability

This section reviews common methods for building empirical bases for observed climate variability, and then applies these methods separately to each data product and time period. Singular value decomposition (SVD) will provide a convenient basis for the covariability of SST and wind stress, while principal components analysis (PCA) will provide a basis for the part of the stress not linearly coupled to SST.

3.3.1   Singular value decomposition

Towards the development of the deterministic model, we briefly describe SVD and its use for finding coupled patterns in data. Further details are given by Bretherton et al. (1992), Newman and Sardeshmukh (1995), and Cherry (1996, 1997).

Let **X** be an $n \times p$ data matrix, whose rows represent snapshots of a data field at different times. The data values are denoted x_{li} where $l = 1, \ldots, n$ is the time index and $i = 1, \ldots, p$ is the space index. We assume **X** is centered in time, namely $\sum_{l=1}^{n} x_{li}/n = 0$ for all spatial gridpoints i. Let **Y** be another time-centered data matrix with dimensions $n \times q$, and let $'$ denote a matrix transpose. Then the cross-covariance of **X** and **Y** is given by the $p \times q$ matrix

$$\mathbf{C} \equiv \frac{\mathbf{X'Y}}{n-1} \tag{3.1}$$

By definition, SVD produces

$$\mathbf{C} = \widetilde{\mathbf{A}} \mathbf{D} \widetilde{\mathbf{B}}' \tag{3.2}$$

where nondimensional matrices are tagged with a tilde ($\sim$). $\mathbf{D}$ is a diagonal matrix of dimension $r \times r$, where $r \equiv \min(p, q)$. The diagonal elements of $\mathbf{D}$ are called the *singular values* of $\mathbf{C}$, denoted d_k for $k = 1, \ldots, r$. The matrices $\widetilde{\mathbf{A}}$ and $\widetilde{\mathbf{B}}$ have dimensions $p \times r$ and $q \times r$ and are unitary:

$$\widetilde{\mathbf{A}}' \widetilde{\mathbf{A}} = \widetilde{\mathbf{B}}' \widetilde{\mathbf{B}} = \mathbf{I} \tag{3.3}$$

where $\mathbf{I}$ is the $r \times r$ identity matrix. The columns of $\widetilde{\mathbf{A}}$ and $\widetilde{\mathbf{B}}$ are called the left and right *singular vectors* of $\mathbf{C}$, denoted $\widetilde{\mathbf{a}}_k$ and $\widetilde{\mathbf{b}}_k$.

Timeseries of singular vector expansion coefficients are given by the $n \times r$ matrices

$$\mathbf{X}^* \equiv \mathbf{X} \widetilde{\mathbf{A}} \tag{3.4}$$
$$\mathbf{Y}^* \equiv \mathbf{Y} \widetilde{\mathbf{B}} \tag{3.5}$$

Thus the first column of $\mathbf{X}^*$, call it $\mathbf{x}_1^*$, is the timeseries resulting from projection of the data $\mathbf{X}$ onto the first left singular vector $\widetilde{\mathbf{a}}_1$. Using the expansion timeseries, one constructs covariance matrices

$$\mathbf{C}_{x^*x^*} \equiv \frac{\mathbf{X}^{*\prime}\mathbf{X}^*}{n-1} \tag{3.6}$$

$$\mathbf{C}_{y^*y^*} \equiv \frac{\mathbf{Y}^{*\prime}\mathbf{Y}^*}{n-1} \tag{3.7}$$

$$\mathbf{C}_{x^*y^*} \equiv \frac{\mathbf{X}^{*\prime}\mathbf{Y}^*}{n-1} = \mathbf{D} \tag{3.8}$$

The last equality, which results from application of (3.1)–(3.5), shows that d_k is the covariance of the expansion timeseries $\mathbf{x}_k^*$ and $\mathbf{y}_k^*$, and that $\mathbf{x}_{k_1}^*$ and $\mathbf{y}_{k_2}^*$ are uncorrelated for $k_1 \neq k_2$.

One may define a "length" for $\mathbf{C}$ using the Frobenius norm

$$\|\mathbf{C}\|^2 \equiv \sum_{i=1}^{p} \sum_{j=1}^{q} c_{ij}^2 = \sum_{k=1}^{r} d_k^2 \tag{3.9}$$

where the second equality, shown by Strang (1988), is simply an application of the Pythagorean theorem. Now suppose one constructs synthetic timeseries $\mathbf{X}_N$ and $\mathbf{Y}_N$, using only the leading N pairs of singular vectors. Call the covariance matrix of these synthetic timeseries $\mathbf{C}_N$. The cumulative fraction of squared covariance accounted for the first N modes is then given by

$$\frac{\|\mathbf{C}_N\|^2}{\|\mathbf{C}\|^2} = \frac{\sum_{k=1}^{N} d_k^2}{\sum_{k=1}^{r} d_k^2} \tag{3.10}$$

It has been shown (Stewart, 1973) that SVD is in fact the *optimal* way to account for $\|\mathbf{C}\|^2$ with N pairs of patterns. In other words, the leading singular mode patterns $\mathbf{a}_1$ and $\mathbf{b}_1$ have expansion timeseries with the maximum possible covariance of any pair of patterns $\mathbf{a}$ and $\mathbf{b}$, and each successive mode has the maximum possible covariance of any

pair of patterns orthogonal to all earlier pairs. In this sense, SVD of the covariance matrix produces an efficient set of empirical "coupled modes." There is no reason to expect these modes to represent actual *physical* relationships between the data fields, except to the extent that these relationships impart strongly covariant structures in the data (Newman and Sardeshmukh, 1995).

For convenience, we transfer the physical units from the singular vector expansion timeseries to the singular vector patterns. It is convenient to define

$$\begin{aligned} \mathbf{S}_{x*}^2 &\equiv \operatorname{diag}(\mathbf{C}_{x*x*}) \\ \mathbf{S}_{y*}^2 &\equiv \operatorname{diag}(\mathbf{C}_{y*y*}) \end{aligned}$$

where the "diag" operator simply sets off-diagonal elements to zero. Pre(post)-multiplication of a matrix by $\mathbf{S}_{x*}$ then corresponds to multiplying the kth row (column) by the standard deviation of the kth expansion coefficient. Dimensional singular vector matrices $\mathbf{A}$ and $\mathbf{B}$, and nondimensional expansion coefficient matrices $\widetilde{\mathbf{X}}^*$ and $\widetilde{\mathbf{Y}}^*$, are then constructed as follows:

$$\mathbf{A} \equiv \widetilde{\mathbf{A}}\mathbf{S}_{x*} \tag{3.11}$$

$$\mathbf{B} \equiv \widetilde{\mathbf{B}}\mathbf{S}_{y*} \tag{3.12}$$

$$\widetilde{\mathbf{X}}^* \equiv \mathbf{X}^*\mathbf{S}_{x*}^{-1} \tag{3.13}$$

$$\widetilde{\mathbf{Y}}^* \equiv \mathbf{Y}^*\mathbf{S}_{y*}^{-1} \tag{3.14}$$

By construction, the nondimensional expansion coefficients $\widetilde{\mathbf{x}}_k^*$ and $\widetilde{\mathbf{y}}_k^*$ have unit variance, and cross-correlation

$$\widetilde{\mathbf{D}} \equiv \mathbf{S}_{x*}^{-1}\mathbf{D}\mathbf{S}_{y*}^{-1} \tag{3.15}$$

With these definitions, the singular value decomposition (3.2) takes the form

$$\mathbf{C} = \mathbf{A}\widetilde{\mathbf{D}}\mathbf{B}' \tag{3.16}$$

In summary, SVD efficiently partitions the covariance of $\mathbf{X}$ and $\mathbf{Y}$ into a particular set of patterns, namely the r columns of $\mathbf{A}$ and $\mathbf{B}$. The first column of $\mathbf{A}$ is paired with the first column of $\mathbf{B}$, the second with the second, and so on, with successive pairs exhibiting successively less temporal covariance between their respective expansion timeseries. The correlations of these paired timeseries are listed along the diagonal of $\widetilde{\mathbf{D}}$. All other pairings of $\mathbf{A}$ expansion timeseries with $\mathbf{B}$ expansion timeseries are uncorrelated. The patterns of $\mathbf{A}$ are mutually orthogonal but their expansion timeseries may be correlated; the same goes for $\mathbf{B}$.

3.3.2 Principal components analysis

PCA, also called empirical orthogonal function (EOF) analysis, is simply SVD of the data matrix $\mathbf{X}$:

$$\mathbf{X} = \widetilde{\mathbf{A}}_x \mathbf{D}_x \widetilde{\mathbf{B}}_x' \tag{3.17}$$

$$\widetilde{\mathbf{A}}_x' \widetilde{\mathbf{A}}_x = \widetilde{\mathbf{B}}_x' \widetilde{\mathbf{B}}_x = \mathbf{I} \tag{3.18}$$

$\mathbf{D}_x$ is a diagonal matrix of dimension $s \times s$, where $s \equiv \min(n, p)$. $\widetilde{\mathbf{A}}_x$ and $\widetilde{\mathbf{B}}_x$ have dimensions $n \times s$ and $p \times s$. The columns of $\widehat{\mathbf{B}}_x$ are orthonormal patterns, with expansion coefficients

$$\mathbf{X}_x^* \equiv \widetilde{\mathbf{A}}_x \mathbf{D}_x \tag{3.19}$$

From (3.18), it follows that the cross-covariance matrix of these expansion coefficients is

$$\frac{\mathbf{X}_x^{*\prime} \mathbf{X}_x^*}{n-1} = \frac{\mathbf{D}_x^2}{n-1} \tag{3.20}$$

and so the PCA expansion coefficients are uncorrelated. The expansion coefficient variances, given by the diagonal elements of $\mathbf{D}_x^2/(n-1)$, are sequentially maximized and sum to the total variance $\|\mathbf{X}\|^2/(n-1)$.

For convenience, we transfer the physical units from the expansion timeseries to the patterns using

$$\mathbf{B}_x \quad \equiv \quad (n-1)^{-1/2} \widetilde{\mathbf{B}}_x \mathbf{D}_x \tag{3.21}$$

$$\widetilde{\mathbf{X}}_x^* \quad \equiv \quad (n-1)^{1/2} \mathbf{X}_x^* \mathbf{D}_x^{-1} = (n-1)^{1/2} \widetilde{\mathbf{A}}_x \tag{3.22}$$

The nondimensional expansion coefficients so defined have unit variance. With these definitions, the principal components decomposition (3.17) takes the form

$$\mathbf{X} = \widetilde{\mathbf{X}}_x^* \mathbf{B}_x' \tag{3.23}$$

In summary, PCA efficiently partitions the variance of $\mathbf{X}$ into a particular set of patterns, namely the s columns of $\mathbf{B}_x$, with successive patterns exhibiting successively less temporal variance of their expansion timeseries. These patterns are mutually orthogonal and their expansion timeseries are uncorrelated.

3.3.3 SVD applied to the data

In this section we apply SVD to the data, following Gutzler (1993) and Syu and Neelin (1995). The singular vectors of SST will serve as a convenient set of basis vectors for the deterministic wind stress model of Section 3.4.

The anomalies of SST and wind stress are arranged as the rows of $\mathbf{X}$ and $\mathbf{Y}$ as in the last section. The first half of each row of $\mathbf{Y}$ contains τ_x' and the second half contains τ_y'. The 1961–1979 and 1980–1999 periods and the NCEP and FSU wind stress products are treated separately, giving four different cases. The time dimension is $n = 228$ for 1961–1979, and $n = 240$ for 1980–1999. The spatial matrix dimensions are $p = 494$, and $q = 494 \times 2 = 988$ for all cases.

The cumulative fraction of square covariance accounted for by the singular modes is shown in Fig. 3.2. The singular modes efficiently capture the covariation of SST and wind stress regardless of the dataset or time period, with the first 8 modes accounting for over 99% of the square covariance. That the gravest mode accounts for over 84% of the square covariance demonstrates that to first order, ENSO is a standing oscillation. Interestingly, the modes account for the FSU/SSTA covariance more easily than they account for the NCEP/SSTA covariance.
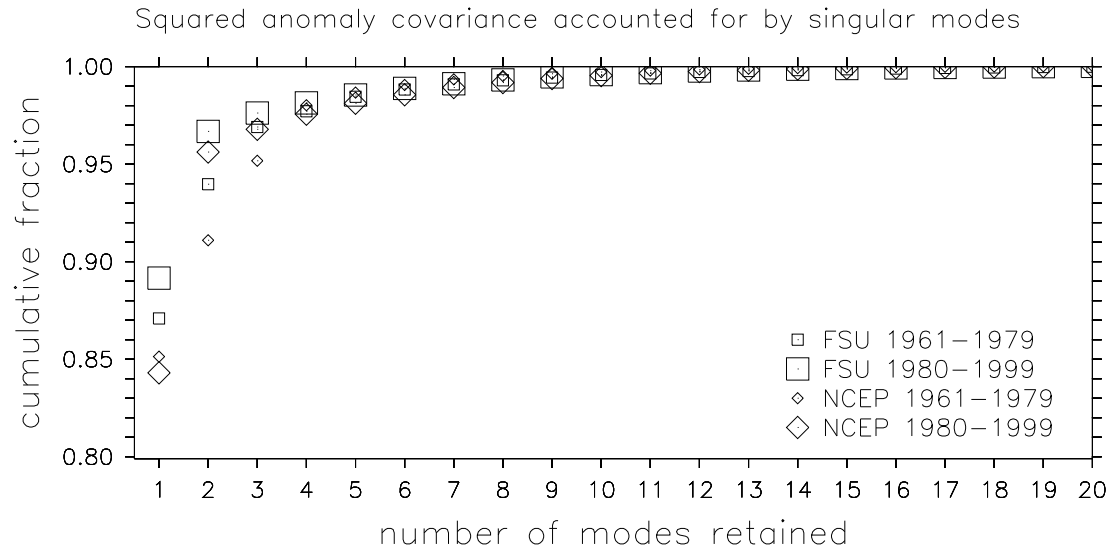
Figure 3.2: Cumulative fraction of squared covariance of monthly-mean tropical Pacific SST and wind stress anomalies, accounted for by the first 20 singular modes.
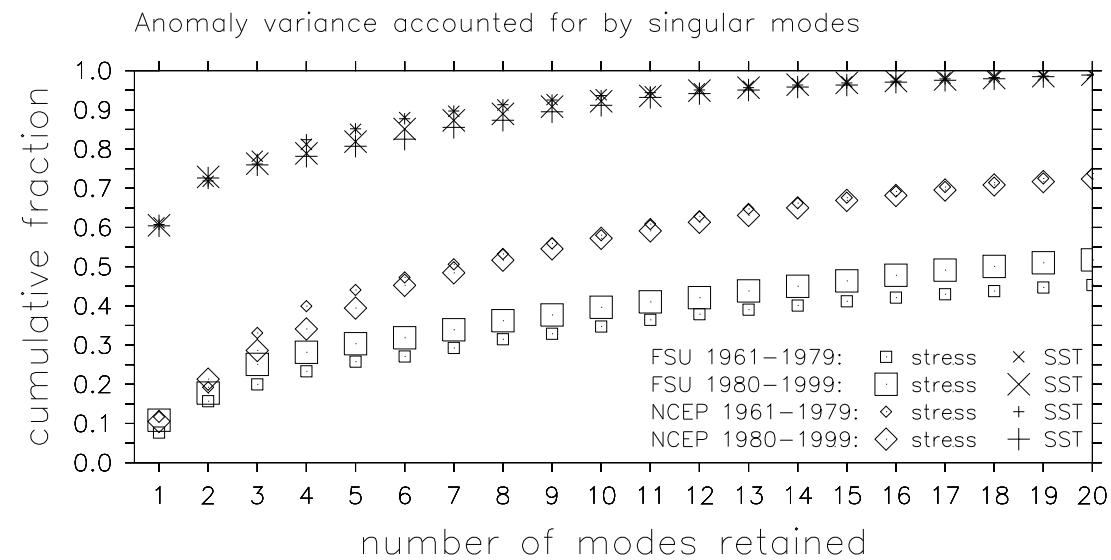
Figure 3.3: Cumulative fraction of variance of monthly-mean tropical Pacific SST and wind stress anomalies, accounted for by the first 20 singular modes.
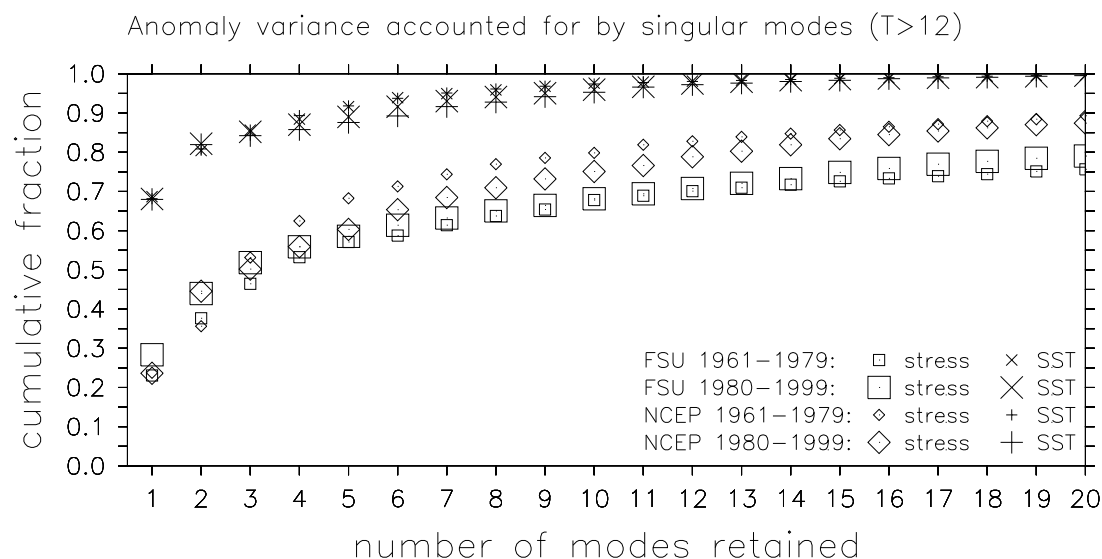
Figure 3.4: Cumulative fraction of interannual variance of tropical Pacific SST and wind stress anomalies, accounted for by the first 20 singular modes.

The singular modes are less efficient at capturing the variances of the fields (Fig. 3.3). The first 8 modes account for more than 85% of the SST variance, but less than 35% of the stress variance for FSU and less than 50% of that for NCEP. This is partly because most of the stress variance occurs at subannual periods irrelevant to SST changes. When the timeseries are filtered to retain only periods greater than one year, the stress variance captured by the first 8 modes increases substantially (Fig. 3.4). However, even on interannual time scales a large fraction of the wind stress does not covary with SSTA. With regard to the explained variance, there is a bigger difference between the FSU and NCEP products than between the 1961–1979 and 1980–1999 time periods, with the SVD capturing less of the total variance in FSU. This is related to the "noisiness" of the FSU stress, which was evident in Fig. 3.1.

The singular vectors $\mathbf{a}_1$, $\mathbf{b}_1$ and $\mathbf{a}_2$, $\mathbf{b}_2$ are shown for each dataset and period in Fig. 3.5. The expansion timeseries for mode 1 (not shown) track standard ENSO indices, such as the NINO3 SSTA and NINO4 τ_x' of Fig. 3.1. In its positive phase, mode 1 is reminiscent of an El Niño event. There is equatorial warming in eastern Pacific, with westerly and equatorward wind anomalies in the central Pacific which converge onto the warm SSTA. Weak easterly anomalies are present over the region of strongest warming in the east, but there are almost no zonal stress anomalies near the coasts.

The SST and wind stress patterns of mode 2 are roughly in quadrature with those of mode 1. Therefore any large-scale propagation of anomalies will be evident in the temporal phasing of the mode expansion coefficients. Fig. 3.6 shows the correlation between the expansion timeseries of mode 1 and those of lagged mode 2. Interestingly, there is a substantial change in the lead/lag relationship between 1961–1979 and 1980–1999. For the earlier period, there is a tendency for the SST pattern of mode 2 to appear 10 months after
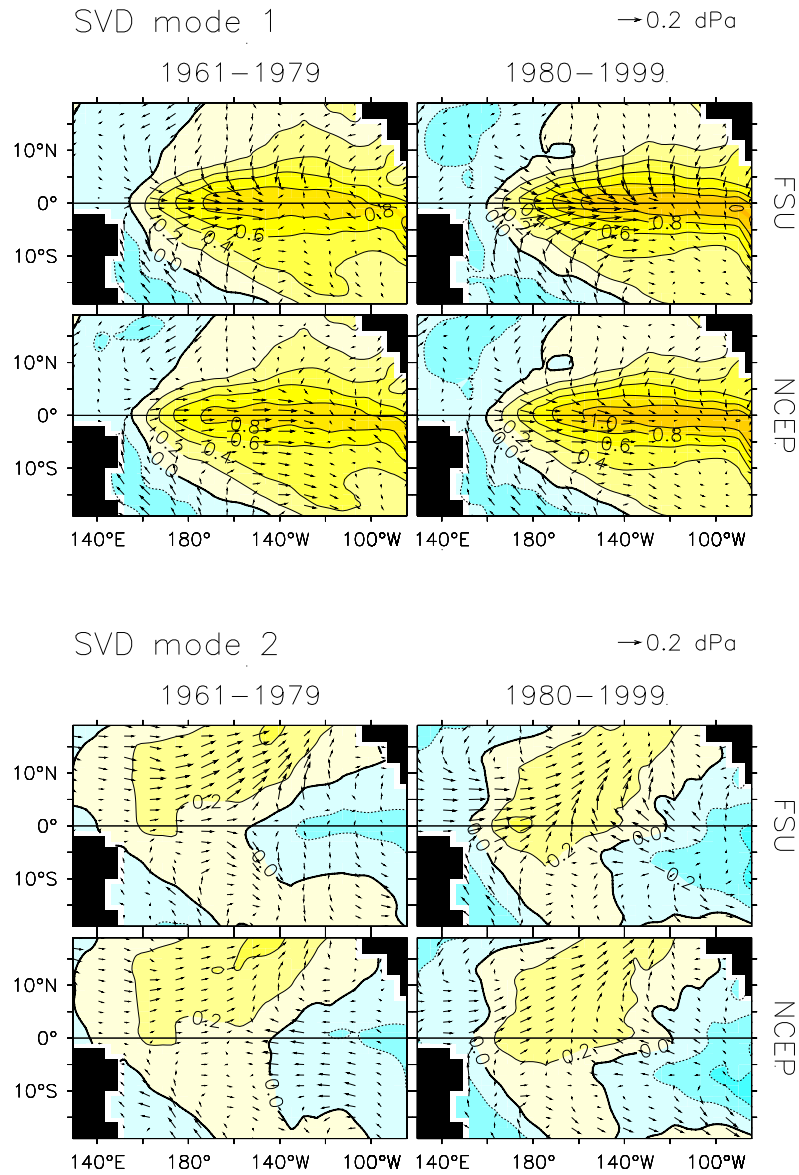
Figure 3.5: Leading singular vectors of the observed covariance of SST (°C) and wind stress anomalies (scale vector indicated).
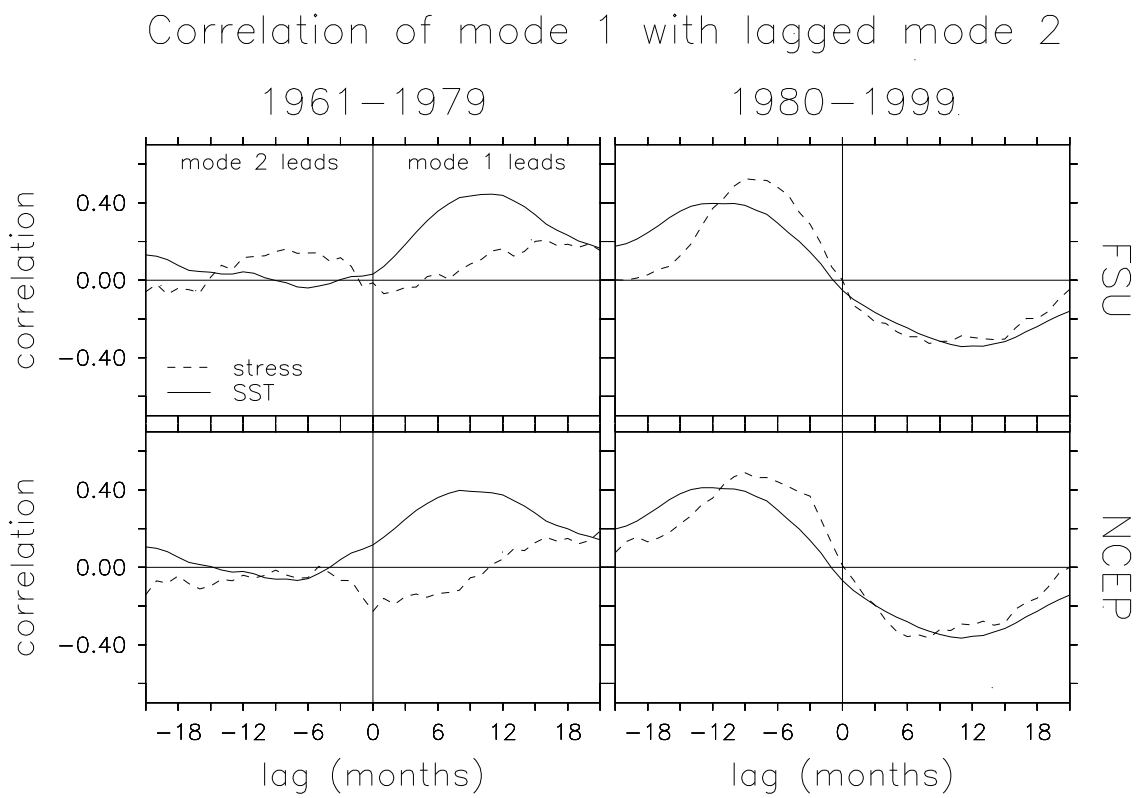
Figure 3.6: Correlation of singular vector expansion coefficients of mode 1 with those of lagged mode 2, for SST anomalies (solid) and wind stress anomalies (dashed).

mode 1, implying westward propagation of SST following the peaks of El Niño and La Niña. For the latter period, the propagation tendency reverses to eastward: mode 2 appears 11 months before mode 1, and again with opposite sign 11 months following mode 1, implying propagation of SST both before and after the peaks of ENSO events. This apparent change in the zonal propagation of SST anomalies in the late 1970s has been noted by Wang (1995) and Trenberth and Stepaniak (2001). It is not yet clear whether this signals a fundamental change in ENSO behavior; perhaps due to the brevity of the observational record, the change in propagation directions is not statistically significant (Harrison and Larkin, 1998). In any case, comparable changes in propagation direction appear to have occurred earlier in the 20th century (Trenberth and Stepaniak, 2001).

What is striking about Fig. 3.6 is that the propagation of SST anomalies during 1961–1979 is not mirrored in the wind stress over that period. During 1980–1999, on the other hand, there is clear southeastward propagation in the wind stress from the northwestern tropical Pacific to the central Pacific just south of the equator: mode 2 appears 8 months prior to mode 1 and again, with opposite sign, 9 months after mode 1.

The basic features of these correlations are similar between the datasets. While this is partly because the same SST product was used in both cases, it is reassuring to see that the primary lag relationship between the modes does not depend on which stress analysis is used.

We now have an empirical basis for the covariation of SST and wind stress, which captures a large fraction of the ENSO signal including the propagation of large-scale anomalies. We shall use this basis in the next section to construct a linear model of the stress anomalies.

3.4   Model for monthly-mean stress anomalies

On monthly time scales, tropical wind stress variability resembles a stochastic boundary-value problem. A reasonable linear model for the stress anomalies is

$$\mathbf{Y} = \mathbf{XW} + \mathbf{E} \tag{3.24}$$

where $\mathbf{W}$ is a $p \times q$ matrix of weights multiplying the instantaneous SST field, and $\mathbf{E}$ is an $n \times q$ matrix of shocks. A priori, we assume these shocks e_{lj} are $NID(0, \sigma_j^2)$; that is, normally and independently distributed in time, with zero mean and a variance that is stationary in time. The shocks may, however, be spatially correlated. We shall reexamine the validity of these assumptions once the model has been fitted.

3.4.1   Deterministic component

Our first task is to estimate the SST weights using the observations. Given our assumptions about the errors, we may use linear regression to help determine $\mathbf{W}$. There are not enough observations to regress each stress point directly onto all SST points, so we proceed by regressing the stress anomalies onto only the "coupled" part of the SST anomalies. Recalling that SVD provides an orthogonal basis that optimally captures the covariation of SST and wind stress anomalies, we truncate the mode expansion to filter

out SSTAs irrelevant to the covariation. A model for the stress data based on the leading N singular vectors of SST anomalies is

$$\mathbf{Y} = \widetilde{\mathbf{X}}^*_N \mathbf{R}_N + \mathbf{E}_N \tag{3.25}$$

where $\widetilde{\mathbf{X}}^*_N$ is the truncated $n \times N$ matrix of nondimensional SST singular vector expansion coefficients, $\mathbf{R}_N$ is the $N \times q$ matrix of weights, and $\mathbf{E}_N$ is the sum of the shocks and the truncation error.

Assuming the truncation error is $NID(0, \sigma_j^2)$, we can estimate the deterministic stress at each gridpoint by linear regression:

$$\widehat{\mathbf{Y}}_N \equiv \widetilde{\mathbf{X}}^*_N \widehat{\mathbf{R}}_N \tag{3.26}$$

$$\widehat{\mathbf{R}}_N \equiv \left(\widetilde{\mathbf{X}}^{*\,\prime}_N \widetilde{\mathbf{X}}^*_N\right)^{-1} \widetilde{\mathbf{X}}^{*\,\prime}_N \mathbf{Y} \tag{3.27}$$

where a "hat" tags matrices estimated from the data. An estimate of the shocks is given by the matrix of residuals

$$\widehat{\mathbf{E}}_N \equiv \mathbf{Y} - \widehat{\mathbf{Y}}_N \tag{3.28}$$

If our assumptions about the shocks and truncation error are valid, then the stress estimate (3.26) is *optimal* for the N modes in that it minimizes the sum of square residuals $\left\|\widehat{\mathbf{E}}_N\right\|^2$ over the data record.

Next we must select the number N of retained modes. To borrow from Einstein, things should be made as simple as possible, no simpler. We therefore build up the model in steps, adding predictors only if they clearly improve the simulation. To ensure that the stress has a smooth spatial dependence on SST, we regress the stress onto the same set of SST modes at all gridpoints. At each point, we quantify the misfit of the N-mode model using the sum of square errors (SSE):

$$\mathrm{SSE}_N = \sum_{l=1}^{n} (y_{jl} - \widehat{y}_{jl})^2 \tag{3.29}$$

where y_{jl} is the observation and $\widehat{y}_{jl}$ is the estimate, using the only the gravest N modes, of the wind stress at a particular gridpoint j and time l.

Now consider two models, one a regression onto N modes and the other a regression onto $N + k$ modes. For the regression model, it will always be the case that $\mathrm{SSE}_{N+k} < \mathrm{SSE}_N$. To check if this reduction in SSE is significant, we examine the ratio

$$f = \frac{(\mathrm{SSE}_N - \mathrm{SSE}_{N+k})/k}{\mathrm{SSE}_{N+k}/(n - 1 - N - k)} \tag{3.30}$$

Under the hypothesis H_0 that the extra k modes are useless as predictors, the numerator and denominator of (3.30) will be independent estimates of the true variance of the random shocks. In this case f will refer to an F distribution with k and $n - 1 - N - k$ degrees of freedom. We define the *significance* as the probability, given H_0, that f could lie as far as it does from unity. If the significance is small, then we may confidently reject H_0 and

Table 3.1: Number of modes retained in each statistical atmosphere model, with the percent of total square covariance, SST anomaly variance, and stress anomaly variance that project onto the singular vectors, and the percent of stress anomaly variance captured by the regression model.

	1961–1979		1980–1999	
	FSU	NCEP	FSU	NCEP
number of modes	4	5	3	5
% square covariance	97.7	98.7	97.6	98.1
% SSTA variance	81.2	85.2	76.3	80.7
% τ' variance				
singular vectors	23.3	44.1	25.1	39.4
regression	12.6	23.0	13.9	19.9

conclude that the extra k modes (taken together) are useful predictors at the gridpoint of interest. We shall consider the change in SSE at a gridpoint to be significant when a two-tailed F test rejects H_0 with 99% confidence.

Using this definition for "significant model improvement" by a set of modes at a single gridpoint, we shall accept a set of modes only if they *significantly improve the model at more than half of the gridpoints.* One can then compute the appropriate number of modes to include using the following algorithm:

1) Begin with $N = N'' = 0$.

2) Determine the minimum number N' of additional SST modes required to produce a significant change in SSE at more than half of the stress gridpoints.

3) If $N' \leq 3$ then set $N = N + 1$, $N'' = N'$, and return to step 2.

4) Set $N = N + N''$ and stop.

This recipe ensures that predictors are included in the model if and only if they significantly improve the model fit, either by themselves or in a small group. Note that if the residual is not $NID(0, \sigma_j^2)$ then the F test will not be strictly valid, and the above procedure may add too many modes to the model. If the model assumptions are not severely violated, the problem can be addressed by increasing the gridpoint confidence level or increasing the number of gridpoints at which significant improvement is required. Otherwise a more sophisticated model may be necessary.

Following the recipe outlined above gives the models summarized in Table 3.1. These models account for a large fraction of the SSTA/τ' covariance and the SSTA variance in the data, but account for less than half of the τ' variance. Clearly most of the stress anomaly is not linearly related to SSTA; this part will be dealt with later.

The first two modes of the deterministic model are shown in Figs. 3.7–3.8 for each dataset and period (SST patterns are repeated from Fig. 3.5). These figures, plus those for higher modes, succinctly represent the entire linear model: projection of an SSTA onto these patterns produces the τ' shown.

For mode 1, the wind stress patterns look very similar to regressions onto NINO3 SST anomalies (Chapter 2), since the SST predictor for this mode has a large loading in
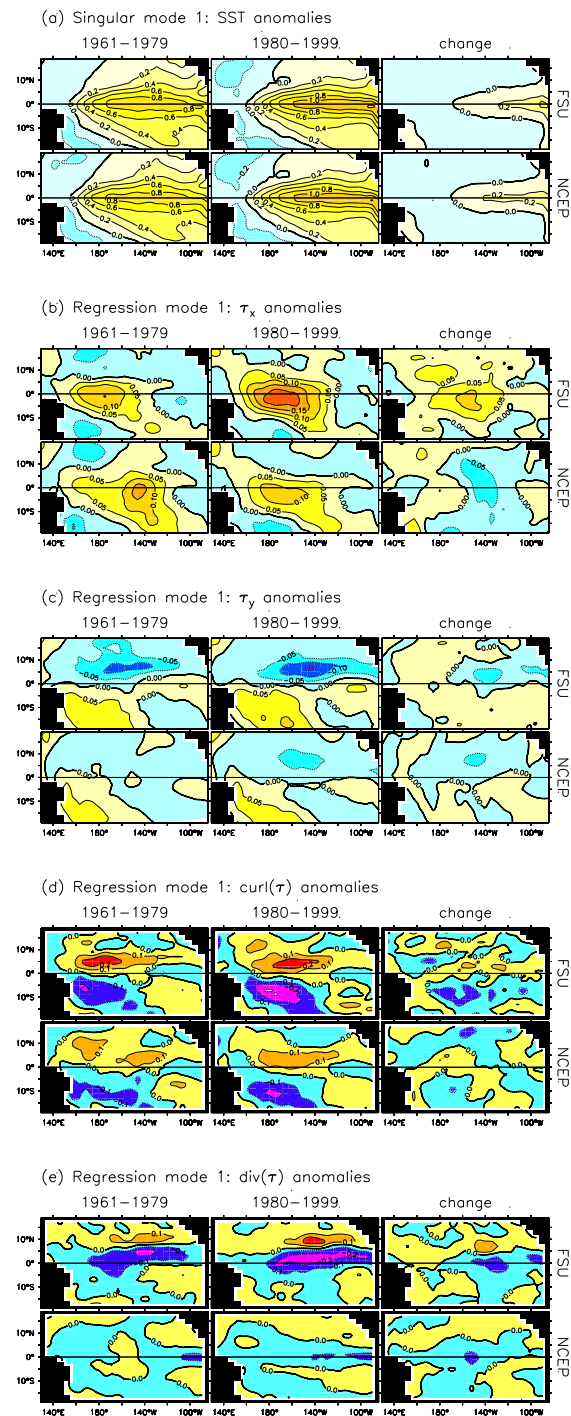
Figure 3.7: Mode 1 of the deterministic wind stress model. In this model, projection onto the (a) SSTA singular vector (°C) produces the corresponding anomalous (b) zonal stress (dPa), (c) meridional stress (dPa), (d) stress curl (0.001 dPa km^{-1}), and (e) stress divergence (0.001 dPa km^{-1}).
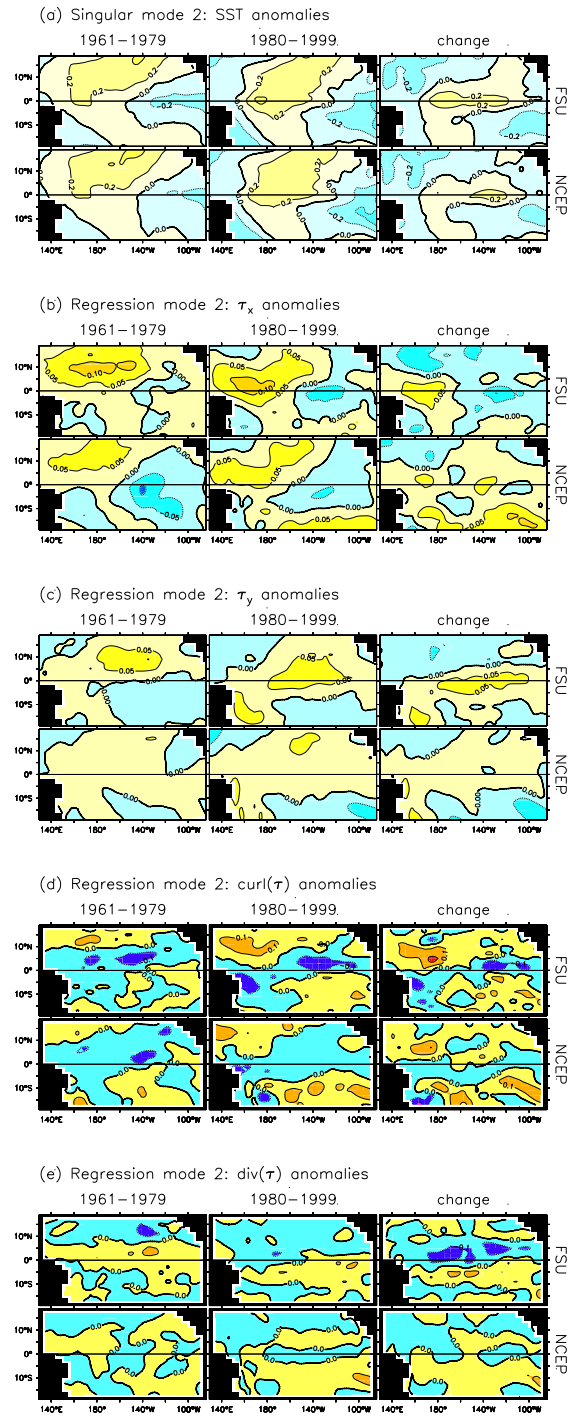
Figure 3.8: As in Fig. 3.7, but for mode 2 of the deterministic wind stress model.

the NINO3 region. The stress response consists of equatorial westerlies and off-equatorial easterlies in the west/central basin, weak easterlies near the eastern boundary, northerlies spanning the northern tropical Pacific, and southerlies across the southwest and equatorial southeast Pacific. There is cyclonic stress curl off-equator in the central basin, with the curl closer to the equator in the north than in the south. The stress response shows anomalous convergence equatorward of the ITCZ and SPCZ, and anomalous divergence poleward of these convergence zones.

There are several differences between the FSU and NCEP responses for mode 1. At the equator, the zonal stress response is weaker in the west Pacific in NCEP than in FSU; NCEP also shows a prominent peak near 145°W during 1961–1979 which is not evident in FSU. NCEP gives weaker meridional stress and convergence anomalies, especially in the vicinity of the climatological convergence zones. The two products also disagree as the nature of changes in the stress response between 1961–1979 and 1980–1999. FSU indicates a strengthening of the τ'_x response, with increased convergence in the equatorial eastern Pacific, while NCEP shows more of a weakening and a westward shift, with little change in the convergence in the east but instead increased convergence in the western and central Pacific.

The stress response for mode 2 is largely in quadrature with that for mode 1, partly due to the orthogonality constraint on the SSTA predictor pattern. For mode 2 there are westerlies in the northwest, and easterlies on and south of the equator in the east. Southerlies appear at and north of the equator, and northerlies appear in the southeast. The FSU and NCEP products again show large differences. The stress response for mode 2 is generally stronger in FSU, except during 1961–1979 when NCEP shows strong easterlies near 140°W. Between 1961–1979 and 1980–1999, FSU indicates a strengthening of the westerly response in the western equatorial Pacific and a weakening in the east, with stronger southerlies along the equator. NCEP shows somewhat smaller and less coherent changes.

By including mode 2 and higher modes, the statistical model can represent the gross wind stress response to SST anomalies, including large-scale propagating features. In summary, the deterministic part of the wind stress anomaly is obtained as follows:

1) Project the SST anomaly field $\mathbf{x}$ onto the leading N singular vectors of SST.

2) Divide through by the variance of the SST expansion coefficients to yield N predictors $\widetilde{\mathbf{x}}^*$.

3) Estimate the stress field from the predictors using the regression model.

In matrix form, the deterministic stress estimate is

$$\widehat{\mathbf{y}}_N = \mathbf{x}\mathbf{A}_N\mathbf{S}_{x^*}^{-2}\widehat{\mathbf{R}}_N \tag{3.31}$$

where $\mathbf{x}$, $\mathbf{A}_N$, and $\mathbf{S}_{x^*}$ have units of °C, and $\widehat{\mathbf{R}}_N$ has units of dPa (dynes cm^{-2}). A comparison of this model with a simpler version used by other authors is given in Appendix A.

3.4.2   Analysis of the residual

Having fit the deterministic model, we now ask to what extent the underlying assumptions are truly valid. In particular, we check whether the residual is really Gaussian noise with stationary variance, as assumed in the regression model. To do this, we obtain the residual stress by subtracting the deterministic model simulation from the data. This residual consists mostly of high-frequency components. It is quite possible that this "noise" plays an important role in the tropical climate system, since it accounts for a large fraction of the total stress variance (Table A.1).

Independence

The regression model assumes that the errors in the wind stress at each point are independent. To check this assumption we examine whether the residual is really uncorrelated in time. The autocorrelation of the residual stress at a lag of one month (not shown) is found to be rather large (exceeding 0.3) near the equator during 1980–1999.

Thus the residual at each point is not simply random from one month to the next. This suggests that the wind stress anomalies may not be a simple linear function of the large-scale SST anomalies. Possible sources of the autocorrelation in the residual include omitted explanatory variables (such as atmospheric moisture, which follows convection rather than SST), an incorrect functional form (e.g. a nonlinear rather than linear dependence on SST), or a combination of both (e.g. nonlinearity interacting with seasonal movements of the tropical convergence zones).

The lack of independence in the residual suggests that more information could be extracted by using a nonlinear or seasonally-dependent statistical model, or by including more predictor variables besides SST. It also indicates that the variance estimates used in the F-test for "significant model improvement" in the last section may be unreliable, leading to too many modes being accepted into the model. Fortunately, the estimates of the regression coefficients are unbiased even in the presence of serial correlation. Thus the model can still be useful, provided the number of accepted modes is sufficiently limited by the other criteria in the acceptance algorithm. Furthermore, our main goal is to correctly *partition* the deterministic and stochastic components and create realistic models for each. The mode selection algorithm must walk a tightrope between accepting too many modes, which would overfit the deterministic model, and accepting too few modes, which would waste information and possibly contaminate the stochastic model.

Normality

The second assumption of the regression model is that the residual at each gridpoint is normally distributed. To check this we use the powerful Shapiro and Wilks's W-test, Applied Statistics Algorithm AS 181 (Royston, 1982). The *significance* of this test is the probability that the test statistic, W, would be as extreme as observed if the data really were normally distributed. A small value of the significance at a gridpoint implies that the residual is probably non-normal at that point.

Significant non-normality is evident in both stress components (not shown), near the dateline and in scattered patches around the basin. This again suggests that a nonlinear

model of the stress may be justified. Two key nonlinearities could be included. The first is the quadratic dependence of the wind stress on wind speed, which in regions of strong trade winds tends to skew stress events toward extreme easterly values. The second is the zonal shift in anomalous trade winds observed during ENSO events, which is likely the result of the dependence of convection on thresholds of total SST. Zonal shifts in convection, which locally appear as nonlinearities, tend to skew the stress towards easterly stress extremes in the western Pacific, and westerly stress extremes in the central/eastern Pacific.

Stationarity

To test whether the variance is constant through time at each gridpoint, we must check whether subsets of the data have variances which are consistent with the overall variance of the dataset. In particular we examine the residual zonal stress averaged over the equatorial band, 2°S–2°N.

To test whether the residual variance is a function of the annual cycle, we bin the data by calendar month, and compute the ratio of monthly binned variances to the overall variance (Fig. 3.9). In each case, the local significance test rejects substantially more than 1% of the points at the 0.01 level. If the null hypothesis were true, the chance of this many local tests being rejected would be small: Fig. B.1 indicates this chance would be less than 5% (except for FSU 1980–1999, which would be less than 30%). This suggests the residual variance is not constant throughout the year at many gridpoints. In the western central Pacific, the variance is particularly strong during boreal winter and spring, and weak during boreal summer and fall.

To check whether the variance changes slowly through time, we bin the data by year and calculate the variance of the data in each of the bins. The ratio of yearly binned variances to the overall variance is shown in Fig. 3.10. Contours surround points where the hypothesis of stationarity of the residual variance is rejected at the 0.01 level, according to a two-tailed F test. Again, the local significance test rejects substantially more than 1% of the points at the 0.01 level. The probability of this many local tests being rejected, if the null hypothesis were true, would be small (less than 5%, Fig. B.1). This suggests that the residual subannual variance is nonstationary from year to year at some of the gridpoints.

Nonstationarity will cause the regression to overfit the noisy periods during boreal spring and the 1960s and 1980s, and underfit the quiet periods during boreal summer and the late 1970s and early 1990s. It is possible that the nonstationarity and non-normality of the residual are related, through some nonlinearity of the wind stress dependence on SST. If this is the case, then a nonlinear transformation applied to the data might improve the model. In the interest of simplicity, however, we shall proceed with the fully linear version, having noted its problems. While significant, the nonstationarity of the residual variance is probably not strong enough to greatly affect the regression model. The model fit should still be accurate, since the SST predictors are only slightly skewed.

Lag correlation with SST anomalies

As noted by Syu and Neelin (1995), the deterministic model acts like a low-pass filter for the wind stress, passing only variability linearly coupled to the slowly-varying SST field.

Figure 3.9: Ratio of binned monthly standard deviation to the standard deviation of the entire residual τ'_x timeseries at the equator. Warm colors indicate above-average variance, cool colors below-average variance. Contours surround points where the hypothesis of stationarity of the residual variance is rejected with 99% confidence, according to a two-tailed F test. Points within solid and dashed contours are rejected for having too much and too little variance, respectively. Labels at the upper-right indicate the fraction of points rejected by the F test.
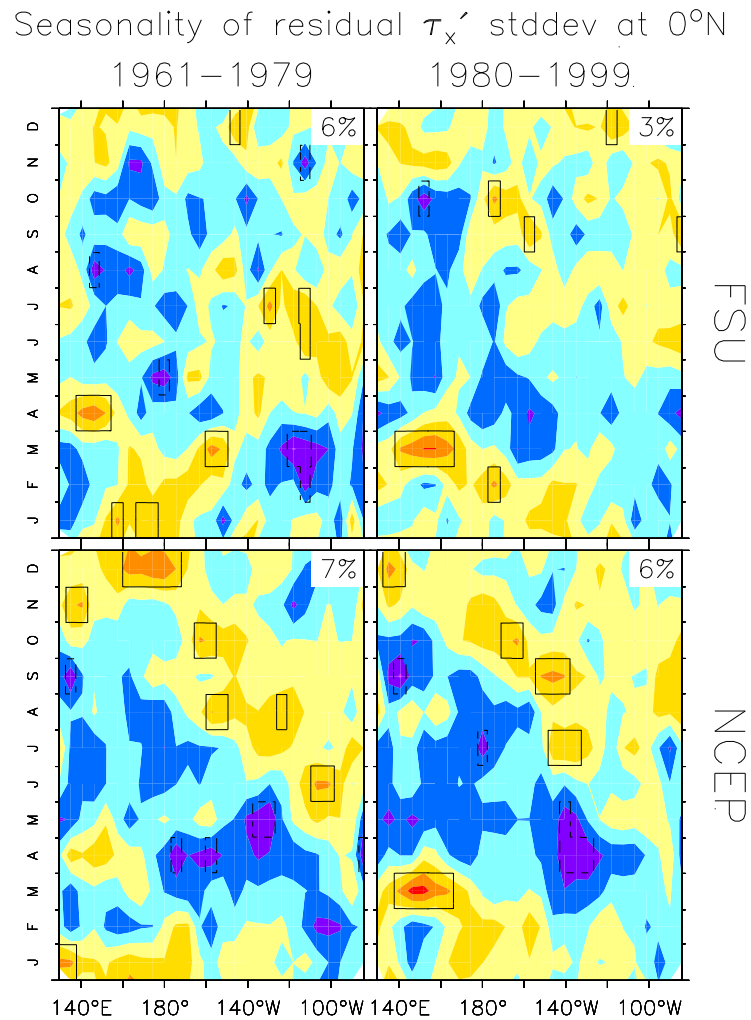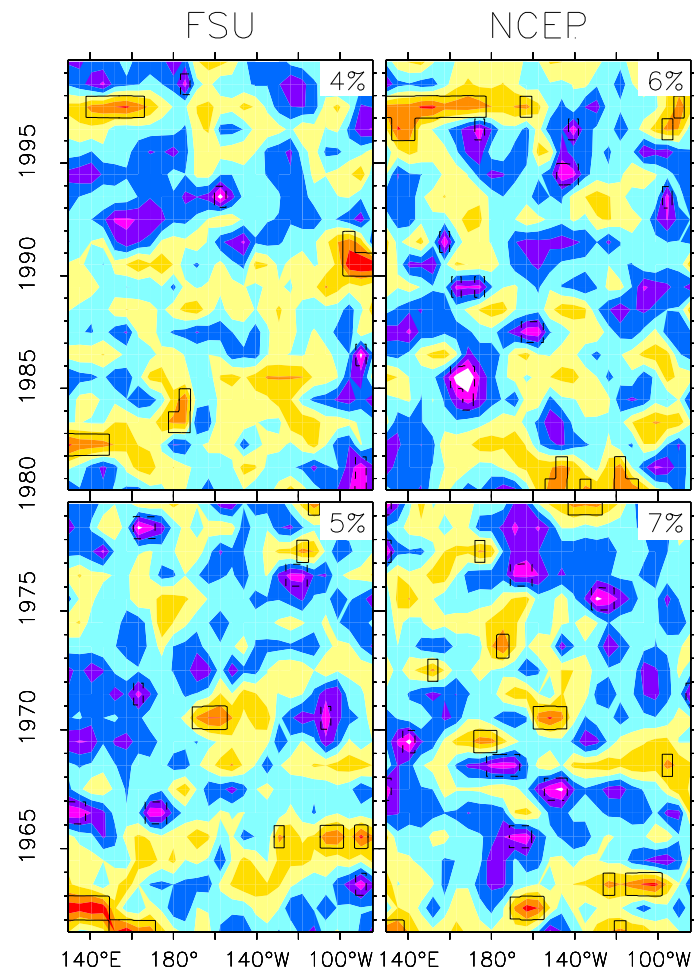
Figure 3.10: Ratio of running annual standard deviation to the standard deviation of the entire residual τ'_x timeseries at the equator. Otherwise as in Fig. 3.9.

Some low-frequency components are present in the residual, however. In particular, the model tends to underestimate the westerly stress response to the strong El Niño event of 1982–83, and misses the easterly stress events in the western Pacific during 1966-67 and 1983–84. It is possible that nonlinearities in convective heating and wind stress emerge at these times, leading to coupling between the residual stress and SST.

In the coupled context, the noisy component of the stress can feed back on the deterministic stress by affecting SST. An unusually strong random westerly wind burst in the west Pacific, for example, would tend to induce an eastward advection of the warm pool and a deepening of the equatorial thermocline in the eastern basin. As a result, after some lag the equatorial SST would tend to increase, the wind stress would respond "deterministically" with a westerly wind anomaly over the central Pacific, and the coupled system could amplify the perturbation into a warm event. One would therefore expect residual stress anomalies to lead SST anomalies, by some characteristic time associated with the transient growth in the coupled system.

Fig. 3.11 shows how equatorial SST anomalies are linked to the residual zonal stress in the western Pacific. The lag correlations are rather weak, since the residual is noisy, but they are statistically significant (at the 0.05 level) over large regions of the diagram. Although Fig. 3.11 indicates that residual wind bursts in the west tend to accompany reversals of the SST-induced stress over the entire basin, it says nothing about cause and effect. One plausible hypothesis is that stochastic wind events in the west Pacific help to bring about ENSO transitions. An alternative hypothesis is that during the transitions between events, the stress anomalies in the west Pacific are more nonlinear, or depend more on smaller-scale SST anomalies. Without dynamical modeling experiments or further physical evidence, it would be difficult to decide which hypothesis is correct.

Nevertheless it is clear that the model and residual stresses are linked in time. In all four cases, westerly stress events in the western equatorial Pacific are preceded 6 to 18 months earlier by cold SSTA in the central Pacific, and followed 2 to 12 months later by warm SSTA in the central and eastern Pacific. The linkage is stronger for FSU than NCEP, and is stronger for 1980–1999 than for 1961–1979. There is tantalizing evidence that the residual stress in the west is related to small-scale anomalies in the zonal SST gradient at zero lag: all cases show anomalously warm SST east of the reference point, and anomalously cold SST west of the reference point. One interpretation is that local coupled feedbacks in the west Pacific amplify random small-scale stress anomalies; these amplified anomalies could then induce Kelvin wave disturbances which give rise to ENSO events through large-scale feedbacks. This picture is consistent with emerging views of possible links between the Madden-Julian Oscillation and ENSO (Zhang et al., 2001a).

3.4.3 Stochastic model

It is important to note that "not knowing the properties of the noise" is very different from "not having any noise." Various types of noise can sustain a damped ENSO, giving rise to sustained interannual variability, whereas in the absence of noise such a system would be quiescent. Stochastic forcing not only feeds energy into a system but also acts as a sort of dynamical averager—stirring up variability that visits a broader range of system dynamics, with random excursions away from asymptotic fixed points and limit cycles. A
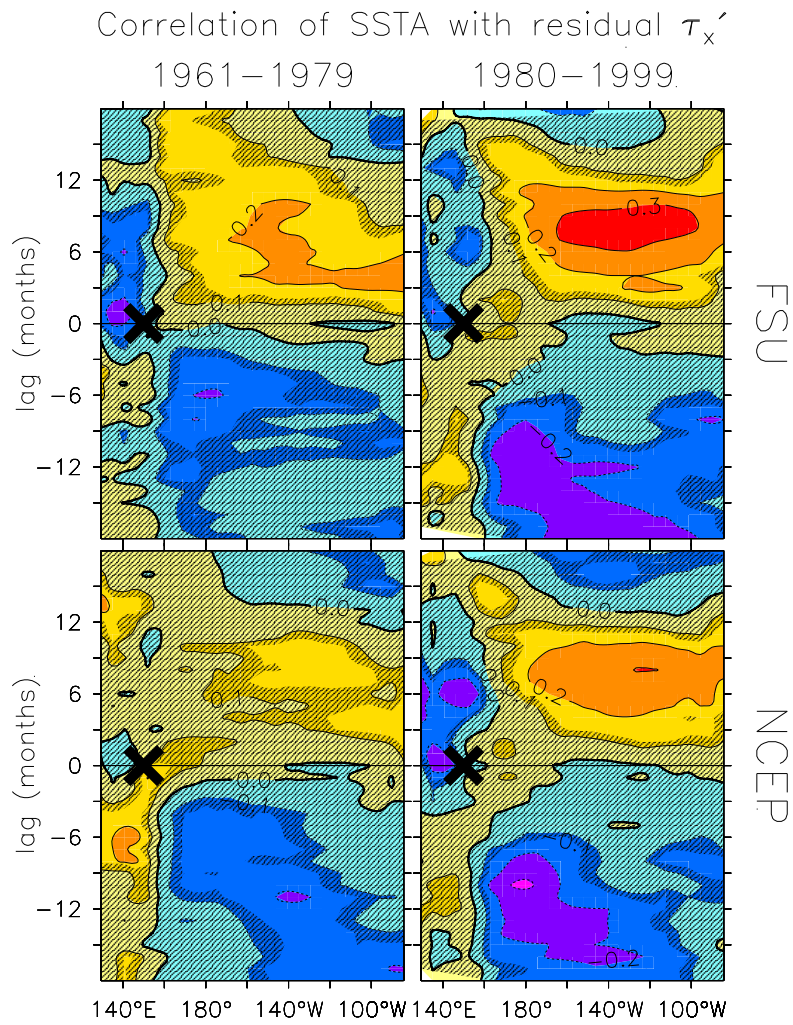
Figure 3.11: Correlation of the lagged equatorial SST anomaly with the residual zonal stress anomaly at a point (marked) on the equator at 150°E. Hatching masks values exceeded by more than 5% of correlations between white noise and the SST anomaly.
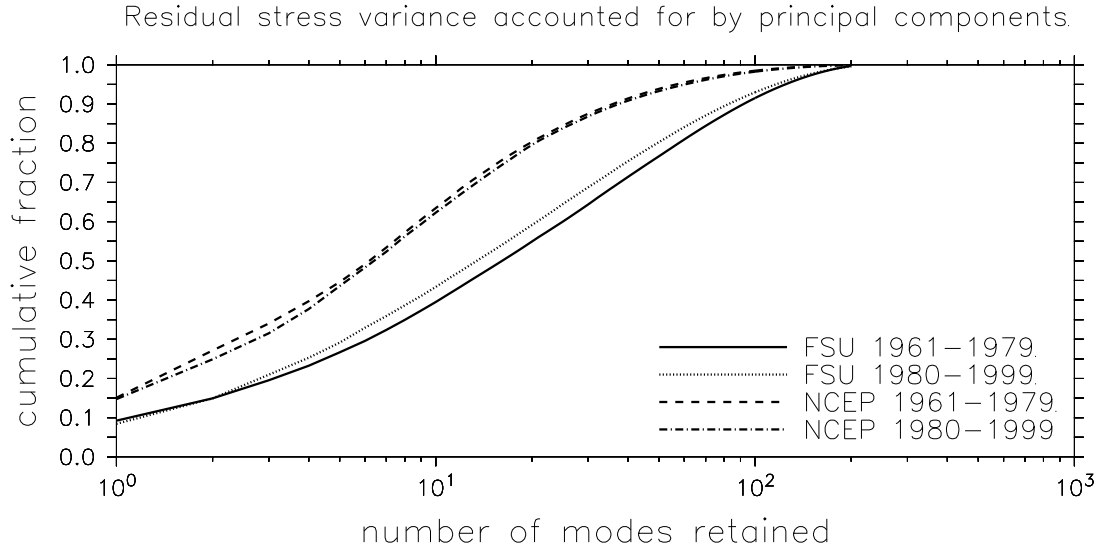
Figure 3.12: Cumulative fraction of residual variance of monthly-mean tropical Pacific SST and wind stress, accounted for by the principal components of the residual. The residual consists of the original data minus the deterministic model estimate.

model with stochastic forcing may also exhibit different sensitivity to parameter changes, since bifurcations and linear modes get smeared out and slow transients begin to dominate the system dynamics.

For these reasons, having a simple, gross estimate of the noise may be better than having no noise at all. Although part of the residual stress in the data may have arisen from observational and analysis errors, there is clearly subannual-scale variability present in the tropical climate system, and while the exact form of the noise is uncertain, one can still model gross aspects like its variance and spatial patterns. In lieu of a more sophisticated model of the residual, we shall approximate it as autocorrelated ("red") noise.

To account for spatial correlations in the residual stress, we decompose $\widehat{\mathbf{E}}_N$ into its principal components using (3.23):

$$\widehat{\mathbf{E}}_N = \widehat{\widetilde{\mathbf{E}}}^*_{N,\widehat{e}} \mathbf{B}'_{N,\widehat{e}} \tag{3.32}$$

The cumulative fraction of residual variance accounted for by the principal components is shown in Fig. 3.12. The fact that the residual has so many degrees of freedom is consistent with the hypothesis that it is mostly noise. The principal components account for the residual variance more efficiently for NCEP than for FSU. For NCEP, over half the variance is accounted for by 7 modes, 90% by 40, and over 99% by 120. For FSU, over half the variance is accounted for by 17 modes, 70% by 40, and over 99% by 180. For NCEP there is little difference in the representation efficiency between 1961–1979 and 1980–1999, while for FSU the efficiency is somewhat greater during the latter period.

The first three PCA patterns of the residual are shown in Fig. 3.13. Although these patterns account for a relatively small fraction of the total residual variance, they are
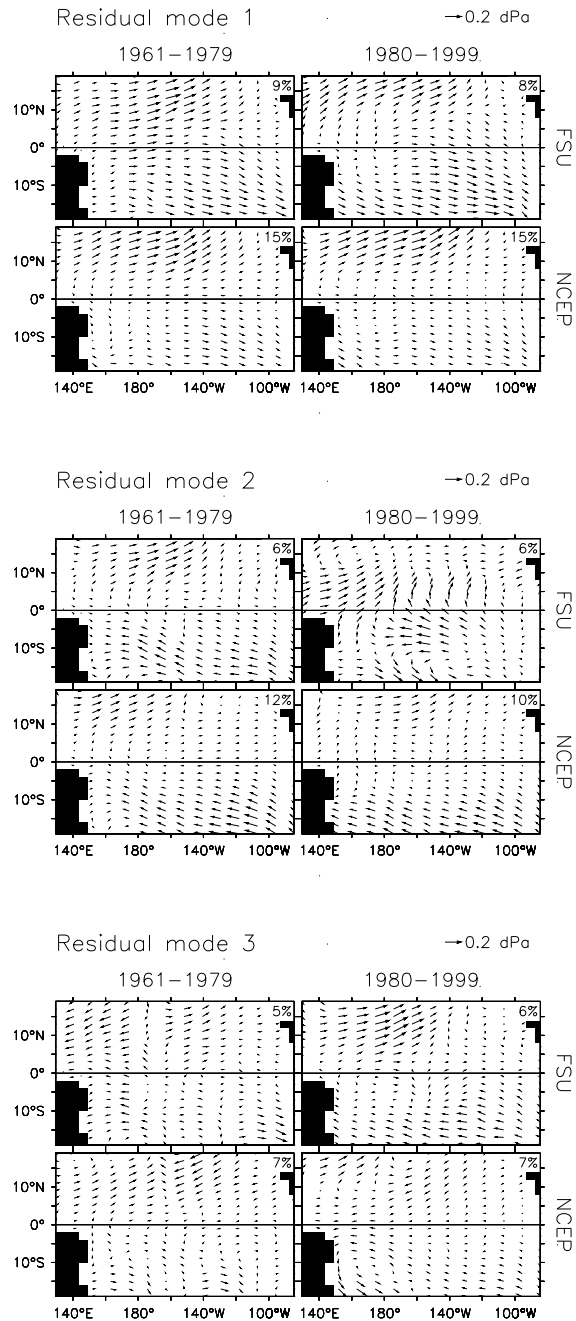
Figure 3.13: Leading principal components of the wind stress residual. The residual consists of the total stress anomaly minus the stress anomaly predicted by the deterministic model. Labels at the upper-right indicate the fraction of residual variance associated with each pattern.

dynamically important because they represent large-scale changes that could affect SST. Most of the patterns show only a weak equatorial signature, but they are associated with changes in the near-equatorial stress curl which could induce equatorial Rossby waves. These waves could then affect SST through equatorial zonal advection, and through reflection into Kelvin waves at the western boundary.

Residual mode 1 represents an overall change in the strength of the trade wind stress, especially north of the equator. The patterns differ between FSU and NCEP, with FSU showing a larger signature in the equatorial and southern tropical Pacific. The patterns also change between 1961–1979 and 1980–1999: FSU shows stronger loading in the off-equatorial western Pacific, with weaker loading in the equatorial western Pacific; similar changes occur in NCEP but to a lesser extent. Residual mode 2 represents more of an antisymmetric change about the equator in the off-equatorial zonal stress. The patterns look fairly similar except for FSU 1980–1999, which shows a much stronger signature near the equator and in the central Pacific. Subsequent modes are heavily constrained by orthogonality, but retain large-scale structures (e.g. residual mode 3).

Although the residual stress modes are coherent in space, their observed projection coefficients are fairly random. Examination of the autocorrelation functions for the residual PCA expansion timeseries indicates that beyond 1-month lag, the autocorrelation of the monthly-mean residual stress is below 0.2 for all modes. The cross-correlations of the PCA timeseries (not shown) are also small at all lags; indeed, the simultaneous cross-correlations are identically zero by (3.20). Thus to an good approximation, the PCA expansion coefficients are random from one month to the next.

We therefore assume that the residual PCA expansion timeseries evolve like red noise, with decorrelation times shorter than one month. Let $\mathbf{f}(t)$ represent the set of expansion coefficients at time t. If for simplicity we assume all the coefficients have the same decorrelation time, the expansion timeseries evolve according to

$$\mathbf{f}(t) = \mathbf{f}(t - \Delta t)e^{-\zeta} + \mathbf{g}(t)\sqrt{1 - e^{-2\zeta}} \qquad (3.33)$$

where Δt is the time step and $\mathbf{g}(t)$ is a random vector whose elements are $NID(0, 1)$; that is, normally and independently distributed with zero mean and homogeneous unit variance. The ratio ζ of the time step to the decorrelation time determines the "color" of the noise. As ζ decreases, the noise spectrum becomes redder, and the noise timeseries take more extended departures from zero. For a decorrelation time of 1 week and a timestep of 1 month, $\zeta \approx 4$ and the noise is practically white in time, $\mathbf{f}(t) \approx \mathbf{g}(t)$, as required by the data.

In summary, the noise residual is modeled using

$$\widehat{\mathbf{E}}_N \approx \mathbf{FB}'_{N,\widehat{e},M} \qquad (3.34)$$

Each column of the $n \times M$ matrix $\mathbf{F}$ is a noise timeseries with a decorrelation time of one week. The $q \times M$ matrix $\mathbf{B}_{N,\widehat{e},M}$ consists of the leading M principal patterns of the residual stress estimated from the leading N singular modes.

While the PCA patterns efficiently represent the variance of the residual, it is possible that the ocean will respond to only part of the noise signal represented by these patterns.

One could imagine using a different basis for the noise, such as a set of "optimal perturbations" which produce maximal growth of SST anomalies over some specified time window (Houtekamer, 1995; Penland and Sardeshmukh, 1995; Moore and Kleeman, 1996, 1997a,b, 1998). Such optimal patterns would be directly relevant to the observed coupled system over recent past. On the other hand, they might not remain optimal in the future if the dynamics or climate of the ocean changes. Furthermore, optimals can differ between reality and models, as well as among different models (Moore and Kleeman, 2001). For generality, therefore, we choose here to model *all* the noise, represented efficiently by the PCA basis, and let subsequent coupled systems select the optimal patterns for themselves.

3.4.4 Full model

Combining (3.31) and (3.34), a model for the full wind stress anomaly field at time t is

$$\mathbf{y}(t) = \mathbf{x}(t)\mathbf{A}_N\mathbf{S}_{x*}^{-2}\widehat{\mathbf{R}}_N + \mathbf{f}(t)\mathbf{B}'_{N,\widehat{e},M} \tag{3.35}$$

which simply says that stress anomalies depend on certain preferred patterns of SST anomalies and noise. The deterministic part of the stress is generated by a regression $\widehat{\mathbf{R}}_N$, estimated from historical data, which relates stress anomalies to dominant coupled SST/stress signals. These nondimensional signals arise from projecting the current SST anomaly $\mathbf{x}$ onto the leading N singular vectors $\mathbf{A}_N$ of historical SST/stress anomalies, and then dividing by the historical SST variance $\mathbf{S}_{x*}^2$. The stochastic part of the stress is generated using random combinations $\mathbf{f}(t)$ of the principal "noise" patterns $\mathbf{B}'_{N,\widehat{e},M}$, which are estimated from the part of the historical data not explained by the deterministic model.

3.5 Discussion

The statistical model (3.35) reproduces many of the observed characteristics of tropical Pacific wind stresses. Analysis of the model errors indicates that the simulation is good, but may not be a complete description of the stress. Thus a few caveats are in order.

The deterministic part of the model depends on large-scale SST anomalies only. In reality, tropical surface winds are forced by pressure gradients which depend on gradients in atmospheric heating. Part of the heating is related to local SST, since conduction, mixing, and radiation convey surface temperatures upward into the atmospheric boundary layer. This local heating then helps determine the locations of large-scale convergence, where further heating is achieved through condensation. Since water vapor is supplied by evaporation over a wide area, part of the local heating depends on nonlocal effects. The present model will capture many of these nonlocal effects, but will miss those that arise from temperature variability outside of the tropical Pacific domain. The deterministic model also neglects effects of local, small-scale SST anomalies on the local circulation; these effects are parameterized by the stochastic model.

The deterministic model is linear. Surface wind stresses, however, depend nonlinearly on the wind; often quadratic dependence is assumed. The winds, in turn, depend non-linearly on the atmospheric heating, since advection and mixing can play roles in the

momentum balance. Positive feedbacks between atmospheric heating and moisture convergence can also produce nonlinearity, since regions of warm SST and mean convergence have a heightened sensitivity to SST anomalies; such a feedback has been incorporated into simple dynamical atmospheric models like that of Zebiak (1986). The present statistical model can only hope to represent the linear part of the above processes. Fortunately, since there is a large amount of data at each gridpoint and the skewness of the residual is not very severe, we expect that the linear regression coefficients will be little affected by the non-normality. While the deterministic model may not completely describe the stress, we can be reasonably confident that it is at least a meaningful *linear* fit to the data.

The model is based on an assumption that the SST/stress relationship and the noise statistics are stationary in time. Analysis of the residual stress indicates that this assumption is not strictly correct: the noise variance changes through the calendar year, and also from year to year. To handle the seasonal nonstationarity, one could block the seasonal effects by fitting a separate model to each month of the calendar year. This time-dependent model would suffer from a substantial reduction in the regression degrees of freedom, but could also benefit from reduced noise variance for each month. It is difficult to statistically quantify the effects of interannual changes on the SST/stress relationships and noise variance, given the present data record. For now, we shall content ourselves with simulating only the most robust, linear part of the wind stress over the entire period 1961–1999.

By removing the seasonal cycle from the data before performing the model fit, we eliminate the assignable seasonal influence of solar forcing on the atmosphere. This is ideal for simulation of anomalies from the seasonal cycle, since it reduces the variance of the data and thereby improves the model fit. It would be easy to repeat the model-fitting exercise using departures from the annual-mean climatology instead of anomalies from the mean seasonal cycle (Syu and Neelin, 1995). Though such a model would be less skillful at predicting anomalies from the seasonal cycle, it would allow simulation of the seasonal cycle itself as well as anomalies from it.

The statistical model is "trained" to respond only to SST anomalies which have analogues in the observed record. It is possible that forcing the statistical model with very unusual SST anomalies could generate an unphysical stress response, which might preclude highly idealized experiments involving observationally rare SST patterns. On the other hand, experience with so-called "constructed analogues" (van den Dool, 1994; Landsea and Knaff, 2000) suggests that skill can be achieved so long as the predictor pattern is representable as some linear combination of observed patterns. Thus it is the stress model may be able to produce a reasonable response even when presented with unusual SST anomalies.

A statistical model is only as good as the data used to build it. If the data has systematic biases, these biases will also show up in the statistical model. Trends were not removed from the data and so have been incorporated into the model. This is desirable if the trends are real, since they provide additional information on the relationship between SST and wind stress to be used by the linear regression. However, if the trends are due only to changes in data density, measurement procedures, or quality control, the model will be a fit to this spurious variability and not to the real system. The primary difficulty is choosing the wind stress product with which to build the model; a consensus product is much needed

to bridge the large gaps between these analyses. Until such a product is available, it may be wise to examine the sensitivity of diagnostic results and model experiments to different wind products. If a statistical model is used, it should not necessarily be viewed as ground truth, given the large uncertainties in the data.

The key to future progress in this area may lie in decoding and successfully modeling the structure of the noise. We have shown that there is some information left in the residual, including spatial and temporal coherence that may be dynamically important for ENSO. More sophisticated stochastic models may be better able to extract this information, which would enhance understanding and modeling of intraseasonal variability and its interactions with ENSO.

Having noted the caveats above, the author believes the statistical model provides a reasonable baseline for simulation of tropical Pacific wind stress anomalies. The model developed here (specifically FSU 1980–1999) will be used in the next chapter to build a fully coupled model of the tropical Pacific climate system.

Chapter 4

Coupled Climate Model

Simplify, simplify.

Thoreau, *Walden*

4.1 Rationale

To ensure the robustness and usefulness of this study, a wide range of climates and model parameters must be explored. A coupled general circulation model would be too costly for this task, both conceptually and computationally. We therefore simplify the dynamics to retain only the processes most relevant to the tropical Pacific climatology and ENSO. Intermediate models, like the one developed in this chapter, have been used extensively over the past decade to construct a vocabulary for ENSO dynamics (see Neelin et al., 1998, for a review). The behaviors found in such models provide essential prototypes for those found in more complex models and in observations. Intermediate models may therefore be viewed as stepping stones to a more complete understanding of tropical climate dynamics.

The use of an intermediate model involves a trade-off between realism and control. Processes such as mixing, clouds, and evaporation are heavily parameterized, so results from the model must necessarily be viewed with caution until verified by more realistic simulations or observations. However, the conceptual and computational efficiency of such a model offers several great advantages. First, it affords the experimenter a large degree of control over the dynamics, which allows hypotheses to be tested cleanly and easily. Second, its computational efficiency provides great freedom for exploration, which allows a wider variety of hypotheses to be tested, and tested more carefully, than would be possible in a GCM. Finally, the simplicity of an intermediate model allows its essential behavior to be understood completely, free from complications arising from secondary processes.

For the purpose of mapping a vast climate parameter space, and translating this map into a physical understanding of ENSO, the benefits of a simplified model here seem to outweigh the costs. The analysis and mapping of intermediate models are further motivated by the need to unify, and put into proper context, the large body of existing literature
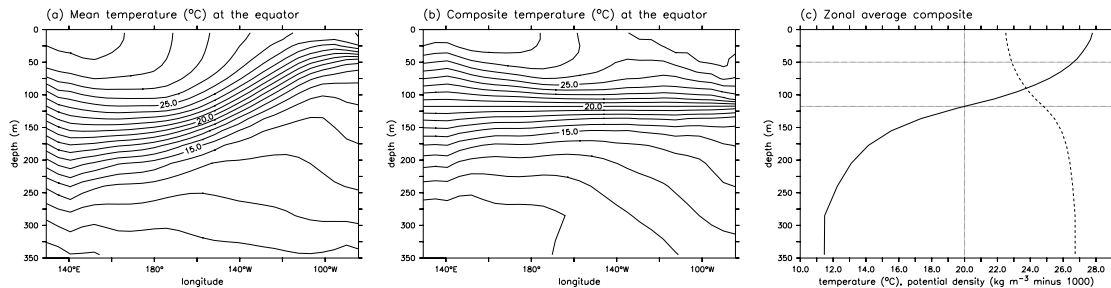
Figure 4.1: Observed vertical thermal structure of the equatorial band (2°S–2°N) during the 1980–1999 period, from the analysis of Behringer et al. (1998). (a) Mean temperature. (b) Composite temperature, obtained as a time average of instantaneous profiles which have been vertically shifted so that their 20°C isotherm lies at the time-mean, zonal-mean depth of the 20°C isotherm. (c) Zonal average composite temperature (solid) and potential density (dashed). Potential density is estimated from the UNESCO equation of state, assuming a reference pressure of 1010 mb and a salinity of 35 parts per thousand.

on such models. The analysis will also be directly applicable to at least some current operational predictions, since intermediate models are still being used for this purpose (Chen et al., 1999).

4.2 Ocean model

4.2.1 Governing equations

Active layer

To a first approximation, the vertical structure of the equatorial Pacific ocean consists of a nearly homogeneous mixed layer near the surface, a sharp thermocline at depth, and a deep bottom layer (Fig. 4.1). A reasonable idealization is a fluid consisting of two vertically-homogeneous layers, with no mixing or friction between the layers. If the bottom layer is assumed to be motionless and infinitely deep, then no horizontal pressure gradients can develop in that layer, and pressure gradients induced by the slope of the sea surface must exactly cancel those induced by the slope of the thermocline. The slope of the thermocline must then be proportional and opposite to the slope of the sea surface.

The average density of active layer is only slightly less than that of the bottom layer, so density variations may be neglected in the equations of motion except where they give rise to pressure gradients (the Boussinesq approximation). Also, because the relative density difference between cold and warm water is much smaller than that between water and air, variations in thermocline slope will be much greater than variations in sea surface height. Surface height variations will therefore play little role in the mass balance of the active layer, and can be neglected in this respect (the rigid lid approximation). Although the surface variations *are* essential for generating pressure gradients within the active layer, these effects can be parameterized in terms of the thermocline slope as noted above.

Let h_1 denote the linear departure of the active (upper) layer depth from its constant reference depth H, and let $\mathbf{U}_1 \equiv (U_1, V_1)$ denote the vertically-integrated horizontal transport of water within the active layer. Restricting attention to long-wave, near-geostrophic flows (wavelengths $\gg 300$ km, times $\gg 1$ day), and integrating vertically over the active layer, the linearized equations for conservation of momentum and mass are given by the *longwave reduced gravity model*

$$\partial_t U_1 \;=\; fV_1 - c^2 \partial_x h_1 + \frac{\tau_x}{\rho} - rU_1 \tag{4.1}$$

$$0 \;=\; -fU_1 - c^2 \partial_y h_1 + \frac{\tau_y}{\rho} - rV_1 \tag{4.2}$$

$$\partial_t h_1 \;=\; -\boldsymbol{\nabla} \circ \mathbf{U}_1 - rh_1 \tag{4.3}$$

where $f = \beta y$ is the equatorial beta-plane approximation to the Coriolis parameter, ρ is the seawater density, r is the dissipation coefficient for mass and momentum, $c^2 = g'H$ is the squared speed of internal gravity waves, $g' = g\Delta\rho/\rho$ is the reduced gravity, and τ_x and τ_y are the zonal and meridional components of the surface wind stress. Note that $\partial_t V_1$ has been eliminated from (4.2) by the assumption of low frequencies and large zonal scales.

The boundary conditions for (4.1)–(4.3) are as follows. There is assumed to be no flow through the northern and southern boundaries. The eastern and western boundaries in reality are thought to be leaky, since they are not perfectly meridional and the western boundary has gaps (Clarke, 1991; Mantua and Battisti, 1994; Kang and An, 1998; Boulanger and Menkes, 1999; Thompson and Battisti, 2000). At the eastern boundary, only a fraction R_e of the zonal transport associated with the impinging Kelvin wave signal is canceled by the generation of long Rossby waves through boundary reflection. Similarly at the western boundary, only a fraction R_w of the zonal transport associated with the impinging Rossby wave signal is canceled by the generation of equatorial Kelvin waves through boundary reflection. In the west, there is a narrow boundary layer where short Rossby waves act to redistribute mass meridionally, and since the long-wave approximation has eliminated short Rossby waves from (4.1)–(4.3), the appropriate western boundary condition must be formulated in terms of the meridionally integrated flow (Cane and Sarachik, 1977). Points close to the model's artificial north/south boundaries will be contaminated by spurious coastal Kelvin waves, so these points are neglected from the flow integral (Battisti, 1988). In summary, the boundary conditions for (4.1)–(4.3) are formulated as

$$V_1 = 0 \quad \text{at} \quad y = y_s, \, y_n \tag{4.4}$$

$$U_{1,Rossby} = -R_e U_{1,Kelvin} \quad \text{at} \quad x = x_e \tag{4.5}$$

$$\int_{y_s}^{y_n} U_{1,Kelvin} \, dy = -R_w \int_{y_s+L(y_s)}^{y_n-L(y_n)} U_{1,Rossby} \, dy \quad \text{at} \quad x = x_w \tag{4.6}$$

where $L(y) = c(\beta y)^{-1}$ is the coastal radius of deformation at latitude y, and $U_{1,Kelvin}$ and $U_{1,Rossby}$ are the Kelvin and Rossby components of the active layer zonal transport.

At the equator and in the limit of no damping, the steady-state thermocline slope is in balance with the zonal wind stress: $\rho g' H \partial_x h_1 = \tau_x$. This implies that the eastern Pacific will be an important dynamical region for ENSO for two reasons. First, the prevailing

easterly trade winds induce a slope in the thermocline, such that it shoals in the eastern Pacific; the presence of strong vertical temperature gradients near the surface in the east then makes vertical entrainment in this region very sensitive to variations in upwelling and thermocline depth. Second, the eastern Pacific is a region of strong vertical motions of the thermocline, since it is impacted by the full force of the zonal wind fetch integrated across the basin. It is this combination of strong *sensitivity* to thermocline depth and strong *activity* of thermocline motions that make the eastern Pacific a key region in the cycle of coupled feedbacks responsible for ENSO.

Given the importance of the thermocline depth in the eastern equatorial Pacific, a special problem then arises due to the linearity of (4.1)–(4.3). If the thermocline depth anomalies are not small compared to the active layer depth, then a more appropriate steady-state zonal balance is $\rho g'(H+h)\partial_x h = \tau_x$ where h denotes the thermocline depth anomaly in nonlinear balance. Comparing this to the linear balance gives $\partial_x h_1 = (1 + h/H)\partial_x h$, which indicates that $\partial_x h_1$ will underestimate the thermocline slope where h is negative, i.e. where the thermocline is shallower than H. This will be the case in the eastern Pacific, where the thermocline is shallow due to the prevailing easterly trade winds.

To improve the thermocline depth simulation in the east Pacific, we therefore introduce scaled versions of the linear thermocline depth and active layer transport for use by the mixed layer model:

$$h = \lambda_h h_1 \tag{4.7}$$
$$\mathbf{U}_{al} = \lambda_u \mathbf{U}_1 \tag{4.8}$$

The coefficients λ_h and λ_u are chosen so that the simulated h (especially in the east Pacific) and $\mathbf{U}_{al}$ (especially in the central Pacific) best agree with observations.

Mixed layer currents

The cold tongue is maintained largely by vertical entrainment of cold water into the mixed layer. This entrainment can be simulated by embedding an Ekman layer into the top of the active layer, following Zebiak and Cane (1987). We assume the wind stress forcing is deposited entirely within a layer of constant depth H_m, so that the total transport in the active layer is given by

$$\mathbf{U}_{al} = \mathbf{U} + \mathbf{U}_i \tag{4.9}$$

where $\mathbf{U}_{al} \equiv H\mathbf{u}_{al}$ is the active layer transport, $\mathbf{U} \equiv H_m\mathbf{u}$ is the mixed layer transport, and $\mathbf{U}_i \equiv (H - H_m)\mathbf{u_i}$ is the interior (non-mixed layer) transport in the active layer. The vertical-average currents in the active layer, mixed layer, and interior layer are denoted by $\mathbf{u}_{al}$, $\mathbf{u}$, and $\mathbf{u}_i$, respectively.

Continuity gives the upwelling velocity at the base of the mixed layer:

$$w = \boldsymbol{\nabla} \circ \mathbf{U} \tag{4.10}$$

Assuming the active layer has uniform density, the pressure gradients in the interior active layer must be the same as those in the mixed layer. The extra flow in the mixed layer which

is not present in the interior must be due to the frictional (Ekman) transport, denoted by

$$\mathbf{U}_s \equiv H_m \mathbf{u}_s \tag{4.11}$$

$$\mathbf{u}_s \equiv \mathbf{u} - \mathbf{u}_i \tag{4.12}$$

Assuming the vertical current structure is in equilibrium with the wind stress, subtracting the momentum equations for the interior active layer from those of the mixed layer gives the shear equations

$$0 = fV_s + \frac{\tau_x}{\rho} - r_s U_s \tag{4.13}$$

$$0 = -fU_s + \frac{\tau_y}{\rho} - r_s V_s \tag{4.14}$$

or

$$\mathbf{U}_s = \frac{r_s \boldsymbol{\tau} - f\hat{k} \times \boldsymbol{\tau}}{\rho \left(f^2 + r_s^2 \right)} \tag{4.15}$$

The coefficient r_s, which controls the viscosity of the mixed layer, strongly affects the equatorial upwelling response to wind stress (Appendix C).

Finally, the mixed layer currents and transports are obtained from the transport budget (4.9):

$$\mathbf{u} = \mathbf{u}_{al} + \left(1 - \frac{H_m}{H} \right) \mathbf{u}_s \tag{4.16}$$

$$\mathbf{U} = \mathbf{U}_s + \frac{H_m}{H} \left(\mathbf{U}_{al} - \mathbf{U}_s \right) \tag{4.17}$$

In summary, the mixed layer transport consists of the Ekman transport plus the fraction of buoyancy-driven transport that occurs within the mixed layer.

Thermodynamics

The model mixed layer is assumed to have uniform temperature in the vertical, i.e. the vertical-average mixed layer temperature is assumed equivalent to SST. The mixed layer temperature equation includes three-dimensional nonlinear advection, horizontal mixing represented by a diffusion term, and surface heat flux represented by linear damping of SST:

$$\partial_t T = -u\partial_x T - v\partial_y T - \mathcal{R}(w)\partial_z T + \kappa \nabla^2 T - \epsilon \left[T - T_0(y) \right] \tag{4.18}$$

where κ is the eddy diffusivity, ϵ is the damping rate, and $\mathcal{R}$ is the ramp function

$$\mathcal{R}(x) \equiv \begin{cases} 0 & : & x \leq 0 \\ x & : & x > 0 \end{cases} \tag{4.19}$$

$T_0(y)$ is the equilibrium surface temperature in the absence of ocean dynamics; it is assumed to have a parabolic structure in the meridional, with a peak at the equator:

$$T_0 = T_0(y = 0) - ay^2 \tag{4.20}$$

Table 4.1: Ocean model grid parameters: minimum and maximum coordinates, spacing, and number of points in longitude and latitude.

Field	x_w	x_e	Δx	n_x	y_s	y_n	Δy	n_y
mixed layer u,v,w,T	129.375°E	84.375°W	5.625°	27	19°S	19°N	2°	20
active layer u_1,h_1	124°E	80°W	2°	79	28.50°S	28.50°N	0.5°	115
active layer v_1	125°E	81°W	2°	78	28.75°S	28.75°N	0.5°	116

The effective vertical entrainment temperature gradient $\partial_z T$ is

$$\partial_z T \equiv \frac{\gamma(T - T_e)}{H_m} \tag{4.21}$$

where γ is the entrainment efficiency. The temperature T_e of water entrained into the mixed layer at depth H_m is parameterized in terms of the thermocline depth h:

$$T_e = T_c + \delta \left[e^{(h-H_m)\Gamma/\delta} - 1 \right] \tag{4.22}$$

$$\delta \equiv T_c - \begin{cases} T_{min} & : & h \leq H_m \\ T_{max} & : & h > H_m \end{cases} \tag{4.23}$$

Direct buoyancy effects of mixed layer temperature changes on the active layer pressure gradients are assumed to be small and are ignored. Changes in SST, however, will feed back indirectly on the ocean dynamics through the wind stress forcing.

4.2.2   Numerics

The horizontal grids for the ocean model are shown in Table 4.1 and Fig. 4.2. Both the active layer and mixed layer models assume a rectangular ocean basin. To adequately resolve equatorial waves, the ocean dynamics are computed on a dense grid, with the meridional velocity grid staggered in x and y relative to the zonal velocity and depth grids to give second order accuracy in space. The mixed layer fields are computed on a lower resolution grid.

The active layer equations (4.1)–(4.3) are integrated forward in time using the method of Cane and Patton (1984). The "Kelvin wave" part of the solution is propagated eastward using the method of characteristics, while the remaining "Rossby wave" part of the solution is propagated westward numerically using an implicit scheme centered in time. In combination with the staggered ocean dynamics grid, this method provides second-order accuracy in time and space and conserves mass and energy away from boundaries. While there are fluxes of mass and energy through the boundaries, these are small and acceptable for our purposes. The great advantage of this scheme is that it allows a very long timestep of 10 days to be used with good accuracy.

Active-layer fields are averaged onto the coarse mixed layer grid prior to the advection computation. After adding the Ekman contribution to the mixed layer currents, the upwelling is computed from (4.10) using centered differences. At the western, southern, and northern boundaries, upwelling is set equal to that computed at the nearest interior point.
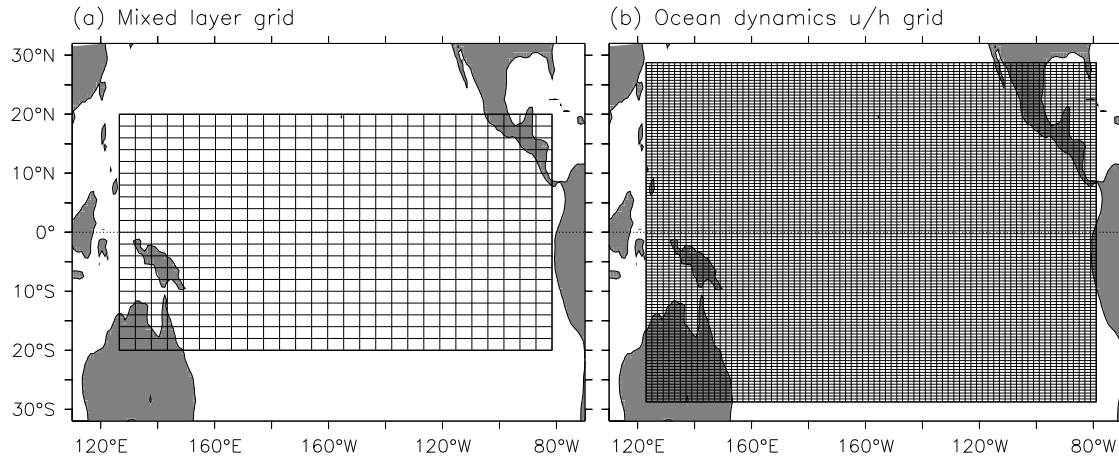
Figure 4.2: Spatial domains and grid boxes for the ocean model. (a) Mixed layer grid boxes for temperature, horizontal velocity, and upwelling. (b) Active layer grid boxes for thermocline depth and zonal velocity; meridional velocity gridpoints are centered at the corners of these boxes. Continents are shown for scale only; the model assumes a rectangular basin.

At the eastern boundary, a boundary condition of no normal flow is assumed in order to simulate coastal upwelling observed off the coast of Peru.

With the currents and thermocline depth fields in hand, the mixed layer temperature tendency equation (4.18) is then integrated forward in time using first-order time-differencing and upwind advection, with no advective flux allowed through model boundaries. At each time step, the upwind direction is determined from the *total* velocity field. This differs slightly from the approach of Zebiak (1985), who simply used the climatological or anomalous velocity field (depending on which advective term was being evaluated) to determine the upwind direction. In the present model, the total velocity sets the upwind direction for every term, giving both a more physically consistent advective scheme and more linear behavior at small amplitudes as expected. The advective scheme is rather dissipative of temperature anomalies at scales comparable to the grid spacing. This dissipation can be considered an implicit horizontal mixing term, which is comparable in magnitude to the explicit mixing included in (4.18). Two nice properties of the advective scheme are that it does not generate artificial temperature anomalies on its own, and it advects temperature anomalies at a speed very close to the true advective speed. In order to ensure numerical stability, the advective timestep adjusts automatically to the speed of the mixed-layer currents and the strength of the horizontal dissipation; the advective timestep is typically on the order of 2–3 days.

4.2.3 Calibration

Observations, models, and theories of ENSO have improved considerably since the pioneering work of Zebiak and Cane (1987). Although some limitations of the original version of the model have been pointed out, subsequent studies have shown that reformulating and

Table 4.2: Ocean model parameters and their standard values.

Parameter	Symbol	Value
Active layer		
density of surface seawater	ρ	1023 kg m^{-3}
thermocline stratification	$\Delta\rho/\rho$	0.005
observed active layer depth	H_{obs}	124 m
resting active layer depth	H_0	143 m
active layer dissipation	r	(18 months)$^{-1}$
western boundary reflectivity	R_w	0.85
eastern boundary reflectivity	R_e	0.85
thermocline depth coefficient	λ_h	1.7
transport coefficient	λ_u	1.0
Mixed layer		
mixed layer depth	H_m	50 m
vertical shear dissipation	r_s	(2 days)$^{-1}$
horizontal eddy diffusivity	κ	4000 m^2 s^{-1}
surface flux coefficient	ϵ	20 W m^{-2} K^{-1}
equatorial equilibrium SST	$T_0(y=0)$	30°C
y-curvature of $T_0(y)$	a	0.0125 K ($^\circ$lat)$^{-2}$
Entrainment parameterization		
entrainment efficiency	γ	0.75
thermocline central temperature	T_c	20°C
minimum T_e	T_{min}	16°C
maximum T_e	T_{max}	30°C
maximum $\partial_h T_e$	Γ	0.17 K m^{-1}

retuning the model can greatly improve its performance (Chang, 1994; Mantua and Battisti, 1995; Wang, 1995; Perigaud and Dewitte, 1996; Dewitte and Perigaud, 1996; Perigaud et al., 1997, 2000a; Cassou and Perigaud, 2000). In addition, although the model was not originally designed to simulate the tropical climatology, Seager et al. (1988) showed that the ocean model framework can successfully reproduce many aspects of this climatology as long as realistic surface fluxes are supplied. The present section builds on this past work by formulating a consistent parameter set that can be used to simulate both the tropical Pacific climatology and ENSO. This motivates a careful comparison of the model simulations against recent observations, and requires a thorough re-tuning of the ocean model. Resulting parameter values for the control run are given in Table 4.2.

Active layer

The linear reduced gravity system (4.1)–(4.3) has four free parameters: the internal gravity wave speed c, the dissipation r, and the boundary reflection coefficients R_e and R_w. The value of c controls the speed of the ocean adjustment to changes in wind stress. Observations suggest that over recent decades, c has been in the range of 2 to 3 m s^{-1} (McPhaden et al., 1998; Neelin et al., 1998), and eigenanalyses of the observed density structure of the ocean indicate first baroclinic mode speeds ranging from 2.4 to 2.9 m s^{-1} and second baroclinic mode speeds ranging from 1.4 to 1.8 m s^{-1} (Busalacchi and O'Brien,

1981; Cane, 1984; Philander, 1990). Intermediate models have typically assumed c to be around 2.9 m s^{-1} (Zebiak and Cane, 1987; Battisti, 1988). Kleeman (1993) tried a range of speeds in a coupled intermediate model and found the best hindcast skill was achieved with c between 2.2 and 2.4 m s^{-1}, i.e. at speeds intermediate between the first and second baroclinic modes. In this study, c must be allowed to vary with H, since effects of changes in the basic state are being tested. We therefore fix the stratification $\Delta\rho/\rho$ at the constant value that gives $c = 2.5$ m s^{-1} when H is set equal to H_{obs}, the observed thermocline depth averaged over the latitudes of strong wave propagation (8°S–8°N). Using the Behringer et al. (1998) ocean analysis for the 1980–1999 period and approximating the thermocline depth by the depth of the 20°C isotherm, we obtain the values given in Table 4.2.

The active-layer dissipation parameter, r, plays a central role in the generation of steady-state currents in response to the climatological wind stress (Yamagata and Philander, 1985). Zebiak and Cane (1987) and Battisti (1988) assumed a rather small value of $r = (30 \text{ months})^{-1}$, which provided a good simulation of the climatological currents and off-equatorial thermocline depth. As pointed out by Mantua and Battisti (1995), however, the single-mode reduced gravity system traps too much energy near the surface, resulting in a basin resonance at periods of 9–11 months (corresponding to a Kelvin wave/Rossby wave circuit) that is much stronger than observed. In a continuously stratified ocean, equatorial waves propagate energy downward and out of the surface layer (Philander, 1990). To represent this process, a few authors have suggested increasing the value of r to $(12 \text{ months})^{-1}$ or more (Picaut et al., 1993; Perigaud and Dewitte, 1996; Thompson and Battisti, 2000). However, if r is too strong then the simulation of the climatological currents and thermocline depth suffers. We therefore choose a value $r = (18 \text{ months})^{-1}$, which is strong enough to attenuate the spurious high-frequency basin-resonant mode but weak enough to give a decent simulation of the off-equatorial climatology.

The boundary reflection coefficients R_e and R_w control the mass flux through the eastern and western boundaries. During a warm event, for example, equatorial westerly stress anomalies generate a Kelvin wave depression in the equatorial thermocline, which propagates eastward. The off-equatorial cyclonic stress curl associated with the equatorial westerlies also generates a Rossby wave elevation in the off-equatorial thermocline, which propagates westward. Both the Kelvin and Rossby signals are associated with eastward equatorial currents. At the eastern and western boundaries, the currents are partially canceled by the generation of reflected waves. The part of the impinging signal that is not canceled (due to imperfect reflection) corresponds to a mass flux through the boundary.

As discussed by An and Kang (2000), this boundary flux is important for controlling the zonal-mean thermocline depth response to changes in wind stress. Depending on the strength of the boundary reflections, the boundary fluxes can act to enhance or inhibit the shoaling of the equatorial zonal-mean thermocline brought about by geostrophic divergence in the interior. For a downwelling Kelvin wave, an imperfect reflection at the *eastern* boundary results in an eastward mass flux *out of* the equatorial band, which helps to *shoal* the equatorial thermocline and *cool* SST through vertical advection. In the presence of a westward background SST gradient, however, the eastward mass flux tends to *warm* SST through zonal advection. The net effect of the eastern boundary flux is therefore a competition between zonal and vertical advective processes. A decrease in R_e can either

lengthen the ENSO period (if the zonal advection effect dominates) or shorten the period (if the vertical advection effect dominates).

Imperfect reflection at the *western* boundary, on the other hand, results in eastward mass flux *into* the equatorial band through that boundary, which serves to *deepen* the equatorial thermocline. In this case, both zonal advection and vertical advection act as a positive feedback on SST anomalies. This delays termination of an event, by counteracting the cooling by equatorial discharge induced by cyclonic off-equatorial wind stress curl. As a result, a decrease in R_w will tend to lengthen the oscillation period. If R_w is so weak that the western boundary flux overwhelms the geostrophic divergence, then the system will no longer oscillate and will instead drift to a new equilibrium.

The actual boundary reflectivities are difficult to estimate, due to the complexity of the coastal geometry and bathymetry. The reflectivity is sensitive not only to the shape and continuity of the boundary, but also to the frequency of the reflecting wave signals. A recent observational estimate of R_e places it around 0.75 (Boulanger and Menkes, 1999). Theoretical estimates of R_w are in the vicinity of 0.8-0.9 (Clarke, 1991; du Penhoat and Cane, 1991), while observational estimates range from 0.7 (Mantua and Battisti, 1994) to nearly 1.0 (Boulanger and Menkes, 1999). Intermediate models have used different values for the reflection coefficients. Zebiak and Cane (1987) and Battisti (1988) assumed perfect reflections at both boundaries; Thompson and Battisti (2000) recommended $R_e = 1.0$, $R_w = 0.7$; Kang and An (1998) and An and Kang (2000) used $R_e = R_w = 0.7$. Experiments with the present model suggest that $R_e = R_w = 0.85$ gives a good simulation of the relative amplitude and phasing of the zonal thermocline slope and zonal-mean thermocline depth. As these values are in the middle of the range of reflectivities suggested by previous work, we adopt them into the standard model (Table 4.2).

Next, a value of λ_h is chosen to optimize the simulation of thermocline depth. For this purpose, H is set equal to H_{obs} and the active layer model is forced with the FSU wind stress anomalies over the 1980–1999 period. Figs. 4.3 and 4.4 show that for the standard value of λ_h in Table 4.2, the model gives a decent simulation of the equatorial thermocline depth anomalies. The amplitude of the thermocline response to the stress appears to be correct, both for the zonal slope and the zonal mean across the basin. That the FSU-forced simulation is poor during 1984–1986 and 1996 may result from problems with the FSU stress product (Chapter 2), perhaps amplified by the basin resonance noted earlier. (Note that forcing the model instead with the NCEP stress anomalies gives a much better simulation during these periods.) Due to the linearity of the model, the simulated thermocline depth variability in the western Pacific is too strong, but this is of little concern since the thermocline is deep in that region and therefore should play little role in directly affecting surface temperatures.

The tropical Pacific surface current variability is less well known than the thermocline depth variability. We expect that $\lambda_u = 1$ should be appropriate, since the equatorial zonal current anomalies are most active in the central and western Pacific where the thermocline depth is not far from H. A comparison of the simulated active-layer current anomalies with measurements reported in the literature (Lagerloef et al., 1999; Wang, 2000b; Wang and McPhaden, 2001; Grodsky and Carton, 2001) indicates that $\lambda_u = 1$ is indeed reasonable, so we adopt this value into the standard model.
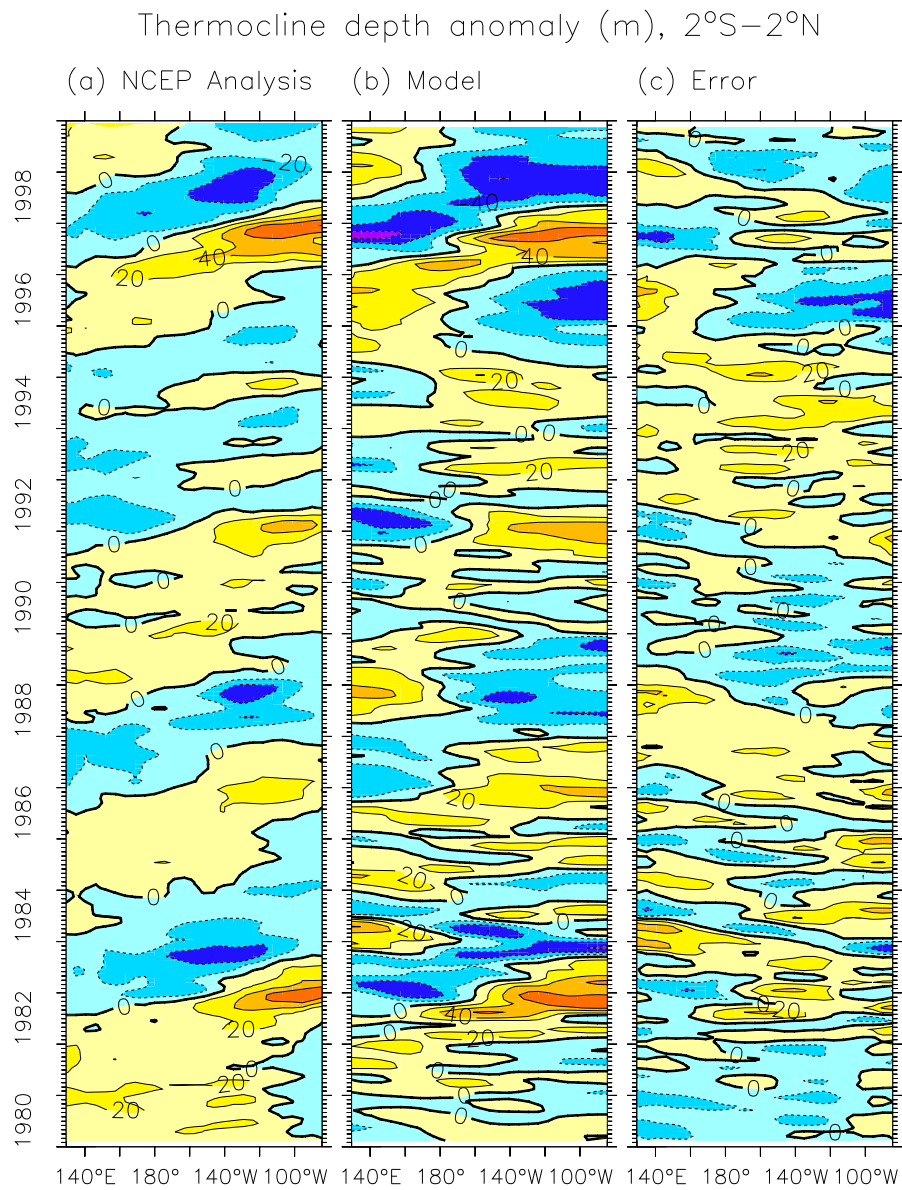
Figure 4.3: Thermocline depth anomaly (m) along the equator, averaged over 2°S–2°N and smoothed with a 3-month triangle filter. (a) Anomalous depth of the 20°C isotherm from the observational analysis of Behringer et al. (1998). (b) Anomalous thermocline depth from the standard active layer model forced by observed FSU stress anomalies. (c) Depth error, model minus observations.
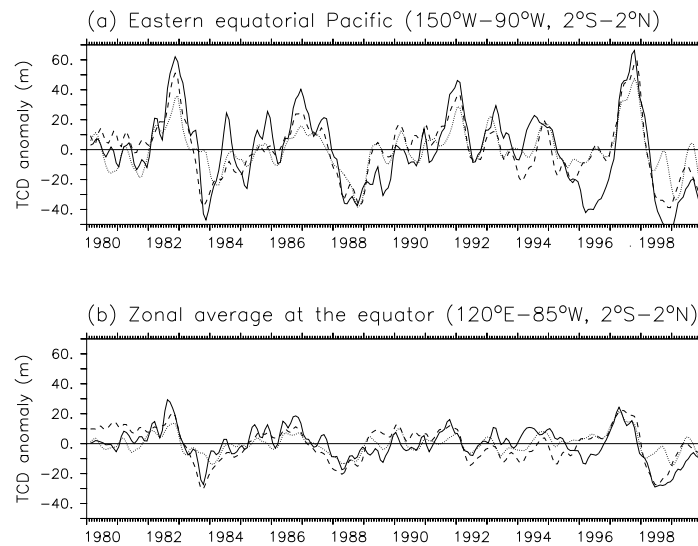
Figure 4.4: Thermocline depth anomaly (m) along the equator, averaged over 2°S–2°N and zonally across the (a) eastern basin, and (b) full basin. Anomalies have been smoothed with a 3-month triangle filter. Dashed line is the 20°C isotherm from the observational analysis of Behringer et al. (1998). Solid line is the standard model forced by FSU stress anomalies, dotted line is forced by NCEP stress anomalies.

Finally, a value for H_0, the thermocline depth in the absence of any wind stress forcing, must be chosen to optimize the simulation of the climatological thermocline depth. The overriding goals for the climatology are (1) a realistic thermocline depth in the eastern Pacific, and (2) a realistic average thermocline depth over the latitudes of strong wave propagation (8°S–8°N). To this end, the model is spun up with the FSU climatological wind stress using various values of H_0. Fig. 4.5 shows that the standard value of H_0 in Table 4.2 results in both a realistic equatorial thermocline depth and a value of H very close to H_{obs}.

Mixed layer currents

The mixed layer has two parameters: a constant depth H_m and a viscosity r_s. Fig. 4.6 shows that in reality, the mixed layer depth varies substantially with location and time. Along the equator, the mixed layer is much shallower in the eastern Pacific than in the central and western Pacific. The equatorial mixed layer is deepest in boreal winter and during El Niño, and shallowest in boreal spring and during La Niña. Clearly a model with a fixed-depth mixed layer may not adequately represent the entrainment processes going on in the real world. Inclusion of a fully interactive mixed layer, however, would complicate the analysis considerably. We instead proceed with the constant-depth mixed layer formulation that has met with much success in understanding and predicting ENSO. Fig. 4.6 indicates that the time-average, zonal-average mixed layer depth near the equator is very close to 50 m (the standard value used by Zebiak and Cane (1987)), so we adopt
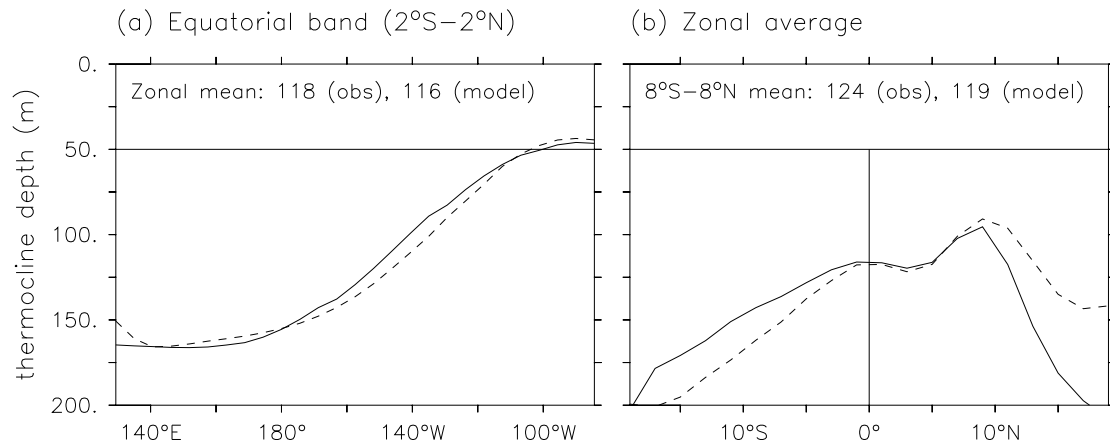
Figure 4.5: Climatology of thermocline depth (m) for the 1980–1999 period. Dashed line is the 20°C isotherm from the observational analysis of Behringer et al. (1998). Solid line is the thermocline depth simulated by the standard model when forced by the climatological FSU stress. (a) Meridional average over the equatorial band, 2°S–2°N; label indicates the zonal mean values over the entire basin. (b) Zonal average over the entire basin; label indicates the meridional means over 8°S–8°N.
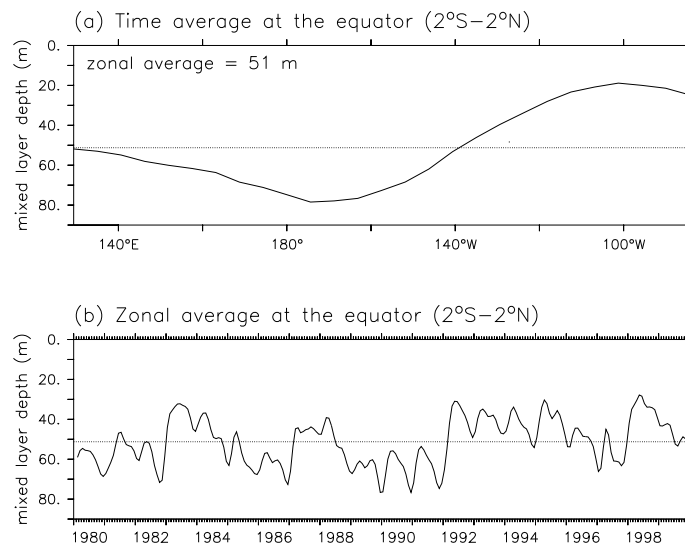
Figure 4.6: Observed mixed layer depth (m), defined as that depth which is 0.5°C cooler than the surface, from the analysis of Behringer et al. (1998). Data are averaged over 2°S–2°N for the 1980–1999 period. (a) Time average. (b) Zonal average over the entire basin. Dotted lines indicate the zonal/time average mixed layer depth, which is labeled in (a).

this value for H_m.

As shown in Appendix C, the mixed layer viscosity r_s controls the intensity and structure of the frictional surface circulation (Ekman flow). Since the upwelling strength is extremely important to the coupled dynamics of the climatology and ENSO, it will be the primary constraint in choosing a value for r_s. For nondivergent winds, (C.8) gives

$$r_s^2 = -\frac{H - H_m}{\rho H}\frac{\beta\tau_x}{w(y=0)} \tag{4.24}$$

The actual mean upwelling along the equator in the Pacific is difficult to estimate. It arises from a divergence of surface currents, so it is highly prone to errors in those currents. Also, because the strongest upwelling occurs in a narrow band near the equator and exhibits large spatial and temporal variability, the data are subject to sizable aliasing and interpolation errors. Weisberg and Qiao (2000) review a number of techniques that have been brought to bear on this problem. A recent estimate by Meinen et al. (2001) suggests that the annual-mean climatological vertical velocity across 50 m depth is 0.28 ± 0.03 m day^{-1} averaged over the region 155°W–95°W, 5°S–5°N. Johnson et al. (2001) obtain a larger value of 0.66 ± 0.19 m day^{-1} averaged over 170°W–95°W, 3.6°S–5.2°N, with a peak zonally-averaged equatorial upwelling velocity of 1.6 ± 0.8 m day^{-1}.

To estimate r_s in the intermediate model, we first average the FSU observed equatorial zonal stress over 170°W–95°W to get $\tau_x = -0.5$ dPa $= -3.73 \times 10^8$ kg m^{-1} day^{-2}. Assuming $H = 125$ m, $H_m = 50$ m, $\rho = 1023$ kg m^{-3}, $\beta = 1.97 \times 10^{-6}$ (m day)$^{-1}$, $w(y=0) = 1.6$ m day^{-1}, equation (4.24) gives $r_s = (1.9$ days$)^{-1}$. Note that there is a fair amount of uncertainty in this parameter, given the large error bars on the observational estimate, and the coarse resolution of the mixed layer model (the closest equatorial points are at 1°S and 1°N). The estimated value is close enough to the $(2.0$ days$)^{-1}$ used in the Zebiak and Cane (1987) model that we simply adopt the latter value. Forcing the full model (including the shallow water component) with the seasonally-varying climatology of FSU vector wind stress from the 1980–1999 period, gives annually-averaged, spatially-averaged simulated upwelling velocities of 0.43 m day^{-1} over 170°W–95°W, 3.6°S–5.2°N; 1.02 m day^{-1} over 170°W–95°W, 2°S–2°N; and 0.39 m day^{-1} over 155°W–95°W, 5°S–5°N. These values are in the midrange of current observational estimates.

Thermodynamics

The entrainment temperature parameterization is plotted along with observations in Fig. 4.7. T_e increases smoothly with thermocline depth from T_{min} to T_{max}, passing through the inflection point (H_m, T_c) where the maximum $\partial_h T_e$ of Γ occurs. The value of T_c is set to 20°C, which is a good fit to the thermocline central temperature along the equator. The entrainment temperature can get no warmer than T_{max}, which is set to the equatorial equilibrium temperature $T_0(y = 0)$, and no colder than T_{min}, which is set to 16°C to prevent excessive cooling in the eastern equatorial pacific during La Niña, when the 20°C isotherm tends to outcrop due to the linearity of the reduced gravity model. The slope of the parameterization at (H_m, T_c), controlled by the parameter Γ, is calibrated by performing a least-squares optimization using 240 months of observed 50 m temperature sections for the 1980–1999 period from the analysis of Behringer et al. (1998).
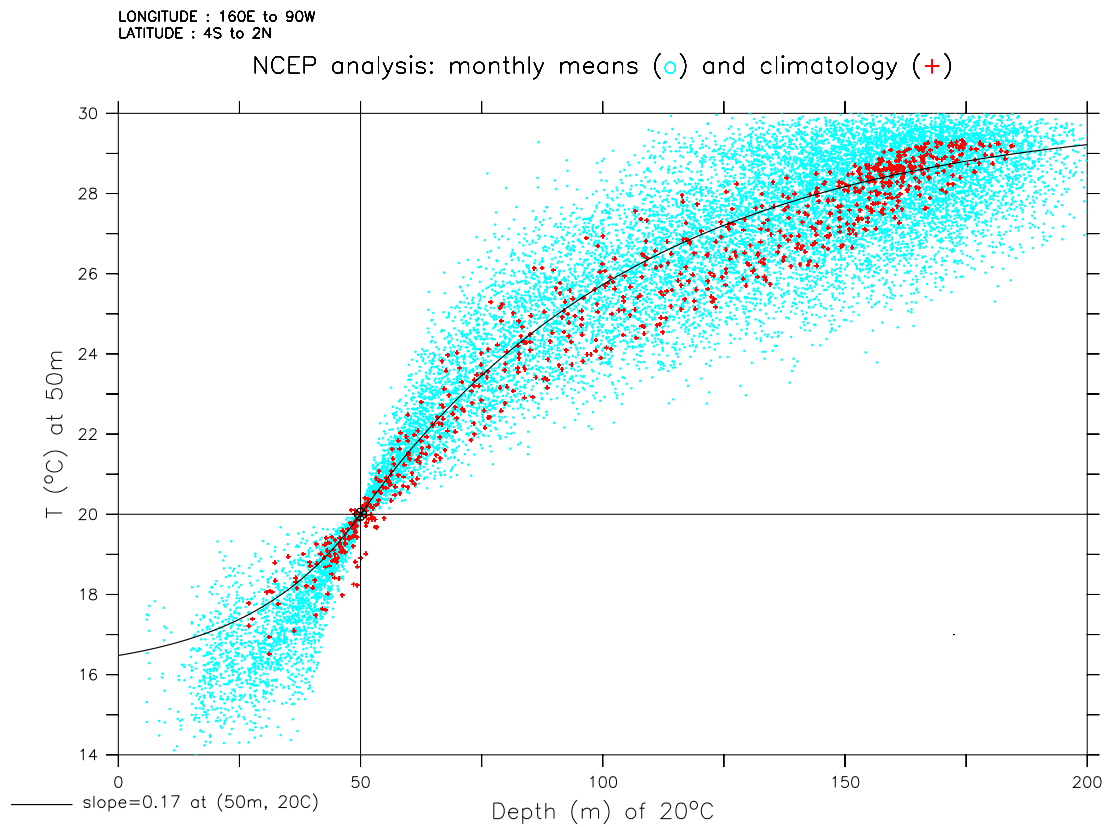
Figure 4.7: Temperature at 50 m depth, versus the depth of the 20°C isotherm, over the region 160°E–90°W, 4°S–2°N. Dots indicate monthly means (1980–1999) from the observational analysis of Behringer et al. (1998); crosses indicate the monthly climatology over this period. Solid line is the model parameterization, which is calibrated to the dots.

Note that the slope of the parameterization would be somewhat less steep if the fit were done to the climatology, since time-averaging of the ever-fluctuating thermocline tends to smooth out the vertical thermal profile. The smoothed climatological profile is the one more relevant to a simulation of climatological SST done with constant winds, since the missing time-mean effects of variability would be implicitly included in the parameterization. For simplicity, however, we shall use the sharper "instantaneous" profile for both the climatology simulation and the anomaly simulations. The steeper T_e parameterization will help to eliminate excessive cooling in the central Pacific where the simulated thermocline is slightly too shallow.

Fig. 4.8 shows a comparison of the model parameterization of T_e anomalies with the observed temperature anomalies at 50 m. The observed anomalies show little propagation except for some eastward propagation in the far eastern Pacific. The parameterized anomalies, on the other hand, show pronounced eastward propagation in the west/central equatorial Pacific, associated with the propagation of thermocline depth anomalies. Thus the parameterization is poorest in the central Pacific (180°W–140°W), where entrainment temperature anomalies are underestimated during ENSO events. This is likely the result of zonal advection below 50 m depth, which is ignored by the exclusive thermocline depth dependence of (4.22). In reality, eastward undercurrent anomalies act on the mean westward gradient of temperature to warm the subsurface in the central Pacific during El Niño, and westward undercurrent anomalies tend to cool the central Pacific during La Niña. In the intermediate model, part of this effect will be accounted for by advection in the mixed layer. However, we expect that the model will probably underestimate the SST variability in the central Pacific.

Many studies have shown that in the tropics and at interannual time scales, the net surface heat flux generally acts as a damper on SST anomalies (Liu and Gautier, 1990; Barnett et al., 1991; Cayan, 1992; Auad et al., 2001), except possibly in the central basin where evaporative changes associated with trade wind variability can sometimes enhance SSTAs (Seager, 1989). In the present model, we parameterize the surface heat flux as a linear restoring of the SST to a latitudinally-dependent temperature field $T_0(y)$, shown in Fig. 4.9 for the standard parameters of Table 4.2. For an SST damping rate of $\epsilon = 20$ W m^{-2} K^{-1}, this parameterization does a good job reproducing the observed surface heat flux, both for the climatology and the anomalies (Fig. 4.10). For the anomalies, the parameterization is better for the east Pacific than for the central Pacific. This is because changes in wind speed, which are not accounted for by the parameterization, induce substantial variability of the latent cooling over the central Pacific.

The entrainment efficiency γ and horizontal eddy diffusivity κ are chosen so that the mixed layer model reproduces observed SSTs when forced with observed wind stresses and entrainment temperatures. Fig. 4.11 shows that for the standard values of these parameters in Table 4.2, the model does a good job reconstructing the observed SST anomalies given the observed stress anomalies and T_e anomalies. There is a slight cold bias in the western Pacific and a slight warm bias near 120°W. The long-term warming trend evident in the NCEP ocean analysis is not reproduced in the intermediate model simulation, perhaps because the latter assumes no change in the radiative equilibrium temperature over the simulation period.
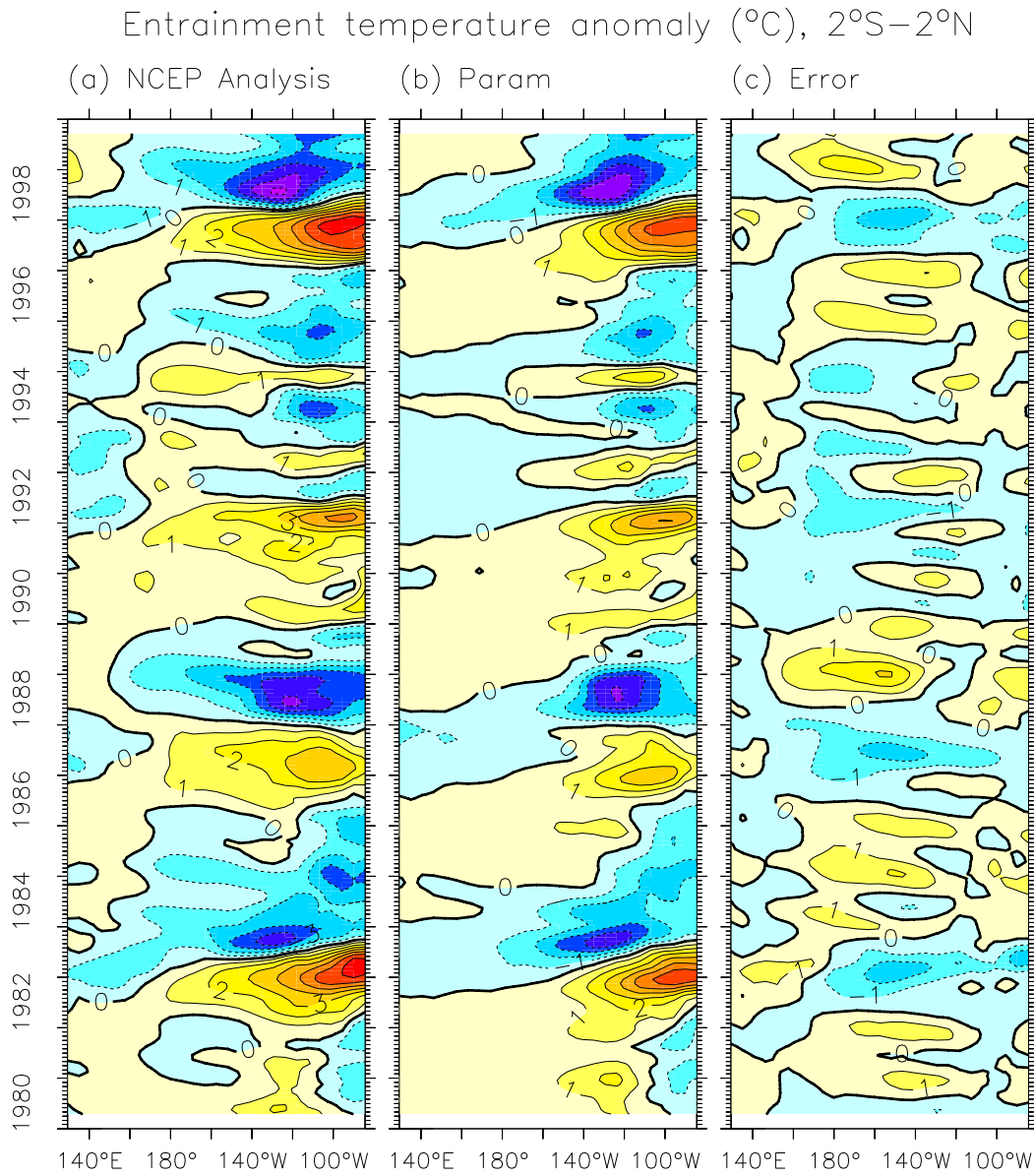
Figure 4.8: Anomalous temperature at 50 m depth, averaged over 2°S–2°N and smoothed with a 7-month triangle filter. (a) Observed anomalies from the analysis of Behringer et al. (1998). (b) Model parameterization in terms of the depth of the 20°C isotherm from Behringer et al. (1998). (c) Parameterization minus observations.
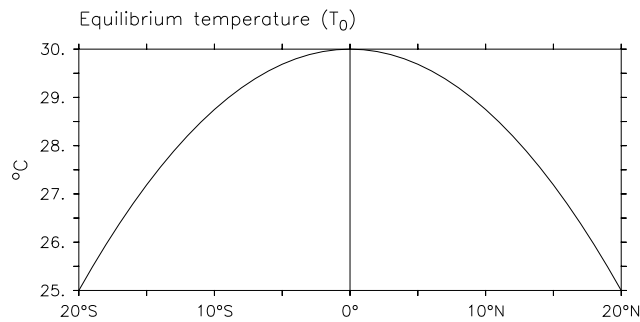
Figure 4.9: Meridional structure of the equilibrium temperature field $T_0(y)$, toward which SST is restored in the intermediate model.
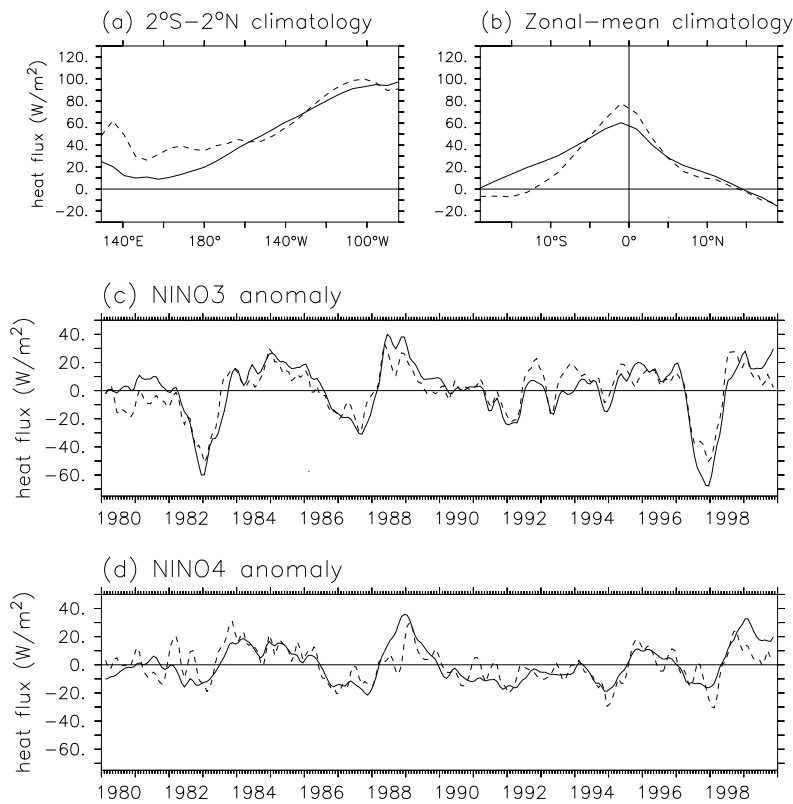
Figure 4.10: Dashed curves are the observed total surface heat fluxes into the ocean from the NCEP reanalysis (Kalnay et al., 1996) over the 1980–1999 period. Solid curves are the parameterized fluxes based on the reanalysis SST. Anomalies are with respect to the monthly climatology and have been smoothed with a 3-month triangle filter. (a) Time-mean heat flux averaged over 5°S–5°N. (b) Time-mean heat flux averaged zonally across the basin. (c) Anomalous heat flux averaged over the NINO3 region (150°W–90°W, 5°S–5°N). (d) Anomalous heat flux averaged over the NINO4 region (160°E–150°W, 5°S–5°N).
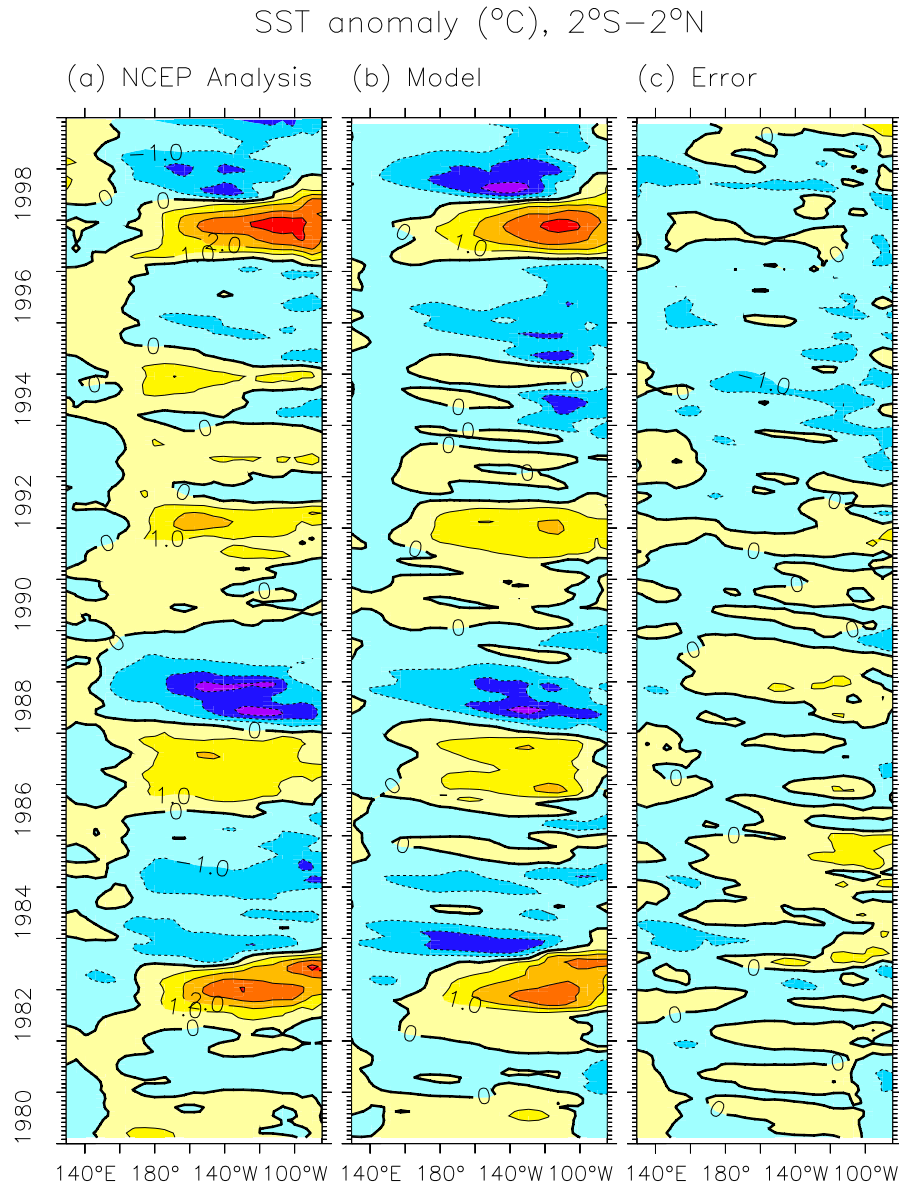
Figure 4.11: SST anomaly (°C), averaged over 2°S–2°N and smoothed with a 3-month triangle filter. (a) Observational analysis of Behringer et al. (1998). (b) Model forced with analyzed stress anomalies from FSU and analyzed 50 m temperature anomalies from Behringer et al. (1998). The climatological temperatures for the model are set equal to the 1980–1999 climatology from the Behringer et al. (1998) analysis, while the climatological currents are simulated by forcing with the FSU stress climatology for that period. (c) SST anomaly error, model minus observations.

4.2.4   Climatology simulation

Mean fields

To simulate the annual-mean climatology of the tropical Pacific ocean, the model is spun up for 10 years using the FSU stress climatology for the 1980–99 period. Fig. 4.12 shows that the model does a good job reproducing the observed thermal structure of the equatorial ocean, although the simulated SST is slightly too warm in the central Pacific. The simulated upwelling at the base of the mixed layer is slightly stronger than, and shifted east of, that in the Behringer et al. (1998) analysis. The simulated zonal current in the mixed layer is more strongly westward than the analyzed zonal current in the upper 50 m, because in the analysis the eastward undercurrent extends above 50 m depth in the eastern Pacific (i.e. in reality the mixed layer is shallower than 50 m in the east). The model also does a decent job simulating the zonal-mean climatological fields (Fig. 4.13). The off-equatorial errors in the subsurface thermal structure are of little concern, because there is very little upwelling in those regions to communicate such errors to the surface.

Climatological heat budget

A time-dependent variable ψ may be split into two components: a climatology (cyclic time-mean) $\overline{\psi}$ and an anomaly ψ' from this climatology: $\psi = \overline{\psi} + \psi'$. The climatology of (4.18) is

$$
\begin{aligned}
\partial_t \overline{T} &= -\overline{u}\partial_x\overline{T} - \overline{u'\partial_x T'} - \overline{v}\partial_y\overline{T} - \overline{v'\partial_y T'} \\
&\quad -\overline{\mathcal{R}(w)}\,\partial_z\overline{T} - \overline{\mathcal{R}'(w)\partial_z T'} \\
&\quad +\kappa\nabla^2\overline{T} - \epsilon(\overline{T} - T_0)
\end{aligned}
\tag{4.25}
$$

where $\mathcal{R}'(w) \equiv \mathcal{R}(w) - \overline{\mathcal{R}(w)}$. This equation describes the exact evolution of the climatological SST, assuming the completeness of (4.18).

The shallow-water model is linear and damped. Thus when the ocean model is forced with steady winds, it converges to a steady state climatology. In this case the climatological mixed layer heat balance is

$$
\begin{aligned}
\partial_t\overline{T}\big|_{model} &= 0 \\
&= -\overline{u}\partial_x\overline{T} - \overline{v}\partial_y\overline{T} - \mathcal{R}(\overline{w})\partial_z\overline{T} + \kappa\nabla^2\overline{T} - \epsilon(\overline{T} - T_0)
\end{aligned}
\tag{4.26}
$$

Note that the eddy terms of (4.25) are absent from (4.26), due to the lack of variability in the climatological wind stress forcing.

The annual-mean surface heat budget, neglecting temporal eddy terms, is shown in Fig. 4.14. The surface flux, which acts to restore the SST to T_0, is the largest single term in the heat budget. The existence of the equatorial cold tongue can be attributed to vertical entrainment, which dominates the heat budget in the east. Horizontal advection, which carries the cooling westward, becomes larger than the vertical entrainment term west of 140°W. Meridional advection carries cold water to the equator from the upwelling zone just south of the equator in the eastern Pacific; it also acts to widen the cold tongue by spreading it poleward. The horizontal mixing (eddy diffusion) also spreads the cold tongue,
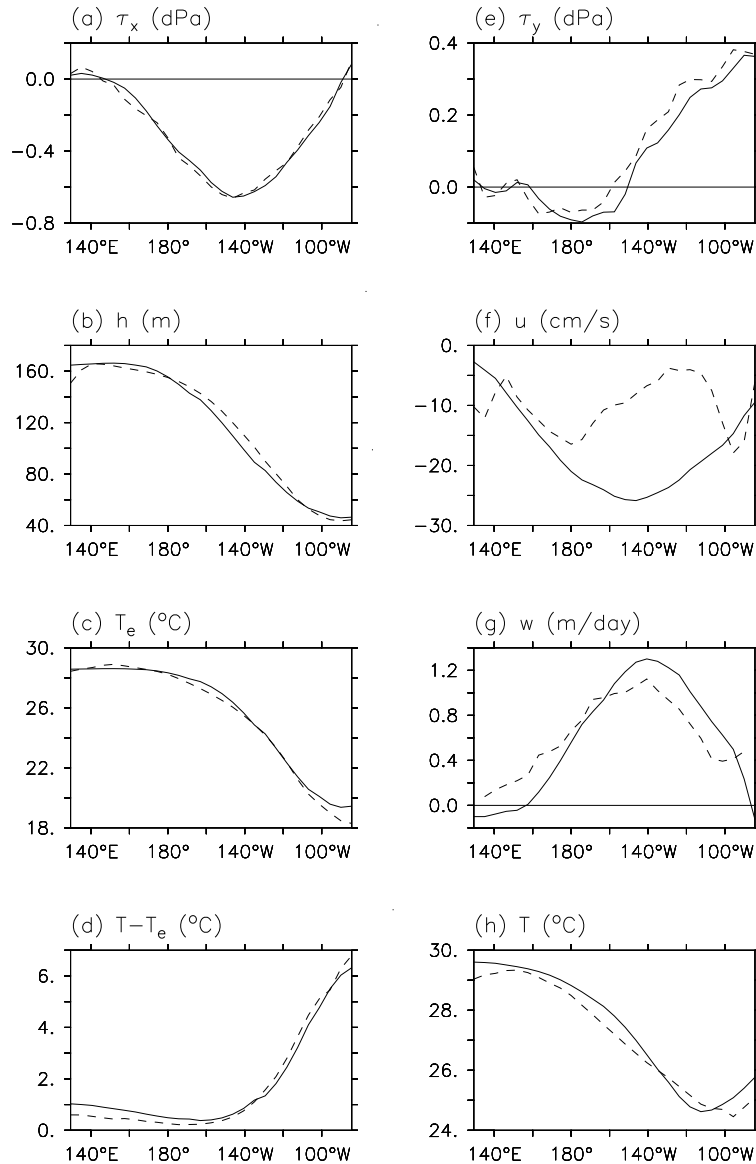
Figure 4.12: Annual-mean oceanic climatological fields at the equator (2°S–2°N). Dashed lines are from the observational analysis of Behringer et al. (1998). Solid lines are from the standard version of the intermediate model forced by the 1980–99 FSU stress climatology. (a) Zonal wind stress, (b) depth of the 20° isotherm, (c) temperature at 50 m, (d) temperature at surface minus that at 50 m, (e) meridional wind stress, (f) zonal current averaged over the top 50 m, (g) vertical velocity at 50 m, (h) SST.
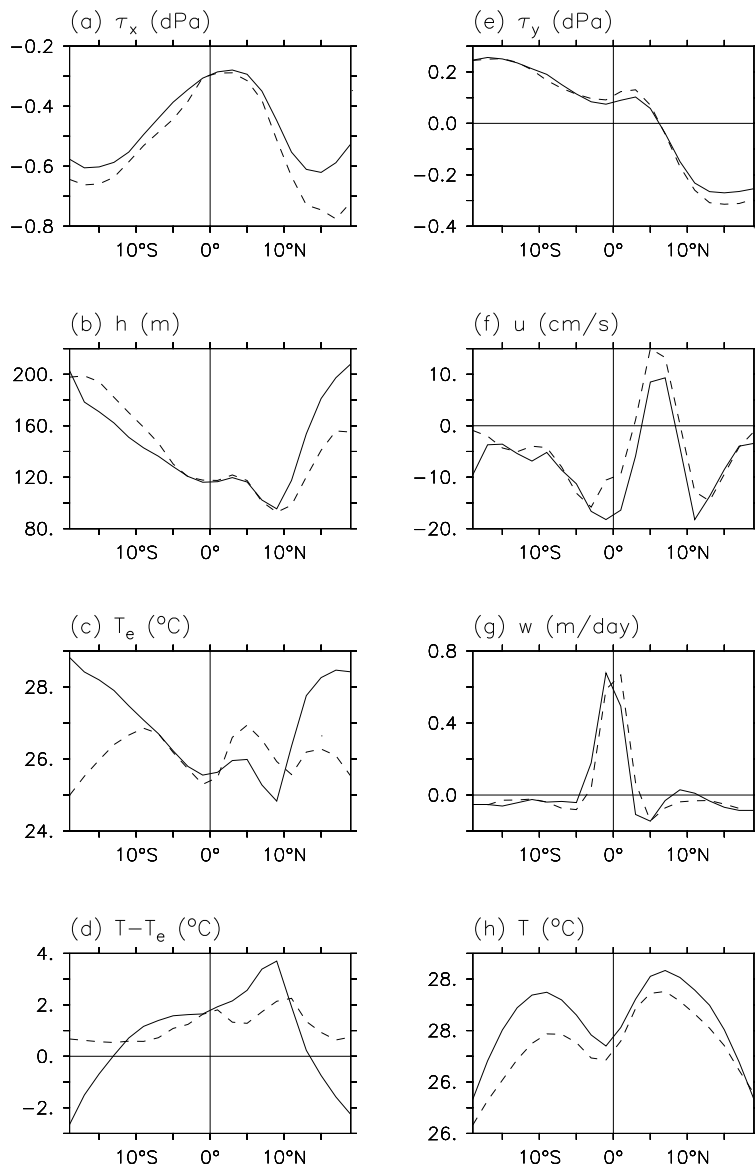
Figure 4.13: As in Fig. 4.12, but for zonal-mean fields.
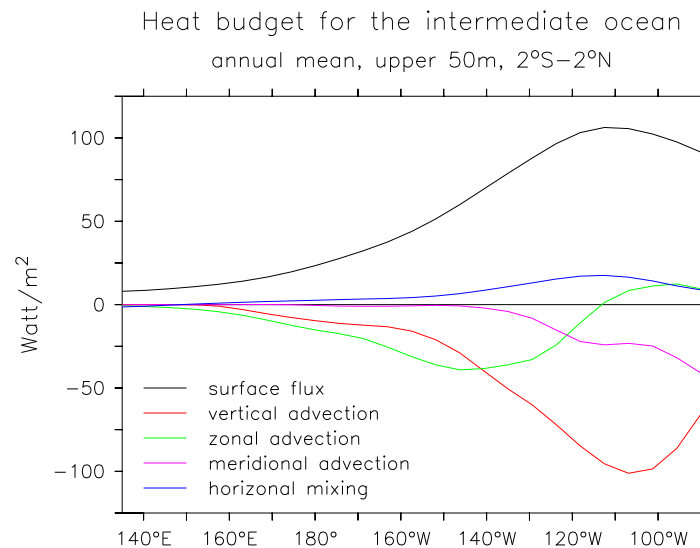
Figure 4.14: Annual-mean surface heat budget (Watts m^{-2}) in the standard model forced by the climatological FSU stresses from 1980–1999. Budget terms are averaged over the equatorial band (2°S–2°N); temporal eddy terms are neglected. Positive values indicate a warming effect on the mixed layer.

by exchanging cold water near the equator with warmer water away from it; mixing thereby acts as a weak damping on the equatorial SST anomalies.

Fig. 4.14 indicates that vertical entrainment will be the key to understanding SST variability in the eastern equatorial Pacific. The other terms in the heat budget are either smaller or act primarily to damp or spread the anomalies generated by entrainment. The longitudinal phase difference between entrainment and zonal advection also suggests that the interplay between these terms may determine whether SST anomalies propagate eastward or westward. This interplay, in turn, is keenly dependent on the structure of the mean state: entrainment dominates in the east because there the thermocline is shallow, and zonal advection dominates in the central Pacific because there the zonal gradient of SST is strong. Thus Fig. 4.14 provides much of the motivation and explanation for the results in this thesis.

4.2.5 ENSO simulation

Next, the climatological fields from Section 4.2.4 are used as the background state for a model simulation forced by observed stress anomalies for 1980–1999. The active layer depth H for the anomaly simulation is taken to be the average, zonally across the basin and meridionally across the 8°S–8°N latitude band, of the thermocline depth from the climatology simulation.
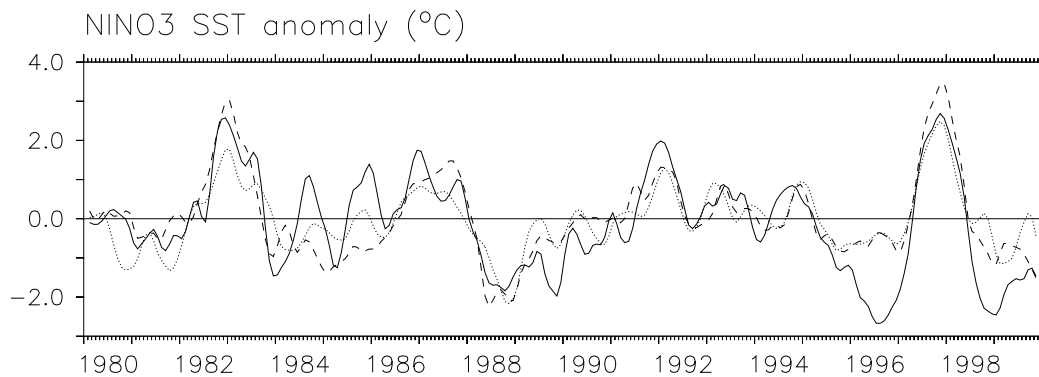
Figure 4.15: SST anomaly (°C) averaged over the NINO3 region (5°S–5°N, 150°W–90°W) and smoothed with a 3-month triangle filter. Dashed line is the observational analysis of Behringer et al. (1998). Solid line is the standard model forced by the FSU stress anomalies; dotted line is forced by the NCEP stress anomalies.

Importance of the stress forcing

Fig. 4.15 illustrates how forcing with different stress products can impact the simulation of SST anomalies. For both the FSU and NCEP stress products, the model underestimates the intensities of the 1984–86 cold period and the 1982–83 and 1997–98 warm events. However, beginning in 1984 the NCEP forcing generally produces NINO3-average SST anomalies with better timing and amplitude than does the FSU forcing. This is especially the case during 1984–87, 1996, and 1998–99. In particular, the NCEP forcing gives much weaker easterly stress anomalies than FSU during the late 1990s, which produces weaker (and more realistic) cold events during that period. Before 1984, however, the NCEP forcing produces somewhat less realistic-looking SST anomalies than does the FSU forcing (see Chapter 2).

Anomaly fields

A comparison between the observed and FSU-forced model SST anomalies at the equator for this period is shown in Fig. 4.16. The simulation looks reasonably similar to the observations, although the model anomalies are more confined to the eastern Pacific than observed. The model shows too much SSTA variance at periods less than one year, due to a similar problem with the thermocline simulation (Fig. 4.3). This could be due to limitations of the stress forcing (Chapter 2), perhaps amplified by the spurious basin resonance noted earlier. The simulated cold events in 1996 and 1998–1999 are too strong, perhaps again due to errors in the FSU stress forcing; and the simulation lacks the observed warming trend, possibly due to the model's neglect of temporal changes in the long-term radiative balance.
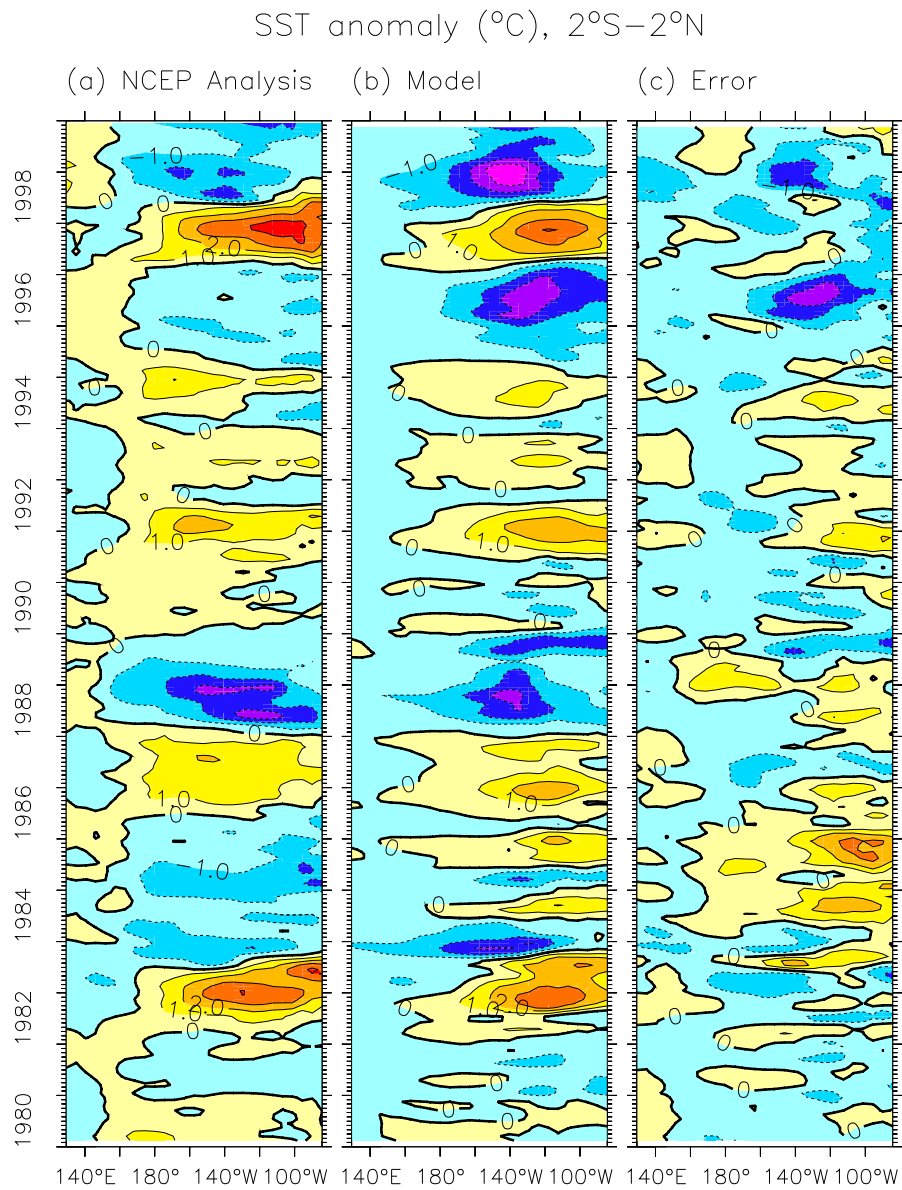
Figure 4.16: SST anomaly (°C) averaged over 2°S–2°N and smoothed with a 3-month triangle filter. (a) Observational analysis of Behringer et al. (1998). (b) Model forced with analyzed stress anomalies from FSU. The climatological background state for the model is simulated by forcing with the FSU stress climatology for that period. (c) SST anomaly error, model minus observations.

Anomalous heat budget

Subtracting (4.25) from (4.18) gives the exact SSTA tendency equation:

$$
\begin{aligned}
\partial_t T' \;=\; & -u'\partial_x\overline{T} - \overline{u}\partial_x T' - (u'\partial_x T')' \\
& -v'\partial_y\overline{T} - \overline{v}\partial_y T' - (v'\partial_y T')' \\
& -\mathcal{R}'(w)\partial_z\overline{T} - \gamma\overline{\mathcal{R}(w)}\partial_z T' - (\mathcal{R}'(w)\partial_z T')' \\
& +\kappa\nabla^2 T' - \epsilon T'
\end{aligned}
\tag{4.27}
$$

The model SSTA tendency equation, on the other hand, is obtained by subtracting (4.26) from (4.18):

$$
\begin{aligned}
\partial_t T'\big|_{model} \;=\; & -u'\partial_x\overline{T} - \overline{u}\partial_x T' - u'\partial_x T' \\
& -v'\partial_y\overline{T} - \overline{v}\partial_y T' - v'\partial_y T' \\
& -\mathcal{R}^*(w)\partial_z\overline{T} - \mathcal{R}(\overline{w})\partial_z T' - \mathcal{R}^*(w)\partial_z T' \\
& +\kappa\nabla^2 T' - \epsilon T'
\end{aligned}
\tag{4.28}
$$

where $\mathcal{R}^*(w) \equiv \mathcal{R}(w) - \mathcal{R}(\overline{w})$. The model SSTA tendency (4.28) differs from the exact SSTA tendency (4.27) because the model climatology neglects the effects of transient eddies (such as ENSO). As a result, anomalies simulated using (4.28) in a fully-coupled model may have nonzero mean.

If one were to assume, for the sake of contradiction, that the primed terms in (4.28) had zero mean, then the time average of (4.28) would be

$$
0 = -\overline{u'\partial_x T'} - \overline{v'\partial_y T'} - \overline{\mathcal{R}^*(w)\partial_z T}
\tag{4.29}
$$

where the last term contains the total $\partial_z T$ due to the nonlinearity of the ramp function. Thus there will be no climate drift if the anomalous currents and temperature gradients are temporally uncorrelated and the total upwelling never changes sign. If the terms on the RHS of (4.29) are large and do not cancel, then the anomalies will develop nonzero mean values, which will then feed back on the climatology through the linear terms in (4.28) as well as through the nonlinear terms. The net effect of the eddy terms on the time mean of (4.28) will provide a measure of their possible role in the observed climatology.

Figs. 4.17 and 4.18 show the anomalous heat budgets at the surface in the eastern and western equatorial Pacific, respectively, for the simulation forced by observed stresses and entrainment temperatures (Fig. 4.11). The anomalous heat budget largely mirrors the climatological heat budget (Fig. 4.14). At 110°W, SST anomalies are generated primarily by mean upwelling acting on the anomalous vertical temperature gradient $(-\mathcal{R}(\overline{w})\partial_z T')$, with a contribution also from anomalous upwelling $(-\mathcal{R}^*(w)\partial_z\overline{T})$. Nonlinear and horizontal advection terms are generally small at 110°W, except during 1982 when anomalous eastward currents make a substantial contribution to the generation of a large warm event.

In contrast, at 170°W the zonal advection terms dominate the heat budget. Here the $-u'\partial_x\overline{T}$ and $-\overline{u}\partial_x T'$ terms act in concert to generate SST anomalies, while the nonlinear term $-u'\partial_x T'$ strongly opposes the generation of anomalies during warm events when the zonal gradient of total SST nearly vanishes. The complexity and nonlinearity of the heat
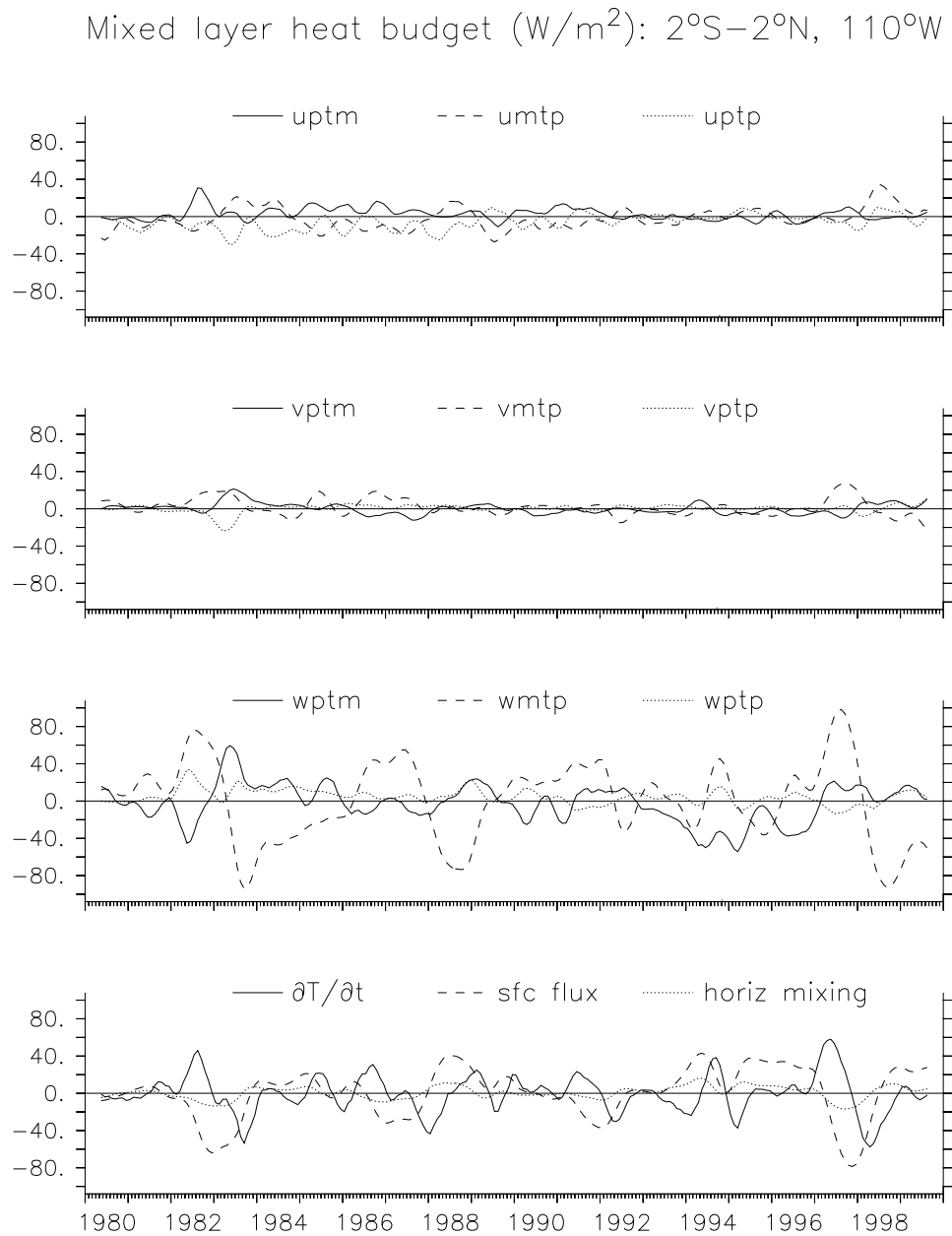
Figure 4.17: Mixed layer temperature tendency terms (Watts m^{-2}) at 110°W for the stress-forced simulation of Fig. 4.16, averaged over 2°S–2°N and smoothed with a 9-month triangle filter.

Mixed layer heat budget (W/m²): 2ºS−2ºN, 170ºW
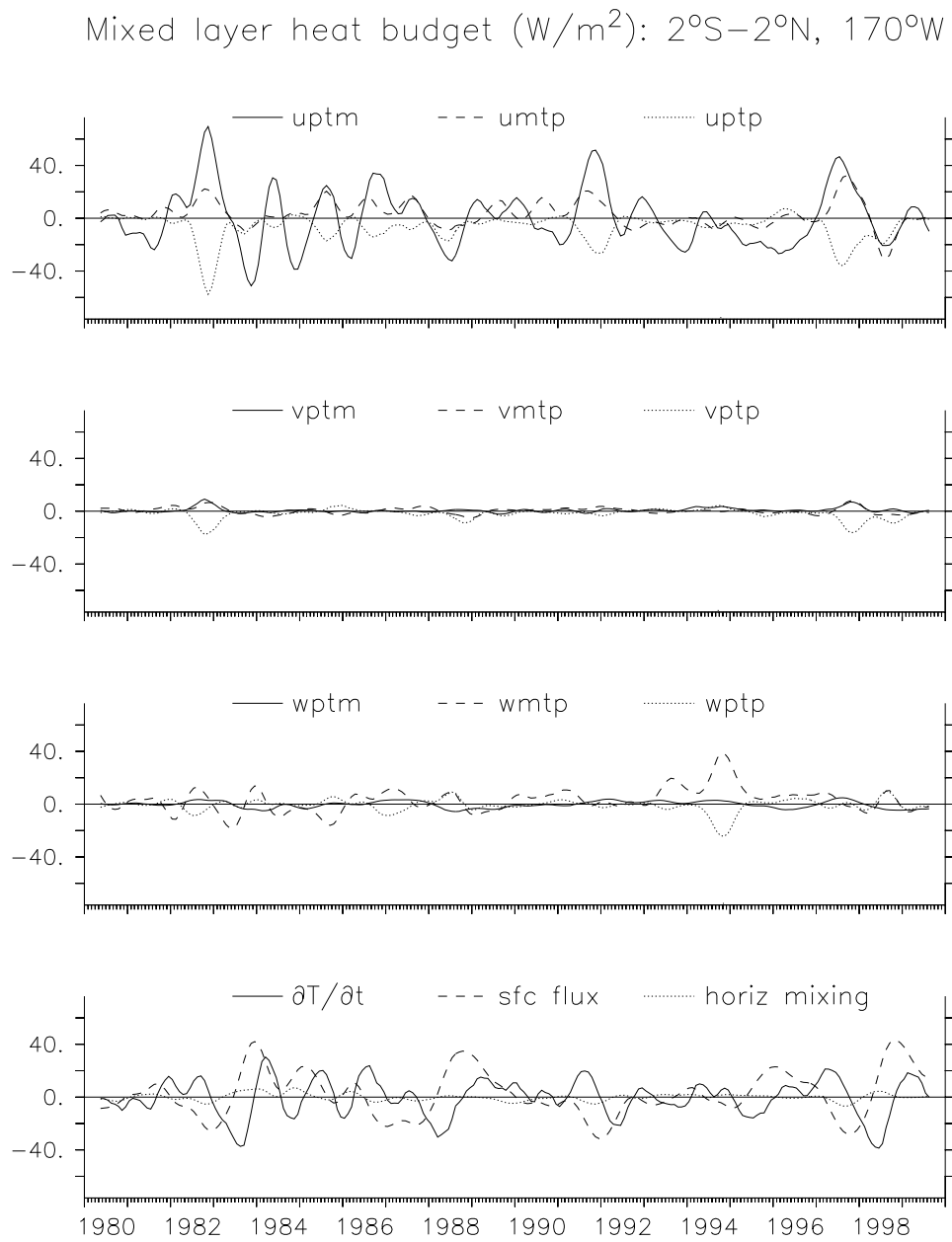
Figure 4.18: As in Fig. 4.17, but at 170°W.

Table 4.3: Stress perturbation parameters and their standard values.

Parameter	Symbol	Value
amplitude (weak)	$\tilde{\tau}_x^*$	0.001 dPa
amplitude (strong)	$\tilde{\tau}_x^*$	0.5 dPa
zonal position	x^*	165°W
meridional position	y^*	0°N
zonal halfwidth	Δx^*	40° lon
meridional halfwidth	Δy^*	10° lon
duration	Δt^*	3 months

budget in the west may be one reason the zonal propagation characteristics of ENSO seem to vary from event to event. Slow changes in the zonal gradient of SST through time may alter the delicate balance of zonal advective terms, changing the temporal phasing of the SST peak in the west relative to that in the east, thereby affecting the zonal propagation characteristics of SST anomalies during ENSO events.

4.3   Coupled model

4.3.1   Control run

Experimental setup

Next, the statistical atmosphere from FSU (1980–1999) is coupled to the dynamical ocean model to produce a hybrid coupled anomaly model (see Appendix D for a caveat regarding anomaly models). The climatology is generated as in Section 4.2.4, except that it is now averaged over the calendar year to produce a time-invariant background state. The anomaly model is then subjected to a transient zonal stress anomaly in the western Pacific, with the form

$$\tau_x^* = \tilde{\tau}_x^* \left[\mathcal{S}(t) - \mathcal{S}(t - \Delta t^*) \right] \exp \left[-\left| \frac{x - x^*}{\Delta x^*} \right|^2 - \left| \frac{y - y^*}{\Delta y^*} \right|^2 \right] \tag{4.30}$$

where $\mathcal{S}$ is the Heaviside step function

$$\mathcal{S}(t) \equiv \begin{cases} 0 & : & t \leq 0 \\ 1 & : & t > 0 \end{cases} \tag{4.31}$$

Standard parameters for the stress perturbation are given in Table 4.3.

Response to a westerly wind event

Fig. 4.19 shows the response of the hybrid coupled model to a strong transient westerly stress anomaly ($\tilde{\tau}_x^* = 0.5$ dPa). The model responds with a strong initial warm event, followed by a regular oscillation with a 3.1 yr period and an e-folding decay timescale of about 10 yr. To first order, the SST anomalies, zonal stress anomalies, and thermocline depth anomalies are best described as developing in place and in phase. The SST anomalies
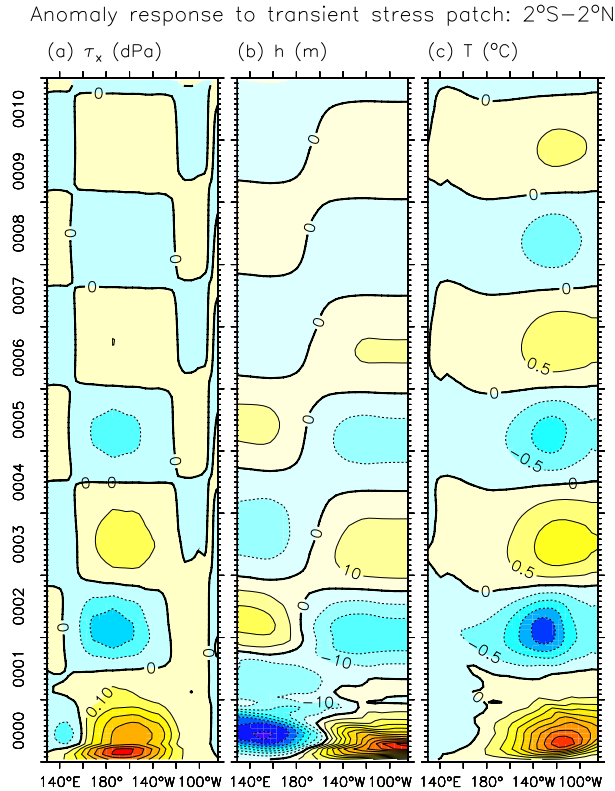
Figure 4.19: Equatorial (2°S–2°N) response of the standard hybrid coupled model to a transient westerly stress perturbation in the central Pacific: (a) zonal stress anomaly (dPa), (b) thermocline depth anomaly (m), (c) SST anomaly (°C). The amplitude of the initial stress perturbation is $\tilde{\tau}_x^* = 0.5$ dPa.

are focused near 120°W during warm events, slightly further west during cold events. The weak SST anomalies west of the dateline show evidence of westward propagation, and there is a slight hint of eastward propagation east of the dateline. The zonal stress shows peak westerly anomalies near 165°W during warm events, and peak easterly anomalies slightly further west during cold events. The thermocline exhibits an east-west seesaw about 170°W, deepening in the east and shoaling in the west during warm events. The thermocline depth near 170°W leads that in the eastern Pacific by a quarter cycle, giving the appearance of eastward propagation of the thermocline depth anomalies between events.

Figs. 4.20 and 4.21 show the heat budget of the mixed layer, starting in year 100 when the oscillation amplitude is significantly reduced and only the least damped mode remains. In this regime, the contributions of the nonlinear terms and $-v'\partial_y \overline{T}$ to the SST budget are small and can be ignored. As noted by Kang et al. (2001), the phase lag between each tendency term and the SSTA reveals the extent to which that term is an instability mechanism which acts to amplify ENSO, or a transitioning mechanism that acts to carry ENSO between warm and cold events. Fig. 4.20 indicates that the surface flux, for example, is a purely stabilizing mechanism in the present model since it is simply a linear damping
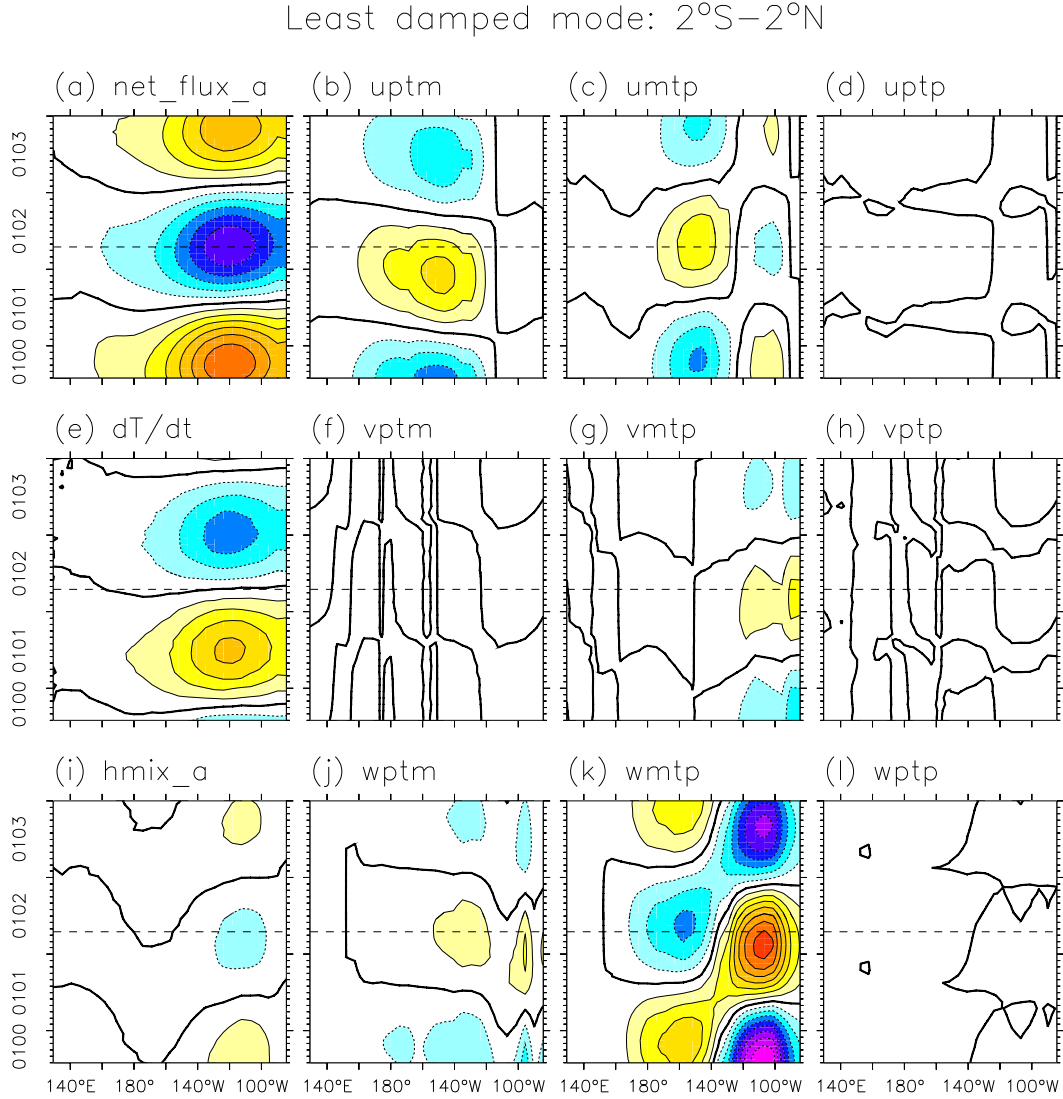
Figure 4.20: Mixed layer temperature tendency terms (averaged 2°S–2°N) for the experiment of Fig. 4.19, long after the initial perturbation when the oscillation is extremely weak and the dynamics are linear. Vertical axis indicates years since perturbation; dashed horizontal line indicates the peak of a warm event. Contour interval is 0.00025 Watts m^{-2}, heavy contour indicates zero; warm colors indicate positive values, cool colors negative values; near-zero values are not shaded. Panels show (a) $-\epsilon T'$, (b) $-u'\partial_x\overline{T}$, (c) $-\overline{u}\partial_x T'$, (d) $-u'\partial_x T'$, (e) $\partial_t T'$, (f) $-v'\partial_y\overline{T}$, (g) $-\overline{v}\partial_y T'$, (h) $-v'\partial_y T'$, (i) $\kappa\nabla^2 T'$, (j) $-\mathcal{R}^*(w)\partial_z\overline{T}$, (k) $-\mathcal{R}(\overline{w})\partial_z T'$, (l) $-\mathcal{R}^*(w)\partial_z T'$. SST anomaly is obtained by dividing the surface flux anomaly in (a) by $-\epsilon$.
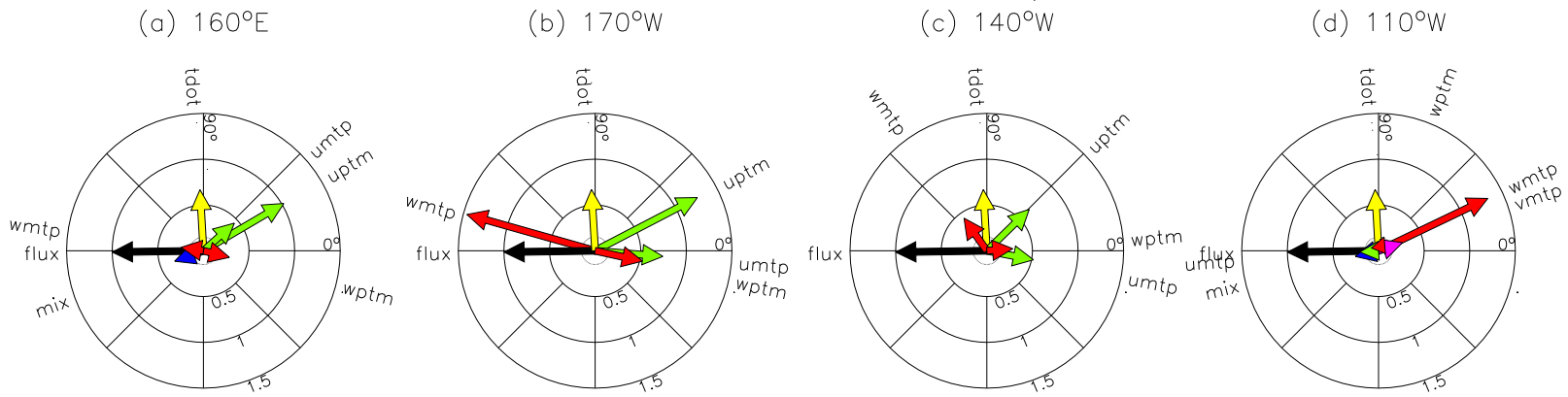
Figure 4.21: Mixed layer temperature tendency phasors (averaged 2°S–2°N) for the experiment of Fig. 4.19, long after the initial perturbation, at longitude (a) 160°E, (b) 170°W, (c) 140°W, (d) 110°W. Each diagram indicates the amplitude (relative to the surface heat flux) and phase lead (relative to local SSTA) of the tendency terms, and reads like a clock: a given phasor leads the one to its right. The peak SST warm anomaly occurs at 0° phase (3 o'clock). The graticule scale is labeled in units of the surface flux damping rate ϵ.

on SSTA.

The $-\mathcal{R}(\overline{w})\partial_z T'$ term plays important but varying roles all across the equatorial Pacific. In the eastern Pacific, $-\mathcal{R}(\overline{w})\partial_z T'$ leads SSTA slightly and therefore plays dual roles as an instability and transition mechanism. In the western/central Pacific, $-\mathcal{R}(\overline{w})\partial_z T'$ is almost perfectly out of phase with SSTA and so acts as a stabilizing mechanism. This is because in the western Pacific the model shows hardly any entrainment temperature anomalies; the vertical temperature gradient therefore follows the surface temperature and SSTAs are damped through mean upwelling.

Zonal advection plays an important role in the central and western Pacific. The $-u'\partial_x\overline{T}$ term, which is most active near $140°$W, leads SSTA slightly more than $-\mathcal{R}(\overline{w})\partial_z T'$ and therefore plays a stronger role as a transitioning mechanism for the simulated ENSO. The transitioning role of $-u'\partial_x\overline{T}$ has been a common theme in recent studies. Picaut and Delcroix (1995) and Picaut et al. (1997), in particular, argued for its importance to the observed ENSO, proposing an advective-reflective conceptual model that depended strongly on zonal advection by Rossby signals reflected from the eastern boundary. The surface current anomalies are also important for redistributing mass within the tropical Pacific Ocean. Goddard and Philander (2000) examined the oceanic energy budget in a wind-forced ocean GCM, and found that the power input to the ocean by the mean wind stress acting on the anomalous currents, which preceded the peak SST anomalies by 3 months, was the greatest generator of available potential energy in the Pacific Ocean at interannual timescales.

The $-\overline{u}\partial_x T'$ term, on the other hand, acts as an SSTA amplifier in the central Pacific (on the western side of the SST anomalies generated by $-\mathcal{R}(\overline{w})\partial_z T'$), and a damper in the eastern Pacific (on the eastern side of the SST anomalies generated by $-\mathcal{R}(\overline{w})\partial_z T'$). Other terms play secondary roles; $-\overline{v}\partial_y T'$ and $-\mathcal{R}^*(w)\partial_z\overline{T}$ act to destabilize ENSO, while $\kappa\nabla^2 T'$ plays more of a stabilizing and "anti-transitioning" role. It is interesting to note that in the western basin, $-\mathcal{R}^*(w)\partial_z\overline{T}$ practically cancels the damping effect of $-\mathcal{R}(\overline{w})\partial_z T'$, so that zonal advection almost entirely controls the evolution of SST anomalies in this region.

The heat budget is somewhat different during the transient phase immediately following the stress perturbation. Fig. 4.22 shows the heat budget of the mixed layer during the first few years after the westerly wind event. Compared to the small-amplitude oscillation in Fig. 4.20, the transient behavior indicates a much stronger role for zonal advection and nonlinearity. The stress perturbation induces strong eastward current anomalies, which act to warm the central Pacific by advecting the warm pool eastward (Fig. 4.22b). As the east Pacific warms, the zonal SST gradient weakens and the effect of $-u'\partial_x\overline{T}$ is strongly opposed by $-u'\partial_x T'$. Vertical advection also contributes strongly to the initial warming in the east Pacific, as less water and warmer water is entrained into the mixed layer. The strong reduction in entrainment also implies a role for $-\mathcal{R}^*(w)\partial_z T'$, which reduces the impact of sub-mixed-layer temperature changes on SST. The warm event peaks soon after the imposed westerly stress is removed, as cold water is conveyed westward by Rossby waves reflected from the eastern boundary, and as the equatorial thermocline continues to shoal due to the strong off-equatorial wind stress curl associated with the atmospheric response to the SST warming. By 18 months the SST has returned to normal, but there is still a cooling tendency due to $-\mathcal{R}(\overline{w})\partial_z T'$ associated with the anomalously shallow equatorial

Figure 4.22: As in Fig. 4.20, but for the years during and immediately after the imposition of a strong westerly stress perturbation. Contour interval is 25 Watts m^{-2}.

thermocline. This cooling carries the system into a weak cold event, and the system settles into the modal behavior shown in Fig. 4.20.

Response to an easterly wind event

Fig. 4.23 shows the response of the model to an easterly stress perturbation ($\tilde{\tau}_x^* = -0.5$ dPa). Clearly, this response is not simply the opposite of that for a westerly wind event. The initial cooling develops rapidly in the central Pacific, due mostly to zonal advection. In contrast with Fig. 4.22, the nonlinear terms $-u'\partial_x T'$ and $-\mathcal{R}^*(w)\partial_z T'$ now act to *enhance* the initial effects of $-u'\partial_x \overline{T}$ and $-\mathcal{R}(\overline{w})\partial_z T'$, as anomalously strong currents act on an anomalously strong cold tongue. The cold event meets an abrupt end, as westerly anomalies develop in the east and cut off the source of cold water from the deep.

Thus we see that there is a fundamental difference in the way simulated strong warm and cold events develop and terminate. Warm events develop in the east via changes in vertical advection, especially that associated with vertical motions of the thermocline; zonal advection plays a secondary role during warm events since the zonal SST gradients are weakened. Cold events develop in the central Pacific via zonal advection, since the zonal SST gradients are enhanced during cold events; vertical advection plays a secondary role during cold events since the temperature of entrained water in the east can get no colder than the saturation temperature below the thermocline.

The simulated warm events, which are associated with westerly stress all along the equator, terminate because the off-equatorial cyclonic wind curl produces geostrophic divergence near the equator. This slowly drains warm water from the equatorial band, shoals the thermocline, and thereby reverses the SST tendency due to vertical advection. Cold events, which are associated with westerly stress near the dateline and easterly stress in the east, terminate due to zonal advection (associated with wave reflection at the eastern boundary, amplified by westerly stress anomalies in the east), and vertical advection (associated with the reduction of upwelling due to the westerly stress anomalies in the east)

4.3.2 Parameter sensitivity of the anomaly model

Before embarking on the climate sensitivity studies in the next chapter, we first investigate the sensitivity of the anomaly model to changes in its dynamical parameters. In these experiments, the background state is held fixed at the standard climatology described in Section 4.2.4. To connect with previous studies, we here introduce a "coupling parameter" μ which multiplies the stress anomalies produced by the statistical atmosphere. We take $\mu = 1.0$ as our standard value. Other important parameters include the active layer coefficients λ_h and λ_u, and the boundary reflectivities R_e and R_w.

Experimental setup

Two regimes are of interest. The first is the small-amplitude regime, where nonlinearities are weak and can be neglected. In this regime, after transient motions have decayed away, oscillations will take the form of a complex exponential that corresponds to the most unstable (or least damped) normal mode of the system. Often, the periods and growth
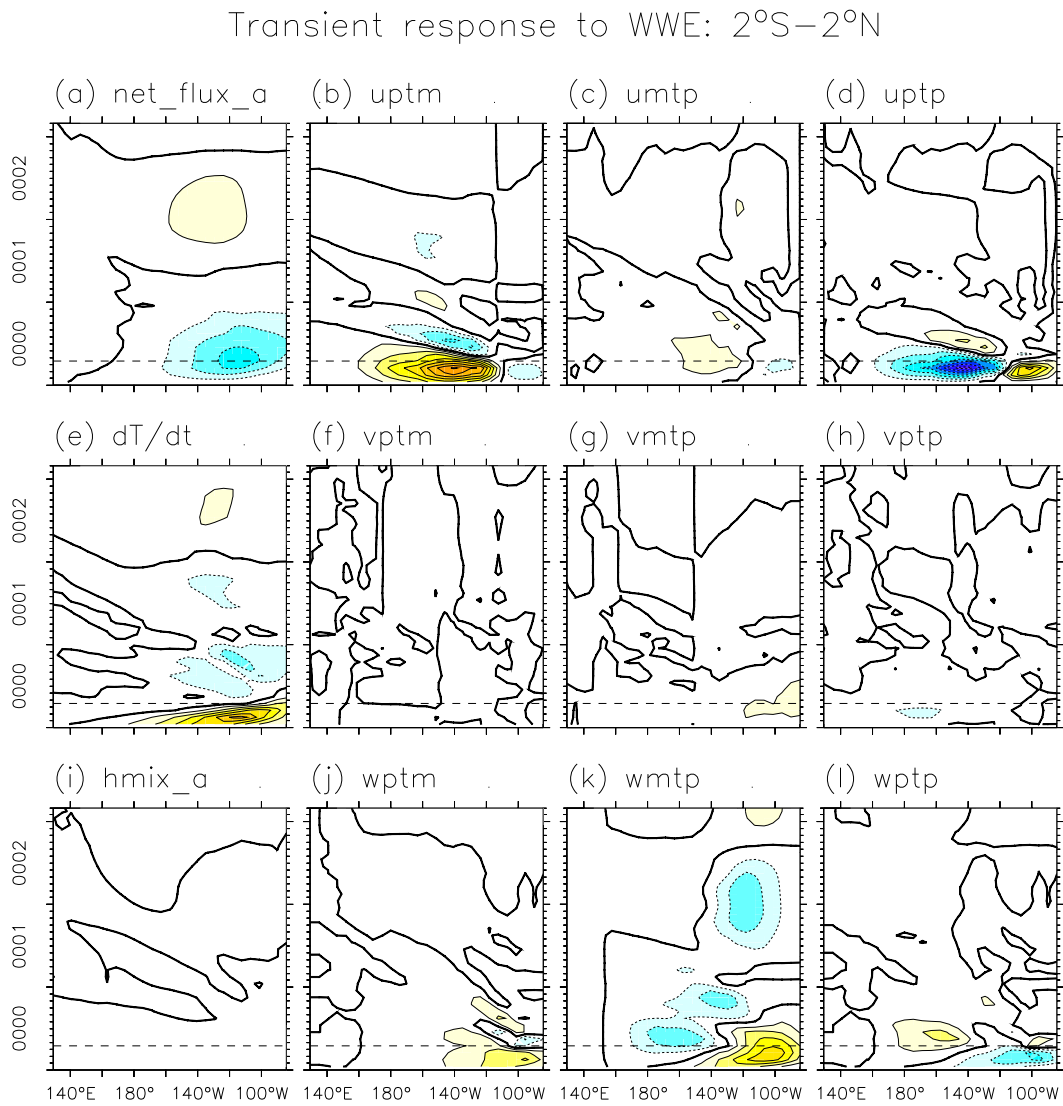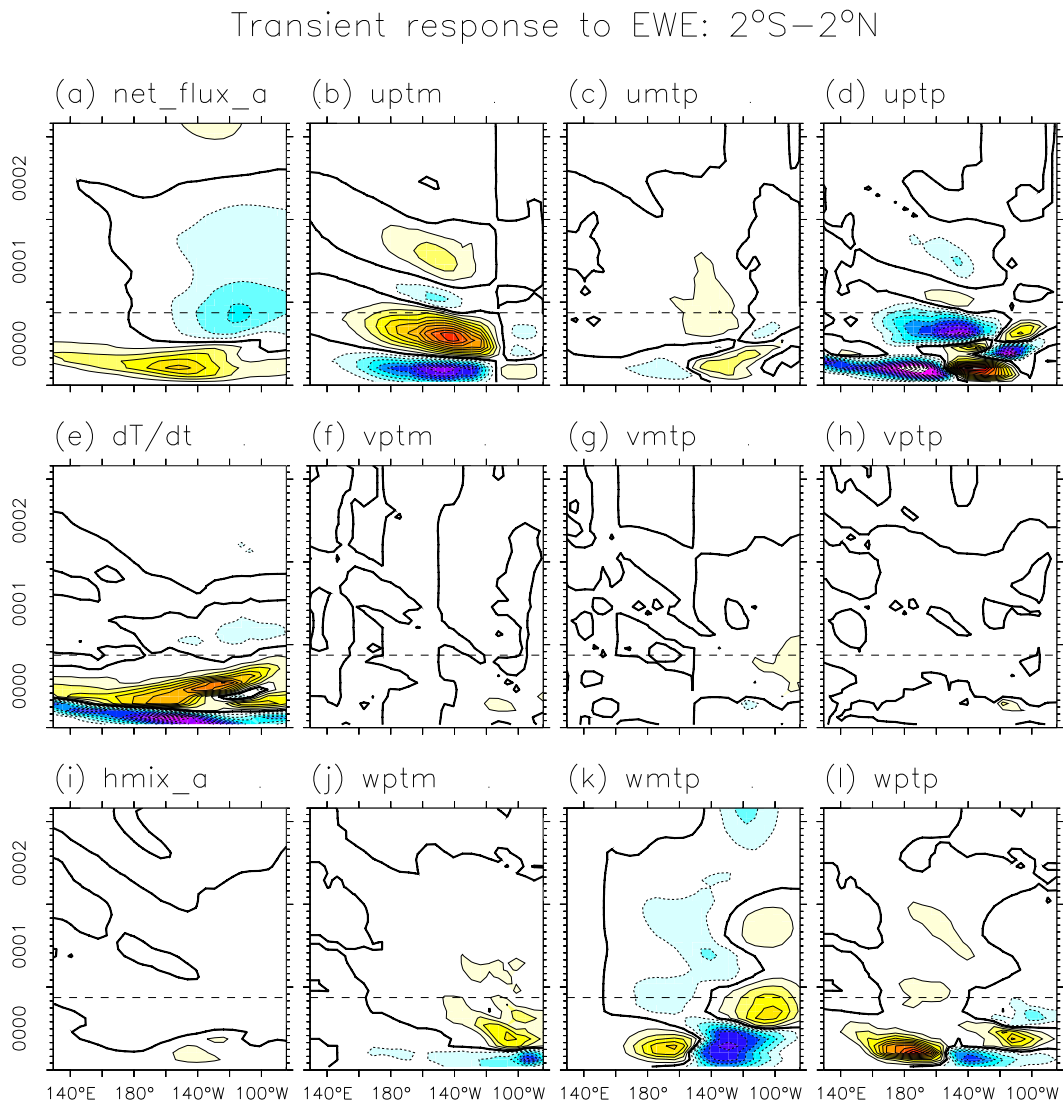
Figure 4.23: As in Fig. 4.22, but for the years during and immediately after the imposition of a strong easterly stress perturbation.
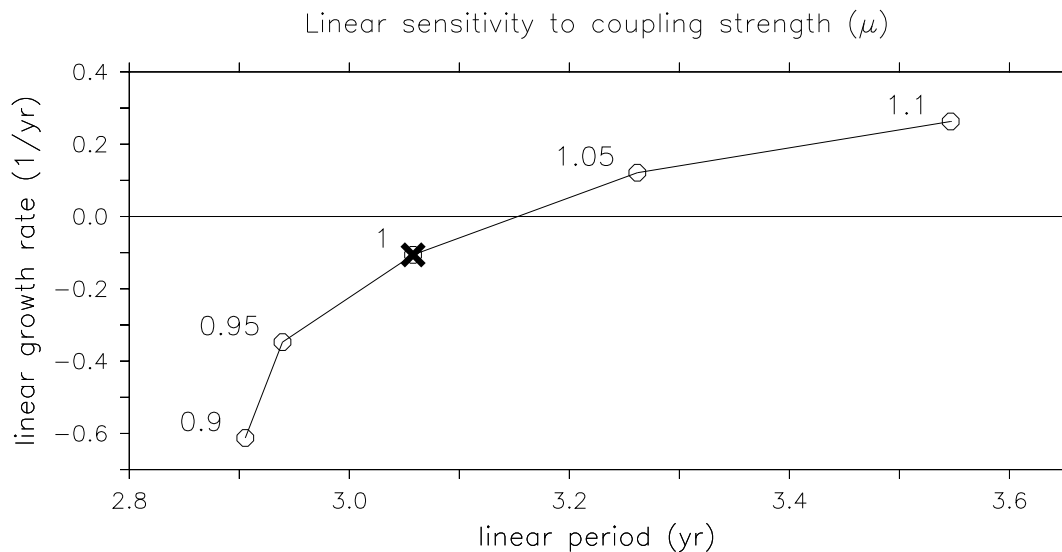
Figure 4.24: Dependence of the model linear growth rate (1/yr) and period (yr) on μ, the strength of the wind stress response to SST anomalies. Values of μ at the open circles are labeled. Standard model corresponds to $\mu = 1.0$ (X).

rates of the normal modes are obtained by casting the system in matrix form and solving the associated eigenproblem. In the present study, we estimate the period by counting the zero-crossings of the timeseries, and then estimate the growth rate by fitting exponential curves to and extrema of the timeseries. For small-amplitude oscillations this technique can recover the period and growth rate of the least damped mode, as long as the growth rate and nonlinear trend are small relative to the frequency. This technique is applied to the present model by perturbing with a very weak stress anomaly ($\tilde{\tau}_x^* = 0.001$ dPa), and then extracting the period and growth rate from the resulting timeseries of NINO3 SSTA.

The second regime of interest is the asymptotic regime, which is reached by the system long after the initial perturbation. The system may reach a stable fixed point, a stable limit cycle, or a strange attractor. Nonlinearity may be important in this regime and the oscillation may be absent or non-sinusoidal. To reach this regime, we perturb the model with a moderate stress anomaly ($\tilde{\tau}_x^* = 0.1$ dPa) and spin up the model for 100 yr. We then extract the time-mean, minimum, maximum, and oscillation period from the subsequent timeseries of NINO3 SSTA.

Sensitivity to air-sea coupling

Fig. 4.24 shows the sensitivity of the linear growth rate and period of the model ENSO to changes in μ, the strength of the wind stress response to SST anomalies. With increasing coupling, both the period and growth rate of the model ENSO increase. The standard coupling $\mu = 1.0$ is just below the neutral stability point. Note that the effect of coupling on the linear period is relatively minor: as μ increases from 0.9 to 1.1, the period goes from 2.9 yr to just under 3.6 yr.
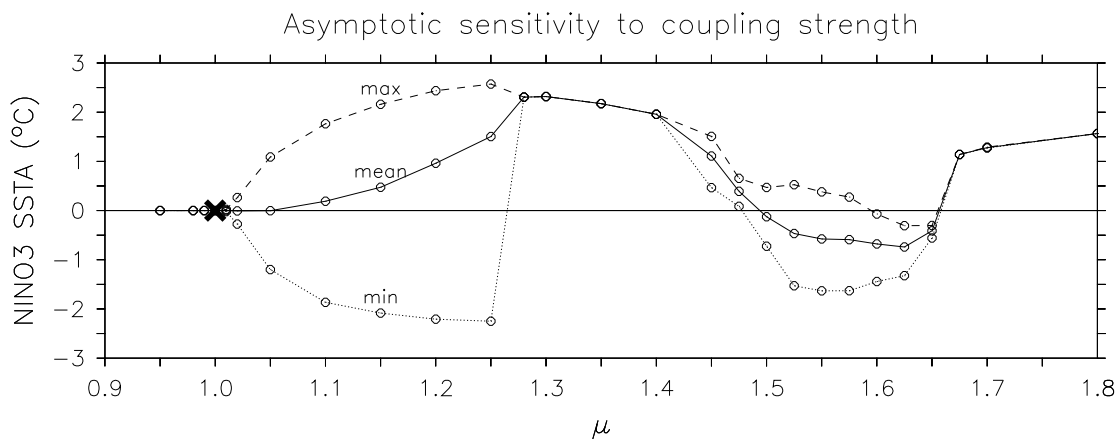
Figure 4.25: Dependence of model asymptotic behavior on μ, the strength of the wind stress response to SST anomalies. For each value of μ, the model is perturbed and then spun up for 100 yr. The minimum, maximum, and time-mean of a subsequent 50 yr timeseries of NINO3 SSTA are then plotted to give an indication of the amplitude and skewness of the model oscillation. The standard model ($\mu = 1.0$) is marked with an X.

The asymptotic sensitivity to coupling strength is shown in Fig. 4.25, for a wider range of μ. As the coupling increases, the system behavior shows several qualitative changes. Above the Hopf bifurcation near $\mu = 1.02$, the oscillation becomes more and more skewed, as warm events lengthen and cold events shorten. Around $\mu = 1.25$ the system plunges into a permanent El Niño. The oscillations appear once more above $\mu = 1.4$, as the model trajectory wanders a thicket of quasi-periodic orbits. Beyond $\mu = 1.65$, the system returns to a permanent El Niño.

Sensitivity to active layer coefficients

Fig. 4.26 shows the sensitivity of the linear growth rate and period to changes in the active layer coefficients. The growth rate increases with increasing λ_h and λ_u, just as it does with an increase in the air-sea coupling coefficient (Fig. 4.24). The period, however, increases with λ_h and decreases with λ_u. Thus along the neutral stability line of Fig. 4.26a, there is a change in the period of the least damped mode. At large λ_h and small λ_u, the mode is dominated by vertical advection, which imparts the slow time scale associated with equatorial recharge/discharge. At small λ_h and large λ_u, the mode is dominated by zonal advection, which introduces two fast time scales: one associated with wave reflection (which reverses the zonal current anomalies), and another associated with zonal propagation (which reverses the upwelling anomalies in the east by displacing the zonal stress anomalies). These two mode types were also evident in Figs. 4.22 and 4.23, except in that case the mode selection was achieved through nonlinearity rather than changes in model parameters. It is interesting to note that the model is most sensitive to the active layer coefficients in the zonal advective regime (small λ_h and large λ_u).
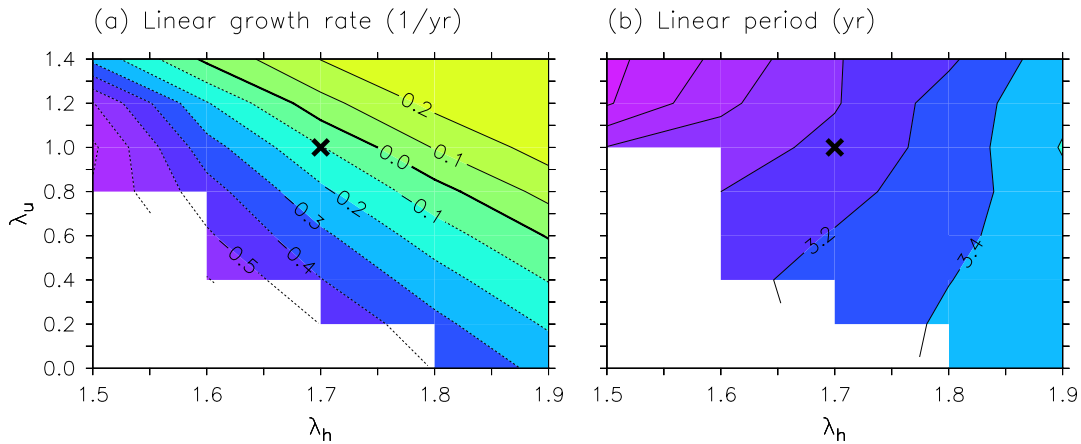
Figure 4.26: Dependence of (a) the linear growth rate (1/yr) and (b) the linear period (yr) on λ_h, the coefficient of active layer depth, and λ_u, the coefficient of active layer currents. Values for the standard model are indicated with an X.
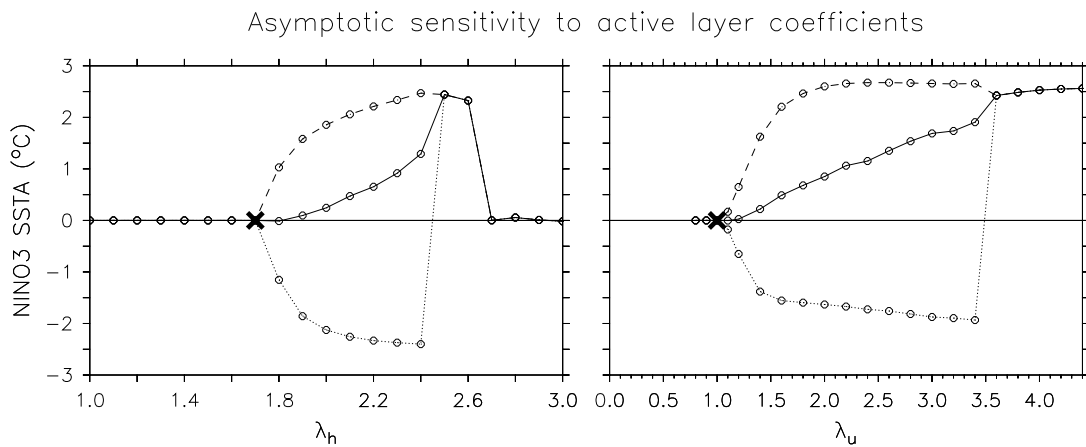
Figure 4.27: As in Fig. 4.25, but for the dependence of model asymptotic behavior on λ_h, the coefficient of thermocline depth anomalies, and λ_u, the coefficient of active layer current anomalies. Standard model corresponds to $\lambda_h = 1.7$, $\lambda_u = 1.0$.
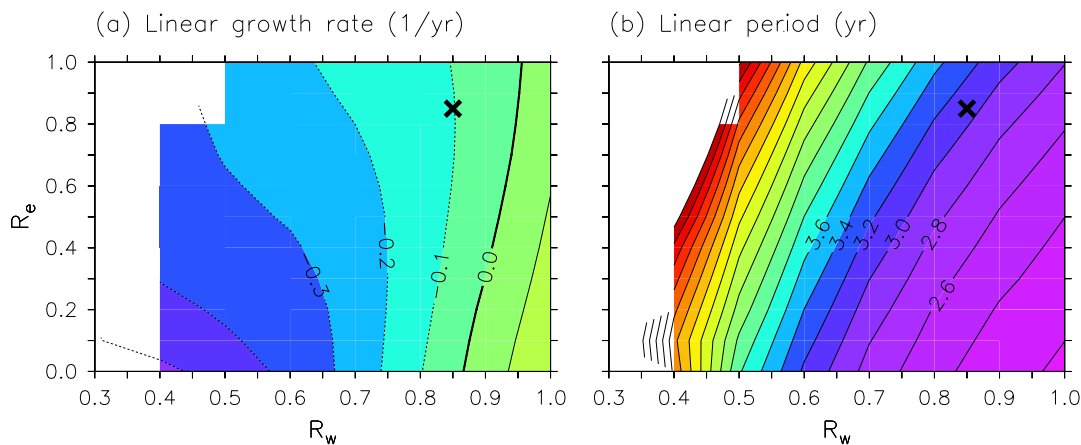
Figure 4.28: As in Fig. 4.26, but for the western and eastern boundary reflectivities R_w and R_e.

The asymptotic response is shown in Fig. 4.27, for a wider range of active layer coefficients. The dependence on these coefficients looks much like the dependence on the coupling strength shown in Fig. 4.25. Above the Hopf bifurcation, the oscillation grows more and more skewed until a permanent warm state is reached. In terms of the bifurcation structure, a 30% increase in μ is roughly equivalent to a 50% increase in λ_h (holding λ_u constant), or a 350% increase in λ_u (holding λ_h constant).

Sensitivity to boundary reflectivity

Fig. 4.28 shows the sensitivity of the linear growth rate and period to changes in the western and eastern boundary reflectivities. The behavior of the anomaly model is more sensitive to R_w than to R_e. As R_w decreases, the western boundary admits a greater zonal mass flux, which serves to recharge equatorial heat content during warm events and discharge equatorial heat content during cold events. As a result, events take longer to terminate, and so the period lengthens. The oscillations also become more stable, because the decrease in reflected feedback reduces a crucial growth mechanism during the onset of events (Battisti and Hirst, 1989). As R_e decreases, on the other hand, the period shortens slightly and the oscillations become either less damped (for $R_w > 0.7$) or more damped (for $R_w < 0.7$). There is a critical threshold for R_w, below which there are no oscillations; this threshold decreases with decreasing R_e, since the eastern boundary assists in the equatorial discharge of heat content associated with the wind stress curl.

The asymptotic sensitivity to boundary reflections is shown in Fig. 4.29. As R_w decreases below the bifurcation value near $R_w = 0.85$, the western boundary flux increases, until near $R_w = 0.4$ it finally overcomes the negative feedbacks associated with the geostrophic divergence in the interior. Beyond this point the model asymptotes to a permanent warm state, which strengthens as R_w decreases further. Decreases in the eastern boundary reflectivity R_e, though they tend to reduce the oscillation damping, have too weak an effect to destabilize the system for the standard R_w.
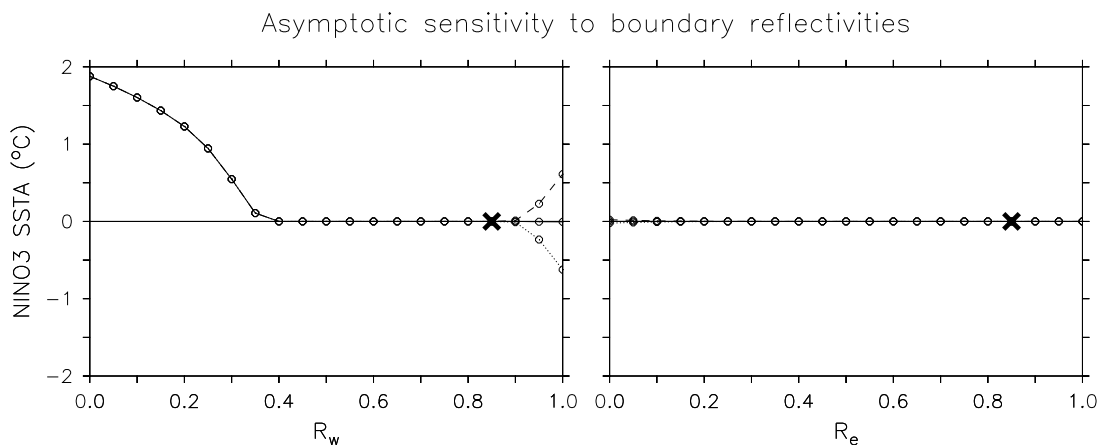
Figure 4.29: As in Fig. 4.25, but for the dependence of model asymptotic behavior on R_w and R_e, the reflectivities of the western and eastern boundaries. Standard model corresponds to $R_w = R_e = 0.85$.

4.3.3 Influence of stochastic forcing

Day-to-day weather is turbulent, so initial uncertainties in the state of the atmosphere grow exponentially in time. The saturation of these errors at small scales produces essentially random noise, which perturbs the slower climate components of the coupled air-sea system. We will therefore refer to the equilibrated chaos associated with atmospheric weather as "noise" or "stochastic forcing," and reserve the word "chaos" for use in describing ENSO behavior in the absence of such noise.

That the model is so close to the stability boundary suggests that a sustained oscillation of reasonable amplitude could be maintained by random forcing. In this section, we incorporate into the model the red noise estimate derived in Chapter 3. This forcing will parameterize the influence of highly unpredictable elements of the tropical climate system, like westerly wind events, the MJO, and day-to-day variations in tropical convection.

Fig. 4.30 shows the influence of the noise amplitude on the distribution of NINO3 SSTA. The particular noise realization is the same in all cases, except that its amplitude is changed. As the noise amplitude increases, the ENSO amplitude increases, the mean and median NINO3 SST become warmer, and the distribution of NINO3 SSTA skews more towards cold events.

The spectral character of the timeseries also changes with increasing noise amplitude. For weak noise (Fig. 4.31), the oscillation is fairly regular, with a sharp spectral peak near 3.2 yr period that is easily distinguished from red noise. Even with this very weak stochastic forcing, the oscillation exhibits large amplitude fluctuations from decade to decade, and slight variations in frequency as well. One might be tempted to infer that something about the dynamics of the system or the noise was different in year 50 than in year 55. Such a conclusion, however, would be erroneous, as both the dynamics and the noise statistics are perfectly stationary in this experiment. The temporal variations result entirely from random coincidences, in which the noise just happens to project strongly onto the system
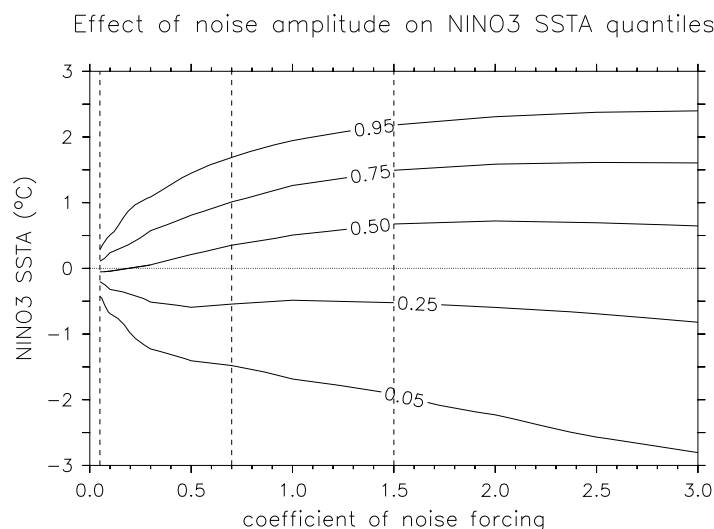
Figure 4.30: Quantiles of NINO3 SSTA (°C) from a 100 yr run forced by wind stress noise, as a function of the noise amplitude. A noise coefficient of 1.0 corresponds to the amplitude estimated from the FSU pseudostress data for 1980–1999. Dashed lines indicate the cases selected for spectral analysis.

dynamics for a time.

For moderate noise amplitude (Fig. 4.32), the spectral peak broadens and there are larger temporal variations in frequency. The time-average spectral signature of the oscillation is still readily distinguished from red noise. The peak period lengthens to 3.7 yr and a substantial short-period tail develops. Amplitude modulation is again evident within the interannual band, although it is weaker and has a shorter period than in the weak-noise case. The spectral variations for this moderate-noise case qualitatively resemble those for observed SST anomalies, shown in Chapter 2.

For strong noise amplitude (Fig. 4.33), the spectrum covers a broad range (0.8 yr to 5 yr) but is still significantly different than red noise. Though it may appear "noisier" than the cases with weaker stochastic forcing, in a sense the timeseries is also more stationary, in that the power within the interannual band shows less extreme temporal variations than before.

Perhaps the most important effect of the noise, regardless of amplitude, is that it induces large temporal variations in ENSO amplitude and frequency. This suggests that any effects of changes in the background state on ENSO may be difficult to discern if the signal-to-noise ratio is small.

4.3.4 Predictability

The skill of a deterministic climate forecast depends on two things: the quality of the forecast system, and the nature of the climate phenomenon to be forecast. A good dynamical forecast system requires a realistic numerical model and accurate initial conditions,
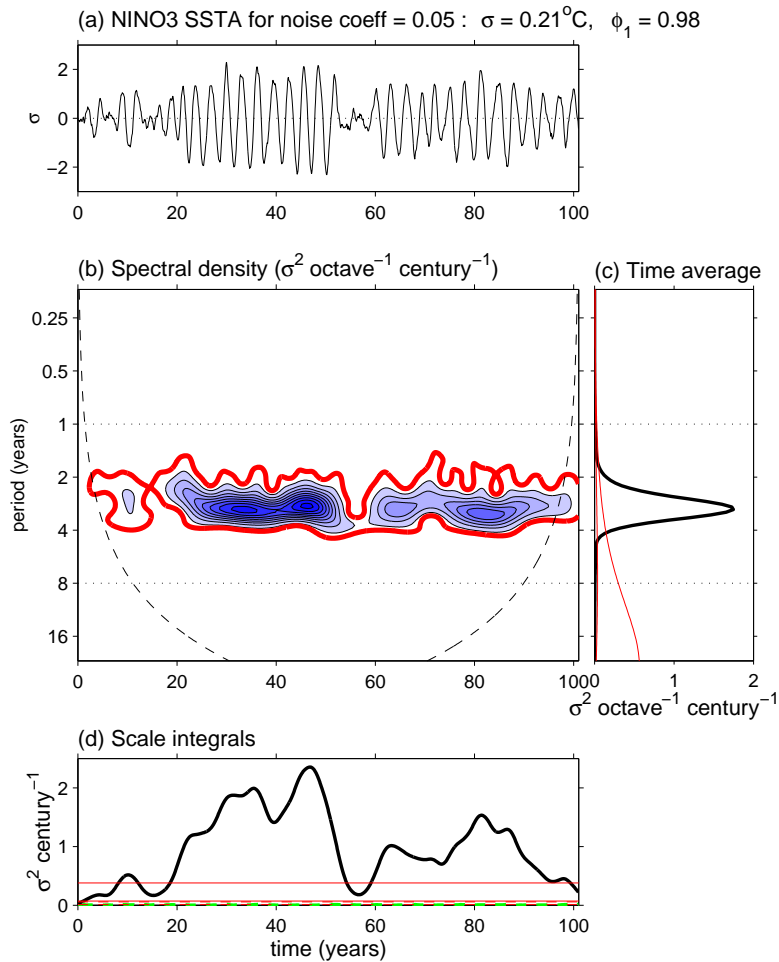
Figure 4.31: Wavelet analysis of NINO3 SST anomalies, simulated by the hybrid model with weak stochastic forcing (0.05 times the FSU estimate for 1980–1999). (a) 100-yr timeseries of standardized monthly anomalies of NINO3 SST. The standard deviation σ and lag-1 autocorrelation ϕ_1 are indicated at the top of the plot. (b) Spectral density of the timeseries, obtained by convolution with a wavenumber-6 Morlet wavelet. The base contour and contour interval are 0.5 σ^2 octave^{-1} century^{-1}. The dashed line ("cone of influence") represents twice the e-folding time for the wavelet response to a spike in the timeseries; below this line the spectral density is underestimated due to edge effects. Thick contour encloses the 95th percentile for red noise realizations with the same σ and ϕ_1 as the timeseries. (c) Time-averaged spectra. Thin lines bracket the central 90% of wavelet spectra calculated from 100-year realizations of the red noise. (d) Running variance in the 0–1 year spectral band (thick dashed) and the 1–8 year band (thick solid). Thin lines bracket the central 90% of running variances calculated from red noise.
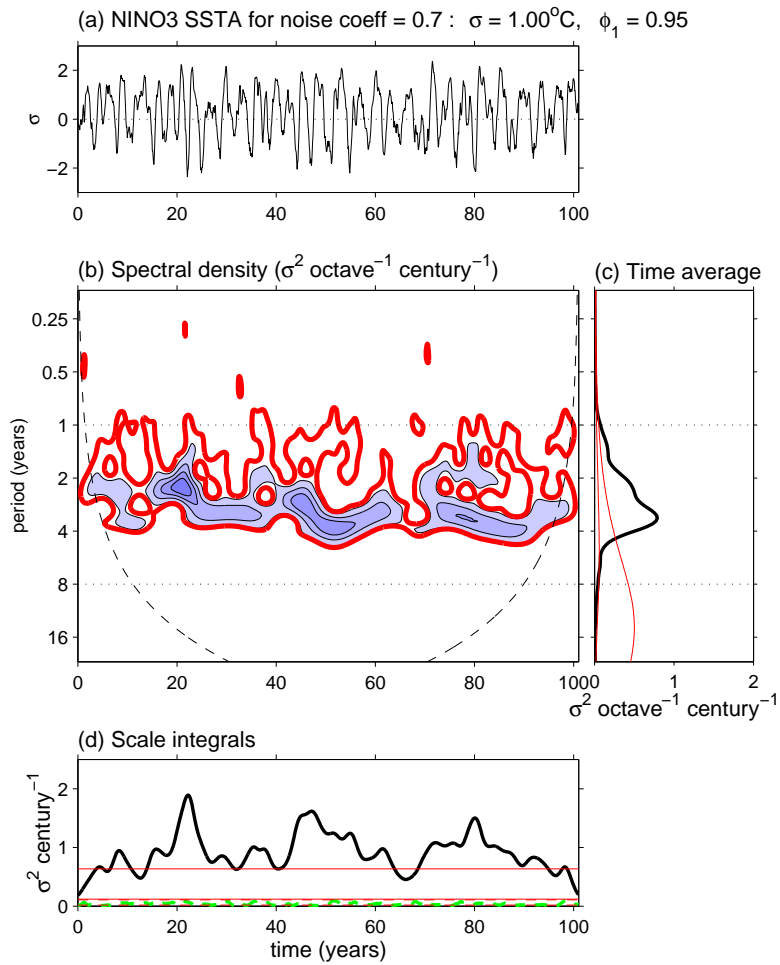
Figure 4.32: As in Fig. 4.31, but for moderate stochastic forcing (0.7 times the FSU estimate for 1980–1999).
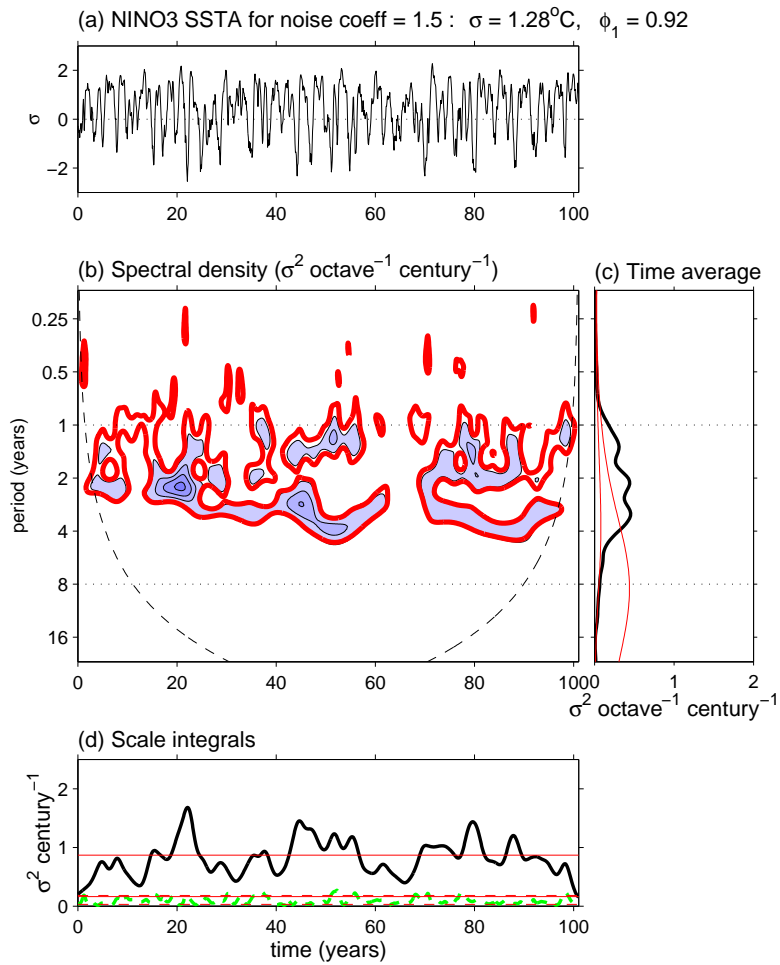
Figure 4.33: As in Fig. 4.31, but for strong stochastic forcing (1.5 times the FSU estimate for 1980–1999).

which the forecaster can control and science can work to improve. What the forecaster cannot control, however, is the climate phenomenon itself, which may have limited predictability even given a perfect forecast system. In this section we explore these natural limits in the context of the intermediate model, by examining the skill of predictions issued using a perfect forecast system and perfect initial conditions.

The nature of predictability

The predictability of ENSO depends on many characteristics of the climate system. Two of these have to do with the noise forcing. The noise *amplitude* is important because it determines the amount of randomness introduced into the system: in the extreme case that the system is simply pure noise, then a climatological forecast (historical event probabilities without reference to the initial conditions) is the best a forecaster can hope to do. The spatial and temporal *structure* of the noise are also important, because they determine the extent to which the noise projects onto the climate phenomenon of interest, i.e. they set the "effective" noise amplitude.

The *probability distribution* of the noise also affects the nature of the forecast problem. If the noise distribution is light-tailed, namely strong events are rare relative to weak events, then forecasts will fail spectacularly just prior to times when a strong noise event does, by chance, occur. Immediately *following* such an event, however, predictability may be enhanced as the system responds deterministically to the unusually strong noise perturbation and retains, for a time, the information associated with that perturbation.

The third characteristic important to ENSO predictability is the lifetime of initial information, which is related to the system dynamics. If ENSO is strongly damped and sustained only by noise, then initial information will rapidly be lost and forecasts cannot hope to improve upon the climatological forecast at long leads. On the other hand, if ENSO is so unstable that it is strongly affected by nonlinearity, then the deterministic system itself may limit predictability at long leads, through sensitive dependence on initial conditions (chaos). It would appear that the best situation for forecasters would be when ENSO is in an intermediate regime where the dynamics are linear, weakly damped and gently sustained by noise. In this case, not only would forecasts following an extreme event would be forgiving of errors in the initial conditions, but they would also yield useful information at long leads while the ENSO signal remained above the weak background noise level.

There is much debate and confusion over the nature of the observed ENSO: is the phenomenon unstable or damped, linear or nonlinear, chaotic or stochastic? Studies which have attempted to classify the system (Jin et al., 1994; Tziperman et al., 1995; Penland and Sardeshmukh, 1995; Chang et al., 1996; Flügel and Chang, 1996; Blanke et al., 1997; Neelin et al., 1998; Thompson and Battisti, 2000, 2001) suggest at least some role for each of the above. ENSO in reality may be a chameleon, changing its colors through the calendar year and from decade to decade. The control run represents a particular type of ENSO which is reasonably consistent with observations, so it is worthwhile investigating the predictability of this system. This control run will also provide a baseline for comparison with the perturbed-climate runs in Chapter 7.
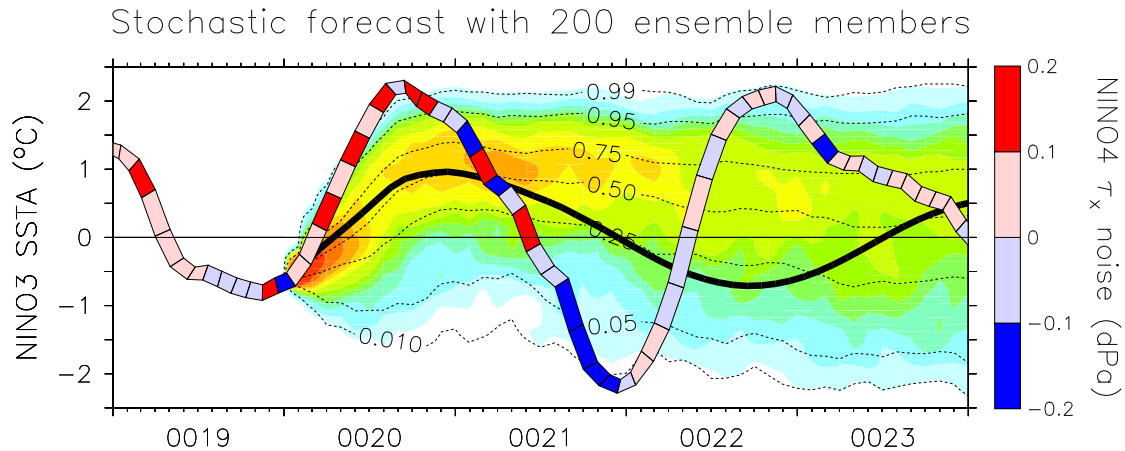
Figure 4.34: Stochastic probability forecast of NINO3 SST anomalies (°C). The stochastic control run is illustrated as a banded tube, where the colors indicate the NINO4 amplitude of zonal stress noise in that run. The control run provides the initial conditions, beginning in year 20, for 200 stochastic forecasts forced by different realizations of the noise. Contours give the fraction of forecasts colder than a given temperature; shading gives the probability density. Solid line shows the response of the model without any noise.

Stochastic probability forecast

To examine the growth of ENSO forecast errors, we perform an idealized prediction experiment. The control run is used to generate the initial conditions for an ensemble of 200 coupled forecasts. Each forecast begins with the same initial condition, which corresponds to the end of a weak cold event at year 20 in the control run. Subsequently, each ensemble member is forced by an independent realization of the noise forcing.

The resulting plume of forecasts (Fig. 4.34) illustrates the fundamental uncertainty of the stochastically driven ENSO, which cannot be reduced by improving the forecast system or initial conditions. The contours represent the cumulative distribution function (CDF) of NINO3 SSTA for the stochastic ensemble, i.e. the fraction of ensemble members colder than a given temperature. (The CDF is the integral, over temperature, of the ensemble probability distribution function (PDF)). The dashed line corresponds to purely deterministic forecast, which is the model ENSO response in the absence of noise.

One year after initialization, both the deterministic forecast and the stochastic ensemble suggest a moderate warming of the eastern Pacific. This indicates that the model was indeed predisposed at year 20 to go into a warm event. Such a warming may be amplified if the noise forcing happens to provide a series of westerly wind events in the western Pacific just after year 20, as illustrated by the striped line, which corresponds to a particular stochastic realization. This run, which is colored according to the noise-induced NINO4 zonal wind stress anomaly, apparently experienced a random series of strong westerly wind bursts during the first half of year 20, which contributed to an unusually strong warm event. The subsequent cold event, furthermore, was unusually strong due to a random series of strong easterly bursts in the latter half of year 21. Although such strong events are rare,

they can occur entirely by chance and cause a deterministic forecast to fail. Such may have been the case operationally for the very strong El Niño of 1997–98 whose amplitude was not well forecast (Landsea and Knaff, 2000), perhaps because it was affected by a series of strong westerly wind bursts in the western Pacific (van Oldenborgh, 2000) which may not have been predictable.

Faced with such situations, the best a forecaster can do is to predict the full probability distribution of system states, so that users can adequately assess the risk of extreme events. This can be done, as in the present case, by using forecast ensembles which explicitly incorporate the noise. Such a probabilistic forecast will incorporate knowledge not only of the initial conditions and deterministic dynamics, but also of the noise statistics and the dynamical system's sensitivity to that noise.

In Fig. 4.34, the spreading of the CDF contours with time corresponds to a loss of deterministic predictability, as the system is affected more and more by random events. Four years after initialization, the impact of the initial condition has been completely obscured by noise, and the stochastic ensemble settles into statistically steady fluctuations with damping balancing the noise excitation. At that point there appears to be little forecast utility left in the ensemble beyond mere climatological probabilities. Thus in the present system, the predictability of ENSO is effectively limited to less than one cycle, consistent with results from previous model studies (Goswami and Shukla, 1991; Latif and Flügel, 1991; Eckert and Latif, 1997).

What insight does the deterministic forecast (dashed line) offer into the evolution of the stochastic ensemble distribution (contours)? For the first year of the forecast, the deterministic run closely tracks the median of the stochastic ensemble, with both showing a warming relative to the equilibrium state. After this, however, the deterministic run transitions into a cold state, while the median of the stochastic runs slowly approaches its stochastic equilibrium value near $0.5°C$ without further fluctuation. Note that although the *individual* stochastic ensemble members are oscillating quite rapidly, most with an even shorter period and stronger amplitude than the deterministic forecast, the phase information associated with the initial conditions has been randomized away by the end of the first year. Thus the temporal phase of the deterministic run does not yield much insight into the evolution of the stochastic ensemble median or quartiles.

Clearly, if the noise amplitude is strong, then to some extent (1) the accuracy of initial conditions may be of little concern, since initial errors will quickly be overwhelmed by noise-induced perturbations, and (2) the asymptotic behavior of the unforced ENSO system (damped or chaotic) may be irrelevant, since the noise continually excites transient variability. To improve forecasts in the stochastic regime, one may have to go beyond improving the initialization and deterministic model behavior, and include an adequate representation of noise and its transient effects on error growth (Moore and Kleeman, 1996, 1997a,b, 1998, 2001).

A measure of predictability

To summarize the information in Fig. 4.34, we shall assume that the ensemble PDF of NINO3 temperature anomalies T is practically normally distributed, with a spread

characterized by its sample variance s^2:

$$s^2 \equiv \frac{N \left\langle |T - \langle T \rangle|^2 \right\rangle}{N - 1} \tag{4.32}$$

where $\langle \ \rangle$ denotes the mean over all N ensemble members. For normal variables, s^2 is an unbiased estimate of the ensemble variance σ^2. For the experiment of Fig. 4.34, σ^2 is initially zero and increases with forecast lead time due to the influence of noise, eventually saturating at the climatological variance σ_c^2. An unbiased estimate of σ_c^2 is given by s_c^2, the sample variance (based on N_c ensemble members) long after initialization. The variance ratio σ^2/σ_c^2, estimated by s^2/s_c^2, is a measure of the uncertainty of a forecast relative to the maximum uncertainty associated with a climatological, or stochastically equilibrated, ensemble. This ratio has often been used in predictability studies, to quantify the "reproducibility" of model trajectories (Hayashi, 1986; Murphy, 1988; Stern and Miyakoda, 1995).

The "predictive power" (PP) of an ensemble forecast may be defined in terms of its "information content," namely the fraction of possible system states which are eliminated by the forecast. One such definition, which arises in information theory, reduces to

$$\mathrm{PP} \equiv 1 - \frac{\sigma}{\sigma_c} \tag{4.33}$$

in the case of univariate normal state vectors (Schneider and Griffies, 1999). For a stochastic forecast, like that in Fig. 4.34, the predictive power of the ensemble will decrease from one toward zero, as noise gradually degrades the information associated with the initial conditions.

The predictive power may be estimated from a given forecast ensemble, to provide an indication of the usefulness of the forecast and to summarize the information in the CDF (Fig. 4.34). A given estimate of the PP will of course differ from the true value. Under the assumption of univariate normal state vectors, however, it is possible to construct an explicit confidence interval for the PP (Appendix E). In general, the larger the ensemble, the better the estimate of the forecast variance, and the tighter the confidence interval for the PP.

Predictability as a function of time

The stochastic ensemble experiment of Fig. 4.34 illustrates the evolution of forecast uncertainty for a single initial condition. To find the "average" decay of predictability with forecast lead time, we must repeat this experiment at multiple points along the control run. In this section we shall consider only ENSO-phase-related effects on predictability, but it should be noted that seasonal effects are also important (Zebiak and Cane, 1987; Battisti, 1988; Latif and Flügel, 1991; Goswami and Shukla, 1991; Balmaseda et al., 1995; Chen et al., 1995; Barnston, 1995; Battisti and Sarachik, 1995; Penland and Sardeshmukh, 1995; Penland, 1996; Flügel and Chang, 1998).

To investigate predictability in the control run, we perform a series of ensemble forecast experiments. Every 2 months the control run is used to initialize 10 new forecasts, which are
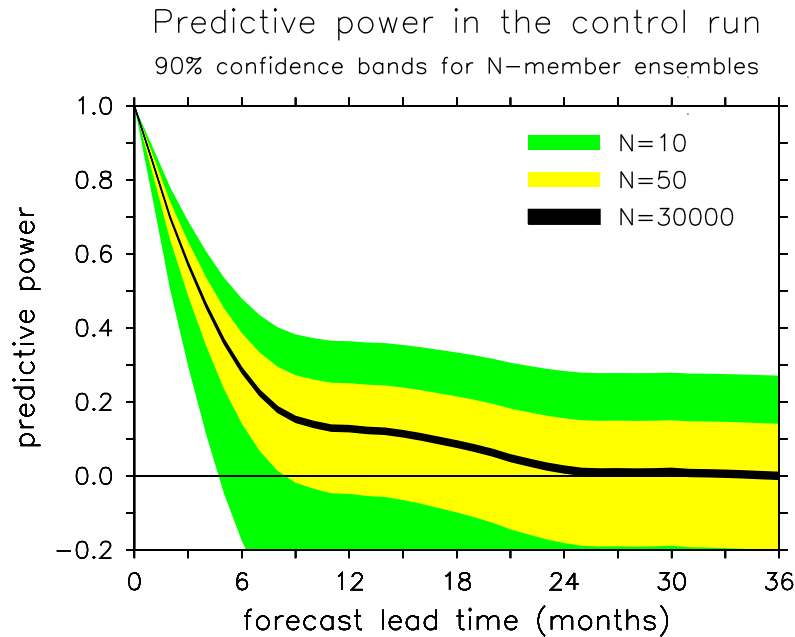
Figure 4.35: Predictability of NINO3 SST anomalies in the stochastic model, as a function of forecast lead time. Shading indicates 90% confidence bands for the predictive power (PP), corresponding to an ensemble of size 10 (green), 50 (yellow), or 30,000 (black). Where the confidence band does not include zero, the PP is greater than zero at the 5% significance level.

initially identical but subsequently diverge under the influence of different noise realizations. This forecast experiment is repeated every 2 months for 500 years, giving a total of 30,000 individual forecasts corresponding to 3,000 different initial conditions. At each lead time, an estimate s^2 of the ensemble variance is obtained by pooling the ensemble sample variance over all 30,000 forecasts. The value of s^2 at 3 years lead is then taken as an estimate s_c^2 of the climatological variance. These estimates of s^2 and s_c^2 are then used to calculate the PP (4.33) and its confidence interval (E.6).

The black band in Fig. 4.35 is the 90% confidence band for the predictability of NINO3 SST anomalies in the stochastic model, as measured by pooling the predictive power over all 30,000 forecasts. Initially, the forecast ensemble provides perfect information (PP = 1) by eliminating all uncertainty in the system state. As forecast lead time increases, the predictability decays due to the influence of noise, and at 6 months less than a third of the initial information remains. With the pooled ensemble of 30,000 forecasts, the confidence interval for the PP is very tight, and it is clear that there is useful information in the ensemble for up to two years beyond initialization.

Unfortunately, operational forecasts using coupled GCMs cannot afford anywhere near this many ensemble members; with present computing resources, a forecast ensemble of 10 is more reasonable. PP confidence bands for small ensembles, obtained by reducing the degrees of freedom in the F-distribution quantiles of (E.6), are shown for the stochastic
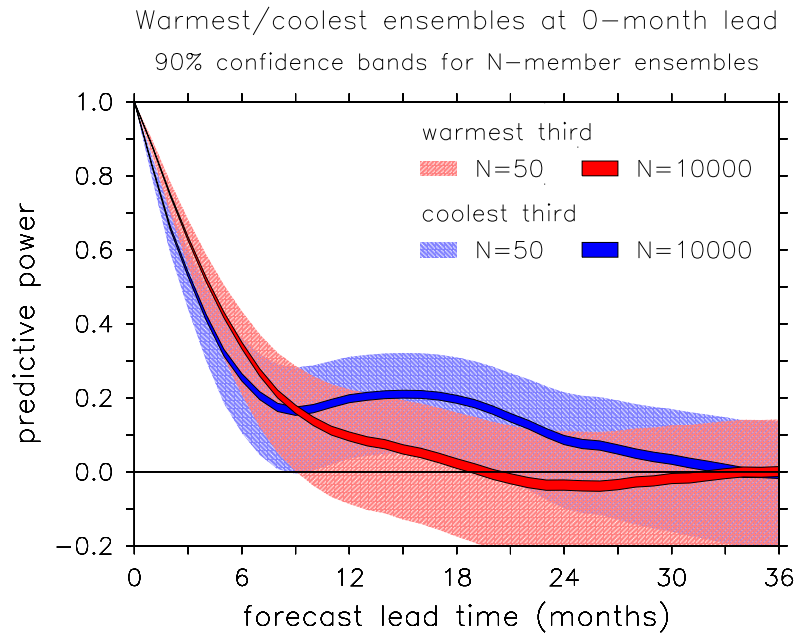
Figure 4.36: As in Fig. 4.35, but divided into forecasts belonging to the warmest and coolest terciles for initial NINO3 SSTA.

model as the lighter-colored bands in Fig. 4.35. For a 10-member ensemble, the predictive power is distinguishable from zero only during the first 5 months of the forecast; beyond this lead time, such a small ensemble cannot reliably detect the small differences between the system PDF and the climatological PDF. Increasing the ensemble size to 50 members, however, increases the precision of the forecast and extends the window of predictability to nearly 9 months.

Predictability for different initial conditions

The coupled model response to wind events is nonlinear (Figs. 4.22 and 4.23) and its stochastic evolution is skewed towards cold events (Fig. 4.30). Thus it is worth asking to what extent the predictability of the model ENSO is affected by the initial conditions of the forecast. To answer this question, the 30,000 forecasts of Fig. 4.35 are stratified according to their initial NINO3 SST anomaly, and classified as "warm starts" (top tercile) and "cold starts" (bottom tercile). Fig. 4.36 shows the evolution of the predictive power, pooled separately over warm and cold starts. With 10,000 ensemble members apiece the confidence bands are very tight, and it is clear that the forecasts from warm starts are the more reproducible during the first 9 months of the forecast. This is likely the result of nonlinearities, such as those described in Section 4.3.1, which during cold events tend to favor coupled instabilities and ruin the forecasts. At longer leads, after most of the system predictability has already been lost, the forecasts with warm starts begin going into cold events, and therefore continue to lose predictability rapidly. The cold starts, on the other hand, by this time begin entering long warm events, such that they retain
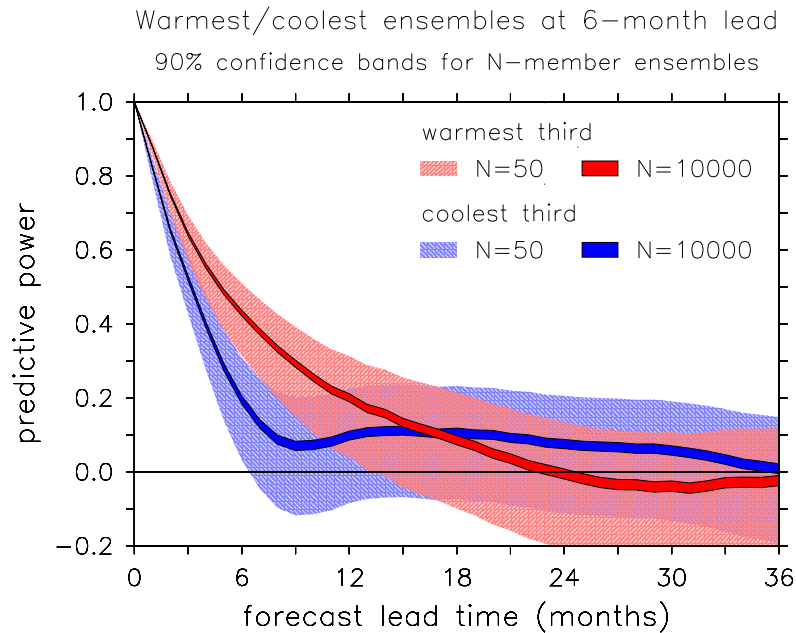
Figure 4.37: As in Fig. 4.36, but divided into forecasts belonging to the warmest and coolest terciles for ensemble-mean NINO3 SSTA at 6 months lead.

significant predictability for nearly two more years.

With an operationally feasible ensemble size of 50, the confidence bands for warm and cold starts overlap for all but the first two months of the forecast. Thus for operational forecasts, it would be hard to distinguish the predictability difference between a forecast with a warm start and one with a cold start. One important difference does emerge, however: the PP for warm starts is significant for only the first 9 months of the forecast, the PP for cold starts remains marginally significant for nearly twice as long. Thus at the 5% significance level, one *could* state that long-lead forecasts from cold starts have predictive power; but one could *not* make the same statement for warm starts.

Are warm events in the model more predictable than cold events? To answer this question, the 30,000 forecasts of Fig. 4.35 are stratified according to their ensemble-mean NINO3 SST anomaly at month 6 of the forecast, and classified as 'warming forecasts" (top tercile) and "cooling forecasts" (bottom tercile). Fig. 4.37 shows the evolution of the predictive power, pooled separately over the warming and cooling forecasts. With 10,000 ensemble members, it is clear that the warming forecasts are the more reproducible during the first year of the forecast. With only 50 ensemble members, this difference is harder to see, but with a few more ensemble members or a slightly less stringent significance test one would be able to state that there is indeed a difference in the predictability for these two types of forecasts. With 50 ensemble members the warming forecasts maintain significant PP past one year, while the cooling forecasts maintain significant PP only for about 6 months.

Thus predictability in the stochastic model does appear to be a function of the initial

condition and the evolution of the ensemble mean. In particular, ensembles which enter warm events early in the forecast tend to have higher predictability than those that enter cold events. Some of these predictability variations would be difficult to see in operationally feasible forecasts, due to the large sampling variability associated with small ensembles. Even for such small ensembles, however, it is possible to distinguish between these forecast cases by testing them against the hypothesis of no predictability: cases which start cold or go warm tend to maintain significant predictability for longer periods.

The predictability variations noted above are related to the skewness of the SST anomalies (Fig. 4.30) in the model. Due to nonlinearities, warm SSTAs tend to persist longer and are less sensitive to wind stress noise than cold SSTAs (Figs. 4.22 and 4.23), which causes warm events to be more predictable than cold events. It is important to note, however, that *observed* NINO3 SST anomalies tend to be skewed toward *warm events*, not cold events as in the coupled model. This is probably due to convective nonlinearities in the real atmosphere, which are neglected by the linear statistical wind stress model. It is likely that in the real world, the sharp peaks of warm events are less predictable than the slow troughs of cold events. Indeed, this is the case in the original Zebiak and Cane (1987) model, which includes a simple parameterization of convective nonlinearity (Samelson and Tziperman, 2001). The key points to take from Figs. 4.36 and 4.37 are that (1) there is a strong link between the predictability of a system and its dynamics, and (2) one must have a large forecast ensemble to reliably detect variations in predictability.

4.4 Summary

The purpose of this chapter has been to develop a coupled model of tropical Pacific climate, which can simulate both the annual-mean climatology and ENSO variability. The resulting intermediate-complexity model is fast, flexible, and conceptually efficient. While the model is based largely on the pioneering work of Zebiak and Cane (1987), several aspects are new. First, the atmosphere is replaced with a statistical model based on recent observations, including an estimate of the intraseasonal variability thought to play some role in observed ENSO events. Second, the ocean model is updated with more realistic boundary conditions, a more consistent advection scheme, and an improved entrainment parameterization. Finally, the ocean model is re-calibrated using newly available observations and results from recent theoretical studies.

Evaluation of the model in both forced and coupled contexts indicates that it does a reasonable job simulating the tropical Pacific climatology and ENSO variability. Some deficiencies remain, however. When the ocean model is forced with observed wind stresses, it shows more activity at short (1–2 year) timescales than do the observations. While this problem may partly be due to inaccuracies in the prescribed stress forcing, it is amplified by an unrealistically strong basin resonance of internal waves. This resonance appears to be related to the inclusion of only a single baroclinic mode in the ocean model which does not propagate downward. In the coupled context, the model SST variability tends to be displaced eastward of that in observations. This may be due to the neglect of wind speed dependence in the parameterization of surface latent heat fluxes, or to the neglect of undercurrent effects on the entrainment temperature. Finally, at large amplitude the

model SST is skewed toward cold events, instead of warm events as in the observations. This may result from the absence of convective nonlinearities in the statistical atmosphere.

Despite these limitations, the model appears realistic enough to warrant a serious investigation into its ENSO behavior. In the absence of noise, the standard version of the model responds to a wind stress perturbation with a damped oscillation and a 3 year period. This oscillation depends essentially on vertical advection in the eastern equatorial Pacific, which affects SST mainly through mean upwelling acting on the anomalous vertical temperature structure of the ocean. Zonal advection also contributes to the oscillation in the central Pacific, where anomalous currents act on the strong climatological gradients at the edge of the warm pool. These two effects show a slight phase lead relative to SST, due to delayed negative feedbacks that arrive from the western boundary in the form of reversed thermocline depth anomalies and zonal current anomalies. These feedbacks, which are associated with equatorial Rossby waves, bring about a reversal of the ENSO event and plunge the system into the opposite phase. Such behavior is consistent with current theories of ENSO evolution, with many GCMs, and with observations.

The model is only marginally stable, and can be rendered unstable by slight changes in the strength of the wind stress feedback or boundary reflectivities, resulting in a sustained, regular oscillation. In the standard (damped) model, a sustained oscillation can be maintained by turning on the intraseasonal noise portion of the atmosphere model, in which case the model spectrum fluctuates in time but is centered near a 3 year period. For realistic noise amplitude, the predictability of the model ENSO is limited to less than one cycle, with higher predictability going into warm events than cold events.

We now have a powerful tool for investigating the climate and variability of the tropical Pacific region. In remaining chapters we shall take advantage of this tool to understand how ENSO behavior is related to the tropical climatology.

Sensitivities of the Tropical Pacific Climatology

. . . a sea-change
Into something rich and strange.

Shakespeare, *The Tempest*

5.1 Introduction

In this chapter we examine the sensitivity of the tropical Pacific climatology to perturbations imposed from outside the coupled system. In the real world, such perturbations might arise from changes in the extratropical Pacific, from changes in heating over the continents, or from random fluctuations within the tropics. These would tend to be amplified by coupled feedbacks, similar to those responsible for ENSO and the strong warm pool/cold tongue climatology observed today.

Coupled GCM studies provide another a clear demonstration of this climate sensitivity. Gudgel et al. (2001), for example, found that replacing predicted low-level clouds with observed clouds over tropical landmasses in a global CGCM led to a substantial strengthening of the Walker circulation and east Pacific cold tongue, and a large reduction in the model's climatological bias. This, in turn, had a positive impact on the model's ENSO forecasts. Studies like these point to the need for better simulation of clouds and other poorly-resolved processes, but they also demonstrate the need for better understanding of how errors in these processes are exported to other aspects of the climate system.

Dijkstra and Neelin (1995) explored many aspects of the climate sensitivity of the tropical Pacific using a simplified version of the Zebiak and Cane (1987) coupled model, namely a meridionally-symmetric equatorial strip in the fast-wave limit, neglecting zonal temperature advection and the climatological annual cycle. Arguing that land-sea contrasts and the Coriolis effect on the Hadley cell produce an "external" component of the trade winds, the authors imposed a weak uniform easterly stress in the model which then provided

a seed for coupled feedbacks. The resulting steady-state climatology was found to be very
sensitive to the strength of the air-sea coupling. The spatial structure of the climatology
was found to depend mostly on internal feedbacks, although the strength of the cold tongue
was sensitive to the strength of the externally-imposed trades. The zonal position of the
cold tongue depended on a competition between two types of feedbacks: a thermocline
feedback, which affected SST east of the stress, and an upwelling feedback, which affected
SST in phase with the stress. Since the model stress response lay slightly west of SST
extrema, only the thermocline feedback was fully consistent with a cold tongue in the
eastern basin; the upwelling feedback tended to drag the cold tongue out into the central
basin. The most important role of the externally-imposed easterlies was to generate mean
upwelling, which enhanced the thermocline feedback and thereby favored a strong cold
tongue in the eastern Pacific.

There remain several unanswered questions. What are the relative roles of equatorial
and off-equatorial winds in determining the tropical climatology? Is the mean state more
sensitive to wind changes in the east or the west? What is the role of the cross-equatorial
southerlies in the eastern Pacific? Are coupled feedbacks sensitive to the nature of the
imposed climate perturbation? How do intraseasonal and interannual variability influence
the climatology?

This chapter addresses these questions and sets the stage for the study of ENSO sensi-
tivity in Chapter 7. We shall assess both the direct effect of a climate perturbation on the
ocean, and the indirect effect that arises from coupled feedbacks with the atmosphere. The
direct effect is simulated by forcing the ocean model of Chapter 4 with a prescribed climate
change, and allowing the climatology to adjust to this change in the absence of coupling
to the statistical atmosphere model. The additional effect of coupling is then simulated
by repeating the adjustment experiment with the atmosphere model turned on. In this
latter case, the simulation will include ENSO variability (discussed in Chapter 7), so the
climatology may include rectified effects of these oscillations.

5.2   Adjustment of the oceanic active layer

5.2.1   Adjustment time scales

The time evolution of the equatorial ocean following a sudden change in wind stress
has been studied in detail (Cane and Sarachik, 1976, 1977, 1979; Gill, 1982; Yamagata
and Philander, 1985; Philander, 1990; Neelin et al., 1998; Philander, 1999). Information
in the active layer can travel no faster than the equatorial Kelvin mode, which conveys
information eastward at the internal gravity wave speed $c = (g'H)^{1/2}$. The next fastest
wave is the gravest Rossby mode, which propagates information westward at speed $c/3$.
As Fig. 5.1 illustrates, the onset of westerly stress in the active layer model produces
Kelvin wave fronts and Rossby wave fronts; the lines crisscrossing the basin correspond
to the fronts that emerge from the boundaries immediately after the onset of the winds.
The dashed line is the front associated with the initial reflection of Rossby waves at the
western boundary; in its wake, the equatorial thermocline shoals and the currents accelerate
westward. The solid line is the front associated with the initial reflection of Kelvin waves
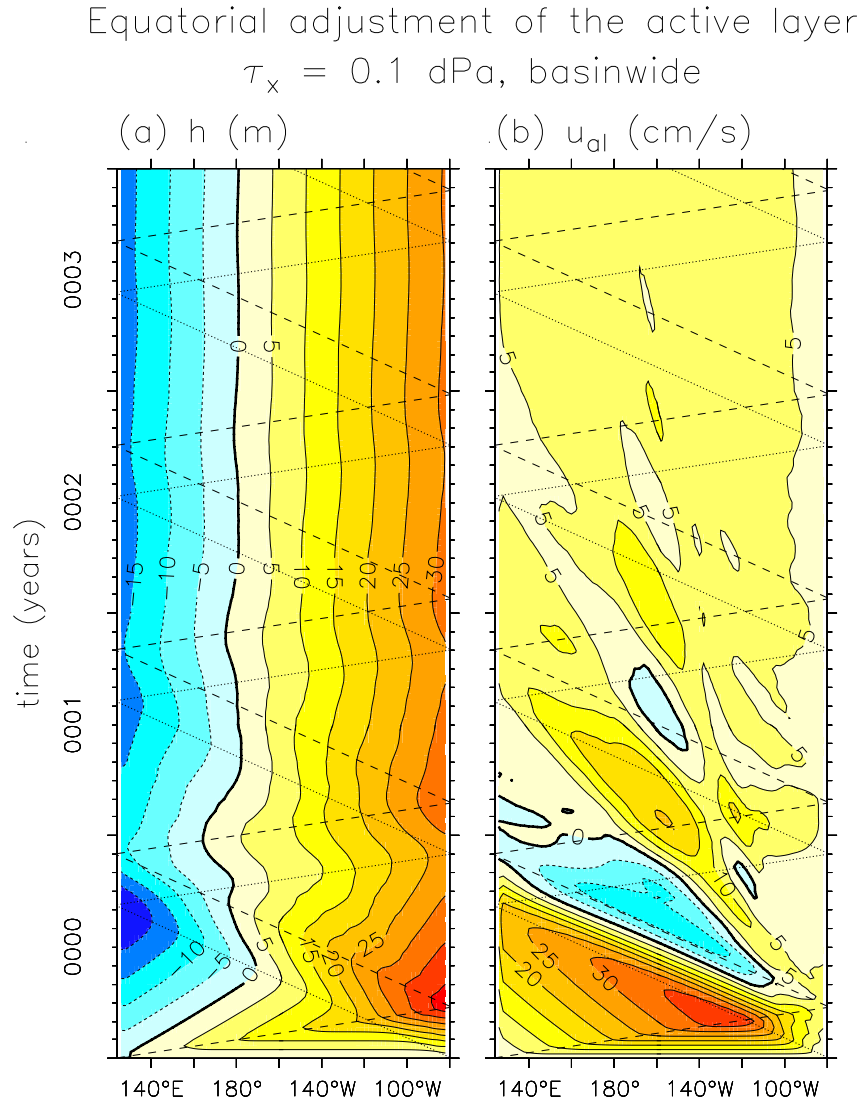
Figure 5.1: Equatorial adjustment of the active layer model to an imposed uniform basin-wide westerly wind stress perturbation of amplitude 0.1 dPa. The stress is turned on at $t = 0$ and held constant thereafter. Shown are the simulated perturbation in (a) thermocline depth (m) and (b) active layer zonal current (cm/s). Warm (cool) colors indicate positive (negative) values. Dashed lines correspond to the front associated with the equatorial Kelvin mode emerging from the western boundary at $t = 0$. Dotted lines correspond to the front associated with the gravest Rossby mode emerging from the eastern boundary at $t = 0$. Compare to Fig. 3.18 of Philander (1990).

at the eastern boundary; in its wake, the equatorial thermocline deepens and the currents accelerate eastward.

The gradual adjustment of the ocean thus proceeds in a series of distinct stages, as the wave fronts cross the basin and reflect at the boundaries. For a basin of zonal width L, the relevant adjustment time scale at the equator is $t_{adjust} = 4L/c$, the time required for one Kelvin-Rossby wave circuit. For the intermediate model, $L = 156°$, $c = 2.42$ m/s and so $t_{adjust} \approx 330$ days. At higher latitudes, the adjustment proceeds more slowly due to the slower speed of Rossby waves, but is nearly complete after two years (Fig. 5.2).

5.2.2 Equilibrium response to uniform westerlies

Fig. 5.3 shows the steady state attained by the active layer after 10 years of continuous forcing by uniform westerly stress. The westerlies have induced a constant zonal slope in the equatorial thermocline, with deepening in the eastern Pacific and shoaling in the western Pacific. This equatorial slope is inhibited by the Newtonian cooling, so that the zonal pressure gradient at the equator does not entirely balance the wind stress. The stress therefore drives steady eastward currents at the equator, which permit viscous friction to complete the zonal momentum budget. The Coriolis force on these currents, which initially had driven a meridional convergence of warm water onto the equator, is now balanced by a poleward pressure gradient force associated with the zonal-mean deepening of the thermocline (and elevation of sea level) at the equator.

Because the boundary reflections are imperfect, zonal currents exist even at the coasts. Mass enters through the western wall via imperfectly-canceled upwelling Rossby waves, and exits through the eastern wall via imperfectly-canceled downwelling Kelvin waves. In the real world, these boundary fluxes would be associated with flow through the Malay Archipelago, and with meridional exchanges via narrow boundary currents.

5.2.3 Response to westerlies with meridional structure

How important are the off-equatorial stresses to the active layer response at the equator? To answer this question, the ocean model is spun up as in the previous section, except that the zonal stress perturbation now has the form

$$\bar{\tau}_x^* = \widetilde{\bar{\tau}_x^*} e^{-y^2/L_y^2} \tag{5.1}$$

i.e., it is constant in the zonal direction, and has a Gaussian shape in the meridional with an equatorial maximum of $\widetilde{\bar{\tau}_x^*}$.

Fig. 5.4 shows how the equilibrium active layer climatology depends on the meridional halfwidth L_y of the zonal stress, when the equatorial stress is held constant. The intriguing result is that the response of the equatorial climatology is sensitive to the off-equatorial structure of the stress. The zonal-mean equatorial thermocline shoals for narrow westerlies, but deepens for wide westerlies. Away from the equator, the zonal-mean thermocline response is the opposite, indicating a net transfer of heat content from the equator to the off-equator (for narrow westerlies) or vice versa (for wide westerlies). Narrow westerlies also produce a stronger eastward zonal-mean current response at the equator, in addition to off-equatorial zonal-mean countercurrents which are absent for wide westerlies.
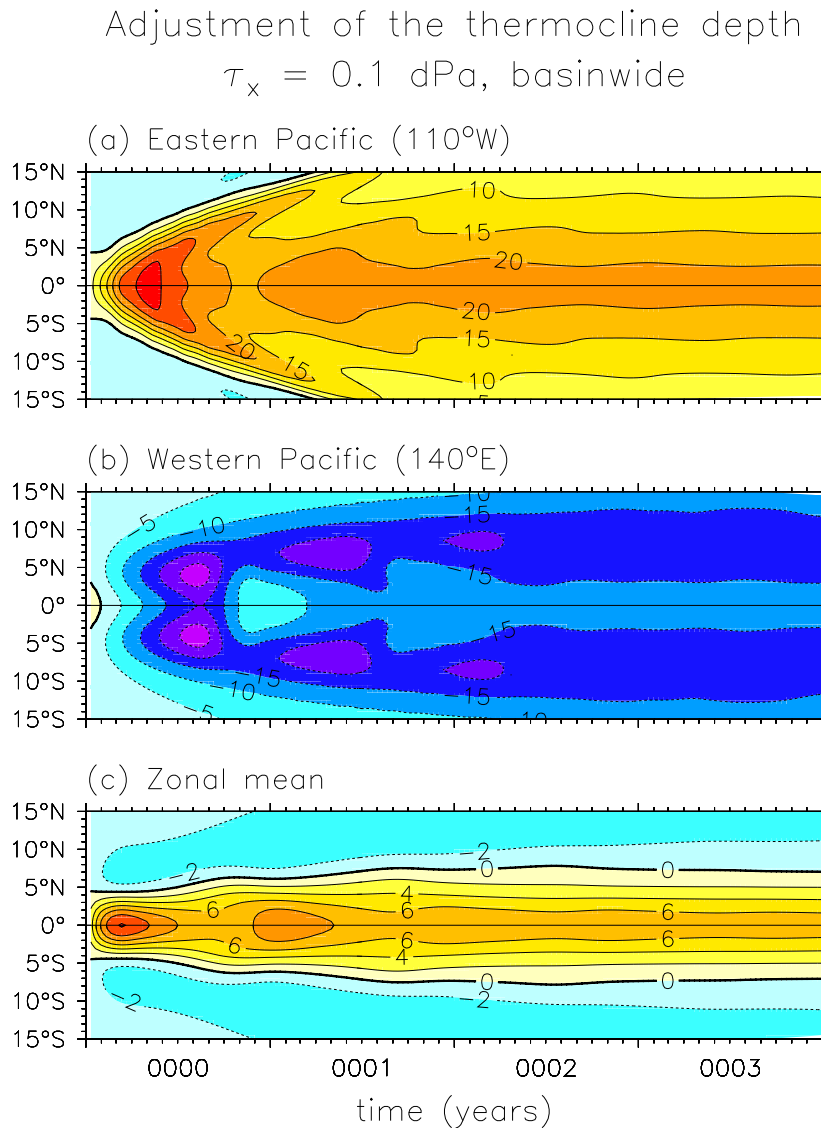
Figure 5.2: Adjustment of the thermocline depth to a uniform basin-wide westerly stress of amplitude 0.1 dPa that is turned on at time $t = 0$. Latitude/time diagrams of the thermocline depth perturbation (m) are shown for (a) the eastern Pacific at 110°W, (b) the western Pacific at 140°E, and (c) the basin zonal average.

Equilibrium active layer for $\tau_x = 0.1$ dPa

(a) h (m)

(b) u_{al} (cm/s)
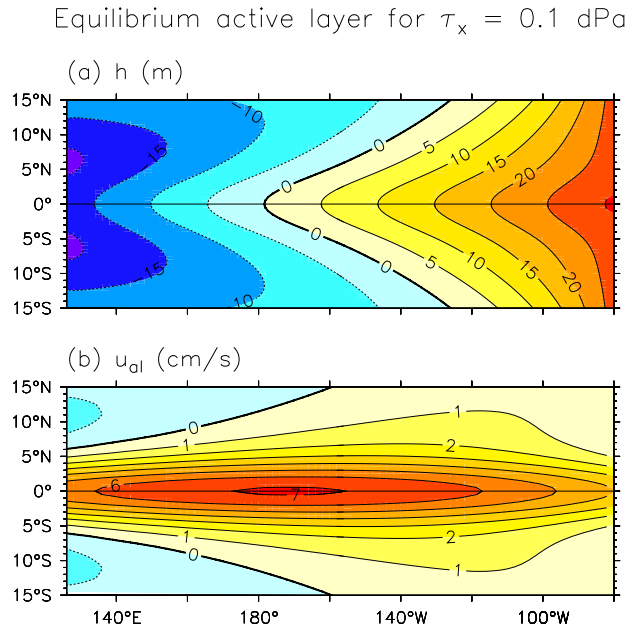
Figure 5.3: Equilibrium active-layer perturbation achieved following 10 yr of forcing by uniform basin-wide westerly stress of amplitude 0.1 dPa. (a) Thermocline depth (m), (b) zonal current (cm/s).

(a) τ_x (dPa)

(b) h (m)

(c) u_{al} (cm/s)
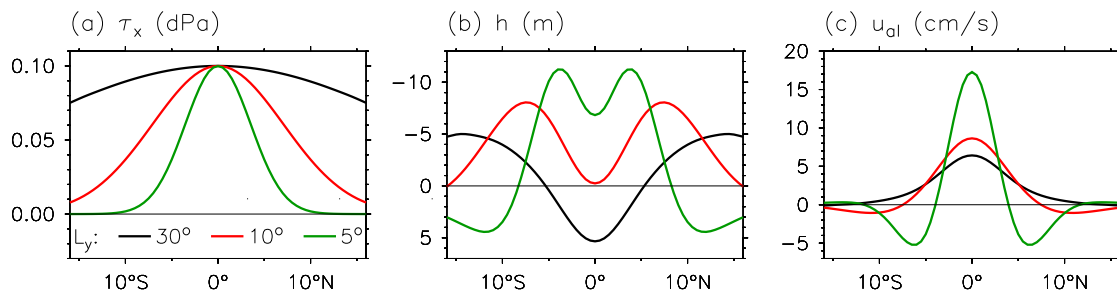
Figure 5.4: Simulated zonal-mean equilibrium response of the active layer to an imposed westerly stress perturbation of amplitude 0.1 dPa, which is zonally constant and has a meridionally Gaussian shape with an e-folding halfwidth of 30° (black), 10° (red), and 5° (green). (a) Imposed zonal stress, (b) equilibrium thermocline depth, (c) equilibrium zonal current.

These results can be understood by considering the steady-state vorticity budget of the active layer. The zonal-mean depth of the equatorial thermocline is determined by a competition between equatorial Ekman pumping and off-equatorial Ekman suction. The former, generated directly by the equatorial westerlies, induces vortex squashing, equatorial convergence, and therefore acts to deepen the equatorial thermocline. The latter, generated by cyclonic curl on the poleward flanks of the stress, induces vortex stretching and poleward flow off-equator, which produces a divergence of water from the equatorial zone and therefore acts to shoal the equatorial thermocline. For a narrow perturbation (small L_y), the off-equatorial Ekman suction dominates and the equatorial thermocline shoals. For a wide perturbation (large L_y), the equatorial Ekman pumping dominates and the equatorial thermocline deepens. Note that there is also some effective zonal mass flux through the boundaries, identified with boundary currents and gaps in the coastline; for westerly stress, the western boundary acts as a source of mass at the equator while the eastern boundary is a sink. At intermediate L_y these three effects cancel and the zonal-mean equatorial thermocline depth is unchanged. For the boundary reflectivities assumed by the model, the critical width of zonal stress for which the zonal-mean thermocline feels no net effect is $L_y \approx 10°$ latitude.

The local deepening of the thermocline near the equator, which is due to equatorial Ekman pumping, is associated with nearly geostrophic zonal currents that are eastward on the poleward flanks of the warm bulge. The off-equatorial cyclonic stress curl, on the other hand, induces a local shoaling of the thermocline, which is associated with currents that are eastward on the equatorward flank of the cold dip and westward on the poleward flank. As L_y decreases, the edges of the westerly stress perturbation draw closer to the equator and sharpen, so that the cyclonic curl near the equator intensifies. Thus meridionally-narrow westerlies give rise to strong equatorial eastward currents, and to westward zonal-mean countercurrents a few degrees away from the equator.

That the equator responds differently to narrow and wide stress perturbations is important, because both types of forcing are present in the real world. The wide-stress case is analogous to the climatological easterlies (Fig. 2.1), which actually *strengthen* away from the equator; this positive off-equatorial curl assists the equatorial Ekman divergence in shoaling the equatorial thermocline. The narrow-stress case resembles the El Niño anomalous stress (Fig. 3.7), which has $L_y \approx 8°$. The equilibrium thermocline response to such narrow stress consists of a zonal-mean shoaling at the equator, and since this shoaling opposes the thermocline deepening in the eastern Pacific observed during El Niño, it has been argued that the equatorial ocean's slow approach to equilibrium (associated with the discharge of equatorial heat content) may be responsible for ENSO (Jin, 1997).

Note that since this recharge/discharge is achieved through the formation and western boundary reflection of oceanic Rossby waves, it is fully compatible with earlier "delayed oscillator" ideas (Battisti, 1988; Suarez and Schopf, 1988) in which wave reflections from the western boundary play a key role. The role of western boundary reflections is simply to cancel enough of the Rossby flux to allow interior geostrophic divergence to control the zonal-mean equatorial thermocline depth.

It is important to understand how changes in equatorial versus the off-equatorial stress

might affect ENSO, since both components are susceptible to model differences and long-term climate variability. The equatorial component of the stress is tightly linked to the warm pool/cold tongue climatology of the ocean, which is very sensitive to changes in external forcings or changes in model dynamics (Dijkstra and Neelin, 1995). The off-equatorial component is more directly tied to strength of the Hadley circulation, which not only differs among climate models (Delecluse et al., 1998; AchutaRao and Sperber, 2002) but also may be subject to future climate change (Rind, 1987; Dai et al., 2001). Section 5.4 will thus explore the relative effects of equatorial and off-equatorial stress changes on the tropical Pacific climatology.

5.3   Design of the climate sensitivity experiments

As indicated by Fig. 5.2, the tropical ocean is very nearly in equilibrium with wind stress variations that occur on time scales longer than a few years. Thus if a given climate parameter is slowly changed during a model run, the simulated climatology will approximately be in equilibrium with that change. This approach is convenient, since only a single run of the model is required, and it is also highly relevant to many kinds of GCM experiments, in which slow variations in anthropogenic or orbital forcings cause changes in climate.

Thus the climate sensitivity experiments are performed as follows. The background state of the anomaly model is in all cases prescribed from the control run climatology described in Section 4.2.4. A climate perturbation is selected, along with a range of parameter values to be tested. An ocean-only climate simulation is then performed by first spinning up the ocean anomaly model for 10 years with the parameter start value, and then running the ocean model for another 500 years as the parameter changes linearly from the start value to the end value. This procedure is then repeated with the statistical stress anomaly model and noise turned on in a fully coupled climate simulation. A control case is also performed by running the coupled stochastic model for 500 years with no climate perturbation imposed. "Noiseless" coupled experiments were also performed, but as these were found to produce climatologies very similar to (though slightly more sensitive than) those in the stochastic cases, they will not be discussed except in connection with Fig. 5.5.

5.4   Changes in mean zonal stress

5.4.1   Equatorial stress

How does the equatorial climatology response to a change in the equatorial trade winds? In nature and in coupled models, such a change could arise due to a change (or model error) in the strength of the Hadley circulation or land-sea temperature contrast, or from a change (or model error) in the effective air-sea coupling of the tropical climate system (Dijkstra and Neelin, 1995).

In our first experiment, a perturbation of the form (5.1) with $L_y = 15°$ is imposed in the intermediate model, and the stress amplitude $\widetilde{\tau_x^*}$ is linearly varied from -0.1 to 0.1 dPa over the course of a 500 year simulation. Fig. 5.5 shows the resulting change in
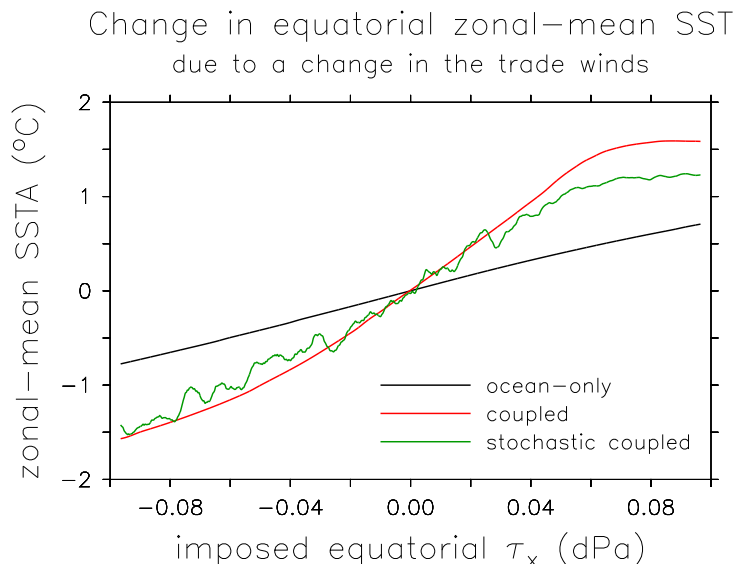
Figure 5.5: Simulated change in the zonal-mean equatorial (2°S–2°N) SST climatology resulting from an imposed equatorial zonal stress perturbation, which is zonally constant and has a meridionally Gaussian shape with an e-folding halfwidth of 15°. Horizontal axis is the strength of the imposed stress perturbation; vertical axis is the SST response. Shown are the response of the uncoupled ocean (black), the coupled ocean/atmosphere without noise (red), and the coupled system with noise (green). All curves are filtered to eliminate periods shorter than 20 years.

zonal-mean equatorial SST for the ocean-only, coupled, and stochastic coupled cases. In all cases the equatorial band warms as the trade winds weaken. The warming is greatest in the coupled cases, where nonlinear saturation is evident for very weak or very strong trades. The coupled system appears to be less sensitive with noise than without.

The equatorial structure of the ocean-only and stochastic coupled cases are shown in Fig. 5.6. The plotted curves represent equatorial 50-year averages from the beginning and end of the sensitivity runs, so that the time averages are centered on ±0.09 dPa. To facilitate comparison with later figures, all data have been scaled by the peak equatorial SST change in the stochastic coupled case, indicated above panel (b). The model surface heat flux may be obtained from (b) by multiplying by a factor of $-\epsilon$. Mixing also tends to oppose SST anomalies in the model, though its effect is smaller than the surface heat flux. Note also that the equilibrium equatorial zonal current in the model looks very similar to τ_x, while the equatorial upwelling looks very similar to $-\tau_x$.

Uncoupled oceanic response

Focusing first on the westerly ocean-only case in Fig. 5.6 (plain red lines), we see that as in Fig. 5.3, zonally-constant equatorial westerlies induce a constant zonal slope in the equatorial thermocline. The deepening of the thermocline in the east is associated with warmer water below the mixed layer, especially in the far eastern Pacific where the mean
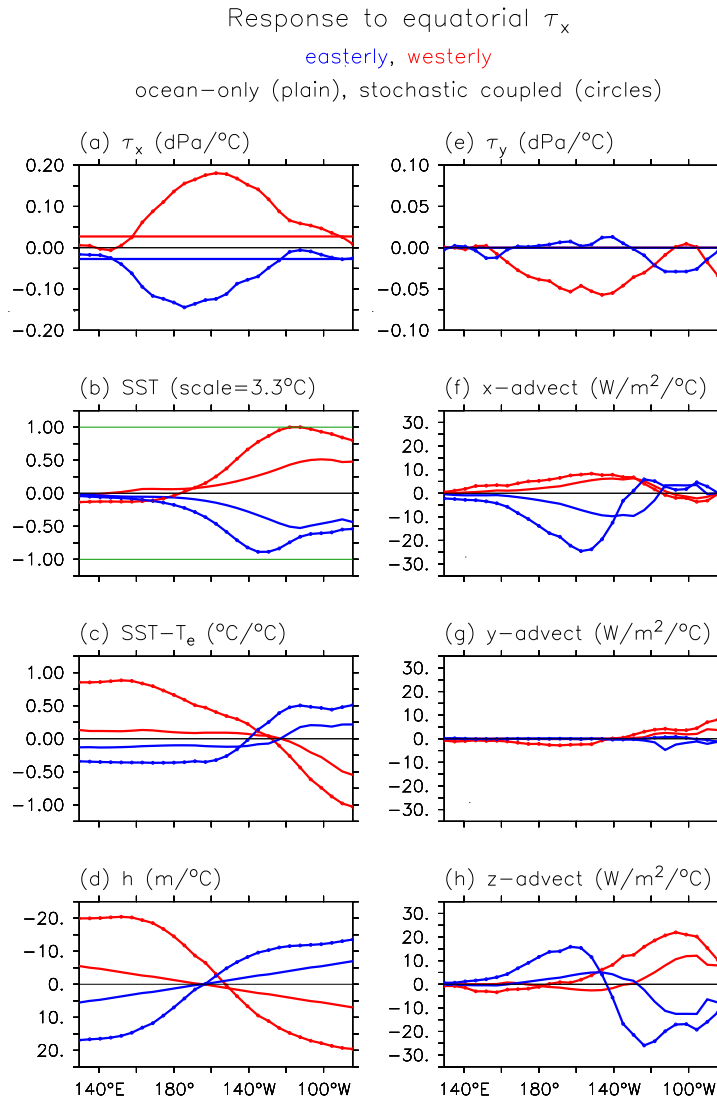
Figure 5.6: Simulated response of the equatorial (2°S–2°N) climatology to an imposed equatorial zonal stress perturbation of amplitude 0.09 dPa, which is zonally constant and has a meridionally Gaussian shape with an e-folding halfwidth of 15°. Red (blue) lines correspond to a westerly (easterly) stress perturbation. Plain lines indicate the ocean response without coupled feedbacks, circled lines the response of the coupled ocean/atmosphere with noise. Fields are scaled by the peak SST change in the coupled case, indicated in panel (b). Panels show the scaled change in (a) zonal stress, (b) SST, (c) temperature difference across the mixed layer, (d) thermocline depth (ordinate reversed), (e) meridional stress; and the mixed layer heating due to (f) zonal, (g) meridional, and (h) vertical advection.

thermocline is shallow. The increase in subsurface temperatures in the east gives a reduced vertical temperature gradient, which produces an eastern warming of SST as warmer water is entrained into the mixed layer from below.

The weakening of the trades also weakens the westward advection of cold water, warming the surface the central Pacific where the mean zonal SST gradient is strong. The surface warming by zonal advection outpaces the increase in T_e, and the vertical temperature gradient steepens. Despite the reduction of upwelling in the central Pacific, the strong increase in $\partial_z T$ results in a net increase in cooling by vertical advection, which mitigates some of the zonal advective warming in the central Pacific.

The effect of meridional advection at the equator is weak, although it does induce some warming in the east as northward currents advect the southern warming (associated with upwelling induced by the cross-equatorial southerly stress, Appendix C) into the equatorial band. Off-equator, meridional advection plays a larger role: there it warms SST as reduced poleward Ekman flow gives anomalously weak meridional spreading of the cold tongue.

An easterly stress perturbation gives largely the opposite response (plain blue lines). In particular, because the active layer model is linear, the thermocline response is exactly opposite from that in the westerly case. Compared to the westerly case, however, the entrainment temperature change in the easterly case is only half as strong in the east, since the T_e parameterization (Fig. 4.7) saturates when the thermocline shoals beyond the model mixed layer depth; cooling is then limited by the temperature of water below the thermocline. Slightly farther west, T_e responds more strongly than in the westerly case, as the thermocline approaches the mixed layer depth from below. Thus T_e west of 110°W reacts more strongly to *strengthening* trades, while T_e east of 110°W reacts more strongly to *weakening* trades. In the central Pacific, zonal advection responds more strongly in the easterly case, as intensified currents carry even colder water westward.

It is interesting to note that despite the strong nonlinearity of the vertical temperature gradient response (c) at the eastern boundary, the vertical advection response at the eastern boundary is nearly linear. For weakened trades the vertical advection response is limited by a lack of equatorial upwelling, while for strengthened trades it is limited by the saturation of T_e. Since the south-equatorial upwelling associated with the cross-equatorial southerlies is unaffected by the imposed zonal stress perturbation, the saturation of T_e is more evident in the southeast than at the equator. This nonlinearity is carried across the equator by the northward currents in the east, limiting the meridional advection response at the equator in the easterly case. Off-equator in the central Pacific (not shown), the sensitivity to the easterly perturbation is enhanced due to a combination of stronger meridional overturning and a stronger poleward temperature gradient.

In summary, the uncoupled SST response to weakening trades is narrower and more asymmetric meridionally, and lies further to the east, than the response to strengthening trades. *Weakening* trades strongly reduce *vertical* temperature gradients in the far eastern Pacific, inducing large changes in vertical advection just south of the equator. *Strengthening* trades strongly enhance *horizontal* temperature gradients in the tropical Pacific, inducing large changes in horizontal advection at the equator. For weak winds, horizontal advection in the central basin is limited by elimination of the cold tongue. For strong winds, vertical advection in the east is limited by saturation of the entrainment temperature when the

thermocline becomes too shallow in the east.

Coupled response

What effect does coupling have on this response? It is obvious from Fig. 5.6 that coupled feedbacks play a major role. Panel (b) indicates that the peak SST change in the equatorial band is nearly twice as strong when coupled (circled lines) than when uncoupled. Considering the rather small change in zonal stress (typical of, say, the difference between observational stress analyses in Fig. 2.1a), the induced SST change is quite large.

Over the central basin, the coupled zonal wind stress response is much larger than the imposed perturbation, and the stronger change in zonal stress produces a larger thermocline slope than in the uncoupled case. Because the coupled stress response is narrow in the meridional (Fig. 3.7), the zonal mean thermocline perturbation is opposite to that in the uncoupled cases, and slightly opposes the thermocline perturbation in the eastern Pacific. The larger thermocline slope in the coupled cases gives rise to a stronger, and more nonlinear, change in the vertical temperature gradient in the eastern Pacific; the T_e nonlinearity produces a vertical advection response which is shifted west in the easterly case relative to the westerly case.

In the central basin, zonal advection is little affected by the coupling in the westerly case; the eastward current anomalies have little effect since the zonal gradient of SST is nearly zero. In the easterly case, however, zonal advection is strongly amplified by the coupling since stronger currents are acting on an increased SST gradient; this produces an intense cooling in the central Pacific which tends to drag the cold tongue westward. This so strongly reduces the vertical temperature gradient that vertical advection acts to damp the cooling in the central basin, despite the stronger vertical currents in the easterly case. Vertical advection thus acts to temper some of the nonlinearity associated with zonal advection in the central Pacific.

The meridional stress response at the equator, shown in panel (e), is weak but highly nonlinear. The SST response in the case with imposed easterlies is nearly symmetric about the equator, so that the cross-equatorial southerlies are little changed. The case with imposed westerlies, on the other hand, shows more warming south of the equator than north of the equator, and the warming response is confined to the eastern Pacific. This pattern of warming corresponds to a strong negative projection onto mode 2 of the wind stress model (Fig. 3.8), and therefore acts to weaken the equatorial southerlies in the central Pacific. It is possible that additional coupled feedbacks not explicitly included in the simulation (e.g. stratus clouds, evaporative heat fluxes) might enhance the asymmetry of the climate response in the real world. This asymmetry, in turn, could be expected to alter the evolution of the annual cycle, which is closely tied to the strength of the climatological southerlies (Chang and Philander, 1994; Li and Philander, 1996; Li and Hogan, 1999; Wang and Wang, 1999).

The net effect of these coupled feedbacks and nonlinearities is to give an SST response in the easterly case which is farther west than in the westerly case. Using the terminology of recent ENSO literature (Hao et al., 1993; Jin and Neelin, 1993a; Neelin et al., 1998; Fedorov and Philander, 2000; An and Wang, 2000; An and Jin, 2001), the effects of coupling on the mean state may be described in terms of "nonlocal" or thermocline feedbacks

$(-\overline{w}\partial_z T')$ and "local" or zonal advective/upwelling feedbacks $(-u'\partial_x T$ and $-w'\partial_z T)$. The former are consistent with an SST response in the east while the latter tend to drag the response westward (Dijkstra and Neelin, 1995). The nonlinearity of T_e favors the thermocline feedback when the thermocline is at intermediate depths, shallow enough to affect entrainment but not so shallow that T_e saturates at the temperature of sub-thermocline waters. The nonlinearity of the zonal advective product $-u'\partial_x T'$, on the other hand, increasingly favors local feedbacks as the cold tongue strengthens and $\overline{T}_x$ increases. The response to easterlies favors local feedbacks over thermocline feedbacks, allowing the SST response to slide west relative to the westerly case.

Fig. 5.6, therefore, establishes three fundamental ideas: (1) coupling strongly amplifies the climate response to perturbations; (2) this enhances nonlinearities which alter the climatological SST budget; (3) these nonlinearities affect the spatial structure of the coupled climate response.

5.4.2 Off-equatorial stress

In the next experiment, we explore the sensitivity of the climatology to a change in the off-equatorial zonal wind stress, which in Section 5.2.3 was shown to be important in the adjustment of active layer. In nature and in coupled models, such a change could arise due to a change in the strength of the Hadley circulation or land-sea temperature contrast. In the intermediate model, a perturbation of the form

$$\overline{\tau}_x^* = \widetilde{\overline{\tau}_x^*} \left(1 - e^{-y^2/L_y^2} \right) \tag{5.2}$$

is imposed with $L_y = 15°$. This perturbation is constant in the zonal direction, zero at the equator, and has an inverted Gaussian shape in the meridional with an off-equatorial maximum of $\widetilde{\overline{\tau}_x^*}$. In other words, it is what one would add to the perturbation (5.1) of the previous section to give a uniform τ_x over the basin.

Because the perturbation has no signature at the equator, it cannot directly affect the strength of equatorial upwelling or the equatorial zonal slope of the thermocline. It can, however, directly affect equatorial climate by changing the zonal-mean depth of the thermocline and the zonal current at the equator, which feel the influence of off-equatorial stress through interior divergence and the boundary conditions (4.5)–(4.6). This experiment thus provides a useful analogue for other processes that could affect the zonal-mean depth of the equatorial thermocline in the real world, such as changes in the thermohaline circulation or changes in subduction in high midlatitudes (Gu and Philander, 1997).

Following the previous experiment, the stress amplitude $\widetilde{\overline{\tau}_x^*}$ is linearly varied from -0.1 to 0.1 dPa over the course of a 500 year simulation. Results for the ocean-only and stochastic coupled cases are shown in Fig. 5.7. The plotted curves represent equatorial 50-year averages from the beginning and end of the sensitivity runs, so that the time averages are centered on ± 0.09 dPa. As in Fig. 5.6, all data have been scaled by the peak equatorial SST change in the stochastic coupled case, indicated above panel (b).
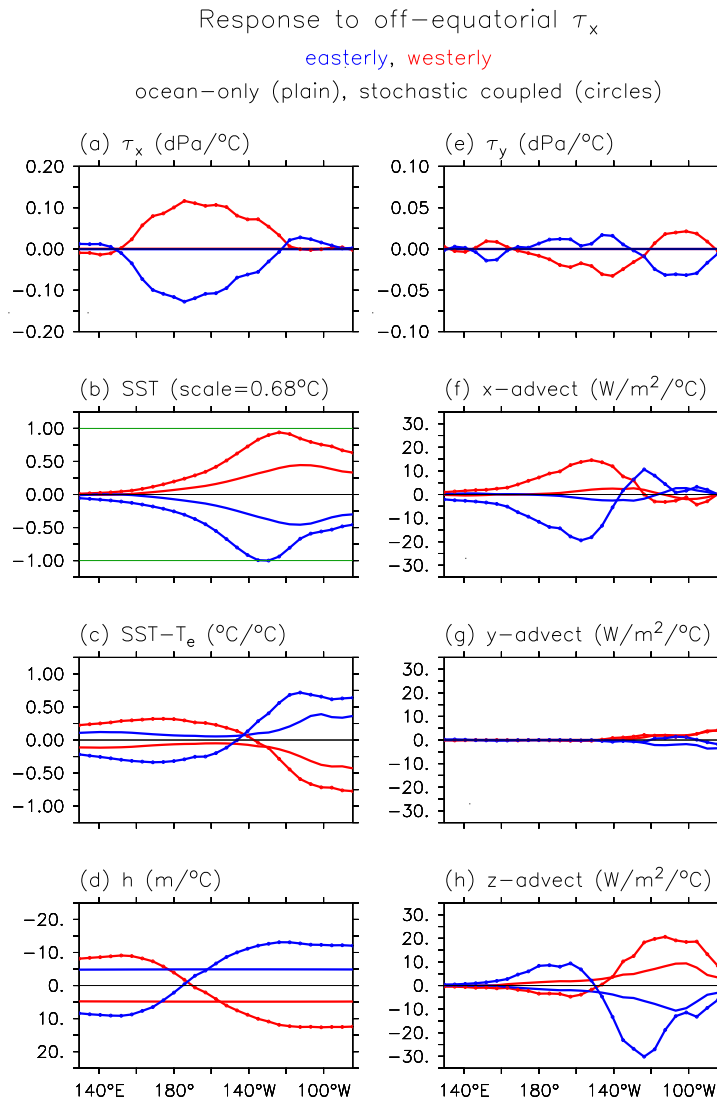
Figure 5.7: Simulated response of the equatorial climatology to an imposed off-equatorial zonal stress perturbation. The perturbation is zonally constant, vanishes at the equator, and has an inverted Gaussian shape in the meridional with an e-folding halfwidth of 15° and a peak off-equatorial amplitude of 0.09 dPa. Red (blue) lines correspond to a westerly (easterly) stress perturbation. Otherwise as in Fig. 5.6.

Uncoupled oceanic response

How much does the off-equatorial wind stress affect the equatorial SST? Focusing first on the westerly ocean-only case in Fig. 5.7 (plain red lines), we see that off-equatorial westerlies induce a zonal-mean deepening of the equatorial thermocline, without changing its zonal slope. The deepening warms the surface by allowing warmer water to be entrained into the mixed layer, especially in the eastern Pacific where the climatological thermocline is shallow. These processes are very similar to the case with equatorial westerlies, although the amplitude of the changes is weaker in this case due to the smaller change in the eastern equatorial thermocline depth.

There is slightly reduced cooling from zonal advection in the central basin, due to a weakening of the easterly currents as the thermocline flattens in the meridional. The increase in T_e as a result of the thermocline deepening in the central basin, however, is strong enough to overcome the zonal advective surface warming, and so produces a reduction in $\partial_z T$ and a vertical advective warming tendency in the central Pacific (in contrast to Fig. 5.6). The change in meridional advection at the equator is even weaker than in Fig. 5.6, since there is little change in the Ekman currents due to absence of any wind stress change at the equator.

Off-equatorial easterlies gives nearly the opposite response (plain blue lines), with an equatorial shoaling of the thermocline and a cooling in the eastern Pacific. There is some nonlinearity evident in the vertical temperature gradient in the east, but it less prominent than in the equatorial-stress case since the overall response is weaker.

Thus the key results from the off-equatorial uncoupled cases are that (1) off-equatorial stress perturbations are felt at the equator, and (2) the zonal asymmetry of the background climatology, namely the shoaling of the thermocline to the east, produces a zonally-asymmetric change in SST even given a zonally-uniform change in equatorial thermocline depth.

Coupled response

How well does the off-equatorial wind stress seed coupled feedbacks? It is again evident that coupled feedbacks greatly amplify the climate response, by a factor of two or more (circled lines). Off-equatorial westerlies produce an eastern warming, which generates a "feedback" westerly stress anomaly at the equator. Because these feedback westerlies are meridionally narrow, they generate equatorial divergence and so the zonal-mean thermocline does not deepen as much as in the uncoupled case. More important, however, is the stronger deepening in the east (where entrainment is most sensitive to thermocline depth) associated with the thermocline slope in the coupled case. Although the feedback stress has a smaller amplitude than the off-equatorial stress, it is very efficient at generating additional climate changes due to its direct equatorial influence on upwelling, zonal currents, and the zonal slope of the thermocline.

It is striking how similar the coupled responses in Fig. 5.7 are to those in Fig. 5.6 (although nonlinearity is not as evident in the present case because the coupled response is weaker). Both cases show a coupled response with roughly the same structure and advective balance, and an SST response to easterlies that is shifted slightly west of the

response to westerlies. Since the coupled feedbacks are so large, the ultimate structure of the coupled response appears largely invariant to the seed perturbation. In this sense, the coupled feedbacks greatly simplify the problem of describing the climate response to external forcing. That the tropical Pacific has a preferred ENSO-like response pattern suggests that one could define a "tropical Pacific climate index" to characterize the climatology as either "El Niño-like" or "La Niña-like". Indeed, in Figs. 5.6 and 5.7 we have already used such an index (the maximum SST change along the equator) to scale the climatological fields for comparison. The problem is then reduced to understanding the sensitivity of this single index.

Thus the key result from the off-equatorial coupled cases is that latitude of the zonal stress perturbation is not essential to structure of the response; more important are the equatorial coupled feedbacks. Neelin and Dijkstra (1995) and Dijkstra and Neelin (1995) provide a firm foundation for understanding of how these coupled feedbacks affect the zonal structure of the climatology. The *amplitude* of the coupled response, on the other hand, *does* depend critically on the seed perturbation, as can be seen by comparing the SST scales in Figs. 5.6 and 5.7; off-equatorial stress is less efficient than equatorial stress at producing equatorial climate changes. In the next section, we quantify this statement by comparing equatorial and off-equatorial zonal stress forcings of different meridional widths.

5.4.3 Meridional width of the stress

Equatorial stress

How sensitive is the climatology to the detailed meridional structure of the climatological zonal stress? To answer this question, the intermediate model is subjected to an equatorial zonal wind stress of the form (5.1), and the meridional width L_y of the perturbation is linearly varied from $5°$ to $30°$ over the course of a 500 year simulation. The amplitude $\widetilde{\tau}_x^* = 0.1$ dPa is held constant in time and is the same for all cases. Model results for the ocean-only and stochastic coupled cases are shown in Fig. 5.8.

Panel (a) indicates that coupled feedbacks substantially amplify the eastern equatorial SST response, and these feedbacks are nonlinear, i.e. the feedback warming for westerlies is greater than the feedback cooling for easterlies. The SST is rather insensitive to the meridional width of the perturbation, indicating that it is the equatorial value of the stress perturbation that dominates the climate response. The SST is slightly less sensitive to narrow imposed stress, because narrow stress induces a zonal-mean thermocline depth change (panel b, see also Fig. 5.4) which in the east opposes the depth change due to the thermocline slope.

The coupled feedback zonal stresses are meridionally narrow (Figs. 3.7–3.8), and so induce an additional shoaling of the zonal-mean thermocline for westerlies, and additional deepening for easterlies. These zonal-mean thermocline changes help to limit the coupled SST response by opposing the slope-related thermocline changes in the east. Compared to the zonally-asymmetric changes, however, the zonal-mean changes are clearly of secondary importance in determining the overall effect on SST. In the westerly case, for example, coupling enhances the surface warming despite a shoaling of the zonal mean thermocline.

The feedbacks also amplify the zonal currents along the equator (panel c of Fig. 5.8).

Equatorial response to imposed equatorial τ_x
ocean−only (plain), stochastic coupled (circles); easterly, westerly

(a) SST_{east} (°C) (b) zonal−mean h (m) (c) zonal−mean u (cm/s)
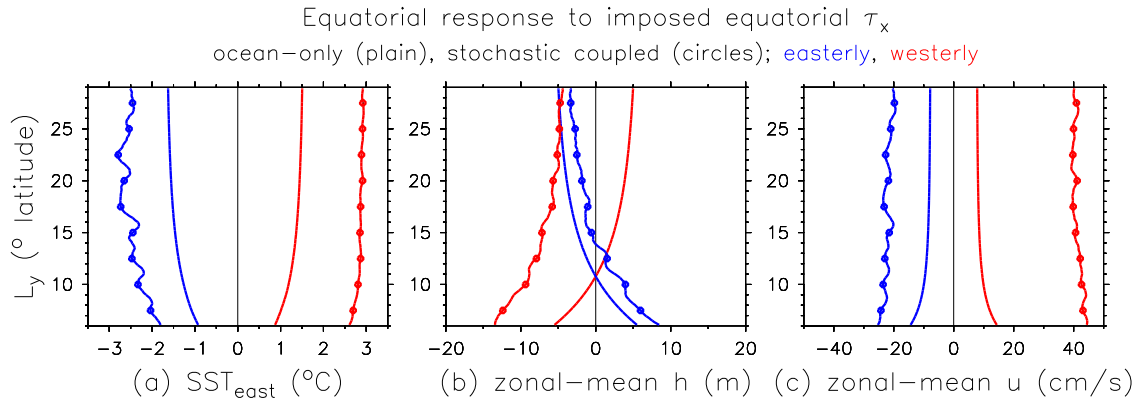
Figure 5.8: Simulated response of the equatorial (2°S–2°N) climatology to an imposed equatorial zonal stress perturbation of amplitude 0.1 dPa, which is zonally constant and has a meridionally Gaussian shape with an e-folding halfwidth of L_y. Red (blue) lines correspond to westerly (easterly) stress perturbations. Plain lines indicate the ocean response without coupled feedbacks, circled lines the response of the coupled ocean/atmosphere with noise. Panels show the long-term mean changes, relative to the control case, of (a) SST averaged over the eastern Pacific (150°W–90°W), (b) zonal-mean thermocline depth, and (c) zonal-mean mixed layer zonal current.

Equatorial response to imposed off−equatorial τ_x
ocean−only (plain), stochastic coupled (circles); easterly, westerly

(a) SST_{east} (°C) (b) zonal−mean h (m) (c) zonal−mean u (cm/s)
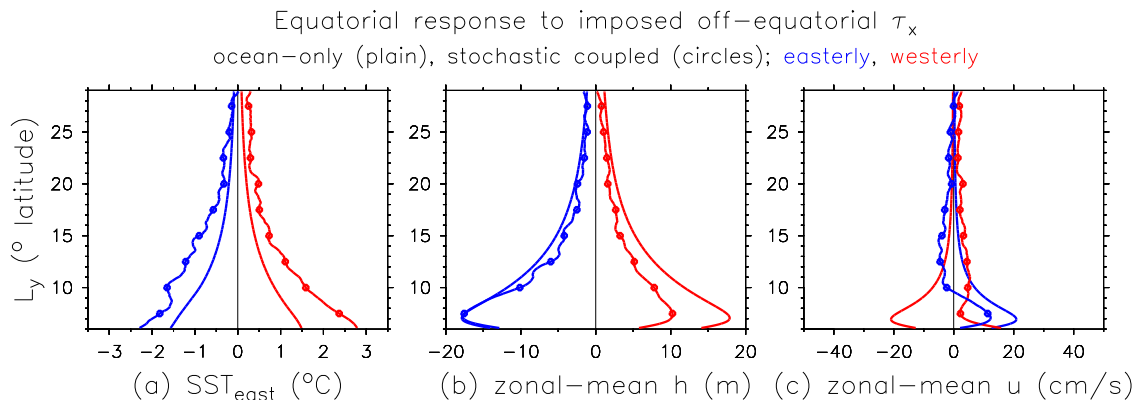
Figure 5.9: Simulated response of the equatorial (2°S–2°N) climatology to an imposed off-equatorial zonal stress perturbation which is zonally constant, vanishes at the equator, and has an inverted Gaussian shape in the meridional with an e-folding halfwidth of L_y and a peak off-equatorial amplitude of 0.1 dPa. Otherwise as in Fig. 5.8.

The effect of coupling on the equatorial zonal-mean thermocline and zonal currents is greatest in the westerly case, because the pattern of SST warming, which is more zonally and meridionally asymmetric than the pattern of cooling, projects more strongly onto mode 2 of the statistical atmosphere (Fig. 3.8) which gives strong cyclonic stress curl in the equatorial eastern Pacific. The feedback westerlies are in effect meridionally "narrower" than the feedback easterlies. Thus the coupled westerly case shows a greater change in the equatorial zonal-mean thermocline and zonal current than does the coupled easterly case. The thermocline change is the more important for SST; e.g. in the westerly case SST warms with increasing L_y despite the slightly weakening current perturbation.

In summary, the SST response is not very sensitive to the meridional width L_y of an imposed equatorial τ_x perturbation. The zonal-mean thermocline depth, on the other hand, *is* sensitive to L_y and also to the width of the feedback stress. The zonal-mean zonal currents are likewise sensitive to L_y. It is therefore possible for two climatologies with similar SSTs to have very different zonal-mean structures below the surface. Such climatologies may also have different mixed layer heat budgets, since widening the stress enhances the effect of thermocline changes on SST, while narrowing the stress enhances the effect of zonal current changes on SST.

Off-equatorial stress

Repeating the experiment instead with a purely off-equatorial zonal wind stress of the form (5.2) results in Fig. 5.9. Here the only way the stress perturbation can affect the equatorial region is by altering the zonal-mean currents and thermocline depth. Panel (c) indicates that the current changes are rather small for all L_y, so the most important effect of off-equatorial westerlies is to induce a deepening of the zonal-mean thermocline at the equator, which then causes a warming of the eastern Pacific that is amplified by coupled feedbacks.

The SST change is strongest when the edges of the imposed stress are close to the equator, so that the near-equatorial stress curl is intense; the SST change in the uncoupled cases is roughly twice as strong for $L_y = 10°$ than for $L_y = 15°$. Narrow stress creates strong Sverdrup divergence, which then strongly affects the zonal-mean thermocline and plants a large seed for equatorial coupled feedbacks to grow. Since the feedback stress is meridionally narrow, it "fills in" the equatorial gap in the imposed stress, canceling part of the zonal-mean response. This is especially the case for the feedback westerlies, since they are narrower than the feedback easterlies.

Comparing Fig. 5.9 to Fig. 5.8, we see that the uncoupled SST responses to off-equatorial and equatorial perturbations are comparable for $L_y \approx 8°$. Coupling, however, is more effective at amplifying the response in the equatorial-stress case, since that case has additional equatorial upwelling and slope-related eastern thermocline depth perturbations generated directly by the imposed stress.

In summary, the tropical Pacific climatology is most sensitive to the part of a zonal stress perturbation that lies on the equator; it is not very sensitive to the part of the stress that is far from the equator. Purely off-equatorial stress perturbations can, if they are near enough to the equator, induce large equatorial changes by affecting the zonal-mean thermocline depth, but off-equatorial stress is less effective than equatorial stress at seeding

coupled feedbacks because it does not induce changes in equatorial upwelling or the zonal slope of the thermocline.

5.4.4   Longitude of the stress

Given the zonal asymmetry of the tropical Pacific climatology and the coupled feedback response, does a change in wind stress forcing in the eastern Pacific affect the climatology differently than a change in the western Pacific? To address this question, we investigate the sensitivity of the climatology to the longitude of an equatorial zonal stress perturbation. In the intermediate model, a bivariate Gaussian perturbation of the form

$$\overline{\tau}_x^* = \widetilde{\overline{\tau}_x^*} \exp\left[-\frac{(x - x_0)^2}{L_x^2} - \frac{y^2}{L_y^2} \right] \tag{5.3}$$

is imposed with $L_x = 40°$ and $L_y = 15°$. This perturbation has an equatorial maximum of $\widetilde{\overline{\tau}_x^*}$ at longitude x_0.

We start by characterizing the structure of the forced and coupled responses to westerly stress perturbations in the east and west. The stress amplitude is held constant at 0.1 dPa, and x_0 is linearly shifted from 125°E to 85°W over the course of a 500 year simulation. Results for the ocean-only and stochastic coupled cases are shown in Fig. 5.10. The plotted curves represent equatorial 50-year averages centered on $x_0 = 170°$E and $x_0 = 130°$W. As in Fig. 5.6, all data have been scaled by the peak equatorial SST change in the stochastic coupled case, indicated above panel (b).

Uncoupled oceanic response

The plain lines in Fig. 5.10 show the uncoupled responses of the equatorial ocean climatology to westerly stress perturbations in the eastern Pacific (case E hereafter) and western Pacific (case W hereafter). The thermocline slope is in zonal phase with the stress, so in case W the thermocline deepens over a large region of the eastern basin, while in case E it deepens only in the east.

These different thermocline responses, together with the stronger change in upwelling in the eastern Pacific in case E, induce changes in $\partial_z T$ and vertical advection that are zonally shifted relative to each other in the same sense as the stress, i.e. case W gives vertical advective warming that lies slightly west of that in case E. Since case E therefore produces a stronger change in $\partial_x T$, it exhibits a stronger central Pacific warming from zonal advection than does case W, but the effect of this zonal advective change is mitigated in case E by increased vertical advective cooling in the central Pacific. The net result is that case E has a stronger warming in the east but a weaker warming in the west.

Coupled response

Coupled feedbacks substantially alter this picture. Compared to the uncoupled responses, the coupled responses (circled lines in Fig. 5.10) look much more similar to each other, since the position of the feedback stress is determined mostly by the model dynamics and is much stronger than the imposed perturbation. As in the uncoupled regime, the SST

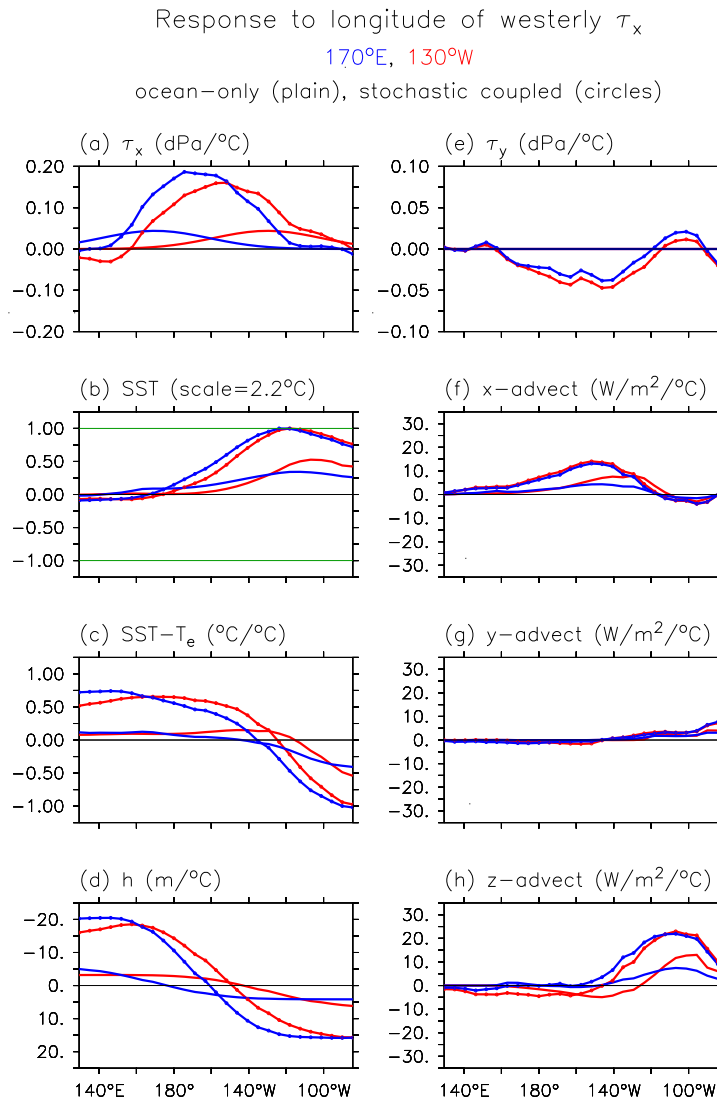Figure 5.10: Simulated response of the equatorial climatology to an imposed equatorial westerly stress perturbation that is zonally localized. The perturbation has a peak equatorial amplitude of 0.1 dPa and a bivariate Gaussian shape with e-folding halfwidths of 40° longitude and 15° latitude. Red (blue) lines correspond to a westerly perturbation with a peak at 130°W (170°E). Otherwise as in Fig. 5.6.

response in case E is shifted eastward of that in case W, but relative to the total SST change the shift is very slight, and the peak SST changes are nearly identical in the two cases. There is also little difference between the advective terms in cases E and W, and the meridional stress change, which is due entirely to coupled feedbacks, is nearly identical between the two cases. It is again evident that the spatial structure of the coupled feedbacks is little affected by the structure of the imposed perturbation, as long as that perturbation is not excessively large. The primary role of the forcing, regardless of zonal position, is to seed coupled feedbacks which then determine the spatial structure of the climatology.

Despite the similarities in the SST climatologies, however, there are important dynamical differences between cases E and W which will be relevant to ENSO variability. This is because the external perturbations persist in the adjusted wind stress, i.e. they are not canceled by the coupled feedbacks. Compared to case E, case W has stronger anomalous westerlies in the west and so shows a stronger deepening of the thermocline over the entire central and eastern Pacific, along with a stronger reduction in $\partial_z T$. Case W also maintains stronger upwelling in the east, as indicated by lack of any westerly anomalies there. Since these fields control the strength of the thermocline feedback and local feedbacks, one can anticipate that the climatologies for E and W (which look rather similar on the surface) may produce quite different ENSO behavior.

Experiments with imposed *easterly* stress perturbations were also performed (not shown). Compared to the westerly experiments, the coupled response in case W is shifted farther to the west of case E. This is because the zonal advective and T_e saturation nonlinearities grow more important as the climatology becomes more La Niña-like (Fig. 5.6). The thermocline is nearer to the surface in the east, and so SST becomes more sensitive to the differences in the thermocline structure associated with the different stress positions. The zonal SST gradient is also stronger in the easterly cases, so the SST also becomes more sensitive to the position of the zonal currents which underlie the stress perturbations.

Longitude of peak zonal stress sensitivity

Where along the equator is the climatology most sensitive to a zonal stress perturbation? Fig. 5.11 shows how the ocean-only and coupled responses depend on the zonal position x_0 of a westerly perturbation. We consider first the ocean-only case (top row). The first column shows the imposed westerly forcing; the equatorial downwelling and zonal current perturbations (not shown) are in zonal phase with and slightly west of the stress, respectively. As the westerlies shift eastward, the zonal slope of the equatorial thermocline shifts eastward, and the zonal extent of deep h in the east decreases. The zonal fetch of the stress perturbation, and therefore the east-west thermocline depth difference, is greatest when x_0 is in the center of the basin. The peak thermocline response in the east occurs for $x_0 \approx 160°W$.

It is interesting to note that when the westerlies in the west, they deepen the zonal-mean h, but when they are in the east, they shoal the zonal-mean h. To understand why, let us consider the wave signals arriving at a point in the center of the basin. For wide stress (here $L_y = 15°$) the equatorial Kelvin signals generated in the region of forcing are stronger than the off-equatorial Rossby signals, so the equatorial response is dominated by the former. When x_0 is in the west, h receives a fresh Kelvin deepening signal arriving
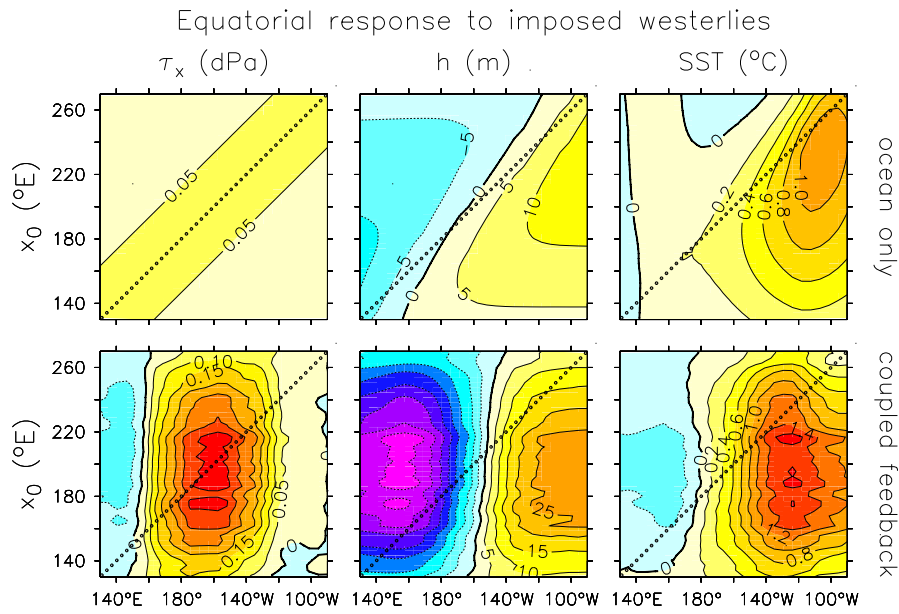
Figure 5.11: Change in the equatorial (2°S–2°N) climatology resulting from a Gaussian westerly stress perturbation with halfwidths of 40° longitude and 15° latitude and a peak value of 0.1 dPa on the equator at longitude x_0 (circles). Left column gives the zonal stress change, center column the thermocline depth change, right column the SST change. Top row shows the forcing and response in the ocean-only case, bottom row the added feedback in the stochastic coupled case. Warm (cool) colors indicate positive (negative) values.
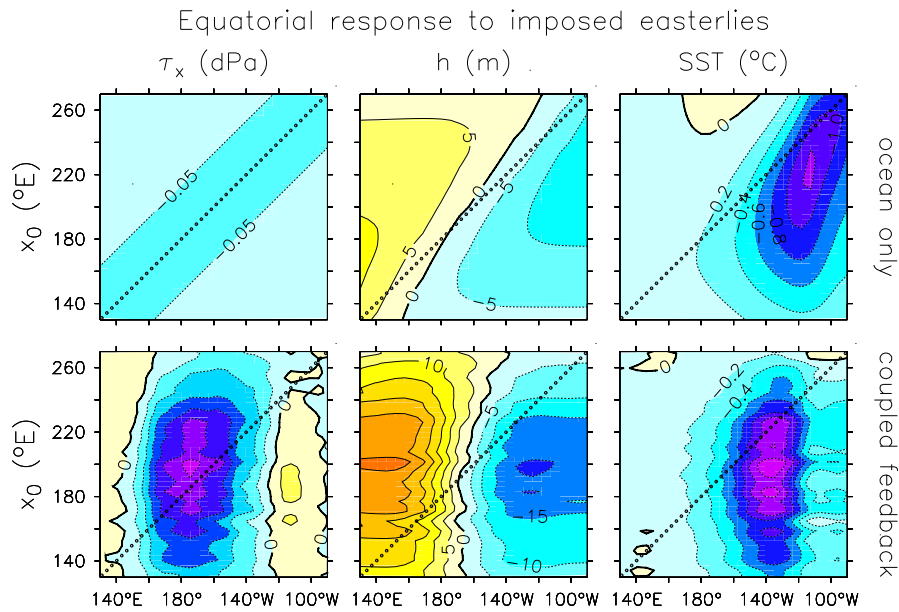
Figure 5.12: As in Fig. 5.11, but for an easterly imposed perturbation.

directly from the region of westerly forcing. When x_0 is in the east, h receives this signal only after a leaky eastern boundary reflection a long Rossby-wave transit westward during which the signal is damped, and a leaky western boundary reflection. These arguments hold at all points interior to x_0, so the zonal-mean thermocline ends up deeper in the case with x_0 in the west than in the east.

As x_0 shifts eastward, the SST response strengthens and becomes more trapped in the east. The peak responses of the SST and its zonal gradient occur for $x_0 \approx 130°$W. When x_0 is very far east, cooling develops in the central basin, where the thermocline shoals but there is little downwelling to oppose the cooling since the westerlies are so far east.

How does coupling affect this picture? The bottom row of Fig. 5.11 shows the air-sea feedback effect in the stochastic coupled case. The feedback response is stronger than the forced response, and consists of peak westerlies near 160°W, and peak warming near 130°W. Strikingly, the position of the feedback response is nearly independent of the position of the westerly forcing: as x_0 crosses the basin from west to east, the feedback stress and thermocline depth shift eastward by less than 20° longitude, and the feedback SST hardly shifts at all. The spatial structure of the feedbacks again appears to be set by the internal dynamics of the coupled system, not the position of the forcing.

The *amplitude* of the feedbacks, however, does depend strongly on x_0. The feedbacks are strongest when the stress forcing lies near the center of the basin ($x_0 \approx 155°$W). Since this is close to the longitude of the feedback stress, it implies that the best seed perturbation for coupled feedbacks is simply one that looks like the feedbacks themselves. Recall that the SST response in the uncoupled case was most sensitive to stress forcing in the eastern Pacific ($x_0 \approx 130°$W). The key point is that *the coupled ocean is sensitive to wind stress forcing in a different location than the uncoupled ocean.*

Fig. 5.12 repeats the experiment but for imposed easterlies instead of westerlies. It is again evident that the coupled feedbacks are very important, that their spatial structure is relatively insensitive to the longitude of the forcing, and that their amplitude is maximized when the forcing lies in the center of the basin. Compared to the case with westerly forcing, however, the forced response in this easterly case is slightly stronger and the coupled feedbacks are slightly weaker. The responses also lie slightly farther west in this case, since zonal advection, which operates mainly in the central basin, plays a larger role when the cold tongue is strong. Unlike the case with westerly forcing, the western Pacific SST has the same sign as that in the east, due to the stronger influence of zonal advection. The SST response is limited in the east by feedback westerlies, which induce local downwelling that reduces the surface cooling.

5.5 Changes in radiative forcing

How does the tropical Pacific climate respond to changes in surface heating that arise from errors in simulated heat fluxes, or from anthropogenic changes in the real world? Given the observed increase in global-mean surface temperature over the past century, and given the accumulation of greenhouse gases in the atmosphere which may drive future climate change, it is worthwhile to examine the possible impacts of such radiative changes on the tropical Pacific.

In the next experiment we impose a uniform heat flux over the entire basin, with an amplitude ranging between -20 Watt m^{-2} (cooling) and 20 Watt m^{-2} (warming) over the course of a 500 year simulation. Results for the ocean-only and stochastic coupled cases are shown in Fig. 5.13. The plotted curves represent equatorial 50-year averages centered on fluxes of ± 10 Watt m^{-2}. As in Fig. 5.6, all data have been scaled by the peak equatorial SST change in the stochastic coupled case, indicated above panel (b).

Uncoupled oceanic response

The plain red line in Fig. 5.13 shows the uncoupled response of the equatorial ocean climatology to imposed heating. The warming is greatest off-equator (not shown) and in the western Pacific, where the ocean circulation is weak and the imposed heating can only be balanced by an increase in the heat flux out of the ocean. This is accomplished through the linear damping term in (4.18), which represents the effect of increased evaporation from the sea surface. In the eastern equatorial Pacific, however, the heating is also balanced by vertical advection (panel h), which has a greater cooling effect due to the increased vertical temperature gradient associated with the warmer SST. Upwelling serves as a "dynamical thermostat" in the east (Clement et al., 1996), so that the eastern equatorial Pacific warms less than the western equatorial Pacific. The eastern equatorial cooling is exported to the western Pacific by zonal advection (panel f) and to the off-equator by meridional advection (not shown). For imposed cooling (plain blue line), the uncoupled response of the ocean is precisely opposite.

Coupled response

Are the homogenizing effects of coupled feedbacks evident for perturbations other than zonal stress? The fascinating thing about Fig. 5.13 is that the coupled feedbacks utterly dominate the response at the equator. In the imposed-warming case (circled red line), the strengthening of the zonal SST contrast by uncoupled processes gives rise to stronger easterlies, which produce greater upwelling at the equator and an even stronger SST contrast. The net result is that the entire equatorial central and eastern Pacific actually *cool down* in the presence of imposed uniform heating. The patterns of the coupled heat flux response are nearly identical in form, mechanism, and nonlinearity to the zonal stress responses shown in Fig. 5.6. An imposed uniform heating of 10 Watt m^{-2} has roughly the same effect on equatorial SST in the model as imposed zonally-uniform equatorial easterly stress of magnitude 0.06 dPa.

This cooling of the equatorial Pacific in response to imposed uniform heating has been noted in other intermediate coupled models (Dijkstra and Neelin, 1995; Clement et al., 1996) and in observations (Kaplan et al., 1998). However, it is not reproduced by the current generation of GCMs, perhaps because weak equatorial upwelling, diffuse simulated thermoclines, and weak air-sea coupling reduce the effects of dynamical feedbacks in those models (Cane et al., 1997). The key point from Fig. 5.13 is that coupled feedbacks may be very important to the climate response at the equator, so it is important to get these feedbacks right if we are to trust model projections of tropical climate changes and the ENSO response to those changes.
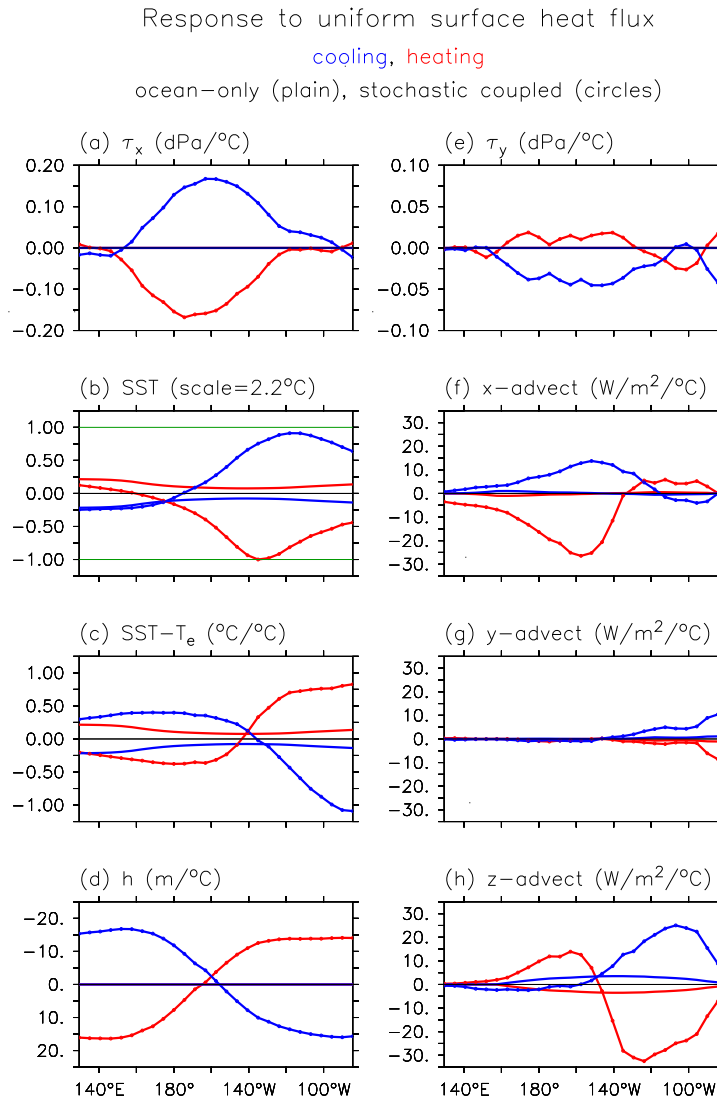
Figure 5.13: Simulated response of the equatorial climatology to an imposed uniform heat flux of 10 Watt m^{-2}. Red (blue) lines correspond to imposed basin-wide heating (cooling). Otherwise as in Fig. 5.6.

5.6 Changes in mean meridional wind stress

The meridional asymmetry of the eastern tropical Pacific mean state results from an ocean-atmosphere instability closely tied to the annual cycle (Philander et al., 1996; Wang and Wang, 1999). The meridional wind stresses ($\overline{\tau}_y$) associated with this climate instability are important, because they generate upwelling south of the equator in the eastern Pacific (Appendix C). This enhances SST/thermocline coupling in that region, in a manner similar to what happens when the zonal trade winds shift eastward (Section 5.4). Thus it is reasonable to expect that a change in the cross-equatorial southerlies might affect ENSO. In nature and in coupled models, such a change might arise due to a change in the land-sea temperature contrast, cloud feedbacks, or the seasonal cycle.

In this section we examine the effect of such a change on the tropical Pacific climatology. In the intermediate model, a meridional stress perturbation is imposed with the form

$$\overline{\tau}_y^* = \widetilde{\overline{\tau}_y^*} \exp\left[-\frac{(x - x_0)^2}{L_x^2} - \frac{y^2}{L_y^2} \right] \tag{5.4}$$

This perturbation is a bivariate Gaussian, with an equatorial maximum of $\widetilde{\overline{\tau}_y^*}$ at longitude x_0. Values of $L_x = 40°$, $L_y = 20°$, and $x_0 = 100°$W correspond roughly to the position and shape of the annual-mean climatology of cross-equatorial southerlies in the eastern Pacific. The stress amplitude $\widetilde{\overline{\tau}_y^*}$ is varied from -0.1 to 0.1 dPa over the course of a 500 year simulation. Results for the ocean-only and stochastic coupled cases are shown in Fig. 5.14. The plotted curves represent equatorial 50-year averages from the beginning and end of the sensitivity runs, so that the time averages are centered on ± 0.09 dPa. As in Fig. 5.6, all data have been scaled by the peak equatorial SST change in the stochastic coupled case, indicated above panel (b).

Uncoupled oceanic response

The uncoupled response of the active layer to the strengthened southerlies (plain red line) resembles that for the uniform change in meridional stress studied by Cane and Sarachik (1977) and Yamagata and Philander (1985); it consists entirely of antisymmetric Rossby waves, which in this case are confined near the eastern boundary especially at high latitudes. The thermocline shoals slightly in the southeast Pacific, and the westward currents intensify in the cold tongue region south of the equator. There are also important changes in the Ekman layer: upwelling increases south of the equator, and there is enhanced cross-equatorial transport in the eastern Pacific.

Together, these changes effect a strengthening of the cold tongue, as more and colder water is upwelled south of the equator, and more of this water is carried northward across the equator. Zonal advection also acts to cool the eastern Pacific by advecting the anomalously cold waters westward. Because the southerly stress perturbation has no effect on *equatorial* upwelling or the equatorial thermocline depth, the changes in vertical advection at the equator are due entirely to the change in SST induced by horizontal advection. Vertical advection thus acts as a damping on the equatorial SST anomalies. For southerly stress the SST cooling is mostly confined to the far eastern Pacific. The SST response to
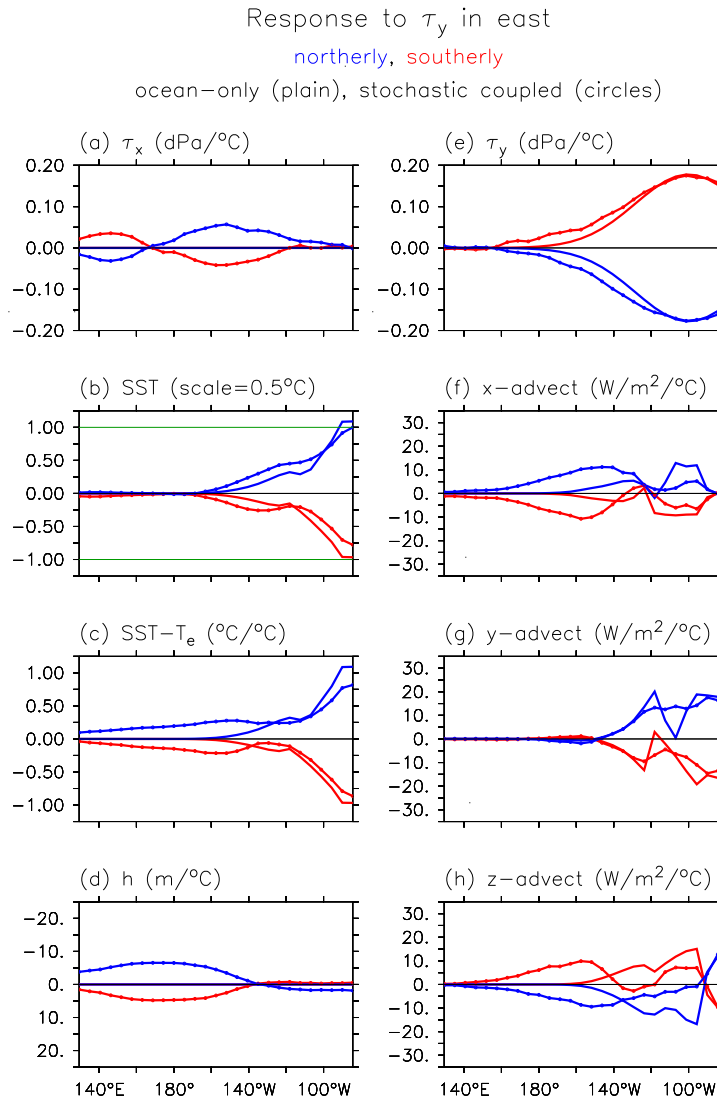
Figure 5.14: Simulated response of the equatorial climatology to an imposed meridional stress perturbation in the eastern equatorial Pacific. The perturbation has a peak amplitude of 0.09 dPa on the equator at 100°W, and a bivariate Gaussian shape with e-folding halfwidths of 40° longitude and 20° latitude. Red (blue) lines correspond to a southerly (northerly) stress perturbation. Otherwise as in Fig. 5.6 except that the ordinate of panel (e) has been changed.

northerly stress is almost exactly opposite, with a warming in the far eastern Pacific; the small amplitude of the response makes the dynamics nearly linear.

Coupled response

We have shown that a wide variety of climate perturbations can produce similar coupled feedbacks, which homogenize the net response. Are these feedbacks universal? Not entirely—the striking thing about Fig. 5.14 is that meridional stress induces very little coupled feedback in the model. The forced SST pattern induced by the meridional stress projects only weakly on the SST patterns of the statistical atmosphere, which are linked more to the observed ENSO zonal stress. Thus there is little feedback generated in either the meridional or the zonal stress. For the zonal stress feedback that *does* arise, there is very little stress in the east (so there is little change in equatorial upwelling in the east), and the fetch in the western Pacific is canceled by that in the central Pacific (so the thermocline depth is nearly unchanged in the east). As a result, vertical advection plays little role except to damp the perturbations induced by horizontal advection.

In the central Pacific, the zonal stress feedback induces slight upwelling changes that enhance the changes induced by the forcing; e.g. in the case of stronger southerlies the τ_x feedback is easterly at the equator and so induces upwelling, which cools the SST in addition to the cooling tendency from stronger southerly-induced upwelling south of the equator. In the western Pacific, the warming by vertical advection (acting on a deepened thermocline) almost exactly cancels the cooling by zonal advection, so that there is almost no change in SST.

Thus the effect of southerly stress on the equatorial climatology of the model is fairly small, is confined to the southeastern Pacific, and produces almost no coupled feedbacks. This is in stark contrast to Figs. 5.6, 5.7, and 5.10, in which the coupled feedbacks dominated the response. Thus, not all climate perturbations are alike: the "seed" perturbation planted by meridional stress does not grow nearly as well as that planted by zonal stress. It should be noted, however, that additional feedbacks not explicitly included in the simulation, such as stratus cloud shading, vertical mixing in the ocean, and evaporative heat fluxes, might enhance the asymmetry of the coupled climate response in the real world.

Despite the small sensitivity of the model to changes in τ_y, it is important to note that the response to meridional stress has a rather different spatial structure than the full climatology. Southerlies shift the upwelling south of the equator and strengthen it, while northerlies do the opposite. This change in the strength and asymmetry of the upwelling, and the additional changes in the structure of the thermocline depth, could be expected to alter the spatial patterns and stability of ENSO variability.

5.7   Sensitivity of a hybrid coupled GCM

In this section, we turn to a more sophisticated model to study the tropical Pacific response to climate changes. The model is a statistical-dynamical hybrid, consisting of a state-of-the-art ocean GCM coupled to a statistical model of the atmosphere. A description of the model and an analysis of a control run are presented in Appendix F. The purpose of
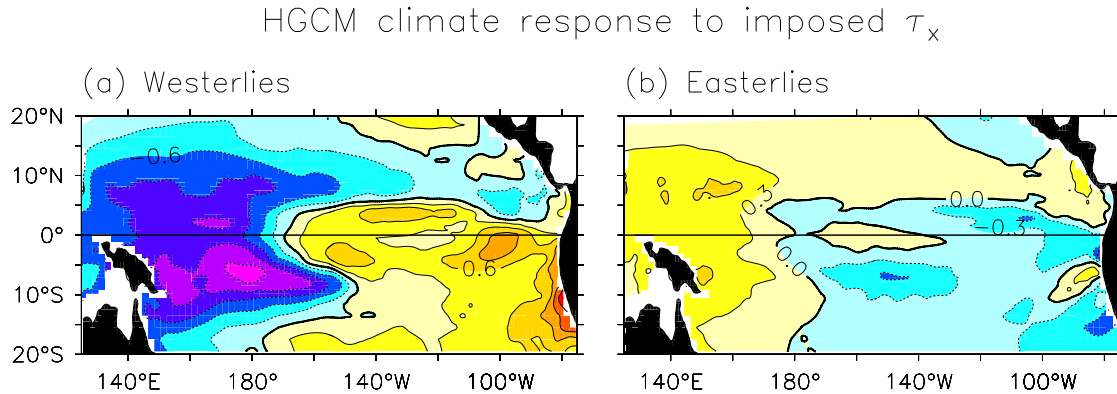
Figure 5.15: Response of the annual-mean tropical Pacific SST climatology to an imposed zonal stress perturbation, as simulated by a hybrid coupled GCM. The imposed perturbation has a peak amplitude of 0.1 dPa on the equator at 140°W and a bivariate Gaussian shape with e-folding halfwidths of 40° longitude and 15° latitude. (a) Imposed westerlies, (b) imposed easterlies. Contour interval is 0.3°C; warm shading indicates a warming, cool shading a cooling.

this section is to show that the GCM has its own unique sensitivity to climate perturbations, though some of the insights gained from the intermediate model apply to this system as well.

5.7.1   Changes in mean zonal stress

We first perform a pair of GCM runs to test the sensitivity of the climatology to a change in equatorial zonal stress. Recall that in the intermediate model, this perturbation was analogous to a whole host of other possible perturbations. Following the model initialization, a zonal stress perturbation of the form (5.3) is imposed with $L_x = 40°$, $L_y = 15°$, $x_0 = 140°$W, and $\widetilde{\tau}_x^* = \pm 1$ dPa. The GCM takes some time to adjust to this change, so the first four years of each run are discarded and the climatology is computed only for the subsequent 16 years. Subtracting the control-run climatology then gives the simulated climate response to the easterly and westerly perturbations.

The change in annual-mean SST for each case is shown in Fig. 5.15. In the westerly case, there is a general weakening of the cold tongue/warm pool contrast, with a warming in the eastern equatorial and southeastern tropical Pacific, and a cooling in the west. The warming is strongest off the coast of Peru, and extends westward along the equator to about 170°W; note that most of the warming occurs off-equator, not on the equator. The cooling in the west is meridionally broad and peaks about 5° south of the equator near the dateline. In the easterly case, the zonal SST contrast strengthens, though the SST change is much weaker than in the westerly case.

The equatorial structures of the responses are shown in Fig. 5.16. As in Fig. 5.6, all data have been scaled by the peak equatorial SST change, indicated above panel (b). As in the intermediate model, it is apparent that coupled feedbacks are important in amplifying
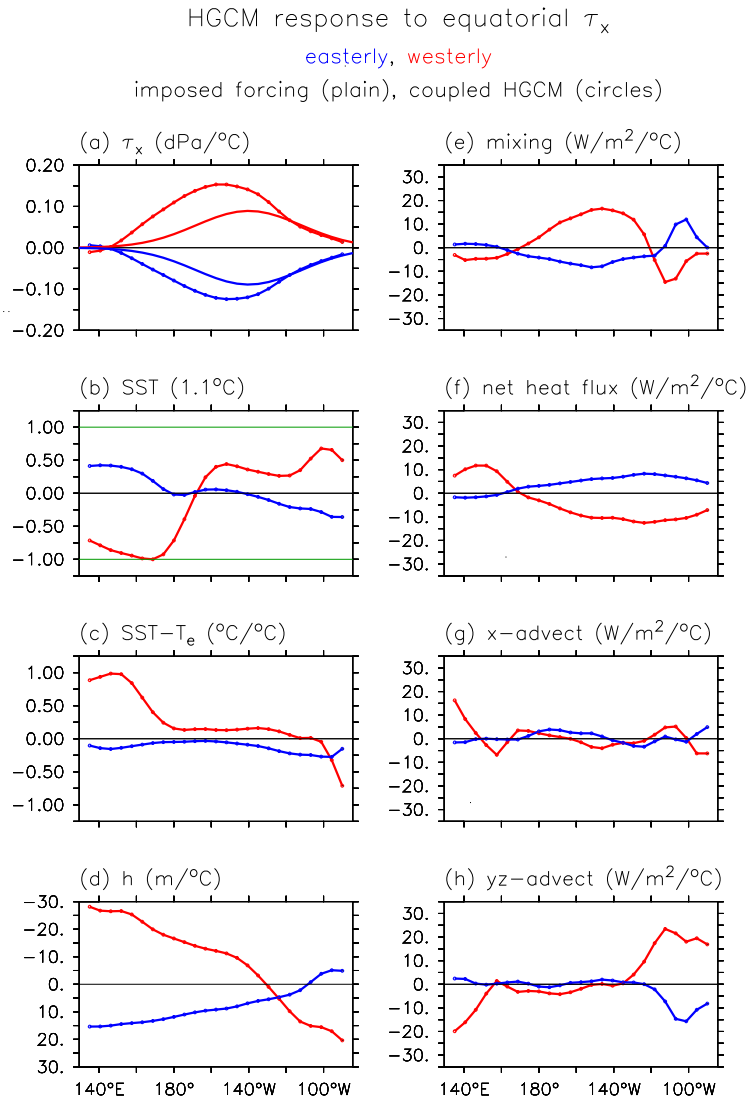
Figure 5.16: Response of the equatorial (2°S–2°N) climatology to an imposed equatorial zonal stress perturbation, as simulated by a hybrid coupled GCM. The imposed perturbation (plain lines in panel a) has a peak amplitude of 0.1 dPa on the equator at 140°W and a bivariate Gaussian shape with e-folding halfwidths of 40° longitude and 15° latitude. Red (blue) lines correspond to a westerly (easterly) stress perturbations. Fields are scaled by the peak SST change indicated in panel (b). Panels show the scaled change in (a) zonal stress, (b) SST, (c) temperature difference across the top 50 m, (d) depth of the 20°C isotherm (ordinate reversed); and the mixed layer heating due to (e) eddy fluxes, (f) surface fluxes, (g) zonal advection, and (h) meridional plus vertical advection.

and modifying the response; the coupled zonal wind stress is about 15° farther west than the imposed forcing. However, the climatological SST response and coupled feedbacks at the equator are only about half as strong as in the intermediate model.

For imposed westerlies, there is some thermocline deepening in the eastern Pacific, but its weakening effect on $\partial_z T$ is overcome by the surface warming except very near the eastern boundary. The weakening of the trades, however, reduces upwelling at and south of the equator, which warms the surface through vertical and meridional advection. This change is opposed in the east by a weakening of the eddy fluxes, which means that less warm off-equatorial is stirred into the equatorial band. In the central Pacific, on the other hand, the change in the eddy flux contributes to the surface warming. (In the control case, the eddy flux had a net cooling effect in the central basin, while in this case it has a net warming effect.) The warming in the central and eastern basin are opposed by an increase in the surface heat flux. In the western and central Pacific, the thermocline shoals strongly, which causes a large increase in $\partial_z T$ in the west and a slight increase in the central basin. In those regions the Ekman currents act on the stronger gradients to cool the surface. Note that there is little change in zonal advection, except for a moderate warming effect in the far western basin which opposes the cooling effects of entrainment and eddy fluxes. The net result of these complex changes is a rather unusual-looking change in SST, with a fairly weak warming plateau in the east, dropping off rapidly to a stronger cooling in the west. The climatological zonal SST gradient is thus weakened for the case with imposed westerlies.

Imposed easterlies have a much smaller effect on the thermocline, but it is interesting to note that h ends up deeper almost everywhere except in the far eastern basin. There is also very little change in the vertical temperature gradient apart from a general weakening all along the equator. In the far eastern basin, stronger upwelling acts to cools the surface despite the weakening of $\partial_z T$. This cooling is balanced by increased eddy warming in the east and decreased heat flux out of the ocean. In the central Pacific, the SST decreases mostly due to a heightened eddy cooling, which is balanced by reduced heat flux out of the ocean. In contrast to the case with imposed westerlies, this case shows little change in the heat balance in the western Pacific. However, the SST warms significantly in the west, since in this region the surface flux does not supply much damping. As in the westerly case, the effect of zonal advection is fairly small. The net result of these changes is a slight increase in the zonal SST contrast.

Thus there are some general similarities with the intermediate model results: in the imposed-westerly case the thermocline flattens, the zonal SST gradient weakens, and the westerlies are enhanced by the coupling; in the imposed-easterly case the opposite happens but the coupled feedbacks are weaker. However, the GCM also shows many differences with the intermediate model. First, the responses are weaker and the $\partial_z T$ changes are smaller in the east, especially in the easterly case. Note that the weaker responses may be partly due to the use of only a single mode in the GCM statistical atmosphere; the SST change patterns are quite different between the easterly and westerly cases, with the latter projecting more strongly onto the leading regression mode. Second, the temperature changes in the west are stronger than in the east. Third, changes in the eddy fluxes play a larger role, while zonal advection and surface fluxes play smaller roles. The HGCM
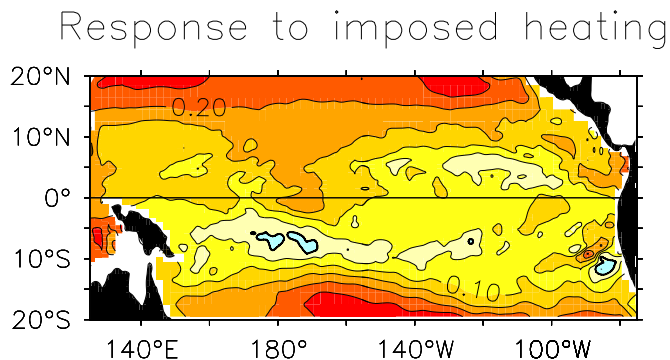
Figure 5.17: Response of the annual-mean tropical Pacific SST climatology to an imposed uniform 1 Watt m^{-2} heating perturbation, as simulated by a hybrid coupled GCM. Contour interval is 0.05°C; warm (cool) shading indicates a warming (cooling), and the heavy line is the zero contour.

appears to be even more nonlinear than the intermediate model, with westerlies giving much stronger feedbacks than easterlies. Again, this is partly due to the changes in high-frequency mixing associated with the change in the climatology and the change in variability (discussed in Chapter 7). Finally, the GCM shows a more complex change in SST, with more off-equatorial structure than in the intermediate model.

5.7.2   Change in radiative forcing

We next test the "dynamical thermostat" hypothesis of Clement et al. (1996) and Cane et al. (1997). Recall that the intermediate model, which represented horizontal mixing as a constant diffusion and surface heat fluxes as a linear damping of SST anomalies, produces a *cooling* response to imposed uniform radiative heating, in accord with the dynamical thermostat. Will the hybrid GCM do the same?

To find out, we impose a weak uniform heating of 1 Watt m^{-2} over the entire basin in the GCM. The imposed heat flux is held constant and the model is integrated for 28 years. As before, the first four years of the run are discarded; only the last 24 years are analyzed.

The change in annual-mean SST for this case is shown in Fig. 5.17. There is warming nearly everywhere, but it is strongest away from the equator. The weakest warming occurs between 2–12°S and in the east Pacific between 2–7°N. There is a slight increase in the zonal SST gradient near the equator, but it is fairly small compared to the overall warming. The dynamical thermostat appears to be weak in this model, as it is in most GCMs.

To see why, we examine the equatorial structure of the response (Fig. 5.18). As in Fig. 5.16, all data have been scaled by the peak equatorial SST change, indicated above panel (b). Note that the coupled response to the imposed heat flux is weaker than in the intermediate model, even after accounting for the factor-of-ten difference in the strength of the forcing. The imposed heating induces a general warming, which gives a *westerly* response in the central basin despite the slight strengthening of the zonal SST gradient. These westerlies push the thermocline down in the east, which reduces $\partial_z T$ and leads to
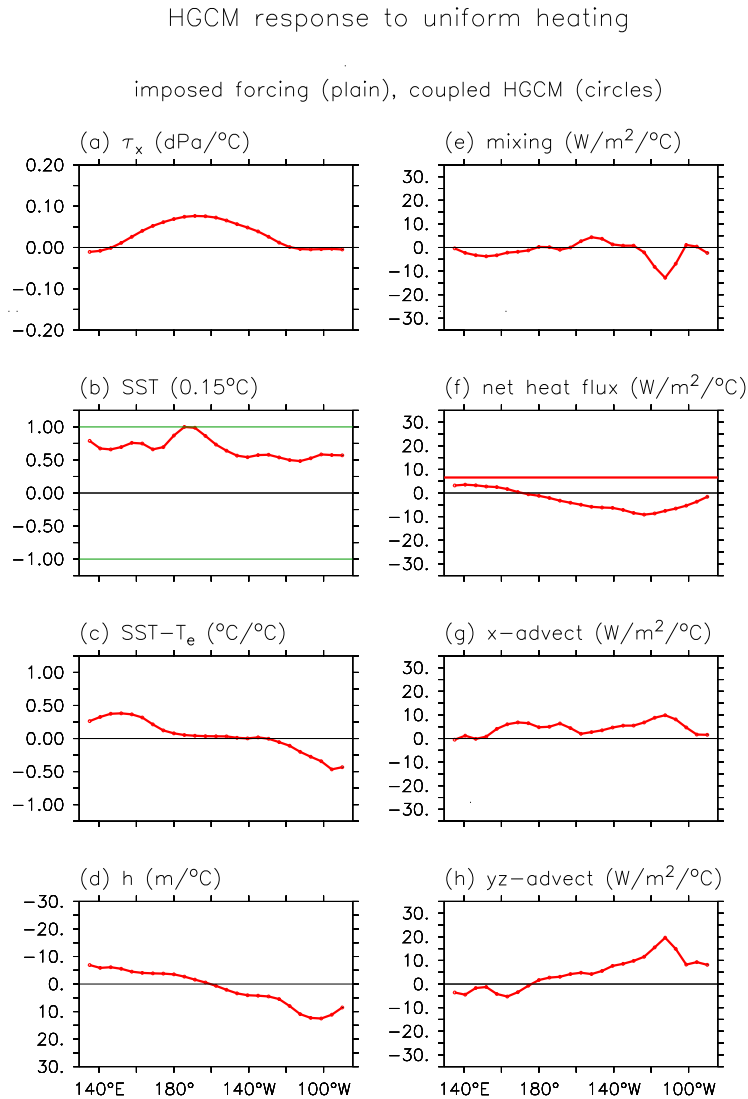
Figure 5.18: Response of the equatorial (2°S–2°N) climatology to an imposed uniform 1 Watt m^{-2} heating perturbation (plain line in panel f), as simulated by a hybrid coupled GCM. Fields are scaled by the peak SST change indicated in panel (b). Panels show the scaled change in (a) zonal stress, (b) SST, (c) temperature difference across the top 50 m, (d) depth of the 20°C isotherm (ordinate reversed); and the mixed layer heating due to (e) eddy fluxes, (f) surface fluxes, (g) zonal advection, and (h) meridional plus vertical advection.

Ekman-induced warming in the east. This eastern warming is countered by the increased cooling by heat fluxes and a reduction in heating from eddy fluxes. The SST warming also leads to an increase in $\partial_z T$ in the western Pacific, where increased cooling by Ekman and eddy fluxes helps to limit the surface warming. In the central equatorial Pacific, the feedback westerlies reduce upwelling and weaken the westward currents, which enhances the warming in that region. The warming of the ocean is more strongly damped by the surface heat flux feedback in the east than in the west.

It is clear from Fig. 5.18 that the changes in surface heat flux (and to a lesser extent, the eddy flux) are the primary reason for the increased SST gradient. Note that this is a rather different asymmetry-generating mechanism than in the intermediate model, where the surface flux acted to *damp* the enhanced gradient; in that case the gradient was generated by the entrainment cooling in the east, associated with the strong thermocline slope generated by *easterly* feedback stress. In the present case there is a *competition* between the zonal stress feedback (which acts to reduce $\partial_x T$) and the surface heat flux feedback (which acts to enhance $\partial_x T$). This competition produces little net change in the zonal gradient, and therefore limits the amplification of the perturbation by coupled feedbacks.

5.8 Discussion

The importance of feedbacks

This chapter has examined the sensitivity of the tropical Pacific climatology to perturbations imposed from outside the coupled system. A recurring theme is that these perturbations can be strongly amplified by coupled feedbacks. With the exception of imposed meridional stress, which produces hardly any coupled feedbacks in the intermediate model, most perturbations are accompanied by strong feedback zonal stress in the central Pacific and associated large changes in the east Pacific cold tongue.

Climate drift

This amplification by feedbacks means that even a good climate model with small dynamical errors can exhibit large climate drift. Consider an ocean model which is tuned to give realistic tropical SSTs when forced by one of the climatological wind stress analyses of Fig. 2.1. If the analyzed trades are weaker than they should be, then the tuned ocean model will be hypersensitive to the trade winds. Coupling such an ocean to a realistic atmosphere model would then give an equatorial cold bias which would be amplified by coupled feedbacks. The trade winds simulated by the CGCM would be too strong, not only compared to the (unknown) truth, but also compared to the analyzed stresses which were too weak in the first place.

Tuning

That the coupled feedbacks have a different pattern from the forced response raises an important point: the root of model bias may not be in the same place as the bias itself.

To improve the performance of a coupled model, one must think carefully about how model deficiencies may be seeding coupled feedbacks, and how those feedback effects are amplifying and redistributing errors throughout the simulation. Instead of tuning locally for the processes one most cares about (like regional SST or precipitation); it may be more effective to improve processes and fields (like central Pacific equatorial zonal stress) that most effectively seed coupled feedbacks, and processes (like equatorial upwelling) that set the strength and spatial structures of these feedbacks.

Attribution

A related issue involves attribution of climate changes that are observed in the real world and in paleoclimate data. The amplification and modification of small perturbations by coupled feedbacks may make it difficult to determine what change occurred and where it occurred. We have seen that a change in zonal stress off-equator, on the equator, or at different longitudes along the equator, and even a change in surface heat flux, can provoke similar responses from the tropical Pacific climatology. Thus it may not be possible to unambiguously deduce the causes of real equatorial climate changes without very detailed climate data and realistic model simulations.

Identification of model problems

In the intermediate model, the spatial structure of the coupled feedbacks appears to be determined mostly by the model dynamics, and not so much by the imposed perturbation. This is actually quite fortunate, because it implies that the feedback effects may be readily identifiable and easy to extract from a given simulation. Taking these results to their logical extreme, one may propose a "straw man" procedure for diagnosing problems in a coupled model.

Suppose one had a coupled climate model which was perfect in every way, except that it had an unknown problem which affected its wind stress field. Suppose that the error directly affected *only* the stress field, such that the direct stress error $\mathbf{E}$ could equivalently be viewed as arising from an external source; an example might be an incorrect value for the surface drag coefficient. Coupled feedbacks would tend to modify the stress error (and other dynamical fields) to produce a total stress bias $\mathbf{B}$ relative to the real world. If the coupled feedback response pattern $\mathbf{P}$ were known to be independent of the stress error, then the stress bias would be $\mathbf{B} = \mathbf{E} + f\mathbf{P}$ with f a scalar representing the feedback strength. The problem of diagnosing $\mathbf{E}$ would then be reduced to estimating f. One could imagine guessing an f, estimating the direct error as $\widehat{\mathbf{E}} = \mathbf{B} - f_{guess}\mathbf{P}$, imposing the opposite of this error in the climate model, spinning up the new climatology, and then diagnosing the new stress bias; repeating this procedure to find the minimum bias would then produce an optimal estimate for $\mathbf{E}$. In the example with an incorrect surface drag coefficient, $\mathbf{E}$ might exhibit patterns very much like the climatological stress, which would point to the drag coefficient as the source of the problem.

Such a procedure is useful mostly for its conceptual value, as it allows one to make quick mental estimates of where model errors lie. A more general procedure for finding model errors would be to compute the "flux adjustments" necessary to correct the model

climatology, say by spinning up the coupled model with a restoring to observations (e.g., Manabe and Stouffer (1988)). The flux adjustment fields would then give some indication of the direct error sources, and subtracting these adjustments from the unadjusted fluxes would give a measure of the structure and amplitude of the feedback error.

The observational network

Yet another issue has to do with the observational network. Naturally one would like to have good observations available at the "pulse points" where the coupled climate system is most sensitive to changes. The hybrid intermediate model suggests that the zonal stress in the central equatorial Pacific is one such key field. We have seen that the feedbacks in the intermediate model resemble those responsible for ENSO and the warm pool/cold tongue climatology, which suggests that one may be able to deduce the active feedback structures simply by observing the natural climate variability of the coupled system. This is fortunate, since it implies that the extensive observing system currently in place to study ENSO may also be extremely useful for detecting longer-term climate changes. It also suggests that paleoclimate data in these regions may be unusually useful in detecting and deducing past climate changes. It is important to remember, however, that the intermediate model indicates that the off-equatorial wind stress can also influence the equatorial climatology. Although this influence is small, it is probably important enough to warrant its consideration in modeling and forecasting of the equatorial Pacific.

Model dependence

As shown in Section 5.7, the climate change resulting from a given perturbation, and the mechanisms that produce this change, can be rather model-dependent. The great strengths of the HGCM are its more realistic treatment of the ocean (including eddy fluxes), its more sophisticated treatment of the surface heat fluxes, and the inclusion of the seasonal cycle. However, some of these assets might conceivably be liabilities as well, e.g. if the mixing parameterization were incorrect (a possibility, given the OGCM's climatological cold bias), or if the single-mode linear atmosphere model were inappropriate for the climate sensitivity experiments (since the positions of the wind stress and surface heat flux responses are fixed in space). The main strengths of the intermediate model, on the other hand, are its more flexible treatment of the wind stress response to SST anomalies, and its well-tuned (albeit very simple) dynamics.

Simplicity of the climate manifold

That the coupling produces similar climate change patterns in the intermediate model for different imposed perturbations greatly simplifies the study of ENSO sensitivity to climate, since the problem is largely reduced to mapping the ENSO response to "El Niño-like" and "La Niña-like" climate states. For a given climate perturbation, one can simply refer to the climatology scale (above panels (b) in the equatorial structure diagrams) to deduce the structure and amplitude of the change in the mean state, and then use this index assess the ENSO response from the sensitivity diagrams that will be presented in

Chapter 7. It is hoped that together, these diagrams will prove quite useful to both theorists and climate modelers.

Theory of ENSO
Sensitivity to Climate

All perception of truth is the detection of an analogy.

Thoreau, *Journal*, 1851

In this chapter we examine the role of the background state in the dynamics of ENSO, by examining the processes that drive sea surface temperature changes in the equatorial Pacific. We first review the primary modes that contribute to interannual oscillations, and examine previous model results regarding the sensitivity of ENSO to the climatology. We then investigate the influence of nonlinearity and the climatology on these modes and propose a way of distinguishing between them based on the relative phasing of terms in the SST tendency equation. Phasor diagrams prove useful for clarifying the individual roles of the tendency terms and their sensitivities to climate change.

6.1   Literature review

6.1.1   Prototype modes

Comprehensive reviews of ENSO theory are given by Neelin et al. (1998) and Philander (1999). In this section we shall focus only on the aspects most relevant to understanding the ENSO sensitivity to the tropical climatology. Two basic types of coupled ocean-atmosphere modes appear relevant to the observed ENSO: a "delayed-oscillator" or "recharge" mode (Fig. 6.1) which depends on slow oceanic adjustment to remote wind forcing (Wyrtki, 1985; Schopf and Suarez, 1988; Suarez and Schopf, 1988; Battisti and Hirst, 1989; Schneider et al., 1995; Jin, 1996; Li, 1997; Jin, 1997), and "SST" modes (Fig. 6.2) that depend more on local wind forcing, anomalous zonal currents, and anomalous upwelling (Zebiak, 1985; Hirst, 1986; Neelin, 1991; Hao et al., 1993; Jin and Neelin, 1993a,b; Dijkstra and Neelin, 1999). ENSO in the real world appears to be a hybrid mode, with ocean adjustment setting the time scale and the SST mode setting the spatial structure and propagation
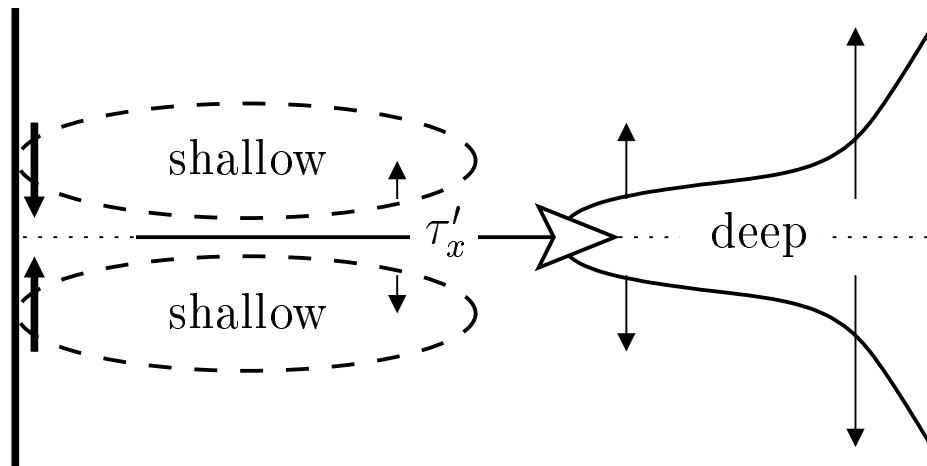
Figure 6.1: View of the recharge/delayed oscillator mode from above. An equatorially-confined westerly stress anomaly induces a rapid deepening of the thermocline in the equatorial eastern Pacific, which warms the surface there via mean upwelling and enhances the westerly stress anomaly. Meanwhile, strong cyclonic stress curl off-equator induces a broad shoaling of the thermocline in the western Pacific and slowly discharges warm water from the equatorial zone. Narrow western boundary currents return some warm water to the equator but not enough to compensate for the discharge in the interior. As the equatorial thermocline shoals, the warm event decays as the remaining wind forcing continues discharging water from the equator. The system is then carried into a cold event by an anomalously shallow equatorial thermocline and associated westward current anomalies, and the cycle repeats with opposite sign.
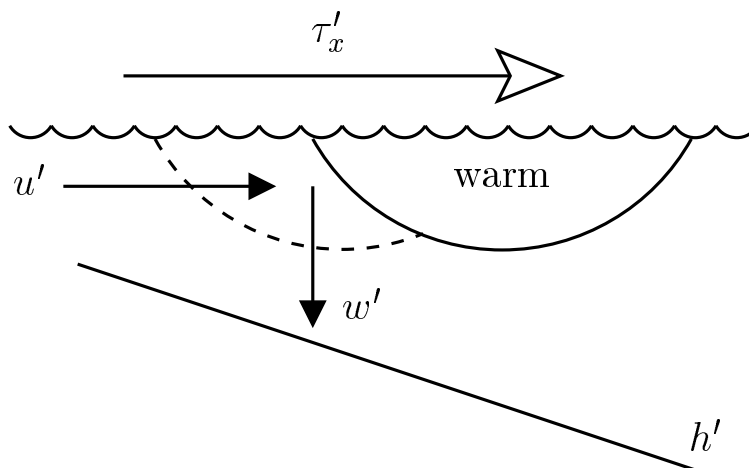
Figure 6.2: Structure of the SST mode, represented as a vertical section through the oceanic active layer and lower troposphere at the equator. A warm anomaly induces anomalous westerly wind stress to the west, which induces downwelling anomalies local to the stress and westerly current anomalies slightly west of the stress. The anomalous currents thus favor *westward* propagation by acting on the mean upward and westward thermal gradients to induce warming to the west of the warm anomaly. In the fast-wave limit, the thermocline is anomalously deep to the east of the stress anomaly, which favors *eastward* propagation of the SST anomaly if the mean upwelling is strong enough.

of SST anomalies (Jin and Neelin, 1993a). If the modal period is long enough (a few years), as appears to be the case for the observed ENSO, individual Kelvin and Rossby wavefronts may not be apparent; hence the relevance of a "fast-wave limit" for the SST mode in which the subsurface ocean is assumed to adjust instantaneously to the wind stress (Neelin, 1991). Variability at shorter periods (a year or less), on the other hand, can evolve as a coupled Rossby mode that depends primarily on zonal advection at the equator and resonant interactions with the eastern and western boundaries (Hirst, 1986; Mantua and Battisti, 1995); such modes have been found to play a role in some models (e.g. that of Zebiak and Cane, 1987).

The zonal propagation of SST anomalies in the fast-wave limit is set by a competition between "thermocline feedbacks" and "local" or "advective" feedbacks (Hirst, 1985, 1986, 1988; Hao et al., 1993; Jin and Neelin, 1993a; An and Jin, 2000, 2001). Thermocline feedbacks are associated with the equatorial thermocline slope, which responds fairly rapidly to changes in zonal wind stress; a westerly stress anomaly induces a deepening of the thermocline in the east, which warms the surface in the east through mean upwelling and drags the stress anomaly eastward. The local advective feedbacks are associated with the anomalous zonal currents and upwelling, which respond locally to stress anomalies that are generally shifted west of the SST anomalies; a warm SST anomaly induces westerlies to the west, which induce local downwelling and eastward currents that drag the SST anomaly westward. Thus thermocline and local advective feedbacks tend to favor eastward and westward propagation, respectively. If both feedbacks are present, the propagation

can be slowed or halted; in the latter case, a standing SST oscillation may arise if oceanic adjustment is delayed.

The stability and period of the delayed/recharge oscillator likewise results from a competition of feedbacks (Battisti and Hirst, 1989; Jin, 1997; An and Jin, 2001). The first is local growth in the equatorial eastern Pacific, which is accomplished by a basinwide positive feedback: during El Niño, the trade winds slacken and deepen the thermocline in the east, which inhibits cooling of the surface in the east, weakens the zonal SST gradient, and thereby further weakens the trades. The second process is a delayed negative feedback that results from slow adjustment of the thermocline. In response to meridionally-confined wind anomalies such as occur during ENSO, geostrophic divergence in the interior and western boundary currents discharge (during El Niño) or recharge (during La Niña) warm surface waters at the equator, which raises or lowers the thermocline in opposition to the eastern Pacific anomaly generated by the zonal slope of the thermocline. Eventually, this slow adjustment affects the surface waters sufficiently to bring about a reversal of the event. Zonal currents, which are linked geostrophically to the zonal-mean thermocline depth at the equator, also contribute to the decay by advecting cold water westward (following an El Niño) or warm water eastward (following La Niña). The combination of rapid adjustment of the equatorial thermocline slope, and delayed adjustment of the equatorial zonal-mean thermocline induced by off-equatorial ocean memory, are thus essential for this mode. The period and growth rate of this delayed/recharge oscillator are surprisingly complex functions of the adjustment time, the strength of the delayed feedbacks, and the strength of local growth processes in the eastern equatorial Pacific (Battisti and Hirst, 1989).

These "prototype modes" can be hard to characterize simply by looking at SST; their similar spatial structures can belie their internal mechanisms and thus their sensitivities to externally-imposed changes. The best way to distinguish them is to examine the balances and relative phasings of the processes which affect SST. We shall develop a framework for this in Sections 6.2 and 6.3.

6.1.2   Influence of the background state

On equatorial waves

From the shallow-water equations (4.1)–(4.3) it is evident that the depth of the thermocline affects the speed and amplitude of equatorial waves. Using an intermediate model, Zebiak and Cane (1987) found that a shoaling of the zonal-mean thermocline, by amplifying the thermocline-slope response to wind stress and delaying the adjustment of the zonal-mean thermocline to changes in wind stress, tended to increase the amplitude and period of ENSO; Dewitte (2000) found similar results. Other authors have expanded on how the structure of the climatology can influence the amplitude, propagation, and dispersion of Kelvin and Rossby waves in a multilevel ocean (Busalacchi and Cane, 1988; Yang, 1991; Yang and Yu, 1992; Yang and O'Brien, 1993).

The background state can also affect the propagation of equatorial waves in the atmosphere. Wang and Xie (1996) found that increased mean vertical westerly wind shear tended to weaken Rossby waves in the lower troposphere, with little impact on Kelvin

waves. Since it is the Rossby component that conveys the westerly stress response westward from regions of anomalous heating, it is conceivable that a long-term change in the strength of the Walker Cell could affect the structure of the wind stress response to SST anomalies. The mean vertical wind shear can also affect the surface stress profile of intraseasonal convective disturbances like the MJO, which appear to be important for modifying ENSO evolution. Takayabu et al. (1999), for example, argued that background westerly shear contributed to the rapid demise of the 1997–98 El Niño: westerly shear altered an MJO disturbance so that it produced predominantly easterly stress anomalies, which in May 1998 reinitiated upwelling on an unusually strong subsurface temperature gradient in the eastern Pacific.

In conceptual models

Results from simple conceptual models provide some insight into the climate sensitivities of ENSO. Battisti and Hirst (1989) analyzed a simple delayed-oscillator model, and found that a strengthening of local growth mechanisms in the east Pacific, or an increase in the delay time for negative feedbacks, favored longer-period and faster-growing oscillations. A strengthening of the delayed feedbacks, on the other hand, favored stronger and shorter-period oscillations. Pure growth and no oscillations obtained if the local growth mechanisms were too strong relative to the delayed feedbacks.

Jin (1996) explored the sensitivity of ENSO to the tropical climatology using a conceptual model of the recharge oscillator. He found that ENSO did not occur if the climatological cold tongue/trade winds were too weak, since a lack of equatorial mean upwelling resulted in SST being too insensitive to thermocline motions in the east. ENSO also did not occur if the cold tongue was too strong, since in this case waters could get no colder in the east and SST again became insensitive to thermocline motions.

In intermediate models

Several studies in intermediate-complexity models have also investigated the sensitivity of ENSO to the climatological background state. Wakata and Sarachik (1991, 1992), building on the work of Hirst (1988), explored the sensitivities of equatorial coupled modes in a bounded basin. They found that both increased air-sea coupling and increased mean upwelling tended to favor oscillations with stronger growth rates and longer periods. Growth rates also tended to increase with the zonal tilt of the thermocline, the strength of the east-west SST contrast, and the meridional width of the equatorial upwelling. The upwelling width also strongly affected the period and propagation tendency of the unstable modes: narrow upwelling inhibited the influence of the thermocline on the surface, favoring zonal advective mechanisms and a westward-propagating mode, while wide upwelling favored thermocline mechanisms and an eastward-propagating mode.

Dijkstra and Neelin (1999) examined the ENSO sensitivity to trade wind strength using the simple model of Jin and Neelin (1993a), with coupled climatologies simulated as in Dijkstra and Neelin (1995). They found only a small region of model parameter space that supported both a realistic climatology and a realistic ENSO, and both were very sensitive to the external component of the trade winds. With increasing air-sea coupling,

the climatology became more La Niña-like, the subsurface temperature saturated in the eastern Pacific, SST in the east became less sensitive to wave dynamics, local growth mechanisms (such as $-u'\partial_x\overline{T}$ and $-w'\partial_z\overline{T}$) dominated the delayed feedbacks, and thus ENSO did not occur. At moderate coupling, oscillations were possible, but only when the tradewind forcing was strong enough that delayed thermocline feedbacks were sufficient to transition the system between warm and cold events. The ENSO frequency was found to increase with increasing trade wind strength. As in Jin (1996), the oscillations were most robust at intermediate wind strength, where coupled feedbacks were strong enough to produce ENSO growth, but not so strong as to produce saturation of the climatological subsurface temperature in the eastern Pacific.

Attempting to explain observed decadal changes in ENSO, Wang and An (2002) explored the ENSO sensitivity to a zonal shift in the climatological tradewinds by prescribing two different background states in the Zebiak and Cane (1987) model. These climatologies were interpolated between the standard model climatology and observed decadal averages from before and after the 1976–77 climate shift, corresponding to an eastward shift in the trade winds. The former case gave a weak ENSO with a 3-year period and westward propagation, while the latter gave a strong ENSO with a 4-year period, eastward propagation, and an eastward shift of the variability relative to the former case. The authors argued for the primacy of the zonal shifts in wind convergence and mean upwelling between the two climatologies, which caused corresponding shifts in the sensitivity of the winds to SST and the sensitivity of the zonal SST gradient to thermocline motions. These changes, by shifting anomalous variability eastward, also lengthened the ENSO period by increasing the time required for negative feedbacks (associated with Rossby waves) to reflect from the western boundary. The increased delay, in turn, enhanced the amplitude of ENSO by allowing more time for growth due to air-sea feedbacks in the eastern basin. The shift in propagation from westward to eastward was identified with a shift in mechanism from $-u'\partial_x\overline{T}$ to $-\overline{w}\partial_z T'$, due to a reduction in the climatological zonal SST contrast in the central Pacific and an increase in mean upwelling the eastern Pacific. An and Jin (2000) and Wang and An (2001) likewise investigated the consequences for ENSO of the 1976 climate shift (see Section 1.1.6).

Other clues are provided by studies that investigated the role of seasonal variations in the background state on the behavior of ENSO. Zebiak and Cane (1987) and Battisti and Hirst (1989) found that climate anomalies tend to be seeded in boreal spring, when the ITCZ is close to the equator, and then grow in boreal summer, as the equatorial upwelling and zonal SST gradient strengthen. Wang and Fang (1996), using a simpler conceptual model, found peak instability in boreal spring, arguing that it was due to the strong vertical temperature gradient (which enhanced positive feedbacks) and weakened upwelling (which reduced negative feedbacks) at that time of year. Wang and Fang (2000), using a more complete intermediate model, examined runs with perpetual-April and perpetual-October radiative forcing. The April case, which produced an El Niño-like background state with weak upwelling and weak vertical temperature gradients, supported longer-period interannual oscillations than the October case which produced a more La Niña-like climatology.

Several studies with intermediate models have mapped the properties of the prototype

modes as a function of changes in key *dynamical* parameters, such as the air-sea coupling strength, the oceanic adjustment time, the strength of currents in the surface layer, and the strength of damping by surface fluxes (Neelin, 1991; Hao et al., 1993; Jin and Neelin, 1993a,b; Neelin and Jin, 1993). To connect these results with observable *climate* parameters, Fedorov and Philander (2000, 2001) prepared complementary maps of the linear stability properties of these modes as a function of the strength of the mean trade winds, the zonal-mean depth of the thermocline, and the sharpness of the thermocline in the vertical. Two important results from these studies are that the linear behavior of ENSO can be very sensitive to parameter and climate changes, and that the sensitivity itself can depend critically on where one stands in parameter space. Perigaud et al. (2000b) and Fedorov (2002) extended some of these results to the time-dependent regime, showing how the response of the coupled ocean-atmosphere system to westerly wind bursts can be sensitive to the depth of the equatorial thermocline.

In coupled GCMs

A number of studies with coupled GCMs have investigated the influence of the background state on interannual variability. Moore (1995) examined the influence of climatological flux adjustments in a coupled GCM. The unadjusted model exhibited a fairly uniform cold bias with weak trades and a thermocline that was too flat, and interannual variability resembling a westward-propagating SST mode. With flux adjustments of surface heat and freshwater only, the model produced an El Niño-like warming of the mean state, and eastward-propagating SST anomalies. Additional flux adjustment of the wind stress produced stronger mean trades and upwelling, and a westward-propagating SST mode amplified by an enhanced convective response to SST anomalies. Increasing the air-sea coupling led to the emergence of delayed-oscillator modes in both the unadjusted and fully flux-adjusted versions of the model.

Li and Hogan (1999) also examined the influence of flux adjustments in a coupled GCM. Their unadjusted model had a climatological cold tongue that was detached from the eastern boundary, and supported only a weak westward-propagating SST mode. With flux adjustments, the cold tongue attached to the eastern boundary, the east-west SST contrast increased, and the simulated ENSO became stronger.

Gordon et al. (2000) explored the influence of low clouds on the climatology and variability of a coupled GCM, which in its control state with simulated clouds showed an El Niño-like warm bias. Specifying only 80% of the observed marine stratocumulus clouds enhanced the cold tongue and produced stronger ENSO variability. Specifying the full observed stratocumulus produced an even stronger cold tongue, with *weaker* ENSO variability than in the control. The ENSO spectra were similar among these cases, but that a 20% change in climatological stratus could have such a large effect on the ENSO amplitude was surprising.

Codron et al. (2001) found that changing a few parameterizations in their coupled GCM produced an El Niño-like warming of the mean state, and an ENSO that was stronger, had a longer period and produced SST anomalies that were stationary instead of westward-propagating. The authors argued that these ENSO changes in the updated model were

due to a strengthening of the wind stress response to SST anomalies, a reduction in the off-equatorial wind stress curl (which reduced the effects of negative feedbacks on zonal average thermocline depth at the equator), and the better confinement of the stress anomalies to the western/central Pacific.

6.1.3 Summary

Several important points have emerged from this review. First, the SST mode and the delayed/recharge oscillator are useful prototypes for describing the time scale, growth rate, spatial structure, and propagation characteristics of ENSO in observations and models. Second, the behavior of these modes, and the merger between them, is controlled by the structure of the background state. The climatology affects the propagation of equatorial waves, the nature of the air/sea coupling, and the strength of the direct and delayed feedbacks that are essential for oscillations and growth. Studies with intermediate models and coupled GCMs have demonstrated the importance to ENSO behavior of the air-sea coupling strength, the structure of the wind stress response to SST anomalies, and the relative balance of thermocline feedbacks and local advective feedbacks. Key climate parameters that appear to affect ENSO in climate models are the depth of the thermocline in the eastern equatorial Pacific, the strength of the zonal SST gradient along the equator, the strength and width of the equatorial mean upwelling, and the intensity of surface wind convergence near the equator.

Although the sensitivities of ENSO are complex, it should be possible to summarize them in a clear diagram that illustrates the relative importance and phasing of the various processes that affect SST. Such a diagram should permit a clear identification of the mechanism in a given model, afford an easy comparison with other models, and also lend insight into climate sensitivities. The next two sections develop just such a diagram, which will be used to support the analyses of the intermediate model and GCM simulations in Chapter 7.

6.2 ENSO sensitivity in the intermediate model

6.2.1 Linearization of the SSTA tendency

The role of the climatology in ENSO evolution is clarified by examining small perturbations about the climatology. We will concentrate on regions of mean upwelling, namely the cold tongue, since these show the largest SST variations during ENSO. Under these conditions the nonlinearities in the SSTA tendency equation (4.28) are weak, and so a linearized version is appropriate:

$$
\begin{aligned}
\partial_t T'\big|_{linear} &= -(u'\partial_x + v'\partial_y + w'\partial_z)\overline{T} \\
&\quad -(\overline{u}\partial_x + \overline{v}\partial_y + \overline{w}\partial_z)T' \\
&\quad +(\kappa\nabla^2 - \epsilon)T'
\end{aligned}
\tag{6.1}
$$

For the intermediate model, we may further linearize the entrainment temperature dependence on thermocline depth by assuming $T'_e \approx bh'$. It is also useful to decompose the

thermocline depth anomaly into a zonal-mean part h'_m and a zonal-perturbation part h'_p. The effect of subsurface temperature changes on SST is then given by the sum of three terms:

$$-\overline{w}\partial_z T' = \frac{\gamma\overline{w}}{H_m}\left(bh'_m + bh'_p - T'\right) \tag{6.2}$$

6.2.2 Local dispersion relation

To understand the effects of these processes on SST evolution during ENSO, we may examine the evolution of a normal mode:

$$\left(T', u', v', w'\right) = \mathrm{Re}\left[\left(\widetilde{T}', \widetilde{u}', \widetilde{v}', \widetilde{w}'\right)e^{\omega t}\right] \tag{6.3}$$

where ω is the complex frequency of the mode, and $\left(\widetilde{T}', \widetilde{u}', \widetilde{v}', \widetilde{w}'\right)$ are complex amplitudes which vary with location. Applying (6.1) to (6.3) yields the dispersion relation

$$\begin{aligned}
\omega &= -\frac{\widetilde{u}'}{\widetilde{T}'}\partial_x\overline{T} - \frac{\widetilde{v}'}{\widetilde{T}'}\partial_y\overline{T} - \frac{\widetilde{w}'}{\widetilde{T}'}\partial_z\overline{T} \\
&\quad -\overline{u}\frac{\widetilde{\partial_x T'}}{\widetilde{T}'} - \overline{v}\frac{\widetilde{\partial_y T'}}{\widetilde{T}'} - \overline{w}\frac{\widetilde{\partial_z T'}}{\widetilde{T}'} \\
&\quad +\kappa\frac{\widetilde{\nabla^2 T'}}{\widetilde{T}'} - \epsilon
\end{aligned} \tag{6.4}$$

This says that ω is controlled by the amplitudes and phases of the tendency terms *relative* to those for SSTA, since for complex numbers ψ_1 and ψ_2,

$$\frac{\psi_2}{\psi_1} = \frac{|\psi_2|}{|\psi_1|}\exp\left[i\left(\theta_{\psi_2} - \theta_{\psi_1}\right)\right] \tag{6.5}$$

where $\theta_{\psi_2} - \theta_{\psi_1}$ is the phase lead of ψ_2 ahead of ψ_1.

For the intermediate model, we may further apply the normal mode structure to the vertical advection term to yield

$$-\overline{w}\frac{\widetilde{\partial_z T'}}{\widetilde{T}'} = \frac{\gamma\overline{w}b}{H_m}\left(\frac{\widetilde{h}'_m}{\widetilde{T}'} + \frac{\widetilde{h}'_p}{\widetilde{T}'}\right) - \frac{\gamma\overline{w}}{H_m} \tag{6.6}$$

6.2.3 Local phase relationships

The dispersion relation (6.4) is illustrated in Fig. 6.3, as a sum of the dominant temperature tendency terms in the complex plane. This schematic, which is loosely based on the intermediate model control run (Fig. 4.21), gives a sort of "frequency budget" for a hypothetical growing mode. The angle of each tendency term from the positive real axis indicates its phase lead ahead of SSTA, so the effect of each term on the mode stability is clear. A stabilizing term is associated with a vector that points to the left; a destabilizing term is associated with a vector that points to the right. An upward-pointing vector (90° phase lead) corresponds to a term which has no effect on stability, but instead contributes
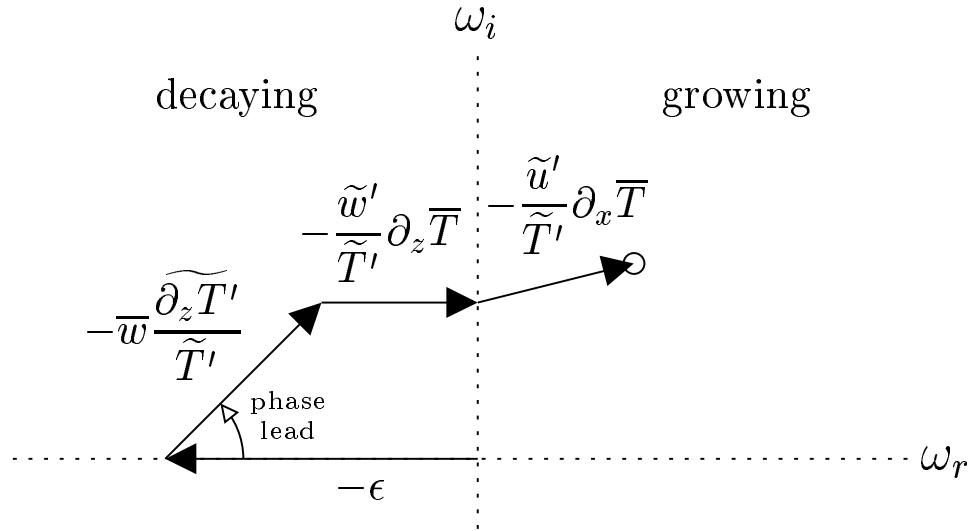
Figure 6.3: Schematic illustration of the complex frequency of SST anomalies (circle), which results from a combination of advective and surface flux tendencies (vectors). Real axis (ω_r) is the e-folding growth rate of the SSTA envelope: positive is growing, negative is decaying. Imaginary axis (ω_i) is the angular frequency in time. The counter-clockwise angle of each vector from the positive real axis indicates its phase lead ahead of SSTA.

to the oscillation itself, as an "inertia" which carries the system past equilibrium points. Conversely, a vector that points downward (90° phase lag) corresponds to an "anti-inertial" term which opposes oscillations and acts to decrease their frequency.

In the control run the surface heat flux is a pure damping term, so it is 180° out of phase with SSTA. The *linear* dependence of the heat flux on SSTA further implies there is a fundamental timescale, ϵ^{-1}, which is independent of location or amplitude. Plotted as the first term in the vector sum, the surface flux provides an invariant scale and "anchor" for the remaining terms.

For the hypothetical mode pictured in Fig. 6.3, the $-\frac{\widetilde{w}'}{\widetilde{T}'}\partial_z\overline{T}$ term associated with anomalous upwelling has a phase angle of 0°. This is because the zonal stress, which is the main driver of equatorial upwelling, is in phase with SSTA over most of the basin. The westerly stress response to warm events induces Ekman convergence and downwelling at the equator, reducing the inflow of cold water from the deep. As a result, $-\frac{\widetilde{w}'}{\widetilde{T}'}\partial_z\overline{T}$ is a pure destabilizer which opposes damping and tries to push the system away from equilibrium.

The $-\overline{w}\frac{\widetilde{\partial_z T'}}{\widetilde{T}'}$ and $-\frac{\widetilde{u}'}{\widetilde{T}'}\partial_x\overline{T}$ tendency terms are also destabilizers: anomalous westerly stress produces anomalous eastward flow and a deepening of the thermocline in the east, both of which act to warm SST in the east and enhance the westerly stress. These feedbacks are not coincident with SSTA, however, and therefore play a role in the transitions between events. Because they lead SSTA, these terms serve to increase the frequency of the oscillations by accelerating the system through the equilibrium state.
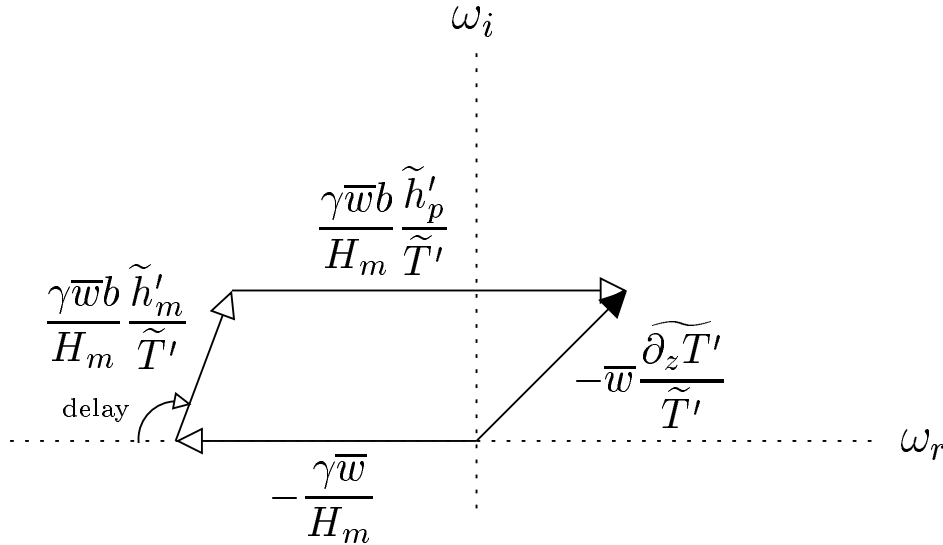
Figure 6.4: Resolution of the frequency effect of equatorial eastern Pacific subsurface temperature changes, $-\overline{w}\frac{\widetilde{\partial_z T'}}{\widetilde{T'}}$, into three components: an SSTA damping $-\frac{\gamma\overline{w}}{H_m}$, a positive feedback $\frac{\widetilde{h'_p}}{\widetilde{T'}}$ from the rapid adjustment of the thermocline slope, and a delayed negative feedback $\frac{\widetilde{h'_m}}{\widetilde{T'}}$ from the slow adjustment of the zonal-mean thermocline depth. Otherwise as in Fig. 6.3.

The complex role of these terms arises from the combined effects of direct feedbacks, associated with rapid adjustment of the equatorial thermocline slope via equatorial Kelvin waves, and delayed negative feedbacks, associated with slow adjustment of the zonal-mean thermocline depth through off-equatorial Rossby waves and boundary reflections. To illustrate for $-\overline{w}\frac{\widetilde{\partial_z T'}}{\widetilde{T'}}$, we refer to (6.6) and concentrate on regions of mean upwelling so that all parameters in that equation are positive. Fig. 6.4 illustrates this sum in the complex plane, with phasors appropriate for the eastern equatorial Pacific in both the intermediate model and observations (Jin, 1997; An and Kang, 2000).

The pure damping effect of $-\frac{\gamma\overline{w}}{H_m}$ is completely determined by the basic state. When SST increases, the vertical temperature gradient increases, and entrainment provides a greater heat flux into the mixed layer to oppose the SST change. The damping increases as the entrainment rate increases or as the mixed layer shoals.

The pure growth effect associated with the equatorial thermocline slope, h'_p, arises because adjustment of the slope is accomplished mainly by equatorial Kelvin waves, which require only a month or two to reach the eastern boundary. At interannual timescales, the anomalous slope is nearly in phase with the zonal wind stress anomaly and therefore with SSTA. When surface warms in the east, the trades weaken and the thermocline rapidly deepens in the east. This warms the subsurface, decreases the entrainment cooling of the mixed layer, and thereby reinforces the initial SST change.

The transitioning effect associated with the zonal-mean thermocline depth h'_m is more

subtle, as there are several processes which affect the heat content of the equatorial band. First, the *generation* of equatorial waves, in response to wind stress changes, produces meridional divergence in the basin interior. A westerly stress perturbation initially gives rise to equatorial downwelling, vortex squashing, convergence onto the equator, and a downwelling Kelvin signal; off-equator, meridional divergence shoals the thermocline and produces a pair of upwelling Rossby signals. Wave *reflections* are also essential, as when wave signals reach the boundaries, they generate narrow boundary currents which pump mass off-equator. Rossby waves reflected from the eastern boundary are eroded by dissipation as they propagate westward, and so are unable to propagate the thermocline depression far into the interior; the thermocline slope they produce is too strong to balance the westerly stress and so poleward currents develop which further discharge mass from the equatorial band. If the boundaries are gappy or slanted, or downward wave propagation is taken into account, then the reflections will be *imperfect* and some mass will effectively leak through the boundaries; at the equator, mass leaks in through the western boundary and out through the eastern boundary during a westerly event.

At interannual timescales, sharp Kelvin and Rossby wavefronts are absent and one may consider the ocean to be nearly adjusted. For equatorial westerlies, this means that equatorial heat content is being discharged by interior meridional divergence and outflux through the eastern boundary, and recharged by influx through the western boundary. The net effect at the equator is generally a small residual and is therefore sensitive to the magnitude of the stress curl and the reflectivity of the boundaries. For westerly stress anomalies, h'_m is discharged at the equator when (1) the wind stress anomaly is narrow in the meridional so that it produces strong interior divergence from the equatorial band, and (2) the boundaries are reflective enough in the west and leaky enough in the east that there is little net influx through the boundaries in the equatorial band.

These conditions are met in the intermediate model control run, and so there is a delayed negative feedback on the eastern Pacific thermocline depth, illustrated schematically by the $\widetilde{h}'_m$ phasor in Fig. 6.4. Interestingly, the phase delay is greater than $90°$ so the "negative feedback" is actually a destabilizing term. This component is also a *transitioner* which carries the system between events. The off-equator responds only slowly to changes in wind stress, so the discharge of equatorial heat content remains strong even after a warm event has ended and westerlies have decayed away. This plunges the system into a cold event and the cycle repeats with opposite sign. Thus the net effect of subsurface temperature changes on SST, $-\overline{w}\frac{\widetilde{\partial_z T'}}{\widetilde{T'}}$, results from a delicate balance of strong and competing effects.

Similar arguments hold for $-\frac{\widetilde{u}'}{\widetilde{T'}}\partial_x \overline{T}$, since the thermocline depth and zonal current are dynamically linked through geostrophy (An and Jin, 2001). Differentiating (4.2), in the inviscid limit without meridional convergence of the meridional wind stress, gives

$$U_1(y = 0) = -\frac{c^2}{\beta} \, \partial_{yy}h_1|_{y=0} \tag{6.7}$$

so that the depth-averaged component of the equatorial zonal current is related to the meridional curvature of the thermocline. When the equatorial thermocline is depressed relative to the off-equator, there will be eastward geostrophic currents at the equator. Thus the slow discharge of heat content out of the equatorial band during warm events

is associated with the development of westward equatorial current anomalies, which act in concert with the equatorial shoaling to reverse the SSTA tendency and transition the system into a cold event. The smaller Ekman component of the equatorial zonal current is in phase with the zonal stress, since from (4.13)

$$U_s(y = 0) = \frac{\tau_x(y = 0)}{\rho r_s} \tag{6.8}$$

Thus the zonal advection term $-\frac{\widetilde{u}'}{\widetilde{T}'} \partial_x \overline{T}$ plays both transitioning and destabilizing roles in the control run.

6.2.4   Effects of changes in the background state

Figs. 6.3 and 6.4 summarize the linear dynamics of the control run in a concise way. Since these diagrams explicitly represent the role of the mean state, they may be useful in understanding and predicting the ENSO response to climate changes.

A change the background state has two effects. First, it selects *which* processes dominate the SST tendency; this is represented by the *magnitude* of the vectors in the phasor diagram. Second, it alters *how* those processes affect the growth rate and period; this is represented by the *phase* of the vectors in the phasor diagram. The latter is the more complicated effect, since the phasing of some terms may depend on the detailed spatial structure of the mode.

Let us explore the effect of changing a single basic state parameter in each tendency term, with the amplitudes and phases of all other tendency terms held fixed. Taking Figs. 6.3 and 6.4 as an example, one could predict that increasing the climatological vertical temperature gradient $\partial_z \overline{T}$ would destabilize the ENSO mode but have no effect on its frequency. Increasing the mean upwelling $\overline{w}$, the mean zonal temperature gradient $\partial_x \overline{T}$, or the entrainment temperature sensitivity b to thermocline depth would destabilize the mode as well, but would also increase its frequency. Increasing the phase delay of the equatorial recharge (Fig. 6.4), as might happen if the anomalous stress response shifted east or if the wave speed c slowed from reduced active layer depth H, would tend to increase the growth rate and decrease the frequency of ENSO. If nonlinearities are weak, then the net impact of multiple changes in tendency terms will simply be the vector sum of the individual changes in the complex plane.

Thus an SST tendency phasor diagram can provide a clear picture of the mechanism and sensitivity of a climate model at any given point in space. We shall use such a diagram in Chapter 7 to help analyze and compare results from the intermediate model and GCM.

6.3   Sensitivity of the SST mode

In this section, we invoke the fast-wave limit and various other reasonable assumptions to permit a complete nonlocal description of the SST mode (Fig. 6.2; Neelin, 1991). The SST mode is common in coupled GCMs, especially when the oceanic resolution is so coarse that mean equatorial upwelling is weak (Cane, 1992; Neelin et al., 1992; Moore,

1995; Delecluse et al., 1998; Li and Hogan, 1999). It also appears to play a role in higher-resolution GCMs and the real world, where it determines the spatial structure and propagation of SST anomalies. There is evidence that related "mobile modes" were important in the 1993–94 warm event (Delcroix, 1998), and may also be relevant to the observed seasonal cycle (Chang, 1994; Chang and Philander, 1994; Xie, 1994).

6.3.1 Equatorial fast-wave limit

Focusing on the equator and assuming meridional symmetry, we begin with the linearized SSTA equation (6.1) in the absence of horizontal mixing:

$$\partial_t T' = -u'\partial_x \overline{T} - \overline{u}\partial_x T' - w'\partial_z \overline{T} - \overline{w}\partial_z T' - \epsilon T' \tag{6.9}$$

The anomalous vertical temperature gradient is linearized as

$$\partial_z T' = \frac{\gamma}{H_m}\left(T' - bh'\right) \tag{6.10}$$

Ignoring dissipation and focusing on low-frequency motions so that the fast-wave limit is valid, (4.1) and (4.7) become

$$\partial_x h' = \frac{\lambda_h \tau'_x}{\rho c^2} \tag{6.11}$$

In this limit the active-layer currents vanish ($u_{al} = 0$), and the surface currents are due entirely to the part of the Ekman circulation not balanced by pressure gradients. Combining (4.15)–(4.16) then gives

$$u' = \frac{B\tau'_x}{\rho r_s H_m} \tag{6.12}$$

where

$$B \equiv \frac{H - H_m}{H} \tag{6.13}$$

Anomalous equatorial upwelling is given by (C.8), which in the limit of small r_s reduces to

$$w' = -\frac{B\beta\tau'_x}{\rho r_s^2} \tag{6.14}$$

For simplicity, we assume the zonal stress anomaly is proportional to the SST anomaly with a zonal phase shift. As we will be looking at normal modes with a sinusoidal structure in the zonal direction, we can induce a zonal phase shift by multiplying the SSTA by a complex scalar A:

$$\tau'_x = AT' = |A|\,e^{i\theta_A}T' \tag{6.15}$$

so that the stress anomaly is shifted eastward relative to the SST anomaly by a phase angle of θ_A. Observations indicate $\theta_A \approx -60°$, i.e. a westward shift of the stress anomaly relative to SSTA.

6.3.2 SST mode dispersion relation

Applying the normal mode structure

$$\left(T', h', u', w', \tau_x'\right) = \left(\widetilde{T}', \widetilde{h}', \widetilde{u}', \widetilde{w}', \widetilde{\tau_x}'\right) e^{\omega t - ikx} \tag{6.16}$$

with k strictly positive, and substituting these solutions into (6.9)–(6.15) gives

$$\omega = -\frac{\widetilde{u}'}{\widetilde{T}'}\partial_x\overline{T} + ik\overline{u} - \frac{\widetilde{w}'}{\widetilde{T}'}\partial_z\overline{T} - \overline{w}\frac{\widetilde{\partial_z T'}}{\widetilde{T}'} - \epsilon \tag{6.17}$$

$$\frac{\widetilde{u}'}{\widetilde{T}'} = \frac{BA}{\rho r_s H_m} \tag{6.18}$$

$$\frac{\widetilde{w}'}{\widetilde{T}'} = -\frac{\beta BA}{\rho r_s^2} \tag{6.19}$$

$$\frac{\widetilde{\partial_z T'}}{\widetilde{T}'} = \frac{\gamma}{H_m}\left(1 - \frac{ib\lambda_h A}{k\rho c^2}\right) \tag{6.20}$$

where all parameters are positive, except for $\overline{u}$ and $\partial_x\overline{T}$ which are negative and A which is complex. Combining these equations gives the dispersion relation

$$\omega = \frac{BA}{\rho r_s}\left(\frac{\beta \partial_z\overline{T}}{r_s} - \frac{\partial_x\overline{T}}{H_m}\right) + \frac{ib\lambda_h A\gamma\overline{w}}{k\rho c^2 H_m} - \left(\frac{\gamma\overline{w}}{H_m} + \epsilon\right) + ik\overline{u} \tag{6.21}$$

where the terms have been grouped according to their phase. The first term, which is in phase with the wind stress anomaly, represents the anomalous currents acting on the mean temperature structure. The second term, which is shifted 90° east of the stress anomaly, represents the effect of subsurface temperature changes acting through mean upwelling. The third term represents a pure damping in phase with the SST anomaly. The final term simply Doppler-shifts the frequency as the wavetrain is advected by the mean zonal currents.

6.3.3 SST mode phase relationships

Dynamical parameters for the intermediate model are listed in Table 4.2, and for the control run at 140°W in the equatorial Pacific we have $H = 120$ m, $c = 2.4$ m/s, $B = 0.58$, $|A| = 0.2$ dPa/°C, $\theta_A = -60°$, $\partial_x\overline{T} = -7.7 \times 10^{-7}$ °C/m, $\partial_z\overline{T} = 0.013$°C/m, $b = 0.075$°C/m, $\overline{u} = -0.25$ m/s, $\overline{w} = 1.5 \times 10^{-5}$ m/s. Assuming a zonal wavelength of 100° longitude, roughly two-thirds the size of the basin, gives $k = 5.7 \times 10^{-7}$ m^{-1}. For these parameters the SST mode has a period of about 1 year, is strongly damped (3 month e-folding time), and propagates westward with a phase speed of about 30 cm/s. The dispersion relation for these parameters is illustrated schematically in Fig. 6.5. This diagram completely describes the SST mode, including its structure, period, growth rate, propagation, parameter sensitivity, and climate sensitivity.

Propagation is essential to the frequency of this mode. Standing modes of this type can only arise if the SSTA phase propagation exactly opposes $\overline{u}$ (i.e. a Doppler-shifted standing mode), or if external forcing and/or delayed oceanic adjustment are present. The
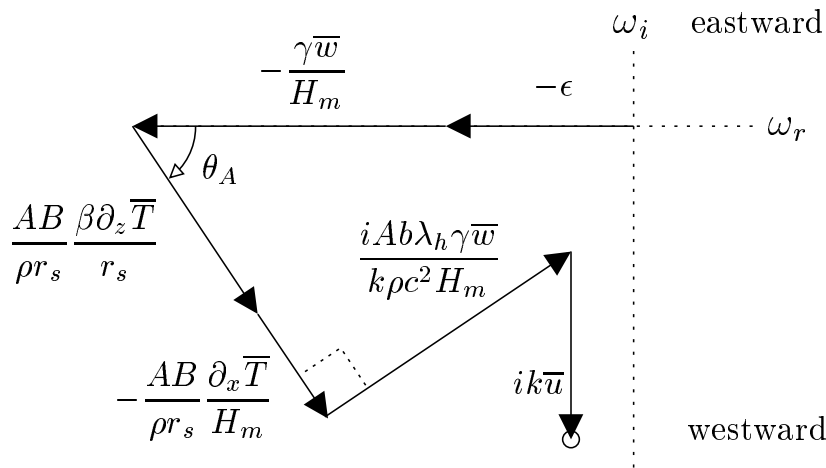
Figure 6.5: Schematic illustration of the complex frequency of SST anomalies for the SST mode (circle), which results from a combination of advective and surface flux tendencies (vectors). The mode has a sinusoidal structure in the zonal direction with positive wavenumber k. Real axis (ω_r) is the e-folding growth rate of the mode: positive is growing, negative is decaying. Imaginary axis (ω_i) is the angular frequency in time: positive is eastward-propagating, negative is westward-propagating. The counter-clockwise angle of each vector from the positive real axis indicates its eastward phase shift relative to SSTA. Vector directions and magnitudes approximate those seen in the intermediate model, for reasonable values of the parameters.

phase propagation arises from a competition of local and nonlocal processes. A westerly stress anomaly, for example, induces a warming *local* to the stress by reducing equatorial upwelling and advecting the warm pool eastward. However, it also induces a *nonlocal* warming by deepening the thermocline a quarter-cycle east of the stress anomaly, which warms that location via mean upwelling. The phase θ_A of the stress anomaly relative to SSTA is therefore key in determining the direction of propagation, as can be seen in Fig. 6.5. As θ_A increases from $-90°$ to $0°$ and the stress becomes more aligned with SST, the "current feedback" goes from inducing westward propagation to inducing growth, while the "thermocline feedback" goes from inducing growth to inducing eastward propagation. Thus the dynamics and sensitivity of the SST mode depend fundamentally on the zonal phase of the stress response to SSTA.

The strength of the thermocline feedback is proportional to the zonal wavelength, since as the wavelength increases the ocean integrates over a larger fetch of the stress anomalies and this results in a larger perturbation in the thermocline. For the observed phasing near $\theta_A = -60°$, it is clear that modes with long zonal wavelengths (small k) are more unstable (and propagate westward more slowly) than modes with short wavelengths. Thus variability will tend to favor the basin scale, where (for the parameters listed above) the SST mode is unstable and nearly stationary. At this scale one would expect boundary reflections to enter into the dynamics of the SST mode. For this reason, variability in coupled models and observations is often described in terms of "mixed modes" which involve elements of both the SST mode and basin wave dynamics modes. In these terms the SST mode can be viewed as controlling the growth and spatial structure of the variability, while ocean dynamics (including equatorial recharge/discharge) control the transitions and thereby set the time scale of the variability.

6.3.4 Effects of background changes on the SST mode

The climate sensitivity of the SST mode is clear from Fig. 6.5. Strengthening the mean temperature gradients $\partial_x \overline{T}$ and $\partial_z \overline{T}$ would destabilize this mode and increase its westward phase speed. Strengthening the mean zonal currents $\overline{u}$ would not affect the stability of the mode, but would increase the westward phase speed by advecting the mode westward. Increasing the mean upwelling $\overline{w}$ would strengthen the thermocline feedback and reduce the westward phase speed; the effect of $\overline{w}$ on the mode stability would depend on the strength of the subsurface temperature anomalies, as the increased upwelling would also act to damp SST anomalies. Increasing the sensitivity b of the entrainment temperature to thermocline depth anomalies (as might occur with a change in the climatological thermocline depth) would strengthen the thermocline feedback, destabilizing the SST mode and slowing its westward propagation. Finally, an increase in the active layer depth H would increase c and B, which in the absence of other changes would favor the current feedback over the thermocline feedback, leading to greater westward propagation, although the effect on stability would be parameter-dependent.

6.4 Summary

This chapter has provided a theoretical basis for understanding the effect of the tropical Pacific climatology on ENSO. A review of previous studies indicated that two coupled modes, the delayed/recharge oscillator and the SST mode, are useful prototypes for understanding ENSO behavior in a wide variety of models. Changes in climate parameters, such as the depth of the thermocline in the eastern Pacific, the intensity of the zonal SST contrast, and the strength of equatorial upwelling, affect the properties of these modes and the merger between them. A local linear analysis of the SST tendency equation in the intermediate model motivated a phasor diagram which illustrates key mechanisms and indicates climate sensitivities. Analysis of the SST mode in the fast-wave limit provided further insight into the structure and propagation of equatorial SST anomalies. The theoretical insights and phasor diagrams developed here are applied in the next chapter, which explores the simulated ENSO sensitivity to climate changes in the intermediate model and the hybrid coupled GCM.

Simulated ENSO Sensitivity to Climate

Knock on the sky and listen to the sound.

Zen saying

This chapter examines the sensitivity of tropical Pacific interannual variability to changes in the climatological background state. Chapter 5 showed that although a wide variety of climate perturbations can affect the equatorial Pacific, the equatorial structure of the response tends to be similar in each case. Due to strong coupled feedbacks like those active in ENSO, the Pacific climatology generally responds with either an El Niño-like warming (with a weakened zonal SST gradient, relaxed trades, relaxed currents, and a flatter thermocline) or a La Niña-like cooling (with a sharper zonal SST gradient, stronger trades, stronger currents, and a steeper thermocline slope).

This chapter therefore focuses primarily on the ENSO sensitivity to a single climate parameter, the strength of the equatorial zonal wind stress. Section 7.1 draws on the ideas of Chapter 6 to explain how the growth of small disturbances is affected by the strength of the climatological equatorial trades, and investigates the extent to which the ENSO sensitivity to other climate parameters resembles the sensitivity to trade wind strength. Section 7.2 then considers how a change in the equatorial trades affects the transient ENSO response to strong wind events, and extends the climate sensitivity map to stronger values of the air-sea coupling. Section 7.3 discusses the effects of climate changes in the stochastic context, focusing on ENSO predictability and the extent to which observed ENSO changes can be detected and attributed to climate changes. Section 7.4 concludes with a climate sensitivity analysis of a hybrid coupled GCM.

7.1 Small-amplitude regime

How is the linear behavior of ENSO affected by a change in climate? In this section, we examine the stability of the tropical Pacific climatology to small perturbations, in

the absence of stochastic excitation. The results in this linear regime will prove relevant not only to the growth of forecast errors, but also to the behavior of ENSO at realistic amplitudes.

7.1.1 Design of the experiments

To explore the sensitivity of a small-amplitude ENSO to climate changes, we perform a suite of experiments in the intermediate model. The plan is to impose a climate perturbation, spin up the model to its new climatology, kick the model with a transient disturbance and characterize the resulting variability. The initial background state of the anomaly model is prescribed from the control run climatology described in Section 4.2.4. For a prototype we consider first the effect of a change in the strength of the trade winds, by imposing an equatorial zonal stress perturbation of the form (5.1), which is constant in the zonal direction, and has a Gaussian shape in the meridional with a meridional halfwidth of $15°$ latitude and an equatorial maximum of $\widetilde{\tau_x^*}$.

The first task is to spin up the model onto its new attractor. Experience suggests that the adjustment to the attractor is most rapid when the climate perturbation is phased in gradually instead of all at once. Thus we linearly increase the amplitude of the climate perturbation from zero to the value of interest over a period of 20 years (Stage I), after which the perturbation parameter is held constant. To attenuate any further effects of the adjustment, the model is run for another 30 years (Stage II) prior to collecting data.

The next task is to characterize the attractor prior to the disturbance. The model trajectory is recorded for 10 years (Stage III). Over the range of trade wind strengths in this experiment, the attractor is generally found to be either a stable fixed point or a very weak limit cycle. (We have observed no evidence of multiple or strange attractors at the standard coupling, though we have not mounted a systematic search.) Thus the attractor appears to be well-characterized by its time-mean state.

The final task is to ping the model with a transient disturbance and characterize the response (Stage IV). At the beginning of year 60 the model is subjected to a slight weakening of the trade winds as in Section 4.3.1, with a peak stress perturbation amplitude of $\tilde{\tau}_x^* = 0.02$ dPa for 3 months on the equator at $165°$W. This perturbation is weak enough to keep the response fairly linear, but still strong enough to knock the trajectory far off of any weak limit cycle. The subsequent evolution of the model is recorded for 10 years, and the reference state from Stage III is subtracted to give a timeseries of anomalies. This brings the total model time required for each linear climate change experiment to 70 years.

Stages I–IV are then repeated at different values of the perturbation parameter, spanning the range of interest. For the prototype case this corresponds to 11 experiments with $\widetilde{\tau_x^*}$ running from -0.1 dPa to 0.1 dPa at intervals of 0.02 dPa. Altogether, the total model time required for the sensitivity map is 770 years.

7.1.2 Overview of the equatorial-trades prototype

Equatorial SST anomalies

How does the evolution of small disturbances depend on the strength $\widetilde{\tau_x^*}$ of the equatorial trades? Fig. 7.1 summarizes the response of SST anomalies to a small disturbance, for

different strengths of the climatological equatorial wind stress. The model SSTA generally evolves like a standing oscillation, though there is some westward propagation in the west and eastward propagation in the east. For strong mean trades (a), ENSO has a short period and the SST variability is focused near 140°W. In contrast, for weak mean trades (f), ENSO has a long period and is active farther east, with weak SST anomalies of opposite sign in the western Pacific. The ENSO mode is damped in nearly all of these regimes, but the damping rate varies with the trade wind strength: the oscillation is least damped when the trades are either very strong (a) or close to their normal strength (c), and are most damped when the trades are very weak (f) or only moderately strengthened (b).

Focusing on the first year after perturbation, it is evident that the short-term transients have a somewhat simpler dependence on the strength of the trades than do the modal properties. The initial warming is most intense when the trades are only slightly stronger than in the control (c), suggesting that the control run is nearly optimal for the initial growth of SSTA errors.

Heat budget phasors

What is responsible for these changes in ENSO behavior? The phasor diagrams in Fig. 7.1 show the relative roles of advection, surface heat fluxes, and mixing in the evolution of the SST anomalies. The phasor plots are derived as follows. At the longitude and time scale of peak equatorial SSTA variance, the differenced tendency terms are analyzed as a function of scale and time using a Morlet wavenumber-6 mother wavelet. The wavelet phase (relative to SSTA) and amplitude (relative surface heat flux) of each tendency term are computed, vector-averaged over the middle third of the timeseries, and then plotted together as a phasor in the diagram. The diagram reads like a clock, with the SSTA peak occurring at 3 o'clock: an arrow that points to the right is in phase with SSTA, and an arrow that points upward leads SSTA by 90°. The phasors are plotted in order of decreasing amplitude so that they do not hide each other. Processes with an amplitude less than 15% of the surface heat flux, i.e. inside the dotted circle, are not plotted but are accumulated in a residual phasor which is plotted only if it lies outside the dotted circle.

The phasors in the diagram are labeled in shorthand, with "m" denoting the background state of the control run (not the perturbed model climatology), and "p" denoting a perturbation from this background state. Thus changes in "uptm" $(-u'\partial_x\overline{T})$ isolate dynamical changes in the amplitude and phase of the zonal currents relative to SSTA, unconfounded by changes in mean SST. Similarly, "wmtp" $(-\overline{w}\partial_z T')$ isolates amplitude and phase changes in the anomalous vertical temperature structure, unconfounded by changes in mean upwelling. The additional effects of changes in the climatological fields, which result directly from the imposed zonal stress, are represented by terms such as "uptp" $(-u'\partial_x T')$. The total SSTA tendency ("tdot" or $\partial_t T$) is the vector sum of all of the individual tendency phasors.

Fig. 7.1 shows that the ENSO mechanism at the longitude of peak SSTA variability is greatly affected by a change in the strength of the trade winds. For the control case (d), the oscillation is almost entirely due to $-\overline{w}\partial_z T'$, which plays both destabilizing and transitioning roles. In this case the $-w'\partial_z\overline{T}$, $-\overline{v}\partial_y T'$, and $-u'\partial_x\overline{T}$ terms, while small, help to maintain the oscillation amplitude in the face of strong damping by the surface heat
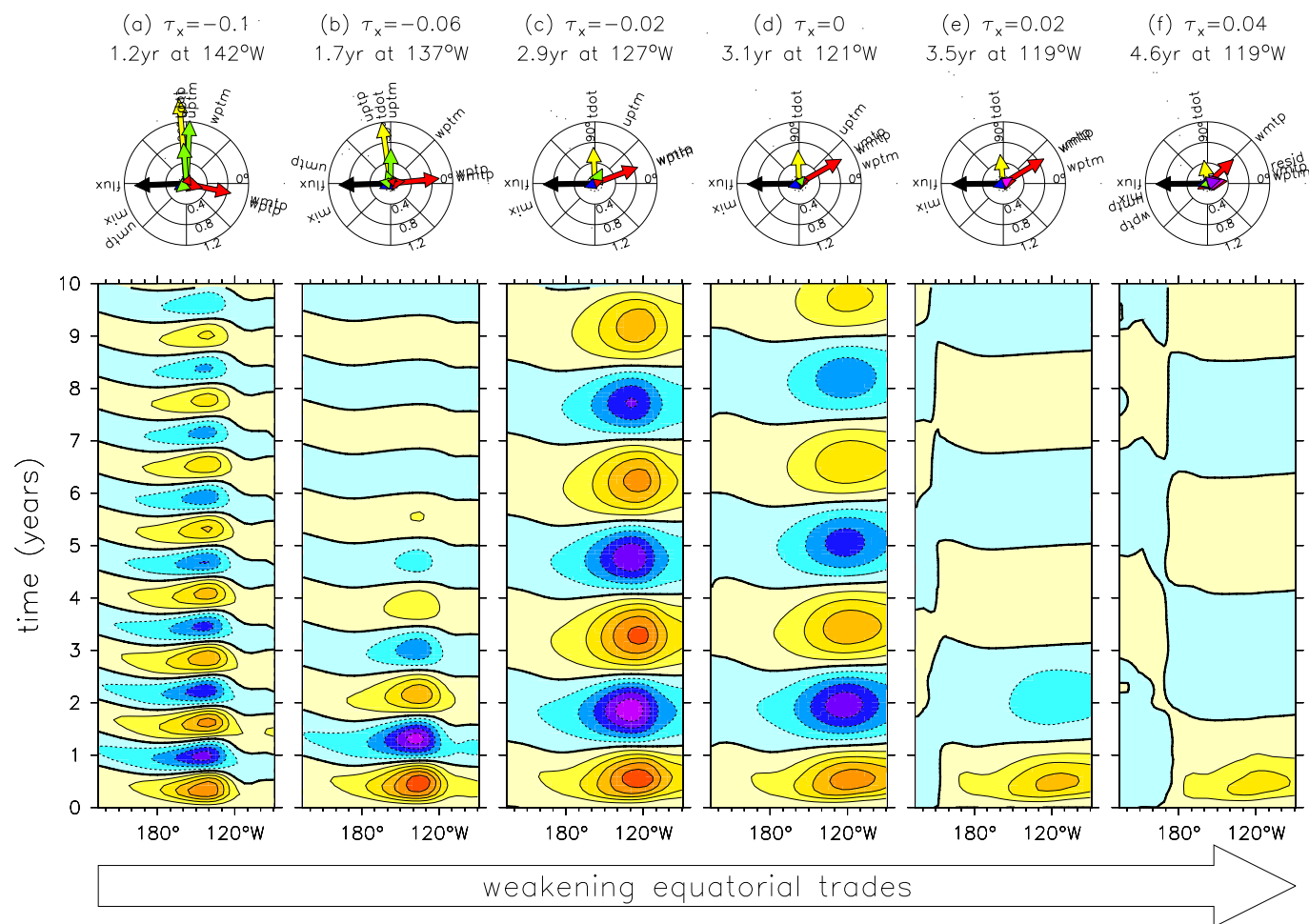
Figure 7.1: Change in ENSO due to a change in mean trade winds, as simulated by the noiseless intermediate model. Time-longitude plots (bottom row) show the equatorial (2°S–2°N) evolution of SST errors induced by a weak westerly wind burst in the central Pacific at the start of year 0. The errors are small (contour interval is 0.1°C) and so the dynamics are nearly linear. Labels at top indicate the amplitude of the imposed climate perturbation (trades weaken to the right), the oscillation period, and the longitude of peak variance. Phasors (middle row) show the amplitude (relative to surface heat flux) and phase lead (relative to local SSTA) of the temperature tendency terms in the equatorial band at the longitude of peak variance.

flux and weak dissipation by horizontal mixing.

As the trades strengthen, $-\overline{w}\partial_z T'$ comes more and more into phase with SSTA, eventually becoming a pure destabilizer. The destabilizing effect of $-\overline{w}\partial_z T'$ is also enhanced by stronger mean upwelling associated with the intensified trades. It is now *zonal* advection that plays the role of the "transitioner," the inertia that carries the system past the climatological equilibrium. The increased zonal advection is largely due to the strengthening of the equatorial zonal current anomalies, but there is also a contribution from the steeper $\partial_x \overline{T}$ which increases the SST sensitivity to the zonal currents.

As the trades weaken, on the other hand, the deepening of the climatological thermocline in the east and the reduction of in equatorial upwelling decrease the SST sensitivity to thermocline motions. This weakening of $-\overline{w}\partial_z T'$ leads to an increase in both the oscillation period and the damping rate of ENSO. The growth effect of this term is further weakened by the increase in the phase lead of $-\overline{w}\partial_z T'$ ahead of SSTA. For very weak trades, equatorial upwelling in the east disappears. At this point, the only thermal connection between surface and subsurface is south of the equator, associated with upwelling induced by the cross-equatorial southerlies. This meridional asymmetry leads to an increased role for meridional advection as a destabilizing term at the equator. The $-w'\partial_z \overline{T}$ term also enters as a destabilizer, as the eastward shift of the statistical stress response brings stronger upwelling variations into the east Pacific region of strong $\partial_z \overline{T}$.

Linear evolution of forecast errors

Given these results, what can we say about how small errors might evolve in a forecast situation? Fig. 7.1 can be interpreted in terms of the evolution of small SST forecast errors, arising from an unanticipated westerly wind burst in the western Pacific. For weak stochastic forcing, a succession of easterly and westerly bursts would result in a linear superposition of the responses shown in Fig. 7.1.

On the basis of this figure one can then say several things about predictability in the linear context. First, errors will tend to grow more rapidly (during the first 1–3 months after the disturbance) when the climatological trades are strong than when they are weak. Second, the saturated error is likely to be greatest when the trades are just slightly stronger than in the control run, since this case has both the strongest peak error value (which occurs around month 7) and also the strongest sustained error amplitude; interestingly, empirical analysis of *observed* SSTAs (Penland and Sardeshmukh, 1995) suggests that the maximum error growth due to modal interference does indeed tend to peak at around 7 months lead. Third, the errors will tend to lie farther west when the climatological trades are strong than when they are weak. And finally, for episodic stochastic forcing, one can expect a "return of predictability" a year or so after a large wind burst, as the SSTA error crosses zero. The return time is simply half the oscillation period, and so increases as the climatological trades weaken.

7.1.3 Evolution of the equatorial vertical structure

What is going on below the surface to cause these changes in the mechanism and behavior of ENSO? In this section we examine vertical slices of the simulated equatorial

fields along the equator. This reveals how changes in the vertical thermal structure of the ocean, and in the zonal phasing of the stress anomalies, have a large impact on the oscillation amplitude and period.

Control run

Fig. 7.2 shows equatorial snapshots from the small-amplitude control run. The imposed westerly stress disturbance weakens equatorial upwelling and generates eastward equatorial current anomalies, associated with an eastward-moving equatorial Kelvin wave and a westward-moving off-equatorial Rossby wave pair. As the Kelvin wave propagates into the eastern Pacific, it deepens the local thermocline and induces a subsurface warming in the east. The mean upwelling $\overline{w}$ then conveys the subsurface signal into the mixed layer, especially in the central Pacific were $\overline{w}$ is strongest. The downwelling anomalies in the central Pacific contribute to the SST increase as less cold water is advected into the mixed layer. The result is a surface warming that is shifted $\sim 20°$ west of the subsurface warming. The SST increase then gives rise to westerly stress anomalies, which peak $\sim 50°$ west of the SSTA. These stress anomalies, in turn, further weaken the equatorial upwelling, strengthen the eastward currents, and enhance the deepening of the thermocline in the east to complete the feedback cycle and plunge the system into a warm event.

Note that as the El Niño is developing, the thermocline is gradually shoaling in the off-equatorial western Pacific. This shoaling is achieved by upwelling long Rossby wave signals, which radiate westward from the region of strong cyclonic curl on the poleward flanks of the westerly stress anomalies in the central basin. The discharge of heat content from the western off-equatorial Pacific gradually drains the equatorial band of heat content as well, as short Rossby waves convey mass poleward along the western boundary and induce upwelling Kelvin wave signals at the equator. The shoaling of the equatorial thermocline erodes the surface warming, which peaks about 7 months after perturbation. Following the peak, mass continues to drain out of the equatorial band, until the surface temperature, winds, and thermocline slope return to normal around month 14.

The system, however, is still out of balance. Note that at this point (1) the equatorial thermocline is everywhere shallower than normal, (2) the surface currents are westward all along the equator, and (3) the draining of heat content out of the equatorial band continues, due to the anomalously shallow thermocline in the off-equatorial western Pacific. Because the climatological thermocline is shallower in the east, the overall shoaling of the thermocline induces a greater cooling of T_e in the east than in the west. Entrainment on the zonally-asymmetric $\partial_z T'$ then generates an anomalous westward SST gradient, which produces easterly stress anomalies that further enhance the equatorial cooling.

The key point is that slow equatorial recharge/discharge processes, which produce a phase lead of the thermocline depth ahead of SSTA in the east Pacific, are central to the oscillation in the control case. Also important are the zonal current anomalies, which reverse in the central basin even before the winds disappear. By month 13, for example, easterly currents have developed at the equator despite the continued presence of westerly stress. These westward currents act on the climatological westward SST gradient to produce a cooling tendency in the central Pacific, which hastens the demise of the warm event.

Together, these factors cause the system to overshoot the climate equilibrium and sow

Control case: linear response
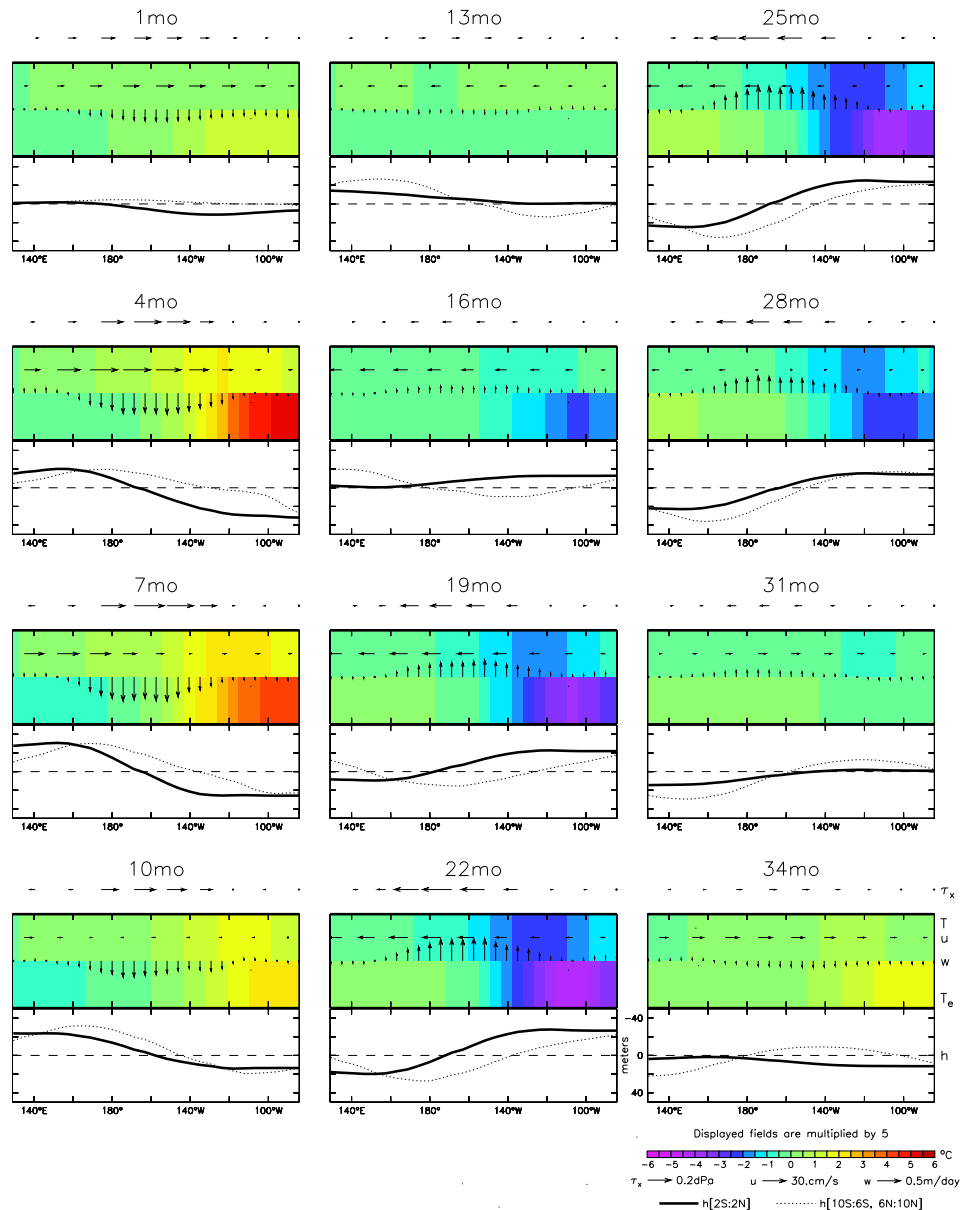
Figure 7.2: Equatorial snapshots at three-month intervals from the small-amplitude control case. Time flows down each column then left to right, and is indicated above each panel in terms of months since a weak westerly stress perturbation was imposed. Bottom right panel gives contour/vector keys for all panels. Vectors indicate anomalies of (top to bottom) zonal surface stress, mixed layer zonal current, and upwelling velocity at the mixed layer base. Shading indicates the anomalous temperature in the well-mixed surface layer (top) and at 50 m depth (bottom). Bottom subpanel shows the thermocline depth anomaly (ordinate reversed), at the equator (2°S–2°N, solid) and off-equator (6–10° N/S, dotted).

the seeds of a cold event, which develops rapidly as easterly winds amplify the thermocline slope, upwelling and easterly currents along the equator. Because the easterly winds are associated with anticyclonic curl off-equator, the western Pacific thermocline gradually deepens via downwelling Rossby signals and their reflection into downwelling Kelvin signals. By month 25 the western Pacific is recharged of heat content, and as this mass begins streaming into the equatorial band along the western boundary, the cold event reaches its peak. By month 34, the system has come full cycle and is poised to begin another El Niño.

In the off-equatorial thermocline, one can see a series of bumps and dips moving slowly westward with a wavelength slightly greater than the width of the Pacific, and a speed of roughly 0.25 m s^{-1}. One might be tempted to infer that coupled Rossby waves were somehow propagating coherently from the eastern to the western boundary, triggering equatorial changes by reflecting as Kelvin waves. As pointed out by Battisti (1989), however, the off-equatorial signal is more the *product* of the equatorial events than the cause of them. In particular, note that the amplitude of the off-equatorial anomaly weakens markedly as it moves into the central basin (during the transitions between ENSO events), and then strengthens again as it approaches the western boundary (as an ENSO event reaches its peak). The off-equatorial western Pacific thermocline signal arises more from ENSO-associated wind curl in the western/central basin than from coupled Rossby signals propagating in from the east. Rather than thinking of the ENSO period in the control run as being related to the time required for off-equatorial thermocline depth anomalies to propagate from the eastern boundary to the western boundary, it is better to think of the period as being set by the time required for the off-equatorial signal in the west (which is generated directly by ENSO stress curl) to reverse the equatorial zonal currents, erode the equatorial zonal-mean thermocline depth, and thereby feed back on the equatorial SST and off-equatorial stress curl.

Case with strong mean trades

How does a strengthening of the climatological trades alter this picture? Fig. 7.3 shows equatorial snapshots from the strong-trades case. As described in Section 7.1.2, the variability in this case has a shorter period and is shifted farther west than in the control run. One key difference in the structure of this mode is that despite substantial thermocline variability in the eastern Pacific, Fig. 7.2 indicates very little change in entrainment temperature along the South American coast. This is because the climatological thermocline is so shallow in the east that T_e is relatively insensitive to variations in h (see Fig. 4.7). In the real world, a desensitizing effect like this could arise due to a shoaling of the mixed layer depth as thermocline approaches the surface.

Such a change in the subsurface anomaly structure has a profound effect on the simulated ENSO. During the initial warming in the central basin, the separation of the SST anomalies from the coast gives rise to easterly stress anomalies in the far eastern Pacific. These easterlies generate anomalous upwelling, which acts on the strong $\partial_z T$ in the east and to further suppress warming there. As a result, there is hardly any warming in the east despite the anomalously deep thermocline. This opens the door for even stronger easterly stress anomalies in the east, and since the easterlies and associated upwelling are displaced slightly westward of the cold peak, they act to propagate the cold SSTA westward. By
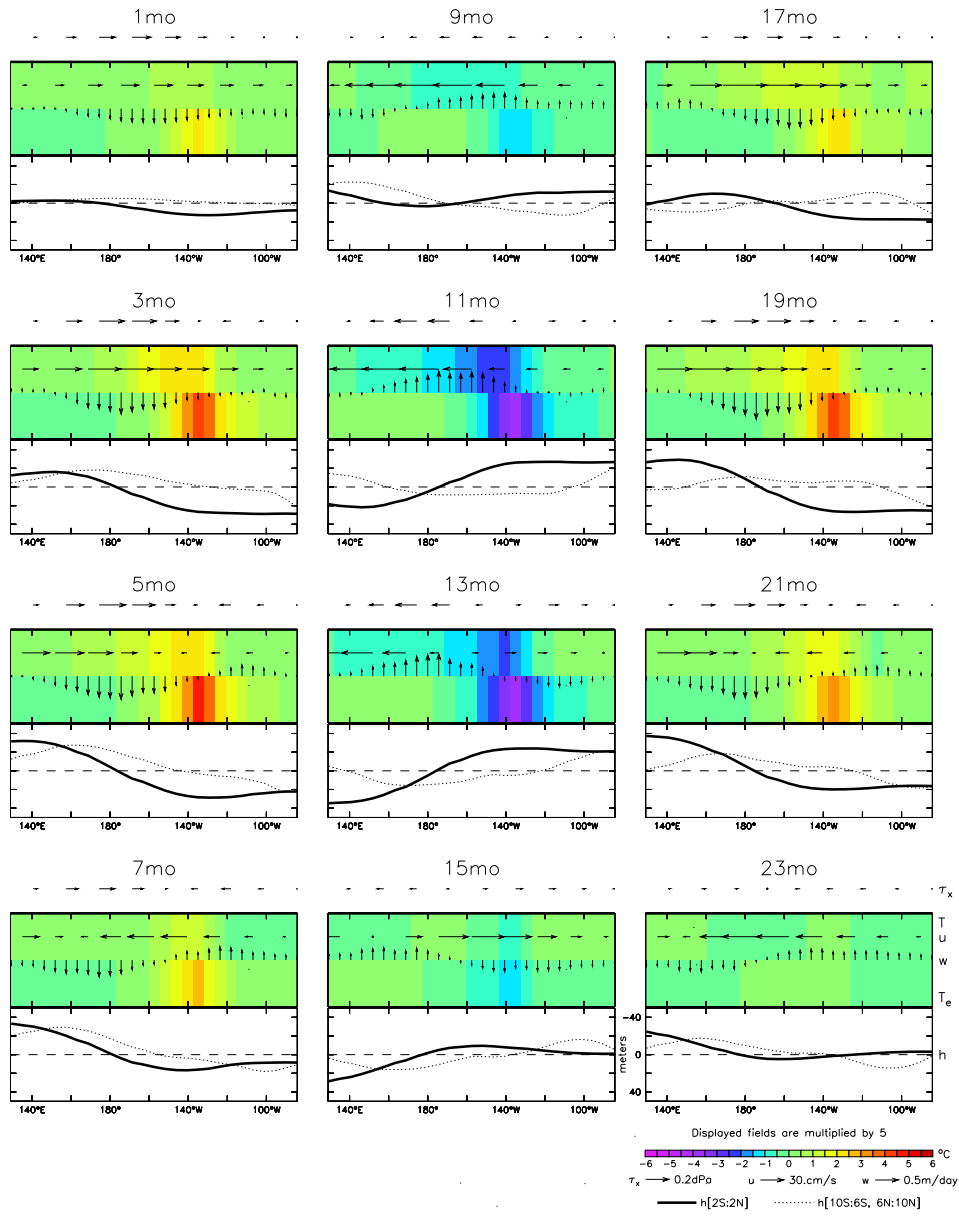
Figure 7.3: Equatorial snapshots at two-month intervals from the small-amplitude case with strengthened trades ($\widetilde{\tau_x^*} = -0.1$ dPa). Otherwise as in Fig. 7.2.

month 9, the easterlies have propagated into the central Pacific to displace the westerly anomalies that had prevailed there, and the cycle then repeats with the opposite sign.

The model ENSO in this case thus resembles the so-called "SST mode," of the type described by Neelin (1991). The propagation of this mode depends on a competition between zonal/vertical advection by the anomalous currents, and vertical advection by mean upwelling acting on the anomalous thermocline. During the first few months after perturbation, the westerly current anomalies in the central Pacific are displaced to the west of the westerly stress anomalies, which are themselves displaced to the west of the surface warming. Since the zonal advective warming is displaced west of the SSTA, it tends to induce westward propagation of the modal structure. This propagation however, is opposed by upwelling on the anomalously deep thermocline, which induces a surface warming far to the east of westerly stress anomalies. Near 140°W, where $\partial_h T_e$ reaches its maximum, both processes are important and the SSTA does not propagate. Only where the thermocline effect is weak, such as in the western Pacific where the thermocline is very deep, and in the far eastern Pacific where T_e saturates, is westward propagation evident.

The meridional structure of the thermocline in this case undulates in a manner very similar to the control run, with warm water flowing off-equator during warm events and onto the equator during cold events. In contrast to the control run, however, these thermocline motions have a relatively small effect on the evolution of surface temperatures compared to zonal advection. The La Niña-like mean state, with its strong $\partial_x T$ in the central Pacific and saturated T_e in the eastern Pacific, naturally favors the zonal advective effect over the thermocline effect, and zonally-propagating mechanisms over meridional recharge/discharge mechanisms.

The amplitude of the oscillation is maintained by entrainment on in-phase thermocline depth anomalies near 140°W, which amplify SSTA near the peak of each cycle. The seed for localized feedbacks is planted by the development of SSTAs in the eastern Pacific which are of opposite sign to those in the central Pacific. The east Pacific SSTAs are induced by an atmospheric bridge, which generates upwelling anomalies that act on the strong $\partial_z T$ in the east. Rossby wave signals emanating from the eastern boundary, which are enhanced by the early wind reversal in the east, provide the delayed negative feedback essential for oscillation. The Rossby signals induce a strong westward-propagating reversal of the equatorial zonal current anomalies, which then act on the strong $\partial_x T$ to transition the system between warm and cold events. Because the timescale in this case is set by a resonant interaction involving zonal advection and eastern boundary reflections, it depends fundamentally on the speed of coupled Rossby waves.

Case with weak mean trades

What is the effect of a *weakening* of the climatological trades? Fig. 7.4 shows equatorial snapshots from the weak-trades case. In this case the westerly stress disturbance induces only a slight warming of the surface in the east. The climatological thermocline is so deep in the eastern Pacific that T_e is relatively insensitive to motions of the thermocline, and $\partial_x \overline{T}$ and $\partial_z \overline{T}$ are weakened so that zonal current and upwelling anomalies have less of an effect on SST. Thus the equatorial positive feedbacks are weak and the oscillation is rapidly damped. The off-equatorial Rossby signals, which are induced entirely by the coupled wind
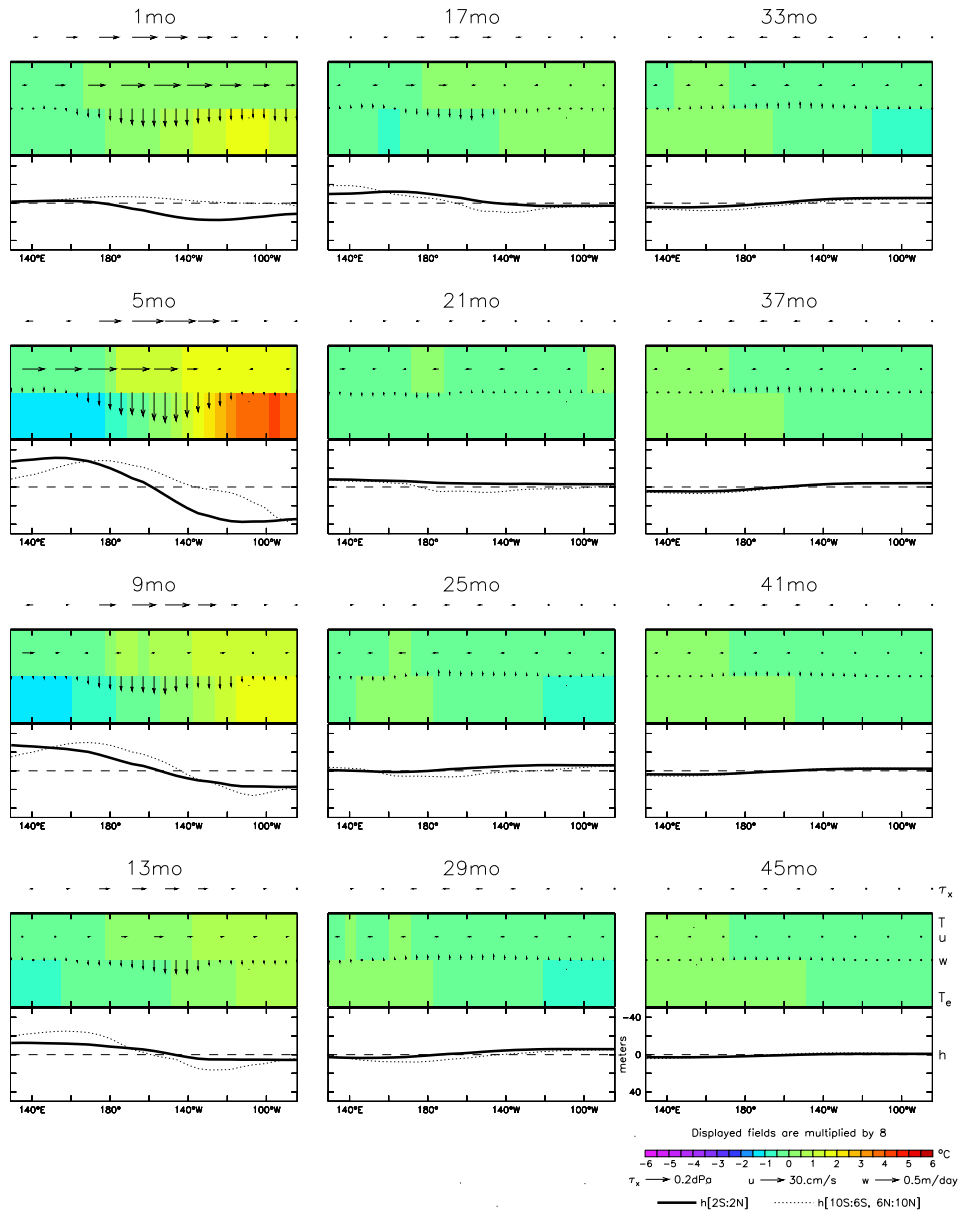
Figure 7.4: Equatorial snapshots at four-month intervals from the small-amplitude case with weakened trades ($\widetilde{\tau^*_x} = 0.04$ dPa). Otherwise as in Fig. 7.2.

stress, are generated farther east than in the control run and so take longer to reach the western boundary and reflect as Kelvin signals. The delayed negative feedback is therefore more attenuated by dissipation, and so takes longer to overcome the direct feedbacks in the eastern Pacific. This increased turnaround time is then reflected in an increased oscillation period.

Comparison of the transient responses

Given a transient disturbance, how quickly do the differences among these cases become apparent in the response? Fig. 7.5 shows simultaneous equatorial snapshots for the three cases during the first few months after perturbation. After only one month, the on- and off-equatorial thermocline looks nearly identical among the three cases—but significant differences are apparent in the entrainment temperature, with the warming of T_e strongest and farthest west in the strong-trades case, and weakest in the weak-trades case. By month 2, the strong-trades case shows the most rapid warming of SST, due to the stronger T_e anomalies at 140°W and the stronger effect of zonal advection acting on an enhanced $\overline{T}_x$. The weak-trades case, on the other hand, shows very little SST warming at month 2.

By month 3, it is possible to discern differences in the strengths of the equatorial zonal current and upwelling anomalies, which are strongest in the strong-trades case. One can also see differences in the equatorial wind stress response, with easterly anomalies forming over the east Pacific in the strong-trades case, while the other two cases show almost no stress anomalies in the east.

At month 4, there are clear differences in the thermocline structures for the west Pacific, where the strong-trades case shows a greater shoaling both on- and off-equator. By month 5, as this shoaling continues to affect the equatorial thermocline, the strong-trades case begins to show westward current anomalies developing in the east Pacific, while the other two cases continue to show little or no zonal current anomalies in the east. The zonal displacements of the stress responses are also clear at month 5, with the westerly stress anomalies (and associated upwelling, zonal currents, and zonal thermocline slope) farthest west in the strong-trades case and farthest east in the weak-trades case.

7.1.4 Change in the mixed layer heat budget

Which of the structural changes noted in the last section are *quantitatively* most relevant to the changes in ENSO? Fig. 7.6 shows the mixed layer heat budget along the equator for each of the three cases. This figure tracks changes at *fixed* locations, complementing the diagrams of Fig. 7.1 which followed the shifting position of peak SSTA variance. The middle row of Fig. 7.6, which corresponds to the control case, is essentially a rescaled version of Fig. 4.21 for reference. As the climate is altered, one can see substantial changes in the ENSO mechanism all along the equator.

110°W

In the far eastern Pacific, where the climatological thermocline is shallowest, the heat budget in the control run is quite simple. It consists essentially of two terms: $-\overline{w}\partial_z T'$ and
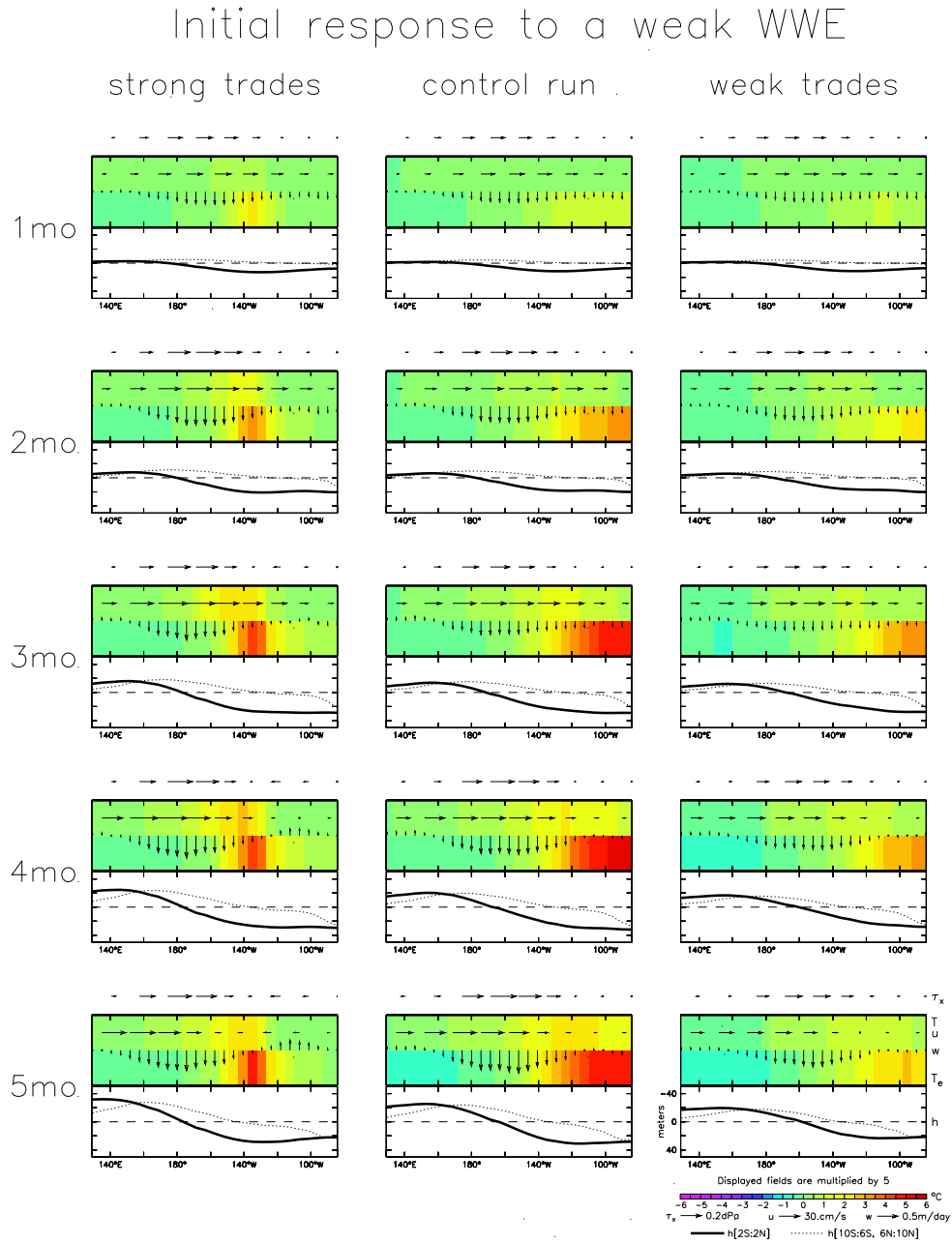
Figure 7.5: Comparison of the small-amplitude cases of Figs. 7.2–7.4, soon after the initial perturbation. Time flows down each column as a sequence of monthly snapshots, and all snapshots have the same scale (indicated in the bottom-right panel). Left column is the case with strengthened trades ($\widetilde{\tau_x^*} = -0.1$ dPa), center column is the control case, right column is the case with weakened trades ($\widetilde{\tau_x^*} = 0.04$ dPa).
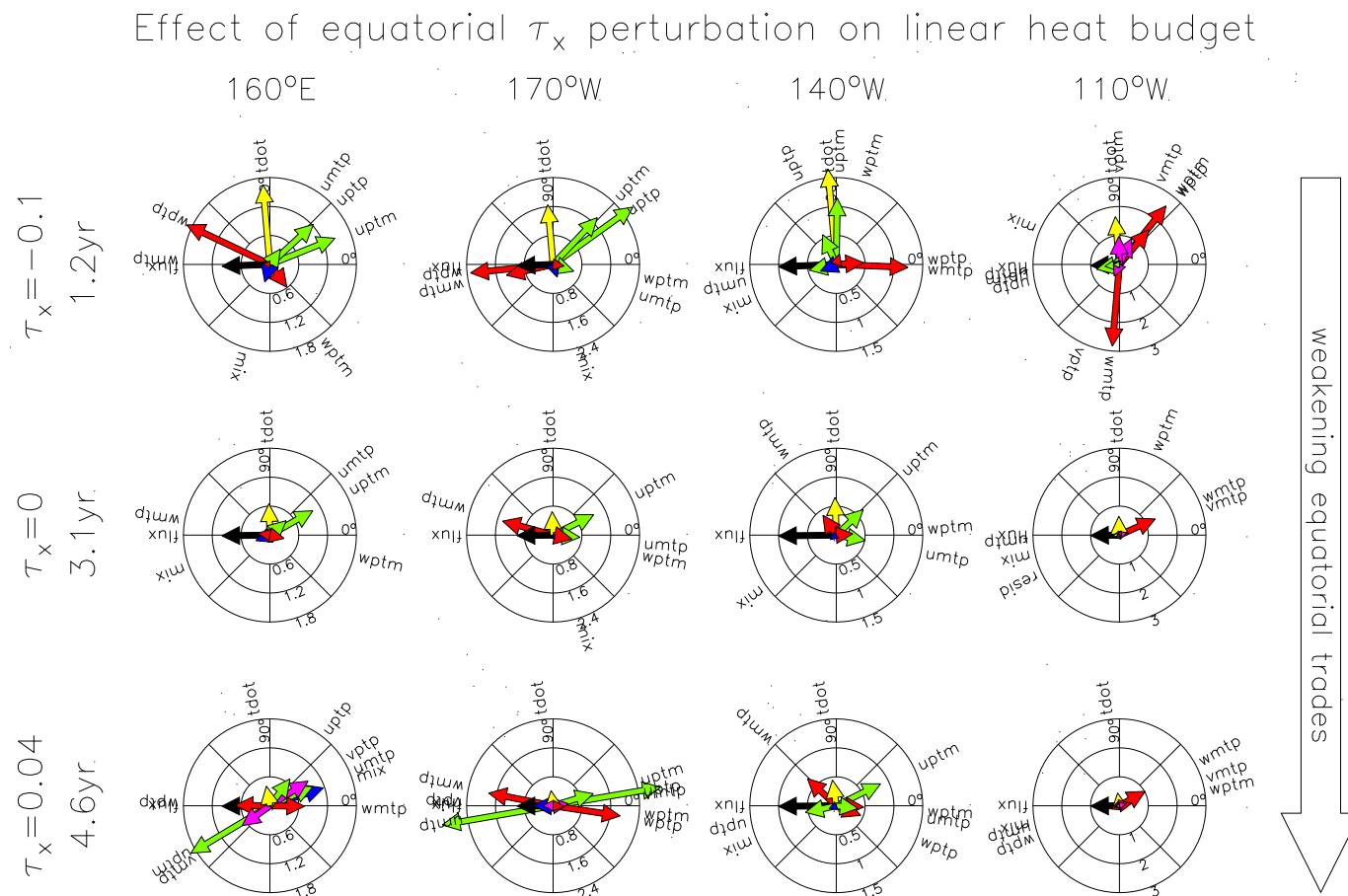
Figure 7.6: Comparison of equatorial mixed layer heat budget phasors for the small-amplitude cases of Figs. 7.2–7.4. The phasor diagrams are as described in Fig. 7.1 and Section 7.1.2. Middle row is the control case, top row is the case with strengthened trades ($\widetilde{\tau_x^*} = -0.1$ dPa), bottom row is the case with weakened trades ($\widetilde{\tau_x^*} = 0.04$ dPa). Each column corresponds to a given longitude, progressing from west on the left to east on the right. Diagrams at the same location, i.e. within a given column, have the same scale.

the surface heat flux. The $-\overline{w}\partial_z T'$ term leads local SSTA slightly, and is thus responsible for the oscillatory tendency in the east. There are only small contributions from $-\overline{u}\partial_x T'$ and $-\overline{v}\partial_y T'$, which stabilize and destabilize the oscillation, respectively.

For weakened climatological trades, the heat budget at 110°W remains quite simple, but there are important differences from the control case. The $-\overline{w}\partial_z T'$ term is relatively weaker than in the control run, due to the reduced $\partial_h T_e$ as a result of the deepened mean thermocline in the east. Because $-\overline{w}\partial_z T'$ is the dominant transitioning and growth mechanism, its reduced amplitude relative to surface flux results in a longer period and a greater damping rate for the oscillations. There is also a larger role for $-w'\partial_z \overline{T}$, since the equatorial zonal stress anomalies are displaced farther east than in the control run. This term is destabilizing, but has little effect on the oscillation period since it is nearly in phase with SSTA. Finally, the $-w'\partial_z T'$ term, which represents effects of reduced mean upwelling and $\partial_z T$, acts to further stabilize the oscillations and increase their period.

For strengthened climatological trades, the heat budget in the east is entirely different. Thermocline depth anomalies now *lag* local SSTA by a quarter cycle, and their effect on SSTA through $-\overline{w}\partial_z T'$ is much stronger relative to the surface flux than in the control run. The large anti-transitioning effect of this term, however, is more than compensated by changes in the meridional Ekman overturning circulation. Strong upwelling anomalies, induced by SSTAs farther west and acting on an enhanced $\partial_z \overline{T}$, overwhelm the effects of the thermocline depth variations to control the evolution of SSTA in the east. The transition between events is hastened by meridional advection, as warming south of the equator and weakening of the cross-equatorial currents occur a quarter-cycle ahead of the equatorial warming. Zonal advection plays a damping role at 110°W, which is as strong as the surface heat flux. The heat budget at this location is thus truly three-dimensional, and involves a very active set of competing processes which, amazingly, nearly balance and produce little net change in SSTA.

140°W

The heat budget at 140°W is generally more complex than at 110°W. In the control run, SST anomalies at 140°W are generated primarily by zonal advection, as eastward current anomalies appear prior to warm events and as SST changes farther east are advected westward by the climatological currents. The $-w'\partial_z \overline{T}$ term, an important destabilizer that is in phase with SSTA, becomes more active as one approaches the peak trade wind activity in the central Pacific. The $-\overline{w}\partial_z T'$ term plays more of a damping role at 140°W, as the SST changes induced by zonal advection have a larger effect on $\partial_z T$ than the subsurface changes induced by local movements of the deep thermocline. The thermocline motions do, however, induce a phase lag in the damping so that $-\overline{w}\partial_z T'$ remains important to the oscillation frequency.

In the weak-trades case, the zonal current variations at 140°W are stronger for a given SSTA than in the control case, due to the eastward shift of the wind response. These current anomalies, however, are much less effective at inducing SST anomalies, because of the weakening of $\partial_x \overline{T}$. The damping effect of $-\overline{w}\partial_z T'$ is also reduced by the weaker mean upwelling. The $-w'\partial_z \overline{T}$ term, on the other hand, plays a larger role due to the eastward shift of the wind variability.

In the strong-trades case, there is a very interesting budget at 140°W with clearly different roles for zonal and vertical advection. The anomalous zonal currents are in quadrature with local SSTA, so that $-u'\partial_x\overline{T}$ plays a purely transitioning role. The thermocline depth, on the other hand, is in phase with local SSTA and thus $-\overline{w}\partial_z T'$ plays a purely destabilizing role. One can think of $-u'\partial_x\overline{T}$ as the "inertia" for this oscillation and $-\overline{w}\partial_z T'$ as the power source: the oscillation passes through the zero-anomaly point due to the disequilibrium zonal currents, and then receives a boost due to advection on the anomalous thermocline at the event peak. The effects of these terms are further enhanced by the strong zonal SST gradient and strong equatorial upwelling in the strong-trades case, leading to a high-frequency, energetic oscillation at 140°W. The instability is largely balanced by the damping effect of incoming advection from farther east, where the SST anomalies are not as strong, and by the horizontal entrainment of off-equatorial waters by high-frequency eddies (here parameterized as horizontal diffusion).

170°W

At 170°W, near the peak of zonal stress variability, the control run shows even stronger roles for $-u'\partial_x\overline{T}$ and $-w'\partial_z\overline{T}$ which act to destabilize the oscillation. The damping effect of $-\overline{w}\partial_z T'$ is also stronger, because at this location (1) the thermocline depth hardly varies, and (2) $\partial_h T_e$ is weak because the climatological thermocline is deep. Thus the SSTA tends to dominate $\partial_z T'$, and the damping by $-\overline{w}\partial_z T'$ surpasses even the surface heat flux. The finite adjustment time of the active layer to the stress is again essential to the oscillation, as it induces a slight lead of the $-u'\partial_x\overline{T}$ term ahead of SSTA, and a lag of the $-\overline{w}\partial_z T'$ damping behind SSTA.

In the weak-trades case, the climatological thermocline flattens and the ENSO patterns shift eastward. In this case, the node in thermocline variability lies slightly *east* of 170°W, so the local thermocline is actually *elevated* when SST is warmer than normal. As this produces a strong $\partial_z T$ during warm events, one might expect mean upwelling to provide a strong damping for SSTA. This damping cannot materialize, however, because there is no mean upwelling at 170°W in the weak-trades case. A similar situation holds for zonal advection: although strong SST anomalies develop to the east, these cannot much affect 170°W due to the weakening of the mean zonal currents at that location. The zonal current anomalies do play an important destabilizing and transitioning role at 170°W but their effect is likewise attenuated by the reduction of the mean zonal temperature gradient. Anomalous upwelling plays a destabilizing role due to the proximity of the tradewind variability and the strengthening of $\partial_z\overline{T}$ at 170°W.

In the strong-trades case, the generation of SSTAs at 170°W is mostly due to zonal advection by anomalous currents, which act on an enhanced $\partial_x\overline{T}$. In contrast to the heat budget at 140°W, the $-u'\partial_x\overline{T}$ and $-u'\partial_x T'$ terms at 170°W lead local SSTA by substantially less than 90° phase, and therefore play destabilizing as well as transitioning roles. The SST anomalies generated by zonal advection are strongly damped by vertical advection, because in the strong-trades case (1) the mean upwelling is enhanced, (2) there is very little thermocline variability at 170°W, and (3) $\partial_h T_e$ is weak due to the deepened mean thermocline at 170°W.

160°E

In the far western Pacific, SST anomalies in the control run develop mostly due to zonal advection. The zonal current and SST gradient are weakest just prior to warm events, so that less and warmer water is advected in from the cold tongue. Anomalous upwelling also plays a small role as a destabilizer, due to the proximity of the tradewind variability. The SST changes induced by these processes are then damped by surface heat fluxes, horizontal mixing, and mean upwelling.

The weak-trades case is special, because SSTA in the west Pacific is out of phase with that in the eastern and central Pacific. Thus at 160°E, a local *warming* occurs during a La Niña event. Vertical advection cannot play any direct role at 160°E, because there is no net upwelling to convey T_e variations to the surface. The meridional currents are also weak in this case, and so cannot much affect the equatorial temperature despite the reasonably strong meridional temperature gradients that develop. The net effect of zonal advection is also weakened due to the lack of strong temperature gradients. As a result, there is very little SSTA variability at 160°E. The SSTAs that *do* develop are mostly transported in by the mean zonal currents and horizontal mixing from farther east, where weak upwelling generates warm anomalies during La Niña, as the thermocline deepens in the west.

The strong-trades case at 160°E is dynamically more interesting. Here the warm anomalies are generated by zonal advection on the strong $\partial_x T$, amplified by strong zonal current anomalies associated with the resonant coupled Rossby wave. In contrast to the control run, there is now mean easterly stress and upwelling at 160°E. The water is entrained into the mixed layer from below remains relatively unperturbed due to the deep climatological thermocline, and thus has mainly a damping effect on local SSTA. Following the peak warming there is a slight reduction in upwelling which opposes the transition to the cold event, but this is more than compensated by the slight phase lag of the T_e cooling behind the local surface warming, which hastens the transition.

Discussion

There are several key points to take from Fig. 7.6. The mixed layer heat budget in the intermediate model is complex, with significant contributions from surface fluxes, vertical advection, and zonal advection, and even meridional advection and mixing at various points along the equator. This complexity may provide a clue as to how ENSO can behave so differently in different models. As the total SSTA tendency is a small residual of many large tendency terms, a relatively small change in any given term can have a significant impact on the oscillation amplitude and period. In particular, the surface heat flux, which tends to be heavily parameterized in the current generation of climate models, appears to be a first-order term in the ENSO heat budget nearly everywhere along the equator.

What maintains the ENSO amplitude? The power source for the oscillation, ultimately, is the sun, which heats the ocean surface. The warm ocean then warms and moistens the overlying atmospheric boundary layer. Differential heating of the atmospheric boundary layer produces horizontal pressure gradients at the surface, which contributes to the generation of surface winds. The moist air also represents a vast reservoir of latent heat, which is

gathered up by the circulation, focused into convective regions, and tapped upon condensation of water vapor into cloud droplets. The differential heating of atmospheric columns above the boundary layer contributes to the horizontal pressure gradients at the surface, driving additional winds which then affect the oceanic thermocline, currents, and surface temperature. The statistical atmosphere parameterizes the variations in the strengths and locations of boundary layer heating and convective heating into a simple relationship between the SST and wind stress anomalies, whereby warm anomalies in the east generate westerly stress anomalies over the central Pacific. The ENSO *amplitude* is then maintained by a positive feedback cycle, whereby deepening of the thermocline in the east acts through climatological Ekman overturning to warm the surface, which induces westerly stress anomalies that further deepen the thermocline in the east. One can think of ENSO as self-regulating the conversion of thermal and latent energy (provided by the sun) into the mechanical work and available potential energy fluctuations associated with the oscillation.

What sets the ENSO period? Ocean-atmosphere feedbacks provide not only an essential power boost, but also off-equatorial wind stress curl that pumps water between the equator and off-equator to facilitate the transitions between events. The continents are also important, as they reflect wave signals back and forth across the basin; when local feedbacks dominate, as in the case with strong trades, basin resonance of coupled Rossby waves can be essential to the ENSO period. Advection by the anomalous equatorial zonal currents $(-u'\partial_x\overline{T})$, which is associated with the meridional curvature of the equatorial thermocline and the propagation of equatorial waves, appears to be a key mechanism in the transitions between warm and cold events, and is largely what sets the oscillation period. The related slow adjustment of the zonal-mean thermocline depth, which is associated with the equatorial recharge/discharge of heat content, is also important in the transition, as it tends to produce a phase lead of vertical advection $(-\overline{w}\partial_z T')$ ahead of SST anomalies in the east Pacific.

The heat budget in the weak-trades case closely mirrors that of the control run in the eastern Pacific, although important differences are apparent in the western/central Pacific. The weakening of the zonal SST gradient in this case reduces the transitioning role of zonal advection, which leads to a decrease in the oscillation frequency. Deepening of the thermocline in the east Pacific, furthermore, reduces the destabilizing role of vertical advection, which leads to stronger damping of the oscillation and also shifts the position of maximum variability eastward where the entrainment temperature is most sensitive to thermocline depth.

In the strong-trades case, on the other hand, the strengthening of the zonal SST gradient enhances the transitioning role of zonal advection. This leads to an increase in the oscillation frequency, and the saturation of the entrainment temperature in the eastern Pacific shifts the peak variability into the central Pacific. The short period of this mode is nearly resonant with coupled Rossby waves, and so one can see westward propagation of SST anomalies in the eastern and western Pacific.

One interesting observation from Fig. 7.6 is that climate changes affect not only the *magnitude* of the tendency terms, but also their *phase* relative to local SSTA, which alters their roles in the oscillation. The role of $-u'\partial_x\overline{T}$ at 140°W, for example, goes from destabilizing to transitioning as the trades strengthen. This then affects the sensitivity to

further climate changes. For weak trades, changes in $\partial_x \overline{T}$ alone will have little effect on the oscillation frequency, since in this case it is the thermocline variations (not the zonal currents) that bring about the transition. For strong trades, on the other hand, the zonal current variations are the key transition mechanism and changes in $\partial_x \overline{T}$ can have a major effect on the oscillation frequency.

The heat budget phasors can also yield useful information on *what* and *where* to observe the real ocean and atmosphere in order to improve modeling and forecasting of ENSO. If the SSTA evolution at a given location is most strongly dependent on $-u'\partial_x \overline{T}$ for the transition, then by monitoring the anomalous zonal currents at that location (either directly or through a proxy like sea level) one can effectively anticipate changes in SST. And if SSTA *growth* is found to depend strongly on $-\overline{w}\partial_z T'$, one may be able to identify weak-upwelling conditions with conditions of high predictability. The climate sensitivity experiments also indicate that the ENSO observing system and modeling requirements may change if the climate changes.

Finally, the phasor diagrams are an excellent diagnostic for comparing numerical models to each other and to observational analyses, and for identifying parts of a simulation that require improvement for more realistic ENSO variability. Although different models may have similar-looking ENSOs when one looks only at equatorial SST, they may have very different mechanisms and therefore different sensitivities to climate change. Phasor diagrams of the mixed layer heat budget are one way to verify that a model is simulating the "right" kind of ENSO for the right reasons.

7.1.5 Responses to other climate perturbations

Having examined the prototype tradewind-strength case in detail, we next ask: To what extent does this prototype mirror the effects of other climate perturbations? Fig. 7.7 summarizes the effects on ENSO of all the perturbations discussed in Chapter 5. Panel (a) corresponds to the imposed zonally-uniform change in the strength of the equatorial trades that we have examined so far: as the trades weaken, the oscillation period increases and the variability shifts eastward, consistent with the analysis of Section 7.1. The amplitude is greatest when the trades are very strong or near-normal, and weakest when the trades are weak or only moderately strengthened.

Radiative forcing

Panel (b) shows the ENSO response to an imposed basinwide change in the surface heat flux. Chapter 5 showed that since the climate response to uniform heating produces a strengthening of the zonal SST gradient and associated zonal stress, the resultant climate change is very similar to that for an imposed change in the strength of the equatorial trades. Panel (b) indicates that the ENSO change is similar as well. With increasing heating, the climatological trades weaken, the ENSO period lengthens and the SST variability shifts eastward. There are two active regimes associated with the zonal-advective mode (for strong heating) and the vertical-advective mode (for weak heating), and two inactive regimes (for cooling or for moderate heating). The ENSO-mapping between (a) and (b) is similar to the climate-mapping between Figs. 5.6 and 5.13, with a 10 Watt m^{-2} heating
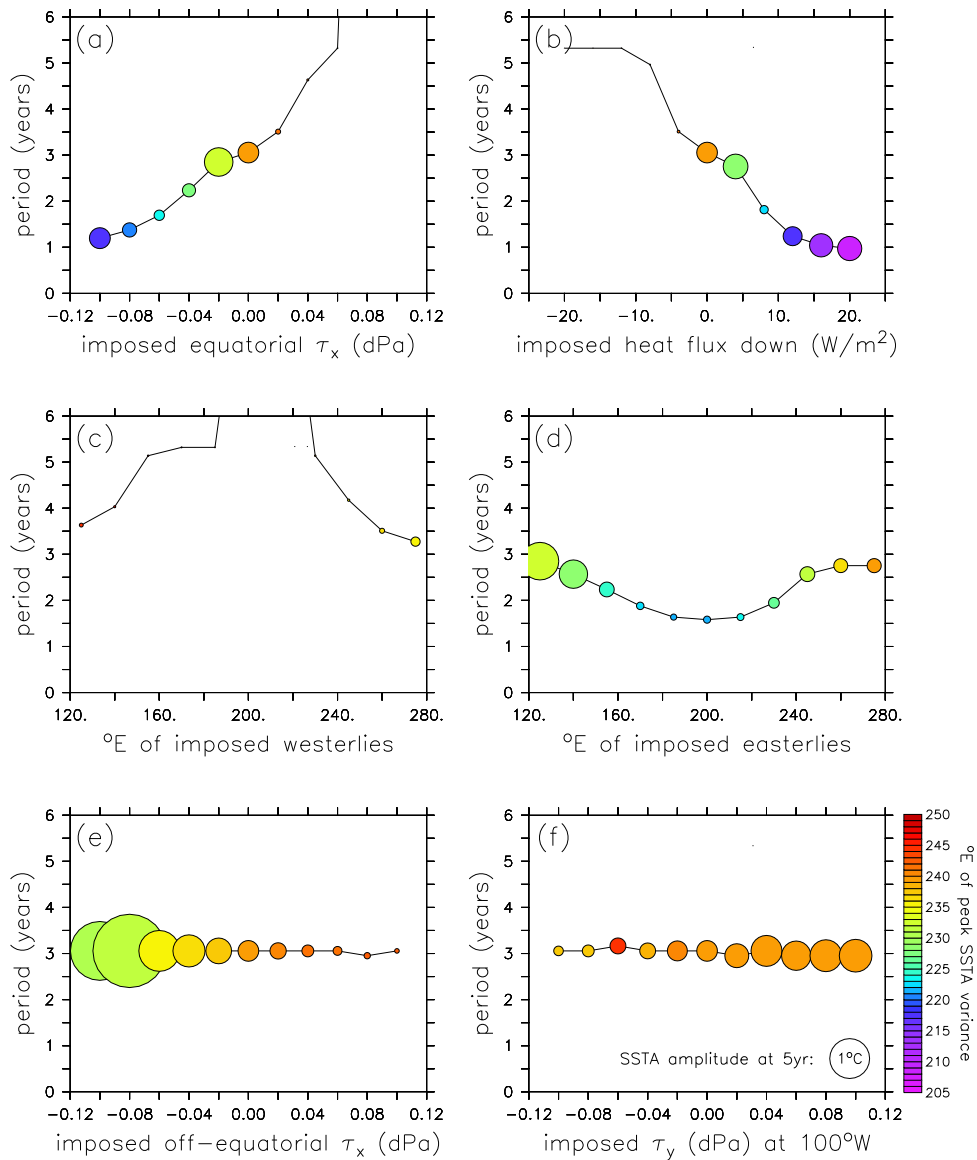
Figure 7.7: Changes in the intermediate model ENSO for the climate perturbations of Chapter 5. Abscissa gives the (a) imposed zonally-uniform zonal stress at the equator, (b) imposed heat flux into the ocean, (c) longitude of local weakening of the equatorial trades, (d) longitude of local strengthening of the equatorial trades, (e) imposed zonally-uniform zonal stress off-equator, and (f) imposed meridional stress in the eastern Pacific. Ordinate gives the ENSO period, dot color the longitude of peak equatorial SSTA variance, and dot radius the SSTA oscillation amplitude at this longitude, 5 years after the imposition of a weak westerly stress anomaly in the central Pacific. The key to dot size and color for all panels is given in (f).

giving roughly the same change as an imposed 0.06 dPa easterly stress.

Longitude of the stress

Panels (c) and (d) show the importance of the zonal position of an equatorial τ_x perturbation. Chapter 5 showed that the effect of a stress perturbation on the coupled climatology is greatest when it lies over the central basin, where it can effectively seed coupled feedbacks by altering both the extent of shallow thermocline in the east and the strength of equatorial upwelling in the east Pacific region of shallow thermocline. Here we see that the effect on ENSO is likewise greatest when the τ_x perturbation lies in the central basin. Off-center perturbations affect the ENSO amplitude and longitude slightly more when they are in the west than in the east, since the east Pacific thermocline depth and central Pacific zonal SST gradient are more responsive to perturbations in the west (Figs. 5.11 and 5.12).

Off-equatorial stress

Panel (e) shows the effect of an off-equatorial zonal stress perturbation on the simulated ENSO. As the off-equatorial trades weaken, the variability weakens and shifts eastward. Interestingly, the ENSO *period* is hardly affected by such a perturbation. When the off-equatorial trades are strong enough, the climatology becomes unstable and a limit cycle develops.

Meridional stress

Panel (f) shows the effect of a change in the cross-equatorial southerlies in the eastern Pacific. The period is hardly affected, and there are only small changes in the amplitude and position of the variability, with ENSO strengthening only slightly as the southerlies strengthen.

Similarity of the results

Recalling that Chapter 5 showed that coupled feedbacks tend to homogenize the climate response, it is interesting to compare results from the various ENSO sensitivity experiments on a common footing. Fig. 7.8 overlays the results from all the experiments in Fig. 7.7 as a function of the strength of the climatological trades in the central Pacific. The results lie essentially along the same curve, indicating that the period is a fairly robust function of the coupled trade wind strength regardless of the type of imposed perturbation. The strongest amplitudes occur at near-normal and very strong trades, and the weakest amplitudes at weak and moderately strong trades, just as in the prototype case that we have examined in detail. And for the most part, the ENSO variability at strong trades and short periods occurs farther west than that at weak trades and long periods.

The off-equatorial τ_x-perturbation case is something of an exception, in that the period changes less rapidly with the equatorial trades while the amplitude changes more rapidly. Recall that the off-equatorial stress can only *directly* affect the *zonal-mean* depth of the equatorial thermocline. A zonally-uniform change in thermocline depth induces less of a change in zonal SST gradient than does a change the slope of the thermocline, and therefore
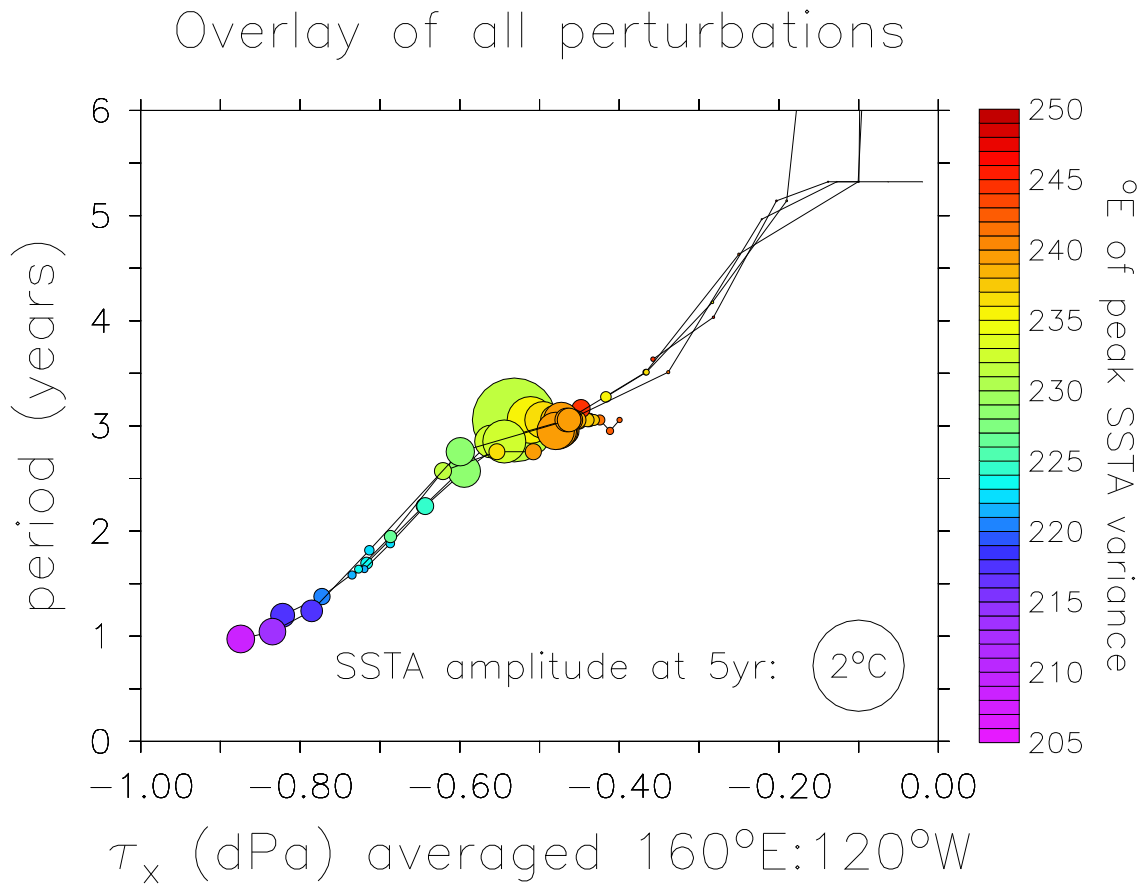
Figure 7.8: Linear ENSO properties as a function of the strength of the equatorial trade winds, for all of the climate-change cases examined in Chapter 5. Horizontal axis is the mean zonal stress (averaged over the region 170°E–120°W, 2°S–2°N), vertical axis is the oscillation period. Dot radius is proportional to the amplitude of the oscillation 5 years after the imposition of a transient westerly stress perturbation. Dot color indicates the longitude of peak equatorial SST anomaly variance.

results in a smaller change in zonal stress with weaker coupled feedbacks. The upshot is that compared to an imposed change in the equatorial trades, an imposed change in the off-equatorial trades induces a larger change in the subsurface temperature structure relative to the surface temperature structure. Now recall that $-u'\partial_x\overline{T}$ is a transitioning mechanism which depends exclusively on the mixed layer SST gradients, while $-\overline{w}\partial_z T'$ is more of a destabilizing mechanism which depends on the subsurface structure. Examination of the heat budget phasors for the off-equatorial case (not shown) confirms that there is a larger change in $-\overline{w}\partial_z T'$ relative to $-u'\partial_x\overline{T}$, and consequently a greater effect on the amplitude than the period, than in the equatorial case.

Despite this, Fig. 7.8 is remarkable because it shows that in the coupled context, ENSO behavior is determined primarily by strength of the equatorial trades—the "El Niño-ness" or "La Niña-ness" of the climatology. This confirms the relevance of the prototype case, and allows us to forgo detailed analysis of the other climate-change cases. Instead, we turn to the effects of climate change on ENSO in nonlinear and stochastic regimes.

7.2   Nonlinear regime

The previous section focused on ENSO behavior in the small-amplitude regime, and at a value of air-sea coupling where unforced oscillations are damped. In this section, we consider the effect of increasing coupling, which tends to destabilize the oscillations and allows them to grow large enough that nonlinearities become important. We also take a step closer to the stochastic context, by examining the response of the system to strong transient wind stress disturbances.

7.2.1   ENSO sensitivity at increased coupling

Is the ENSO sensitivity to climate any different if the wind stress depends more strongly on SST anomalies? This is an important question, since (1) the strength of the stress response in the real world is unclear, due to sparse observations and uncertain analyses; (2) the effective "coupling strength" may vary with time, due to changes in the mean state and ENSO structure; and (3) current atmospheric models have a range of different stress responses to SSTAs.

Fig. 7.9 shows how the strength μ of the wind stress anomaly response to SSTAs affects the intermediate model sensitivity to the trade winds. At the standard coupling ($\mu = 1$) ENSO is damped, except at very strong climatological trades where a weak 1.2-year oscillation is sustained. As coupling increases, another sustained regime appears, with a period of about 3 years at near-normal trades. Around $\mu = 1.07$, these two regimes merge and there are sustained oscillations for all $\widetilde{\tau}_x^* < 0.02$ dPa, with period increasing as the trades weaken. As coupling increases further, so do the amplitude, period, and skewness of the oscillations, as well as the critical tradewind strength required for sustained variability.

Thus it appears that the lengthening of the period with a weakening of the trades is robust to large changes in coupling, even as the oscillations grow large enough to feel the influence of nonlinearity. The stability structure is also fairly robust to moderate changes in coupling, with peak ENSO growth/amplitude at strong and intermediate trades. Note that
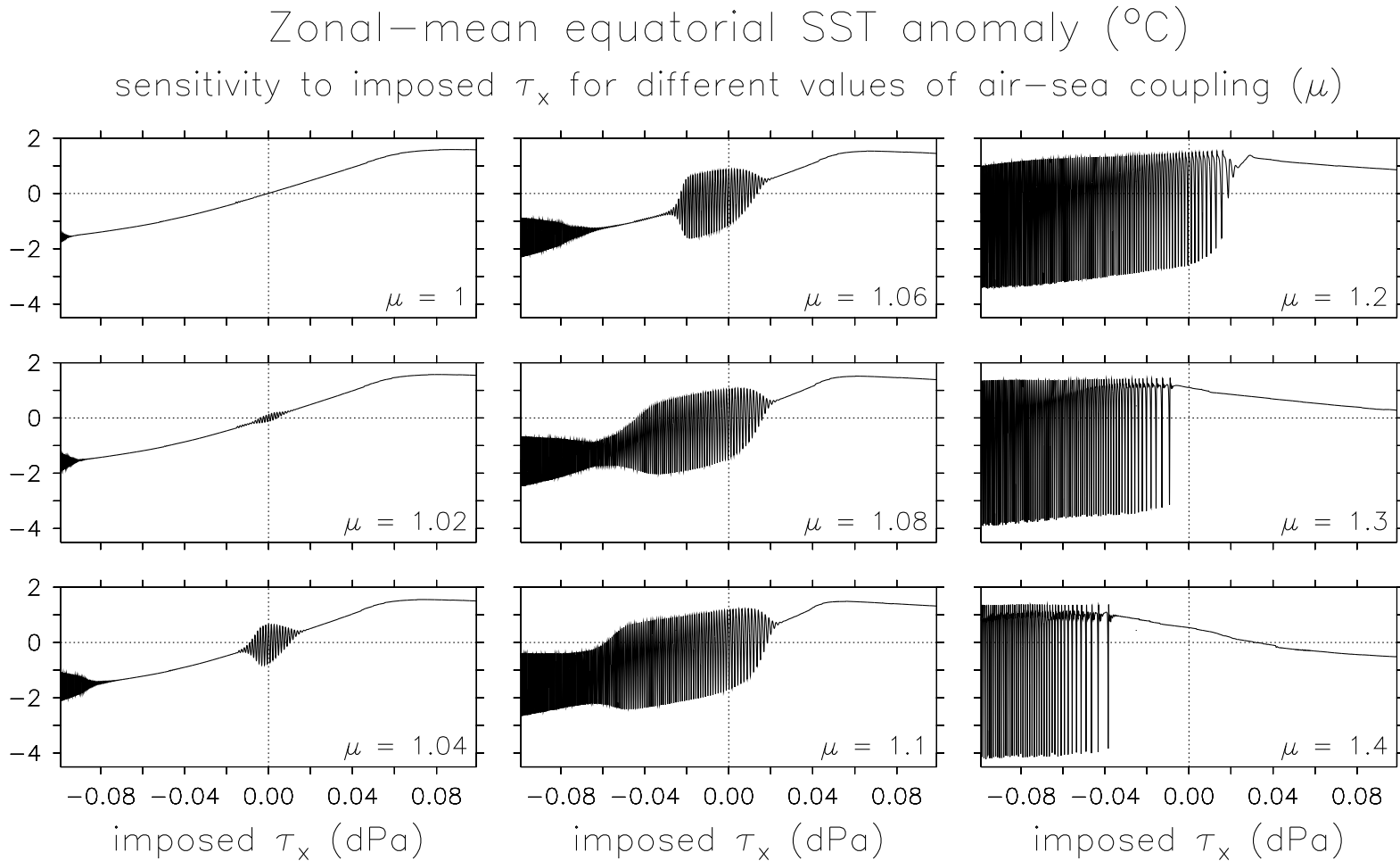
Figure 7.9: ENSO sensitivity to the time-mean strength of the trade winds, for different air-sea coupling strengths. Each panel shows zonal-mean equatorial (2°S–2°N) SST anomalies from a 500-year run of the intermediate model, in which the mean equatorial trade winds are gradually weakened over the course of the simulation. The imposed zonal stress perturbation is given on the horizontal axis, with tic marks every 0.02 dPa (50 years).

even with a coupling strength 40% higher than the standard value, sustained oscillations cannot exist when the trades are very weak.

As an aside, note that at very strong coupling the zonal-mean climatological SST actually *cools* as the imposed τ_x perturbation becomes more westerly. In this case, feedback easterlies in the western Pacific induce upwelling on the shallow thermocline there, which cools the surface. This induces more easterlies slightly west of the cooling, and creating a positive feedback cycle that generates a cold tongue in the central Pacific instead of the eastern Pacific.

7.2.2   Response to strong transient wind events

Does the ENSO response to *strong* transient wind stress differ from its response to weak stress disturbances? And how does this response change as climate changes? This section addresses these questions in the context of the intermediate model.

Fig. 7.10 shows how the intermediate model response to strong wind stress kicks changes as the climatology changes. A westerly kick (top panel) generally produces an initial warming, an easterly kick (bottom panel) a cooling. Following the first cycle, the oscillations decay away much as in the small-amplitude case (Fig. 7.1), and also reflect the stability properties at moderately higher coupling (Fig. 7.9). As the mean trades weaken, the oscillation period increases and the damping rate exhibits local minima for strong and near-normal mean trades. For very weak trades, there is essentially no lasting response to transient stress.

Fig. 7.11 focuses more closely on the initial SSTA cycle following a stress kick. For weak kicks (column a), the system is approximately linear and easterly and westerly kicks induce nearly opposite responses. The initial zonal-mean SSTA response corresponds to about 10°C per dPa of stress kick for strong mean trades, 13°C/dPa at normal trades, and less than 2°C/dPa at weak trades. Since the transient behavior is a superposition of normal modes, some of which decay rapidly but project strongly on the initial disturbance, the timing of the first peak is not directly tied to the period of the least-damped mode. Indeed, the bottom panel of (a) shows that the timing of the first peak is nearly independent of the tradewind strength, while the period of the least damped mode (roughly the time between the first and third extrema) varies strongly with the tradewind strength.

Is the response to strong kicks any different? Comparing (b) to (a) in Fig. 7.11, it is clear that a 0.2 dPa kick is generally less efficient at generating SSTA disturbances than is a 0.02 dPa kick. Some exceptions are at strong trades, where strong westerly kicks are more efficient than weak westerly kicks at inducing initial warming (W1), and at weak trades, where strong easterly kicks are more efficient than weak easterly kicks at inducing initial cooling (E1). The amplitude of the third peak relative to the kick (W3, E3), indicates that for strong-to-moderate climatological trades, strong kicks are roughly half as efficient as weak kicks at putting energy into the least-damped mode.

How is the *timing* of the response affected by nonlinearity? The answer is illustrated by the bottom row of Fig. 7.11. For near-normal tradewind strengths, the first El Niño following an easterly kick (E2) occurs several months sooner than in the linear case. For strong trades, the initial El Niño following a westerly kick (W1) is delayed about a month relative to the linear case, while the initial La Niña following an easterly kick (E1) comes

Zonal—mean equatorial SST anomaly
with stress kicks (3mo at 0.2 dPa, 165°W) every 25yr
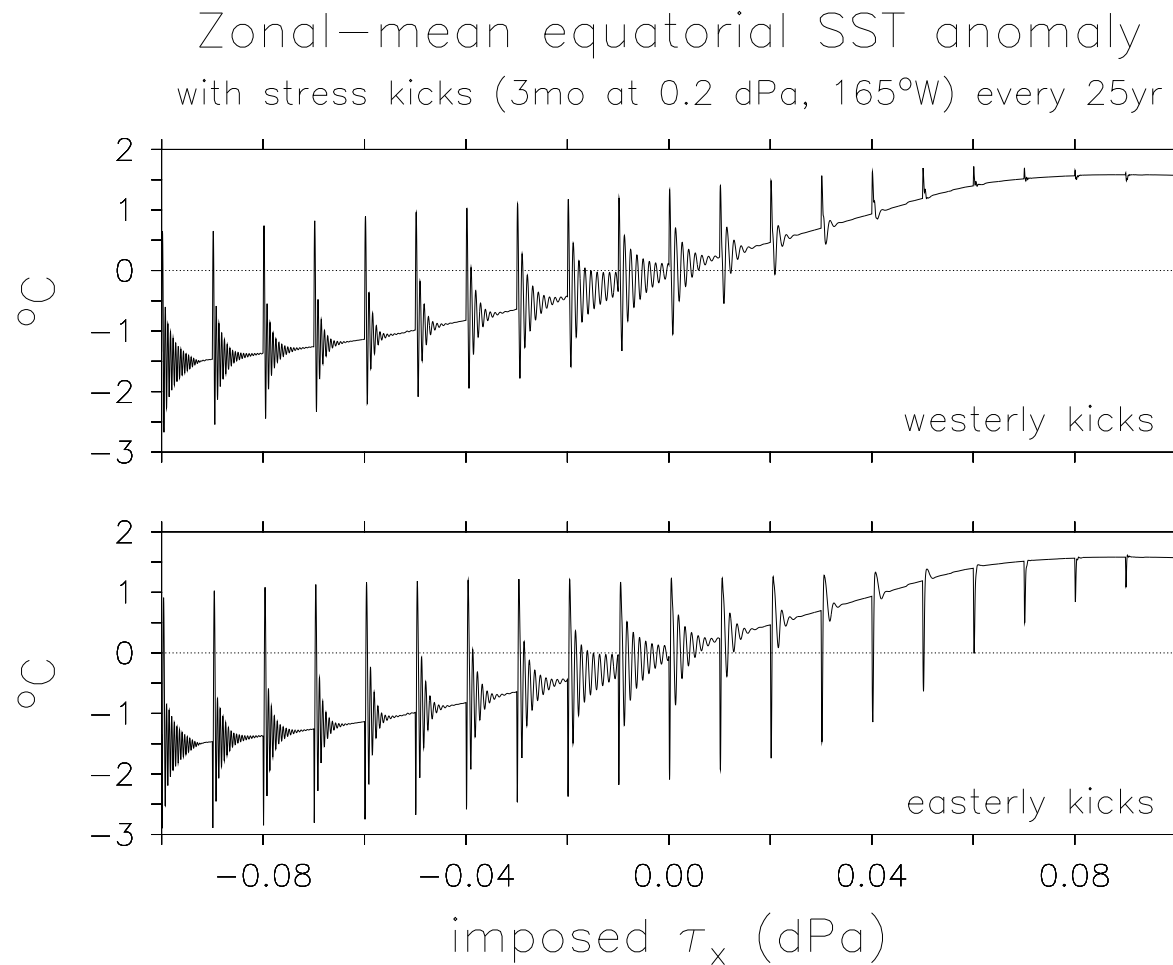
Figure 7.10: Simulated ENSO response to transient wind events. Zonal-mean equatorial (2°S–2°N) SST anomalies are shown from a 500-year run of the intermediate model, during which the mean equatorial trade winds are gradually weakened (horizontal axis indicates the imposed zonal stress perturbation). Meanwhile, the system is subjected to a series of transient wind stress events which occur every 25 years. Top panel shows the response to westerly events, bottom panel shows the response to easterly events. Each stress event lasts for 3 months and has a bivariate Gaussian spatial structure, with a peak amplitude of 0.2 dPa on the equator at 165°W, and e-folding halfwidths of 40° longitude and 10° latitude.
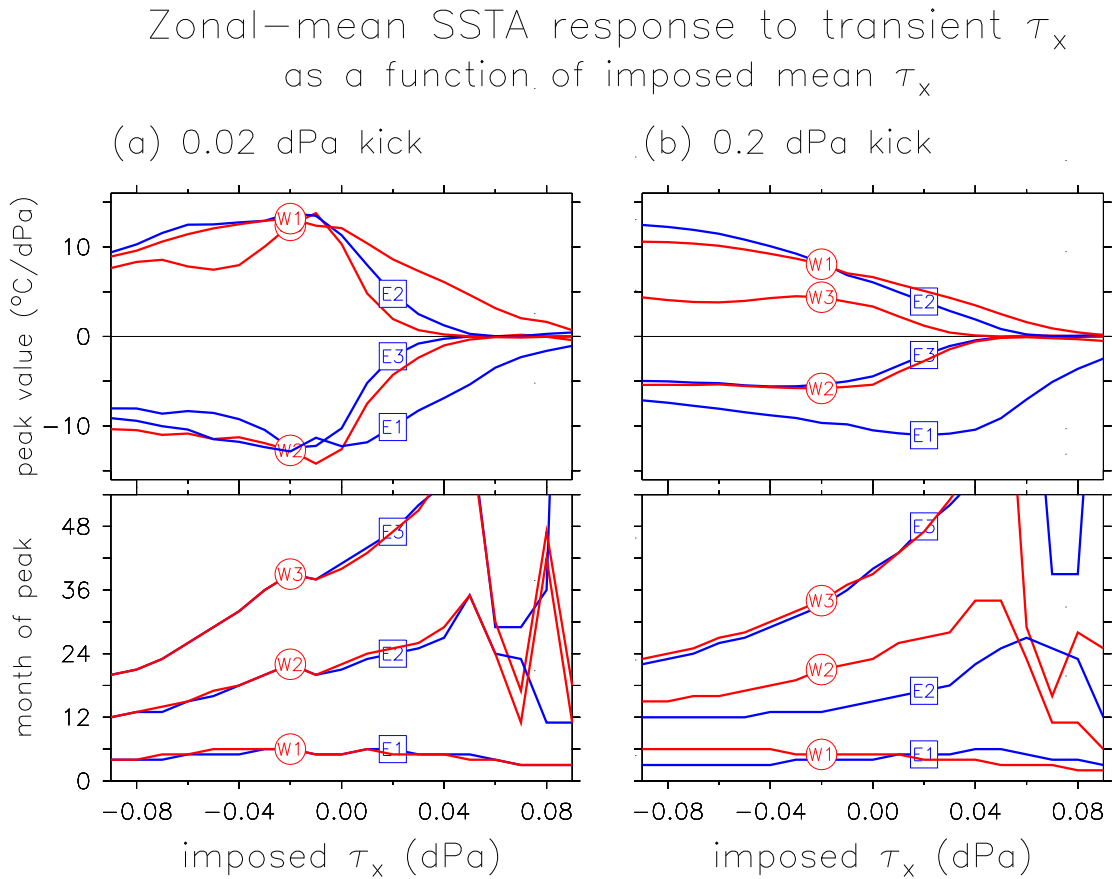
Figure 7.11: Transient response statistics for zonal-mean equatorial SST anomalies, as a function of the climatological tradewind strength. As in Fig. 7.10, the intermediate model is subjected to a series of transient stress kicks, whose peak values are given at the top of each column: (a) is for the weak kicks of Section 7.1 and (b) is for the stronger kicks of Fig. 7.10. Horizontal axis gives the imposed *climatological* stress perturbation at the time of the kick. Top row gives the first three SSTA extrema following the stress kick, and bottom row gives the months they occur. For a westerly kick, W1 indicates the first event (warm), W2 the second (cold), and W3 the third (warm). For an easterly kick, E1 indicates the first event (cold), E2 the second (warm), and E3 the third (cold).

Figure 7.12: Ratios of magnitudes of the peak zonal-mean SST anomalies shown in the upper-right panel of Fig. 7.11. Horizontal axis gives the imposed climatological stress perturbation.

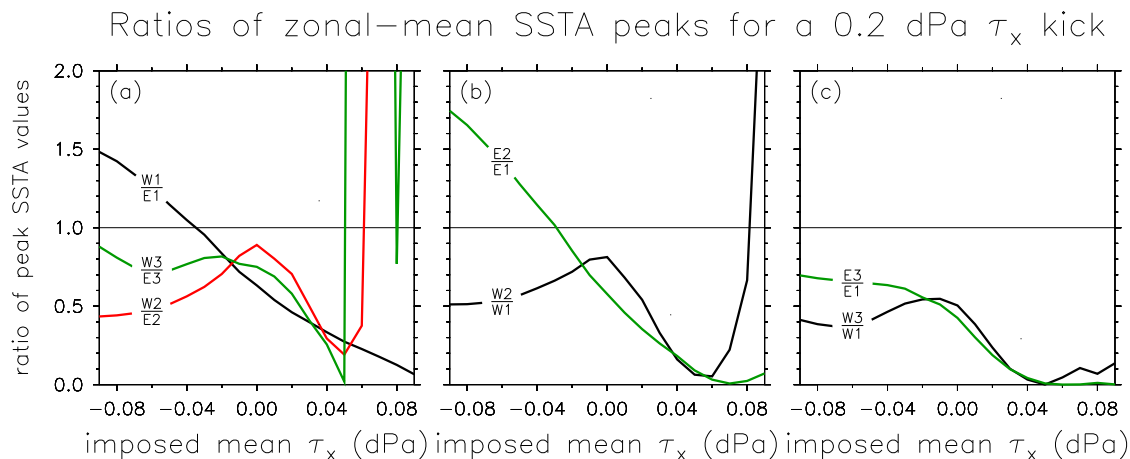roughly a month sooner than in the linear case. For weak trades, the responses shift in the opposite sense, with E1 occurring slightly later than W1. Thus although the linear period grows *longer* as the trades weaken, the first warm event actually appears progressively *sooner* following a strong westerly kick. Despite these changes in the transient behavior, the phase of the modal response (W3, E3) is remarkably insensitive to the strength of the kick, or to whether it is easterly or westerly.

How does the initial SSTA response to a strong westerly kick differ from that for an easterly kick? In addition to the timing differences noted above, there are also substantial differences in amplitude. Panel (a) of Fig. 7.12 shows ratios of the SSTA peak responses for westerly versus easterly kicks. Focusing on the first SSTA peak (W1, E1), we see that for strong trades, a westerly kick induces a stronger initial peak than does an easterly kick. As the trades weaken, westerly kicks induce progressively weaker initial peaks relative to easterly kicks, and at very weak trades the westerly kicks have almost no effect. Note that this change is related to the skewness change evident at higher coupling (Fig. 7.9). The same nonlinearities are responsible in both contexts: if the trades are too strong, easterly kicks cannot affect SST due to the outcropping of the thermocline in the east; if the trades are too weak, westerly kicks cannot affect SST due to the absence of mean upwelling at the equator.

Focusing on the second and third SSTA peaks, it is clear that at the strong-to-intermediate tradewinds where such peaks occur, they tend to be stronger for easterly kicks than for westerly kicks. In the stochastic context, at strong trades one can expect more "modal" variability to arise from easterly kicks, but more "transient" variability to arise from westerly kicks. This is also evident in panel (c), which compares the third SSTA peak to the first.

How strong is the immediate aftermath of the initial event? The answer again depends on the strength of the climatological trades. It is evident from Fig. 7.9 that for strong

trades, the first warm event after a westerly kick is more than twice as strong as the subsequent cold event. As the trades weaken, the cold aftermath disappears, until for very weak trades there is almost no initial warming and instead only a slight cooling in response to a westerly kick. Panel (b) of Fig. 7.12 summarizes such changes by showing the ratios W2/W1 and E2/E1. For strong trades, an easterly kick induces a much stronger aftermath than does a westerly kick. In this case the warm aftermath of the easterly kick is stronger than the initial cold event; in fact, as can be seen in panel (b) of Fig. 7.11, it is stronger even than the initial warm event following a westerly kick! As the mean trades weaken, the warm aftermath of an easterly kick becomes progressively weaker relative to the initial cold event. The cold aftermath of a westerly kick, however, shows a local maximum relative to the initial warming when the trades are near-normal. For very weak trades, an easterly kick produces a fairly strong initial cold spike without any warm aftermath, while a westerly kick produces hardly any response.

Having considered the effect of individual stress disturbances on the ENSO system, we are now prepared to enter a more realistic regime—one that includes continual excitation by random wind stress variability.

7.3   Stochastic regime

In this section, we consider the effects of climate changes on a stochastically-excited ENSO. This context is arguably more realistic than those we have considered so far, given the large intraseasonal wind stress signals present in observational analyses (Chapter 2). The two key questions are: (1) Do the changes in the modal and transient behavior we have seen up to this point also apply in stochastic regime? and (2) How large a climate change must occur before its effect on ENSO can be distinguished from natural variations?

To answer these questions, we take advantage of the stochastic hybrid coupled intermediate model developed in Chapters 3 and 4. Noise of moderate amplitude is used (as in Fig. 4.32 and Chapter 5), so that the ENSO variability mimics the amplitude, distribution, spectrum, and spectral variations of observed SST anomalies (Fig. 2.11). The climate-change cases correspond to the 500-year stochastic runs of Chapter 5, in which the strength of the equatorial trades are gradually weakened over the course of the simulation. To ensure good statistics for the hypothesis tests, a 5000-year control run is also performed in which no climate perturbation is imposed.

7.3.1   Overview of the stochastic timeseries

Control run

The first 500 years of the 5000-year stochastic control run are shown in Fig. 7.13. There are rather strong natural fluctuations in the strength of the ENSO activity from decade to decade, and from century to century. That these fluctuations are due entirely to the statistically-steady noise forcing illustrates a key point: in the stochastic context, temporal variations in ENSO behavior may arise from pure chance, and need not be due to fundamental changes in the climate system. Thus any suspected effect on ENSO of an
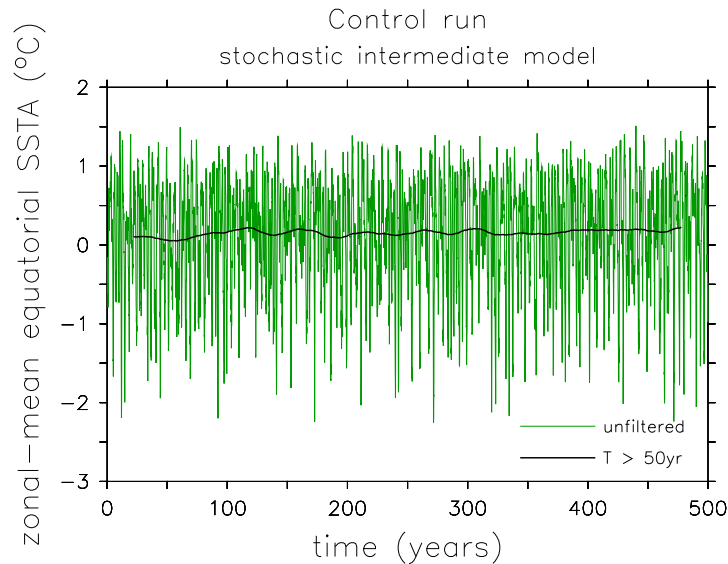
Figure 7.13: Zonal-mean equatorial (2°S–2°N) SST anomalies from a 500-year control run of the stochastic intermediate model. Green line is the monthly anomaly timeseries; black line filters out periods shorter than 50 years.

imposed climate forcing should always be tested against a hypothesis of no climate change at all.

Effect of changing equatorial trades

Fig. 7.14 shows how the stochastic model responds to a change in the strength of the trade winds. The horizontal axis is the same as in Fig. 7.13, but has been relabeled to indicate the strength of the imposed climatological zonal stress perturbation. Note that the simulations of Figs. 7.13 and 7.14 are driven by the same particular realization of the wind stress noise, so any differences between the two timeseries must arise entirely due to the imposed mean zonal stress and associated dynamical changes.

As the trade winds weaken, the equatorial band warms up; it is apparent that the climate response is nonlinear, i.e. that the long-term mean SST is less sensitive to strong $\overline{\tau}_x$ perturbations than to weak ones. Also as the trades weaken, ENSO becomes less active. The ENSO behavior at weak trades appears to be quite different from anything in the control run, so the climate perturbation does indeed appear to have an impact on ENSO. The remaining sections will refine and quantify these statements.

7.3.2 Distribution

The quantiles of zonal-mean equatorial SST anomalies from the control run are shown in Fig. 7.15. The shaded bands indicate the uncertainty that results from trying to characterize the quantiles using timeseries of various lengths. The sample quantiles for a 10-year timeseries are highly variable, suggesting that it may be difficult to see the effects of climate
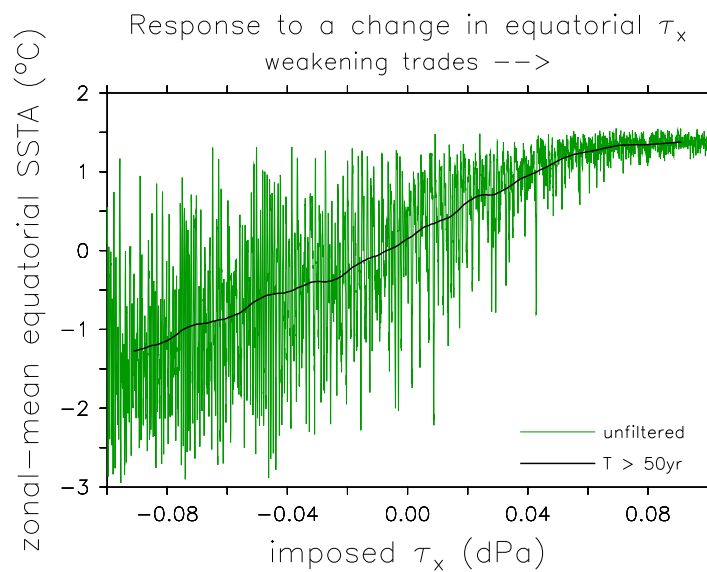
Figure 7.14: Simulated response of equatorial Pacific SST to a change in the strength of the trade winds. The imposed zonal stress perturbation is zonally constant and has a meridionally Gaussian shape with an e-folding halfwidth of 15°. Horizontal axis indicates the amplitude of the imposed zonal stress, which changes linearly from −0.1 dPa (easterly) to 0.1 dPa (westerly) over the course of a 500 year stochastic simulation. Otherwise as in Fig. 7.13.
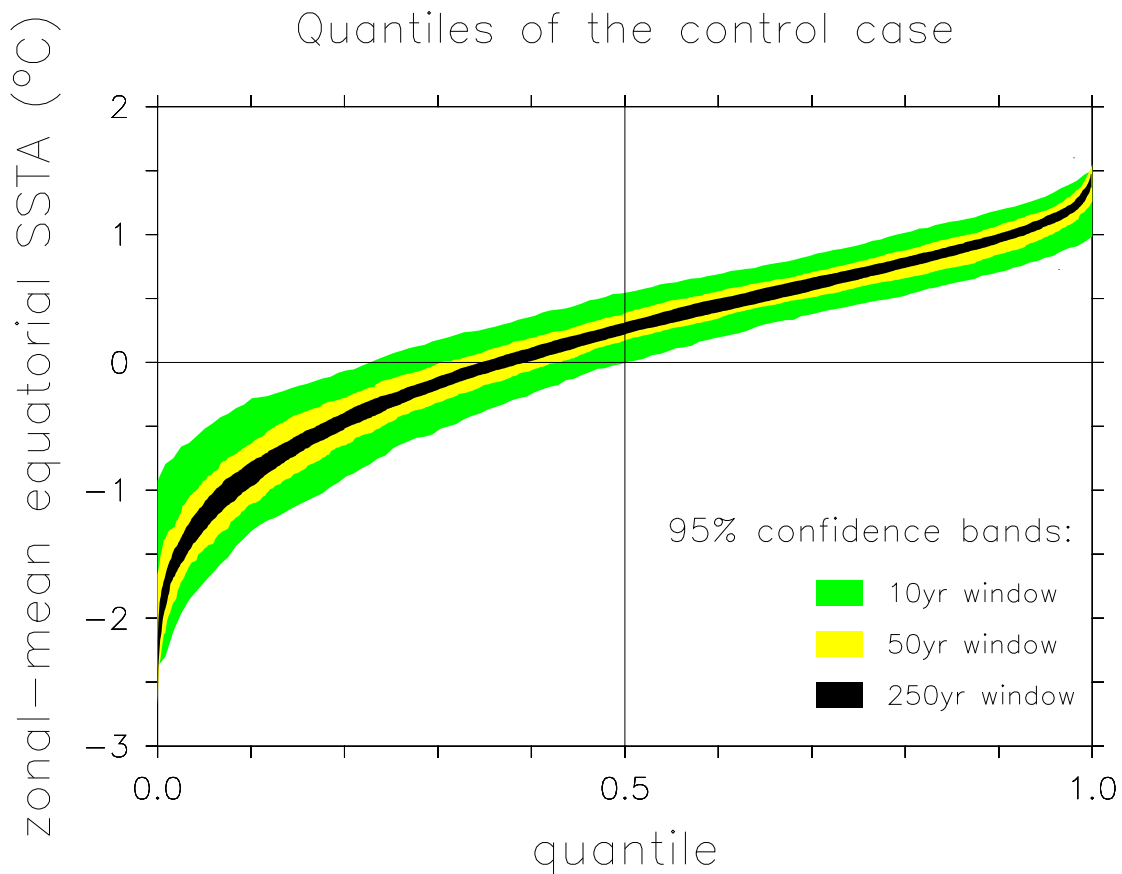
Figure 7.15: Quantile function for zonal-mean equatorial (2°S–2°N) SST anomalies, based on the control run of the stochastic intermediate model. Horizontal axis indicates the fraction of SSTA values smaller than the value given on the vertical axis. The shaded bands are 95% confidence intervals for the quantiles, based on a 5000 year simulation divided into non-overlapping windows of length 10 years (green), 50 years (yellow), and 250 years (black). Thus the green band indicates that for any given 10 year timeseries, to 95% confidence the coldest SSTA will lie between −2.7°C and −0.7°C, the median between −0.1°C and 0.6°C, and the warmest between 0.9°C and 1.5°C.
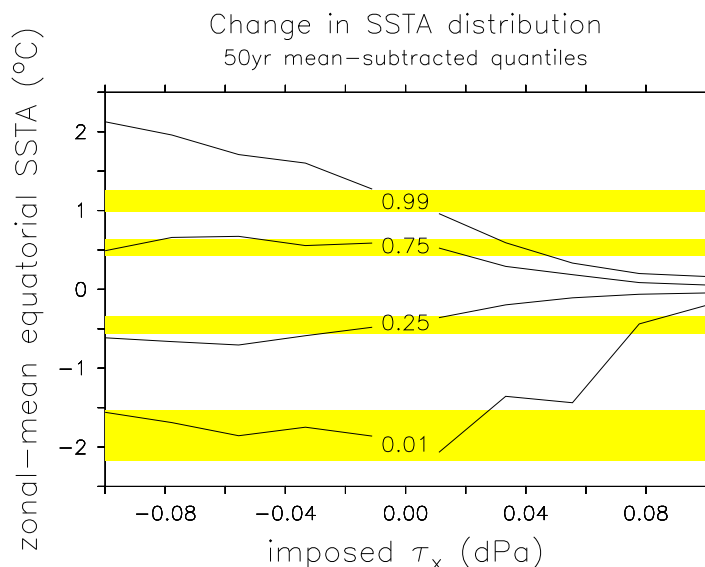
Figure 7.16: Change in the distribution of zonal-mean equatorial (2°S–2°N) SST anomalies, for the experiment of Fig. 7.14. The 500-year simulation is divided into 10 non-overlapping windows, each of length 50 years. For each window, the mean is subtracted and then the quantiles are computed and plotted (solid lines). Repeating this procedure in the 5000-year control run yields 95% confidence bands (shaded) for the unperturbed 50-year quantiles.

change on the distribution at these time scales. To reliably detect changes in the SSTA distribution, it clearly helps to have long timeseries.

The cold-skewness of the control-run SSTAs is evidenced by the shift of the median above zero, and by the stronger amplitude of cold events relative to warm events. (Note that *observed* SSTAs over the last century appear to be skewed toward *warm* events, rather than cold events as in the model; thus the quantile function for the observations would resemble an upside-down version of Fig. 7.15.) The confidence intervals are widest at the lowest quantiles, indicating that a shift in the cold events (here the strong La Niñas) will be harder to detect than an equivalent shift in the median or warm events.

How does the distribution of these SST anomalies change as climate changes? Fig. 7.16 shows what happens to the SSTA quantiles as the trades weaken. A 50-year running mean has been subtracted from the quantiles so that changes are easier to see, and the shaded bands indicate the control-run confidence bands for 50-year timeseries. For strong trades, warm events are significantly strengthened compared to the control, and the SSTA distribution becomes positively skewed; changes in the magnitude of the coldest 1% of events, however, are not detectable even at 50-year timescales. For weak trades, ENSO is significantly weakened and the SSTA distribution becomes even more negatively skewed than in the control. In the weak-trades case, all four quantiles are significantly different from those in the control run, and the changes in the most extreme events can be detected even with 10-year timeseries. In short, the change in distribution due to ENSO *suppression* (for weak trades) is more easily detected than that due to ENSO *conversion* from a slow
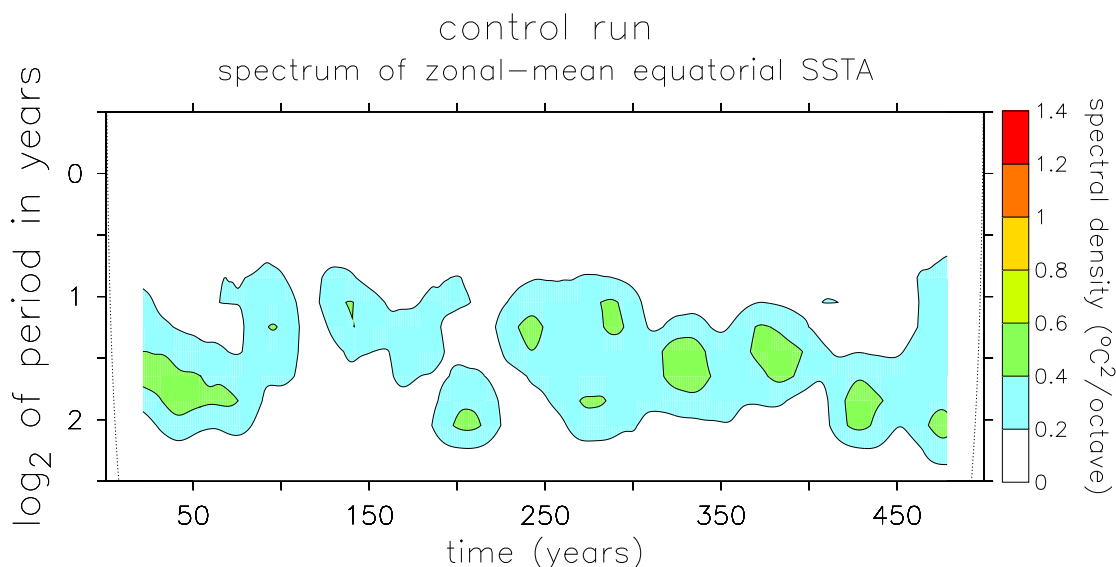
Figure 7.17: Spectral modulation in the stochastic intermediate model control run, based on a wavelet analysis of the unfiltered timeseries shown in Fig. 7.13. Horizontal axis indicates the model time in years. Vertical axis indicates the base-2 logarithm of the period in years. Contours indicate the wavelet power density, which has been smoothed to eliminate modulations at periods shorter than 50 years. Dotted lines indicate the "cone of influence," below which the wavelet power is reduced by zero padding at the beginning and end of the timeseries.

to a fast mode (for strong trades).

7.3.3 Spectrum

Fig. 7.17 shows the "natural" slow variation in the spectrum of zonal-mean equatorial SST anomalies from the stochastic control run. The power in the interannual band varies from century to century, simply due to random fluctuations in the statistically-steady noise. There are also apparent shifts in the dominant period of oscillation: between years 375 and 425, for example, the period shifts from 2.7 to 3.6 years for no reason other than chance. Again, one must be careful to test supposed climate-induced ENSO changes against the hypothesis of stationarity.

To support these tests, we present confidence bands for the control spectrum in Fig. 7.18. The shaded bands indicate the uncertainty that results from trying to characterize the spectrum using short timeseries. The sample spectrum for a 10-year timeseries is extremely variable, suggesting that spectral changes in the interannual band will be difficult to detect at decadal scales. Even for timeseries as long as 250 years, the spectral density in the interannual band can vary by nearly a factor of two. It is important to note, however, that away from the spectral peak the confidence bands narrow substantially. This suggests that it may be relatively easy to detect a *shift* in the spectrum towards longer or shorter periods, which would increase variability in bands that are inactive in the control run.
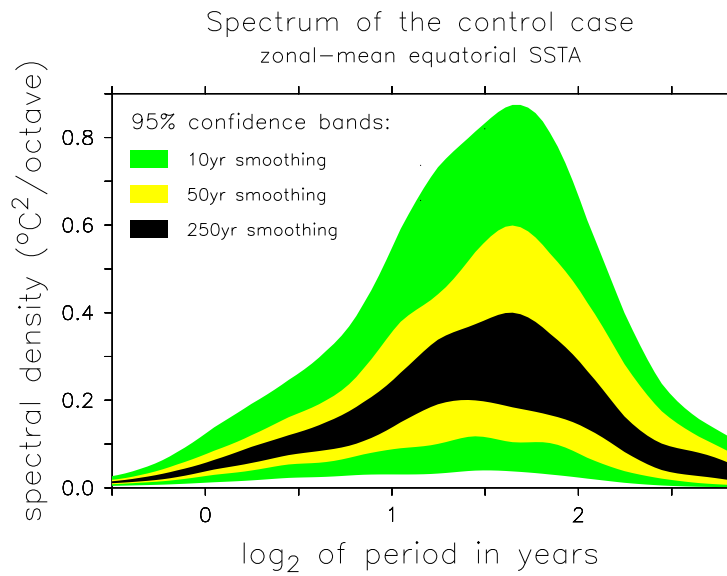
Figure 7.18: Wavelet power spectral density of zonal-mean equatorial (2°S–2°N) SST anomalies, based on the control run of the stochastic coupled intermediate model. Horizontal axis indicates the base-2 logarithm of the period in years. The shaded bands are 95% confidence intervals for the spectrum, based on a 5000 year simulation smoothed to eliminate modulations at periods shorter than 10 years (green), 50 years (yellow), and 250 years (black). Thus the green band indicates that on time scales longer than 10 years, to 95% confidence the spectral density at 2 years will lie between 0.03 and 0.55°C^2/octave.
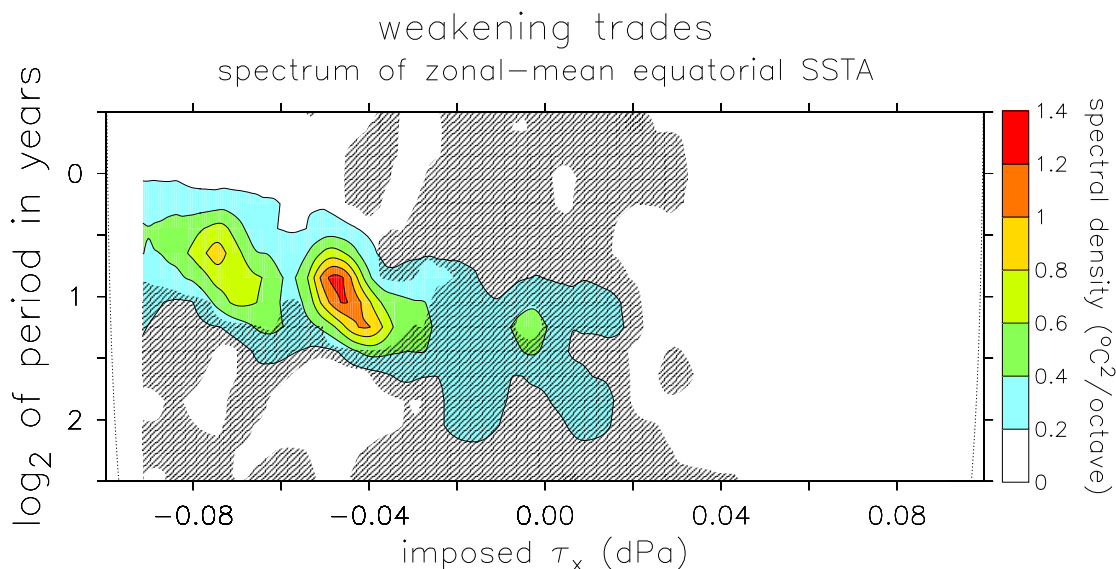
Figure 7.19: Spectral response of the stochastic intermediate model to a weakening of the equatorial trade winds, based on a wavelet analysis of the unfiltered 500-year timeseries shown in Fig. 7.14. Hatching indicates regions that are within the 95% confidence bounds for the 50-year smoothed density in a very long (5000-year) control run. Otherwise as in Fig. 7.17.

How does the period of the stochastic ENSO change as climate changes? Fig. 7.19 shows that as the equatorial trades winds weaken, the ENSO period tends to increase as expected from Sections 7.1 and 7.2. Note that this spectrum is directly comparable to Fig. 7.17 since it is driven by the same realization of the wind stress noise; this is why the two spectra look similar when the imposed zonal stress is near zero. The apparent "resonances" that arise near $\widetilde{\tau}_x^* = -0.07$ dPa and $\widetilde{\tau}_x^* = -0.05$ dPa, and the apparent "anti-resonance" at $\widetilde{\tau}_x^* = -0.06$ dPa, are likely due to chance variations in the stochastic forcing since similar features are found at these times in the control run.

On timescales of 50 years or longer, these spectral changes are robust enough to be distinguished from natural variability. For strong trades $(\widetilde{\tau}_x^* \leq -0.03$ dPa$)$, short periods are significantly *more* active than in the control, while for weak trades $(\widetilde{\tau}_x^* \geq 0.03$ dPa$)$, all periods are significantly *less* active than in the control. Note that at periods of about 3 years, where the control run is most active, the spectral effect of strengthening trades is undetectable even with 50-year timeseries. Instead, the ENSO fingerprint of climate change most clearly revealed in the increased variability in the 1–2 year band, which was relatively inactive in the control run. The key point is this: perhaps the best place to look for evidence of past and future changes is not in the spectral band where ENSO is most active today, but instead at the shorter and longer timescales that are now relatively quiet. These "edge bands" may well be the most sensitive to climate changes that induce shifts in the spectrum.
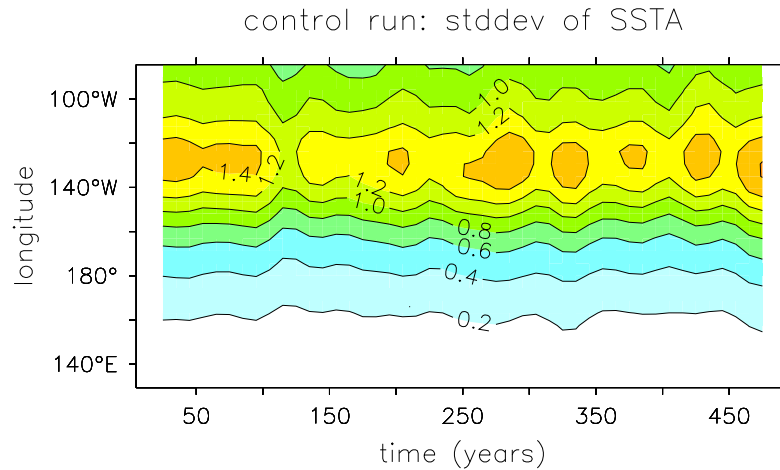
Figure 7.20: Running standard deviation of SST anomalies along the equator (2°S–2°N) in the control run of the stochastic intermediate model. Horizontal axis is the model time in years, vertical axis is longitude. Contours indicate the standard deviation, computed by high-pass filtering the SSTA to eliminate periods longer than 8 years, squaring the result, low-pass filtering to eliminate periods shorter than 50 years, and then taking the square root.

7.3.4 Spatial structure

Fig. 7.20 shows the random modulation of the equatorial SST variability in the control run. While there are variations in the ENSO amplitude as noted earlier, the zonal structure of the variability is rather fixed in time, with a peak amplitude near 130°W and little variability in the western Pacific. Confidence bands for the standard deviation are given in Fig. 7.18.

How does the equatorial structure of ENSO change as climate changes? Fig. 7.22 shows that as the climatological trades weaken, the SST variability shifts eastward, again as expected from Sections 7.1 and 7.2. On timescales of 50 years or more, these changes are readily distinguishable from the stochastic control run. For strong trades ($\widetilde{\tau^*_x} \leq -0.02$ dPa), the SSTA variability is significantly stronger than the control in the western and central Pacific, and significantly weaker in the far eastern Pacific. For weak trades ($\widetilde{\tau^*_x} \geq 0.02$ dPa), the variability is significantly weaker than the control, everywhere along the equator except in the far western Pacific. Again, the implication for ENSO-change studies is that the best place to look for the influence of climate may not where ENSO is most active today, but instead farther west, at the edge of the present variability, where paleodata are likely to be most sensitive to climate-induced zonal shifts in ENSO over time.

7.3.5 Predictability

Given that the distribution, spectrum, and structure of ENSO are all significantly affected by changes in the climatology, is ENSO predictability affected as well? Again, we must first appreciate the natural stochastic variations in predictability. Fig. 7.23 shows
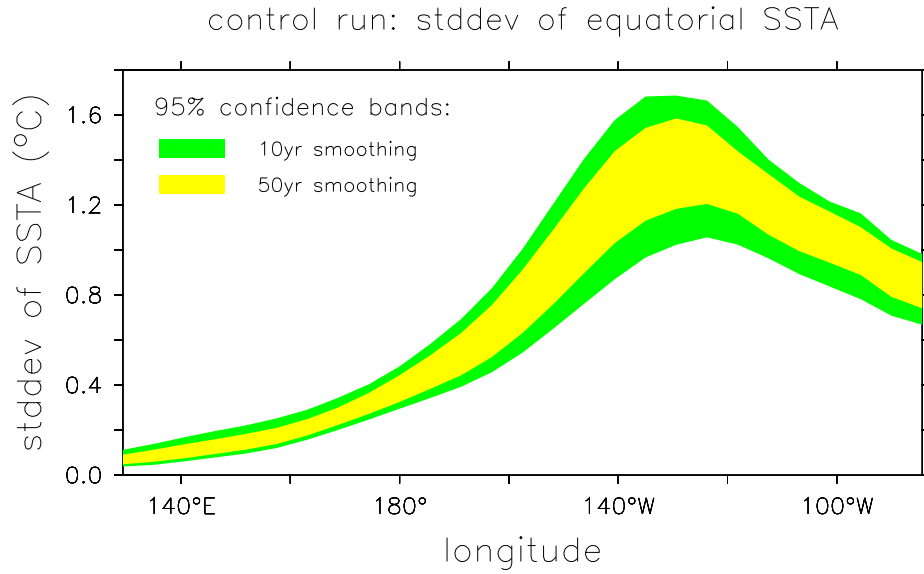
Figure 7.21: Confidence bands for the running standard deviation of SST anomalies along the equator (2°S–2°N) in the control run of the stochastic intermediate model. The standard deviation is computed by high-pass filtering the SSTA to eliminate periods longer than 8 years, squaring the result, low-pass filtering, and then taking the square root. The shaded bands are 95% confidence intervals for the standard deviation for a low-pass filter that eliminates periods shorter than 10 years (green) or 50 years (yellow).
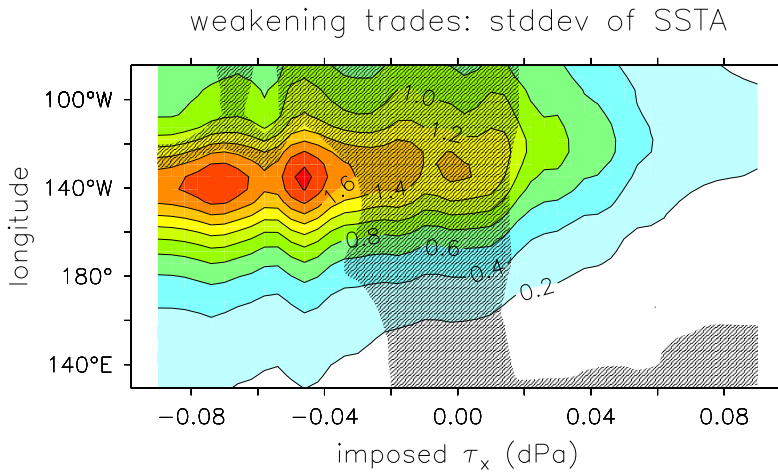
Figure 7.22: Running standard deviation of equatorial SSTA as the equatorial trade winds gradually weaken. Horizontal axis indicates the amplitude of the imposed stress; otherwise as in Fig. 7.20. Hatching indicates regions that are within the 95% confidence bounds for the standard deviation in the control run.

how the predictive power (PP) of the control-run ENSO varies over long time scales, due to the stochastic excitation. The predictive power of a large ensemble does not appear to fluctuate much at time scales longer than 50 years, at least not for those early lead times where the PP significantly greater than zero, and the window of significant predictability generally lasts about 7–10 months. Confidence bands for the smoothed PP are shown in Fig. 7.24.

How does the predictability of ENSO then change as climate changes? Fig. 7.25 shows that as the climatological trades weaken, the predictability window begins to close. This is consistent with Figs. 7.10–7.12, which showed that as the climatological trades weaken, the SSTA response to a wind stress kick becomes more transient—i.e. it dissipates initial information more rapidly. For strong trades, forecasts yield useful information for a full year after initialization, but for weak trades the forecasts become useless after only three months. Fortunately, the predictability appears to be greatest when the ENSO signal is strong, which is presumably the regime where one most depends on forecasts.

These changes are readily distinguishable from the control run, if one examines the average predictability over periods longer than 50 years. For strong trades ($\widetilde{\tau_x^*} \leq -0.02$ dPa), the PP is significantly enhanced at forecast leads of 5–12 months. For weak trades ($\widetilde{\tau_x^*} \geq 0.01$ dPa), the PP is significantly reduced at all leads where the forecasts are useful.

7.3.6 Summary

In the stochastic regime, the effect of climate perturbations on ENSO appears to be similar to that in the absence of noise (Sections 7.1 and 7.2). Compared to the control run, experiments with weakened trades exhibit an ENSO that is weaker, more skewed towards La Niña, and less predictable, with a longer period and an SSTA pattern that is shifted eastward. Experiments with strengthened trades, on the other hand, show an ENSO that is more skewed towards El Niño and more predictable, with a shorter period and an SSTA pattern that is shifted westward.

Whether these changes can be detected in the stochastic context depends on two things: the magnitude of the climate change and the duration of the timeseries. Nearly all of the ENSO changes described above are detectable in 50-year timeseries given an imposed 0.04 dPa change in equatorial zonal-mean stress. This is roughly 30–40% of the standard deviation of interannual zonal stress anomalies observed over the past few decades (Fig. 2.5a), and is the same order of magnitude as the change observed between 1960-79 and 1980–99 (Fig. 2.1a). This suggests that the ENSO variations observed over the past several decades could well be linked to changes in the climatology. The results in this section further suggest that these changes should be most detectable at the "edges" of the present-day ENSO variability, where the statistics can most clearly reveal shifts in the distribution, spectrum, and spatial pattern of variability.

Unfortunately, as noted in Chapter 2, the *disparity* between observational analyses is also the same order of magnitude as the climate and ENSO changes we wish to detect. Thus the attribution of ENSO changes to climate changes, while plausible, may be hard to justify without improved analyses or the accumulation of additional data. On the other hand, the large climate differences in the analyses, combined with the discernable effect of climate on ENSO, may be one clue as to why ENSOs differ among coupled GCMs,
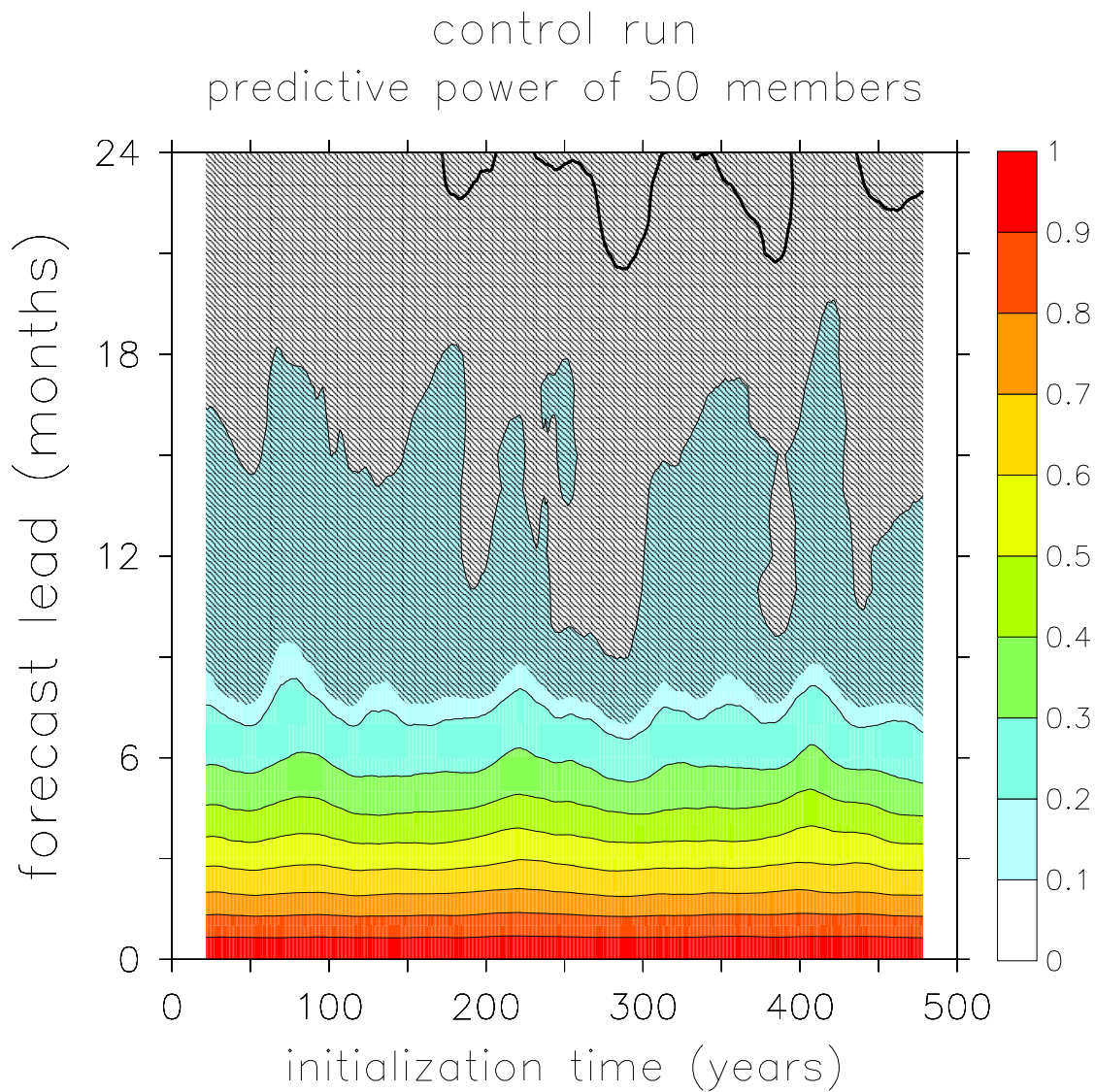
Figure 7.23: Predictive power (PP) of 50 ensemble members, in the control run of the stochastic intermediate model. Horizontal axis is the model initialization time in years. Vertical axis is the forecast lead time. Contours indicate the PP, which has been smoothed in time to eliminate amplitude modulations at periods shorter than 50 years. Hatching indicates regions of insignificant PP, where the probability of positive PP is less than 95%.
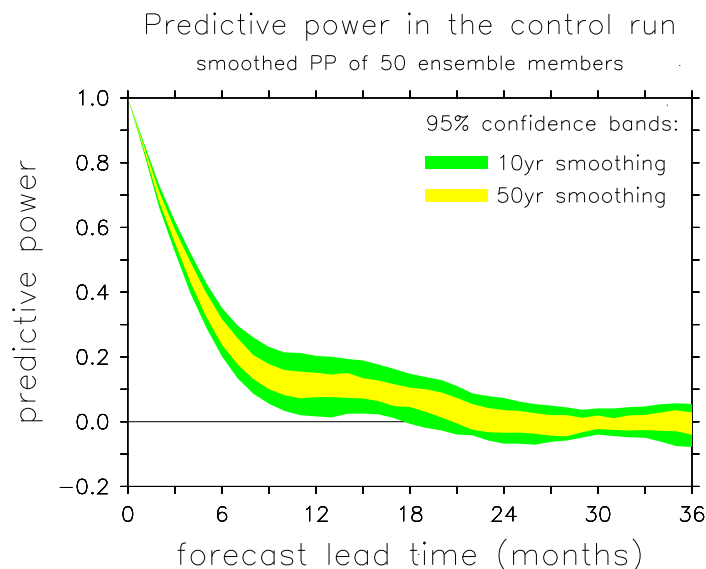
Figure 7.24: Smoothed predictive power (PP) of zonal-mean equatorial (2°S–2°N) SST anomalies in the control run of the stochastic intermediate model. The shaded bands are 95% confidence intervals for PP smoothed by a low-pass filter that eliminates PP variations at periods shorter than 10 years (green) or 50 years (yellow).

and between the models and observations. Uncoupled atmosphere or ocean GCMs, forced by erroneous analyses and tuned to reproduce erroneous analyses, may drift toward an erroneous climate when coupled and thereby alter the simulated ENSO.

7.4 Hybrid coupled GCM experiments

Having found a significant impact of the background state on ENSO in the intermediate model, we now ask: Does a coupled GCM exhibit similar sensitivity?

7.4.1 Design of the experiments

To answer this question, we turn to a hybrid coupled model consisting of an ocean GCM coupled to a statistical atmosphere (Appendix F). Compared to the intermediate model, the ocean GCM is a much more sophisticated treatment of ocean dynamics and mixing, with full nonlinearity and a seasonally-varying background state. The statistical atmosphere in this case includes a nonlocal representation of both the wind stress and the surface heat fluxes, but supports only a single degree of freedom and so cannot represent propagating features or changes in the stress anomaly patterns.

The hybrid GCM is roughly 10,000 times more expensive to run than the intermediate model, so we must choose our experiments carefully. Fortunately, the intermediate model results offer useful guidance in this regard. Based on Section 7.1, the climate parameter of greatest interest appears to be the strength of the equatorial zonal stress, which can

Figure 7.25: Predictive power as the equatorial trade winds gradually weaken. Horizontal axis indicates the amplitude of the imposed zonal stress. Hatching that ramps up to the right indicates regions that are within the 95% confidence bounds for PP in the control run. Otherwise as in Fig. 7.23.

stand in for a wide range of possible climate changes as far as ENSO is concerned. Second, from Section 7.3 it appears that many of the ENSO changes observed in the most realistic stochastic regime tend to be evident even when no noise is present, so we can forgo long stochastic runs in the HGCM.

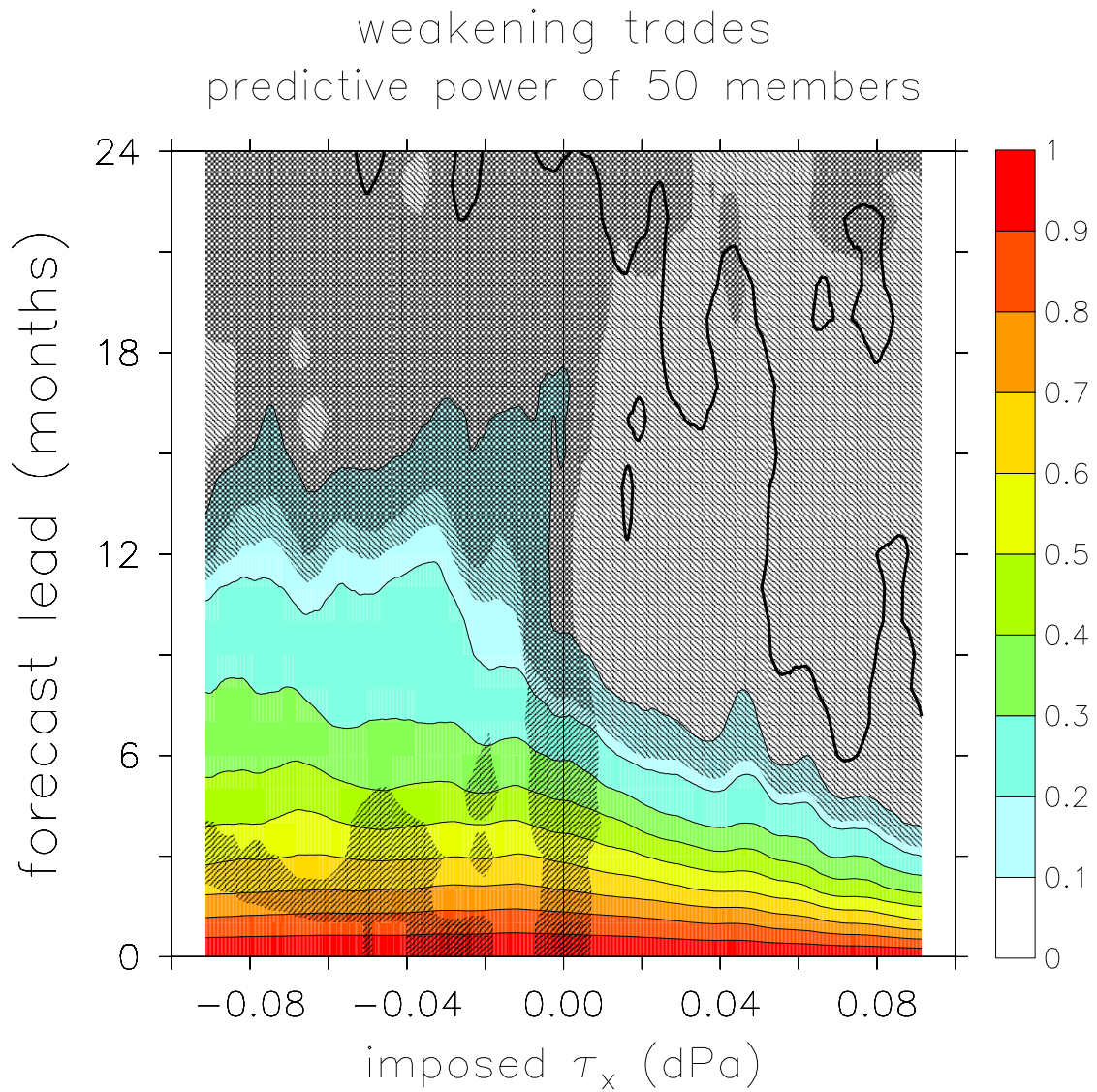Thus we perform two perturbation experiments, subjecting the HGCM to a zonal wind stress perturbation which is constant in time and has the spatial form (5.3) with $L_x = 40°$, $L_y = 15°$, and an equatorial maximum of $\widetilde{\tau_x^*} = \pm 0.1$ dPa at longitude $x_0 = 140°$W. The GCM is spun up for 4 years, and the subsequent 16 years are used to compute a monthly climatology that is subtracted from the total fields to yield monthly anomalies. (The climatologies for these experiments were described in Chapter 5.) Advection terms are computed on the model grid from the monthly-mean climatology and anomalies, and then averaged over the top 50 m of the ocean. Subtracting the vertically-averaged total advection and surface heat flux terms from the total temperature tendency then gives a residual heating, which is assumed to arise from high-frequency mixing. Finally, the advection, surface flux, and mixing fields are averaged onto a coarse ($2°$ lat $\times$ $5.625°$ lon) grid for ease of comparison with the intermediate model.

7.4.2   Overview of the equatorial-trades prototype

Equatorial SST anomalies

Fig. 7.26 shows the equatorial evolution of SST anomalies in the control and perturbed HGCM cases, beginning four years after initialization. The control exhibits a sustained oscillation with a period of about 3.3 years, a peak-to-peak NINO3 SSTA amplitude of about $2.3°$C, and westward propagation of SST anomalies in the central Pacific. For strengthened trades, the model ENSO is damped and has a slightly shorter period of 3.1 years. For weakened trades, the HGCM exhibits a sustained series of long warm events punctuated every 5.5 years by short, strong cold events, which is very similar to the behavior of the intermediate model at high coupling (Fig. 7.27).

Heat budget phasors

What is responsible for these changes in behavior? The phasor diagrams in Fig. 7.26 indicate the relative roles of advection, surface heat fluxes, and mixing in the evolution of zonal-mean SST anomalies in the hybrid coupled GCM. The diagrams are prepared as in Section 7.1.2, except that here "m" refers to the background state of the altered model climatology (as opposed to the control climatology), and "p" refers to perturbations from this altered background state. Thus changes in the "uptm" term, for example, represent changes in both the mean SST gradient and the anomalous zonal current variability.

In the control case, the primary terms affecting the temperature of the top 50 m of the ocean are the surface flux, $-\overline{w}\partial_z T'$, and $-u'\partial_x \overline{T}$. The surface flux provides a strong damping, which lags the SSTA slightly and so facilitates the transition between warm and cold phases. The $-\overline{w}\partial_z T'$ term is largely responsible for maintaining the oscillation amplitude in the face of damping by the surface flux. The $-u'\partial_x \overline{T}$ term, which is nearly in quadrature with SSTA, plays a strong transitioning role and is the largest factor in determining the oscillation period.
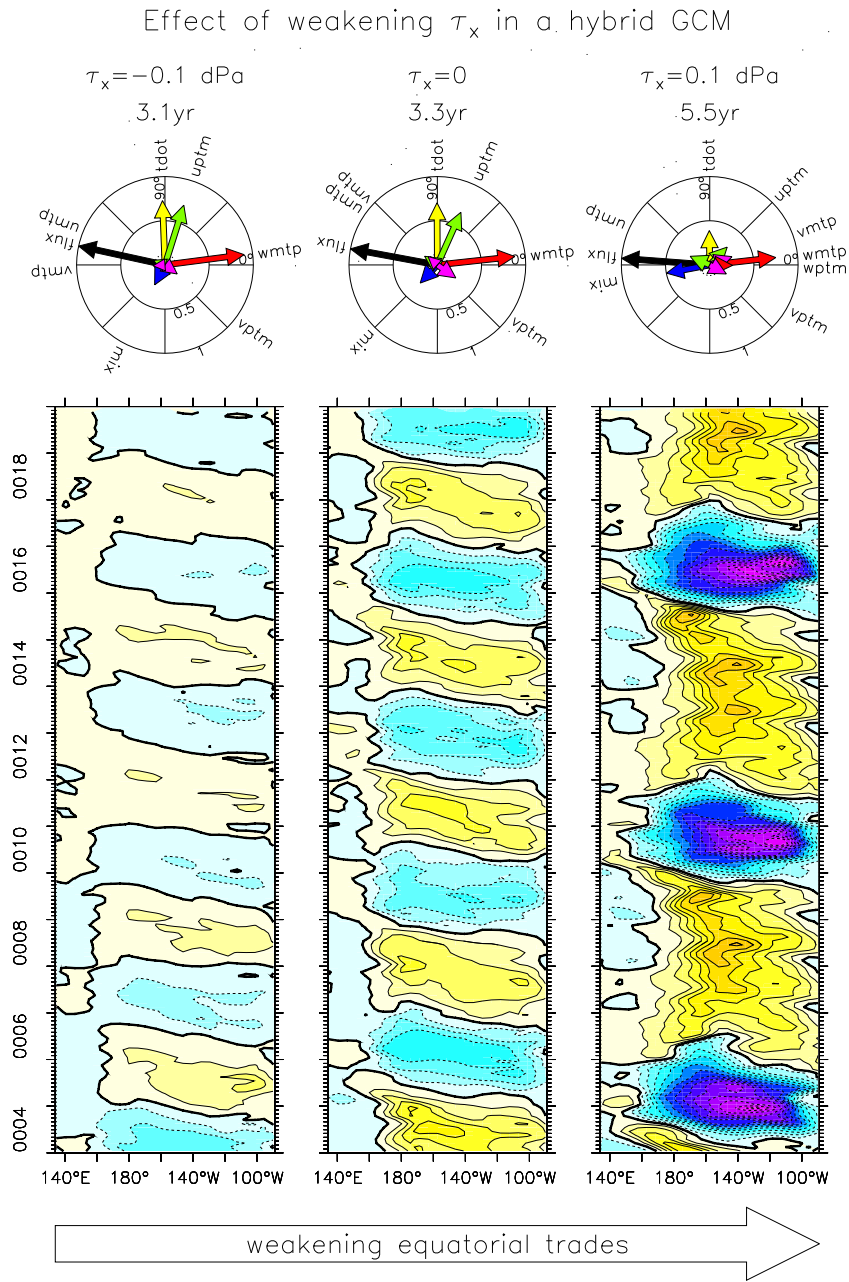
Figure 7.26: Change in ENSO due to a change in mean trade winds, as simulated by a hybrid coupled GCM. Time-longitude plots (bottom row) show the equatorial (2°S–2°N) evolution of SST anomalies, for a period of 16 years beginning four years after initialization. Contour interval is 0.5°C, with a thick line at 0°C; warm (cool) colors indicate positive (negative) anomalies. Labels at top indicate the amplitude of the imposed climate perturbation (the trades winds weaken to the right) and the oscillation period. Phasors (middle row) show the amplitude (relative to surface heat flux) and phase lead (relative to local SSTA) of the temperature tendency terms, averaged zonally across the basin in the equatorial band.
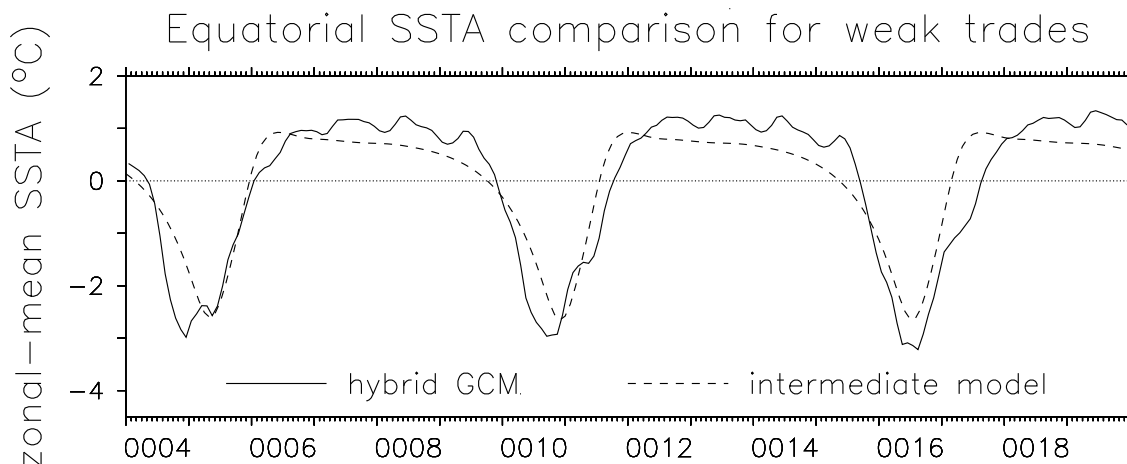
Figure 7.27: Comparison of zonal-mean equatorial (2°S–2°N) SST anomalies from two models. Solid line corresponds to the GCM weak-trades case; dashed line corresponds to the intermediate model with $\mu = 1.2$ and imposed zonally-constant westerly stress with peak amplitude 0.011 dPa at the equator. Horizontal axis indicates years since initialization.

In the strong-trades case, the zonal-mean heat budget is only subtly changed from the control case. A slight weakening of $-v'\partial_y\overline{T}$ reduces the coupled instability relative to the control, and is responsible for the gradual damping of the oscillation. The weakening of $-v'\partial_y\overline{T}$ also reduces its anti-transitioning effect, which along with the strengthening of $-u'\partial_x\overline{T}$ and the increased phase lead of $-\overline{w}\partial_z T'$ ahead of SSTA, is responsible for the slightly shorter period relative to the control case.

The weak-trades case, on the other hand, differs markedly from the control. The weakening of the climatological cold tongue in the east greatly reduces the transitioning role of zonal advection during warm events, which contributes to the lengthening of the oscillation period. Both $-w'\partial_z\overline{T}$ and $-\overline{v}\partial_y T'$ become important destabilizers, opposing the damping of equatorial SSTAs by mixing and $-\overline{u}\partial_x T'$. It is clear from the skewness of the oscillation that nonlinearities are playing a key role in this case.

7.4.3 Evolution of the equatorial vertical structure

What is going on below the surface to cause these changes in the mechanism and behavior of the HGCM ENSO? In this section we examine vertical slices of the simulated equatorial fields along the equator, exactly as in the intermediate model case. We will show that there are several key differences between the models in how the equatorial structure of ENSO responds to changes in the climatology.

Control run

Fig. 7.28 shows equatorial snapshots from the HGCM control run, at 3-month intervals beginning in January of year 7. The story begins with anomalous eastward currents and an anomalously deep thermocline all along the equator. Eastward advection of the warm pool
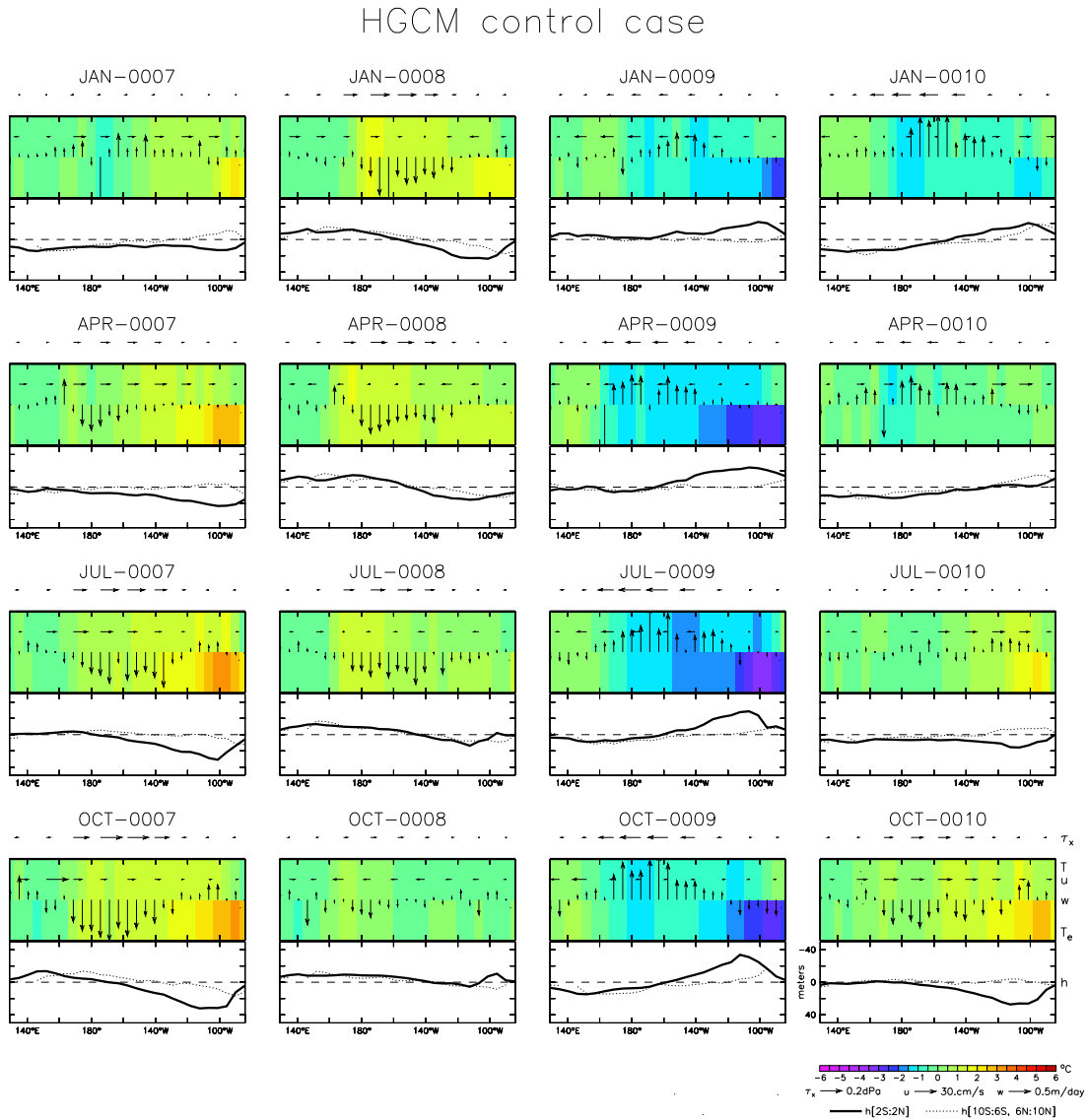
Figure 7.28: Equatorial snapshots at three-month intervals from the HGCM control case. Time flows down each column then left to right. Bottom right panel gives contour/vector keys for all panels. Vectors indicate anomalies of (top to bottom) zonal surface stress, average zonal velocity of the top 50 m of the ocean, and upwelling velocity at 50 m depth. Shading indicates the anomalous temperature in the well-mixed surface layer (top) and at 50 m depth (bottom). Bottom subpanel shows the anomalous depth of the 20°C isotherm (ordinate reversed), at the equator (2°S–2°N, solid) and off-equator (6–10° N/S, dotted).

and warmer entrainment into the mixed layer leads to a warming of the central and eastern Pacific, which then incites westerly stress anomalies over the central basin. These stress anomalies induce anomalous downwelling in the central basin and enhance the deepening of the thermocline in the east, completing a positive feedback loop that launches the system into a warm event.

Meanwhile, the thermocline begins to shoal in the west and off-equator in October of year 7, as upwelling Rossby signals arrive from the region of anomalous stress forcing. Gradually, this off-equatorial shoaling draws heat content from the equatorial waveguide along the western boundary. A reversal of the equatorial current anomalies begins in the eastern Pacific around January of year 8, and then spreads westward, cooling the surface and weakening the westerly stress anomalies. This reduces the thermocline slope and shoals the thermocline in the east, so that cooler water is entrained into the eastern Pacific mixed layer (October of year 8). As the westward current anomalies and shallow thermocline continue to cool the mixed layer past the climatological equilibrium, the system is propelled into a cold event, which then evolves in the opposite sense as the warm event.

Thus ENSO in the HGCM control run appears to be largely of the "recharge" or "delayed oscillator" type, with a period set by slow ocean adjustment via internal waves. Elements of "SST mode" behavior are also evident, such as in the westward-propagating SST anomalies which lag behind similarly-propagating the zonal current anomalies. The control ENSO is thus a hybrid mode, with meridional recharge providing the "overshoot" necessary to initiate events, but with coupled surface dynamics determining the subsequent spatial structure and propagation of the anomalies.

Several differences are evident between the HGCM ENSO and that in the intermediate model. The HGCM does not exhibit coherent westward propagation of off-equatorial thermocline depth anomalies, presumably due to the downward propagation of Rossby waves emerging from the eastern boundary. The thermocline depth anomalies in the western Pacific are also weaker in the HGCM, since in nonlinear balance the deep warm layer in the west requires less of a surface slope to balance the wind stress than does a linear active-layer model (Section 4.2.1). In the western and central Pacific, the HGCM temperature anomaly at 50 m generally tracks closely to the SST anomaly due to the deep mixed layer there; the intermediate model, in contrast, often showed substantial differences developing between T_e' and T' in the west, which led to overly strong SSTA-damping due to mean upwelling.

Case with strong mean trades

The GCM case with strengthened trades evolves in a manner so similar to the control run that scaled equatorial snapshots for the two cases look nearly identical. We therefore postpone discussion of this case to Section 7.4.4.

Case with weak mean trades

Fig. 7.29 shows equatorial snapshots from the hybrid GCM case with weakened trades, beginning in January of year 6. The warm event is sustained for nearly 3.5 years, during which time there are strong equatorial westerly stress anomalies, downwelling anomalies,
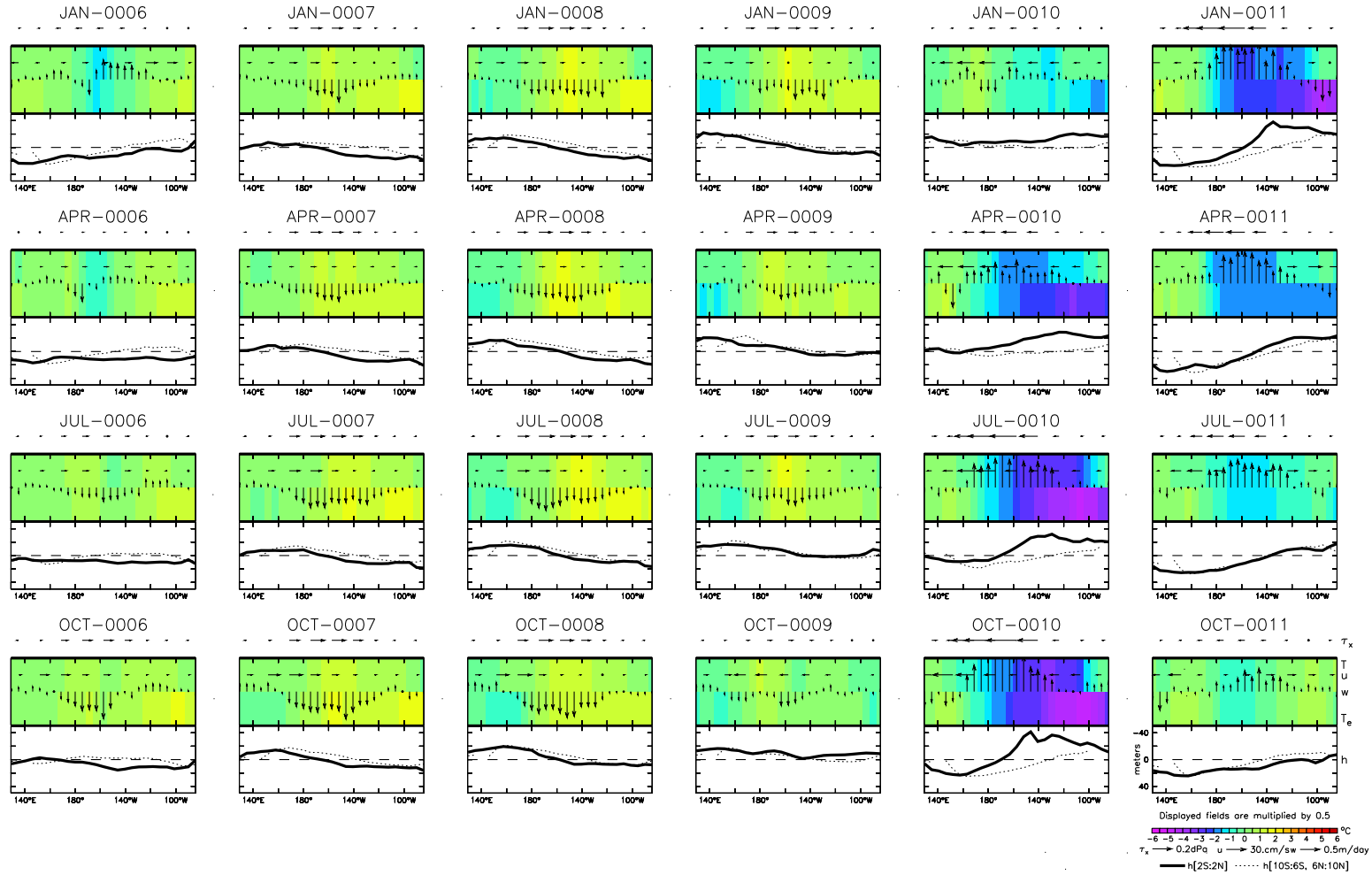
HGCM weak-trades case

Figure 7.29: Equatorial snapshots at three-month intervals from the HGCM case with weakened trades ($\widetilde{\tau^*_x} = 0.1$ dPa). Otherwise as in Fig. 7.28.

and eastward current anomalies in the central Pacific, and a deepened thermocline in the east. An east-west sloshing of the SST anomalies is also apparent during the warm event, as the SSTAs are advected by the seasonally-varying mixed-layer currents, which are eastward in boreal spring and early summer but westward the rest of the year.

The continued presence of westerly stress anomalies slowly generates a sizable shoaling of the off-equatorial thermocline in west, which gradually drains heat content from the equatorial band along the western boundary. This can have only a limited effect the SST anomaly, however, since total upwelling is nearly shut off and there is only a weak zonal SST gradient upon which the zonal current anomalies can act. The warm event is thus prolonged, decaying slowly via surface fluxes, until eventually the warm surface temperatures erode and the trade easterlies are reestablished.

As the westerly anomalies weaken, the equatorial zonal current anomalies reverse and the equatorial thermocline shoals in the east (October of year 9), bringing an end to the warm event. The strengthening of the easterly stress ignites an explosive cooling, as fresh upwelling begins to act on an ever-increasing vertical temperature gradient in the east. Meanwhile, the paucity of heat content in the off-equatorial western basin continues to siphon mass out of the equatorial band, further shoaling the equatorial thermocline and enhancing the westward advection of the cold tongue. A combination of strong upwelling, strong westward currents, and a strong shoaling of the thermocline in the east produces a sizable cold event which quickly recharges the heat content in the off-equatorial western Pacific. During these strong cold events, energetic tropical instability waves develop just off-equator, and contribute to the restoration of warm temperatures by stirring in warm off-equatorial water. The cooling peaks as the westward current anomalies weaken (October of year 9), and then terminates as the current anomalies reverse and the thermocline deepens in the east (October of year 11).

Thus nonlinearities appear to play a key role in the HGCM ENSO for weak climatological trades. The disappearance of upwelling and the zonal SST contrast during warm events is important for lengthening the oscillation period, since it delays the surface adjustment to changes in the meridional structure of the thermocline. This delay is also important for generating the strong cold events that quickly recharge the equatorial heat content, since it allows excessive negative heat content anomalies to develop off-equator during warm events.

This nonlinear delay mechanism is more severe than in the weak-trades case of the intermediate model at standard coupling, but it does play a significant role in the latter at higher coupling where the equatorial easterly stress disappears during warm events (Figs.7.9 and 7.27). Such a comparison is probably appropriate, since the intermediate model at "normal" trades can only support sustained oscillations (such as those in the HGCM control run) when the coupling is stronger than the standard value. The nonlinearity responsible for the HGCM cold-skewness at weak trades is also echoed in the stochastic intermediate model at standard coupling, where the SSTA distribution goes from warm-skew to cold-skew as the trades weaken (Fig. 7.16). In a broader sense, the nonlinearity associated with the weakening of the *climatological* zonal SST gradient is even responsible for the increase in the period of the intermediate model ENSO at small amplitudes (Fig. 7.1), since as the climatological trades go from "strong" to "normal" the transitioning effect of $-u'\partial_x\overline{T}$ is

reduced. Thus many elements of the HGCM ENSO response to changes in the equatorial trades actually mirror those found in the intermediate model.

7.4.4 Change in the mixed layer heat budget

What is the quantitative change in the HGCM ENSO mechanism as climate changes, and how is it related to the intermediate model? Fig. 7.30 shows the mixed layer heat budget along the equator for each of the three HGCM cases. As in the intermediate model, the change in the strength of the climatological trades induces substantial changes in the ENSO mechanism along the equator. A glance at Fig. 7.30 shows that these changes are complex and spatially-dependent. We shall consider them one at a time, at four key longitudes along the equator.

110°W

In the far eastern Pacific of the HGCM control run, $-\overline{w}\partial_z T'$ and $-\overline{v}\partial_y T'$ act in concert as destabilizers, maintaining the oscillation amplitude in the face of surface heat fluxes and mixing. Since the destabilizers lag SSTA slightly they delay the transitions between events, which serves to lengthen the ENSO period. The $-u'\partial_x \overline{T}$ term, on the other hand, is nearly in quadrature with local SSTA and thus plays a strong transitioning role. Note that the surface flux and mixing terms are also important transitioners, since the damping associated with them lags SSTA by 20–30°. The $-w'\partial_z \overline{T}$ and $-v'\partial_y \overline{T}$ terms, which are rather weak at 110°W, both act to damp the local oscillation but play opposite roles in the transition.

Some differences from the intermediate model control run (Fig. 7.6) are already evident. In the intermediate model at 110°W, zonal advection and mixing were negligible, and the surface flux played only a damping role, meridional advection was less important, and $-\overline{w}\partial_z T'$ led instead of lagged SSTA. The heat budget in the HGCM is more reminiscent of the intermediate model *strong-trades case* between 110–140°W, which makes sense since the HGCM control run is known to have an overly strong cold tongue at the equator (Fig. F.4h).

In the HGCM strong-trades case, $-\overline{w}\partial_z T'$ plays a larger role, and it along with $-\overline{v}\partial_y T'$ become more purely destabilizing than in the control case. This, together with the slightly stronger $-u'\partial_x \overline{T}$, accelerates the transitioning mechanism and slightly increases the oscillation frequency. The frequency increase is largely opposed by the change in mixing, which strengthens and becomes a slight anti-transitioner. The increased damping of the ENSO oscillation at strong trades results from increased dissipation of equatorial anomalies by mixing, probably related to stronger TIWs associated with the enhanced current shear at strong trades.

In the weak-trades case, $-\overline{w}\partial_z T'$ is weaker and more purely destabilizing than in the control. The $-u'\partial_x \overline{T}$ term also plays less of a transitioning role due to the weakened zonal SST gradient; surprisingly, the strongest transitioning term is now the surface heat flux. The precise period of ENSO again depends on a subtle balance, with significant contributions from mixing (a transitioner) and $-w'\partial_z \overline{T}$ (an anti-transitioner). The reduced
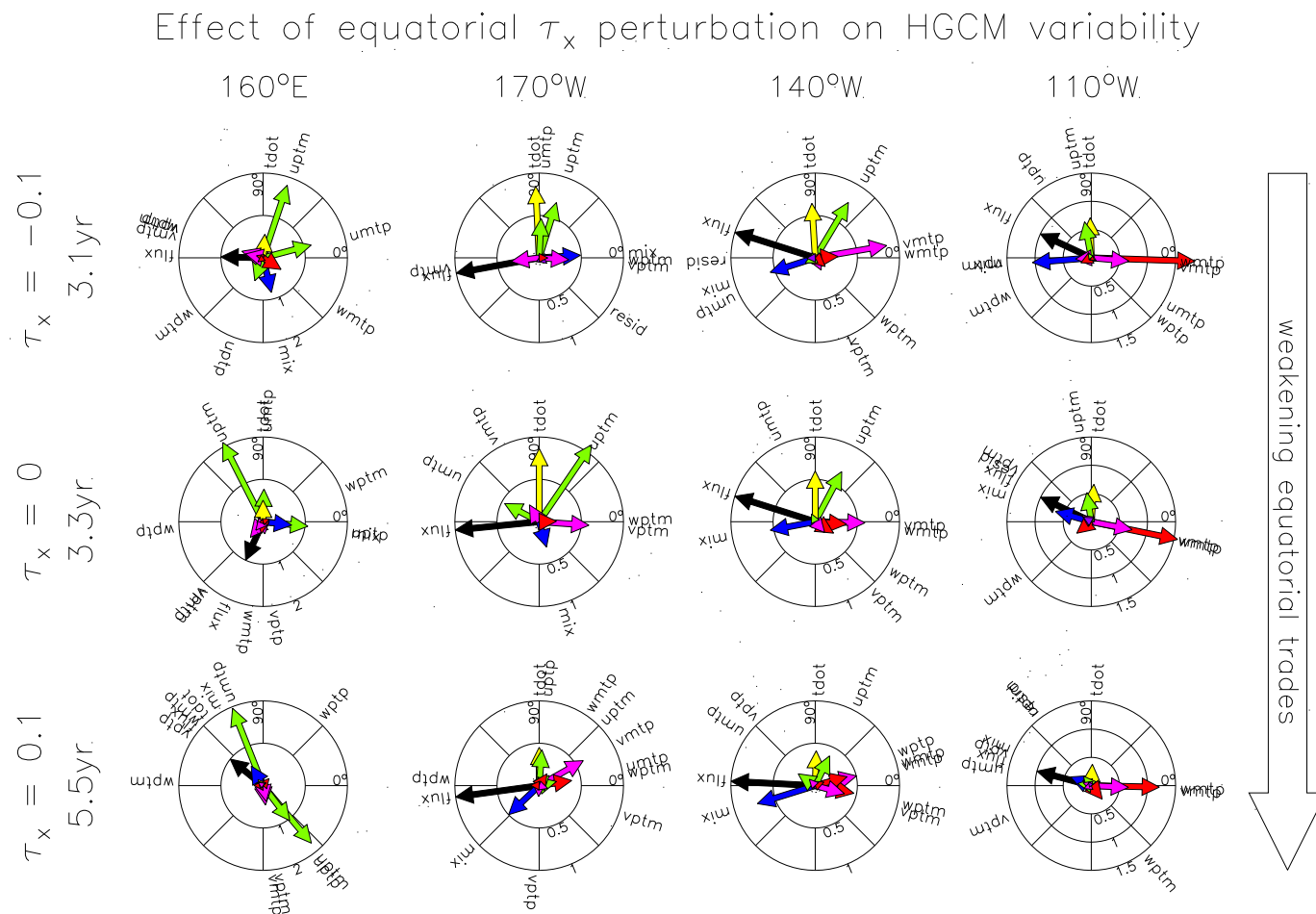
Figure 7.30: Comparison of equatorial mixed layer heat budget phasors for the hybrid GCM cases of Figs. 7.28–7.29. The phasor diagrams are as described in Fig. 7.1 and Section 7.1.2. Middle row is the control case, top row is the case with strengthened trades ($\widetilde{\overline{\tau}}_x^* = -0.1$ dPa), bottom row is the case with weakened trades ($\widetilde{\overline{\tau}}_x^* = 0.1$ dPa). Each column corresponds to a given longitude, progressing from west on the left to east on the right. Diagrams at the same location, i.e. within a given column, have the same scale.

lag of $-w'\partial_z\overline{T}$ behind SSTA has also changed the role of $-w'\partial_z\overline{T}$ from a damper to a destabilizer.

140°W

In the central/eastern Pacific, the HGCM control run shows a smaller role for $-\overline{w}\partial_z T'$ than in the far eastern Pacific. The destabilization is now mostly due to $-\overline{v}\partial_y T'$, with assistance from $-\overline{w}\partial_z T'$, $-u'\partial_x\overline{T}$, $-w'\partial_z\overline{T}$, and $-v'\partial_y\overline{T}$ that balances the damping by the surface fluxes and mixing. The $-u'\partial_x\overline{T}$ term plays a more active role in the transition than it did farther east, which along with the surface flux acts to balance the now anti-transitioning effect of the mixing.

For strong trades, the strong meridional asymmetry of the cold tongue enhances $-\overline{v}\partial_y T'$, which is not only the top destabilizer at 140°W but is also an important transitioner. The $-u'\partial_x\overline{T}$ term is also stronger than in the control, which helps to shorten the oscillation period slightly. There is little change in the roles of the surface fluxes and mixing relative to the control, so the damping of ENSO in the strong-trades case appears to result from more subtle changes, including reduced $-\overline{w}\partial_z T'$ and increased $-\overline{u}\partial_x T'$.

The heat budget of the weak-trades case is even more complex. The $-\overline{w}\partial_z T'$, $-\overline{v}\partial_y T'$, $-w'\partial_z\overline{T}$, and $-v'\partial_y\overline{T}$ terms have roughly the same magnitude and all contribute to the destabilization. The $-u'\partial_x\overline{T}$ term is weaker relative to the surface flux than in the control, though it is still the dominant transitioner at 140°W. The increased period in this case is mainly due to the weakening of the $-u'\partial_x\overline{T}$ transitioner, a reduction in the phase lag of the surface flux damping, and to stronger mixing (which has an anti-transitioning effect). The $-\overline{u}\partial_x T'$ term also enters as an important local damper and transitioner at 140°W, as temperature anomalies are advected slowly westward by the mean currents.

170°W

In the western/central Pacific, the HGCM control run has both a strong climatological westward SST gradient and strong interannual zonal current variations, so there is a stronger role for $-u'\partial_x\overline{T}$ than further east. This term is by far the most important transitioner, and is even the most important destabilizer (slightly ahead of $-v'\partial_y\overline{T}$). The $-\overline{u}\partial_x T'$ and $-\overline{v}\partial_y T'$ terms also appear as damping/transitioning terms. Note that the surface flux and mixing have taken on stronger anti-transitioning roles at this longitude. The $-\overline{w}\partial_z T'$ term no longer plays a role, since at this longitude the thermocline depth does not fluctuate much, and the thermocline is so deep that it has little influence on the temperature of water entrained into the mixed layer.

In the strong-trades case, $-u'\partial_x\overline{T}$ is weaker and plays a more purely transitioning role than in the control run. The only other significant transitioner is $-\overline{u}\partial_x T'$, which also more of a transitioner than it was in the control case. The effect of mixing is stronger than in the control, due to stronger temperature gradients and stronger TIWs in the strong-trades case. Since increased mixing during cold events imports cold water from farther east, mixing acts as a destabilizer at 170°W, which assists $-v'\partial_y\overline{T}$ in the face of damping by $-\overline{v}\partial_y T'$ and strong surface fluxes.

In the weak-trades case, $-u'\partial_x\overline{T}$ is much weaker than in the control. For weak trades, zonal advection occurs almost exclusively during the transitions into cold events, when a strong westward SST gradient appears at 170°W; the rest of the time the zonal SST gradient is very weak at this longitude. This nonlinearity is evident in the large role for $-u'\partial_x T'$, which is nearly identical to the total temperature tendency (since the remaining terms, though large, almost cancel). Nonlinearity is thus very important to the oscillation in the weak-trades case. The transition at this longitude is assisted by $-\overline{v}\partial_y T'$ and opposed by mixing and surface fluxes. The $-w'\partial_z\overline{T}$ term plays a significant role as a destabilizer, and a host of other terms ($-\overline{u}\partial_x T'$, $-\overline{w}\partial_z T'$, $-v'\partial_y T'$) also contribute to the destabilization and transition at 170°W.

160°E

In the western Pacific, the HGCM control run once again shows a large transitioning role for $-u'\partial_x\overline{T}$. In contrast to further east, however, $-u'\partial_x\overline{T}$ also acts as a damper since it leads local SSTAs by more than 90°. In this case the damping by $-u'\partial_x\overline{T}$ is even stronger than that due to the surface heat flux, which has now taken on more of an anti-transitioning role along with meridional and vertical advection. Other zonal advective terms also contribute to the oscillation: $-\overline{u}\partial_x T'$ is a transitioner while $-u'\partial_x T'$ is a destabilizer. Mixing also contributes to local growth by importing anomalous SSTAs from farther east. Thus the total SSTA tendency in the western Pacific of the control run is but a small residual of many large terms that nearly balance.

In the strong-trades case, $-u'\partial_x\overline{T}$ is more of a destabilizer at 160°E than in the control. The $-u'\partial_x T'$ term also plays a different role than in the control run, acting as an anti-transitioner which opposes $-u'\partial_x\overline{T}$ to a small extent. The $-\overline{u}\partial_x T'$ term contributes slightly to the transition, but in contrast to the control plays a much larger role as a destabilizer. The $-\overline{w}\partial_z T'$ term has a dual destabilizing/anti-transitioning effect which is essentially canceled by meridional advection. Mixing is an anti-transitioner, again in contrast to the control run where it was a destabilizer.

In the weak-trades case, the SSTA hardly varies at all at 160°E, except during La Niñas when cold water encroaches from the east. This balance results from a near-perfect cancellation between $-u'\partial_x\overline{T}$, $-u'\partial_x T'$, $-v'\partial_y\overline{T}$, and $-\overline{v}\partial_y T'$ on the one hand (which act as destabilizers and anti-transitioners), and $-\overline{u}\partial_x T'$, surface flux, and mixing on the other hand (which act as stabilizers and transitioners). Note that the role of the surface flux in this case is very different from in the control run.

Heat budget summary

There are several general points to take from Fig. 7.30. The mixed layer heat budget in the hybrid coupled GCM is even more complex than in the intermediate model, with significant contributions from surface heat fluxes, mixing, and full three-dimensional advection everywhere along the equator. The surface fluxes and mixing, in particular, are first-order terms and both show substantial phase changes relative to SSTA at different longitudes and between the control and perturbed-trades cases. This is in contrast to the intermediate model, which assumes simply that surface fluxes act as a linear damping of

local SSTAs. The contribution of fluxes and mixing to the ENSO frequency in the HGCM illustrates the complexity of modeling ENSO, since both of these processes involve highly nonlinear and small-scale variability that is heavily parameterized in the current generation of coupled GCMs. This may be yet another reason why different models simulate such different ENSOs, and why they often show poor agreement with observations.

In the HGCM, the strong-trades case evolves in much the same way as the control run, and its heat budget closely mirrors that of the control, apart from a larger role for zonal advection in the east and a more complex array of differences in the western/central Pacific. The weak-trades case is very different from the control, with a decreased role for zonal advection and with nonlinearities playing a key role in determining the oscillation period and skewness.

7.5 Chapter summary and discussion

This chapter has examined the sensitivity of ENSO to changes in the climatological background state, using a hierarchy of ocean-atmosphere models. In the simplest case, an intermediate model is perturbed slightly and then allowed to evolve under the influence of climatological trades of varying strengths. The results show that as the trades weaken, the oscillation period increases and the pattern of SST anomalies shifts eastward. Oscillations are rapidly damped when the trades are weak, but are less damped at intermediate and strong trades. For weak trades, a weakened zonal SST gradient inhibits the transitioning effect of zonal advection, and the increased depth of the thermocline in the east inhibits the growth of SST anomalies by desensitizing the entrainment temperature to vertical motions of the thermocline. For strong trades, the increased zonal SST gradient enhances the transitioning effect of zonal advection, while the outcropping of the thermocline in the east causes the SST variability to shift westward into the central basin. Similar results are found for other types of climate perturbations, whose primary effect is to set into motion coupled feedbacks that set the climatological strength of the equatorial trades.

The climate-induced changes of stability and period in the intermediate model are echoed in the nonlinear regime. As the air-sea coupling increases, a sustained ENSO appears first at intermediate and strong trades, just where control case showed the weakest damping of ENSO in response to small kicks; and as in the control run, the period of the sustained ENSO lengthens as the trades weaken. For strong wind stress kicks, a new wrinkle is added by short-term transients, which are strong relative to the subsequent modal oscillations and are heavily influenced by nonlinearity. The transients too are affected by the climatology, but they bear little direct relation to the properties of the least-damped mode.

In the stochastic regime, too, climate has a significant impact on ENSO: As the trades weaken, ENSO shifts to longer periods, weaker amplitudes, and farther east, and ENSO forecasts lose predictive power. Whether these ENSO changes can be detected in the face of natural variability depends on both the magnitude of climate change and the length of the timeseries. Wind stress changes of the magnitude seen in observations over the past century, and on the order of the differences between observational analyses, appear to be just at the edge of detectability for ENSO changes in 50-year timeseries. If ENSO is as

strongly influenced by random events as the intermediate model, then interdecadal ENSO changes may be difficult to attribute to changes in the climatology. Paleodata, such as coral records and deep-ocean sediments, may be the only records long enough to cope with the significance issue and thus may prove invaluable for discerning real-world ENSO/climate relationships. Such data, of course, are beset with their own special problems: they are generally only local and indirect measures of ENSO, they may be confounded with non-ENSO effects, and it can be difficult to establish a reliable time axis for the data.

A change in the equatorial trades is also found to have a large effect on ENSO in a hybrid coupled GCM. As in the intermediate model, as the trades weaken the oscillation becomes more skewed towards cold events and shows an increased period. The HGCM is most reminiscent of the intermediate model high coupling and strengthened trades, where the intermediate model mimics the sustained variability and overly-strong cold tongue found in the HGCM. In this case the period at weak trades is strongly affected by nonlinearities, in particular the elimination of the cold tongue and equatorial upwelling during warm events, which delay the transitions from warm to cold events.

The indirect mapping between the HGCM and intermediate model underscores the importance of a broad view of ENSO, one which encompasses both its climate sensitivity and model-dependence. Well-thought-out sensitivity maps for sophisticated coupled GCMs, though expensive, would likely be invaluable tools for diagnosing problems; and similar maps for the real world (constructed from paleodata) would also be beneficial for the modeling community. Understanding these many sensitivities may well be the key to improving ENSO forecasting in the future.

Chapter 8

Conclusion

I hate quotations. Tell me what you know.

Ralph Waldo Emerson, *Journal*, 1822

8.1 Summary

8.1.1 The questions

The central question of this dissertation has been: *How do changes in the tropical Pacific climatology affect ENSO?* This question was motivated by the need to understand the wide range of ENSO simulations among general circulation models, the need to understand historical and paleo changes in ENSO, and the desire to predict what may happen to ENSO in the future.

The path to the answer has spawned a number of secondary questions: How have the tropical Pacific climatology and ENSO variability changed over the observed record, and what are the uncertainties in these changes? How should one model the climatology and ENSO, and how sensitive is the model to its uncertain parameters? How do different types of plausible changes affect the climatology, and what is the role of air-sea coupling in the response? How do these climate changes affect the mechanism and behavior of ENSO? What is the role of transients and nonlinearity, and how detectable are the ENSO changes in the stochastic context?

8.1.2 The answers

We have proposed answers to all of these questions, based on a detailed analysis of the observations, exploration of the ENSO sensitivity to climate in a hierarchy of theoretical and numerical models, and interpretation of the model results in terms of the mixed layer energy budget and coupled mode theory.

An analysis of observations (Chapter 2) indicated large differences among the available wind stress analyses. We conclude that the true stresses, their decadal changes, and their

dependence on tropical SSTs remain very uncertain. These differences should be kept in mind when arguing for effects of climate changes based on recent ENSO behavior, when forcing ocean models for tuning and analysis, or when building statistical atmosphere models from the available stress products. Better understanding of what *really* happened to the stresses over the past four decades must come from improved analyses, including consistency checks with stress-interactive variables like the oceanic thermal structure.

In Chapter 3 a statistical atmosphere model was constructed using what appear to be the most reliable stress data (FSU 1980–99). This model includes a deterministic component, which depends linearly on large-scale SST anomalies, and a stochastic component that reproduces the observed spatial correlations and variance of intraseasonal stress anomalies not linearly related to large-scale SSTs. A key result from this chapter was that the stochastic component appears to be a very important contributor to the overall stress in the real world.

In Chapter 4 an intermediate-complexity ocean model was developed and calibrated, to enable realistic simulation of the tropical Pacific climatology and ENSO using a consistent set of parameters. The statistical atmosphere was then coupled to the ocean model to yield a stochastic/dynamic hybrid that gives a reasonable simulation of observed and GCM-simulated ENSO behavior, including its spatial structure, temporal spectrum, and mechanism. To provide a context for the climate sensitivity study, the linear stability, asymptotic properties, sensitivity to noise forcing, and predictability characteristics of the coupled model were mapped over a range of important (and uncertain) model parameters. The results were then interpreted physically, to build intuition regarding ENSO behavior. A new paradigm for ENSO forecasts is suggested, which downplays the uncertainty in the initial conditions and instead focuses on the influence of future random events.

Chapter 5 presented results from idealized experiments with the intermediate model, designed to test the sensitivity of the tropical Pacific climatology to imposed long-term perturbations. These perturbations were well-motivated by observed and hypothetical future changes in the real world; they included the strength of the equatorial and off-equatorial zonal wind stress, the longitude of the equatorial zonal stress, the meridional stress in the eastern equatorial Pacific, and radiative forcing of the surface ocean. The results suggest that because coupled feedbacks tend to dominate the time-mean response, a perturbed tropical Pacific climatology generally comes to resemble either an ENSO warm state (with weakened trades and flattened thermocline) or an ENSO cold state (with enhanced trades and steeper-sloping thermocline), with different perturbations more or less efficient at forcing these changes. Similar experiments in a hybrid coupled GCM yielded qualitatively different responses than in the intermediate model, particularly for changes in radiative forcing. Both models have limitations and it is not clear which model is more representative of the real world. If the climate manifold is indeed as simple as the intermediate model suggests, then the ENSO climate-sensitivity problem is largely reduced to one of understanding the ENSO response to El Niño-like and La Niña-like backgrounds.

The warm and cold climate extremes are found to support very different modes of interannual variability, due to thermodynamic changes which control the structure of the oscillations. Changes in the climatology operate through nonlinearities to modify the coupling between components of the ENSO system, thereby altering the mechanisms that

produce SST anomalies. In Chapter 6 the effects of climate on the dominant coupled modes are illustrated by appealing to the phasing of the SST tendency terms relative to local SST. Phasor diagrams are proposed to simplify and unify the discussion of interannual coupled modes. Processes in phase with local SST produce pure growth, while those that lead SST by a quarter cycle contribute purely to the oscillation frequency. The climatology can be seen as modifying not only the relative *amplitudes* of the growth and transition mechanisms ("which tendency terms are important"), but also their *phase* relative to SST ("the role of a given tendency term").

Chapter 7 applies these ideas to altered-climate simulations of ENSO in the intermediate model and hybrid GCM. For weakened trades, the transitioning effect of zonal advection in the intermediate model is inhibited by weak zonal SST gradients, and so the oscillation has a longer period than in the control run. The oscillation pattern also shifts eastward and weakens due to the increased depth of the mean thermocline, which desensitizes the entrainment temperature to vertical motions of the thermocline. For strong trades, the opposite happens: transitions are accelerated by zonal advection on enhanced zonal SST gradients, increasing the oscillation frequency, and the outcropping of the thermocline in the east causes SST variability to shift westward. Altering the strength of the equatorial trades in the hybrid GCM also results in large changes in the ENSO behavior, but in this case nonlinearities and mixing play key roles. The GCM results appear to be related to the intermediate model behavior at high coupling, suggesting that a broad view of ENSO variability (including sensitivities to both model parameters and climate parameters) can help link together different results from disparate models.

The effects of altered climates on the ENSO period, amplitude, and zonal structure largely persist in the nonlinear, transient, and stochastic ENSO regimes, though a few important differences are noted. In the stochastic case, detectability is hindered by random ("natural") modulations that affect ENSO behavior even in the absence of climate changes. In this case, long timeseries are required for unambiguous attribution of ENSO changes to climate changes, suggesting that paleo data may be essential for solidifying our understanding of climatology/ENSO interactions in the near future.

8.1.3   Contributions

Contributions of this dissertation to the climate community include:

1. A tropical Pacific wind stress comparison, which documents the essential features, changes, and uncertainties of a critical climate field in two widely-used operational analyses.

2. A new coupled model of ENSO, which improves upon an existing widely-used class of models. The model is capable of simulating the ocean climatology as well as coupled anomalies, and is carefully calibrated using newly available climate data to yield more realistic ENSO variability in forced, coupled, and stochastic modes. The model sensitivity analysis will be a valuable guide to potential users of the model.

3. A new way of thinking about ENSO forecasts, which downplays the uncertainty of the initial conditions and instead focuses on the influence of future random events.

4. Maps of the tropical Pacific coupled equilibrium response to relevant time-mean forcings, and a physical interpretation of these maps. The similarity of the responses to different forcings suggests that the strength of the equatorial trade winds is an essential metric for the climatology.

5. Mapping and understanding of the ENSO response to altered climates, with a demonstration of the similarity of ENSO responses to different time-mean forcings. Sensitivity maps are presented for linear, nonlinear, transient, and stochastic regimes.

6. A wavelet phasor diagram that compactly summarizes the roles of time-varying tendency terms in the growth rate and frequency of an oscillation. These diagrams are powerful tools for comparing the thermodynamics of different models as a function of location, frequency, and time.

7. Quantitative evaluation of the detectability of climate-induced changes in the ENSO probability distribution, spectrum, zonal structure, and predictability, in the context of short stochastic timeseries and small forecast ensembles.

8.2 Outlook

Much work remains before the links between ENSO and the climatology of the tropical Pacific are fully understood. Several more interesting studies could be done in the intermediate model:

- A study of the climate/ENSO response to *localized* changes in surface heat fluxes, relevant to the uncertain changes in cloud radiative forcings in a greenhouse world.

- A study of the climate/ENSO response to changes in thermocline depth and dispersion, relevant to the thermocline stratification errors in GCMs and to interdecadal temperature anomalies that reach the equator from midlatitudes.

- Inclusion of a seasonally-varying background state, a more realistic model for surface heat fluxes, and seasonally-to-interannually varying wind stress noise to see how these affect the ENSO sensitivity to climate changes.

Other essential items and avenues for further research on this topic include:

- Continued expansion of the historical and paleo data archives, with improved analyses of ocean-atmosphere fields for the past century (especially for the surface wind stress and subsurface ocean).

- Consolidation of existing paleodata into a reference dataset for use by climate modelers.

- More detailed model ENSO intercomparisons, with increased emphasis on subsurface oceanic fields and the thermodynamics of the mixed layer.

- Analysis of a very long control run of a coupled GCM that simulates reasonably realistic interannual and interdecadal variability.

- Systematic climate-sensitivity studies with ENSO-resolving CGCMs, including idealized climates, paleoclimates for which proxy data exist, and climates with increased atmospheric greenhouse gas concentrations.

Studies like these should help us better understand, predict, and coexist with our ever-changing climate system. Considering the tremendous progress of the last two decades, the outlook is bright indeed.

Regression Versus a Simpler Stress Model

A simpler SVD-based statistical model of wind stress anomalies has been used by several authors (Syu and Neelin, 1995; Blanke et al., 1997; Cassou and Perigaud, 2000). In this model, the stress singular vector expansion coefficients $\widetilde{\mathbf{Y}}^*$ are assumed equal to the SST singular vector expansion coefficients $\widetilde{\mathbf{X}}^*$. This model takes the form

$$\widehat{\mathbf{Y}}_N = \widetilde{\mathbf{X}}^*_N \mathbf{B}'_N \tag{A.1}$$

which essentially replaces the regressed $\boldsymbol{\tau}'$ anomalies in Figs. 3.7–3.8 with the singular vectors of $\boldsymbol{\tau}'$ shown in Fig. 3.5.

A comparison of the regression estimate (3.26) with the estimate (A.1) is shown in Table A.1. For unfiltered stress data, the two models have nearly the same residual variance ("error") of monthly-means. On this basis, it might at first appear that the regression is not much of an improvement over (A.1). However, the regression is superior in several important ways.

First, because the wind stress is noisy, improvements in the deterministic part of the model are hard to discern in the monthly data. Filtering the stress to retain only interannual variations shows that (A.1) gives a mean square error 12% larger than the regression model for these time scales. Presumably these are the time scales most important to ENSO.

More importantly, model (A.1) assumes that the singular mode expansion coefficients are perfectly correlated. In fact, these correlations drop off rapidly after the gravest mode (Fig. A.1). For higher modes, (A.1) will overestimate the influence of SST on the wind stress by nearly a factor of two. This is why the model variance of (A.1) is nearly twice as large as the regression, and why the skill of (A.1) actually gets *worse* as the number of modes increases. Thus an important benefit of the regression (3.26) is its more accurate representation of the air-sea coupling strength.

Finally, from Table A.1 it is clear that the regression model is optimal (in a least squares sense) because the model and residual variances sum to the total variance for the unfiltered data. The regression model is close to optimal for the interannual wind stress as well. That (A.1) fits the data fairly well, even though its variance is so much greater than the optimal estimate, indicates that it is probably an overfit to the data. This problem is even more apparent for the interannual stress anomalies. Thus while (A.1) shows good

Table A.1: Analysis of variance of the 1980–1999 FSU wind stress anomalies for two different models $\widehat{\mathbf{Y}}_N$, both based on $N = 3$ modes. Results are shown for unfiltered data, and for data filtered to retain only periods greater than one year. Variances are expressed as a percentage of the total variance of the wind stress anomalies (40.8 dPa^2 unfiltered, 10.7 dPa^2 interannual). The regression model corresponds to $\widehat{\mathbf{Y}}_N = \widetilde{\mathbf{X}}_N^* \widehat{\mathbf{R}}_N$. The direct SVD model corresponds to $\widehat{\mathbf{Y}}_N = \widetilde{\mathbf{X}}_N^* \mathbf{B}_N'$.

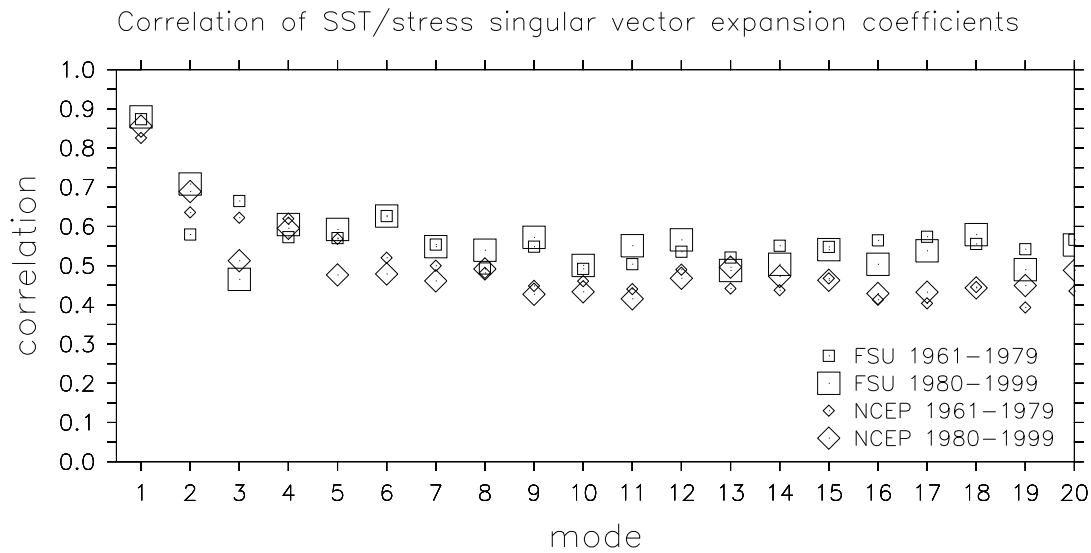|	Regression	Direct SVD
Total τ'		
model variance	13.9	25.1
residual variance	86.1	89.4
sum	100.0	114.5
Interannual τ'		
model variance	41.2	71.5
residual variance	54.8	61.6
sum	96.0	133.1

Figure A.1: Correlation of SST singular vector expansion coefficients with stress singular vector expansion coefficients.

skill in reconstructing the training data, it would perform much worse given a different realization of the noise. Obviously the purpose of the model is to forecast the unknown, not the known. Therefore we proceed using the regression estimate (3.26).

Field Significance

To determine the field significance of a collection of local hypothesis tests performed on a grid, one must find the probability of rejecting at least x of the N gridpoints at significance level p, assuming the null hypothesis is true. If this probability is small, then one may confidently reject the null hypothesis, and infer that the field as a whole was not generated by the assumed reference process.

If there were no spatial correlations in the residual, then this problem would be equivalent to finding the probability of x successes in N trials, where the probability of success in any single trial is p. If X is a hypothesized number of successes, then the binomial distribution (Wilks, 1995) gives the probability of observing $X = x$ successes:

$$Pr\{X = x\} = \binom{N}{x} p^x (1-p)^{N-x} \tag{B.1}$$

The probability of *at least* x successes is then

$$Pr\{X \geq x\} = \sum_{i=x}^{N} \binom{N}{i} p^i (1-p)^{N-i} \tag{B.2}$$

$$= 1 - \sum_{i=0}^{x-1} \binom{N}{i} p^i (1-p)^{N-i} \tag{B.3}$$

This probability is shown in Fig. B.1, using unconnected symbols, for the cases of Fig. 3.9 ($N = 324$) and Fig. 3.10 ($N = 513$ for 1961–1979, $N = 540$ for 1980–1999). In each case the probability of "success" is taken to be the local significance level, $p = 0.01$, and the number of trials N is taken to be the number of gridpoints tested.

In the presence of spatial correlation, one can redefine N to be an "effective" number of gridpoints, which decreases as the correlation increases. For the wind stress residual, assuming a conservative zonal decorrelation scale of $40°$ longitude gives $N \approx 3$. The binomial probabilities associated with this value of N are shown in Fig. 3.9 using symbols connected by lines. The figure indicates that in this spatially-correlated case, roughly two to four times as many points must be rejected by the local significance test to attain field significance.
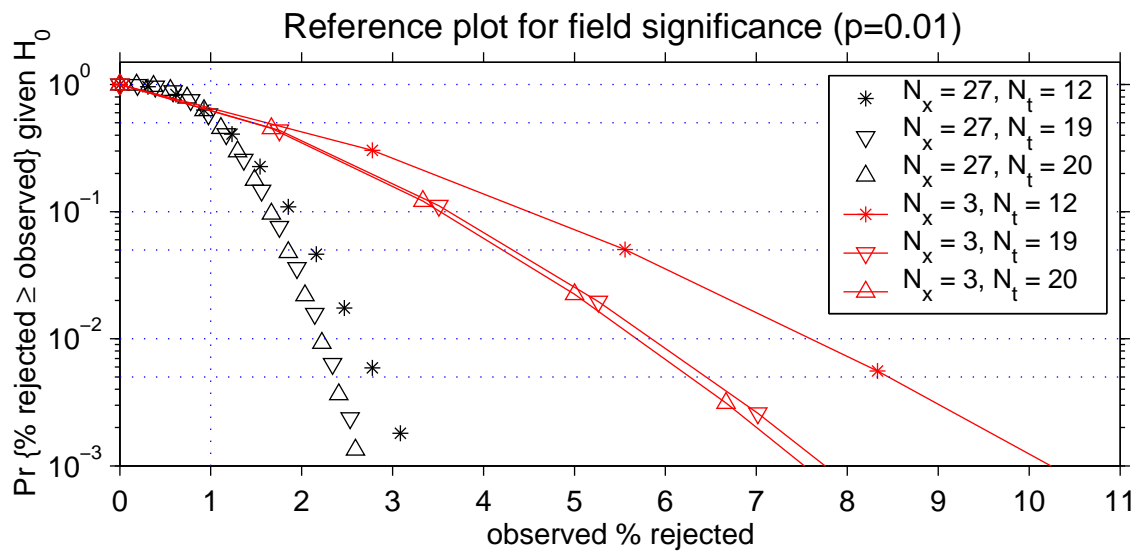
Figure B.1: Reference plot for evaluating field significance of the local hypothesis tests of Figs. 3.9 and 3.10. Abscissa gives the observed percentage of points rejected by the local test at significance level $p = 0.01$. Ordinate gives the binomial probability that the percent rejected could have been greater than or equal to that observed, assuming the null hypothesis were true. Unconnected symbols correspond to the assumption of no spatial correlation, such that $N_x = 27$ is the number of zonal gridpoints. Line-connected symbols correspond to an assumed zonal decorrelation scale of $40°$ longitude, such that the effective number of zonal gridpoints is $N_x = 3$. Asterisks ($N_t = 12$) correspond to the 12 calendar months of Fig. 3.9. Triangles ($N_t = 19$ and $N_t = 20$) correspond to the years 1961–1979 and 1980–1999 in Fig. 3.10.

Upwelling in the Intermediate Model

In the intermediate model, upwelling at the base of the mixed layer is given by the divergence of mixed layer transport (4.10):

$$w = \nabla \circ \mathbf{U} \tag{C.1}$$

where from (4.17),

$$\mathbf{U} = \mathbf{U}_s + \frac{H_m}{H}\left(\mathbf{U}_{al} - \mathbf{U}_s\right) \tag{C.2}$$

The divergence of the active-layer transport is given by (4.3) and (4.7)–(4.8):

$$\boldsymbol{\nabla} \circ \mathbf{U}_{al} = -\frac{\lambda_u}{\lambda_h}(\partial_t h + rh) \tag{C.3}$$

The Ekman transport is given by (4.15):

$$\mathbf{U}_s = \frac{r_s \boldsymbol{\tau} - f\hat{k} \times \boldsymbol{\tau}}{\rho\left(f^2 + r_s^2\right)} \tag{C.4}$$

Solving (C.1)–(C.4) for w away from boundaries gives

$$
\begin{aligned}
w = \quad & - \quad \frac{H_m \lambda_u}{H \lambda_h}(\partial_t h + rh) \\
& + \quad \frac{H - H_m}{\rho H(f^2 + r_s^2)}\left[r_s \mathrm{div}(\boldsymbol{\tau}) + f\mathrm{curl}(\boldsymbol{\tau}) + \frac{\beta(f^2 - r_s^2)\tau_x - 2\beta f r_s \tau_y}{f^2 + r_s^2}\right]
\end{aligned}
\tag{C.5}
$$

The first term arises from the shallow water dynamics and is quite small, on the order of 0.05 m day^{-1} for standard parameter values. The remaining terms immediately suggest a rescaling of y:

$$\tilde{y} \equiv \frac{\beta}{r_s}y = \frac{f}{r_s} \tag{C.6}$$

Dropping the first term in (C.5) and substituting for y then gives

$$w = \frac{H - H_m}{\rho H(\tilde{y}^2 + 1)}\left[\frac{\mathrm{div}(\boldsymbol{\tau})}{r_s} + \frac{\tilde{y}\mathrm{curl}(\boldsymbol{\tau})}{r_s} + \frac{\beta}{r_s^2}\left(\frac{\tilde{y}^2 - 1}{\tilde{y}^2 + 1}\tau_x - \frac{2\tilde{y}}{\tilde{y}^2 + 1}\tau_y\right)\right] \tag{C.7}$$

It is enlightening to examine this solution at three key latitudes:

$$w(\tilde{y} = 0) \;\; = \;\; \frac{H - H_m}{\rho H} \left(\frac{\text{div}(\boldsymbol{\tau})}{r_s} - \frac{\beta \tau_x}{r_s^2} \right) \tag{C.8}$$

$$w(\tilde{y} = \pm 1) \;\; = \;\; \frac{H - H_m}{2\rho H} \left(\frac{\text{div}(\boldsymbol{\tau})}{r_s} \pm \frac{\text{curl}(\boldsymbol{\tau})}{r_s} \mp \frac{\beta \tau_y}{r_s^2} \right) \tag{C.9}$$

$$w(|\tilde{y}| \gg 1) \;\; = \;\; \frac{H - H_m}{\rho H} \frac{\text{curl}(\boldsymbol{\tau})}{r_s \tilde{y}} \tag{C.10}$$

In all three cases, the upwelling increases as H_m shoals relative to H. Equation (C.8) indicates that at the equator, upwelling is generated both by stress divergence and by easterly stress, with the latter effect usually dominating. The viscosity parameter r_s exerts a strong control over the equatorial upwelling, with w scaling like r_s^{-2}. Equation (C.9) indicates that at $y = r_s \beta^{-1}$, the direct effect of the easterlies vanishes; here the upwelling is generated by stress divergence, cyclonic stress curl, and equatorward stress. To the extent that the wind stress is large in scale, (C.9) indicates that the meridional winds will be important for generating upwelling slightly away from the equator, with the strength of the upwelling scaling like r_s^{-2}. Finally, (C.10) indicates that upwelling far from the equator is entirely due to the wind stress curl; this upwelling decreases with increasing r_s and increasing latitude.

It is interesting to compare the effects of easterlies versus southerlies. For spatially constant easterlies, (C.7) becomes

$$w = \frac{\beta}{\rho r_s^2} \frac{H - H_m}{H} \frac{\tilde{y}^2 - 1}{(\tilde{y}^2 + 1)^2} \tau_x \tag{C.11}$$

The upwelling zone extends to $y = \pm r_s \beta^{-1}$, and so widens with increasing r_s. Integrating over the latitudes of upwelling gives

$$\int_{-1}^{1} w \, d\tilde{y} = -\frac{\beta}{\rho r_s^2} \frac{H - H_m}{H} \tau_x \tag{C.12}$$

For spatially constant southerlies, on the other hand, (C.7) becomes

$$w = \frac{\beta}{\rho r_s^2} \frac{H - H_m}{H} \frac{-2\tilde{y}}{(\tilde{y}^2 + 1)^2} \tau_y \tag{C.13}$$

The upwelling is a maximum at $y = -3^{-1/2} r_s \beta^{-1}$. Integrating over the latitudes of upwelling gives

$$\int_{-\infty}^{0} w \, d\tilde{y} = \frac{\beta}{\rho r_s^2} \frac{H - H_m}{H} \tau_y \tag{C.14}$$

Comparison of (C.12) and (C.14) shows that for equal magnitudes of wind stress, *southerlies* induce as much total upwelling *south* of the equator as *easterlies* do *straddling* the equator. South of $y = (1 - 2^{1/2}) r_s \beta^{-1}$, southerlies induce stronger upwelling than easterlies of equal magnitude.

Flux Correction

In the present study we rely on coupled anomaly models, i.e. models in which the climatology in the control run is flux-corrected. It should be noted that Neelin and Dijkstra (1995) have found important dynamical differences between fully-coupled and flux-corrected climatologies. In the latter case, the climatology cannot respond to changes in air-sea coupling, and so as coupling increases the flux-corrected trade winds become too weak relative to the fully-coupled case. These "spurious westerlies" in the flux-corrected case can allow spurious climate equilibria to exist, which can then affect the model variability.

The present model shows a warm equilibrium at high coupling in the absence of noise (Fig. 4.25), which may well be an artifact of the flux correction. That the remnants of this fixed point at lower coupling may interact with the model's stochastic variability can be inferred from Fig. 4.30, which shows the model SST anomalies have negative skewness, i.e. a tendency to linger in warm states. The hybrid GCM, which is also an anomaly model, shows this negative skewness as well (Fig. 7.26). Observed SST anomalies, on the other hand, show positive skewness (Figs. 2.14 and Fig. 2.15).

Unfortunately, it is difficult to maintain a realistic climatology in the present intermediate model without flux correction. There are two main problems. First, the shallow-water model is linear, and so cannot simultaneously simulate both the climatological thermocline's zonal mean depth (which determines the speed of internal waves, and the sensitivity of the thermocline slope to wind stress changes) and its depth in the eastern Pacific (which is crucial to ENSO coupled feedbacks). To simulate a fully-coupled climatology in the present model would require $H = H_0$, which would weaken the wind-thermocline coupling relative to observations. In the flux-corrected case, however, we may achieve a realistic climatological thermocline (Fig. 4.5) without sacrificing realistic wave speed and thermocline sensitivity (Fig. 4.4).

The second problem in simulating a fully-coupled climatology is that many climate processes, such as those involving clouds, evaporation, and vertical mixing, are heavily parameterized in the intermediate model and in the HGCM. Although these parameterizations may be reasonable for simulating ENSO variability, they give rise to errors in simulating the climatology which are then strongly amplified by coupled feedbacks. Prescribing the climatological winds from observations circumvents this problem, allowing us to escape the chain of feedbacks which leads to climate drift.

We have therefore opted for flux correction as a way to obtain a realistic climatology. The concerns noted by Neelin and Dijkstra (1995) are valid but difficult to address directly. Indeed, a prime motivation for the present study is the inability of even many state-of-the-art GCMs to achieve a realistic climatology in the absence of flux correction (Fig. 1.4).

Interval Estimate for the Predictive Power

It is possible to give an interval estimate for the predictive power (PP) under the assumption of univariate normal state vectors. Given (4.32) and the discussion afterward, the quantity

$$\chi^2_{N-1} \equiv \frac{(N-1)s^2}{\sigma^2} \tag{E.1}$$

follows a chi-square distribution on $N-1$ degrees of freedom. Similarly, the quantity

$$\chi^2_{N_c-1} \equiv \frac{(N_c-1)s_c^2}{\sigma_c^2} \tag{E.2}$$

follows a chi-square distribution on $N_c - 1$ degrees of freedom. The ratio of chi-square variables

$$
\begin{aligned}
F_{N-1,N_c-1} &\equiv \frac{\chi^2_{N-1}/(N-1)}{\chi^2_{N_c-1}/(N_c-1)} \\
&= \frac{s^2/s_c^2}{\sigma^2/\sigma_c^2}
\end{aligned}
\tag{E.3}
$$

then follows an F distribution on $N-1$ and $N_c - 1$ degrees of freedom. By definition of the F-distribution quantiles $F_{N-1,N_c-1,\alpha/2}$ and $F_{N-1,N_c-1,1-\alpha/2}$ we have

$$P\left\{F_{N-1,N_c-1,\alpha/2} < F_{N-1,N_c-1} < F_{N-1,N_c-1,1-\alpha/2}\right\} = 1 - \alpha \tag{E.4}$$

which implies

$$P\left\{\frac{s^2/s_c^2}{F_{N-1,N_c-1,1-\alpha/2}} < \frac{\sigma^2}{\sigma_c^2} < \frac{s^2/s_c^2}{F_{N-1,N_c-1,\alpha/2}}\right\} = 1 - \alpha \tag{E.5}$$

Substituting from (4.33) then gives a $1 - \alpha$ confidence interval for the PP:

$$P\left\{1 - \frac{s/s_c}{F^{1/2}_{N-1,N_c-1,\alpha/2}} < \mathrm{PP} < 1 - \frac{s/s_c}{F^{1/2}_{N-1,N_c-1,1-\alpha/2}}\right\} = 1 - \alpha \tag{E.6}$$

Hybrid Coupled GCM

The hybrid GCM used in this study consists of an ocean general circulation model coupled to a statistical model of the surface wind stress and heat fluxes, as in Harrison et al. (2002). Relevant details from that paper are repeated here for convenience, with an additional description of the model climatology and interannual variability.

F.1 Ocean model

The ocean component is the GFDL Modular Ocean Model (MOM) version 3. The horizontal domain of the model, shown in Fig. F.1, extends from 120°E–70°W, 40°S–40°N, with a sponge condition within 10° of the northern and southern boundaries. The zonal grid spacing is a uniform 1°. The meridional grid spacing is a uniform 0.33° below 10° latitude, gradually increases between 10° and 15° latitude, and is a uniform 1° poleward of 15° latitude. The model has 16 fixed vertical levels, with 10 in the top 250 m of the ocean; the vertical grid spacing increases with depth as shown in Fig. F.2. A rigid lid is assumed at the ocean surface. The primitive equations are solved on an Arakawa B grid and advection is computed using centered differences. Vertical mixing is the Richardson number dependent scheme of Pacanowski and Philander (1981); horizontal mixing is the nonlinear scheme of Smagorinsky (1963).

Starting from a resting state with observed temperature and salinity (Levitus and Boyer, 1994), the ocean model is spun up for 25 years using observed climatological monthly surface fluxes of momentum and heat. The surface wind stresses are converted from the FSU pseudostress product (Stricherz et al., 1997), using an air density of $\rho_a = 1.2$ kg m^{-3} and a drag coefficient of $c_d = 1.2 \times 10^{-3}$. Outside the 30°S–30°N domain of FSU, the stresses are taken from Hellerman and Rosenstein (1983). The heat fluxes consist of the OSU analysis (Esbensen and Kushnir, 1981), with an additional restoring of the top level toward observed SST at a rate of 50 Watt m^{-2} °C^{-1}. Surface salinities are restored toward their observed climatological values at a rate 0.01 kg m^{-2} s^{-1} PSU^{-1}. The restoring for the top model level temperature and salinity corresponds to an e-folding time scale of approximately 5 days.
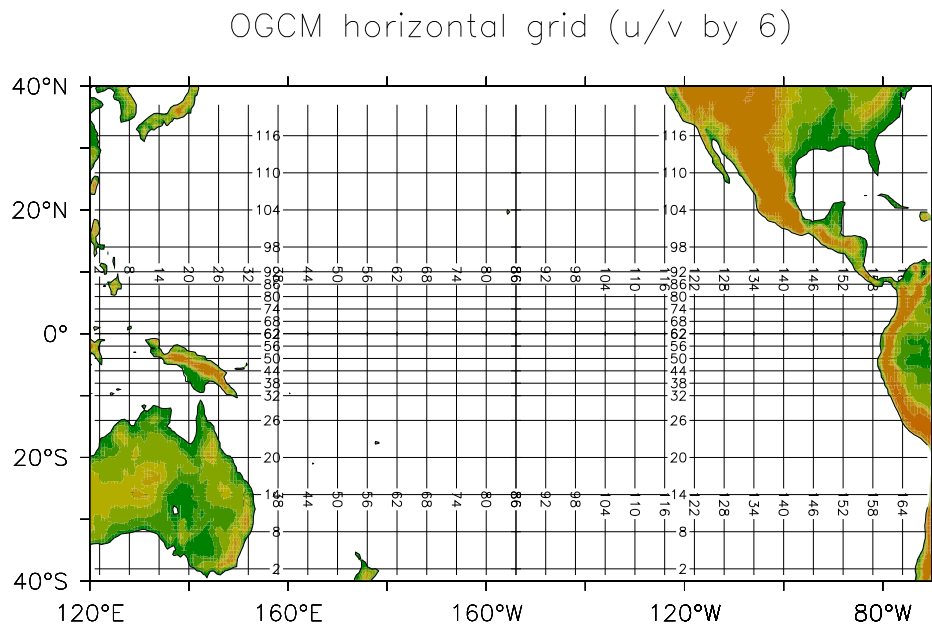
Figure F.1: Horizontal velocity grid of the ocean general circulation model. Gridpoints lie at the line intersections; only every sixth row and column of points is plotted. The temperature and vertical velocity lie on a grid staggered in latitude and longitude with respect to the grid shown.
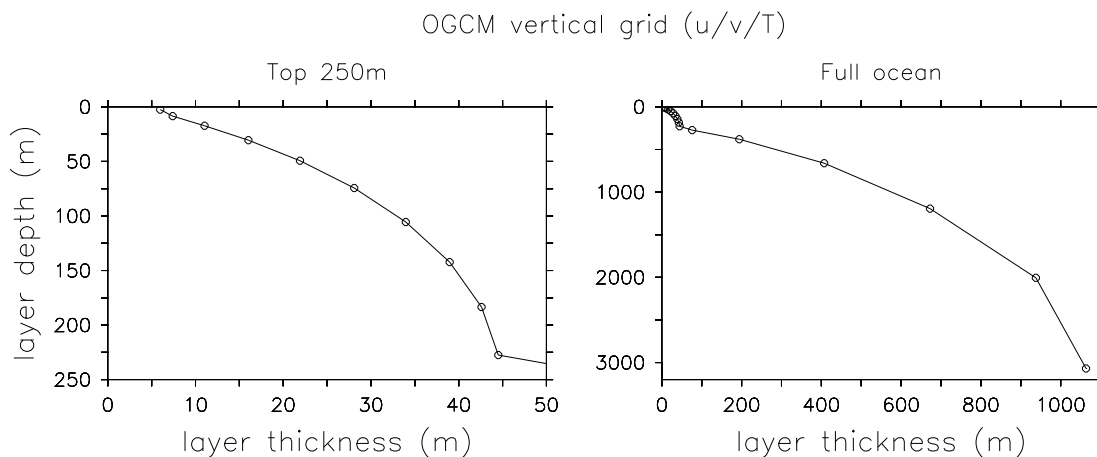
Figure F.2: Vertical grid of the ocean general circulation model. Gridpoints of temperature and horizontal velocity lie at the depths indicated by the circles; layer thicknesses are indicated on the horizontal axis. The vertical velocity grid is staggered in the vertical with respect to the grid shown.

F.2 Statistical atmosphere model

The statistical atmosphere model is very similar to the stress models developed in Chapter 3. Wind stress, latent heat flux, radiative heat flux models are each developed separately (sensible and freshwater fluxes are not included). Harrison et al. (2002) compared several such models based on different flux analyses; here we use the version based on the 1979–1993 period from the ECMWF product (Gibson et al., 1997). SST data are taken for the same period from the analysis of Reynolds and Smith (1994).

The data fields are first interpolated onto a $3° \times 3°$ grid covering the ocean between 20°S–20°N. Monthly climatologies are subtracted from the data to give monthly anomalies, which are then detrended by removing the least-squares linear fit to the timeseries at each gridpoint. As in Chapter 3, the flux models are constructed by performing linear regressions of the observed anomalies onto the leading singular vector patterns of observed flux/SST covariance. Only the gravest regression mode is included in this case, and there is no stochastic component.

F.3 Coupled model

Following the spinup of the ocean climatology, the ocean GCM is coupled to the statistical atmosphere anomaly model. The ocean model climatology is maintained by the imposition of the climatology of restoring terms simulated during the last 10 years of ocean spinup. An additional heat flux is also imposed to damp SST anomalies at a rate of 1 Watt m^{-2} °C^{-1}, which corresponds approximately to a restoring time scale of 100 days for the top model layer.

The coupled simulation is initialized with a perturbation from the model climatology, and then is integrated forward in time for 20 years, with output of monthly-average fields. The first four years of the run are considered a transition to the coupled statistical equilibrium and are discarded; only the last 16 years are analyzed. A 12-month climatology is computed from these 16 years of data, and then subtracted from the total fields to give monthly anomaly fields.

F.3.1 Climatology

Annual mean

The annual-mean equatorial temperature structure of the coupled model is shown in Fig. F.3. The simulated ocean is about 1–2°C too cold near the surface in the central and eastern Pacific, and slightly too cold in the western Pacific. Thus $\partial_z T$ is too weak at 50 m depth in the east and the zonal SST gradient is somewhat too strong. The model also has a 2–4°C cold bias below 160 m. These problems are likely related to limitations of the vertical mixing scheme, and perhaps also to errors in the climatological stress forcing, since this forcing is rather uncertain (see Chapter 2). However, the simulated depth of the 20°C isotherm is generally quite good, as is the vertical stratification in the vicinity of the thermocline.

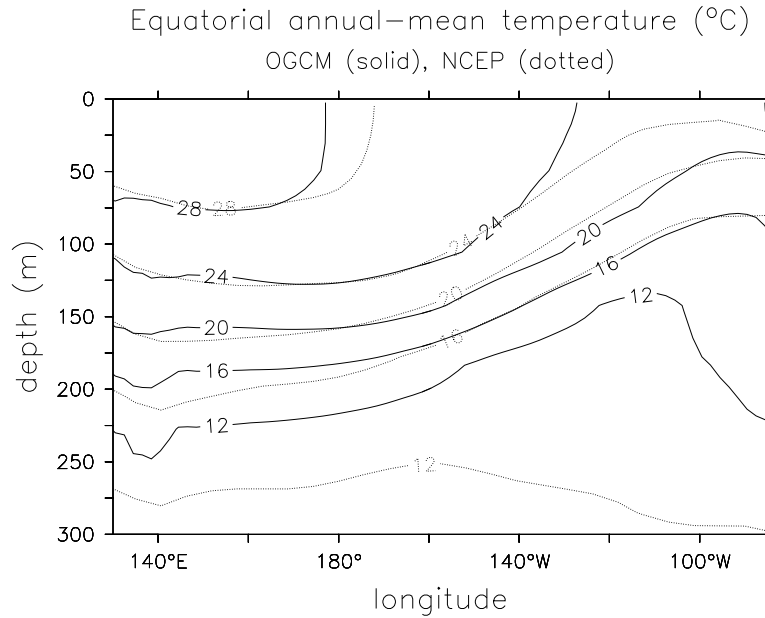Figure F.3: Vertical section of climatological annual-mean temperature along the equator (2°S–2°N). Solid contours indicate the climatology of the hybrid coupled GCM control run. Dotted contours indicate the 1980–99 climatology from the observational analysis of Behringer et al. (1998).

The annual-mean structure of the equatorial ocean simulated by the model is shown in Fig. F.4. The GCM cold bias at the surface, evident in panel (h), weakens the stratification near the surface in the east (panel d), which promotes vertical mixing. Compared to the NCEP analysis, the GCM has more easterly mixed layer currents in the east, more westerly currents in the west, and stronger upwelling at 50 m depth in the central/eastern Pacific. Note that similar biases in the mixed layer currents were found in the intermediate model (Fig. 4.12). This suggests that either both models are missing some fundamental physics, or that the FSU wind stress forcing is flawed, or that the NCEP ocean analysis is incorrect.

The equatorial heat budget of the top 50 m of the model is shown in Fig. F.5. The equatorial eastern Pacific is cooled primarily through vertical advection. Additional cooling occurs through meridional advection, which peaks around 125°W, and zonal advection, which provides a broad cooling throughout the central basin. Vertical advection is responsible for all of the cooling at the eastern boundary, while zonal advection is responsible for nearly all of the cooling at the dateline. The advective cooling is almost balanced by the surface heat flux, which is into the ocean all along the equator. Adding the advective tendency to the surface flux gives a nonzero residual which is identified with sub-monthly eddies. This eddy flux provides a warming in the east, which is roughly one third as strong as the warming due to surface flux, and a weak cooling in the western Pacific.

Compared to the intermediate model (Fig. 4.14), the GCM has a more active heat budget due to its stronger cold tongue. The cooling due to vertical advection is shifted farther east in the GCM, and the cooling due to zonal advection is zonally broader due to
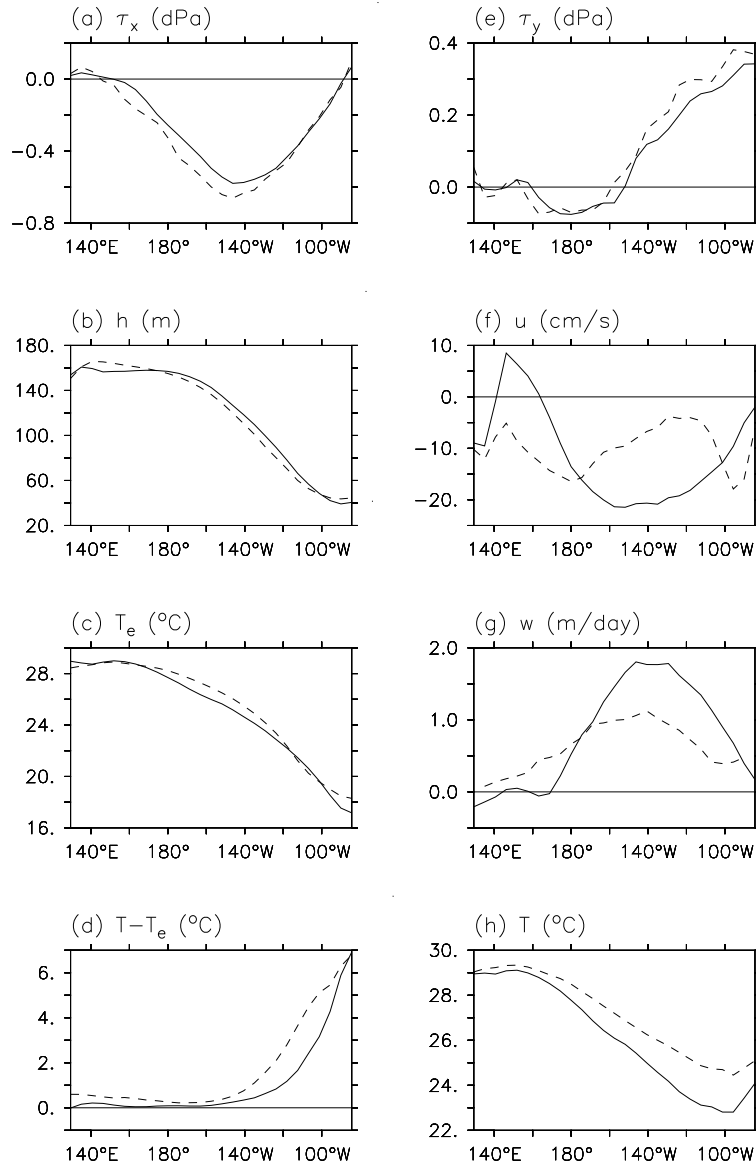
Figure F.4: Annual-mean oceanic climatological fields at the equator (2°S–2°N). Dashed lines are from the observational analysis of Behringer et al. (1998), solid lines are from the control run of the hybrid coupled GCM. (a) Zonal wind stress, (b) depth of the 20° isotherm, (c) temperature at 50 m, (d) temperature at surface minus that at 50 m, (e) meridional wind stress, (f) zonal current averaged over the top 50 m, (g) vertical velocity at 50 m, (h) SST.
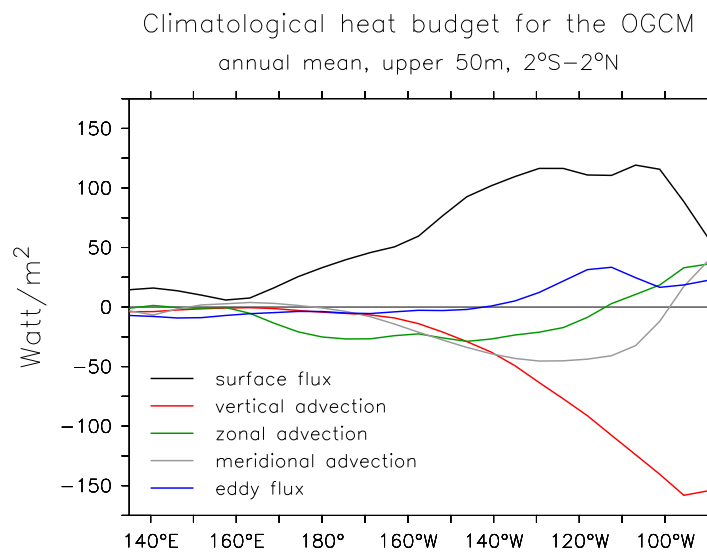
Figure F.5: Annual-mean climatological heat budget of the equatorial band (2°S–2°N), for the top 50 m of the hybrid coupled GCM. Positive values correspond to a warming tendency. Advection and surface fluxes are computed on the full model grid using the total monthly-mean currents and temperatures from the control run, so that effects of the annual cycle and ENSO are included but sub-monthly eddy fluxes are not. The eddy flux tendency is then defined as the heating required to balance the effects of monthly-mean surface flux and advection.

a gentler zonal SST gradient than in the intermediate model. Meridional advection plays rather different roles in these models: in the intermediate ocean, it provides strong cooling at the eastern boundary, while in the GCM, it *warms* the eastern boundary and cools farther west. The eastern boundary warming by meridional advection is a major reason that the GCM also shows a relatively smaller role for surface heat flux in the east.

The GCM eddy fluxes in the east Pacific are largely driven by tropical instability waves (TIWs), which are active in the model as well as in observations (McPhaden et al., 1998; Stockdale et al., 1998; Masina and Philander, 1999a,b; Chelton et al., 2001; Polito et al., 2001; Zhang, 2001). These waves have a period of 20–40 days and so are not well resolved by monthly averages. Comparing Figs. F.5 and 4.14 shows that the amplitude and position of the eddy heat fluxes in the GCM is reasonably well captured by the diffusion term in the intermediate model. Note, however, that the intermediate model assumes a constant diffusivity, i.e. it assumes the eddies have constant amplitude. In reality, TIWs are strongest when the trade winds and cold tongue are strongest, such as during boreal autumn and La Niña. Thus the intermediate model will probably tend to underestimate mixing in the east Pacific during La Niña, and overestimate it during El Niño. The intermediate model also does not capture the small amount of eddy cooling in the central and western Pacific that is evident in the GCM.

Annual cycle

The annual cycle of SST in the model (Fig. F.6) is strongest off-equator and in the vicinity of the cold tongue. Near the coast of South America, SST is warmest in March–April. The annual signal propagates westward along the equator through the calendar year, such that SST peaks in October near the dateline. Associated with these annual variations in SST are seasonal changes in the surface wind stress and currents (not shown), which also propagate westward along the equator. In the central equatorial Pacific, upwelling tends to peak near the end of the calendar year, when the easterly trade winds are at their strongest. The westward equatorial surface currents, on the other hand, are strongest in the central Pacific during August–October and weakest April–June.

F.3.2   Simulated ENSO

Fig. F.7 shows the evolution of the equatorial fields in the hybrid coupled GCM. After four years the model has settled into a self-sustained ENSO with a period of about 3.3 years and a NINO3 SSTA amplitude of about 1.25°C. The oscillation fairly regular, although it is modulated somewhat by the seasonal cycle. Westward propagation of SST anomalies is evident in the central Pacific. Although there is evidence of eastward propagation of the thermocline depth anomalies, the bulk of the thermocline signal in the east is in phase with SSTA in the east. The zonal stress along the equator slightly lags the SSTA in the east, and is more in phase with SSTA in the western Pacific.

The off-equatorial structure of the simulated ENSO cycle is shown in Fig. F.8. The peak SST variability occurs off the coast of Peru, and just south of the equator in the central Pacific. There is westward propagation of SST anomalies almost everywhere in the basin, not just at the equator, and there is a strong poleward spreading of the SST
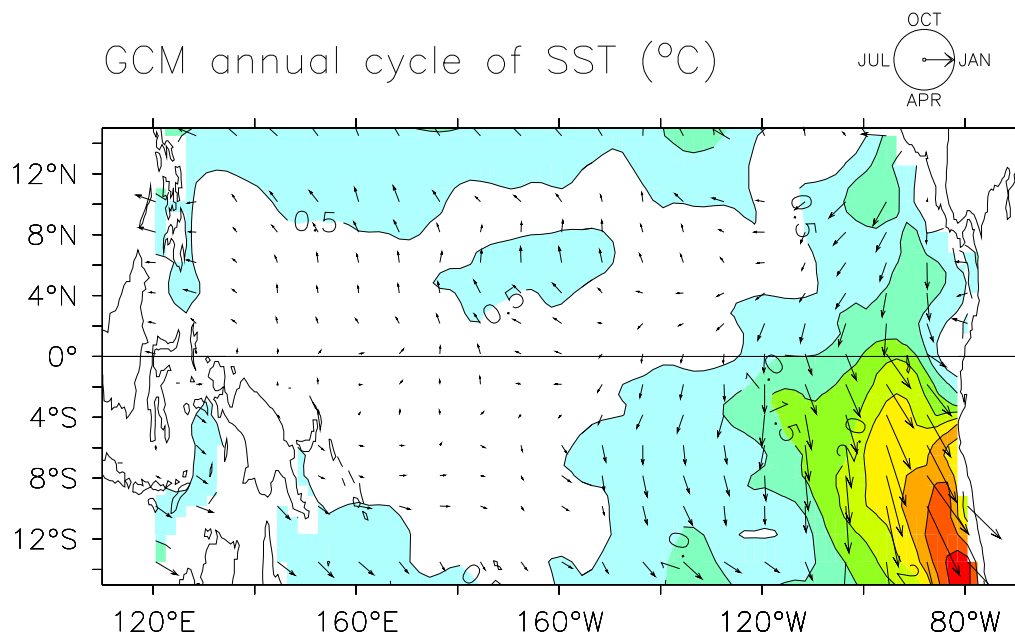
Figure F.6: Annual harmonic of SST from the climatology of the hybrid coupled model. Vectors indicate the month of warmest SST, i.e. rightward-pointing vectors indicate a January peak, downward-pointing vectors an April peak. The vector length corresponds the amplitude of the annual harmonic and is indicated by the contours (°C).
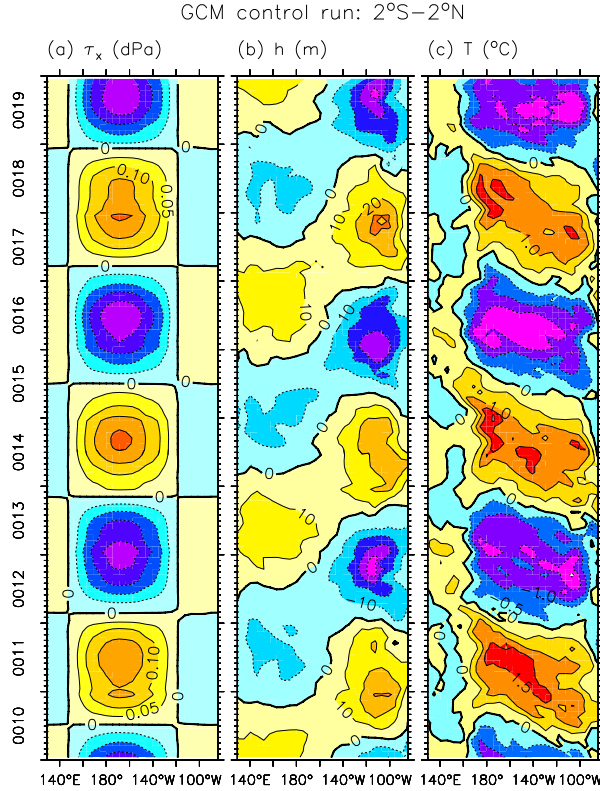
Figure F.7: Representative timeseries of anomaly fields from the hybrid coupled GCM control run, averaged over the equatorial band (2°S–2°N). (a) Zonal stress anomaly (dPa), (b) anomalous depth (m) of the 20°C isotherm, (c) SST anomaly (°C).

anomalies following the equatorial peak.

Fig. F.9 shows the equatorial heat budget for a single ENSO cycle in the GCM. The largest term, $-\overline{w}\partial_z T'$, is active east of 140°W and is a strong amplifier of SSTA in the east. The next largest term is the surface heat flux, which provides a strong damping of SST anomalies across the central and eastern Pacific. The eddy heat fluxes also damp SSTA strongly in the east. The destabilizing effect of $-\overline{w}\partial_z T'$ on the SSTA is enhanced by the meridional advection terms: $-\overline{v}\partial_y T'$ in the eastern basin, and $-v'\partial_y \overline{T}$ in the central basin. All of these terms are nearly in phase or perfectly out of phase with SSTA in the east, and none of these terms shows much sign of zonal propagation.

Enter $-u'\partial_x \overline{T}$, which is active in the central basin and propagates westward at roughly 30 cm s^{-1} (i.e. a 1.7-year basin-crossing time). In the eastern Pacific, this term is nearly in quadrature with SSTA. The $-\overline{u}\partial_x T'$ term is also somewhat in quadrature with SSTA, but no other terms have the amplitude of $-u'\partial_x \overline{T}$ at the crossing points between warm and cold events. Thus $-u'\partial_x \overline{T}$ appears to be an essential oscillation mechanism in the GCM.

The $-w'\partial_z \overline{T}$ term plays a fairly small role except possibly at the far eastern boundary, but even in the east its effect not very coherent with the model ENSO. The nonlinear terms generally small, though they do have rectified effects on the mean state: $-v'\partial_y T'$
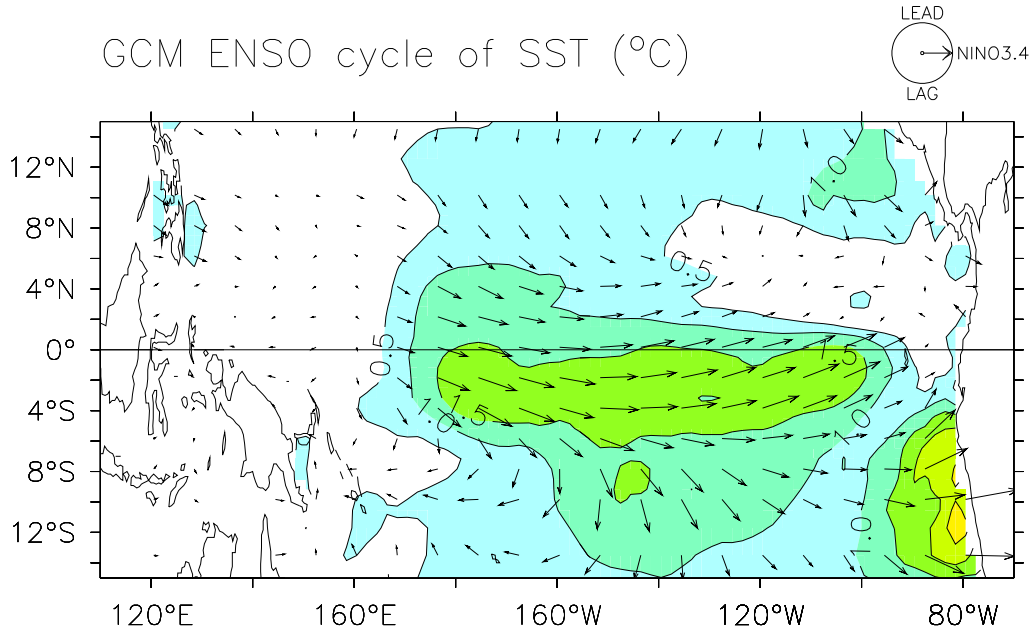
Figure F.8: Amplitude and phase of the ENSO cycle of SST anomalies in the hybrid coupled model. Vectors indicate the SSTA phase relative to the average over the NINO3.4 region (170°W–120°W, 5°S–5°N), i.e. rightward-pointing vectors indicate a peak coincident with NINO3.4 SSTA, downward-pointing vectors a lag of a quarter cycle behind NINO3.4 SSTA. The vector length corresponds the amplitude of the ENSO harmonic and is indicated by the contours (°C). The period of the cycle is 3.3 years.

induces a warming all along the equator, while $-u'\partial_x T'$ and $-w'\partial_z T'$ induce cooling near the dateline and near the eastern boundary, respectively.

There are many similarities between the GCM ENSO and that in the intermediate model control run (Fig. 4.20). In both cases, $-\overline{w}\partial_z T'$ is the dominant destabilizer in the east, surface flux is the primary damping, and $-u'\partial_x \overline{T}$ is a key transitioner in the central Pacific. There are also important differences. Compared to the intermediate model, the GCM shows a greater role for eddy fluxes, which act as an extra damping in the east; the $-\overline{w}\partial_z T'$ term does not lead SSTA as much in the east; and $-\overline{w}\partial_z T'$ does not act as a damping in the central Pacific. The effects of meridional advection are stronger in the GCM, while the effect of $-\overline{u}\partial_x T'$ is weaker.
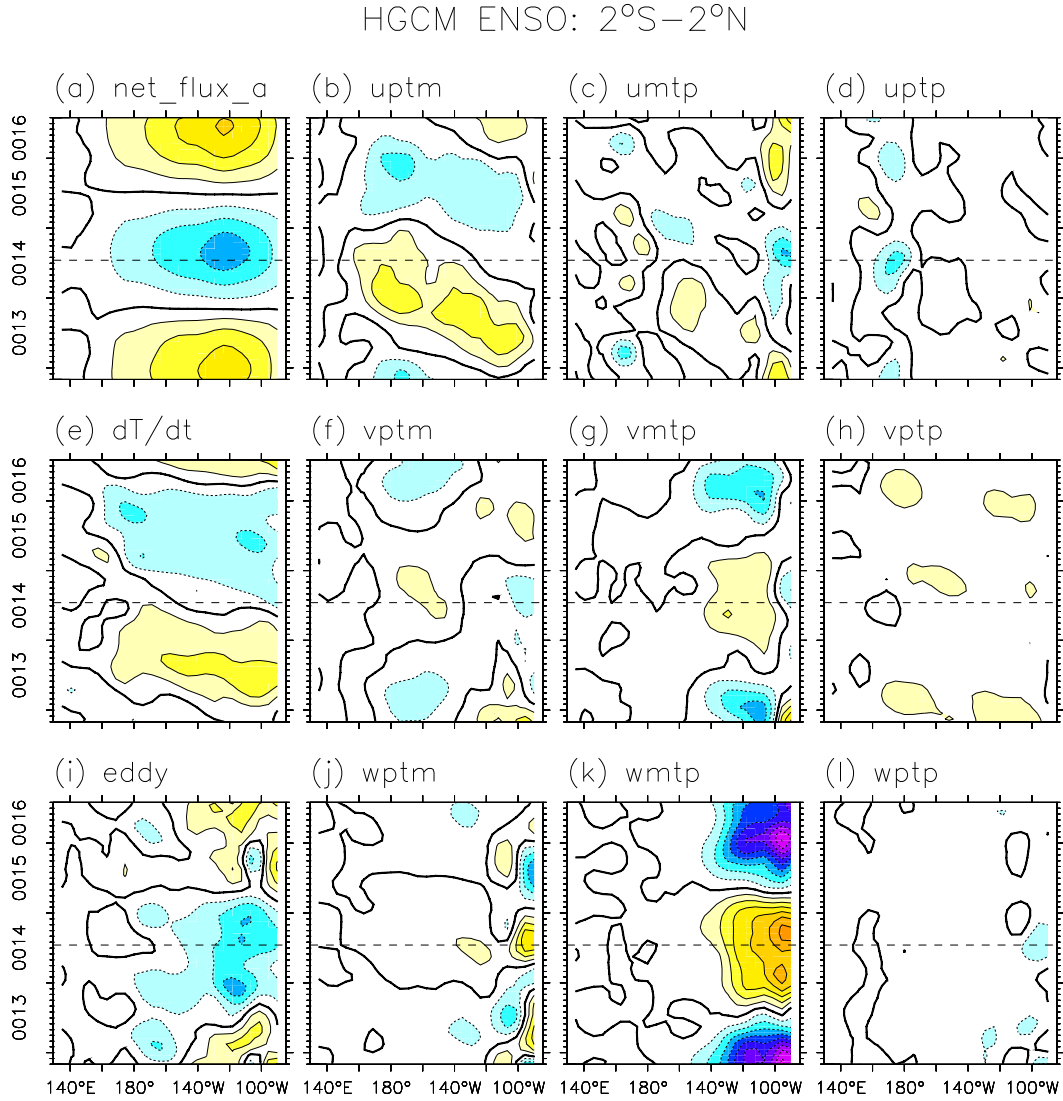
Figure F.9: Temperature anomaly tendency terms for a single ENSO cycle from the hybrid coupled GCM control run, averaged 2°S–2°N and over the upper 50 m of the ocean. Vertical axis indicates years since initialization; dashed line indicates the peak of a warm event. Contour interval is 10 Watts m^{-2}, heavy contour indicates zero; warm colors indicate positive values, cool colors negative values; near-zero values are not shaded. Panels show (a) net heat flux into the ocean, (b) $-u'\partial_x\overline{T}$, (c) $-\overline{u}\partial_x T'$, (d) $-u'\partial_x T'$, (e) $\partial_t T'$, (f) $-v'\partial_y\overline{T}$, (g) $-\overline{v}\partial_y T'$, (h) $-v'\partial_y T'$, (i) eddy flux, (j) $-w'\partial_z\overline{T}$, (k) $-\overline{w}\partial_z T'$, (l) $-w'\partial_z T'$.

Symbols and Definitions

Scalars (real or complex) are indicated by italic Roman or Greek type (u, U, τ_x). Vectors are indicated by bold type ($\mathbf{u}$, $\mathbf{U}$, $\boldsymbol{\tau}$). Matrices are indicated by uppercase bold sans serif type ($\mathbf{M}$).

Diacritical marks

$\overline{\psi}$	time mean of ψ
ψ'	temporal anomaly of ψ: $\psi' \equiv \psi - \overline{\psi}$
ψ^*	rotated coordinates; or perturbation
$\widehat{\psi}$	estimate of ψ from data
$\widetilde{\psi}$	nondimensional ψ; or amplitude of ψ
$\mathbf{M}'$	matrix transpose
$\mathbf{M}^*$	matrix of expansion coefficients (rotated timeseries)
$\widetilde{\mathbf{M}}$	nondimensional matrix

Operators

$|\psi|$	absolute value (magnitude) of ψ: $|\psi|^2 \equiv \mathrm{Re}(\psi)^2 + \mathrm{Im}(\psi)^2$
$\|\psi\|$	norm of ψ, e.g. the sum of squares of all elements of ψ
$\langle \psi \rangle$	ensemble mean of ψ
curl	vertical component of vector curl
∂_ψ	partial derivative with respect to ψ
$\mathcal{H}\{x(t)\}$	Hilbert transform: $\mathcal{H}\{x(t)\} \equiv \dfrac{1}{\pi} \displaystyle\int_{-\infty}^{\infty} \dfrac{x(t')}{t' - t}\, dt'$

$\mathcal{R}(x)$ ramp function: $\mathcal{R}(x) \equiv x\mathcal{S}(x) = \begin{cases} 0 & : & x \leq 0 \\ x & : & x > 0 \end{cases}$

$\mathcal{R}'(w)$ $\mathcal{R}(w) - \overline{\mathcal{R}(w)}$

$\mathcal{R}^*(w)$ $\mathcal{R}(w) - \mathcal{R}(\overline{w})$

$\mathrm{Re}(\psi)$ real part of ψ

$\mathcal{S}(x)$ Heaviside step function: $\mathcal{S}(x) \equiv \begin{cases} 0 & : & x \leq 0 \\ 1 & : & x > 0 \end{cases}$

∇^2 horizontal Laplacian operator: $\nabla^2 \equiv \partial_x^2 + \partial_y^2$

Roman symbols (lowercase)

a curvature parameter for T_0

b linear sensitivity of entrainment temperature anomalies to thermocline depth anomalies: $T_e' \approx bh'$

c shallow water gravity wave speed $= (g'H)^{1/2}$

c_d drag coefficient (nondimensional)

e the base of the natural logarithm: $e \equiv \lim_{x \to \infty} \left(1 + \dfrac{1}{x}\right)^x$

f Coriolis parameter on the equatorial beta plane $= \beta y$; or statistic used in the F-test for variance

g acceleration of gravity at sea level $= 9.81$ m s^{-2}

g' reduced gravity $= g\Delta\rho/\rho$

h thermocline depth anomaly

h_1 linear thermocline depth anomaly

h_m zonal-mean thermocline depth anomaly

h_p zonal-perturbation thermocline depth anomaly: $h_e = h - h_m$

i zonal index; or imaginary unit $(-1)^{1/2}$

j meridional index

k singular value index; or zonal wavenumber

l time index

n number of time points

n_x total number of longitudinal gridpoints

n_y total number of latitudinal gridpoints

p number of SST gridpoints

q number of wind stress gridpoints

r dissipation coefficient for active layer mass and momentum; or number of singular values

r_s damping of active layer shear current (mixed layer viscosity)

s number of principal components; or sample standard deviation

s_c sample standard deviation of the climatological ensemble

t time coordinate

$\mathbf{u}$ average mixed layer current $= (u, v)$

$\mathbf{u}_1$ linear average active layer current

$\mathbf{u_a}$ surface wind $= (u_a, v_a)$

$\mathbf{u}_{al}$ average active layer current

$\mathbf{u}_i$ average active layer current below the mixed layer

$\mathbf{u}_s$ vertical shear current at base of mixed layer $= (u_s, v_s)$

w upwelling at base of mixed layer

x zonal coordinate (positive eastward)

x^* longitude of transient zonal stress patch

x_0 longitude of climatological stress perturbation

x_e longitude of easternmost gridpoint

x_w longitude of westernmost gridpoint

y meridional coordinate (positive northward)

$\tilde{y}$ meridional coordinate nondimensionalized by upwelling scale

y^* latitude of transient zonal stress patch

y_n latitude of northernmost gridpoint

y_s latitude of southernmost gridpoint

z vertical coordinate (positive upward)

Roman symbols (uppercase)

A — complex coupling factor $A = |A|\, e^{i\theta_A}$, converts SST anomalies to zonal stress anomalies in the simplified equatorial model. The stress anomalies are shifted eastward relative to the SST anomalies by the phase angle θ_A.

B — fraction of the active layer occupied by the unmixed layer: $B \equiv \dfrac{H - H_m}{H}$

F_{ν_1,ν_2} — distribution of a ratio of independent chi-square variables with ν_1 and ν_2 degrees of freedom: $F_{\nu_1,\nu_2} \equiv \dfrac{\chi^2_{\nu_1}/\nu_1}{\chi^2_{\nu_2}/\nu_2}$

H — active layer depth

H_0 — active layer depth in the absence of wind stress

H_m — mixed layer depth

H_{obs} — observed active layer depth averaged over the domain of wave propagation

$\mathrm{Im}(\psi)$ — imaginary part of ψ

L_e — equatorial radius of deformation $= \left(\dfrac{c}{2\beta}\right)^{1/2} \approx 230\text{ km} \approx 2.1^\circ$ latitude

L_x — zonal halfwidth of climatological stress perturbation

L_y — meridional halfwidth of climatological stress perturbation

M — number of principal components in the noise model for the residual stress anomalies

N — number of singular modes in the regression model for stress anomalies

N_e — number of ensemble members

$P\{E\}$ — probability of event E

PP — predictive power

R_e — reflectivity of the eastern boundary

R_w — reflectivity of the western boundary

T — mixed layer temperature (SST)

$T_0(y)$ — equilibrium SST in the absence of ocean dynamics

$T_0(y = 0)$ — value of T_0 at the equator

T_c — thermocline central temperature

T_e temperature of water entrained into the mixed layer

T_{min} minimum temperature in T_e parameterization

U mixed layer transport $= H_m \mathbf{u}$

$\mathbf{U}_1$ linear total active layer transport $= (U_1, V_1)$

$\mathbf{U}_{1,Kelvin}$ Kelvin component of $\mathbf{U}_1$

$\mathbf{U}_{1,Rossby}$ Rossby component of $\mathbf{U}_1$

$\mathbf{U}_{al}$ total active layer transport $= H \mathbf{u}_{al}$

$\mathbf{U}_i$ active layer transport below the mixed layer $= (H - H_m) \mathbf{u}_{al}$

$\mathbf{U}_s$ shear transport $= H_m \mathbf{u}_s$

Greek symbols (lowercase)

β variation of Coriolis parameter with latitude at the equator
$= 2.28 \times 10^{-11}$ (m s)$^{-1}$ $= 1.97 \times 10^{-6}$ (m day)$^{-1}$
$\approx 2.51 \times 10^{-6}$ (°lat s)$^{-1}$ ≈ 0.217 (°lat day)$^{-1}$

γ mixed layer entrainment efficiency

δ temperature increment in T_e parameterization

ϵ linear damping coefficient for SST

ζ ratio of time step to noise decorrelation time

κ horizontal eddy diffusivity in the mixed layer

λ_h coefficient of thermocline depth

λ_u coefficient of active layer currents/transport

ϕ_1 lag-1 autocorrelation

ρ density of seawater

ρ_a density of surface air

μ coefficient of wind stress anomalies (coupling strength)

σ^2 variance

σ_c^2 climatological variance

ω complex frequency in time: $\omega = \omega_r + i\omega_i$

ω_i angular frequency in time

ω_r	e-folding growth rate in time
$\boldsymbol{\tau}$	vector wind stress on the ocean surface $= (\tau_x, \tau_y)$
τ_x^*	transient zonal stress patch
θ_ψ	phase angle of ψ
$\tilde{\tau}_x^*$	amplitude of transient zonal stress patch
$\bar{\tau}_x^*$	perturbation to climatological zonal stress
$\bar{\tau}_y^*$	perturbation to climatological meridional stress
$\widetilde{\bar{\tau}_x^*}$	amplitude of perturbation to climatological zonal stress
$\widetilde{\bar{\tau}_y^*}$	amplitude of perturbation to climatological meridional stress
χ_ν^2	chi-square variable with ν degrees of freedom

Greek symbols (uppercase)

Δx	grid spacing in zonal direction
Δy	grid spacing in meridional direction
Δx^*	zonal halfwidth of transient zonal stress patch
Δy^*	meridional halfwidth of transient zonal stress patch
Δt	time step
Δt^*	duration of transient zonal stress patch
Γ	maximum $\partial_h T_e$ in T_e parameterization

Matrices

$\mathbf{A}$	dimensionalized left singular vectors of $\mathbf{C}$
$\mathbf{A}_N$	leading N SST singular vectors
$\widetilde{\mathbf{A}}$	left singular vectors of $\mathbf{C}$
$\mathbf{B}$	dimensionalized right singular vectors of $\mathbf{C}$
$\widetilde{\mathbf{B}}$	right singular vectors of $\mathbf{C}$
$\mathbf{B}_{N,\widehat{e}}$	dimensionalized principal component patterns of the residual stress estimated from N singular modes
$\mathbf{B}_{N,\widehat{e},M}$	leading M dimensionalized principal component patterns of the residual stress estimated from N singular modes

$\mathbf{C}$	temporal covariance of observed SST/stress anomalies $= (n-1)^{-1}\mathbf{X}'\mathbf{Y}$
$\mathbf{D}$	diagonal matrix of singular values of $\mathbf{C}$
$\widetilde{\mathbf{D}}$	nondimensionalized diagonal matrix of singular values of $\mathbf{C}$
$\mathbf{E}$	matrix of shocks (spatially-correlated Gaussian noise)
$\mathbf{E}_N$	random shocks plus truncation error
$\widehat{\mathbf{E}}_N$	matrix of residuals (estimate of $\mathbf{E}_N$ from the data)
$\widehat{\widetilde{\mathbf{E}}}^*_{N,\widehat{e}}$	nondimensionalized principal component expansion coefficients of the residual stress estimated using N singular modes
$\mathbf{F}$	red noise model for residual stress principal components
$\mathbf{I}$	identity matrix
$\mathbf{R}_N$	regression of stress anomalies onto the leading N singular vectors of SST
$\widehat{\mathbf{R}}_N$	estimate of $\mathbf{R}_N$ from the data
$\mathbf{S}_{x^*}$	diagonal matrix of SST singular vector expansion coefficient standard deviations
$\mathbf{S}_{y^*}$	diagonal matrix of stress singular vector expansion coefficient standard deviations
$\mathbf{X}$	observed SST anomalies
$\mathbf{X}^*$	singular vector expansion coefficients of SST anomalies
$\widetilde{\mathbf{X}}^*$	nondimensionalized singular vector expansion coefficients of SST anomalies
$\widetilde{\mathbf{X}}^*_N$	leading N nondimensionalized singular vector expansion coefficients of SST anomalies
$\mathbf{Y}$	observed wind stress anomalies
$\mathbf{Y}^*$	singular vector expansion coefficients of stress anomalies
$\widetilde{\mathbf{Y}}^*$	nondimensionalized singular vector expansion coefficients of stress anomalies
$\widehat{\mathbf{Y}}_N$	estimate of deterministic stress anomaly from the leading N singular modes

Units and Conversions

dPa   MKS unit of wind stress = 0.1 Pa
        = 1 dyne cm^{-2} = 7.46 × 10^8 kg m^{-1} day^{-2}

cm   centimeter

dyne   CGS unit of force = g cm s^{-2} = 10^{-5} N

°C   Celsius temperature scale, or Celsius degree

km   kilometer

K   Kelvin temperature scale, or Kelvin unit

° lat   degree latitude ≈ 1.11 × 10^5 m at the equator

° lon   degree longitude ≈ 1.11 × 10^5 m at the equator

m   meter

N   Newton (MKS unit of force)

Pa   MKS unit of wind stress = 1 N m^{-2}

s   second

W   Watt (unit of power)

yr   year

Abbreviations and Acronyms

Abbreviations

H_0	null hypothesis
ka	thousand years ago
$NID(\mu, \sigma^2)$	normally and independently distributed with mean μ and variance σ^2
NINO3	eastern equatorial Pacific region (150°W–90°W, 5°S–5°N)
NINO3.4	central equatorial Pacific region (170°W–120°W, 5°S–5°N)
NINO4	western/central equatorial Pacific region (160°E–150°W, 5°S–5°N)
umtp	zonal advection component $-\overline{u}\partial_x T'$
uptm	zonal advection component $-u'\partial_x \overline{T}$
uptp	zonal advection component $-u'\partial_x T'$
vmtp	meridional advection component $-\overline{v}\partial_y T'$
vptm	meridional advection component $-v'\partial_y \overline{T}$
vptp	meridional advection component $-v'\partial_y T'$
wmtp	vertical advection component $-\overline{w}\partial_z T'$
wptm	vertical advection component $-w'\partial_z \overline{T}$
wptp	vertical advection component $-w'\partial_z T'$

Acronyms

AGCM	atmospheric general circulation model
CGS	centimeter-gram-second system of units
CGCM	coupled atmosphere/ocean general circulation model

ENSO	El Niño-Southern Oscillation
EOF	empirical orthogonal function
EWE	easterly wind event
FSU	Florida State University; or the FSU pseudostress analysis
GCM	general circulation model
GFDL	Geophysical Fluid Dynamics Laboratory
HGCM	hybrid coupled general circulation model
ITCZ	Intertropical Convergence Zone
MJO	Madden-Julian Oscillation
MKS	meter-kilogram-second system of units
MOM	Modular Ocean Model
MSD	mean square deviation
NAO	North Atlantic Oscillation
NCAR	The National Center for Atmospheric Research
NCEP	The National Centers for Environmental Prediction; or the NCEP/NCAR reanalysis
OGCM	oceanic general circulation model
OLR	outgoing longwave radiation
PCA	principal components analysis
PDO	Pacific Decadal Oscillation
PP	predictive power
RMS	root mean square
SOI	Southern Oscillation Index (surface air pressure at Tahiti minus that at Darwin, Australia)
SPCZ	South Pacific Convergence Zone
SSE	sum of square errors
SST	sea surface temperature
SSTA	sea surface temperature anomaly

SVD	singular value decomposition
TIW	tropical instability wave
UNESCO	United Nations Educational, Scientific, and Cultural Organization
WWE	westerly wind event

Bibliography

AchutaRao, K. and K. R. Sperber, 2002: Simulation of the El Niño Southern Oscillation: Results from the Coupled Model Intercomparison Project. *Climate Dyn.*, **19**, 191–209. 4, 7, 8, 9, 145

AMS Council, 2001: Statement on seasonal to interannual climate prediction. *Bull. Amer. Meteor. Soc.*, **82**, 701–710. 2

An, S.-I. and F.-F. Jin, 2000: An eigen analysis of the interdecadal changes in the structure and frequency of ENSO mode. *Geophys. Res. Lett.*, **27**, 2573–2576. 13, 177, 180

An, S.-I. and F.-F. Jin, 2001: Collective role of thermocline and zonal advective feedbacks in the ENSO mode. *J. Climate*, **14**, 3421–3432. 149, 177, 178, 186

An, S.-I. and I.-S. Kang, 2000: A further investigation of the recharge oscillator paradigm for ENSO using a simple coupled model with the zonal mean and eddy separated. *J. Climate*, **13**, 1987–1993. 92, 93, 185

An, S.-I. and B. Wang, 2000: Interdecadal change of the structure of the ENSO mode and its impact on the ENSO frequency. *J. Climate*, **13**, 2044–2055. 13, 22, 26, 38, 45, 56, 149

Anderson, D. L. T., E. S. Sarachik, P. J. Webster, and L. M. Rothstein, 1998: The TOGA Decade: Reviewing the progress of El Niño research and prediction. *J. Geophys. Res.*, **103**, 14 167–14 510. 2

Andreasen, D. H., A. C. Ravelo, and A. J. Broccoli, 2001: Remote forcing at the last glacial maximum in the tropical Pacific ocean. *J. Geophys. Res.*, **106**, 879–897. 15

Auad, G., J. Miller, J. O. Roads, and D. Cayan, 2001: Pacific ocean wind stress and surface heat flux anomalies from NCEP reanalysis and observations: Cross-statistics and ocean model responses. *J. Geophys. Res.*, **106**, 22 249–22 265. 24, 99

Balmaseda, M. A., D. L. T. Anderson, and M. K. Davey, 1994: ENSO prediction using a dynamical ocean model coupled to statistical atmospheres. *Tellus*, **46A**, 497–511. 56

Balmaseda, M. A., M. K. Davey, and D. L. T. Anderson, 1995: Decadal and seasonal dependence of ENSO prediction skill. *J. Climate*, **8**, 2705–2715. 132

Barnett, T. P., G. Hegerl, T. Knutson, and S. Tett, 2000: Uncertainty levels in predicted patterns of anthropogenic climate change. *J. Geophys. Res.*, **105**, 15 525–15 542. 16

Barnett, T. P., M. Latif, N. Graham, M. Flügel, S. Pazan, and W. White, 1993: ENSO and ENSO-related predictability. Part I: Prediction of equatorial sea surface temperature with a hybrid coupled ocean-atmosphere model. *J. Climate*, **6**, 1545–1566. 56

Barnett, T. P., M. Latif, E. Kirk, and E. Roeckner, 1991: On ENSO physics. *J. Climate*, **4**, 487–515. 99

Barnett, T. P., D. W. Pierce, M. Latif, D. Dommenget, and R. Saravanan, 1999: Inter-decadal interactions between the tropics and midlatitudes in the Pacific basin. *Geophys. Res. Lett.*, **26**, 615–618. 12, 13

Barnston, A. G., 1995: Our improving capability in ENSO forecasting. *Weather*, **50**, 419. 132

Barnston, A. G., M. H. Glantz, and Y. He, 1999a: Predictive skill of statistical and dynamical climate models in SST forecasts during the 1997–98 El Niño episode and the 1998 La Niña onset. *Bull. Amer. Meteor. Soc.*, **80**, 217–243. 4

Barnston, A. G., A. Leetmaa, V. E. Kousky, R. E. Livezey, E. A. O' Lenic, H. M. van den Dool, A. J. Wagner, and D. A. Unger, 1999b: NCEP forecasts of the El Niño of 1997–98 and its U.S. impacts. *Bull. Amer. Meteor. Soc.*, **80**, 1829–1852. 4

Barnston, A. G., et al., 1994: Long-lead seasonal forecasts—Where do we stand? *Bull. Amer. Meteor. Soc.*, **75**, 2097–2114. 2

Battisti, D. S., 1988: Dynamics and thermodynamics of a warming event in a coupled tropical atmosphere-ocean model. *J. Atmos. Sci.*, **45**, 2889–2919. 86, 92, 93, 132, 144

Battisti, D. S., 1989: On the role of off-equatorial oceanic Rossby waves during ENSO. *J. Phys. Oceanogr.*, **19**, 551–559. 200

Battisti, D. S. and A. C. Hirst, 1989: Interannual variability in a tropical atmosphere-ocean model: Influence of the basic state, ocean geometry and nonlinearity. *J. Atmos. Sci.*, **46**, 1687–1712. 18, 123, 175, 178, 179, 180

Battisti, D. S. and E. S. Sarachik, 1995: Understanding and predicting ENSO. *Rev. Geophys.*, **July 1995 Suppl.**, 1367–1376. 132

Battisti, D. S., E. S. Sarachik, and A. C. Hirst, 1999: A consistent model for the large-scale steady surface atmospheric circulation in the tropics. *J. Climate*, **12**, 2956–2964. 40

Behringer, D. W., M. Ji, and A. Leetmaa, 1998: An improved coupled model for ENSO prediction and implications for ocean initialization. Part I: The ocean data assimilation system. *Mon. Wea. Rev.*, **126**, 1013–1021. 26, 85, 92, 94, 95, 96, 97, 98, 100, 102, 103, 104, 107, 108, 266, 267

Blanke, B., J. D. Neelin, and D. Gutzler, 1997: Estimating the effect of stochastic wind stress forcing on ENSO irregularity. *J. Climate*, **10**, 1473–1486. 56, 129, 253

Boer, G. J., G. Flato, and D. Ramsden, 2000: A transient climate change simulation with greenhouse gas and aerosol forcing: Projected climate to the twenty-first century. *Climate Dyn.*, **16**, 427–450. 16, 17

Bonekamp, H., G. J. van Oldenborgh, and G. Burgers, 2001: Variational assimilation of tropical atmosphere-ocean and expendable bathythermograph data in the Hamburg Ocean Primitive Equation ocean general circulation model, adjusting the surface fluxes in the tropical ocean. *J. Geophys. Res.*, **106**, 16 693–16 709. 23

Bony, S., K.-M. Lau, and Y. C. Sud, 1997: Sea surface temperature and large-scale circulation influences on tropical greenhouse effect and cloud radiative forcing. *J. Climate*, **10**, 2055–2077. 17

Boulanger, J.-P. and C. Menkes, 1999: Long equatorial wave reflection in the Pacific ocean from TOPEX/POSEIDON data during the 1992–1998 period. *Climate Dyn.*, **15**, 205–225. 86, 93

Bretherton, C. S., C. Smith, and J. M. Wallace, 1992: An intercomparison of methods for finding coupled patterns in climate data. *J. Climate*, **5**, 541–560. 58

Busalacchi, A. J., R. M. Atlas, and E. C. Hackert, 1993: Comparison of Special Sensor Microwave Imager vector wind stress with model-derived and subjective products for the tropical Pacific. *J. Geophys. Res.*, **98**, 6961–6977. 24

Busalacchi, A. J. and M. A. Cane, 1988: The effect of varying stratification on low-frequency equatorial motions. *J. Phys. Oceanogr.*, **18**, 801–812. 178

Busalacchi, A. J. and J. J. O'Brien, 1981: Interannual variability of the equatorial Pacific in the 1960's. *J. Geophys. Res.*, **86**, 10 901–10 907. 91

Bush, A. B. G., 1999: Assessing the impact of mid-Holocene insolation on the atmosphere-ocean system. *Geophys. Res. Lett.*, **26**, 99–102. 14

Bush, A. B. G. and S. G. H. Philander, 1998: The role of ocean-atmosphere interactions in tropical cooling during the last glacial maximum. *Science*, **279**, 1341–1344. 15

Cane, M. A., 1984: Modeling sea level during El Niño. *J. Phys. Oceanogr.*, **14**, 1864–1874. 92

Cane, M. A., 1992: Comments on "The fast-wave limit and interannual oscillations". *J. Atmos. Sci.*, **49**, 1947–1949. 187

Cane, M. A., A. C. Clement, A. Kaplan, Y. Kushnir, D. Pozdnyakov, R. Seager, S. E. Zebiak, and R. Murtugudde, 1997: Twentieth century sea surface temperature trends. *Science*, **275**, 957–960. 16, 161, 169

Cane, M. A. and P. Molnar, 2001: Closing of the Indonesian seaway as a precursor to east African aridification around 3–4 million years ago. *Nature*, **411**, 157–162. 15

Cane, M. A. and R. J. Patton, 1984: A numerical model for low-frequency equatorial dynamics. *J. Phys. Oceanogr.*, **14**, 1853–1863. 89

Cane, M. A. and E. S. Sarachik, 1976: Forced baroclinic ocean motions: I. The linear equatorial unbounded case. *J. Mar. Res.*, **34**, 629–665. 139

Cane, M. A. and E. S. Sarachik, 1977: Forced baroclinic ocean motions: II. The linear equatorial bounded case. *J. Mar. Res.*, **35**, 395–432. 86, 139, 163

Cane, M. A. and E. S. Sarachik, 1979: Forced baroclinic ocean motions: III. The linear equatorial basin case. *J. Mar. Res.*, **37**, 355–398. 139

Cane, M. A., S. E. Zebiak, and S. C. Dolan, 1986: Experimental forecasts of El Niño. *Nature*, **321**, 827–832. 3

Cane, M. A., S. E. Zebiak, and Y. Xue, 1995: Model studies of the long-term behavior of ENSO. *Natural Climate Variability on Decade-to-Century Time Scales*, National Academy Press, 442–457. 14

Cardone, V. J., J. G. Greenwood, and M. A. Cane, 1990: On trends in historical marine wind data. *J. Climate*, **3**, 113–127. 22

Casey, K. S. and P. Cornillon, 2001: Global and regional sea surface temperature trends. *J. Climate*, **14**, 3801–3818. 10

Cassou, C. and C. Perigaud, 2000: ENSO simulated with intermediate coupled models and evaluated with observations over 1970–1998. Part II: Role of the off-equatorial ocean and meridional winds. *J. Climate*, **13**, 1635–1663. 22, 38, 40, 56, 91, 253

Cayan, D. R., 1992: Latent and sensible heat flux anomalies over the northern oceans: Driving the sea surface temperature. *J. Phys. Oceanogr.*, **22**, 859–881. 99

Cess, R. D., G. L. Potter, and Coauthors, 1989: Interpretation of cloud-climate feedback as produced by 14 atmospheric general circulation models. *Science*, **245**, 513–516. 17

Cess, R. D., G. L. Potter, and Coauthors, 1990: Intercomparison and interpretation of climate feedback processes in 19 atmospheric general circulation models. *J. Geophys. Res.*, **95**, 16 601–16 615. 17

Chang, P., 1994: A study of the seasonal cycle of sea surface temperature in the tropical Pacific Ocean using reduced gravity models. *J. Geophys. Res.*, **99**, 7725–7741. 91, 188

Chang, P., L. Ji, H. Li, and M. Flügel, 1996: Chaotic dynamics versus stochastic processes in El Niño-Southern Oscillation in coupled ocean-atmosphere models. *Physica D*, **98**, 301–320. 19, 129

Chang, P. and S. G. H. Philander, 1994: A coupled ocean-atmosphere instability of relevance to the seasonal cycle. *J. Atmos. Sci.*, **51**, 3627–3648. 149, 188

Chao, Y., M. Ghil, and J. C. McWilliams, 2000: Pacific interdecadal variability in this century's sea surface temperatures. *Geophys. Res. Lett.*, **27**, 2261–2264. 10, 12

Chelton, D. B., et al., 2001: Observations of coupling between surface wind stress and sea surface temperature in the eastern tropical Pacific. *J. Climate*, **14**, 1479–1498. 269

Chen, D., M. A. Cane, and S. E. Zebiak, 1999: The impact of NSCAT winds on predicting the 1997/1998 El Niño: A case study with the Lamont-Doherty Earth Observatory model. *J. Geophys. Res.*, **104**, 11 321–11 327. 24, 85

Chen, D., S. E. Zebiak, A. J. Busalacchi, and M. A. Cane, 1995: An improved procedure for El Niño forecasting: Implications for predictability. *Science*, **269**, 1699–1702. 25, 132

Chen, J., B. E. Carlson, and A. D. Del Genio, 2002: Evidence for strengthening of the tropical general circulation in the 1990s. *Science*, **295**, 838–841. 12

Cherry, S., 1996: Singular value decomposition analysis and canonical correlation analysis. *J. Climate*, **9**, 2003–2009. 58

Cherry, S., 1997: Some comments on singular value decomposition analysis. *J. Climate*, **10**, 1759–1761. 58

Clarke, A. J., 1991: On the reflection and transmission of low-frequency energy at the irregular Western Pacific Ocean boundary. *J. Geophys. Res.*, **96**, 3289–3305. 86, 93

Clarke, A. J. and A. Lebedev, 1996: Long-term changes in the equatorial Pacific trade winds. *J. Climate*, **9**, 1020–1029. 10, 23

Clarke, A. J. and A. Lebedev, 1997: Interannual and decadal changes in equatorial wind stress in the Atlantic, Indian, and Pacific oceans and the eastern ocean coastal response. *J. Climate*, **10**, 1722–1729. 10, 22, 23

Clement, A. C., M. A. Cane, and R. Seager, 2001: An orbitally driven tropical source for abrupt climate change. *J. Climate*, **14**, 2369–2375. 15

Clement, A. C., R. Seager, and M. A. Cane, 1999: Orbital controls on the El Niño/Southern Oscillation and the tropical climate. *Paleoceanogr.*, **14**, 441–456. 15

Clement, A. C., R. Seager, M. A. Cane, and S. E. Zebiak, 1996: An ocean dynamical thermostat. *J. Climate*, **9**, 2190–2196. 16, 17, 161, 169

Codron, F., 2001: Sensitivity of the tropical Pacific to a change of orbital forcing in two versions of a coupled GCM. *Climate Dyn.*, **17**, 187–203. 14

Codron, F., A. Vintzileos, and R. Sadourny, 2001: Influence of mean state changes on the structure of ENSO in a tropical coupled GCM. *J. Climate*, **14**, 730–742. 18, 181

Cole, J., 2001: A slow dance for El Niño. *Science*, **291**, 1496–1497. 14, 15

Colinvaux, P., 1972: Climate and the Galápagos Islands. *Nature*, **240**, 17–20. 14

Collins, M., 2000a: The El Niño-Southern Oscillation in the Second Hadley Centre Coupled Model and its response to greenhouse warming. *J. Climate*, **13**, 1299–1312. 17

Collins, M., 2000b: Understanding uncertainties in the response of ENSO to greenhouse warming. *Geophys. Res. Lett.*, **27**, 3509–3512. 17

Curtis, S. and S. Hastenrath, 1999: Long-term trends and forcing mechanisms of circulation and climate in the equatorial Pacific. *J. Climate*, **12**, 1134–1144. 10

da Silva, A. M., C. C. Young, and S. Levitus, 1994: Atlas of Surface Marine Data 1994, Vol. 1: Algorithms and Procedures. NOAA Atlas NESDIS 6, U.S. Department of Commerce, 83 pp., Washington, D.C. 22, 23, 26

D'Agostino, R. B. and M. A. Stephens, (Eds.) , 1986: *Goodness-of-fit techniques*. Dekker, New York, 560pp. 49

Dai, A., T. M. L. Wigley, B. A. Boville, J. T. Kiehl, and L. E. Buja, 2001: Climates of the twentieth and twenty-first centuries simulated by the NCAR Climate System Model. *J. Climate*, **14**, 485–519. 16, 145

D'Arrigo, R., R. Villalba, and G. Wiles, 2001: Tree-ring estimates of Pacific decadal climate variability. *Climate Dyn.*, **18**, 219–224. 12

Davey, M. K., M. Huddleston, K. R. Sperber, and model data contributors, 2000: STOIC: A study of coupled GCM climatology and variability in tropical ocean regions. STOIC project report, CLIVAR-WGSIP, 41 pp. 6

Davey, M. K., M. Huddleston, K. R. Sperber, and model data contributors, 2002: STOIC: A study of coupled model climatology and variability in tropical ocean regions. *Climate Dyn.*, **18**, 403–420. 4, 6, 8

Delcroix, T., 1998: Observed surface oceanic and atmospheric variability in the tropical Pacific at seasonal and ENSO timescales: A tentative overview. *J. Geophys. Res.*, **103**, 18 611–18 633. 188

Delecluse, P., M. K. Davey, Y. Kitamura, S. G. H. Philander, M. Suarez, and L. Bengtsson, 1998: Coupled general circulation modeling of the tropical Pacific. *J. Geophys. Res.*, **103**, 14 357–14 373. 3, 145, 188

DeVries, T. J., L. Ortlieb, A. Diaz, L. Wells, and C. Hillaire-Marcel, 1997: Determining the early history of El Niño. *Science*, **276**, 965–966. 14

DeWitt, D. G. and E. K. Schneider, 1998: The tropical ocean response to a change in orbital forcing. Technical Report 56, COLA. 14

Dewitte, B., 2000: Sensitivity of an intermediate ocean-atmosphere coupled model of the tropical Pacific to its oceanic vertical structure. *J. Climate*, **13**, 2363–2388. 178

Dewitte, B. and C. Perigaud, 1996: El Niño-La Niña events simulated with Cane and Zebiak's model and observed with satellite or in situ data. Part II: Model forced with observations. *J. Climate*, **9**, 1188–1207. 25, 91

Diaz, H. F. and R. S. Pulwarty, 1994: An analysis of the time scales of variability in centuries-long ENSO-sensitive records in the last 1000 years. *Climatic Change*, **26**, 317–342. 14

Dijkstra, H. A. and J. D. Neelin, 1995: Ocean-atmosphere interaction and the tropical climatology. Part II: Why the Pacific cold tongue is in the east. *J. Climate*, **8**, 1343–1359. 28, 138, 145, 150, 153, 161, 179

Dijkstra, H. A. and J. D. Neelin, 1999: Coupled processes and the tropical climatology. Part III: Instabilities of the fully coupled climatology. *J. Climate*, **12**, 1630–1643. 18, 175, 179

du Penhoat, Y. and M. A. Cane, 1991: Effect of low-latitude western boundary gaps on the reflection of equatorial motions. *J. Geophys. Res.*, **96**, 3307–3322. 93

Dunbar, R. B., G. M. Wellington, M. W. Colgan, and P. W. Glynn, 1994: Eastern Pacific sea surface temperature since 1600 A.D.: The δ^{18}O record of climate variability in Galápagos corals. *Paleoceanogr.*, **9**, 291–315. 12, 14

Dutton, J. F., C. J. Poulsen, and J. L. Evans, 2000: The effect of global climate change on the regions of tropical convection in CSM1. *Geophys. Res. Lett.*, **27**, 3049–3052. 17

Easterling, D. R., G. A. Meehl, C. Parmesan, S. A. Chagnon, T. R. Karl, and L. O. Mearns, 2000: Climate extremes: Observations, modeling, and impacts. *Science*, **289**, 2068–2074. 17

Eckert, C. and M. Latif, 1997: Predictability of a stochastically forced hybrid coupled model of El Niño. *J. Climate*, **10**, 1488–1504. 56, 131

Enfield, D. B., 2001: Evolution and historical perspective of the 1997–1998 El Niño-Southern Oscillation event. *Bull. Marine Sci.*, **63**, 7–25. 5

Enfield, D. B. and L. Cid, 1991: Low-frequency changes in El Niño-Southern Oscillation. *J. Climate*, **4**, 1137–1146. 13

Enfield, D. B. and A. M. Mestas-Nuñez, 1999: Interannual-to-multidecadal climate variability and its relationship to global sea surface temperatures. *Inter-Hemispheric Climate Linkages*, V. Markgraf, Ed., Academic Press, 17–29. 12, 14

Esbensen, S. and V. Kushnir, 1981: The heat budget of the global ocean — an atlas based on estimates from surface marine observations. Technical Report 29, Clim. Res. Inst., Oregon State Univ., Corvallis, OR. 263

Farrell, J., T. Pedersen, S. Calvert, and B. Nielsen, 1995: Glacial-interglacial changes in the equatorial Pacific ocean. *Nature*, **377**, 514–517. 14

Fedorov, A. V., 2002: The response of the coupled tropical ocean-atmosphere to westerly wind bursts. *Quart. J. Roy. Meteor. Soc.*, **128**, 1–23. 18, 181

Fedorov, A. V. and S. G. Philander, 2000: Is El Niño changing? *Science*, **288**, 1997–2002. 18, 149, 181

Fedorov, A. V. and S. G. Philander, 2001: A stability analysis of tropical ocean-atmosphere interactions: Bridging measurements and theory for El Niño. *J. Climate*, **14**, 3086–3101. 18, 181

Flügel, M. and P. Chang, 1996: Impact of dynamical and stochastic processes on the predictability of ENSO. *Geophys. Res. Lett.*, **23**, 2089–2092. 129

Flügel, M. and P. Chang, 1998: Does the predictability of ENSO depend on the seasonal cycle? *J. Atmos. Sci.*, **55**, 3230–3243. 132

Fu, R., A. D. Del Genio, W. B. Rossow, and W. T. Liu, 1992: Cirrus-cloud thermostat for tropical sea surface temperatures tested using satellite data. *Nature*, **358**, 394–397. 16

Gagan, M. K., L. K. Ayliffe, D. Hopley, J. A. Cali, G. E. Mortimer, J. Chappell, M. T. McCulloch, and M. J. Head, 1998: Temperature and surface-ocean water balance of the mid-Holocene tropical western Pacific. *Science*, **279**, 1014–1017. 14

Galanti, E. and E. Tziperman, 2000: ENSO's phase locking to the seasonal cycle in the fast-SST, fast-wave, and mixed mode regimes. *J. Atmos. Sci.*, **57**, 2936–2950. 28

Gibson, J., P. Kållberg, S. Uppala, A. Nomura, A. Hernandez, and E. Serrano, 1997: ECMWF Reanalysis Project Report Series. Technical Report 1, ECMWF, Shinfield Park, Reading, United Kingdom. 265

Giese, B. S. and J. A. Carton, 1999: Interannual and decadal variability in the tropical and midlatitude Pacific ocean. *J. Climate*, **12**, 3402–3418. 12

Giese, B. S., S. C. Urizar, and N. S. Fuckar, 2002: Southern hemisphere origins of the 1976 climate shift. *Geophys. Res. Lett.*, **29**, doi:10.1029/2001GL013268. 12

Gill, A. E., 1980: Some simple solutions for heat-induced tropical circulation. *Quart. J. Roy. Meteor. Soc.*, **106**, 447–462. 23

Gill, A. E., 1982: *Atmosphere-Ocean Dynamics*. Academic Press, San Diego, 662pp. 139

Goddard, L., S. J. Mason, S. E. Zebiak, C. F. Ropelewski, R. Basher, and M. A. Cane, 2001: Current approaches to seasonal to interannual climate predictions. *Int. J. Climatol.*, **21**, 1111–1152. 2

Goddard, L. and S. G. Philander, 2000: The energetics of El Niño and La Niña. *J. Climate*, **13**, 1496–1516. 116

Gordon, C. T., A. Rosati, and R. Gudgel, 2000: Tropical sensitivity of a coupled model to specified ISCCP low clouds. *J. Climate*, **13**, 2239–2260. 181

Goswami, B. N. and J. Shukla, 1991: Predictability of a coupled ocean-atmosphere model. *J. Climate*, **4**, 3–22. 131, 132

Goswami, B. N. and M. A. Thomas, 2000: Coupled ocean-atmosphere inter-decadal modes in the tropics. *J. Meteor. Soc. Japan*, **78**, 765–775. 12

Graham, N. E., 1994: Decadal-scale climate variability in the tropical and North Pacific during the 1970s and 1980s: Observations and model results. *Climate Dyn.*, **10**, 135–162. 12, 24, 34, 45

Grodsky, S. A. and J. A. Carton, 2001: Intense surface currents in the tropical Pacific during 1996–1998. *J. Geophys. Res.*, **106**, 16 673–16 684. 93

Gu, D. and S. G. H. Philander, 1995: Secular changes of annual and interannual variability in the tropics during the past century. *J. Climate*, **8**, 864–876. 3, 13, 45

Gu, D. and S. G. H. Philander, 1997: Interdecadal climate fluctuations that depend on exchanges between the tropics and extratropics. *Science*, **275**, 805–807. 12, 16, 150

Gudgel, R. G., A. Rosati, and C. T. Gordon, 2001: The sensitivity of a coupled atmospheric-oceanic GCM to prescribed low-level clouds over the ocean and tropical landmasses. *Mon. Wea. Rev.*, **129**, 2103–2115. 138

Gutzler, D. S., 1993: Modes of large-scale ocean-atmosphere interaction in the tropical Pacific. *Proc. 17th Annual NOAA Climate Diagnostics Workshop*, Norman, OK, Natl. Ocean. Atmos. Admin., 77–80, nTIS PB93–183895. 61

Hao, Z., J. D. Neelin, and F.-F. Jin, 1993: Nonlinear tropical air-sea interaction in the fast-wave limit. *J. Climate*, **6**, 1523–1544. 18, 149, 175, 177, 181

Harrison, D. E., W. S. Kessler, and B. S. Giese, 1989: Ocean circulation model hindcasts of the 1982–83 El Niño: Thermal variability along the ship-of-opportunity tracks. *J. Phys. Oceanogr.*, **19**, 397–418. 22, 24

Harrison, D. E. and N. K. Larkin, 1997: Darwin sea level pressure, 1876–1996: evidence for climate change? *Geophys. Res. Lett.*, **24**, 1779–1782. 10, 14

Harrison, D. E. and N. K. Larkin, 1998: ENSO sea surface temperature and wind anomalies, 1946–1993. *Rev. Geophys.*, **36**, 353–399. 3, 26, 66

Harrison, M. J., A. Rosati, B. J. Soden, E. Galanti, and E. Tziperman, 2002: An evaluation of air-sea flux products for ENSO simulation and prediction. *Mon. Wea. Rev.*, **130**, 723–732. 24, 56, 263, 265

Hartmann, D. L., 2002: Tropical surprises. *Science*, **295**, 811–812. 12

Hartmann, D. L. and M. L. Michelson, 1993: Large-scale effects on the regulation of tropical sea surface temperature. *J. Climate*, **6**, 2049–2062. 16

Hayashi, Y., 1986: Statistical interpretations of ensemble-time mean predictability. *J. Meteor. Soc. Japan*, **64**, 167–181. 132

Hazeleger, W., M. Visbeck, M. Cane, A. Karspeck, and N. Naik, 2001: Decadal upper ocean temperature variability in the tropical Pacific. *J. Geophys. Res.*, **106**, 8971–8988. 13

Hellerman, S. and M. Rosenstein, 1983: Normal monthly wind stress over the world ocean with error estimates. *J. Phys. Oceanogr.*, **13**, 1093–1104. 24, 263

Hirst, A. C., 1985: Free equatorial instabilities in simple coupled atmosphere-ocean models. *Coupled Ocean-Atmosphere Models*, J. C. J. Nihoul, Ed., Elsevier, Amsterdam, 153–165. 177

Hirst, A. C., 1986: Unstable and damped equatorial modes in simple coupled ocean-atmosphere models. *J. Atmos. Sci.*, **43**, 606–630. 18, 175, 177

Hirst, A. C., 1988: Slow instabilities in tropical ocean basin-global atmosphere models. *J. Atmos. Sci.*, **45**, 830–852. 177, 179

Houtekamer, P. L., 1995: The construction of optimal perturbations. *Mon. Wea. Rev.*, **123**, 2181–2196. 81

Hu, Z.-Z., L. Bengtsson, E. Roeckner, M. Christoph, A. Bacher, and J. M. Oberhuber, 2001: Impact of global warming on the interannual and interdecadal climate modes in a coupled GCM. *Climate Dyn.*, **17**, 361–374. 17

Huang, B. and Z. Liu, 2001: Temperature trend of the last 40 yr in the upper Pacific ocean. *J. Climate*, **14**, 3738–3750. 10, 17

Huang, R. X. and J. Pedlosky, 2000: Climate variability of the equatorial thermocline inferred from a two-moving-layer model of the ventilated thermocline. *J. Phys. Oceanogr.*, **30**, 2610–2626. 12

Hughen, K. A., D. P. Schrag, S. B. Jacobsen, and W. Hantoro, 1999: El Niño during the last interglacial period recorded by a fossil coral from Indonesia. *Geophys. Res. Lett.*, **26**, 3129–3132. 15

Ji, M., D. W. Behringer, and A. Leetmaa, 1998: An improved coupled model for ENSO prediction and implications for ocean initialization. Part II: The coupled model. *Mon. Wea. Rev.*, **126**, 1022–1034. 26

Jin, F.-F., 1996: Tropical ocean-atmosphere interaction, the Pacific cold tongue, and the El Niño-Southern Oscillation. *Science*, **274**, 76–78. 18, 175, 179, 180

Jin, F.-F., 1997: An equatorial ocean recharge paradigm for ENSO. Part I: Conceptual model. *J. Atmos. Sci.*, **54**, 811–829. 144, 175, 178, 185

Jin, F.-F., 2000: Low frequency modes of tropical ocean dynamics. *J. Climate*, **14**, 3874–3881. 12

Jin, F.-F., Z.-Z. Hu, M. Latif, L. Bengtsson, and E. Roeckner, 2001: Dynamical and cloud-radiation feedbacks in El Niño and greenhouse warming. *Geophys. Res. Lett.*, **28**, 1539–1542. 16, 17

Jin, F.-F. and J. D. Neelin, 1993a: Modes of interannual tropical ocean-atmosphere interaction–a unified view. Part I: Numerical results. *J. Atmos. Sci.*, **50**, 3477–3503. 18, 149, 175, 177, 179, 181

Jin, F.-F. and J. D. Neelin, 1993b: Modes of interannual tropical ocean-atmosphere interaction–a unified view. Part III: Analytical results in fully coupled cases. *J. Atmos. Sci.*, **50**, 3523–3540. 18, 175, 181

Jin, F.-F., J. D. Neelin, and M. Ghil, 1994: El Niño on the devil's staircase: Annual subharmonic steps to chaos. *Science*, **264**, 70–72. 129

Johnson, G. C. and M. J. McPhaden, 1999: Interior pycnocline flow from the subtropical to the equatorial Pacific ocean. *J. Phys. Oceanogr.*, **29**, 3073–3089. 12

Johnson, G. C., M. J. McPhaden, and E. Firing, 2001: Equatorial Pacific ocean horizontal velocity, divergence, and upwelling. *J. Phys. Oceanogr.*, **31**, 839–849. 97

Jones, P. D., T. J. Osborn, and K. R. Briffa, 2001: The evolution of climate over the last millennium. *Science*, **292**, 662–667. 14

Kachi, M. and T. Nitta, 1997: Decadal variations of the global atmosphere-ocean system. *J. Meteor. Soc. Japan*, **75**, 657–675. 12

Kalnay, E., M. Kanamitsu, R. Kistler, and Coauthors, 1996: The NCEP/NCAR 40-year reanalysis project. *Bull. Amer. Meteor. Soc.*, **77**, 437–471. 25, 101

Kang, I.-S. and S.-I. An, 1998: Kelvin and Rossby wave contributions to the SST oscillation of ENSO. *J. Climate*, **11**, 2461–2469. 86, 93

Kang, I.-S., S.-I. An, and F.-F. Jin, 2001: A systematic approximation of the SST anomaly equation for ENSO. *J. Meteor. Soc. Japan*, **79**, 1–10. 113

Kang, I.-S. and J.-S. Kug, 2000: An El Niño prediction system using an intermediate ocean and a statistical atmosphere. *Geophys. Res. Lett.*, **27**, 1167–1170. 56

Kang, I.-S. and J.-S. Kug, 2002: El Niño and La Niña sea surface temperature anomalies: Asymmetry characteristics associated with their wind stress anomalies. *J. Geophys. Res.*, **107**, doi:10.1029/2001JD000393. 38

Kaplan, A., M. A. Cane, Y. Kushnir, A. C. Clement, M. B. Blumenthal, and B. Rajagopalan, 1998: Analyses of global sea surface temperature 1856–1991. *J. Geophys. Res.*, **103**, 18 567–18 589. 11, 161

Kelly, K. A., S. Dickinson, M. J. McPhaden, and G. C. Johnson, 2001: Ocean currents evident in satellite wind data. *Geophys. Res. Lett.*, **28**, 2469–2472. 22

Kelly, K. A., S. Dickinson, and Z. Yu, 1999: NSCAT tropical wind stress maps: Implications for improving ocean modeling. *J. Geophys. Res.*, **104**, 11 291–11 310. 24

Kerr, R. A., 1993: El Niño metamorphosis throws forecasters. *Science*, **262**, 656–657. 4, 13

Kerr, R. A., 1999a: Big El Niños ride the back of slower climate change. *Science*, **283**, 1108–1109. 12

Kerr, R. A., 1999b: El Niño grew strong as cultures were born. *Science*, **283**, 467–468. 14

Kerr, R. A., 2000a: Globe's "missing warming" found in the ocean. *Science*, **287**, 2126–2127. 10

Kerr, R. A., 2000b: Second thoughts on skill of El Niño predictions. *Science*, **290**, 257–258. 4

Kestin, T. S., D. J. Karoly, J.-I. Yano, and N. A. Rayner, 1998: Time-frequency variability of ENSO and stochastic simulations. *J. Climate*, **11**, 2258–2272. 13, 14

Kirtman, B. P., 1997: Oceanic Rossby wave dynamics and the ENSO period in a coupled model. *J. Climate*, **10**, 1690–1704. 22, 38, 56

Kirtman, B. P. and E. K. Schneider, 1996: Model-based estimates of equatorial Pacific wind stress. *J. Climate*, **9**, 1077–1091. 23

Kirtman, B. P. and P. S. Schopf, 1998: Decadal variability in ENSO predictability and prediction. *J. Climate*, **11**, 2804–2822. 4, 14, 18, 22

Kleeman, R., 1991: A simple model of the atmospheric response to ENSO sea surface temperature anomalies. *J. Atmos. Sci.*, **48**, 3–18. 40

Kleeman, R., 1993: On the dependence of hindcast skill on ocean thermodynamics in a coupled ocean-atmosphere model. *J. Climate*, **6**, 2012–2033. 92

Kleeman, R., R. A. Colman, N. R. Smith, and S. B. Power, 1996: A recent change in the mean state of the Pacific basin climate: Observational evidence and atmospheric and oceanic responses. *J. Geophys. Res.*, **101**, 20 483–20 499. 12, 13

Kleeman, R., J. P. McCreary, and B. A. Klinger, 1999: A mechanism for generating ENSO decadal variability. *Geophys. Res. Lett.*, **26**, 1743–1746. 12, 14, 26

Kleeman, R. and A. M. Moore, 1997: A theory for the limitation of ENSO predictability due to stochastic atmospheric transients. *J. Atmos. Sci.*, **54**, 753–767. 22

Kleeman, R., G. Wang, and S. Jewson, 2001: Surface flux response to interannual tropical Pacific sea surface temperature variability in AMIP models. *Climate Dyn.*, **17**, 627–641. 8, 24, 25, 56

Knaff, J. A. and C. W. Landsea, 1997: An El Niño-Southern Oscillation climatology and persistence (CLIPER) forecasting scheme. *Wea. Forecasting*, **12**, 633–652. 4

Knutson, T. R. and S. Manabe, 1995: Time-mean response over the tropical Pacific to increased CO_2 in a coupled ocean-atmosphere model. *J. Climate*, **8**, 2181–2199. 16

Knutson, T. R. and S. Manabe, 1998: Model assessment of decadal variability and trends in the tropical Pacific ocean. *J. Climate*, **11**, 2273–2296. 12, 16

Knutson, T. R., S. Manabe, and D. Gu, 1997: Simulated ENSO in a global coupled ocean-atmosphere model: Multidecadal amplitude modulation and CO_2 sensitivity. *J. Climate*, **10**, 138–161. 17

Kug, J.-S., I.-S. Kang, and S. E. Zebiak, 2001: The impacts of the model assimilated wind stress data in the initialization of an intermediate ocean and the ENSO predictability. *Geophys. Res. Lett.*, **28**, 3713–3716. 24

Lagerloef, G. S. E., G. T. Mitchum, R. B. Lukas, and P. P. Niiler, 1999: Tropical Pacific near-surface currents estimated from altimeter, wind, and drifter data. *J. Geophys. Res.*, **104**, 23 313–23 326. 93

Landsea, C. W. and J. A. Knaff, 2000: How much skill was there in forecasting the very strong 1997–98 El Niño? *Bull. Amer. Meteor. Soc.*, **81**, 2107–2119. 4, 5, 56, 82, 131

Landsteiner, M. C., M. J. McPhaden, and J. Picaut, 1990: On the sensitivity of Sverdrup transport estimates to the specification of wind stress forcing in the tropical Pacific. *J. Geophys. Res.*, **95**, 1681–1691. 22, 24

Latif, M., 1987: Tropical ocean circulation experiments. *J. Phys. Oceanogr.*, **17**, 246–263. 22, 24

Latif, M., 1998: Dynamics of interdecadal variability in coupled ocean-atmosphere models. *J. Climate*, **11**, 602–624. 12

Latif, M. and M. Flügel, 1991: An investigation of short-range climate predictability of the El Niño/Southern Oscillation in the tropical Pacific. *J. Geophys. Res.*, **96**, 2661–2673. 131, 132

Latif, M., R. Kleeman, and C. Eckert, 1997: Greenhouse warming, decadal variability, or El Niño? An attempt to understand the anomalous 1990s. *J. Climate*, **10**, 2221–2239. 13, 14, 45

Latif, M., K. Sperber, and CMIP participants, 2001: ENSIP: The El Niño Simulation Intercomparison Project. *Climate Dyn.*, **18**, 255–276. 4, 8, 9, 56

Latif, M., et al., 1998: A review of the predictability and prediction of ENSO. *J. Geophys. Res.*, **103**, 14 375–14 393. 3, 4

Lau, K. M., C.-H. Sui, M.-D. Chou, and W. K. Tao, 1994: An inquiry into the cirrus-cloud thermostat effect for tropical sea surface temperature. *Geophys. Res. Lett.*, **21**, 1157–1160. 16

Lau, K.-M. and H. Weng, 1995: Climate signal detection using wavelet transform: How to make a time series sing. *Bull. Amer. Meteor. Soc.*, **76**, 2391–2402. 45

Lau, K.-M. and H. Weng, 1999: Interannual, decadal-interdecadal, and global warming signals in sea surface temperature during 1955–97. *J. Climate*, **12**, 1257–1267. 12

Lea, D. W., D. K. Pak, and H. J. Spero, 2000: Climate impact of late quaternary equatorial Pacific sea surface temperature variations. *Science*, **2000**, 1719–1724. 15

Legler, D. M. and J. J. O'Brien, 1988: Tropical Pacific wind stress analysis for TOGA, IOC Time series of ocean measurements. IOC Technical Series 33, UNESCO. 25

Levitus, S., J. I. Antonov, T. P. Boyer, and C. Stephens, 2000: Warming of the world ocean. *Science*, **287**, 2225–2229. 10

Levitus, S. and T. P. Boyer, 1994: World Ocean Atlas 1994 Volume 4: Temperature. NOAA Atlas NESDIS 4, U.S. Department of Commerce, Washington, D.C. 263

Li, T., 1997: Phase transition of the El Niño-Southern Oscillation: A stationary SST mode. *J. Atmos. Sci.*, **54**, 2872–2887. 175

Li, T. and T. F. Hogan, 1999: The role of the annual-mean climate on seasonal and interannual variability of the tropical Pacific in a coupled GCM. *J. Climate*, **12**, 780–792. 149, 181, 188

Li, T. and S. G. H. Philander, 1996: On the annual cycle of the eastern equatorial Pacific. *J. Climate*, **9**, 2986–2998. 149

Lindzen, R. S. and S. Nigam, 1987: On the role of sea surface temperature gradients in forcing low-level winds and convergence in the tropics. *J. Atmos. Sci.*, **44**, 2418–2436. 23, 29

Linsley, B. K., G. M. Wellington, and D. P. Schrag, 2000: Decadal sea surface temperature variability in the subtropical south Pacific from 1726 to 1997 A.D. *Science*, **290**, 1145–1148. 12

Liu, W. T. and C. Gautier, 1990: Thermal forcing on the tropical Pacific from satellite data. *J. Geophys. Res.*, **95**, 13 209–13 217. 99

Liu, Z., 1998: The role of ocean in the response of tropical climatology to global warming: The west-east SST contrast. *J. Climate*, **11**, 864–875. 16

Liu, Z. and B. Huang, 1997: A coupled theory of tropical climatology: warm pool, cold tongue, and Walker Circulation. *J. Climate*, **10**, 1662–1679. 16

Liu, Z. and B. Huang, 2000: Cause of tropical Pacific warming trend. *Geophys. Res. Lett.*, **27**, 1935–1938. 10

Liu, Z., J. Kutzbach, and L. Wu, 2000a: Modeling climate shift of El Niño variability in the Holocene. *Geophys. Res. Lett.*, **27**, 2265–2268. 14, 15

Liu, Z., S. Shin, P. Behling, W. Prell, M. Trend-Staid, S. P. Harrison, and J. Kutzbach, 2000b: Dynamical and observational constraints on tropical Pacific sea surface temperatures at the last glacial maximum. *Geophys. Res. Lett.*, **27**, 105–108. 15

Liu, Z. and R.-H. Zhang, 1999: Propagation and mechanism of decadal upper-ocean variability in the north Pacific. *Geophys. Res. Lett.*, **26**, 739–742. 12

Lorenz, E. N., 1963: Deterministic nonperiodic flow. *J. Atmos. Sci.*, **20**, 130–141. 2

Lorenz, E. N., 1975: Climatic predictability. *The Physical Basis of Climate and Climate Modelling*, World Meteorological Organization, Geneva, Switzerland, No. 16 in Global Atmospheric Research Programme Publication Series, 132–136, report of the International Study Conference in Stockholm, 29 July – 10 August 1974. 2

Manabe, S. and R. J. Stouffer, 1988: Two stable equilibria of a coupled ocean-atmosphere model. *J. Climate*, **1**, 841–866. 173

Mann, M. E., R. S. Bradley, and M. K. Hughes, 2000: Long-term variability in the El Niño Southern Oscillation and associated teleconnections. *El Niño and the Southern Oscillation: Multiscale variability and its impacts on natural ecosystems and society*, H. F. Diaz and V. Markgraf, Eds., Cambridge University Press, Cambridge, United Kingdom, 357–412. 14

Mann, M. E. and J. Park, 1994: Global-scale modes of surface temperature variability on interannual to century timescales. *J. Geophys. Res.*, **99**, 25 819–25 833. 12, 13

Mantua, N. J. and D. S. Battisti, 1994: Evidence for the delayed oscillator mechanism for ENSO: The "observed" oceanic Kelvin mode in the western Pacific. *J. Phys. Oceanogr.*, **24**, 691–699. 86, 93

Mantua, N. J. and D. S. Battisti, 1995: Aperiodic variability in the Zebiak-Cane coupled ocean-atmosphere model: Air-sea interactions in the western equatorial Pacific. *J. Climate*, **8**, 2897–2927. 91, 92, 177

Masina, S. and S. G. H. Philander, 1999a: An analysis of tropical instability waves in a numerical model of the Pacific ocean. 1. Spatial variability of the waves. *J. Geophys. Res.*, **104**, 29 613–29 635. 269

Masina, S. and S. G. H. Philander, 1999b: An analysis of tropical instability waves in a numerical model of the Pacific ocean. 2. Generation and energetics of the waves. *J. Geophys. Res.*, **104**, 29 637–29 661. 269

McCreary, J. P. and D. L. T. Anderson, 1991: An overview of coupled ocean-atmosphere models of El Niño and the Southern Oscillation. *J. Geophys. Res.*, **Feb. 1996 Suppl.**, 3125–3150. 19

McPhaden, M. J., A. J. Busalacchi, and J. Picaut, 1988: Observations and wind-forced model simulations of the mean seasonal cycle in tropical Pacific sea surface topography. *J. Geophys. Res.*, **93**, 8131–8146. 22, 24, 29

McPhaden, M. J. and D. Zhang, 2002: Slowdown of the meridional overturning circulation in the upper Pacific ocean. *Nature*, **415**, 603–608. 10, 13

McPhaden, M. J., et al., 1998: The Tropical Ocean-Global Atmosphere observing system: A decade of progress. *J. Geophys. Res.*, **103**, 14 169–14 240. 3, 22, 40, 56, 91, 269

Mechoso, C. R., A. W. Robertson, and Coauthors, 1995: The seasonal cycle over the tropical Pacific in coupled ocean-atmosphere general circulation models. *Mon. Wea. Rev.*, **123**, 2825–2838. 8

Meehl, G. A., G. J. Boer, C. Covey, M. Latif, and R. J. Stouffer, 2000a: The Coupled Model Intercomparison Project (CMIP). *Bull. Amer. Meteor. Soc.*, **81**, 313–318. 16

Meehl, G. A., G. W. Branstator, and W. M. Washington, 1993: Tropical Pacific interannual variability and CO_2 climate change. *J. Climate*, **6**, 42–63. 17

Meehl, G. A., W. D. Collins, B. Boville, J. T. Kiehl, T. M. L. Wigley, and J. M. Arblaster, 2000b: Response of the NCAR Climate System model to increased CO_2 and the role of physical processes. *J. Climate*, **13**, 1879–1898. 16

Meehl, G. A., P. R. Gent, J. M. Arblaster, B. L. Otto-Bliesner, E. C. Brady, and A. Craig, 2001a: Factors that affect the amplitude of El Niño in global coupled climate models. *Climate Dyn.*, **17**, 515–526. 8

Meehl, G. A., R. Lukas, G. N. Kiladis, K. M. Weickmann, A. J. Matthews, and M. Wheeler, 2001b: A conceptual framework for time and space scale interactions in the climate system. *Climate Dyn.*, **17**, 753–775. 48

Meehl, G. A. and W. M. Washington, 1996: El Niño-like climate change in a model with increased atmospheric CO_2 concentrations. *Nature*, **382**, 56–60. 16

Mehta, V., E. Lindstrom, and Coauthors, 2000: Proceedings of the NASA Workshop on Decadal Climate Variability. *Bull. Amer. Meteor. Soc.*, **81**, 2983–2985. 10, 13

Meinen, C. S., M. J. McPhaden, and G. C. Johnson, 2001: Vertical velocities and transports in the equatorial Pacific during 1993–99. *J. Phys. Oceanogr.*, **31**, 3230–3248. 97

Meissner, T., D. Smith, and F. Wentz, 2001: A 10 year intercomparison between collocated Special Sensor Microwave Imager oceanic surface wind speed retrievals and global analyses. *J. Geophys. Res.*, **106**, 11 731–11 742. 24

Mestas-Nuñez, A. M. and D. B. Enfield, 2001: Eastern equatorial Pacific SST variability: ENSO and non-ENSO components and their climatic associations. *J. Climate*, **14**, 391–402. 12

Michaud, R. and C. A. Lin, 1992: Monthly summaries of merchant ship surface marine observations and implications for climate variability studies. *Climate Dyn.*, **7**, 45–55. 22

Moore, A. M., 1995: Tropical interannual variability in a global coupled GCM: sensitivity to mean climate state. *J. Climate*, **8**, 807–828. 18, 181, 187

Moore, A. M. and R. Kleeman, 1996: The dynamics of error growth and predictability in a coupled model of ENSO. *Quart. J. Roy. Meteor. Soc.*, **122**, 1405–1446. 81, 131

Moore, A. M. and R. Kleeman, 1997a: The singular vectors of a coupled ocean-atmosphere model of ENSO. Part I: Thermodynamics, energetics and error growth. *Quart. J. Roy. Meteor. Soc.*, **123**, 953–981. 81, 131

Moore, A. M. and R. Kleeman, 1997b: The singular vectors of a coupled ocean-atmosphere model of ENSO. Part II: Sensitivity studies and dynamical interpretation. *Quart. J. Roy. Meteor. Soc.*, **123**, 983–1006. 81, 131

Moore, A. M. and R. Kleeman, 1998: Skill assessment for ENSO using ensemble prediction. *Quart. J. Roy. Meteor. Soc.*, **124**, 557–584. 81, 131

Moore, A. M. and R. Kleeman, 2001: The differences between the optimal perturbations of coupled models of ENSO. *J. Climate*, **14**, 138–163. 81, 131

Moron, V., R. Vautard, and M. Ghil, 1998: Trends, interdecadal and interannual oscillations in global sea-surface temperatures. *Climate Dyn.*, **14**, 545–569. 12

Morrissey, M. L., 1990: An evaluation of ship data in the equatorial western Pacific. *J. Climate*, **3**, 99–112. 22

Murphy, J. M., 1988: The impact of ensemble forecasts on predictability. *Quart. J. Roy. Meteor. Soc.*, **114**, 463–493. 132

National Research Council, (Ed.) , 1995: *Natural climate variability on decade-to-century time scales.* National Academy Press, Washington, D.C., 630pp. 10

Navarra, A., (Ed.) , 1999: *Beyond El Niño: Decadal and interdecadal climate variability.* Springer-Verlag, Berlin, Germany, 374pp. 10

Neelin, J. D., 1990: A hybrid coupled general circulation model for El Niño studies. *J. Atmos. Sci.*, **47**, 674–693. 22, 38, 56

Neelin, J. D., 1991: The slow sea surface temperature mode and the fast-wave limit: Analytic theory for tropical interannual oscillations and experiments in a hybrid coupled model. *J. Atmos. Sci.*, **48**, 584–606. 18, 175, 177, 181, 187, 202

Neelin, J. D., D. S. Battisti, A. C. Hirst, F.-F. Jin, Y. Wakata, T. Yamagata, and S. Zebiak, 1998: ENSO theory. *J. Geophys. Res.*, **103**, 14 261–14 290. 18, 19, 23, 84, 91, 129, 139, 149, 175

Neelin, J. D. and H. A. Dijkstra, 1995: Ocean-atmosphere interaction and the tropical climatology. Part I: The dangers of flux correction. *J. Climate*, **8**, 1325–1342. 153, 260, 261

Neelin, J. D. and F.-F. Jin, 1993: Modes of interannual tropical ocean-atmosphere interaction–a unified view. Part II: Analytical results in the weak-coupling limit. *J. Atmos. Sci.*, **50**, 3504–3522. 18, 181

Neelin, J. D., et al., 1992: Tropical air-sea interaction in general circulation models. *Climate Dyn.*, **7**, 73–104. 8, 187

Newman, M. and P. D. Sardeshmukh, 1995: A caveat concerning singular value decomposition. *J. Climate*, **8**, 352–361. 58, 60

Nitta, T. and S. Yamada, 1989: Recent warming of tropical sea surface temperature and its relationship to the Northern Hemisphere circulation. *J. Meteor. Soc. Japan*, **67**, 375–383. 45

Noda, A., K. Yamaguchi, S. Yamaki, and S. Yukimoto, 1999: Relationship between natural variability and CO_2-induced warming pattern: MRI AOGCM experiment. *10th Symposium on Global Change Studies*, American Meteorological Society, Boston, Massachusetts, 359–362. 16

Nurnberg, D., 2000: Taking the temperature of past ocean surfaces. *Science*, **289**, 1698–1699. 15

Otto-Bliesner, B. L., 1999: El Niño/La Niña and Sahel precipitation during the middle Holocene. *Geophys. Res. Lett.*, **26**, 87–90. 14, 15

Pacanowski, R. C. and S. G. H. Philander, 1981: Parameterization of vertical mixing in numerical models of tropical oceans. *J. Geophys. Res.*, **86**, 1903–1916. 263

Penland, C., 1996: A stochastic model of IndoPacific sea surface temperature anomalies. *Physica D*, **98**, 534–558. 132

Penland, C. and P. D. Sardeshmukh, 1995: The optimal growth of tropical sea surface temperature anomalies. *J. Climate*, **8**, 1999–2024. 22, 81, 129, 132, 197

Perigaud, C. and B. Dewitte, 1996: El Niño – La Niña events simulated with Cane and Zebiak's model and observed with satellite or in situ data. Part I: Model data comparison. *J. Climate*, **9**, 66–84. 91, 92

Perigaud, C., F. Melin, and C. Cassou, 2000a: ENSO simulated by intermediate coupled models and evaluated with observations over 1970–1998. Part I: Role of the off-equatorial variability. *J. Climate*, **13**, 1605–1634. 91

Perigaud, C., S. E. Zebiak, F. Melin, J.-P. Boulanger, and B. Dewitte, 1997: On the role of meridional wind anomalies in a coupled model of ENSO. *J. Climate*, **10**, 761–773. 91

Perigaud, C. M., C. Cassou, B. Dewitte, L.-L. Fu, and J. D. Neelin, 2000b: Using data and intermediate coupled models for seasonal-to-interannual forecasts. *Mon. Wea. Rev.*, **128**, 3025–3049. 181

Peterson, E. Q. and L. Hasse, 1987: Did the Beaufort scale or the wind climate change? *J. Phys. Oceanogr.*, **17**, 1071–1074. 22

Philander, S. G., 1990: *El Niño, La Niña, and the Southern Oscillation*. Academic Press, San Diego, 293pp. 92, 139, 140

Philander, S. G. H., 1999: A review of tropical ocean-atmosphere interactions. *Tellus*, **51A**, 71–90. 139, 175

Philander, S. G. H., D. Gu, D. Halpern, G. Lambert, N.-C. Lau, T. Li, and R. C. Pacanowski, 1996: Why the ITCZ is mostly north of the equator. *J. Climate*, **9**, 2958–2972. 28, 163

Picaut, J. and T. Delcroix, 1995: Equatorial wave sequence associated with warm pool displacements during the 1986–1989 El Niño-La Niña. *J. Geophys. Res.*, **100**, 18 393–18 408. 116

Picaut, J., F. Masia, and Y. du Penhoat, 1997: An advective-reflective conceptual model for the oscillatory nature of the ENSO. *Science*, **277**, 663–666. 116

Picaut, J., C. Menkes, J.-P. Boulanger, and Y. du Penhoat, 1993: Dissipation in a Pacific equatorial long wave model. *TOGA Notes*, **10**, 11–15. 92

Pierce, D. W., T. P. Barnett, and M. Latif, 2000a: Connections between the Pacific ocean tropics and midlatitudes on decadal timescales. *J. Climate*, **13**, 1173–1194. 13

Pierce, D. W., T. P. Barnett, N. Schneider, R. Saravanan, D. Dommenget, and M. Latif, 2000b: The role of ocean dynamics in producing decadal climate variability in the North Pacific. *Climate Dyn.*, **18**, 51–70. 13

Pierrehumbert, R. T., 1995: Thermostats, radiator fins, and the local runaway greenhouse. *J. Atmos. Sci.*, **52**, 1784–1806. 16

Polito, P. S., J. P. Ryan, W. T. Liu, and F. P. Chavez, 2001: Oceanic and atmospheric anomalies of tropical instability waves. *Geophys. Res. Lett.*, **28**, 2233–2236. 269

Pontaud, M., J.-P. Cerón, M. Kimoto, F. Pluviaud, L. Terray, and A. Vintzileos, 2000: CoPIVEP: A theory-based analysis of coupled processes and interannual variability in the equatorial Pacific in four coupled GCMs. *Climate Dyn.*, **16**, 917–933. 8

Posmentier, E. S., M. A. Cane, and S. E. Zebiak, 1989: Tropical Pacific climate trends since 1960. *J. Climate*, **2**, 731–736. 10, 22

Putman, W. M., D. M. Legler, and J. J. O'Brien, 2000: Interannual variability of synthesized FSU and NCEP-NCAR reanalysis pseudostress products over the Pacific ocean. *J. Climate*, **13**, 3003–3016. 25

Quinn, W. H., V. T. Neal, and S. E. Antunez de Mayolo, 1987: El Niño occurrences over the past four and a half centuries. *J. Geophys. Res.*, **92**, 14 449–14 461. 13

Rajagopalan, B., U. Lall, and M. A. Cane, 1997: Anomalous ENSO occurrences: An alternate view. *J. Climate*, **10**, 2351–2357. 14

Ramage, C. S., 1987: Secular change in reported surface wind speeds over the ocean. *J. Climate Appl. Meteor.*, **26**, 525–528. 22

Ramanathan, V. and W. D. Collins, 1991: Thermodynamic regulation of ocean warming by cirrus clouds deduced from observations of the 1987 El Niño. *Nature*, **351**, 27–32. 16

Rasmusson, E. M. and T. H. Carpenter, 1982: Variations in tropical sea surface temperature and surface wind fields associated with the Southern Oscillation / El Niño. *Mon. Wea. Rev.*, **110**, 354–384. 3

Rasmusson, E. M., X. Wang, and C. F. Ropelewski, 1995: Secular variability of the ENSO cycle. *Natural Climate Variability on Decade-to-Century Time Scales*, National Academy Press, 458–471. 13

Ravelo, A. C. and N. J. Shackleton, 1995: Evidence for surface water circulation changes at site 851 in the eastern tropical pacific ocean. *Proceedings of the Ocean Drilling Program*, N. G. Pisias, L. A. Mayer, T. R. Janecek, A. Palmer-Julson, and T. H. van Andel, Eds., 503–516. 14

Reynolds, R. W., K. Arpe, C. Gordon, S. P. Hayes, A. Leetmaa, and M. J. McPhaden, 1989: A comparison of tropical Pacific surface wind analyses. *J. Climate*, **2**, 105–111. 24

Reynolds, R. W. and T. M. Smith, 1994: Improved global sea surface temperature analyses. *J. Climate*, **7**, 929–948. 11, 37, 265

Rind, D., 1987: The doubled CO_2 climate: Impact of the sea surface temperature gradient. *J. Atmos. Sci.*, **44**, 3235–3268. 17, 145

Rodbell, D. T., G. O. Seltzer, D. M. Anderson, M. B. Abbott, D. B. Enfield, and J. H. Newman, 1999: An ∼15,000-year record of an El Niño-driven alluviation in southwestern Ecuador. *Science*, **283**, 516–520. 14

Roulston, M. S. and J. D. Neelin, 2000: The response of an ENSO model to climate noise, weather noise and intraseasonal forcing. *Geophys. Res. Lett.*, **27**, 3723–3726. 22

Royston, J. P., 1982: Algorithm AS181: The W Test for Normality. *Appl. Statist.*, **31**, 176–180. 72

Saji, N. H. and B. N. Goswami, 1997: Intercomparison of the seasonal cycle of tropical surface stress in 17 AMIP atmospheric general circulation models. *Climate Dyn.*, **13**, 561–585. 24, 25, 56

Samelson, R. M. and E. Tziperman, 2001: Instability of the chaotic ENSO: the growth-phase predictability barrier. *J. Atmos. Sci.*, **58**, 3613–3625. 136

Sandweiss, D. H., J. B. Richardson III, E. J. Reitz, H. B. Rollins, and K. A. Maasch, 1996: Geoarchaeological evidence from Peru for a 5000 years B.P. onset of El Niño. *Science*, **273**, 1531–1533. 14

Sandweiss, D. H., J. B. Richardson III, E. J. Reitz, H. B. Rollins, and K. A. Maasch, 1997: Determining the early history of El Niño. *Science*, **276**, 966–967. 14

Santer, B. D., J. J. Hnilo, T. M. L. Wigley, J. S. Boyle, C. Doutriaux, M. Fiorino, D. E. Parker, and K. E. Taylor, 1999: Uncertainties in "observational" estimates of temperature change in the free atmosphere. *J. Geophys. Res.*, **104**, 6305–6333. 45

Schneider, E. K., 2002: Understanding differences between the equatorial Pacific as simulated by two coupled GCMs. *J. Climate*, **15**, 449–469. 8

Schneider, E. K., B. Huang, and J. Shukla, 1995: Ocean wave dynamics and El Niño. *J. Climate*, **8**, 2415–2439. 175

Schneider, N., A. J. Miller, M. A. Alexander, and C. Deser, 1999a: Subduction of decadal north Pacific temperature anomalies: Observations and dynamics. *J. Phys. Oceanogr.*, **29**, 1056–1070. 12

Schneider, N., S. Venzke, A. J. Miller, D. W. Pierce, T. P. Barnett, C. Deser, and M. Latif, 1999b: Pacific thermocline bridge revisited. *Geophys. Res. Lett.*, **26**, 1329–1332. 13

Schneider, T. and S. M. Griffies, 1999: A conceptual framework for predictability studies. *J. Climate*, **12**, 3133–3155. 132

Schopf, P. S. and M. J. Suarez, 1988: Vacillations in a coupled ocean-atmosphere model. *J. Atmos. Sci.*, **45**, 549–566. 175

Seager, R., 1989: Modeling tropical Pacific sea surface temperature: 1970–87. *J. Phys. Oceanogr.*, **19**, 419–434. 99

Seager, R. and R. Murtugudde, 1997: Ocean dynamics, thermocline adjustment, and regulation of tropical SST. *J. Climate*, **10**, 521–534. 16

Seager, R., S. E. Zebiak, and M. A. Cane, 1988: A model of the tropical Pacific sea surface temperature climatology. *J. Geophys. Res.*, **93**, 1265–1280. 91

Setoh, T., S. Imawaki, A. Ostrovskii, and S.-I. Umatani, 1999: Interdecadal variations of ENSO signals and annual cycles revealed by wavelet analysis. *J. Oceanogr.*, **55**, 385–394. 13

Shinoda, T., H. H. Hendon, and J. Glick, 1999: Intraseasonal surface fluxes in the tropical western Pacific and Indian oceans from NCEP Reanalyses. *Mon. Wea. Rev.*, **127**, 678–693. 24

Silverman, B. W., 1986: *Density Estimation for Statistics and Data Analysis*. Chapman and Hall, 175pp. 49

Smagorinsky, J., 1963: General circulation experiments with the primitive equations. Part I: The basic experiment. *Mon. Wea. Rev.*, **91**, 99–164. 263

Smith, S. D., 1988: Coefficients for sea surface wind stress, heat flux, and wind profiles as a function of wind speed and temperature. *J. Geophys. Res.*, **93**, 15 467–15 472. 22

Smith, S. R., D. M. Legler, and K. V. Verzone, 2001: Quantifying uncertainties in NCEP reanalyses using high-quality research vessel observations. *J. Climate*, **14**, 4062–4072. 24, 25

Smith, T. M., R. W. Reynolds, R. E. Livezey, and D. C. Stokes, 1996: Reconstruction of historical sea surface temperatures using empirical orthogonal functions. *J. Climate*, **9**, 1403–1420. 26, 37

Stahle, D. W., et al., 1998: Experimental dendroclimatic reconstruction of the Southern Oscillation. *Bull. Amer. Meteor. Soc.*, **79**, 2137–2152. 14

Stephens, C., S. Levitus, J. Antonov, and T. P. Boyer, 2001: On the Pacific ocean regime shift. *Geophys. Res. Lett.*, **28**, 3721–3724. 12

Sterl, A., 2001: On the impact of gap-filling algorithms on variability patterns of reconstructed oceanic surface fields. *Geophys. Res. Lett.*, **28**, 2473–2476. 22

Stern, W. and K. Miyakoda, 1995: Feasibility of seasonal forecasts inferred from multiple GCM simulations. *J. Climate*, **8**, 1071–1085. 132

Stewart, G., 1973: *Introduction to Matrix Computations*. Academic Press, 441pp. 59

Stockdale, T. N., A. J. Busalacchi, D. E. Harrison, and R. Seager, 1998: Ocean modeling for ENSO. *J. Geophys. Res.*, **103**, 14 325–14 355. 269

Strang, G., 1988: *Linear algebra and its applications*. Harcourt, Brace, and Jovanovitch, 505pp. 59

Stricherz, J. N., D. M. Legler, and J. J. O'Brien, 1997: TOGA pseudostress atlas 1985–1994. II: Tropical Pacific Ocean. COAPS Tech. Rep. 97-2, COAPS/The Florida State University, 155 pp., Tallahassee, FL. 25, 263

Suarez, M. J. and P. S. Schopf, 1988: A delayed action oscillator for ENSO. *J. Atmos. Sci.*, **45**, 3283–3287. 144, 175

Sun, D.-Z. and Z. Liu, 1996: Dynamic ocean-atmosphere coupling: A thermostat for the tropics. *Science*, **272**, 1148–1150. 16

Syu, H.-H. and J. D. Neelin, 1995: Seasonal and interannual variability in a hybrid coupled GCM. *J. Climate*, **8**, 2121–2143. 56, 61, 73, 82, 253

Takayabu, Y. N., T. Iguchi, M. Kachi, A. Shibata, , and H. Kanzawa, 1999: Abrupt termination of the 1997–98 El Niño in response to a Madden-Julian oscillation. *Nature*, **402**, 297–282. 179

Talley, L. D., 1995: Some advances in understanding of the general circulation of the Pacific Ocean, with emphasis on recent U.S. contributions. *Rev. Geophys.*, **July 1995 Suppl.**, 1335–1352. 12

Taylor, P. K., 2001: Intercomparison and validation of ocean-atmosphere energy flux fields. Joint WCRP/SCOR Working Group on Air-Sea Fluxes Final Report. WMO/TD 1036, WCRP-112, 306 pp., Geneva, Switzerland. 25

Tett, S. F. B., 1995: Simulation of El Niño/Southern Oscillation like variability in a global AOGCM and its response to CO_2 increase. *J. Climate*, **8**, 1473–1502. 16, 17

Thompson, C. J. and D. S. Battisti, 2000: A linear stochastic dynamical model of ENSO. Part I: Model development. *J. Climate*, **13**, 2818–2832. 86, 92, 93, 129

Thompson, C. J. and D. S. Battisti, 2001: A linear stochastic dynamical model of ENSO. Part II: Analysis. *J. Climate*, **14**, 445–466. 19, 129

Timmermann, A., 1999: Detecting the nonstationary response of ENSO to greenhouse warming. *J. Atmos. Sci.*, **56**, 2313–2325. 14, 17

Timmermann, A., 2001: Changes of ENSO stability due to greenhouse warming. *Geophys. Res. Lett.*, **28**, 2061–2064. 17

Timmermann, A. and F.-F. Jin, 2002: A nonlinear mechanism for decadal El Niño amplitude changes. *Geophys. Res. Lett.*, **29**, doi:10.1029/2001GL013369. 14

Timmermann, A., J. Oberhuber, A. Bacher, M. Esch, M. Latif, and E. Roeckner, 1999: Increased El Niño frequency in a climate model forced by future greenhouse warming. *Nature*, **398**, 694–697. 16, 17

Tomita, T., B. Wang, T. Yasunari, and H. Nakamura, 2001: Global patterns of decadal-scale variability observed in sea surface temperature and lower-tropospheric circulation fields. *J. Geophys. Res.*, **106**, 26 805–26 815. 12

Torrence, C. and G. P. Compo, 1999: A practical guide to wavelet analysis. *Bull. Amer. Meteor. Soc.*, **79**, 61–78. 3, 13, 45

Torrence, C. and P. J. Webster, 1998: The annual cycle of persistence in the El Niño/Southern Oscillation. *Quart. J. Roy. Meteor. Soc.*, **124**, 1985–2004. 3, 13, 45

Torrence, C. and P. J. Webster, 1999: Interdecadal changes in the ENSO-monsoon system. *J. Climate*, **12**, 2679–2690. 3, 45

Tourre, Y. M., B. Rajagopalan, Y. Kushnir, M. Barlow, and W. B. White, 2001: Patterns of coherent decadal and interdecadal climate signals in the Pacific basin during the 20th century. *Geophys. Res. Lett.*, **28**, 2069–2072. 12

Trenberth, K. E. and T. J. Hoar, 1996: The 1990–1995 El Niño-Southern Oscillation event: Longest on record. *Geophys. Res. Lett.*, **23**, 57–60. 14

Trenberth, K. E. and T. J. Hoar, 1997: El Niño and climate change. *Geophys. Res. Lett.*, **24**, 3057–3060. 14

Trenberth, K. E. and J. W. Hurrell, 1994: Decadal atmosphere-ocean variations in the Pacific. *Climate Dyn.*, **9**, 303–319. 12, 13, 45

Trenberth, K. E. and J. W. Hurrell, 1999: Comments on "The interpretation of short climate records, with comments on the North Atlantic and Southern Oscillations". *Bull. Amer. Meteor. Soc.*, **80**, 2721–2722. 14

Trenberth, K. E., W. G. Large, and J. G. Olson, 1990: The mean annual cycle in global ocean wind stress. *J. Phys. Oceanogr.*, **20**, 1742–1760. 24

Trenberth, K. E. and D. P. Stepaniak, 2001: Indices of El Niño evolution. *J. Climate*, **14**, 1697–1701. 13, 66

Tudhope, A. W., et al., 2001: Variability in the El Niño-Southern Oscillation through a glacial-interglacial cycle. *Science*, **291**, 1511–1517. 2, 14, 15

Tziperman, E., M. A. Cane, and S. E. Zebiak, 1995: Irregularity and locking to the seasonal cycle in an ENSO prediction model as explained by the quasi-periodicity route to chaos. *J. Atmos. Sci.*, **52**, 293–306. 129

Tziperman, E., M. A. Cane, and S. E. Zebiak, 1997: Mechanisms of seasonal–ENSO interaction. *J. Atmos. Sci.*, **54**, 61–71. 28

Urban, F. E., J. E. Cole, and J. T. Overpeck, 2000: Influence of mean climate change on climate variability from a 155-year tropical Pacific coral record. *Nature*, **407**, 989–993. 10

van den Dool, H. M., 1994: Searching for analogues, how long must we wait? *Tellus*, **46A**, 314–324. 82

van Oldenborgh, G. J., 2000: What caused the onset of the 1997–1998 El Niño? *Mon. Wea. Rev.*, **128**, 2601–2607. 131

Vimont, D. J., D. S. Battisti, and A. C. Hirst, 2002: Pacific interannual and interdecadal equatorial variability in a 1000-yr simulation of the CSIRO coupled general circulation model. *J. Climate*, **15**, 160–178. 12

Wakata, Y. and E. S. Sarachik, 1991: Unstable coupled atmosphere-ocean basin modes in the presence of a spatially varying basic state. *J. Atmos. Sci.*, **48**, 2060–2077. 18, 179

Wakata, Y. and E. S. Sarachik, 1992: Effects of the meridional extent of mean equatorial upwelling on atmosphere-ocean coupled instabilities over an unbounded ocean. *J. Meteor. Soc. Japan*, **70**, 843–854. 18, 179

Wallace, J. M., E. M. Rasmusson, T. P. Mitchell, V. E. Kousky, E. S. Sarachik, and H. von Storch, 1998: On the structure and evolution of ENSO-related climate variability in the tropical Pacific: Lessons from TOGA. *J. Geophys. Res.*, **103**, 14 241–14 259. 10

Wang, B., 1995: Interdecadal changes in El Niño onset in the last four decades. *J. Climate*, **8**, 267–285. 13, 66, 91

Wang, B. and S.-I. An, 2001: Why the properties of El Niño changed during the late 1970s. *Geophys. Res. Lett.*, **28**, 3709–3712. 13, 180

Wang, B. and S.-I. An, 2002: A mechanism for decadal changes of ENSO behavior: Roles of background wind changes. *Climate Dyn.*, **18**, 475–486. 13, 18, 45, 180

Wang, B. and Z. Fang, 1996: Chaotic oscillations of tropical climate: A dynamic system theory for ENSO. *J. Atmos. Sci.*, **53**, 2786–2802. 180

Wang, B. and Z. Fang, 2000: Impacts of shortwave radiation forcing on ENSO: A study with a coupled tropical ocean-atmosphere model. *Climate Dyn.*, **16**, 677–691. 180

Wang, B. and T. Li, 1993: A simple tropical atmosphere model of relevance to short-term climate variations. *J. Atmos. Sci.*, **50**, 260–284. 29, 40

Wang, B. and Y. Wang, 1996: Temporal structure of the Southern Oscillation as revealed by waveform and wavelet analysis. *J. Climate*, **9**, 1586–1598. 3, 13, 45

Wang, B. and Y. Wang, 1999: Dynamics of the ITCZ-equatorial cold tongue complex and causes of the latitudinal climate asymmetry. *J. Climate*, **12**, 1830–1847. 149, 163

Wang, B. and X. Xie, 1996: Low-frequency equatorial waves in vertically sheared zonal flow. Part I: Stable waves. *J. Atmos. Sci.*, **53**, 449–467. 178

Wang, C., 2000a: On the atmospheric responses to tropical Pacific heating during the mature phase of ENSO. *J. Atmos. Sci.*, **57**, 3767–3781. 28

Wang, C., 2001a: A unified oscillator model for the El Niño-Southern Oscillation. *J. Climate*, **14**, 98–115. 19

Wang, C., 2001b: On the ENSO mechanisms. *Adv. Atmos. Sci.*, **18**, 674–691. 19

Wang, W., 2000b: The surface-layer heat balance in the equatorial Pacific ocean. Part II: Interannual variability. *J. Phys. Oceanogr.*, **30**, 2989–3008. 93

Wang, W. and M. J. McPhaden, 2001: Surface layer temperature balance in the equatorial Pacific during the 1997–98 El Niño and 1998–99 La Niña. *J. Climate*, **14**, 3393–3407. 93

Ward, N. M., 1992: Provisionally corrected surface wind data, worldwide ocean-atmosphere surface fields, and Sahelian rainfall variability. *J. Climate*, **5**, 454–475. 22, 23

Ward, N. M. and B. J. Hoskins, 1996: Near-surface wind over the global ocean 1949–1988. *J. Climate*, **9**, 1877–1895. 23

Washington, W. M., et al., 2000: Parallel climate model (PCM) control and transient simulations. *Climate Dyn.*, **16**, 755–774. 16

Weaver, A. J., 1999: Extratropical subduction and decadal modulation of El Niño. *Geophys. Res. Lett.*, **26**, 743–746. 12, 13

Weisberg, R. H. and L. Qiao, 2000: Equatorial upwelling in the central Pacific estimated from moored velocity profilers. *J. Phys. Oceanogr.*, **30**, 105–124. 97

Wells, L. E. and J. S. Noller, 1997: Determining the early history of El Niño. *Science*, **276**, 966. 14

White, W. B. and D. R. Cayan, 1998: Quasi-periodicity and global symmetries in interdecadal upper ocean temperature variability. *J. Geophys. Res.*, **103**, 21 335–21 354. 12

Wielicki, B. A., et al., 2002: Evidence for large decadal variability in the tropical mean radiative energy budget. *Science*, **295**, 841–844. 12

Wilks, D. S., 1995: *Statistical methods in the atmospheric sciences.* Academic Press, San Diego, 467pp. 256

Wright, D. G. and K. R. Thompson, 1983: Time-averaged forms of the nonlinear stress law. *J. Phys. Oceanogr.*, **13**, 341–345. 22

Wright, P. B., 1988: On the reality of climatic changes in wind over the Pacific. *J. Climatol.*, **8**, 521–527. 10, 22

Wu, L., Z. Liu, and H. E. Hurlburt, 2000: Kelvin wave and Rossby wave interaction in the extratropical-tropical Pacific. *Geophys. Res. Lett.*, **27**, 1259–1262. 13

Wunsch, C., 1999: The interpretation of short climate records, with comments on the North Atlantic and Southern Oscillations. *Bull. Amer. Meteor. Soc.*, **80**, 245–255. 14

Wyrtki, K., 1985: Water displacements in the Pacific and the genesis of El Niño cycles. *J. Geophys. Res.*, **90**, 7129–7132. 175

Xie, S.-P., 1994: On the genesis of the equatorial annual cycle. *J. Climate*, **7**, 2008–2013. 188

Yamagata, T. and S. G. H. Philander, 1985: The role of damped equatorial waves in the oceanic response to winds. *J. Oceanogr. Soc. Japan*, **41**, 345–357. 92, 139, 163

Yang, F., A. Kumar, and W. Wang, 2001: Seasonal dependence of surface wind stress variability on SST and precipitation over the tropical Pacific. *Geophys. Res. Lett.*, **28**, 3171–3174. 24, 38

Yang, J., 1991: A coupled atmosphere-ocean model in the tropics with various climatological backgrounds. Ph.D. thesis, Florida State University, 140pp. 178

Yang, J. and J. O'Brien, 1993: A coupled atmosphere-ocean model in the tropics with different thermocline profiles. *J. Climate*, **6**, 1027–1040. 18, 178

Yang, J. and L. Yu, 1992: Propagation of equatorially trapped waves on a sloping thermocline. *J. Phys. Oceanogr.*, **22**, 573–582. 178

Yang, Y. J., T. Y. Tang, and R. H. Weisberg, 1997: Basin-wide zonal wind stress and ocean thermal variations in the equatorial Pacific ocean. *J. Geophys. Res.*, **102**, 911–927. 24

Yu, B. and G. J. Boer, 2002: The roles of radiation and dynamical processes in the El Niño-like response to global warming. *Climate Dyn.*, **19**, 539–553. 16, 17

Yu, Z. and D. W. Moore, 2000: Validating the NSCAT winds in the vicinity of the Pacific Intertropical Convergence Zone. *Geophys. Res. Lett.*, **27**, 2121–2124. 24

Yukimoto, S., M. Endoh, and A. Noda, 2000: ENSO-like interdecadal variability in the Pacific ocean as simulated in a coupled general circulation model. *J. Geophys. Res.*, **105**, 13 945–13 963. 12

Zebiak, S. E., 1985: Tropical atmosphere-ocean interaction and the El Niño / Southern Oscillation phenomenon. Ph.D. thesis, Massachusetts Institute of Technology, 261pp. 90, 175

Zebiak, S. E., 1986: Atmospheric convergence feedback in a simple model for El Niño. *Mon. Wea. Rev.*, **114**, 1263–1271. 82

Zebiak, S. E., 1990: Diagnostic studies of Pacific surface winds. *J. Climate*, **3**, 1016–1031. 23

Zebiak, S. E. and M. A. Cane, 1987: A model El Niño-Southern Oscillation. *Mon. Wea. Rev.*, **115**, 2262–2278. 28, 87, 90, 92, 93, 95, 97, 132, 136, 138, 177, 178, 180

Zhang, C., 2001: Intraseasonal perturbations in sea surface temperatures of the equatorial eastern Pacific and their association with the Madden-Julian Oscillation. *J. Climate*, **14**, 1309–1322. 269

Zhang, C., H. H. Hendon, W. S. Kessler, and A. J. Rosati, 2001a: A workshop on the MJO and ENSO. *Bull. Amer. Meteor. Soc.*, **82**, 971–976. 76

Zhang, R.-H., 1998: Decadal variability of temperature at a depth of 400 meters in the north Pacific ocean. *Geophys. Res. Lett.*, **25**, 1197–1200. 12

Zhang, R.-H., T. Kagimoto, and S. E. Zebiak, 2001b: Subduction of decadal north Pacific thermal anomalies in an ocean GCM. *Geophys. Res. Lett.*, **28**, 2449–2452. 12

Zhang, R.-H. and Z. Liu, 1999: Decadal thermocline variability in the north Pacific ocean: Two pathways around the subtropical gyre. *J. Climate*, **12**, 3273–3296. 12

Zhang, R.-H., L. M. Rothstein, and A. J. Busalacchi, 1998: Origin of upper-ocean warming and El Niño change on decadal scales in the tropical Pacific ocean. *Nature*, **391**, 879–882. 12

Zhang, R.-H., L. M. Rothstein, and A. J. Busalacchi, 1999: Interannual and decadal variability of the subsurface thermal structure in the Pacific ocean: 1961–90. *Climate Dyn.*, **15**, 703–717. 12

Zhang, Y., J. M. Wallace, and D. S. Battisti, 1997: ENSO-like interdecadal variability: 1900–93. *J. Climate*, **10**, 1004–1020. 12